INTRAVITAL MICROSCOPY IMAGING OF LEUKOCYTES

EDITED BY: Elzbieta Kolaczkowska, Craig N. Jenne and Connie Wong
PUBLISHED IN: Frontiers in Immunology

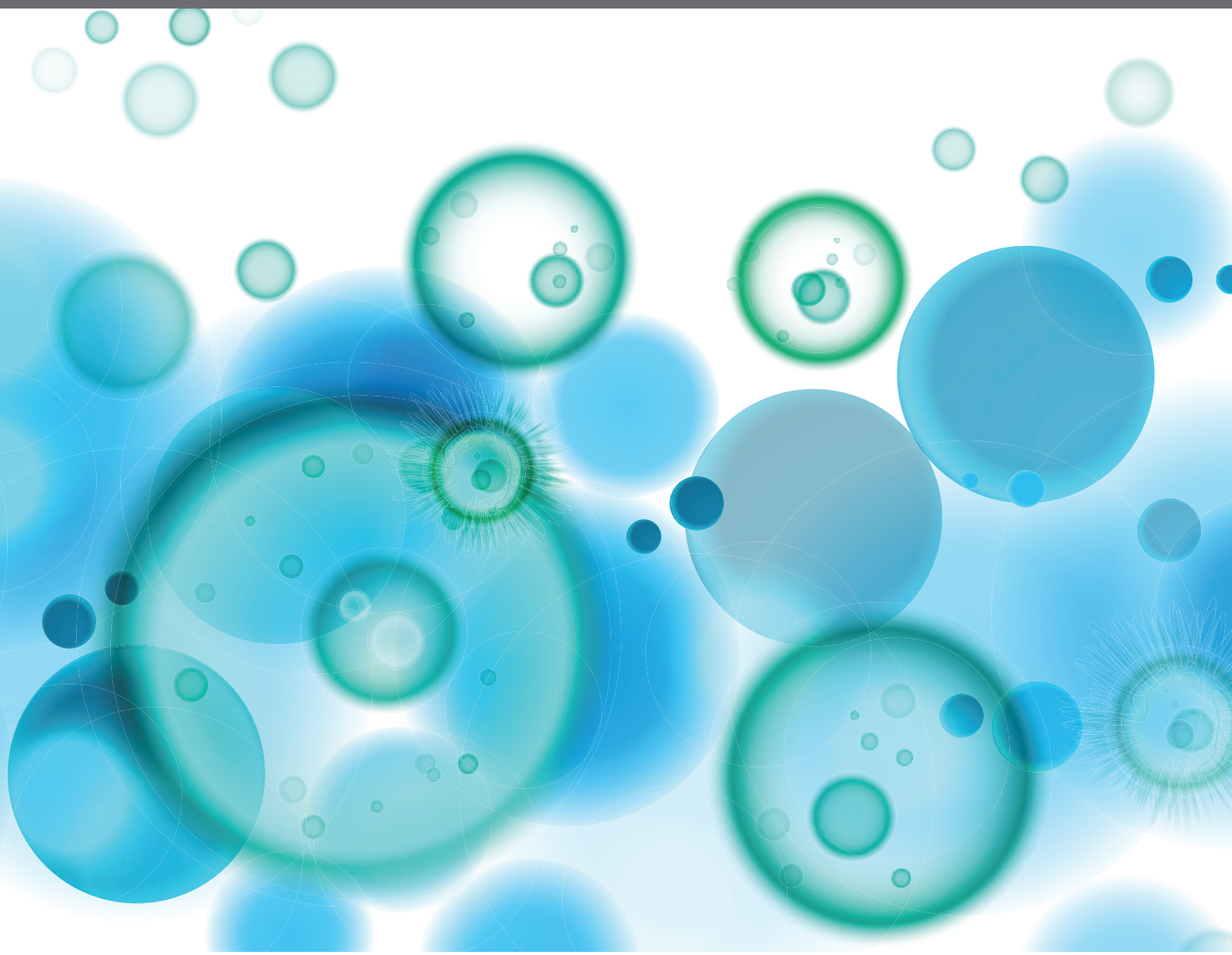

frontiers Research Topics

frontiers

ISSN 1664-8714
ISBN 978-2-88966-138-1
DOI 10.3389/978-2-88966-138-1

About Frontiers

Frontiers is more than just an open-access publisher of scholarly articles: it is a pioneering approach to the world of academia, radically improving the way scholarly research is managed. The grand vision of Frontiers is a world where all people have an equal opportunity to seek, share and generate knowledge. Frontiers provides immediate and permanent online open access to all its publications, but this alone is not enough to realize our grand goals.

Frontiers Journal Series

The Frontiers Journal Series is a multi-tier and interdisciplinary set of open-access, online journals, promising a paradigm shift from the current review, selection and dissemination processes in academic publishing. All Frontiers journals are driven by researchers for researchers; therefore, they constitute a service to the scholarly community. At the same time, the Frontiers Journal Series operates on a revolutionary invention, the tiered publishing system, initially addressing specific communities of scholars, and gradually climbing up to broader public understanding, thus serving the interests of the lay society, too.

Dedication to Quality

Each Frontiers article is a landmark of the highest quality, thanks to genuinely collaborative interactions between authors and review editors, who include some of the world's best academicians. Research must be certified by peers before entering a stream of knowledge that may eventually reach the public - and shape society; therefore, Frontiers only applies the most rigorous and unbiased reviews.
Frontiers revolutionizes research publishing by freely delivering the most outstanding research, evaluated with no bias from both the academic and social point of view. By applying the most advanced information technologies, Frontiers is catapulting scholarly publishing into a new generation.

What are Frontiers Research Topics?

Frontiers Research Topics are very popular trademarks of the Frontiers Journals Series: they are collections of at least ten articles, all centered on a particular subject. With their unique mix of varied contributions from Original Research to Review Articles, Frontiers Research Topics unify the most influential researchers, the latest key findings and historical advances in a hot research area! Find out more on how to host your own Frontiers Research Topic or contribute to one as an author by contacting the Frontiers Editorial Office: researchtopics@frontiersin.org

INTRAVITAL MICROSCOPY IMAGING OF LEUKOCYTES

Topic Editors:
Elzbieta Kolaczkowska, Jagiellonian University, Poland
Craig N. Jenne, University of Calgary, Canada
Connie Wong, Monash University, Australia

Citation: Kolaczkowska, E., Jenne, C. N., Wong, C. eds. (2020). Intravital Microscopy Imaging of Leukocytes. Lausanne: Frontiers Media SA.
doi: 10.3389/978-2-88966-138-1

Table of Contents

frontiers in Immunology

EDITORIAL
published: 10 September 2020
doi: 10.3389/fimmu.2020.02137

Editorial: Intravital Microscopy Imaging of Leukocytes

Connie H. Y. Wong[1], *Craig N. Jenne*[2] *and Elzbieta Kolaczkowska*[3]*

[1] Centre for Inflammatory Diseases, Department of Medicine, School of Clinical Sciences at Monash Health, Monash University, Clayton, VIC, Australia, [2] Department of Microbiology, Immunology and Infectious Diseases, University of Calgary, Calgary, AB, Canada, [3] Department of Experimental Hematology, Institute of Zoology and Biomedical Research, Jagiellonian University, Krakow, Poland

Keywords: intravital microscopy (IVM), intravital imaging, leukocytes, inflammation, eye, heart, liver, lymph nodes

Editorial on the Research Topic

Intravital Microscopy Imaging of Leukocytes

The capacity to image motile leukocytes in three dimensions in tissues and organs, *in situ*, over time (the 4th dimension), in a living organism, presents a unique and powerful tool that allows for real-time investigation of their function and behavior. The approach of "seeing" cells in the live animal is called intravital imaging or *in vivo* microscopy (IVM). Recent advancements in microscope technologies, new strains of reporter mice, novel surgical approaches, and broad access to fluorochrome conjugated monoclonal antibodies, have led us to now visualize, at sub-cellular level, deep into living tissues. To reach this stage, many obstacles had to be overcome. For example, imaging of the lung required the opening of the chest cavity without the lung collapsing. Similarly, imaging of organs with strong autonomic innervation (heart, intestines) needs to overcome the dynamic tissue movements. As these technical challenges have been met and overcome, we are now only beginning to reveal the true life of the leukocyte. The goal of this Research Topic was to bring together some of the latest methodological developments in the field of IVM as well as some novel findings both in terms of unstudied diseases, and leukocyte function and cellular fate.

Immune cells play a pivotal role in both maintaining and restoring homeostasis in our bodies. Resident leukocytes are either strategically located in tissues prone to infection (e.g., skin, body cavities), or actively patrol vasculature of some organs (e.g., lung, liver). Once infection or injury occurs, these resident immune cells alert other immune cells, facilitating robust cellular recruitment when needed. In these functions, leukocytes are actively supported by platelets, blood components that in recent years have become highly appreciated as critical helpers and regulators of the immune response. Montague et al. review imaging approaches that have allowed for the study of platelets at the single cell level. These studies have provided great insight into the roles of platelets in both hemostasis and in infection/inflammation, reveling rapid and dramatic shape changes, alterations in adherence and interactions with other blood cells, plasma proteins, and vascular structures. In many respects, the ability to image platelet activation, in real-time, has fundamentally changed our understanding of these multifaceted blood components.

During the inflammatory response to virtually any disorder, the first leukocytes to be recruited to the afflicted tissue are neutrophils. These cells are traditionally regarded as the simple, dispensable foot-soldiers of innate immunity and are largely underappreciated. In this Research Topic, several papers focus on neutrophils, analyzing their behavior and function during sterile (Davis et al.), viral (Pizzagalli et al.), or bacterial (Cichon et al.) inflammation/infection as well as during cancer (Sody et al.). In the latter context, Sody et al. show that tumor associated neutrophils, or TANs, are associated with poor prognosis of cancer, and migrate in a unique fashion into solid tumors via

OPEN ACCESS

Edited and reviewed by:
Florent Ginhoux,
*Singapore Immunology Network (A*STAR), Singapore*

***Correspondence:**
Elzbieta Kolaczkowska
ela.kolaczkowska@uj.edu.pl

Specialty section:
This article was submitted to Antigen Presenting Cell Biology, a section of the journal Frontiers in Immunology

Received: *01 July 2020*
Accepted: *06 August 2020*
Published: *10 September 2020*

Citation:
Wong CHY, Jenne CN and Kolaczkowska E (2020) Editorial: Intravital Microscopy Imaging of Leukocytes. Front. Immunol. 11:2137. doi: 10.3389/fimmu.2020.02137

both CXCR2-dependent and -independent mechanisms. Clearly, neutrophils are not only engaged in the first-line of defense but are also involved in adaptive immunity and antigen presentation (1). Pizzagalli et al. report that, upon challenge of mice with attenuated influenza virus (vaccination), neutrophils are "seen" transporting viral particles from the site of infection to the draining lymph nodes. Although lymph node imaging is typically challenging due to their location deep within draining tissues, the rather superficial and accessible location of the popliteal lymph node allows for efficient and clear imaging of this secondary lymphoid tissue, making it one the most frequently imaged lymph nodes [(2), Lopez et al.]. Further developing the ability to image lymph nodes, Lopez et al. have established a method for visualizing the mandibular draining lymph nodes of the eye to study corneal immune responses. It is within these lymph nodes that antigen presentation occurs as inflammation progresses, and it is the dendritic cells (DCs) that play a critical role in lymphocyte activation during the dry eye disease (DED) adaptive immune response. Two papers included in this Research Topic focus on the morphology and kinetics of these DCs in both the eye and lymph nodes of animals affected by DED (Jamali et al.; Ortiz et al.).

Historically, one of the most challenging tissues to image in the live organism is the heart. This difficulty is due to both continual tissue movement (beating) needed to maintain normal tissue perfusion throughout the animal and due to its location deep within the chest. In fact, it has only been in the last decade that high resolution imaging of the living, beating heart of an intact animal has been possible. In this Research Topic, two groups have provided reviews of the key advancements, techniques and knowledge gained from intravital imaging of the heart and the coronary microcirculation with an emphasis on vascular health and leukocyte trafficking (Allan-Rahill et al.; Kavanagh and Kalia). Key in these imaging advancements is the development of a technique that involves the installation of a glass window and a gentle vacuum-mediated tissue stabilization, allowing for fixation of a single field of view for imaging (Allan-Rahill et al.; Kavanagh and Kalia). Although not yet developed for the beating heart, imaging of other tissues can utilize long-term implantable windows, allowing for visualization of a tissue or organ, in a single animal, over an extended period of time (days-weeks), creating the possibility to follow a given pathological process (e.g., tumor progression) over time (3). Sedin et al. developed a system of highly controlled vacuum chambers to stabilize the kidney during IVM for several hours with minimal disruption of local milieu. One of the important, yet not often addressed, shortcomings of window application in IVM is maintenance of the local temperature of the imaged tissue. Ahl et al. constructed a tissue-stabilizing system via 3D printing that aids in the control of tissue temperature underneath the window allowing for imaging of skin or muscle for several hours. The temperature maintenance is also a key methodological issue in the study by Ortiz et al. who have developed an imaging platform heated by circulating water in the region of the lacrimal gland of the eye.

The spectrum of technical issues faced by the IVM users also includes organ autofluorescence. It is an intrinsic parameter that depends on naturally present, endogenous fluorophores, and in the case of the liver, this phenomenon can provide real-time information on the morphology and functional properties of this organ (4). Davis et al. report on strategies to accommodate this autofluorescence and with a methodological approach, they were able to study leukocyte behavior during non-alcoholic fatty liver disease (NAFLD), a disorder rarely studied with IVM due to the high autofluorescence associated with lipidemic liver. The liver is frequently a target for metabolic-induced damage and perturbations as highlighted during the study of another disease affecting this organ, Wilson's disease, resulting from a point mutation leading to copper accumulation in the liver and brain. Cichon et al. contrasted this condition with that of Menkes disease, a condition in which there is not enough copper available. In either case, during sepsis, the organ is affected by either diminished production of neutrophil extracellular traps (NETs) or decreased neutrophil infiltration, respectively, conditions that are readily tracked and characterized using IVM.

In this Research Topic, we present a selection of papers on both latest developments in research on leukocytes in various tissues and organs, along with novel, or improved methodology, for intravital imaging. Studies and reviews presented in this Research Topic cover multiple tissues/organs and they include the ear (Sody et al.), eye (Jamali et al.; Lopez et al.; Ortiz et al.), heart (Allan-Rahill et al.; Kavanagh and Kalia), kidney (Sedin et al.), liver (Cichon et al.; Davis et al.), lymph nodes (Lopez et al.; Pizzagalli et al.), muscle and skin (Ahl et al.). We have come a long way since the nineteenth century when Augustus Waller and Julius Cohnheim observed the vasculature within the tongue of a live frog using very simple light microscopes (5). Contemporary IVM continues to evolve, embracing new technology and methodology that expands the repertoire of organs, deep-set tissues, and cell types that can be imaged as well as analytical tools that enable a better comprehension of obtained data. By embracing these developments, we are now better equipped than ever to reveal the true life of a leukocyte in health and disease.

AUTHOR CONTRIBUTIONS

All: inviting contributors, handling and tracking submissions, acting as associate editors for selected manuscripts, inviting reviewers, co-authoring and revising the manuscript. EK: coordinating the team work, drafting the manuscript.

FUNDING

CW was supported by the CSL Centenary Fellowship. CJ was supported by the Canada Research Chairs Program. EK was supported by a grant [No. 2018/29/B/NZ6/00713] from the National Science Center, Poland (NCN).

REFERENCES

1. Vono M, Lin A, Norrby-Teglund A, Koup RA, Liang F, Lore K. Neutrophils acquire the capacity for antigen presentation to memory CD4(+) T cells *in vitro* and *ex vivo*. *Blood.* (2017) 129:1991–2001. doi: 10.1182/blood-2016-10-744441
2. Secklehner J, Lo Celso C, Carlin LM. Intravital microscopy in historic and contemporary immunology. *Immunol Cell Biol.* (2017) 95:506–13. doi: 10.1038/icb.2017.25
3. Alieva M, Ritsma L, Giedt RJ, Weissleder R, van Rheenen J. Imaging windows for long-term intravital imaging: general overview and technical insights. *Intravital.* (2014) 3:e29917. doi: 10.4161/intv.29917
4. Croce AC, De Simone U, Freitas I, Boncompagni E, Neri D, Cillo U, et al. Human liver autofluorescence: an intrinsic tissue parameter discriminating normal and diseased conditions. *Lasers Surg Med.* (2010) 42:371–8. doi: 10.1002/lsm.20923
5. Hwa C, Aird WC. The history of the capillary wall: doctors, discoveries, and debates. *Am J Physiol Heart Circ Physiol.* (2007) 293:H2667–79. doi: 10.1152/ajpheart.00704.2007

Conflict of Interest: The authors declare that the research was conducted in the absence of any commercial or financial relationships that could be construed as a potential conflict of interest.

frontiers in Immunology

ORIGINAL RESEARCH
published: 25 June 2019
doi: 10.3389/fimmu.2019.01419

Distinct Spatio-Temporal Dynamics of Tumor-Associated Neutrophils in Small Tumor Lesions

Simon Sody[1], Mohib Uddin[2], Anika Grüneboom[3†], André Görgens[4,5], Bernd Giebel[4], Matthias Gunzer[3] and Sven Brandau[1]*

[1] Department of Otorhinolaryngology, University Hospital Essen, University Duisburg-Essen, Essen, Germany, [2] Respiratory Global Medicines Development (GMD), AstraZeneca, Gothenburg, Sweden, [3] Institute for Experimental Immunology and Imaging, University Hospital Essen, University Duisburg-Essen, Essen, Germany, [4] Institute for Transfusion Medicine, University Hospital Essen, University Duisburg-Essen, Essen, Germany, [5] Department of Laboratory Medicine, Karolinska Institutet, Stockholm, Sweden

OPEN ACCESS

Edited by:
Craig N. Jenne,
University of Calgary, Canada

Reviewed by:
Mia Phillipson,
Uppsala University, Sweden
Victor Naumenko,
National University of Science and Technology MISiS, Russia

***Correspondence:**
Sven Brandau
sven.brandau@uk-essen.de

†Present Address:
Anika Grüneboom,
Department of Internal Medicine 3 - Rheumatology and Immunology, Friedrich-Alexander-University Erlangen-Nürnberg (FAU) and University Hospital Erlangen, Erlangen, Germany

Specialty section:
This article was submitted to Inflammation, a section of the journal Frontiers in Immunology

Received: 05 February 2019
Accepted: 05 June 2019
Published: 25 June 2019

Citation:
Sody S, Uddin M, Grüneboom A, Görgens A, Giebel B, Gunzer M and Brandau S (2019) Distinct Spatio-Temporal Dynamics of Tumor-Associated Neutrophils in Small Tumor Lesions. Front. Immunol. 10:1419. doi: 10.3389/fimmu.2019.01419

Across a majority of cancer types tumor-associated neutrophils (TAN) are linked with poor prognosis. However, the underlying mechanisms, especially the intratumoral behavior of TAN, are largely unknown. Using intravital multiphoton imaging on a mouse model with neutrophil-specific fluorescence, we measured the migration of TAN in distinct compartments of solid tumor cell lesions *in vivo*. By longitudinally quantifying the infiltration and persistence of TAN into growing tumors in the same animals, we observed cells that either populated the peripheral stromal zone of the tumor (peritumoral TAN) or infiltrated into the tumor core (intratumoral TAN). Intratumoral TAN showed prolonged tumor-associated persistence and reduced motility compared to peritumoral TAN, whose velocity increased with tumor progression. Selective pharmacological blockade of CXCR2 receptors using AZD5069 profoundly inhibited recruitment of TAN into peritumoral regions, while intratumoral infiltration was only transiently attenuated and rebounded at later time points. Our findings unravel distinct spatial dynamics of TAN that are partially and differentially regulated via the CXCR2 signaling pathway.

Keywords: tumor-associated neutrophils, neutrophil granulocytes, intravital imaging, multiphoton microscopy, tumor microenvironment, tumor immunology, CXCR2, AZD5069

INTRODUCTION

During the last decade, a high intratumoral frequency of tumor-associated neutrophils (TAN) was established as a strong predictor of poor clinical outcome in the majority of solid tumor entities (1–3). In fact, in a recent transcriptomic analysis of ∼18.000 human tumor samples from 14 solid tumors neutrophils (secondary to mast cells) showed the strongest correlation with adverse cancer outcomes (1).

Despite this well-established prognostic role in the clinical setting, the mechanisms underlying a disease-promoting activity of neutrophils are still poorly understood. Murine studies have identified a variety of neutrophil-mediated pro-tumorigenic factors (4). Production of neutrophil-derived matrix metalloproteinases like MMP-9 were shown to release VEGF-A from the extracellular matrix (ECM) and thereby constitute a major source of pro-angiogenic factors in the tumor microenvironment (5–8). In addition, neutrophils can influence invasiveness and metastatic potential of tumor cells by angiotropism (9) or neutrophil granule-derived enzymes,

that actively remodel the ECM and mutually activate tumoral proteases to promote the invasion of tumor cells (10). Priming of lung pre-metastatic niches through neutrophil MMPs enhanced the metastatic spread of mammary tumors (11). Likewise, human neutrophils, after CXCR2-dependent recruitment (12), and MAPK activation have the ability to induce multiple tumor promoting mechanisms (6), which includes the cortactin-mediated induction of tumor cell invasion and metastasis in patients (13). Further, immunosuppressive neutrophils with myeloid-derived suppressor cell activity (PMN-MDSC) can drive tumor immune evasion (14–16).

Despite this important role of neutrophils in malignant disease, until recently, even in murine models, mechanistic studies on the recruitment and intratumoral biology of TAN were limited to histological tissue analyses, *ex vivo* investigations or depletion of neutrophils by antibodies without a direct observation of the live cells within the tumor. To a large extent, this has been based on existing models such as lys-EGFP, c-fms-EGFP, and hMRP8-Cre that were not neutrophil specific and hence also included the analysis of "contaminating" cells from the myelomonocytic and dendritic lineages (17–19). As such, immune-mediated mechanisms of neutrophil recruitment to the sites of tumor are incompletely understood.

Experimental murine studies and clinical correlation analyses have identified ligands for CXCR2 as major drivers of TAN recruitment into tumor lesions, involving CXCL1/KC, CXCL2/MIP-2, CXCL5/LIX, CXCL6, and MIF (12, 20–23). Consequently, at least in murine models, many of the disease-promoting effects of neutrophils can be attenuated by CXCR2 blockade (24–26). In contrast to human neutrophils, where CXCR1 and CXCR2/IL-8 interaction is a major chemoattractant (27), in mice, CXCR1 has a redundant capacity for neutrophil trafficking whilst playing a predominant role in regulating degranulation (28). Neutrophil effector functions and trafficking to tissues are also context-dependent. While neutrophils were initially considered as purely pathogen-clearing innate effector cells, to date, complex and adaptable functions in infection, inflammation and cancer are emerging (29, 30).

In this study, we used AZD5069 to modulate recruitment of TAN into tumor lesions *in vivo*. AZD5069 is a small molecule antagonist with over 100-fold selectivity for CXCR2 relative to CXCR1 receptor, that does not adversely affect neutrophil-mediated host immunity (31, 32). Beyond a potential immuno-oncological target (20), AZD5069 has been extensively studied as an orally active immunotherapy in chronic respiratory diseases, including COPD (33, 34), bronchiectasis (35) and severe asthma (36, 37). In murine tumor models CXCR2 blockade has been shown to modulate neutrophil trafficking to sites of chronic inflammation, subsequently reduced tumor and metastasis formation and enhanced treatment efficacy in distinct therapeutic conditions (38–41).

To directly image different phases of neutrophil invasion into locally growing tumors, we used a recently established mouse model, termed Catchup (42). This allowed us to uncover time-dependent changes in frequency, localization, and migratory patterns of neutrophils in small tumor lesions. We found that neutrophils localized in either intratumoral or peritumoral regions revealed distinct migratory patterns. Surprisingly, blockade of the CXCR2 chemokine receptors, previously believed to selectively inhibit migration of neutrophils into tumors and other inflammatory tissue lesions, was shown to markedly attenuate peritumoral stromal TAN, whilst only transiently blocking the recruitment of TAN into the early tumor cell lesion. These findings have important implications for the precision targeting of TAN in emerging cancer combination immunotherapies.

Abbreviations: 2PM, two-photon microscopy; a.dest, distilled water; ADCC, antibody-dependent cellular cytotoxicity; BP, bandpass; COPD, chronic obstructive pulmonary disease; ECM, extracellular matrix; $FetCO_2$, end-tidal CO_2-fraction; G-MDSC, granulocytic myeloid-derived suppressor cells; HNC, head and neck cancer; HNSCC, head and neck squamous cell carcinoma; i.d., intradermal; i.p., intraperitoneal; i.v., intravenous; LP, longpass; MIP, maximum intension projection; NIR, near infrared; PBS, Phosphate buffered saline; SHG, second harmonic generation; TAN, Tumor-associated neutrophils; TME, Tumor microenvironment.

MATERIALS AND METHODS

Animals

All animal experiments were performed in accordance with the animal ethics committee of the state of North Rhine–Westphalia, Germany, and German guidelines for experimental animal welfare. Generation of Catchup$^{IVM-red}$ was previously described (42). Catchup$^{IVM-red}$ mice were bred in the animal facility of the Centre for Medical Biotechnology of the University Duisburg Essen and housed under specific pathogen-free conditions in individually ventilated cage racks. Both male and female Catchup$^{IVM-red}$ mice were used at any age between 3 and 6 month, but animals were sex- and age-matched in each experiment as much as possible.

Tumor Cell Culture

The murine oropharyngeal cell line MOPC (C57BL/6-derived, HPV16 E6/E7$^-$) was kindly provided by J. Lee (Sanford Research/University of South Dakota, Sioux Falls, SD, USA) and cultured as described previously (43). MOPC^{EGFP} cells were generated by lentiviral gene transfer using a pCL6IEGwo empty vector (44) as previously described (45). Cells were washed twice in phosphate buffer saline (PBS) before injection into mouse dermis under sterile conditions.

Tumor Model

Syngeneic murine HNSCC line MOPC^{EGFP} were injected superficially in the dermis of the outer dorsal ear for intravital microscopy. Approximately 3 min before tumor cell injection the ear was depilated using commercially available depilatory cream, applied <2 min. Under Ketamin/Xylazin (100/20 mg/kg body weight) anesthesia ∼10 µl of $20*10^6$/ml cell suspension in PBS was injected into the ear dermis using a 30-gauge cannula.

Contralateral Day 3 Tumor

In one experiment, on day 3 after tumor cell inoculation, AZD5069 and vehicle-treated Catchup$^{IVM-red}$ mice were injected with a second tumor into the contralateral outer ear

dermis. Tumor injection and CXCR2 blockade was performed as described below.

CXCR2 Antagonism

CXCR2 was blocked with small molecule antagonist AZD5069, which was provided by AstraZeneca. AZD5069 was diluted in vehicle solution consisting of 1.14% w/w HP-β-cyclodextrin and 0.5% Hydroxy propyl methyl cellulose (HPMC 6 cps) in 0.1 mM Carbonate buffer (pH 9.5–10). One-hundred microliter of 10 mM AZD5069 or vehicle solution only (for control group) was continuously administered twice daily (12 h interval) via oral gavage starting 12 h before tumor cell injection.

Intravital 2-Photon Microscopy

Imaging of $MOPC^{EGFP}$ tumors in the outer dermis of the dorsal ear was performed non-invasively on costume build water heated aluminum stage. The ear was gently mounted on pre-warmed aluminum block using Vaseline, covered with a cover slip and encumbered with a 1 cm diameter metal ring. PBS was used as immersion medium beneath and above cover slip sealed with Vaseline to prevent drain. Long term anesthesia was controlled via intubation narcosis and mechanical ventilation (1.5% Isoflurane in O_2) using capnography to maintain physiologic ventilation (expiratory CO_2: ∼20 mmHg). Mice were injected with 10 µL of a 1 mM QTracker® 655 (Life Technologies, Darmstadt, Germany) solution i.v. to visualize blood vessels before constant observation in a Leica TCS SP8 MP microscope (Leica Microsystems, Mannheim, Germany) with simultaneous detection via hybrid-reflected light detectors and photomultiplier tubes with a HCX IRAPO L253/0.95 water objective. If not otherwise indicated excitation was performed at 960 nm using a Coherent Chameleon Vision II Ti:Saph-Laser (Coherent LaserSystems, Göttingen, Germany). The following filter settings were used: collagen (second harmonic generation, SHG) BP485/30; neutrophils (tdTomato transgene) BP585/50, blood vessels (QTracker®) BP660/30, tumor cells (EGFP) BP525/50. Raw data were reconstructed with Imaris (Bitplane, Zurich, Switzerland) for quantitative analysis and generation of representative pictures and videos.

Statistical Analysis

Data were analyzed using GraphPad Prism Software (GraphPad Software, Inc., La Jolla, CA, USA). Statistical significance was assessed with paired or unpaired two-tailed *t*-test for the comparison of two groups and two-way ANOVA with Bonferroni post-tests for the comparison of multiple groups if not otherwise indicated. Results were considered statistically significant at $p \leq 0.05$.

RESULTS

Establishment of a Longitudinal Intravital Imaging System to Monitor TAN Mobility and Migration During Early Engraftment of Tumor Cells

At first, we established technical requirements crucial for high quality, unperturbed, longitudinal imaging of TAN in early tumor cell lesions. Maintaining body temperature is important for preserving normal physiology of mice during prolonged and longitudinal imaging. Common heating pads are unsuitable for this purpose, since periodical heating leads to relevant material expansion and contraction with enormous shifts in z-direction. To circumvent this problem, we designed a water heated aluminum stage with an external heating unit, which was constantly perfused with 36°C warm water. After narcosis, depilation of the ear, tumor cell injection and *i.v.* blood labeling the mouse ear was gently mounted with petroleum jelly (Vaseline®) in prone position on pre-warmed aluminum block and covered with a glass cover slip. For stable long-term imaging conditions (>1 h) endotracheal intubation and controlled isoflurane narcosis (1.5% Isoflurane in 100% O_2) with constant capnometry ($FetCO_2$ = 2–3%) proved successful. Continuous capnometry ensured appropriate ventilation, sufficient narcosis depth, tolerability and an adjusted recovery phase. For short-term imaging periods (<1 h) *i.p.* ketamine narcosis without endotracheal intubation was sufficient. Using these procedures intravital imaging was performed on days 0, 3, and 6 (**Figure 1A**).

To this end, following the adoptive transfer of ∼150,000 cells of the HNC cell line $MOPC^{EGFP}$ (45), an appropriate superficial tumor cell lesion was identified with epifluorescence and navigation through oculars. The autofluorescence of epidermal cells followed by overlay with the second harmonic generation (SHG) signal of the basal membrane during multiphoton acquisition permitted navigation through skin layers (**Figure 1B**). Mean size of the lesion analyzed inside the field of view increased over time from ∼0.007 mm^3 (day 0, 120–180 min after injection) to 0.017 mm^3 (day 6) (**Figure 1C**). Within the tumor cell lesion, we identified TAN in two distinct regions relative to the tumor cell mass. The center of a compact tumor lesion, consisting of densely packed tumor cells, was considered intratumoral and TAN localized in this area were designated intra-TAN. The directly adjacent, SHG signal/collagen rich, area within the field of view was termed peritumoral compartment. The peritumoral compartment was defined as a maximum distance of 250 µm from the tumor margin, which was expected to be in reach of paracrine tumoral conditioning factors, but without direct tumor cell contact (**Figure 1D**; **Supplementary Video 1**). TANs in this region were termed peri-TAN. Using our model, we could routinely record longitudinal sessions of TAN imaging in single tumor lesions from day 0 (up to 3 h post tumor cell injection) until days 3 and 6 post injection (**Figure 1E**).

This experimental model therefore has provided a reliable method for longitudinal monitoring of unmanipulated TAN in small newly established tumor cell lesions with high resolution and in the context of two different spatial compartments of the tumor microenvironment.

Dynamics of Early Neutrophil Infiltration Into the Tumor Lesion

Due to their small size, very early tumor lesions are not readily accessible to classical histological preparation and analysis. Hence, intravital 2PM was especially suited to monitor

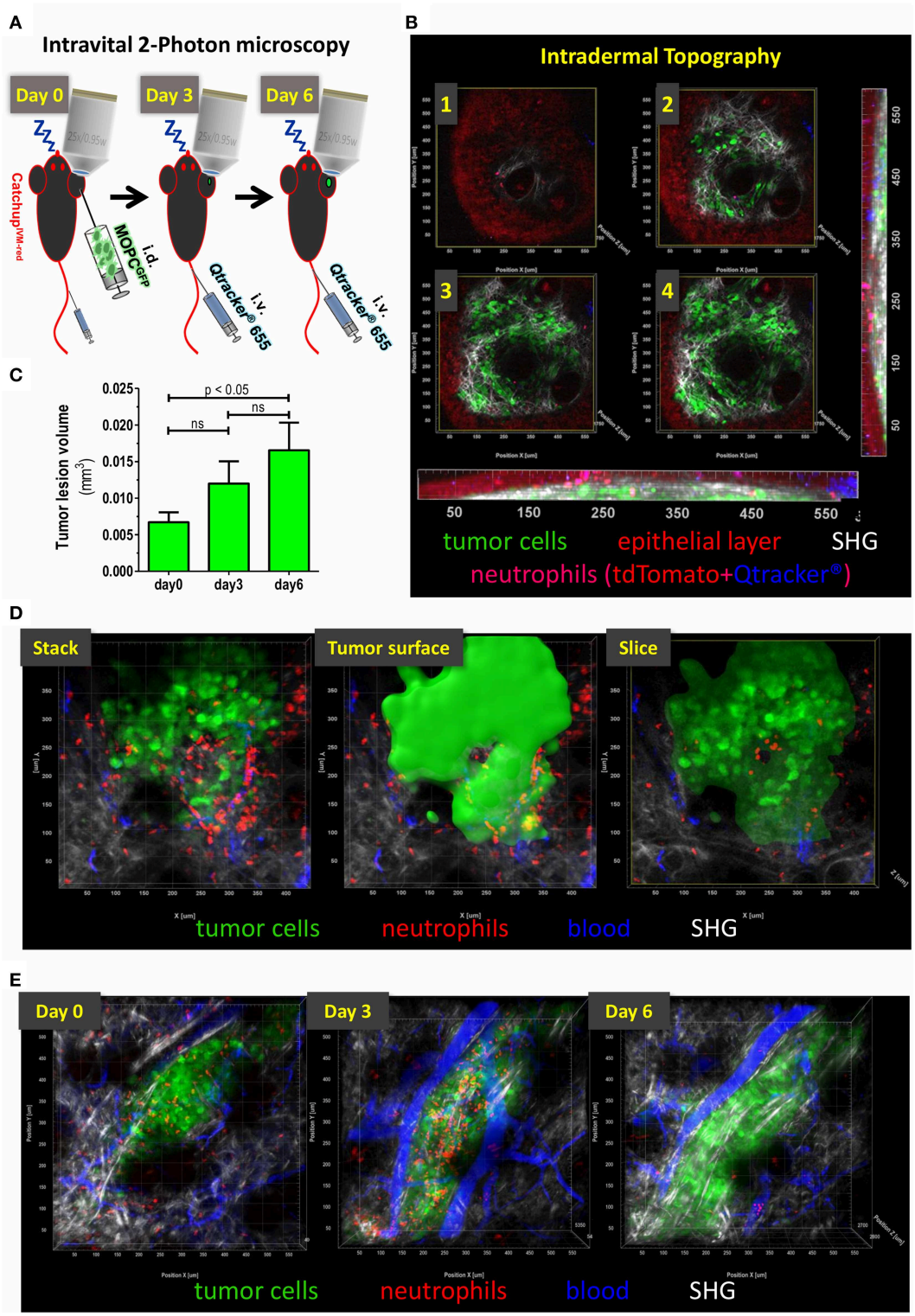

FIGURE 1 | Topography of small intradermal lesions of tumor cells. **(A)** Experimental scheme for longitudinal analysis of spatio-temporal dynamics of TAN. After narcosis Catchup$^{IVM-red}$ mice were intradermally injected with MOPC^{EGFP} cells into the dorsal ear skin (day 0). Directly before imaging Qtracker® vascular label 655 was injected i.v. into the tail vein or retrobulbar to visualize blood vessels. Imaging procedure on the same tumor lesion was repeated on days 3 and 6. **(B)** Images 1–4 show single cross sections in different depth in a multidimensional 2-Photon stack of an advanced tumor (>day 10). Orthogonal maximum intension projection (MIP) in the x-z-plane (bottom) and y-z-plane (right). Epidermal layer shows a weak autofluorescent signal in the tdTomato emission spectrum (red). Neutrophils show highly

(Continued)

FIGURE 1 | fluorescent tdTomato signals and weakly accumulate Qtracker® over time (here 1.5 h post-injection is shown). After fluorescence overlay, neutrophils are displayed in magenta. This enables additional differentiation from autofluorescence by mixed color. Only residual Qtracker® (blue) from leakage or clotting and no blood staining is visible since *i.v.* injection occurred 1.5 h prior to image acquisition in this case. MOPC^{EGFP} tumor cells are in green. Collagen fibers of the basal membrane and dermal matrix are visualized through SHG signal (white). Image 1 represents the epidermal-basal membrane border. **(C)** Means (+/– SEM) of tumor lesion volumes at different time points after tumor cell injection. Day 0 = 120–180 min after tumor cell injection. $N = 6$ animals. **(D)** Definition of tumoral compartments. Tumor volume was assessed by semi-automated surface generation of tumor cells (solid green). TAN inside tumor surface area were termed "intratumoral," cells outside were designated as "peritumoral." Cross-section through tumor volume reveals intra- vs. peritumoral TAN. **(E)** Intravital multidimensional 2-Photon images of representative tumor cell lesions in MIP from days 0 (120 min after tumor cell injection), 3, and 6 are depicted. 3D reconstruction was performed with Imaris® (Bitplane).

immune cell dynamics in these very early tumor cell lesions. **Supplementary Video 2** records TAN infiltration between 45 and 120 min after tumor cell injection. At 60 min post injection, high numbers of highly migratory neutrophils started to infiltrate the tumor lesion (**Supplementary Video 2**). This influx followed sigmoid kinetics over the first 3 h (**Figure 2A**) and at 3 h post injection substantial numbers of neutrophils infiltrated the tumor injection site. In order to test whether the injection procedure itself may cause accumulation and recruitment of neutrophils we monitored injections of PBS (**Figure 2E**). While PBS injection indeed stimulated the recruitment of a smaller number of neutrophils, this influx was clearly low-level compared to the tumor cell-induced recruitment (**Figures 2B,E**). In addition, neutrophils, induced by this initial mechanical stimulus, showed short persistence and almost completely disappeared from the injection site by days 3 and 6 (**Figures 2C–E**).

We next investigated numbers and migration of individual TAN. While intra-TAN were mostly in contact with the carcinoma cells themselves, peri-TAN were in contact with the surrounding normal or stromal tissue and the extracellular matrix. At 2–3 h post injection, a substantial number of neutrophils was present in both compartments. At day 3 the frequency of peri-TAN was already strongly decreased from 322 cells/0.015 mm^3 (day 0) to 79 cells/0.015 mm^3, with further reduction by day 6 (**Figures 2B–D**). In contrast, intra-TAN frequencies remained at high levels until day 3 and only decreased to lower levels by day 6 (**Figures 1B**, **2B–D**).

We next quantified and compared the motility of TAN in these two compartments. At day 0, both intra-TAN and peri-TAN were highly migratory displaying an average velocity of 8.8 μm/min. This velocity was comparable to neutrophils recruited in response to PBS injection, suggesting that tumor cells strongly increased recruitment of neutrophils over the injection trigger as such (**Figure 2B**), but did not further modulate their speed (**Figure 2F**). We did not compare migratory properties of intra- vs. peri-TAN at day 0, since neutrophils rapidly interchanged between compartments at this early point in time, making a clear allocation impossible. Instead the comparison of velocity of intra-TAN and peri-TAN was performed starting at day 3 and then followed up for at least 10 additional days. We observed that the velocities of intra-TAN strongly decreased during tumor development and TAN in larger developed tumors (day 14 or later) displayed a rather sessile phenotype (**Figures 2G–I** and **Supplementary Video 3**). Interestingly, and in contrast to directly tumor cell-associated neutrophils, peri-TAN increased their velocity over time. By day 14, this resulted in a substantial difference in velocity of intra- vs. peritumoral TAN (**Figure 2I**). Next, we analyzed the directionality of TAN migration over time. At day 0 (1 to 3 h after injection) the infiltration of neutrophils into the lesion was directional (**Figure 2J**, directionality > 0.5). In contrast, at days 3 and 6, the overall directionality of TAN decreased over time, with peritumoral TAN constantly displaying a slightly higher directionality than intratumoral TAN (**Figures 2K,L**). **Supplementary Video 4** supports this finding.

In conjunction, these data establish previously unknown time-dependent differences in recruitment, persistence and migratory behavior of TAN located in either the intratumoral or the peritumoral area of the tumor microenvironment.

Effect of CXCR2 Blockade on TAN Recruitment Into Tumors

We have previously shown that TAN in this MOPC tumor model express high amounts of CXCR2 on their surface (45). Expression of CXCR2 ligands in the tumor microenvironment is believed to be a major pathway of TAN recruitment in murine tumor models (20, 46–48) and even in human HNC patients (3). Given the tumor-promoting role of TAN, interference with CXCR2/CXCR2-ligand interaction, has been proposed as a means to limit the pro-tumorigenic activity of TAN. Against this background, we investigated how CXCR2 blockade would affect frequencies and migratory patterns of TAN in this model. Consistent with this idea the small molecule CXCR2 antagonist, AZD5069 effectively blocked the influx of TAN into both the intratumoral and peritumoral areas at early time points after tumor cell inoculation (left columns, 2–3h, **Figures 3A,B**). However, unexpectedly, intratumoral TAN rebounded by days 3 and 6 despite AZD5069 treatment. Thus, CXCR2 blockade was unable to limit the recruitment of intra-TAN to intratumoral areas at days 3 and 6 (**Figure 3A**, compare **Figure 3D** for the respective still images of videos). This inability was in contrast to the durable inhibitory effect of AZD5069 on the frequency of peri-TAN, which did not show a significant rebound (**Figure 3B**). In fact, in most experiments CXCR2 blockade still maintained peri-TAN density to levels below 70 cells/0.015 mm^3 on days 3 and 6 (**Figure 3B**) while intra-TAN reached levels comparable to or even higher than control mice by day 3 and later (**Figure 3A**). This rebound of intra-TAN occurred despite reduced levels of circulating neutrophils in AZD5069-treated mice until day 6 (**Supplementary Figure 1**). To confirm that AZD5069 was still generally active at day 3, we injected a second tumor at the contralateral side at this time point (**Figure 3C**). In this tumor, CXCR2 blockade still effectively inhibited the immediate recruitment of TAN into the tumor lesion at 2–3 h post injection. This indicates the *in vivo* activity

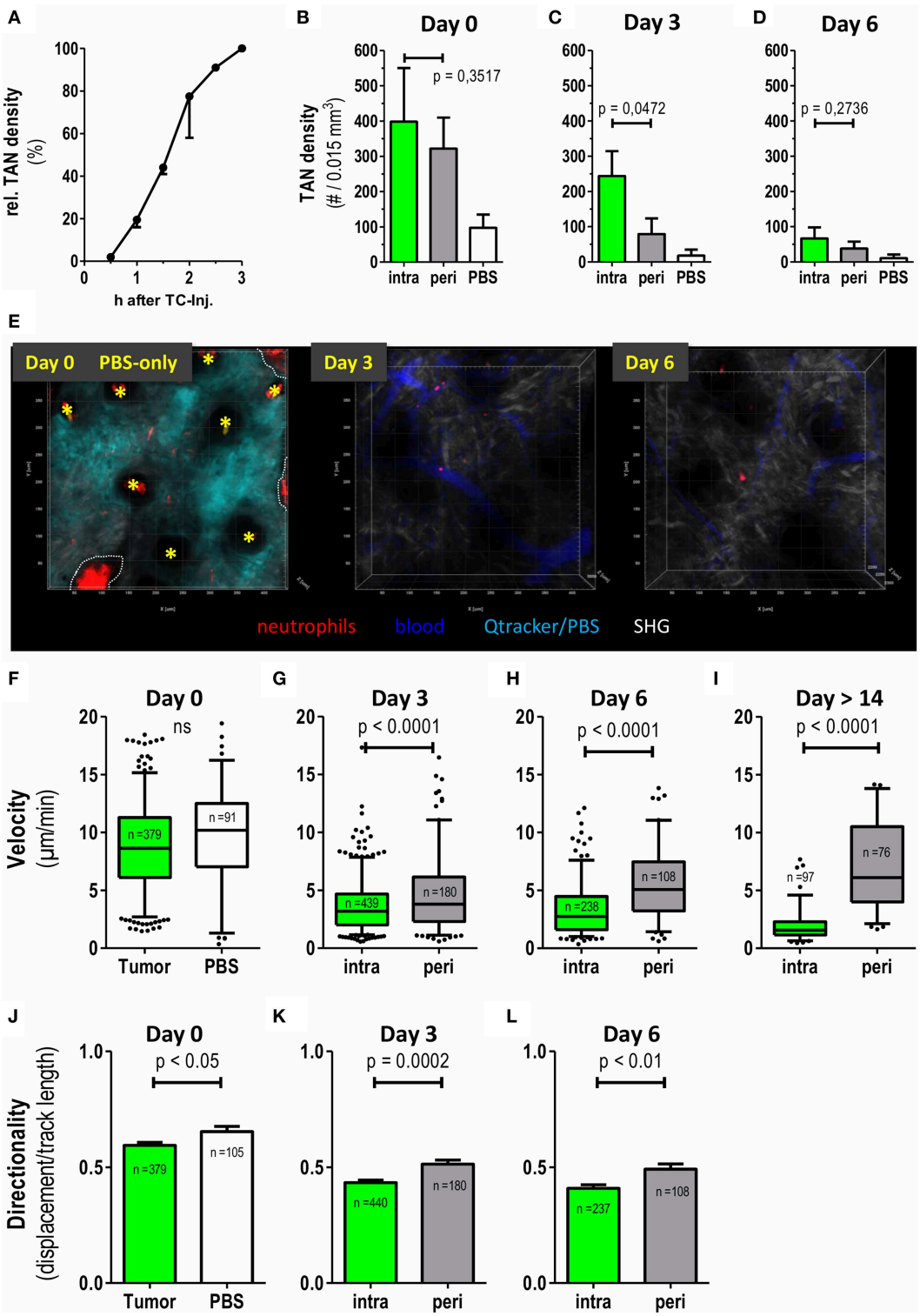

FIGURE 2 | Differential recruitment and migratory patterns of intratumoral vs. peritumoral neutrophils. Catchup$^{IVM-red}$ mice were injected with MOPC^{EGFP} cells into the dorsal ear dermis. TAN infiltration and motility was assessed by transdermal intravital 2PM. **(A)** Time course of TAN recruitment during the first 3 h after tumor cell inoculation. TAN density at 3 h was defined as 100% (mean with SEM of 2 representative mice is shown). **(B–D)** Neutrophil densities were quantified in intratumoral (green bars) and peritumoral (gray bars) compartment and after PBS injection only (white bars) at days 0, 3, and 6 and depicted as number of TAN per 0.015 mm^3 tumor tissue volume ($n = 6$ mice for tumor and $n = 2$ mice for PBS). **(E)** Representative 2-D still images generated from three-dimensional multiphoton images in

(Continued)

FIGURE 2 | maximum intension projection (MIP) demonstrating low neutrophil recruitment and persistence in control Catchup$^{IVM-red}$ mice injected with PBS+Qtracker® at day0. At day 0 the Qtracker dye (+PBS) (cyan) was injected into the ear dermis only. On day 3 and 6 blood vessels were labeled by i.v. Qtracker® (blue) injection. Yellow asterisks mark hair follicles (day 0). Dotted white line indicate areas of invaginated epidermal layer (wrinkle) with high red autofluorescence. Scattered neutrophils are represented by cell-associated red signals in the tissue parenchyma. **(F–I)** Velocities of neutrophils in the tumor compartments assessed by semi-automated tracking. **(J–L)** Migration of TAN in **(F–H)** was also analyzed for directionality (track length/displacement). **(F–L)** $n = 4$ for tumor bearing mice, $n = 2$ for PBS, $n = 3$ in **(I)** and cumulative number of analyzed single neutrophils depicted in each plot. Statistical significance was assessed with paired *t*-test **(B–D)** and unpaired two-tailed *t*-test **(F–L)**, $\alpha = 0.05$. Mean +/– SEM is shown in bar graphs and 5–95% percentiles in boxplots. 3D reconstruction, quantification and tracking were performed with Imaris® (Bitplane).

of the compound despite the inability to exclude intra-TAN from tumors injected 3 days earlier in the same animal. Strikingly, also in the secondary tumor, AZD5069 lost effects on intra-TAN 3 days post injection (**Figure 3C**) suggesting that this effect is mediated by a change in tumor biology rather than TAN biology. Consistent with observations in primary tumors, in most experiments CXCR2 blockade retained its inhibitory activity on the recruitment of peri-TAN by 3 days post injection also for the 2nd challenge tumor.

Having analyzed the effects of CXCR2 blockade on TAN densities, we then assessed the effect of CXCR2 blockade on fundamental motility parameters of TAN in both compartments. In day 0 intravital imaging showed the trafficking of neutrophils through vasculature directly adjacent to tumor cell lesions. As expected, also signs of neutrophil adhesion and rolling could be observed. Importantly, and confirming data from **Figures 3A,B**, the extravasation of TAN from vessels into the tumor lesion was completely abrogated by CXCR2 blockade at this time point (**Supplementary Video 5**). Since AZD5069 treatment completely prevented TAN recruitment to tumor lesions at the day of injection, motility was subsequently only analyzed at days 3 and 6 post injection. Interestingly, and despite its inability to reduce the recruitment of TAN to the intratumoral lesion at this time point (**Figure 3A**), AZD5069 still significantly reduced the motility of intra-TAN at day 3 (**Figure 3E**). However, at day 6 this effect of CXCR2 blockade on intra-TAN over vehicle treated animals was lost. A similar pattern of response was found for AZD5069 effects on the small numbers of peri-TAN. As depicted in **Figure 3F**, AZD5069 reduced the velocity of peri-TAN only at day 3 and not at day 6. Instead, the small number of peri-TAN, which infiltrated the tumors in the presence of CXCR2 blockade at day 6, seemed to display substantial mobility with a mean velocity above 5 μm/min (**Figure 3F**). In summary, the effects of CXCR2 blockade on the migration demonstrated clear differences between intra- and peri-TAN. In contrast, we observed a coherent effect of CXCR2 blockade on the directionality of TAN migration in both compartments. Here, AZD5069 treatment equally increased the directionality of TAN migration in both compartments (**Figures 3G,H**).

These data show, that, in addition to its distinct inhibitory effects on intra- and peri-TAN recruitment, AZD5069 also affects the intratumoral motility and directionality of these TAN subtypes in small tumor lesions.

DISCUSSION

In this study, we demonstrate the establishment of an experimental system of unperturbed longitudinal tumor-associated neutrophil (TAN) observation in the living mouse. To this end, we used a tumor cell injection model in the murine ear dermis. While this model has many advantages in terms of the imaging technology, it also has apparent limitations. Notably, injection models, particularly with respect to early growth phases do not fully recapitulate the complex multi-component tumor-stroma available in selected chemically induced or transgenic models. Despite these limitations, syngeneic transplantation models are very frequently used for experimental research and important aspects of immuno-oncology are being investigated in such models (45, 47, 49, 50). In terms of *in vivo* imaging, many experimental models to date require major surgical intervention to make tumor lesions accessible to imaging technologies (51, 52). This constitutes a trauma with subsequent effects on immune cell infiltration and behavior. Our model utilizes a minimally invasive procedure allowing for longitudinal long-term observations of the invasion of unperturbed TAN into a growing tumor. Although artificial disruption of tissue integrity occurs during intradermal injection in this model, the degree of damage is comparable to human tumor-associated wounds and inflammation, which are actually induced by invasive malignant progression or iatrogenic biopsies and surgery (53, 54). Our model, therefore, recapitulates certain aspects of regular tumor development in patients with cancer. In addition, we investigated the stimulus by PBS injection itself. By comparing neutrophil dynamics in PBS-only lesions with tumor cell injection, we could show that tumor cells are the major source of neutrophil attraction and exclusively induce persistence in this model. Tumor lesions showed four times greater neutrophil densities than PBS lesions. Further, the neutrophil influx in PBS lesions was transient; and resolved to background by day 3, while TAN recruitment was durable over >6 days of observation.

Interestingly, we observed the formation of densely packed areas of tumor cells within 3 h after tumor cell injection and tumor cells showed tight microscopic cell-contacts. It is tempting to speculate that the injection of tumor cells and the formation of dense tumor cell areas also influences the biology of the surrounding stromal tissue. Our intravital imaging shows effective triggering of TAN recruitment into what we designated "intratumoral" and "peritumoral" (surrounding stromal) areas. Thus, at these early time points, most likely both tumor cell-derived and stromal cell-derived factors trigger TAN recruitment (22, 23, 55). At later time points, intra-TAN showed prolonged persistence and reduced motility, consistent with *in vitro* observations demonstrating recruitment and delayed apoptosis of neutrophils in response to tumor-derived factors (12, 56).

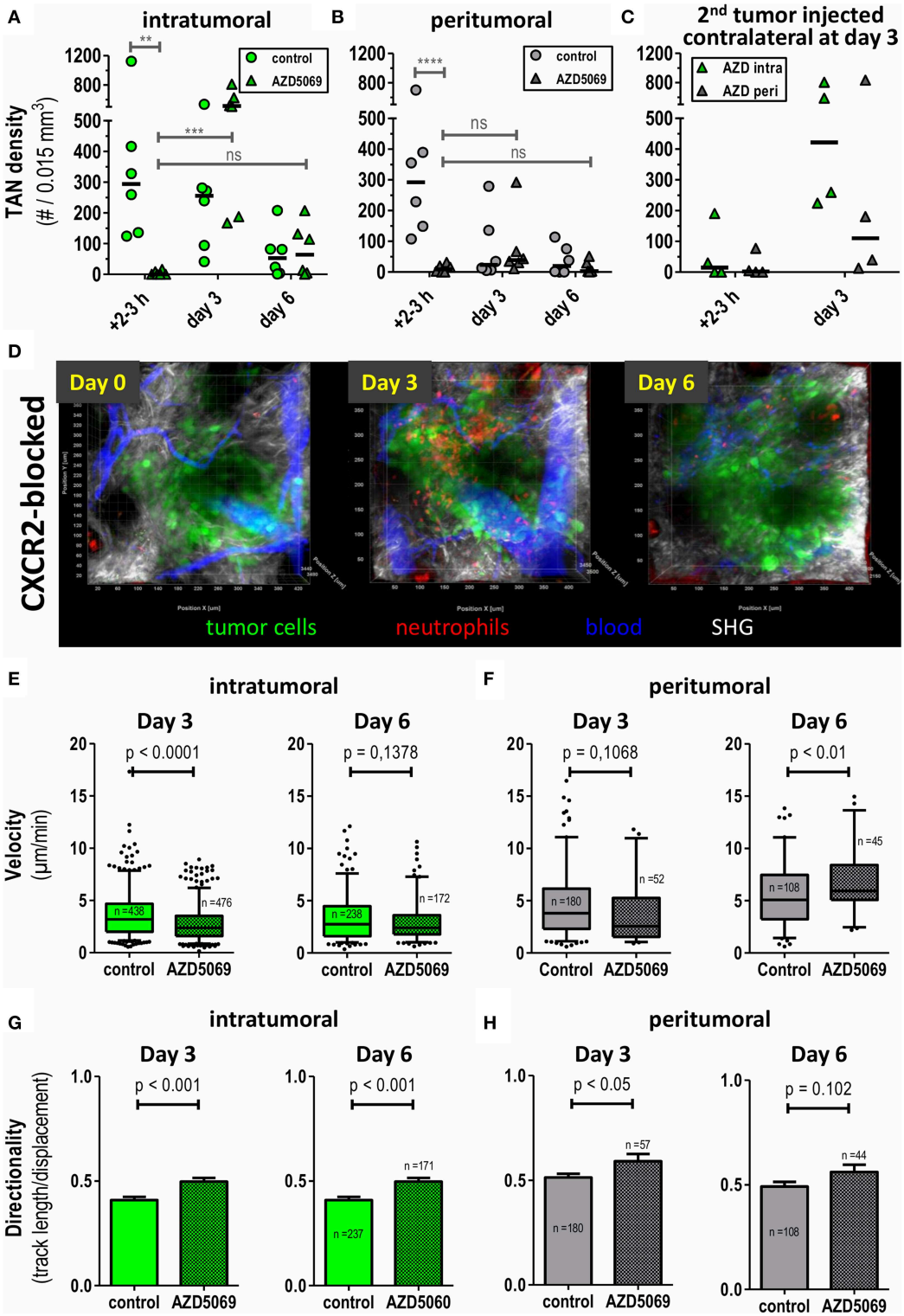

FIGURE 3 | Intratumoral and peritumoral TAN are differentially affected by CXCR2 blockade to AZD5069 treatment. Catchup$^{IVM-red}$ mice were injected with MOPC^{EGFP} cells into the dorsal ear dermis. TAN infiltration and motility was assessed by transdermal intravital 2PM. To block CXCR2 AZD5069 was orally administered twice daily starting from day−1 before tumor cell inoculation until the end of the experiment. Intratumoral **(A)** and peritumoral **(B)** TAN infiltration was quantified as neutrophils per 0.015 mm^3. Note the efficient reduction of both intratumoral and peritumoral TAN by AZD5069 at day 0. Also note the rebound of intratumoral, but not peritumoral, TAN under AZD5069 treatment at days 3 and 6. **(C)** Three days after injection of the primary tumor, AZD5069-treated mice received

(Continued)

FIGURE 3 | a second tumor injection into the contralateral ear dermis. TAN density was determined in intra- and peritumoral areas 2–3 h and 3 days after 2nd tumor injection. **(D)** Intravital multidimensional 2-Photon images of representative tumors of AZD5069 treated mice in maximum intension projection (MIP) on days 0, 3, and 6. Velocities and directionality of intratumoral **(E,G)** and peritumoral **(F,H)** TAN in AZD5069-treated compared to control mice were determined on days 3 and 6 by intravital 2PM and semi-automated tracking (pooled data from $n = 4$ mice per group). Statistical significance of difference was assessed with unpaired two-tailed *t*-test ($\alpha = 0.05$). Data in **(A–C)** are individual mice and the bar represents the median. Data in **(E–F)** are presented as box-plots with whiskers indicating the 5–95% percentile. In **(G–H)** barplots of means with SEM. In **(A–C)** each symbol represents one mouse. $^{**}p < 0.01$, $^{***}p < 0.001$, $^{****}p < 0.0001$, ns $= p > 0.05$. 3D representation, quantification, and tracking were performed with Imaris® (Bitplane).

Most tumors consist of tumor cell islands and surrounding parenchyma or non-malignant stroma cells. Recently, we demonstrated a differential prognostic role of stromal vs. tumoral inflammation in head and neck squamous cell cancer (HNSCC) patients (57). Considering the emerging prognostic relevance of tumor-stroma constitution and sublocalization of immune infiltrates in solid tumors (58, 59), we especially focused on separate analyses of tumoral compartments in this study and could indeed find striking differences in TAN frequencies, motility and CXCR2-dependent regulation with regard to TAN localization.

A key finding was the reduced directionality and velocity of intra-TAN compared with peri-TAN. This reduced migratory activity of intra-TAN could be a possible reason for the persistence of high TAN densities in the intratumoral compartment beyond day 3 as opposed to the rapid decrease of peri-TAN frequencies. Additional evidence for the intratumoral persistence of intra-TAN comes from an analysis of adoptively transferred peripheral blood leukocytes from Catchup$^{IVM-red}$ mice together with tumor cells into the ear dermis of C57BL/6 mice (**Supplementary Figure 2**). Here, we observed viable migrating adoptively transferred TAN until day 3 after transfer, suggesting that at least a certain number of intra-TAN can persist for up to 3 days in the tumor lesion. In contrast, the increased mobility of peri-TAN may lead to an increased chance of contact to distracting cues from sites away from the tumor lesion. It remains to be shown, which mechanisms are active in recruiting peri-TAN away from the tumor. Also delayed apoptosis of intra- vs. peri-TAN is a potential mechanism that might explain our findings (56, 60). New models utilizing photoactivatable GFP-transgenic neutrophils have recently been published (61) and could be used to further decipher the fate and function of intra-TAN after recruitment into the tumor core area.

CXCR2 is a major signaling pathway in neutrophil recruitment in tumors and non-malignant neutrophil-driven inflammatory diseases (34, 62–64). In a previous study, using the same MOPC cell line, we have demonstrated expression of KC and MIF by MOPC tumors (45). Interestingly, in the present study, we observed differential effects of CXCR2 blockade on TAN localized in either the intratumoral or peritumoral tissue areas. The fact that CXCR2 blockade efficiently blocked primary TAN influx on day 0 suggests a major role of the CXCR2 pathway in driving acute TAN recruitment. This is consistent with published intravital data in zebrafish larvae where neutrophil recruitment to wounds is abrogated by CXCR2 antagonists (65). However, in addition tumors may develop CXCR2 independent mechanisms of TAN recruitment which lead to stable TAN infiltration beyond day 3. Alternatively, TAN residing in specialized niches of tumors might produce factors that recruit additional TANs, as has been shown recently for HGF, that is produced by TAN and recruits additional TANs via c-Met signaling (66). Similar observations have been made for neutrophils in necrotic lesions that induce a feed-forward loop for the recruitment of other neutrophils via leukotriene B_4 (67). Future work needs to address, which mechanism is active in our model. Interestingly, in a model of zebrafish wounding additionally to the initial recruitment of neutrophils also the resolution of inflammation seemed to depend on CXCR2 (65).

The chemokine receptor CXCR2 is primarily expressed on mature neutrophils. However, in tumor hosts often an expansion of immature neutrophils occurs (45). Immature circulating neutrophils normally express low or no CXCR2. Evrard et al. recently showed that tumor bearing mice display elevated numbers of immature CD101$^-$ neutrophils in blood and pancreatic tumors compared to naive mice (68). Those cells showed low surface expression of CXCR2. Interestingly, in this model CXCR2$^-$ immature cells were still capable of normal tissue infiltration and interstitial migration. Hence, antagonizing CXCR2 using AZD5069 may selectively allow CXCR2$^-$ immature neutrophils only to infiltrate transplanted tumors in our model. By contrast, CD101$^-$ immature neutrophils only account for 1 to 5 % isolated neutrophils in blood and 5 to 16% of isolated neutrophils from pancreas in animals with low or high tumor burden, respectively (68). However, in our tumor model the numbers of intra-TAN in CXCR2-blocked Catchup$^{IVM-red}$ mice even exceeded those of vehicle treated animals on day 3. In addition, using the same tumor cell line model as in this study, we recently reported that in both, naïve and tumor-bearing C57BL/6 mice, neutrophils in the blood, bone marrow and spleen consistently express considerable amounts of CXCR2 (45). The high TAN content under CXCR2 blockade occurs despite reduced systemic levels of circulating neutrophils (**Supplementary Figure 1**). Next to TAN-intrinsic mechanisms, it might still be possible, that the tumor changes its phenotype in a co-evolution with TAN or other infiltrating immune cells, which should be investigated in future studies. Furthermore, tumor cell triggered differential chemokine modifications in the densely packed intratumoral compartment may differ from chemokine processing and constitution in the peritumoral compartment. For neutrophil activating chemokines, it is known that their effect is modulated by post-translational changes like nitration or binding to glycosaminoglycans (69). Additionally, differential constitution in terms of extracellular matrix or extracellular proteolytic activity of both compartments may lead to differential conformational changes of the present chemokines to predominantly monomers or dimers. Since it was shown for

CXCL1 that monomeric and dimeric form display differential activity in CXCR2 binding leading to a possible fine-tuning of chemokine-receptor pair effects (70), it is plausible that differential chemokine constitution in both compartments may lead to differential migratory properties of TAN.

In summary, our data represent the first targeted observation of unperturbed TAN in the living mouse during very early tumor establishment *in vivo*. Despite known and obvious limitations in terms of tumor cell development, our transplantable tumor model for intravital imaging reflects certain elements of human tumor cell biology and allows longitudinal tracking of spatio-temporal dynamics of unperturbed genetically labeled TAN. Clearly, our data suggest that infiltration of intratumoral lesion and peritumoral stroma are differentially regulated in terms of chemo-attractive and repulsive cues including the respective chemokine receptors and ligands involved. Interestingly, CXCR2 antagonism by AZD5069 is ineffective in preventing $Ly6G^+$ cell recruitment to tumor lesions at latter timepoints. Additional studies are required to decipher the complex bi-directional cross-talk of tumor tissue and TAN responsible for this dynamic interplay. Preliminary data in our group indicate strong tumor promoting features of intratumoral TAN (data not shown). Hence, our intravital system opens the possibility to further functionally characterize these distinct classes of TAN in different tumoral compartments and thereby enables unpreceded insight into TAN biology in the living animal.

ETHICS STATEMENT

This study was carried out in accordance with the recommendations of the animal ethics committee of the state of North Rhine–Westphalia, Germany, and German guidelines for experimental animal welfare. The protocol was approved by the animal ethics committee of the state of North Rhine–Westphalia, Germany.

AUTHOR CONTRIBUTIONS

SB, SS, and MG: conceptualization. SS and AGr: investigation. SS, SB, MG, and MU: writing manuscript. SB, MG, and SS: data curation and analysis. SB, MU, MG, AGr, AGö, and BG: resource. SB, MG, MU, and AGö: reviewing manuscript.

FUNDING

This study was supported by the Else-Kröner Fresenius Foundation through the ELAN programme. The funding agency provided scholarship support and partly funded the consumables used in this study. The funder had no role in planning or executing the research.

ACKNOWLEDGMENTS

The authors gratefully acknowledge advice and technical support by Alexandra Brenzel and Anthony Squire from Imaging Center Essen (IMCES). We thank Anja Hasenberg for support with multiphoton imaging and animal management and Katrin Hahnel for preliminary work and advise. The authors would like to thank Dr Anna Malmgren (AstraZeneca, Gothenburg) for her support in providing the AZD5069 compound for exploratory research.

SUPPLEMENTARY MATERIAL

The Supplementary Material for this article can be found online at: https://www.frontiersin.org/articles/10.3389/fimmu.2019.01419/full#supplementary-material

REFERENCES

1. Gentles AJ, Newman AM, Liu CL, Bratman SV, Feng W, Kim D, et al. The prognostic landscape of genes and infiltrating immune cells across human cancers. *Nat Med*. (2015) 21:938–45. doi: 10.1038/nm.3909
2. Shen M, Hu P, Donskov F, Wang G, Liu Q, Du J. Tumor-associated neutrophils as a new prognostic factor in cancer: a systematic review and meta-analysis. *PLoS ONE*. (2014) 9:e98259. doi: 10.1371/journal.pone.0098259
3. Trellakis S, Bruderek K, Dumitru CA, Gholaman H, Gu X, Bankfalvi A, et al. Polymorphonuclear granulocytes in human head and neck cancer: enhanced inflammatory activity, modulation by cancer cells and expansion in advanced disease. *Int J Cancer*. (2011) 129:2183–93. doi: 10.1002/ijc.25892
4. Coffelt SB, Wellenstein MD, de Visser KE. Neutrophils in cancer: neutral no more. *Nat Rev Cancer*. (2016) 16:431–46. doi: 10.1038/nrc.2016.52
5. Deryugina EI, Zajac E, Juncker-Jensen A, Kupriyanova TA, Welter L, Quigley JP. Tissue-infiltrating neutrophils constitute the major *in vivo* source of angiogenesis-inducing MMP-9 in the tumor microenvironment. *Neoplasia*. (2014) 16:771–88. doi: 10.1016/j.neo.2014.08.013
6. Dumitru CA, Fechner MK, Hoffmann TK, Lang S, Brandau S. A novel p38-MAPK signaling axis modulates neutrophil biology in head and neck cancer. *J Leukoc Biol*. (2012) 91:591–8. doi: 10.1189/jlb.0411193
7. Kuang DM, Zhao Q, Wu Y, Peng C, Wang J, Xu Z, et al. Peritumoral neutrophils link inflammatory response to disease progression by fostering angiogenesis in hepatocellular carcinoma. *J Hepatol*. (2011) 54:948–55. doi: 10.1016/j.jhep.2010.08.041
8. Nozawa H, Chiu C, Hanahan D. Infiltrating neutrophils mediate the initial angiogenic switch in a mouse model of multistage carcinogenesis. *Proc Natl Acad Sci USA*. (2006) 103:12493–8. doi: 10.1073/pnas.0601807103
9. Bald T, Quast T, Landsberg J, Rogava M, Glodde N, Lopez-Ramos D, et al. Ultraviolet-radiation-induced inflammation promotes angiotropism and metastasis in melanoma. *Nature*. (2014) 507:109–13. doi: 10.1038/nature13111
10. Shamamian P, Schwartz JD, Pocock BJ, Monea S, Whiting D, Marcus SG, et al. Activation of progelatinase A (MMP-2) by neutrophil elastase, cathepsin G, and proteinase-3: a role for inflammatory cells in tumor invasion and angiogenesis. *J Cell Physiol*. (2001) 189:197–206. doi: 10.1002/jcp.10014
11. Yan HH, Pickup M, Pang Y, Gorska AE, Li Z, Chytil A, et al. Gr-1+CD11b+ myeloid cells tip the balance of immune protection to tumor promotion in the premetastatic lung. *Cancer Res*. (2010) 70:6139–49. doi: 10.1158/0008-5472.CAN-10-0706
12. Dumitru CA, Gholaman H, Trellakis S, Bruderek K, Dominas N, Gu X, et al. Tumor-derived macrophage migration inhibitory factor modulates the biology of head and neck cancer cells via neutrophil activation. *Int J Cancer*. (2011) 129:859–69. doi: 10.1002/ijc.25991
13. Dumitru CA, Bankfalvi A, Gu X, Eberhardt WE, Zeidler R, Lang S, et al. Neutrophils activate tumoral CORTACTIN to enhance

progression of orohypopharynx carcinoma. *Front Immunol*. (2013) 4:33. doi: 10.3389/fimmu.2013.00033
14. Brandau S, Moses K, Lang S. The kinship of neutrophils and granulocytic myeloid-derived suppressor cells in cancer: cousins, siblings or twins? *Semin Cancer Biol*. (2013) 23:171–82. doi: 10.1016/j.semcancer.2013.02.007
15. Gabrilovich DI, Ostrand-Rosenberg S, Bronte V. Coordinated regulation of myeloid cells by tumours. *Nat Rev Immunol*. (2012) 12:253–68. doi: 10.1038/nri3175
16. Lang S, Bruderek K, Kaspar C, Hoing B, Kanaan O, Dominas N, et al. Clinical relevance and suppressive capacity of human myeloid-derived suppressor cell subsets. *Clin Cancer Res*. (2018) 24:4834–44. doi: 10.1158/1078-0432.CCR-17-3726
17. Abram CL, Roberge GL, Hu Y, Lowell CA. Comparative analysis of the efficiency and specificity of myeloid-Cre deleting strains using ROSA-EYFP reporter mice. *J Immunol Methods*. (2014) 408:89–100. doi: 10.1016/j.jim.2014.05.009
18. Faust N, Varas F, Kelly LM, Heck S, Graf T. Insertion of enhanced green fluorescent protein into the lysozyme gene creates mice with green fluorescent granulocytes and macrophages. *Blood*. (2000) 96:719–26.
19. Sasmono RT, Oceandy D, Pollard JW, Tong W, Pavli P, Wainwright BJ, et al. A macrophage colony-stimulating factor receptor-green fluorescent protein transgene is expressed throughout the mononuclear phagocyte system of the mouse. *Blood*. (2003) 101:1155–63. doi: 10.1182/blood-2002-02-0569
20. Acharyya S, Oskarsson T, Vanharanta S, Malladi S, Kim J, Morris PG, et al. A CXCL1 paracrine network links cancer chemoresistance and metastasis. *Cell*. (2012) 150:165–78. doi: 10.1016/j.cell.2012.04.042
21. Ji H, Houghton AM, Mariani TJ, Perera S, Kim CB, Padera R, et al. K-ras activation generates an inflammatory response in lung tumors. *Oncogene*. (2006) 25:2105–12. doi: 10.1038/sj.onc.1209237
22. Lazennec G, Richmond A. Chemokines and chemokine receptors: new insights into cancer-related inflammation. *Trends Mol Med*. (2010) 16:133–44. doi: 10.1016/j.molmed.2010.01.003
23. Vandercappellen J, Van Damme J, Struyf S. The role of CXC chemokines and their receptors in cancer. *Cancer Lett*. (2008) 267:226–44. doi: 10.1016/j.canlet.2008.04.050
24. Chao T, Furth EE, Vonderheide RH. CXCR2-dependent accumulation of tumor-associated neutrophils regulates T-cell immunity in pancreatic ductal adenocarcinoma. *Cancer Immunol Res*. (2016) 4:968–82. doi: 10.1158/2326-6066.CIR-16-0188
25. Highfill SL, Cui Y, Giles AJ, Smith JP, Zhang H, Morse E, et al. Disruption of CXCR2-mediated MDSC tumor trafficking enhances anti-PD1 efficacy. *Sci Transl Med*. (2014) 6:237–67. doi: 10.1126/scitranslmed.3007974
26. Moses K, Brandau S. Human neutrophils: their role in cancer and relation to myeloid-derived suppressor cells. *Semin Immunol*. (2016) 28:187–96. doi: 10.1016/j.smim.2016.03.018
27. Aul R, Patel S, Summerhill S, Kilty I, Plumb J, Singh D. LPS challenge in healthy subjects: an investigation of neutrophil chemotaxis mechanisms involving CXCR1 and CXCR2. *Int Immunopharmacol*. (2012) 13:225–31. doi: 10.1016/j.intimp.2012.04.008
28. Swamydas M, Gao JL, Break TJ, Johnson MD, Jaeger M, Rodriguez CA, et al. CXCR1-mediated neutrophil degranulation and fungal killing promote Candida clearance and host survival. *Sci Transl Med*. (2016) 8:322ra310. doi: 10.1126/scitranslmed.aac7718
29. Liew PX, Kubes P. The neutrophil's role during health and disease. *Physiol Rev*. (2019) 99:1223–48. doi: 10.1152/physrev.00012.2018
30. Mantovani A, Cassatella MA, Costantini C, Jaillon S. Neutrophils in the activation and regulation of innate and adaptive immunity. *Nat Rev Immunol*. (2011) 11:519–31. doi: 10.1038/nri3024
31. Jurcevic S, Humfrey C, Uddin M, Warrington S, Larsson B, Keen C. The effect of a selective CXCR2 antagonist (AZD5069) on human blood neutrophil count and innate immune functions. *Br J Clin Pharmacol*. (2015) 80:1324–36. doi: 10.1111/bcp.12724
32. Uddin M, Betts C, Robinson I, Malmgren A, Humfrey C. The chemokine CXCR2 antagonist (AZD5069) preserves neutrophil-mediated host immunity in non-human primates. *Haematologica*. (2017) 102:e65–8. doi: 10.3324/haematol.2016.152371
33. Kirsten AM, Forster K, Radeczky E, Linnhoff A, Balint B, Watz H, et al. The safety and tolerability of oral AZD5069, a selective CXCR2 antagonist, in patients with moderate-to-severe COPD. *Pulm Pharmacol Ther*. (2015) 31:36–41. doi: 10.1016/j.pupt.2015.02.001
34. Pedersen F, Waschki B, Marwitz S, Goldmann T, Kirsten A, Malmgren A, et al. Neutrophil extracellular trap formation is regulated by CXCR2 in COPD neutrophils. *Eur Respir J*. (2018) 51:1700970. doi: 10.1183/13993003.00970-2017
35. De Soyza A, Pavord I, Elborn JS, Smith D, Wray H, Puu M, et al. A randomised, placebo-controlled study of the CXCR2 antagonist AZD5069 in bronchiectasis. *Eur Respir J*. (2015) 46:1021–32. doi: 10.1183/13993003.00148-2015
36. O'Byrne PM, Metev H, Puu M, Richter K, Keen C, Uddin M, et al. Efficacy and safety of a CXCR2 antagonist, AZD5069, in patients with uncontrolled persistent asthma: a randomised, double-blind, placebo-controlled trial. *Lancet Respir Med*. (2016) 4:797–806. doi: 10.1016/S2213-2600(16)30227-2
37. Watz H, Uddin M, Pedersen F, Kirsten A, Goldmann T, Stellmacher F, et al. Effects of the CXCR2 antagonist AZD5069 on lung neutrophil recruitment in asthma. *Pulm Pharmacol Ther*. (2017) 45:121–3. doi: 10.1016/j.pupt.2017.05.012
38. Di Mitri D, Toso A, Chen JJ, Sarti M, Pinton S, Jost TR, et al. Tumour-infiltrating Gr-1+ myeloid cells antagonize senescence in cancer. *Nature*. (2014) 515:134–7. doi: 10.1038/nature13638
39. Gong L, Cumpian AM, Caetano MS, Ochoa CE, De la Garza MM, Lapid DJ, et al. Promoting effect of neutrophils on lung tumorigenesis is mediated by CXCR2 and neutrophil elastase. *Mol Cancer*. (2013) 12:154. doi: 10.1186/1476-4598-12-154
40. Jamieson T, Clarke M, Steele CW, Samuel MS, Neumann J, Jung A, et al. Inhibition of CXCR2 profoundly suppresses inflammation-driven and spontaneous tumorigenesis. *J Clin Invest*. (2012) 122:3127–44. doi: 10.1172/JCI61067
41. Steele CW, Karim SA, Leach JDG, Bailey P, Upstill-Goddard R, Rishi L, et al. CXCR2 inhibition profoundly suppresses metastases and augments immunotherapy in pancreatic ductal adenocarcinoma. *Cancer Cell*. (2016) 29:832–45. doi: 10.1016/j.ccell.2016.04.014
42. Hasenberg A, Hasenberg M, Mann L, Neumann F, Borkenstein L, Stecher M, et al. Catchup: a mouse model for imaging-based tracking and modulation of neutrophil granulocytes. *Nat Methods*. (2015) 12:445–52. doi: 10.1038/nmeth.3322
43. Williams R, Lee DW, Elzey BD, Anderson ME, Hostager BS, Lee JH. Preclinical models of HPV+ and HPV- HNSCC in mice: an immune clearance of HPV+ HNSCC. *Head Neck*. (2009) 31:911–8. doi: 10.1002/hed.21040
44. Leurs C, Jansen M, Pollok KE, Heinkelein M, Schmidt M, Wissler M, et al. Comparison of three retroviral vector systems for transduction of nonobese diabetic/severe combined immunodeficiency mice repopulating human CD34+ cord blood cells. *Hum Gene Ther*. (2003) 14:509–19. doi: 10.1089/104303403764539305
45. Moses K, Klein JC, Mann L, Klingberg A, Gunzer M, Brandau S. Survival of residual neutrophils and accelerated myelopoiesis limit the efficacy of antibody-mediated depletion of Ly-6G+ cells in tumor-bearing mice. *J Leukoc Biol*. (2016) 99:811–23. doi: 10.1189/jlb.1HI0715-289R
46. Jablonska J, Wu CF, Andzinski L, Leschner S, Weiss S. CXCR2-mediated tumor-associated neutrophil recruitment is regulated by IFN-beta. *Int J Cancer*. (2014) 134:1346–58. doi: 10.1002/ijc.28551
47. Sharma B, Nannuru KC, Varney ML, Singh RK. Host Cxcr2-dependent regulation of mammary tumor growth and metastasis. *Clin Exp Metastasis*. (2015) 32:65–72. doi: 10.1007/s10585-014-9691-0
48. Singh S, Varney M, Singh RK. Host CXCR2-dependent regulation of melanoma growth, angiogenesis, and experimental lung metastasis. *Cancer Res*. (2009) 69:411–5. doi: 10.1158/0008-5472.CAN-08-3378
49. Fridlender ZG, Sun J, Kim S, Kapoor V, Cheng G, Ling L, et al. Polarization of Tumor-Associated Neutrophil (TAN) phenotype by TGF-?: "N1" versus "N2" TAN. *Cancer Cell*. (2009) 16:183–94. doi: 10.1016/j.ccr.2009.06.017
50. Klein JC, Moses K, Zelinskyy G, Sody S, Buer J, Lang S, et al. Combined toll-like receptor 3/7/9 deficiency on host cells results in T-cell-dependent control of tumour growth. *Nat Commun*. (2017) 8:14600. doi: 10.1038/ncomms14600

51. Headley MB, Bins A, Nip A, Roberts EW, Looney MR, Gerard A, et al. Visualization of immediate immune responses to pioneer metastatic cells in the lung. *Nature*. (2016) 531:513–7. doi: 10.1038/nature16985
52. Lohela M, Casbon AJ, Olow A, Bonham L, Branstetter D, Weng N, et al. Intravital imaging reveals distinct responses of depleting dynamic tumor-associated macrophage and dendritic cell subpopulations. *Proc Natl Acad Sci USA*. (2014) 111:E5086–95. doi: 10.1073/pnas.1419899111
53. Antonio N, Bonnelykke-Behrndtz ML, Ward LC, Collin J, Christensen IJ, Steiniche T, et al. The wound inflammatory response exacerbates growth of pre-neoplastic cells and progression to cancer. *EMBO J*. (2015) 34:2219–36. doi: 10.15252/embj.201490147
54. Rosowski EE, Huttenlocher A. Neutrophils, wounds, and cancer progression. *Dev Cell*. (2015) 34:134–6. doi: 10.1016/j.devcel.2015.07.005
55. Del Prete A, Schioppa T, Tiberio L, Stabile H, Sozzani S. Leukocyte trafficking in tumor microenvironment. *Curr Opin Pharmacol*. (2017) 35:40–7. doi: 10.1016/j.coph.2017.05.004
56. Zhou SL, Zhou ZJ, Hu ZQ, Huang XW, Wang Z, Chen EB, et al. Tumor-associated neutrophils recruit macrophages and T-regulatory cells to promote progression of hepatocellular carcinoma and resistance to sorafenib. *Gastroenterology*. (2016) 150:1646–58 e1617. doi: 10.1053/j.gastro.2016.02.040
57. Höing B, Kanaan O, Altenhoff P, Petri R, Thangavelu K, Schluter A, et al. Stromal versus tumoral inflammation differentially contribute to metastasis and poor survival in laryngeal squamous cell carcinoma. *Oncotarget*. (2018) 9:8415–26. doi: 10.18632/oncotarget.23865
58. Feng Z, Bethmann D, Kappler M, Ballesteros-Merino C, Eckert A, Bell RB, et al. Multiparametric immune profiling in HPV- oral squamous cell cancer. *JCI Insight*. (2017) 2:93652. doi: 10.1172/jci.insight.93652
59. Mezheyeuski A, Bergsland CH, Backman M, Djureinovic D, Sjoblom T, Bruun J, et al. Multispectral imaging for quantitative and compartment-specific immune infiltrates reveals distinct immune profiles that classify lung cancer patients. *J Pathol*. (2017) 244:421–31. doi: 10.1002/path.5026
60. Andzinski L, Wu CF, Lienenklaus S, Kroger A, Weiss S, Jablonska J. Delayed apoptosis of tumor associated neutrophils in the absence of endogenous IFN-beta. *Int J Cancer*. (2015) 136:572–83. doi: 10.1002/ijc.28957
61. Wang J, Hossain M, Thanabalasuriar A, Gunzer M, Meininger C, Kubes P. Visualizing the function and fate of neutrophils in sterile injury and repair. *Science*. (2017) 358:111–6. doi: 10.1126/science.aam9690
62. Boppana NB, Devarajan A, Gopal K, Barathan M, Bakar SA, Shankar EM, et al. Blockade of CXCR2 signalling: a potential therapeutic target for preventing neutrophil-mediated inflammatory diseases. *Exp Biol Med*. (2014) 239:509–18. doi: 10.1177/1535370213520110
63. Eash KJ, Greenbaum AM, Gopalan PK, Link DC. CXCR2 and CXCR4 antagonistically regulate neutrophil trafficking from murinebone marrow. *J Clin Investig*. (2010) 120:2423–31. doi: 10.1172/JCI 41649
64. Waugh DJ, Wilson C. The interleukin-8 pathway in cancer. *Clin Cancer Res*. (2008) 14:6735–41. doi: 10.1158/1078-0432.CCR-07-4843
65. Powell D, Tauzin S, Hind LE, Deng Q, Beebe DJ, Huttenlocher A. Chemokine signaling and the regulation of bidirectional leukocyte migration in interstitial tissues. *Cell Rep*. (2017) 19:1572–85. doi: 10.1016/j.celrep.2017.04.078
66. Glodde N, Bald T, van den Boorn-Konijnenberg D, Nakamura K, O'Donnell JS, Szczepanski S, et al. Reactive neutrophil responses dependent on the receptor tyrosine kinase c-MET limit cancer immunotherapy. *Immunity*. (2017) 47, 789–802 e789. doi: 10.1016/j.immuni.2017.09.012
67. Lammermann T, Afonso PV, Angermann BR, Wang JM, Kastenmuller W, Parent CA, et al. Neutrophil swarms require LTB4 and integrins at sites of cell death *in vivo*. *Nature*. (2013) 498:371–5. doi: 10.1038/nature 12175
68. Evrard M, Kwok IWH, Chong SZ, Teng KWW, Becht E, Chen J, et al. Developmental analysis of bone marrow neutrophils reveals populations specialized in expansion, trafficking, and effector functions. *Immunity*. (2018) 48:364–79. doi: 10.1016/j.immuni.2018.02.002
69. Thompson S, Martinez-Burgo B, Sepuru KM, Rajarathnam K, Kirby JA, Sheerin NS, et al. Regulation of chemokine function: the roles of GAG-binding and post-translational nitration. *Int J Mol Sci*. (2017) 18:E1692. doi: 10.3390/ijms18081692
70. Ravindran A, Sawant KV, Sarmiento J, Navarro J, Rajarathnam K. Chemokine CXCL1 dimer is a potent agonist for the CXCR2 receptor. *J Biol Chem*. (2013) 288:12244–52. doi: 10.1074/jbc.M112.443762

Conflict of Interest Statement: AGö is a consultant for and has equity interest in Evox Therapeutics Ltd., Oxford, UK. MU is an employee of AstraZeneca and holds shares in AstraZeneca.

The remaining authors declare that the research was conducted in the absence of any commercial or financial relationships that could be construed as a potential conflict of interest.

frontiers in Immunology

METHODS
published: 27 August 2019
doi: 10.3389/fimmu.2019.02036

Turning Up the Heat: Local Temperature Control During *in vivo* Imaging of Immune Cells

David Ahl, Olle Eriksson, John Sedin, Cédric Seignez, Emil Schwan, Johan Kreuger, Gustaf Christoffersson and Mia Phillipson**

Department of Medical Cell Biology, Uppsala University, Uppsala, Sweden

Intravital imaging is an invaluable tool for studying the expanding range of immune cell functions. Only *in vivo* can the complex and dynamic behavior of leukocytes and their interactions with their natural microenvironment be observed and quantified. While the capabilities of high-speed, high-resolution confocal and multiphoton microscopes are well-documented and steadily improving, other crucial hardware required for intravital imaging is often developed in-house and less commonly published in detail. In this report, we describe a low-cost, multipurpose, and tissue-stabilizing *in vivo* imaging platform that enables sensing and regulation of local tissue temperature. The effect of tissue temperature on local blood flow and leukocyte migration is demonstrated in muscle and skin. Two different models of vacuum windows are described in this report, however, the design of the vacuum window can easily be adapted to fit different organs and tissues.

Keywords: intravital microscopy, skin, blood flow, leukocytes, vacuum window, confocal microscopy

OPEN ACCESS

Edited by:
Connie Wong,
Monash University, Australia

Reviewed by:
Rohit Jain,
Centenary Institute Australia, Australia
Denise Carmona Cara,
Federal University of Minas Gerais, Brazil

****Correspondence:***
Gustaf Christoffersson
gustaf.christoffersson@mcb.uu.se
Mia Phillipson
mia.phillipson@mcb.uu.se

Specialty section:
This article was submitted to Antigen Presenting Cell Biology, a section of the journal Frontiers in Immunology

Received: *14 June 2019*
Accepted: *12 August 2019*
Published: *27 August 2019*

Citation:
Ahl D, Eriksson O, Sedin J, Seignez C, Schwan E, Kreuger J, Christoffersson G and Phillipson M (2019) Turning Up the Heat: Local Temperature Control During in vivo Imaging of Immune Cells. Front. Immunol. 10:2036. doi: 10.3389/fimmu.2019.02036

INTRODUCTION

Microscopy has a long history as an important tool in life science research. In recent decades, more advanced microscope technologies have been steadily emerging, providing researchers with a plethora of options for visualization of complex biological processes. Intravital microscopy provides unique information about cellular behavior and functions within the living animal. With the invention of the confocal microscope (1) and its ability to optically section the imaged tissue, the possibility of imaging cell-cell interactions *in vivo* was greatly improved. Further technological advances allowed for the introduction of the multiphoton microscope, which improved some of the limiting aspects of confocal microscopy, such as phototoxicity and penetration depth. While these microscopy techniques enable high temporal and spatial resolution imaging, other aspects of *in vivo* imaging remain challenging, and impact the quality of the results. The access to and preparation of the target tissue should enable maintained regulation of homeostasis including stable blood perfusion, innervation and temperature, which otherwise will influence the observed biological processes. In addition, stabilization of the target tissue is crucial for high-resolution imaging, and even very slight movements can prevent acquisition of usable image data. When performing imaging in anesthetized laboratory animals, the breathing of the animal is the most common cause of movement artifacts, also in tissues distal to the lungs. Devices using vacuum for immobilization of the lungs and other organs have been previously described, but has required custom-made metallic parts to function, somewhat increasing the threshold for most researchers to acquire such systems (2–5).

Maintaining proper physiological conditions while exposing the tissue to the microscope objective is important if the benefits of studying biological processes *in vivo* are to be retained. While standard practice is to carefully control the body temperature of the animal with a whole-body heating pad, local tissue temperature of the imaged area is rarely reported. Attaching the tissue to any kind of stabilizing device or imaging window may further increase the risk of heat loss when the ambient-tempered device is in physical contact with the tissue and may act as a heat-sink. Interestingly, the importance of local temperature control when studying immune cell behavior was recently highlighted in a paper by Lin et al. (6) demonstrating that T-cell trafficking and bacterial clearance were affected by febrile temperatures.

In an effort to overcome these challenges, we here utilize 3D printing together with commercially available electronic components to produce a versatile and low-cost *in vivo* imaging platform. The platform consists of a temperature-regulated vacuum window, a vacuum window holder and an operating table with magnetic mounting points. We also present two proof-of-concept applications for the platform: The study of blood flow using heat-induced hyperemia and the effect of local tissue temperature on leukocyte migration.

MATERIALS AND METHODS

3D-Printing

All 3D-printed parts were designed in Fusion 360 (Autodesk Inc., San Rafael, CA, USA). The vacuum window holder and the vacuum windows were printed with a Form 2 3D-printer (Formlabs, Somerville, MA, USA) with 50 μm layers. The vacuum window holder was printed in clear resin (Formlabs). The vacuum windows were printed in Dental SG resin (Formlabs) and post-processed according to Formlabs guidelines to reach biocompatibility. The operating table was 3D-printed in black PLA (polylactic acid) with an Ultimaker 3 Extended 3D printer (Ultimaker B.V., Geldermalsen, The Netherlands) using a 0.8 mm nozzle and 200 μm layers with the ironing feature (Neosanding) enabled when preparing toolpaths in Ultimaker Cura 4.0.0 (Ultimaker). All STL files are available in the **Supplementary Data**.

Magnets

The magnets inserted in the base of the operating table and the vacuum window holder were neodymium disk magnets, of N42 grade with nickel plating and a diameter of 15 mm and a height of 8 mm (Webcraft GmbH, Gottmadingen, Germany).

Electronic Components

The electronic control unit was built using readily available standard components. Specifically, an Arduino UNO Rev3 microcontroller was connected to a MOSFET IRF520 module (Velleman, Gavere, Belgium), a 100 kΩ NTC bead thermistor (NXFT15WF104FA2B100, Murata Electronics, North America) and a 32 AWG nichrome resistance wire.

Animals

Male C57Bl/6J mice [30–35 g (Taconic, Denmark)], male $CX_3CR1^{GFP/+}$/NG2DsRedBAC F1 hybrid mice [25–30 g [B6.129P-Cx3cr1tm1Litt/J, The Jackson Laboratory, (7)] and (Tg(Cspg4-DsRed.T1)1Akik, The Jackson Laboratory, (8)] were used. All animals had access to tap water and pelleted food *ad libitum* throughout the experimental study. For blood flow measurements, fur was removed by shaving the right hind limb of the mice 1 day prior to the experiments. For intravital imaging, the following antibodies were administered through an injection in the tail vein approximately 30 min before start of imaging to visualize leukocytes and blood vessels: anti-mouse Ly6G mAb conjugated to Brilliant Violet 421, anti-mouse CD31 mAb conjugated to Alexa Flour Dye 647. All experiments were approved by the Regional Animal Ethics Committee in Uppsala, Sweden, under the ethical permit number C81/14.

Surgical Preparation, Blood Flow Measurements, IR, and Intravital Imaging

Mice were anesthetized by spontaneous inhalation of isoflurane (Abbott Scandinavia, Sweden) diluted 1.8–2.6 % in a mixture of air and oxygen. The animals were immediately placed on the operating table described in this article, with a heating pad to control and maintain body temperature. IR temperature imaging was performed using a FLIR A40 thermal imaging camera and the FLIR Report Studio software (FLIR, Wilsonville, OR, USA). For the blood flow measurements, the left jugular vein was catheterized with a PE-10 cannula for administration of L-NAME and saline, and the right carotid artery was catheterized and connected to a BP transducer (MLT0380/D) and a Bridge Amplifier (ML221). Blood pressure data was recorded at 1 kHz sampling rate by a PowerLab 4/3 and analyzed in LabChart 7 Pro software (AD Instruments, Oxford, UK). Blood flow was measured using Laser Speckle Contrast Analysis (785 nm laser, 20 μm resolution, PeriCam HR PSI System, Perimed). For intravital imaging, a ∼10 × 10 mm patch of the abdominal skin was carefully dissected from the mouse and turned upside down, creating a skin flap still connected to the mouse abdomen. The vacuum window, described in this article, was covered with an imaging-grade 13 mm No. 1.5 glass coverslip held in place with vacuum grease, where after the inside of the mouse abdominal skin was carefully immobilized using the vacuum. Prior to attachment, the coverslip had been prepared with a 0.5 mm^3 agarose gel (2% in Hanks balanced salt solution, Sigma-Aldrich) containing MIP-2 (0.5μM), (R&D Systems) to induce chemotaxis of leukocytes.

The table was then mounted on a Scientifica MMBP stage connected to a Leica SP8 point-scanning confocal microscope with a Leica HC Fluotar L 25×/0.95-W VISIR objective. Experiments were conducted in a room temperature of 23.5±°C.

Analysis

Data is presented as mean ± SEM and data analysis was performed using GraphPad Prism 6 (GraphPad Software, La Jolla, CA, USA). Student's two-tailed *t*-test was used analyzing two groups and $p < 0.05$ was considered significant.

Intravital time-lapse movies were processed using the Fiji distribution of ImageJ and the TrackMate plugin (9–11).

RESULTS

The purpose of the vacuum window imaging platform is to immobilize tissue from an anesthetized animal to enable *in vivo* high resolution imaging, primarily using an upright confocal or multi photon microscope. In addition, maintained tissue temperature is essential when studying biological parameters. To allow for this, as well as to enable the study of the effects of locally altered temperature, the vacuum window described here was designed to provide both regulation and readout of tissue temperature.

At the center of the *in vivo* imaging platform is a 3D-printed vacuum window (**Figure 1A**). The window was connected to a vacuum source (**Figure 1B**). The negative pressure was regulated through a coarse adjustment valve (**Figure 1C**) and fine-tuned using a negative pressure gauge (**Figure 1D**) and a manually regulated vacuum wastegate (**Figure 1E**). A vacuum trap (**Figure 1F**) was used to protect the vacuum source. Further, the vacuum window was connected to an Arduino microcontroller (**Figure 1G**) through a 4-wire cable, enabling reading of temperature data as well as controlling temperature through a heating wire inside the vacuum window.

Temperature-Regulated Vacuum Window

To enable imaging of tissue, the vacuum window was designed with a circular opening in the head of the window (**Figure 2A**). Importantly, the flat top of the 13 mm vacuum window head serves as the attachment surface for a round glass coverslip (**Figure 2B,** green area), which is hermetically sealed to the window frame using a thin layer of vacuum grease. The vacuum window head was constructed so that it together with the coverslip constitutes the upper half of a vacuum connected chamber (**Figure 2C**). When vacuum is applied through the vacuum channel (**Figure 2D**), tissue positioned below the vacuum window head will be pulled upward and held against the coverslip, enabling imaging through the coverslip. In our experiments, 5–20 mbar was enough negative pressure to get stable attachment of the tissue to the coverslip.

To enable registration of temperature, a thermistor channel (**Figure 2E**) was positioned in the vacuum window, allowing entry of the thermistor wires in the vacuum window body and positioning of the thermistor head as close to the window opening as possible. This channel was designed to also have an opening close to the head of the window to facilitate insertion of the thermistor during assembly. Heat delivery to the window was provided by a 32 AWG nichrome resistance wire inserted in a heating channel in the vacuum window (**Figure 2F**). The heating channel openings were positioned on both sides of the thermistor channel in the vacuum window body, while the channel itself circumvents the vacuum window opening in the head to enable heat transfer to the imaged area when a current is applied to the resistance wire. During assembly, the nichrome wire was first inserted into a PTFE (OD/ID: 0.9 mm/0.4 mm) tube to facilitate insertion into to the heating channel. After assembly of both the thermistor and heating wire, all channel openings were sealed with a cyanoacrylate adhesive. To allow for magnetic attachment to the holder, the top of the vacuum window body was designed with a cutout for a round steel plate (15 × 2 mm) that was glued in place during assembly (**Figure 2G**).

The vacuum window was 3D-printed using a biocompatible resin using a Form 2 printer. STL files for printing the window can be found in the **Supplementary File 1**. Notably, the vacuum window design can easily be adapted to fit a specific organ of interest.

Electronic Control Unit

For measuring and regulating tissue temperature, a control unit was built using an Arduino Uno Rev3 microcontroller (**Figure 3A**) powered by a USB cable connected to a computer (**Figure 3B**). The USB interface was also used for logging thermistor data and setting target temperature. Heating wire power was provided through a MOSFET module connected to a standard computer power supply unit delivering 3.3 V (**Figure 3C**). The vacuum window (**Figure 3D**) was connected to the control unit using a 4-wire cable (**Figure 3E**) with screw terminal connectors in each end to attach the four wires.

The computer connected to the control unit through the USB interface (**Figure 3B**) was running the Arduino IDE software,

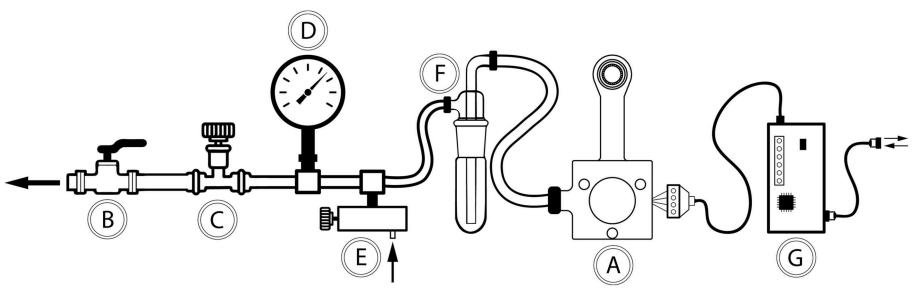

FIGURE 1 | Schematic drawing of the components in the vacuum window *in vivo* imaging platform. **(A)** Vacuum window, **(B)** connection to central vacuum system (ON/OFF), **(C)** coarse vacuum adjustment valve, **(D)** negative pressure gauge, **(E)** vacuum wastegate for fine tuning of negative pressure, **(F)** vacuum trap, **(G)** Arduino microcontroller.

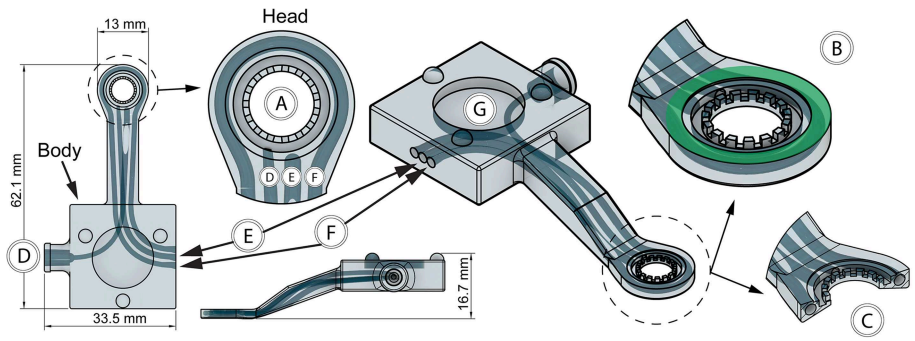

FIGURE 2 | Features of the 3D-printed vacuum window. **(A)** Window opening, **(B)** coverslip attachment surface (green), **(C)** vacuum window head cross section, **(D)** vacuum channel, **(E)** thermistor channel, **(F)** heating wire channel, **(G)** steel plate cutout for kinematic mount.

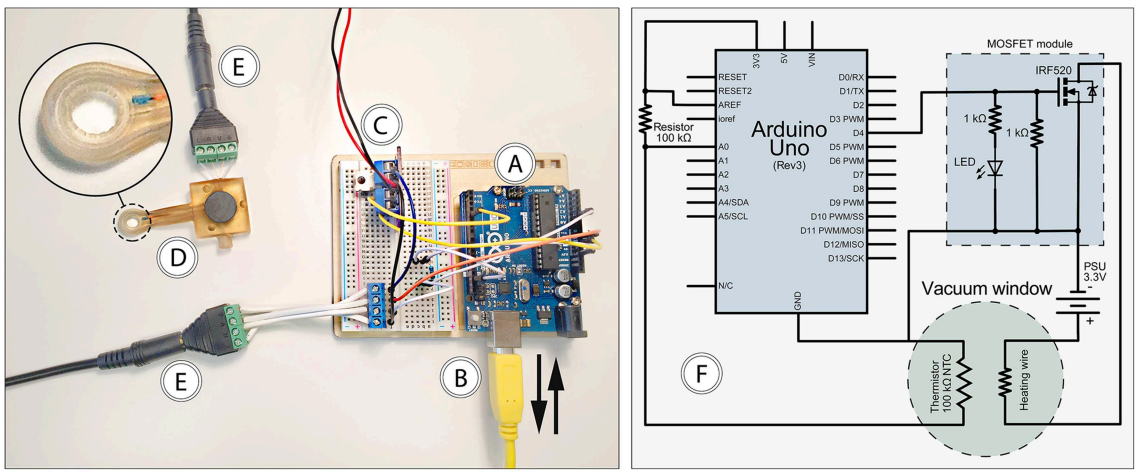

FIGURE 3 | Features of the electronic control unit. **(A)** Arduino Uno, **(B)** USB connection to computer, **(C)** 3.3 V power supply and MOSFET module, **(D)** vacuum window, **(E)** 4-wire cable, **(F)** circuit diagram.

which provided continuous logging of thermistor temperature as well as setting target temperature for the control loop. The control loop was designed so that it reads the temperature of the thermistor, compares it with the set target temperature, and adjusts power output to the heating wire using a PID regulator. ON/OFF functionality of the heating system was achieved with the power switch of the power supply unit. A complete circuit diagram of the control unit is provided in **Figure 3F**. The code for the microcontroller can be found in the **Supplementary File 2**.

Holder and Operating Table

In order to achieve stable immobilization of tissue attached to the vacuum window, a vacuum window holder (to be mounted on a steel plate) and an operating table with magnet attachment points was designed and 3D-printed. STL and Gcode files for printing the holder and operating table can be found in the **Supplementary File 1**.

The operating table (printed in PLA using an Ultimaker 3 Extended 3D printer) had cutouts for a heating pad (**Figure 4A**), M5 thread inserts for mounting of the table on a Scientifica stage (**Figure 4B**), and 15 mm round neodymium magnets (**Figure 4C**). Thread inserts and magnets were glued in place during assembly.

The vacuum window holder was printed in clear resin using a Form 2 printer. After assembly, the height adjustment screw in the base of the holder (**Figure 4D**) can be used to position the vacuum window vertically (**Figure 4E**). The mounting part of the holder consists of a kinematic mount that fits to the vacuum window body. Attachment of the window to the holder is achieved using a neodymium magnet (**Figure 4F**) on the mount and a steel plate in the vacuum window (**Figures 2G**, **4G**).

The height-adjustable holder was mounted on a 2 mm steel plate (**Figure 4H,** red area). Together with the magnetic attachment points on the operating table and the vacuum window, this constitutes a stable tissue immobilizing platform while at the same time providing great flexibility in XYZ positioning of the imaging window (**Figure 4I**). The neodymium magnets also function as attachment points for any other steel plate mounted peripherals, such as holders for tubing (**Figure 5**).

Figure 5 depicts the complete setup mounted with additional magnetically attached holders for tubing on a Scientifica stage for imaging with an upright Leica SP8 confocal microscope.

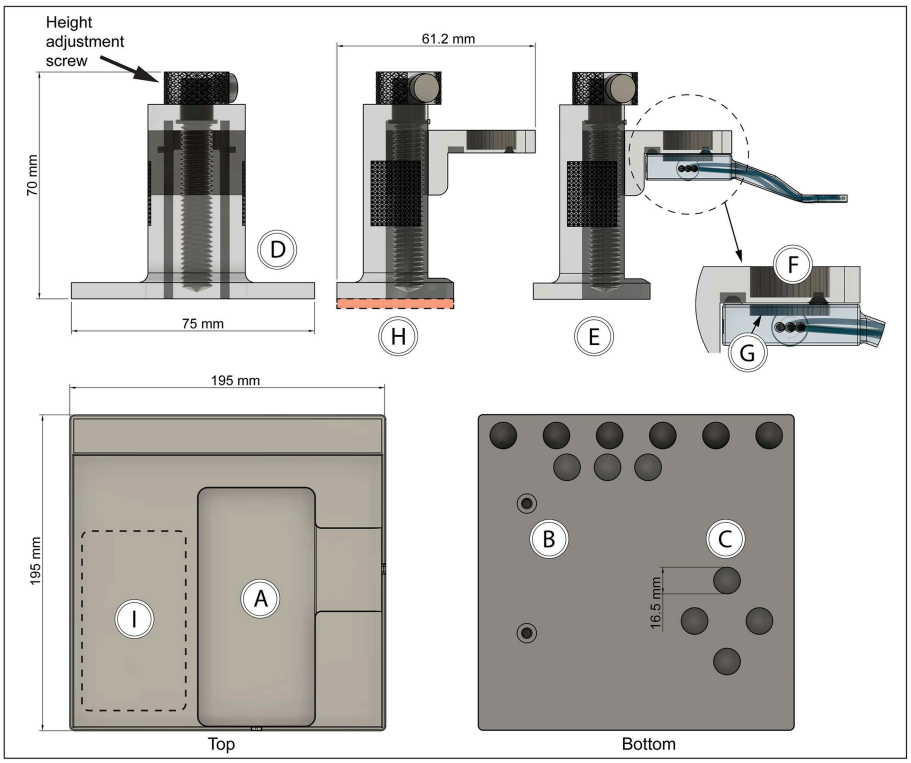

FIGURE 4 | Vacuum window holder and operating table with magnetic attachment points **(A)** Heating pad cutout, **(B)** M5 thread inserts, **(C)** neodymium magnet cutouts, **(D)** height-adjustable vacuum window holder—front view, **(E)** holder side view with vacuum window attached, **(F)** neodymium magnet position on holder, **(G)** steel plate position in vacuum window, **(H)** height-adjustable vacuum window holder—side view, red area indicates position of steel plate, **(I)** holder attachment area on table.

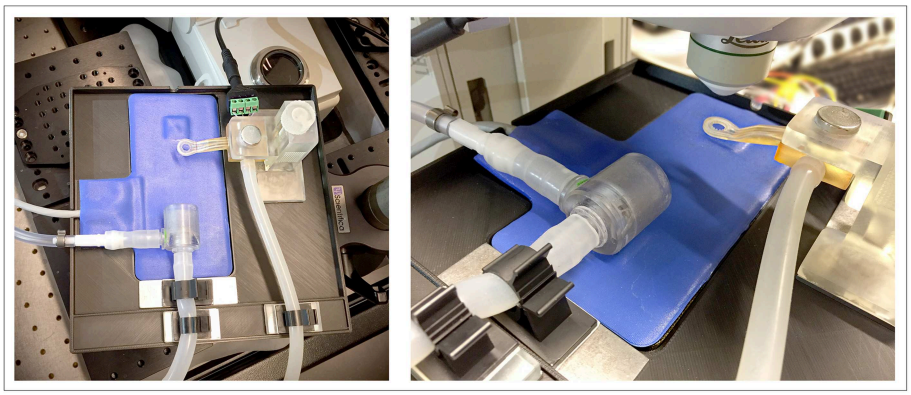

FIGURE 5 | Complete setup of the 3D-printed *in vivo* imaging platform mounted on a Scientifica stage on the Leica SP8 confocal microscope, shown together with heating pad, anesthetic mask and metal plate mounted holders for tubing.

In vivo Temperature Control Dynamics

The thermistor embedded in the vacuum window head was positioned as close as possible to the underlying tissue. However, during heating, the temperature in window opening is expected to be lower due to the distance from the heating wire circumventing the window. In order to elucidate the relationship between the temperature reported by the thermistor and the temperature inside the window viewing area below the coverslip, a set of experiments was performed using a FLIR A40 thermal imaging camera. By setting up temperature measuring points in the acquired IR images using the FLIR Report Studio software, temperature readouts in positions inside and surrounding the viewing area were recorded.

The dynamics of local tissue temperature regulation *in vivo* was tested using two different temperature setpoints with the vacuum window attached to the inside of an abdominal skin flap of an anesthetized C57Bl/6J mouse. First, a physiological tissue temperature of 37°C was used as the setpoint for the temperature control loop. As shown in **Figure 6A**, an overshoot, most pronounced at the window edge containing the heating wire (**Figure 6A,** red line), up to 40°C was briefly reached, followed by an undershoot. After 10 min, a stable temperature of approximately 36°C was reached in the center of the imaging window. The positions of the IR temperature measurement points are shown in **Figure 6B**.

Secondly, a supraphysiological tissue temperature of 42°C was set for the control loop (**Figure 6C**). This setpoint did not produce an overshoot, most likely due to the fact that it appeared to be close to the maximum temperature possible with a 3.3 V power source. This is supported by the power readout (**Figure 6C,** yellow line) from the control unit, showing that maximum power was delivered for the first 5 min, after which power started to be reduced by the control loop. After 10 min, the IR temperature reading inside the window stabilized at approximately 40°C. The positions of the IR temperature measurement points are shown in **Figure 6D**.

In these experiments, both the embedded thermistor and the IR camera reported that the initial tissue temperature inside the window was lower than physiological temperature at around 32–33°C, while the shaved skin of the mouse outside of the window maintained approximately 36°C (**Figures 6A–D**, gray line and marker), indicating that the vacuum window serves as a heat-sink when the heating is turned off and room temperature is lower than skin temperature.

L-NAME Attenuates Heat-Induced Hyperemia in Mouse Hind Limb Skin and Underlying Muscle

Given the ability of the vacuum window presented here to manipulate local tissue temperature, we wanted to test this function in an experimentally relevant setting; the study of heat-induced hyperemia. Heat-induced hyperemia can be used to study functional blood flow regulation, and has previously been achieved by applying heat to an entire limb through tubing containing pre warmed water to increase skin temperature 10°C. The temperature-regulated vacuum window developed here could provide researchers with a tool for more controlled experimental settings, including more precise readout of local tissue temperature. To this end we conducted a set of experiments in anesthetized C57Bl/6J mice using a Laser Speckle Contrast Analysis system, which provides quantitative image data of tissue blood flow. Fur was removed from the hind limb of mice 1 day prior to the day of the experiment. Blood flow was measured with the vacuum window head placed on the exposed skin of the hind limb, and the window opening was selected as the measurement area (**Figure 7A**). Continuous blood flow measurements were performed for 130 min during which the vacuum window heat was turned on with a setpoint of 37°C for two separate periods of 20 min each. Nitric oxide produced by the endothelial nitric oxide synthase (eNOS) is known to regulate blood flow (12, 13). The L-arginine analog L-NAME (N(ω)-nitro-L-arginine methyl ester) is a widely used eNOS inhibitor (14), thereby affecting the ability of vasculature to dilate. After the first heating and a cool-down period of 20 min, a bolus dose (10 mg/kg) of L-NAME was administered, after which continuous infusion (3 mg/ml at 0.35 ml/h) of L-NAME was initiated (**Figure 7B**). The mean blood flow (perfusion units) during 15 min before each heating cycle was considered as the baseline value of blood flow, whereas the plateau phase of the blood flow curve during the heating was considered the hyperemic blood flow value. The difference (delta PFU) between baseline and hyperemia provides a readout of the ability of the animal to regulate blood flow in response to heat. Arterial blood pressure was monitored throughout the experiments (**Figure 7C**). Heating the vacuum window to 37°C produced a marked increase in local blood flow, whereas L-NAME attenuated this increase (**Figure 7D**). These results demonstrate the possibility of using the temperature-regulated vacuum window as a tool for studying functional blood flow.

Leukocyte Migration Speed at Different Tissue Temperatures

The main purpose of the temperature-regulated vacuum window is to provide researchers with a tissue stabilizing tool for *in vivo* imaging that gives the experimenter control over local tissue temperature. To investigate the effects of different tissue temperatures on leukocyte migration, we conducted experiments in anesthetized mice with fluorescently labeled leukocytes.

Neutrophils were immunostained with Ly6G mAb conjugated to Brilliant Violet 421 in $CX_3CR1^{GFP/+}$/NG2DsRedBAC mice, where GFP is expressed by CX_3CR1^{+} cells (predominantly monocytes, macrophages and dendritic cells), and DsRed marks vascular mural cells (pericytes) to provide more detailed information about the vascular morphology. In the imaging data, pericytes (red) can be seen covering arterial vasculature and as smaller dots along capillaries, but are absent on the venous vasculature. Blood vessels were immunostained with CD31 mAb conjugated to Alexa Flour Dye 647.

To induce leukocyte recruitment from the vasculature, an agarose gel containing MIP-2 was attached to the coverslip of the vacuum window before it was lowered onto the inside of an abdominal skin flap. The appearance of immunostained tissue attached to the vacuum window coverslip is demonstrated in **Figure 8**, showing a tile scan that covers the complete window opening of the oval vacuum window. The teeth of the inner window edge are visible (**Figure 8A**) and mark the border between the mouse skin and the plastic material of the window. The MIP-2 gel is also visible as a dark shape blocking light from the stained tissue (**Figure 8B**). A Leica SP8 confocal microscope was used to acquire time-lapse recordings of the migrating leukocytes while the vacuum window was cycled ON-OFF in 20 min intervals with a supraphysiological temperature setpoint of 42°C.

Leukocytes were tracked using the TrackMate plugin for ImageJ (**Figure 9A**), and the speed of the cells was plotted

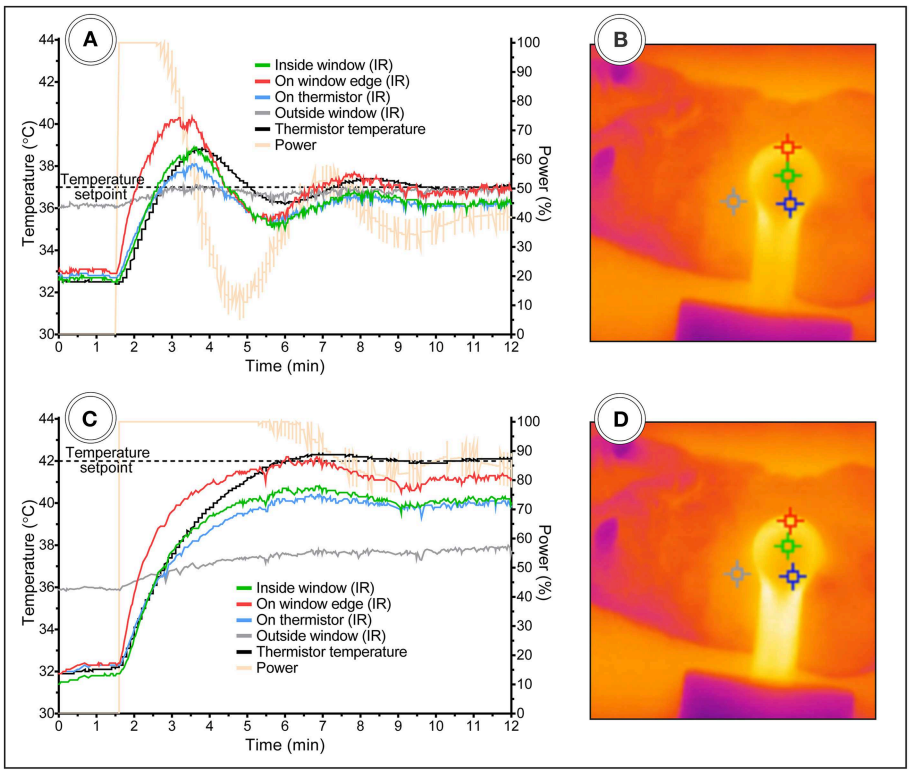

FIGURE 6 | Vacuum window temperature control dynamics in anesthetized mice with skin flap attached to window. Temperature setpoint at **(A)** 37°C and **(C)** 42°C. **(B,D)** Shows the corresponding IR images with temperature measurement points.

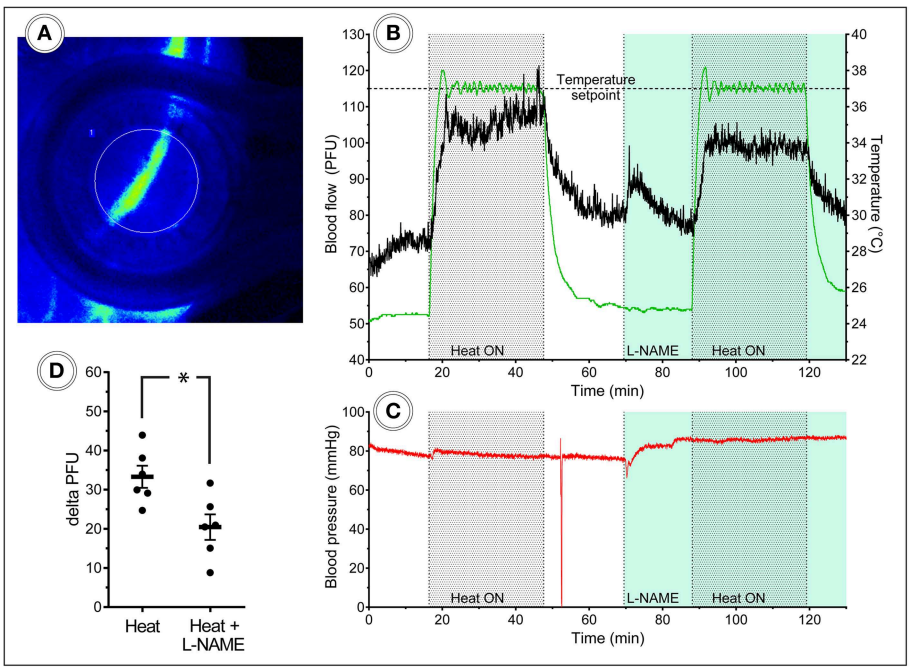

FIGURE 7 | Laser speckle blood flow imaging in the mouse hind limb. **(A)** Laser speckle contrast image of a mouse hind limb with heat turned off, **(B)** 130 min continuous blood flow and **(C)** arterial blood pressure measurements, including two heat challenges and L-NAME administration, **(D)** heat-induced hyperemia is attenuated after L-NAME administration ($n = 6$).

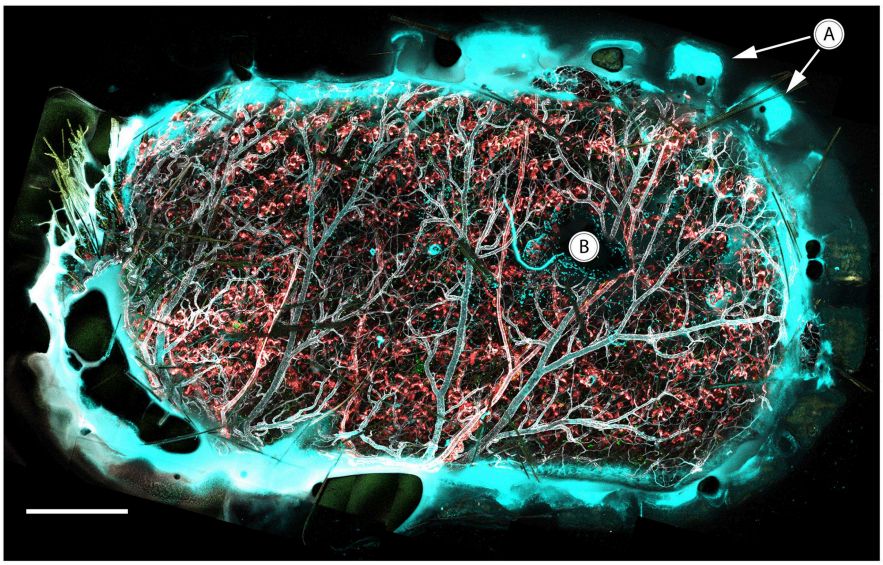

FIGURE 8 | *In vivo* confocal tile scan of the complete vacuum window opening attached to immunostained mouse skin. **(A)** Teeth of the window border lining the tissue, **(B)** MIP-2 gel positioned between the coverslip and underlying tissue. Color code: Ly6G–cyan, CX_3CR1–green, CD31–gray, NG2–red. Scale bar is 400 μm.

for the duration of the experiments. The tracking of cells in these data sets was performed so that only migrating cells were included in the analysis. Time-lapse movies and images visualizing cell tracking from the experiments are available in the **Supplementary Files 3**–**7**. Neutrophil migration speed was increased during the periods of heating (**Figures 9B,C**), while migrating CX_3CR1 cells showed a less clear response to heat (**Figure 9D**), indicating that temperature control is of importance when doing intravital imaging of leukocytes. The NG2-positive cells were not visibly affected by the heat-cycling in these experiments.

DISCUSSION

Here we present the most complete and easily accessible solution to date for enabling *in vivo* imaging of virtually any organ of anesthetized mice. This was achieved by further development of previous designs (3, 4) of vacuum windows to be able to monitor and control temperature of the imaged tissue. The vacuum window was designed with a magnetic mounting system that makes pre-experimental set up of the platform easy.

The readily available and low-cost electronic components together with the supplementary code for the Arduino microcontroller provides the researcher with an easily assembled bare-bones control unit. While the specific electronic parts used in this paper will produce an easy-to-use functional system, most parts can be substituted with alternative components, e.g., in order to achieve a more compact setup and fit it in a small chassis. Addition of fuses and diodes can also easily be made to provide short-circuit protection if required. To further facilitate ease of use of the system, we chose to include a complete operating table in the platform. The neodymium magnets embedded in the bottom of the table provide an attachment area where the vacuum window holder, or any other steel-mounted peripheral device, can be freely positioned while still maintaining excellent stability. This gives the platform great flexibility, allowing researchers to use the temperature-regulated vacuum window at any position of the anesthetized mouse suitable for their specific application. In addition, magnets embedded in the top edge of the table allows for attachment of steel-mounted holders to secure tubing for vacuum and anesthesia. The emergence of low-cost, commercially available 3D printers has led to massive growth of the 3D printing market (15). The scientific community has embraced the opportunity to create custom-built laboratory tools for a wide range of applications (16–19). The *in vivo* imaging platform described in this paper was 3D printed, and all STL files are available for download in order to ease use of the design.

The test of the temperature regulating ability of the vacuum window demonstrated that it is possible to attain stable temperature using both physiological and supraphysiological setpoints within 10 min of operation. Presumably, this time period can be shortened if the vacuum window is pre-heated instead of starting from ambient temperature. Of note is also that without heating turned on, the temperature reported by the IR measurement point inside of the viewing area was significantly lower (32–33°C) than that of the shaved skin of the mouse (36°C). This indicates that the window itself might be acting as a heat sink, lowering temperature in the observed tissue, further emphasizing the importance of being able to control temperature in the vacuum window in order to maintain physiological conditions during imaging. These experiments also provide insight in the relationship between thermistor temperature and tissue temperature. At a temperature setpoint of 37°C, tissue temperature was approximately one degree lower than the thermistor reading, and at a 42°C setpoint, tissue temperature was two degrees lower. We believe that this is due to the fact that the thermistor is positioned closer to the heating

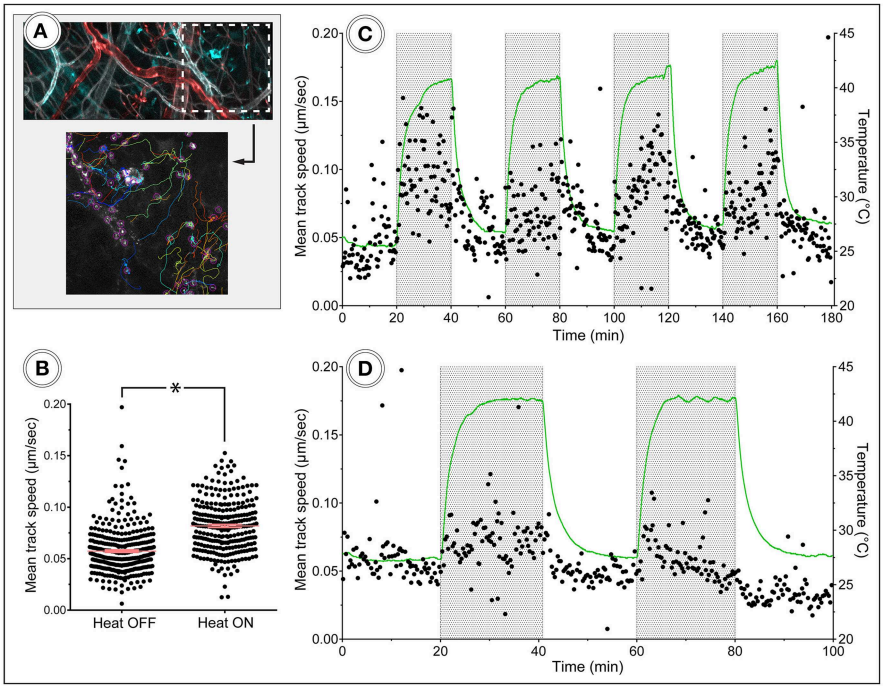

FIGURE 9 | *In vivo* tracking of leukocyte migration during heat challenge. **(A)** Shows a frame from the corresponding time-lapse movie and tracking data. Color code: Ly6G–cyan, CD31–gray, NG2–red. **(B)** Migration speed of neutrophils was increased during heating periods compared to periods without heating. **(C,D)** Show track speed of neutrophils and CX_3CR1 positive cells, respectively, plotted over time with heating periods indicated by gray areas.

wire than to the center of the vacuum window opening, which leads to poorer heat transfer from the wire to the tissue in the center of the window than to the thermistor. Thus, with heating activated, heat transfer becomes a relevant factor which results in 3–5% lower tissue temperature compared to the setpoint of the vacuum window. This difference appears to increase with setpoint temperature. If the temperature regulating function of the vacuum window is to be utilized, and uncertainty below 5% is required, we suggest that the researcher investigates the temperature discrepancy between the thermistor and the center of the vacuum window with the tissue of interest attached to the window.

In order to compare the performance of the temperature-regulated vacuum window to established methods, we conducted a set of experiments on blood flow regulation in the mouse hind limb. These experiments test the ability of the mouse vasculature to up regulate blood flow in response to a local heat increase. Our results show that the vacuum window successfully induces hyperemia without affecting arterial blood pressure, and that administration of L-NAME attenuates this response. Compared to the conventional method of using tubing with pre-heated water, the vacuum window provides a simpler and more effective way of achieving hyperemia, with the added benefit of more precise temperature regulation due to the embedded thermistor.

Tracking migrating cells *in vivo* is associated with several challenges related to the preparation and stabilization of tissue. *Ex vivo* solutions such as explanting lymph nodes or spleens for leukocyte imaging are commonly used to circumvent this, with the drawbacks of disconnecting blood circulation with risk of hypoxia, and removing the organ from its original position and thus losing the possibility of leukocyte trafficking in and out of the organ. Other solutions for *in vivo* imaging may include extracorporeal tissue fixation to a viewing pedestal with the possibility of heat and fluid dissipation. For true physiological readouts, intact tissue within the animal must be handled in such a way so that sufficient blood flow is maintained in order to avoid ischemia, and any mean of stabilizing the tissue must be gentle enough not to cause unnecessary trauma that might affect cell behavior in the imaged area. In our proof-of-concept *in vivo* imaging experiments, the temperature-regulated vacuum window fulfilled the function as a tissue-stabilizing device eliminating artifacts such as those emanating from respiratory movements. When heat was cycled to a supraphysiological setpoint of 42°C to mimic fever, the increased migration speed of neutrophils was apparent, both visually and according to tracking data. CX_3CR1 positive cells showed a much less pronounced migration speed response to heat, indicating that all leukocytes do not respond the same to fever.

Taken together, the present study provides researchers with details on a 3D printed, low-cost *in vivo* imaging platform with a temperature-regulated vacuum window. The presented proof-of-concept experiments demonstrate the function of the vacuum window as a tissue stabilizer as well as the importance of local temperature regulation when performing *in vivo* imaging of leukocytes.

DATA AVAILABILITY

The datasets generated for this study are available on request to the corresponding author.

AUTHOR CONTRIBUTIONS

DA and CS conducted the experiments. DA, JS, OE, JK, ES, GC, and MP designed the method and study. DA, GC, and MP analyzed the data and interpreted the results. DA wrote the manuscript. DA, OE, JK, ES, GC, and MP contributed to the editing of the manuscript.

FUNDING

The work was supported by Swedish Research Council (2018-02552), Ragnar Söderberg foundation, Knut and Alice Wallenberg foundation, Swedish Society for Medical Research, the Göran Gustafsson Foundation, the Family Ernfors Foundation and the Novo Nordisk Foundation.

ACKNOWLEDGMENTS

The authors would like to thank Greger Thornell and Erika Åkerfeldt at the Department of Engineering Sciences, Division of Microsystems Technology, Uppsala University for lending us the FLIR A40 thermal imaging camera as well as providing technical support on the system. 3D printing was performed at U-PRINT: Uppsala University's 3D-printing facility at the Disciplinary Domain of Medicine and Pharmacy.

SUPPLEMENTARY MATERIAL

The Supplementary Material for this article can be found online at: https://www.frontiersin.org/articles/10.3389/fimmu.2019.02036/full#supplementary-material

Supplementary Video 1 | 180 minute *in vivo* time-lapse movie from the Leica SP8 confocal microscope, imaging mouse skin attached to the vacuum window. Neutrophils can be seen migrating during heat-cycling of the vacuum window. Color code: Ly6G–cyan (neutrophils), CD31–gray (blood vessels), NG2–red (pericytes).

Supplementary Video 2 | 100 minute *in vivo* time-lapse movie from the Leica SP8 confocal microscope, imaging mouse skin attached to the vacuum window. CX_3CR1^+-cells can be seen migrating during heat-cycling of the vacuum window. Color code: CX_3CR1–green (monocytes/macrophages/dendritic cells), CD31–gray (blood vessels), NG2–red (pericytes).

Supplementary Images 1–3 | Screenshots from visualization of neutrophil tracking in **Supplementary Video 1** using the TrackMate plugin for ImageJ. Color code: Ly6G–gray (neutrophils), tracks are colorized to facilitate identification of individual tracks.

REFERENCES

1. Minsky M. Memoir on inventing the confocal scanning microscope. *Scanning*. (1988) 10:128–38. doi: 10.1002/sca.4950100403
2. Wagner WW. Pulmonary microcirculatory observations *in vivo* under physiological conditions. *J Appl Physiol.* (1969) 26:375–7. doi: 10.1152/jappl.1969.26.3.375
3. Lamm WJ, Bernard SL, Wagner WW, Glenny RW. Intravital microscopic observations of 15-microm microspheres lodging in the pulmonary microcirculation. *J Appl Physiol.* (2005) 98:2242–8. doi: 10.1152/japplphysiol.01199.2004
4. Looney MR, Thornton EE, Sen D, Lamm WJ, Glenny RW, Krummel MF. Stabilized imaging of immune surveillance in the mouse lung. *Nat Methods*. (2011) 8:91–6. doi: 10.1038/nmeth.1543
5. Christoffersson G, Chodaczek G, Ratliff SS, Coppieters K, von Herrath MG. Suppression of diabetes by accumulation of non-islet-specific CD8+ effector T cells in pancreatic islets. *Sci Immunol.* (2018) 3:eaam6533. doi: 10.1126/sciimmunol.aam6533
6. Lin C, Zhang Y, Zhang K, Zheng Y, Lu L, Chang H, et al. Fever promotes T lymphocyte trafficking via a thermal sensory pathway involving heat shock protein 90 and A4 Integrins. *Immunity*. (2019) 50:137–51.e6. doi: 10.1016/j.immuni.2018.11.013
7. Jung S, Aliberti J, Graemmel P, Sunshine MJ, Kreutzberg GW, Sher A, et al. Analysis of fractalkine receptor CX(3)CR1 function by targeted deletion and green fluorescent protein reporter gene insertion. *Mol Cell Biol.* (2000) 20:4106–14. doi: 10.1128/mcb.20.11.4106-4114.2000
8. Zhu X, Bergles DE, Nishiyama A. NG2 cells generate both oligodendrocytes and gray matter astrocytes. *Development*. (2008) 135:145–57. doi: 10.1242/dev.004895
9. Schindelin J, Arganda-Carreras I, Frise E, Kaynig V, Longair M, Pietzsch T, et al. Fiji: an open-source platform for biological-image analysis. *Nat. Methods*. (2012) 9:676–82. doi: 10.1038/nmeth.2019
10. Schneider CA, Rasband WS, Eliceiri KW. NIH Image to ImageJ: 25 years of image analysis. *Nat Methods*. (2012) 9:671–5.
11. Tinevez JY, Perry N, Schindelin J, Hoopes GM, Reynolds GD, Laplantine E, et al. TrackMate: an open and extensible platform for single-particle tracking. *Methods*. (2017) 115:80–90. doi: 10.1016/j.ymeth.2016.09.016
12. Kellogg DL, Liu Y, Kosiba IF, O'Donnell D. Role of nitric oxide in the vascular effects of local warming of the skin in humans. *J Appl Physiol.* (1999) 86:1185–90. doi: 10.1152/jappl.1999.86.4.1185
13. Johnson JM, Minson CT, Kellogg DL. Cutaneous vasodilator and vasoconstrictor mechanisms in temperature regulation. *Compr Physiol.* (2014) 4:33–89. doi: 10.1002/cphy.c130015
14. Furfine ES, Harmon MF, Paith JE, Garvey EP. Selective Inhibition of Constitutive Nitric Oxide Synthase by L-NG-Nitroarginine. *Biochemistry*. (1993) 32:8512–7. doi: 10.1021/bi00084a017
15. Kianian B. *Wohlers Report 2016: 3D Printing and Additive Manufacturing State of the Industry, Annual Worldwide Progress Report*: *Chapter Title: The Middle East*. 21st ed. Wohlers Associates Inc (2016).
16. Baden T, Chagas AM, Gage GJ, Gage G, Marzullo TC, Marzullo T, et al. Open labware: 3-D printing your own lab equipment. *PLoS Biol.* (2015) 13:e1002086. doi: 10.1371/journal.pbio.1002086
17. Wijnen B, Hunt EJ, Anzalone GC, Pearce JM. Open-source syringe pump library. *PloS ONE*. (2014) 9:e107216. doi: 10.1371/journal.pone.0107216
18. Hernández Vera R, Schwan E, Fatsis-Kavalopoulos N, Kreuger J. A modular and affordable time-lapse imaging and incubation system based on 3D-printed parts, a smartphone, and off-the-shelf electronics. *PloS ONE*. (2016) 11:e0167583. doi: 10.1371/journal.pone.0167583
19. Fatsis-Kavalopoulos N, O'Callaghan P, Xie B, Hernández Vera R, Idevall-Hagren O, Kreuger J. Formation of precisely composed cancer cell clusters using a cell assembly generator (CAGE) for studying paracrine signaling at single-cell resolution. *Lab Chip*. (2019) 19:1071–81. doi: 10.1039/c8lc01153b

Conflict of Interest Statement: The authors declare that the research was conducted in the absence of any commercial or financial relationships that could be construed as a potential conflict of interest.

frontiers in Immunology

ORIGINAL RESEARCH
published: 20 November 2019
doi: 10.3389/fimmu.2019.02621

Characterization of the Dynamic Behavior of Neutrophils Following Influenza Vaccination

Diego Ulisse Pizzagalli[1,2†], Irene Latino[1†], Alain Pulfer[1], Miguel Palomino-Segura[1], Tommaso Virgilio[1], Yagmur Farsakoglu[3], Rolf Krause[2‡] and Santiago F. Gonzalez[1‡]*

[1] Institute for Research in Biomedicine, Università della Svizzera italiana, Bellinzona, Switzerland, [2] Institute of Computational Science, Università della Svizzera italiana, Lugano, Switzerland, [3] Salk Institute, San Diego, CA, United States

Neutrophils are amongst the first cells to respond to inflammation and infection. Although they play a key role in limiting the dissemination of pathogens, the study of their dynamic behavior in immune organs remains elusive. In this work, we characterized *in vivo* the dynamic behavior of neutrophils in the mouse popliteal lymph node (PLN) after influenza vaccination with UV-inactivated virus. To achieve this, we used an image-based systems biology approach to detect the motility patterns of neutrophils and to associate them to distinct actions. We described a prominent and rapid recruitment of neutrophils to the PLN following vaccination, which was dependent on the secretion of the chemokine CXCL1 and the alarmin molecule IL-1α. In addition, we observed that the initial recruitment occurred mainly via high endothelial venules located in the paracortical and interfollicular regions of the PLN. The analysis of the spatial-temporal patterns of neutrophil migration demonstrated that, in the initial stage, the majority of neutrophils displayed a patrolling behavior, followed by the formation of swarms in the subcapsular sinus of the PLN, which were associated with macrophages in this compartment. Finally, we observed using multiple imaging techniques, that neutrophils phagocytize and transport influenza virus particles. These processes might have important implications in the capacity of these cells to present viral antigens.

Keywords: intravital 2-photon, innate immunity, vaccination, neutrophils, data mining, action recognition, cell actions

OPEN ACCESS

Edited by:
Connie Wong,
Monash University, Australia

Reviewed by:
Tri Giang Phan,
Garvan Institute of Medical Research, Australia
Sapna Devi,
The University of Melbourne, Australia

****Correspondence:***
Santiago F. Gonzalez
santiago.gonzalez@irb.usi.ch

[†]These authors have contributed equally to this work

[‡]These authors share last authorship

Specialty section:
This article was submitted to Inflammation, a section of the journal Frontiers in Immunology

Received: *06 September 2019*
Accepted: *22 October 2019*
Published: *20 November 2019*

Citation:
Pizzagalli DU, Latino I, Pulfer A, Palomino-Segura M, Virgilio T, Farsakoglu Y, Krause R and Gonzalez SF (2019) Characterization of the Dynamic Behavior of Neutrophils Following Influenza Vaccination. Front. Immunol. 10:2621. doi: 10.3389/fimmu.2019.02621

INTRODUCTION

The innate immune system plays a critical role in protecting the host during the first hours that follow a new insult (1). This process involves complex cell-to-cell and cell-to-pathogen interactions that are essential for the early recognition of the pathogen and the initiation of the adaptive immune response (2). Although several advances have been made in linking the behavior of innate immune cells to the efficiency of the immune response (3), many questions remain open. This is mainly due to the dynamic nature of the aforementioned interaction patterns, which change over time and are distributed in space (4).

The lymph node (LN) has been the preferred organ to investigate *in vivo* the complexity of cell behavior and cell dynamics in relation to immune functions (5). This organ is highly compartmentalized and is composed of specific regions, which facilitate the coordination of the innate and adaptive immune responses. Indeed, the architecture of the LN further promotes the dynamics of immune cell interactions, such as antigen trafficking between macrophages from

different regions, which is critical for the final effector response (6–10), and the capture and presentation of antigen by LN resident dendritic cells (DC) (11, 12). The migration of different cell populations to the specific regions of the LN follows a complex balance of chemokine gradients that orchestrate its architecture. For instance, CCL21 and CXCL12 act on the vascular endothelium to promote the recruitment of leukocytes via high endothelial venules (HEV) (13, 14). After the extravasation process, CXCL13 and CCL19-21 direct B and T cells toward the B-cell follicle and the T-cell zone, respectively (15–20).

Among the innate cells that migrate to the LN in inflammatory conditions, neutrophils constitute the first line of defense against pathogens (21, 22). These cells have important immunological functions, such as the secretion of antimicrobial compounds (23), and play a key role in tissue cleaning and remodeling (24). Neutrophils are abundant in the circulation in their mature form and are rapidly recruited from the bone marrow upon inflammation (25, 26) via post-capillary vessels (27, 28) or lymphatics (28–31). Neutrophil recruitment to the site of infection is a highly regulated process that involves the initial secretion of pro-inflammatory factors, released by activated macrophages and DC, which regulate the expression of adhesion molecules from vascular endothelial cells (24, 32). Among the different inflammatory cytokines that have shown to be involved in this process, the interleukin-1 (IL-1) family (33–35) and the tumor necrosis factor (TNF) are some of the best-characterized (29). In addition, many other chemokines and receptors are known to be involved (36).

Once recruited to the inflamed tissue, neutrophils can interact with lymphocytes and antigen-presenting cells (APC) influencing the adaptive immune response (24, 37, 38). This was demonstrated in different inflammatory conditions in which neutrophils released B cell-stimulating molecules, such as BAFF or CD40L (39), or induced T cell proliferation and activation (37, 38, 40). T cell response can be further orchestrated by neutrophils influencing both DC priming and T cell function via NETosis or release of granules (41). Moreover, recent evidence has indicated that neutrophils can cooperate with DC, transporting antigens to the site of T cell activation or acting as APC (21, 42, 43).

While the initial recruitment of neutrophils from blood has been extensively characterized (44), their post-recruitment behavior remains widely unknown. One of the few actions previously described regards the formation of aggregates or swarms (22). This process involves the coordinated migration of cells toward a common target (22, 45, 46). During the formation of swarms, the first neutrophils that are recruited can trigger a cascade of secondary chemoattractants, which amplify the recruitment of other neutrophils in a feed-forward manner (47). The main signals triggering neutrophil influx and swarm formation were associated with tissue injury (48, 49). However, in infection models, other factors such as pathogen-derived compounds (50), or molecules released by dying neutrophils (51) can trigger swarm formation. The role of neutrophil swarms has been linked with microbicidal activity, tissue remodeling, and protection of uninfected tissues (21). However, it is unclear how individual neutrophils behave in the swarming environment. Recent studies using infection models have shown that neutrophil swarm growth is correlated with the removal of subscapular sinus macrophages (22). This suggests an interplay between the two populations and a possible involvement of the resident cell population in the initiation and regulation of the process.

To better investigate the behavior of neutrophils following influenza vaccination, imaging techniques are of paramount importance. Among the available imaging methods, 2-photon intravital microscopy (2P-IVM), allows the long-term observation of cells in tissues of living animals. For this reason, in the last two decades, 2P-IVM has become an essential tool for the observation of immune-related mechanisms *in vivo,* highlighting unprecedented mechanisms related to cell migration and cell-to-cell interaction (5). However, an interdisciplinary approach is required to analyze the imaging data generated by this technique. Indeed, the recently established image-based systems biology approach (52) combines microscopy data with computational methods to describe, quantify, and interpret complex biological processes, from imaging data. This combination of methods allowed for instance to uncover different T cell receptor signaling patterns (53) or different types of migration patterns (54) from the tracks of immune cells.

In this work, we employ a cutting-edge imaging analysis methodology to characterize *in vivo* the dynamics of neutrophil recruitment and their migratory patterns following vaccination with UV-inactivated influenza virus. Thus, we highlight the interaction of early recruited neutrophils with the resident macrophage population involved in antigen capturing. Finally, we report how neutrophil behavior changes over time, using a new mathematical model that maps recurrent motility patterns of neutrophils to biological functions.

RESULTS

Neutrophils Are Recruited to the Draining Lymph Node via Blood Following Influenza Vaccination

To study the dynamics of neutrophil recruitment to the popliteal lymph node (PLN) we evaluated the total number of Ly6G+CD11b+ cells by flow cytometry during the first 24 h following footpad administration of influenza vaccine (UV-inactivated influenza virus, strain A/Puerto Rico/8/34). We observed a rapid increase in the number of neutrophils, reaching a peak at 12 h post-vaccination (p.v.) (**Figures 1A,B**). Moreover, we found that the recruitment coincided with an increase in the expression of the early activation marker CD69 in these cells (**Figure 1C**). However, we found that, once in the LN, neutrophils downregulate the expression of the chemokine receptor CXCR4, one of the key regulators of leukocyte trafficking (**Figure 1D**). In addition, we also detect loss and shedding of the receptors CD44, CD62L, and CD49d, which are constitutively expressed in resting neutrophils (**Supplementary Figures 1A–D**). To better characterize the recruitment process, we performed confocal

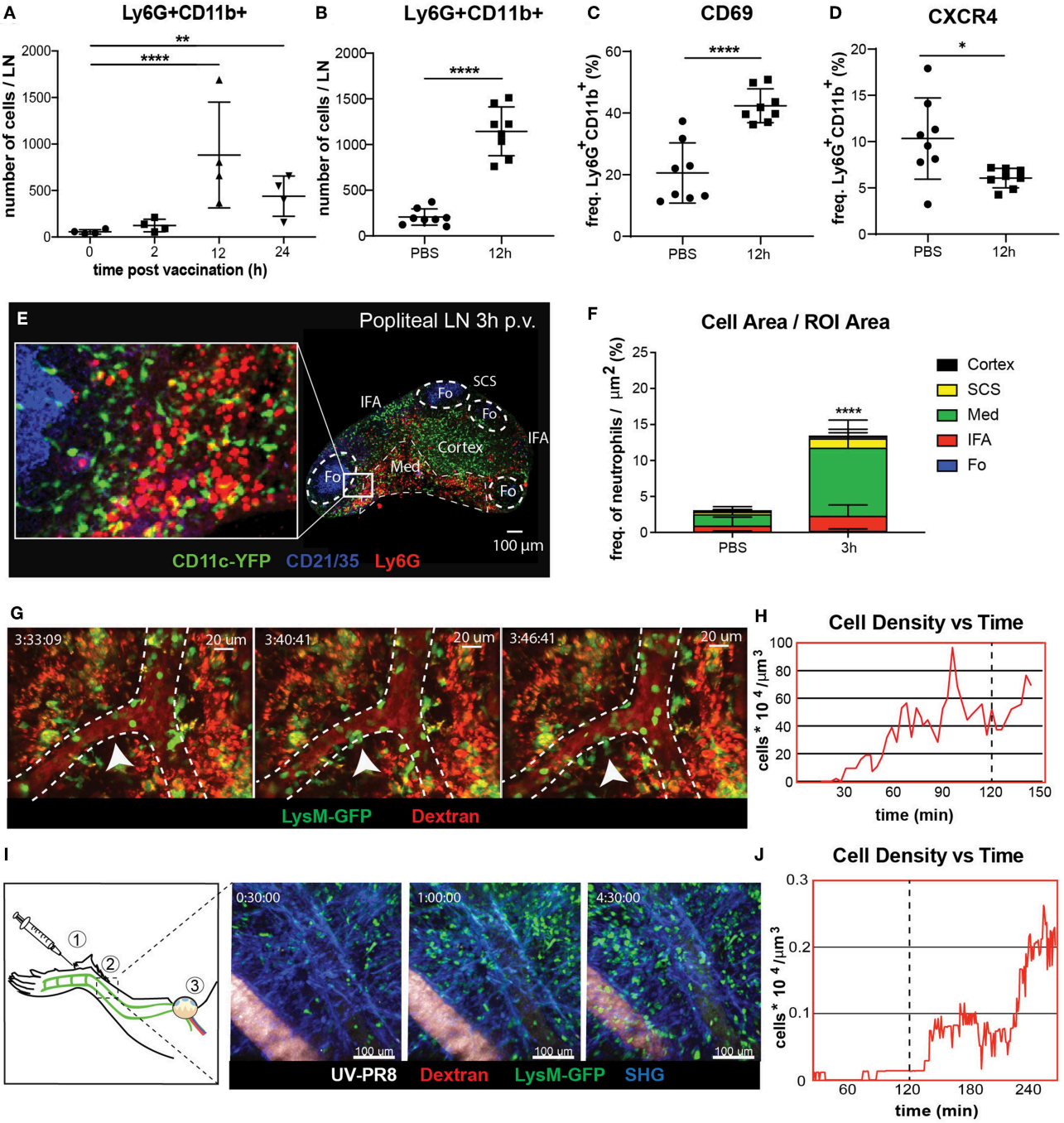

FIGURE 1 | Neutrophil recruitment and distribution into the popliteal lymph node (PLN) after influenza vaccine administration. **(A)** Kinetic of neutrophil recruitment into the PLN during the first 24 h following UV-inactivated influenza virus injection (UV-PR8). **(B)** Flow cytometric analysis showing the recruitment of neutrophils (Ly6G+ CD11b+) at 12 h post-vaccination (p.v.). Percentages of CD69+ **(C)** and CXCR4+ **(D)** cells out of all neutrophils at 12 h p.v. compared with non-vaccinated controls. **(E)** Representative confocal microscopy of LN section showing the distribution of Ly6G+ neutrophils (red) in the LN at 3 h p.v. in a CD11c-YFP animal. **(F)** Quantification plots showing the distribution of neutrophils in the medullary (Med), interfollicular area (IFA), T cell zone (Cortex), follicle (Fo), and subcapsular sinus (SCS) areas of the LN at 3 h p.v.. **(G)** Sequential 2-photon intravital (2P-IV) micrographs showing the recruitment of LysM-GFP neutrophils (green). Blood vessels (red) are labeled by i.v. injection of Rhodamine B isothiocyanate-Dextran. White arrows indicate a hotspot. **(H)** Time series showing increasing density of neutrophils inside high endothelial venules (HEVs) of the PLN following vaccination. **(I**, left) Schematic drawing of the mouse footpad showing the injection site (1), the imaged area (2), and the lymphatic drainage toward the PLN (3). **(I**, right) Sequential 2P-IV micrographs showing the recruitment of LysM-GFP inside the lymphatic vessel in the injection site following UV-PR8 administration. **(J)** Time series showing increasing density of neutrophils inside the draining lymphatic vessel. In all figures, the presented data are representative of at least three independent experiments. Results are given as mean ± SD. ns $p > 0.05$; *$p < 0.05$; **$p < 0.01$; ****$p < 0.0001$.

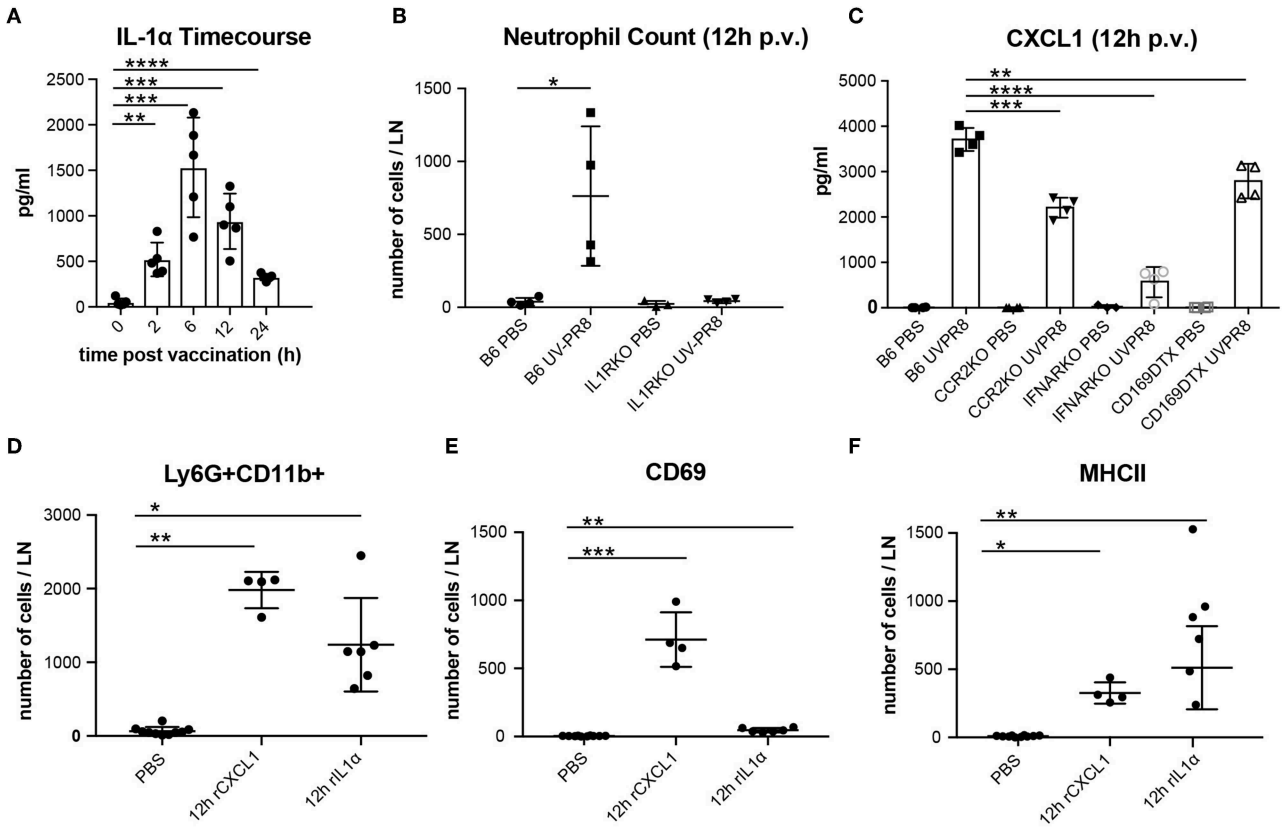

FIGURE 2 | Production of CXCL1 and IL-1α induce recruitment of neutrophils to the PLN in response to vaccination. **(A)** Time course showing the secreted IL-1α in the LN at 0, 2, 6, 12, and 24 h following vaccination. **(B)** Flow cytometric analysis showing the recruitment of neutrophils in the LN in B6 and IL-1R-deficient mice at 12 h p.v.. **(C)** Cytoplex analysis showing the production of CXCL1 in the LN at 12 h p.v. in CCR2 KO, IFNAR KO, and CD169DTR mice compared to B6 controls. Flow cytometric analysis showing the total neutrophils count **(D)**, and the expression of CD69 **(E)**, and MHCII **(F)** after administration of recombinant IL-1α and CXCL1. In all figures, the presented data are representative of at least three independent experiments. Results are given as mean ± SD. ns $p > 0.05$; *$p < 0.05$; **$p < 0.01$; ***$p < 0.001$; ****$p < 0.0001$.

microscopy and quantified the presence of these cells in different areas of the PLN at 3 h p.v. (**Figure 1E**). We observed that, at this early time, neutrophils accumulate in the medullary and interfollicular areas (**Figure 1F**). Next, to evaluate if the recruitment occurs via the blood vessels or the lymphatic system, we monitored *in vivo* the process using intravital 2-photon and electron microscopy. Quantitative analysis of the 2-photon movies acquired in the paracortical blood vessels of LysM-GFP mice showed a prominent increase in the number of neutrophils during the first 2 h p.v. (**Figure 1H**). In addition, we observed the presence of multiple hotspots (55) in the wall of high endothelial venules (HEVs), suggesting a relevant role of these areas in the observed recruitment (**Figure 1G**; **Supplementary Movie 1**). To confirm this observation, we performed electron microscopy in a PLN HEV, which clearly showed neutrophils associated with the blood vessel endothelium as early as 2 h p.v. (**Supplementary Figure 1A**). Interestingly, intravital imaging of the lymphatic vessels, which drain the area in which the vaccine was administered (**Figure 1I**), showed a progressive increase in the number of neutrophils inside the lymphatic vessels during the first 4 h p.v. (**Figure 1I**; **Supplementary Movie 2**). However, this process appeared to be slower than the recruitment that occurs via blood, as we could not detect any neutrophil in the lumen of the lymphatic vessels during the first 2 h p.v. (**Figure 1J**).

The Recruitment of Neutrophils to the LN Involves the Cytokine IL-1α and the Chemokine CXCL1

In a previous study, we observed that the necrotic death of the LN macrophages after the administration of influenza vaccine was followed by the release of the potent inflammatory cytokine IL-1α (6). In this work, we confirmed that IL-1α reaches an early peak (6 h) following vaccination and returns to basal levels at 24 h p.v. (**Figure 2A**). Moreover, we found that IL-1RKO animals show a significant inhibition of neutrophil recruitment in the PLN (**Figure 2B**). To confirm that IL-1α was involved in neutrophil recruitment, we injected a dose of 1 μg of recombinant IL-1α in the mouse footpad, and observed that the injection of this cytokine alone was able to induce the recruitment of neutrophil in the draining PLN at 12 h p.v. (**Figure 2D**). In a previous work, we also observed that

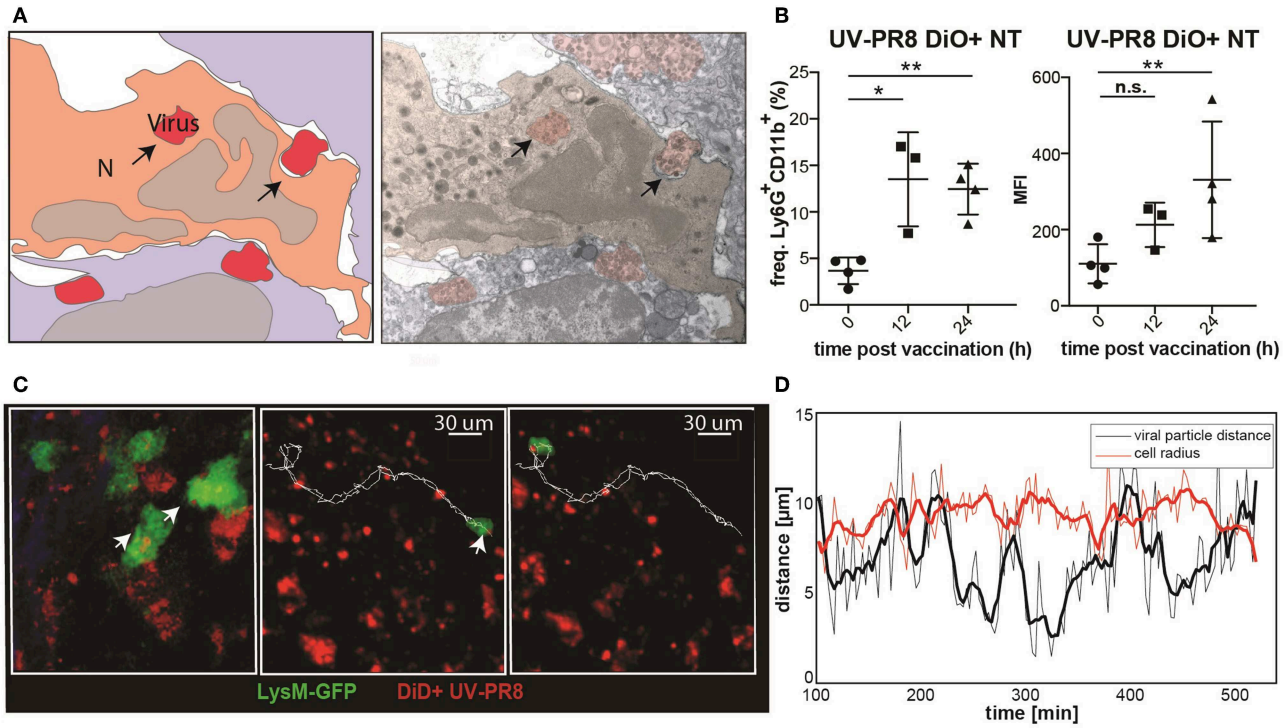

FIGURE 3 | Neutrophils phagocyte and transport influenza virus. **(A)** Schematic drawing (left) of an electron micrograph (right) showing neutrophils in the SCS phagocytizing UV-inactivated influenza virus at 2 h p.v.. **(B)** Flow cytometric analysis indicating the percentage of neutrophils positive for influenza vaccine (DiO labeled, left) and the corresponding MFI analysis (right). **(C)** Intravital 2-photon micrograph showing a LysM-GFP neutrophil (green) phagocytizing DiD labeled UV-PR8 (red) (left). Intravital 2-photon timelapse showing the correlation between the tracks from a UVPR8-positive vesicle and the neutrophil (right). **(D)** Distance of the viral particles from the cell centroid (black line), compared to the cell radius (red line). Results are given as mean ± SD. ns $p > 0.05$; *$p < 0.05$; **$p < 0.01$.

influenza vaccination induced a fast increase of the chemokine CXCL1 (6), a well-known inducer of neutrophil recruitment (56). Therefore, to investigate whether the production of this chemokine was associated with LN macrophages, we measured the secretion of CXCL1 in animals in which LN macrophages (CD169-DTR + Diphtheria toxin) or monocytes (CCR2KO) had been depleted. We observed that, in both cases, the levels of CXCL1 were significantly reduced at 12 h p.v. compared to the control group (**Figure 2C**). However, CXCL1 levels were not completely abrogated. Interestingly, we also observed that the type-I interferon response following vaccination was necessary for the secretion of this chemokine, as IFNARKO animals showed a prominent inhibition of the levels of CXCL1 at 12 h p.v. (**Figure 2C**). Moreover, we also observed that IFNARKO animals display lower number of resident macrophages (**Supplementary Figures 1H,I**), while CCR2KO did not showed any difference (**Supplementary Figure 1G**). However, DTX-treated CD169-DTR mice exhibited a complete depletion of LN macrophages after the administration of the toxin (**Supplementary Figure 1F**). Besides, footpad administration of recombinant CXCL1 (0.5 µg/fp) alone was able to induce a significant recruitment of neutrophils in the popliteal LN (**Figure 2D**). However, we observed significant differences in the effect that both molecules had on the activation of neutrophils. Recombinant CXCL1, but not IL-1α, was able to induce the expression of the early activation marker CD69 in the recruited neutrophils (**Figure 2E**). However, neutrophils recruited after IL-1α administration showed higher levels of MHC II compared to the ones recruited following treatment with CXCL1 (**Figure 2F**).

Neutrophils Phagocytize and Transport Influenza Virus

To examine the capacity of neutrophils to phagocytize UV-inactivated influenza virus (UV-PR8), we performed electron microscopy. Indeed, results showed that a number of neutrophils phagocytized necrotic vesicles containing the UV-PR8 particles (**Figure 3A**, **Supplementary Figure 1J**). To quantify the percentage of neutrophils that phagocytized the virus, we labeled inactivated influenza virus with the lipophilic dye DiO and performed flow cytometric analysis. We found that 15% of the neutrophils were positive at 12 h p.v. (**Figure 3B**). Finally, to assess the capacity of neutrophils to transport phagocytized influenza particles, we performed 2P-IVM in LysM-GFP mice. The dual tracking of DiD-UV-PR8 and LysM-GFP neutrophils confirmed that, after phagocytosis, neutrophils were able to transport the phagocytized virus within the LN during 7 h (**Figure 3C**, representative track, **Supplementary Movie 3**). A volumetric reconstruction further confirmed that viral particles

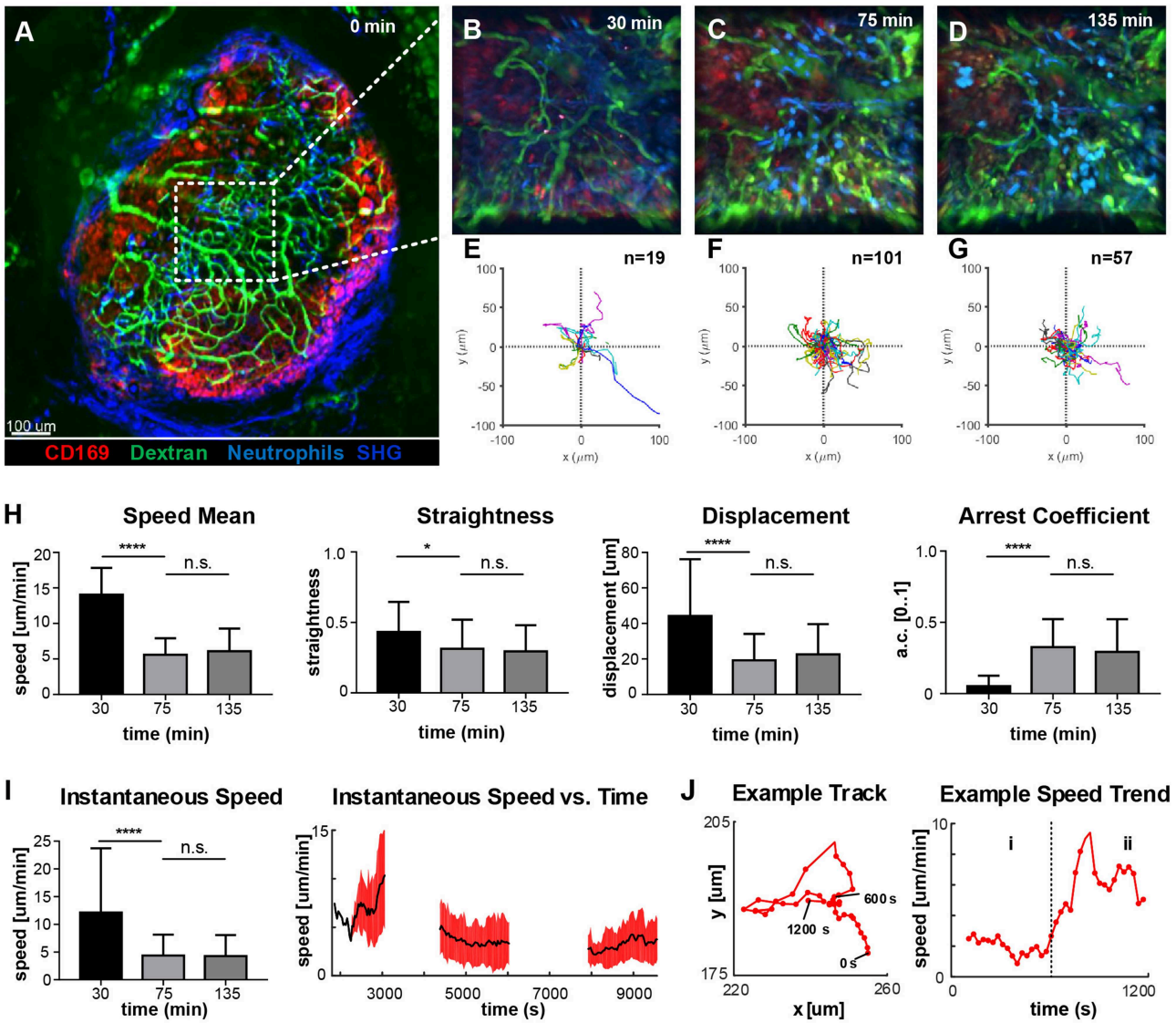

FIGURE 4 | Time-course of neutrophil motility. **(A)**. Low-magnification 2P-IVM micrograph showing the structure of the PLN including vascular network (Fluorescein isothiocyanate-Dextran), CD169+ macrophages (red), collagen scaffold (Second Harmonic Generation–blue) and neutrophils (light-blue) adoptively transferred from a CK6/ECFP animal. Image was acquired immediately after vaccine injection. **(B–D)** Snapshots of representative LN areas at different time points. **(E–G)** Plots of cell tracks with common origin showing four preferential migratory directions at 30 min, more equally distributed directionalities at 75 min and a tendency toward the 1st and 4th quadrants at 135 min. The number of tracks is 19, 101, 57, respectively. **(H)** Cell motility quantification using tracks mean speed, straightness, displacement, and arrest coefficient. **(I)** Boxplots of Instantaneous speed (left) exhibiting high variance at early time points. Instantaneous speed time series (right) showing distinct trends at different time points. **(J)** Representative track (left) acquired at 135 min and the associated time series of the instantaneous speed (right). The same cell exhibits two different trends characterized by low speed (i) and high speed (ii). Results are given as mean ± SD. ns $p > 0.05$; *$p < 0.05$; ***$p < 0.001$; ****$p < 0.0001$.

were internalized, with a distance from the cell centroid smaller than the cell radius (**Figure 3D**).

Neutrophils Change Their Motility Soon After Being Recruited to the LN

To identify the areas of the LN with higher activity, we acquired low-magnification 2P-IVM movies (**Figure 4A**) in a non-fluorescent recipient animal by adoptively transferring neutrophils from a CK6/ECFP donor. Moreover, to visualize the vasculature and the LN macrophages, we administered fluorescein isothiocyanate-dextran (200 kDa) and CD169-PE antibody, respectively. Initially, we imaged an area located in the paracortex of the LN (**Figure 4A**, dashed line), characterized by a high vascularization and active recruitment of neutrophils. Representative snapshots of the acquired movies are shown in **Figures 4B–D**, while the tracks of the analyzed cells are plotted in **Figures 4E–G**. A qualitative analysis of cell migration showed

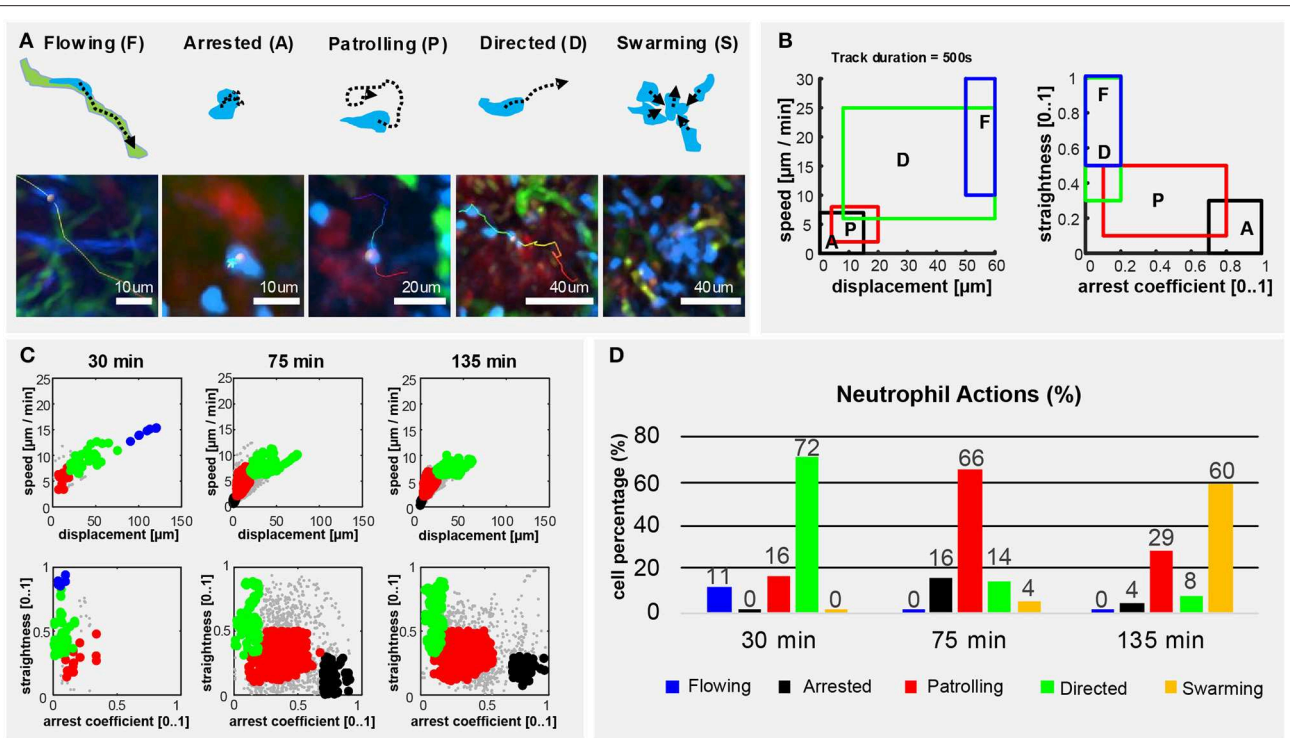

FIGURE 5 | Neutrophils exhibit different actions in the early response to vaccination. **(A)** Graphic representation (up) and 2P-IVM micrographs showing different neutrophil actions in response to influenza vaccination: flowing "F" neutrophils moving inside blood vessels, with long and straight tracks following the vessel structure. Arrested neutrophils "A" exhibit confined tracks and short displacement. Patrolling neutrophils "P" have long, non-straight tracks associated with extensive tissue monitoring. Directed neutrophils "D" exhibit straight tracks with lower migration speed compared to flowing neutrophils. Swarming neutrophils (S) form cell aggregates with high density and large volume. **(B)** Gating strategies used to define and identify the actions according to cell speed, displacement, straightness, and arrest coefficient on track fragments of fixed length (500 s). **(C)** Classification of track fragments at different time intervals (arrested: black, patrolling: red, directed: green, flowing: blue, unspecified: gray). **(D)** Time-course plot showing the percentage of cells performing each of the actions over time, according to our gating strategy.

that at 30 min p.v. neutrophils generated long tracks in four main directions, which were associated with their movement inside the blood vessels (**Figure 4E**; **Supplementary Movie 4**). Once outside the blood vessel (75 min p.v.), neutrophils did not follow any preferential direction (**Figure 4F**; **Supplementary Movie 4**), while at later time points (135 min p.v.) they displayed a collective migration directed toward an area in which cells started to cluster (**Figure 4G**; **Supplementary Movie 4**). Next, we quantified cell migration by computing measures based on entire tracks (**Figure 4H**). We observed a significant change in neutrophil motility occurring within 30–75 min p.v. Indeed, neutrophils at 30 min p.v. were faster, more directional and traveled longer distances with a lower arrest coefficient, compared to later time points. However, no significant difference was observed between 75 and 135 min. These findings, using track-based measures, confirmed a change in the overall motility only after recruitment. Nevertheless, the analysis of the instantaneous speed of neutrophils showed a high variance (**Figure 4I**, left), which was associated with a variable mean over time (**Figure 4I**, right, black line). The observed variability in speed arises from both the differences between distinct cells at the changes of speed that a single neutrophil undergoes over time. An example is provided in **Figure 4J**, where the track of a neutrophil (left) and the plot of the instantaneous speed (right) over time are shown. This example shows the transition between two distinct behaviors that are characterized by low speed and high speed, respectively.

Neutrophils Perform Different Actions Over Time

To describe the long-term and time-varying behavior of each individual neutrophil, we defined, according to previous studies (45, 57–59), five distinct cellular actions based on the motility patterns visually identifiable in the videos (**Figure 5A**). We named them flowing, arrested, patrolling, directed migration and swarming (**Figure 5A**). To detect these actions from imaging data, we divided the track of each neutrophil into multiple fragments (tracklets). Then, we computed morphological and motility measures on each of them. By defining a gating strategy on these measures, each tracklet was associated with an action (**Figure 5B**). Considering each tracklet as a data-point, the proposed gating strategy identified five distinct populations corresponding to the different actions (**Figure 5C**). Following this analysis, we observed that neutrophils perform different actions at different time points (**Figure 5D**). At homeostasis, neutrophils were mostly flowing. Hence, circulating within blood vessels with high speed and directionality

(**Supplementary Figure 2**; **Supplementary Movie 8**). Then, during the first 30 min p.v. neutrophils were mostly associated with capillaries, displaying both flowing and directed migration. This behavior changed when neutrophils started to migrate within the LN (30–75 min p.v.), displaying primarily patrolling, directed, and arrested behaviors. Other neutrophils exhibited a temporarily directed migration. Finally, at 2 h p.v., cluster formation was the predominant neutrophil behavior. This was associated with temporarily directed migration of neutrophils either toward a swarm under formation or from a previously formed swarm to another target. In addition, a small population of neutrophils was arrested (**Figure 5D**). These results confirmed that the time-varying motility of neutrophils can be represented as a sequence of distinct actions which, in turn, are associated with distinct biological processes.

Following Vaccination Neutrophils Form Swarms in the SCS Associated With SCS Macrophages (SSM)

To identify the areas in the LN with high cell motility we performed low magnification (10X) 2P-IVM, which allowed the visualization of the whole organ (**Figure 6A**; **Supplementary Movie 5**). Cells were tracked for a period of 30 min and the percentage of cells migrating from one region to another was computed. We found that at early time p.v. most of the neutrophil migration occurred between the interfollicular (IF) and the SCS areas (**Figure 6B**). To evaluate the presence of areas associated with high neutrophil motility, we measured the average pixel velocity by optical flow, a computer vision method that does not require cell tracking (60). The results showed the presence of hotspots with high motility, which are depicted as lighter areas in the pixel velocity heat map (**Figure 6C**). These hotspots were localized in the SCS and IF area. Interestingly, the hotspots were associated with the regions where swarms were formed (**Figures 6D,E**).

To fully characterize neutrophils swarming behavior, we recorded movies in the SCS region of the LN using different magnifications. Low magnification movies from LysM-GFP mice showed that neutrophils formed large and multiple swarms in association with regions enriched with macrophages (**Figure 6F**; **Supplementary Movie 6**). Such swarms grew in size over time (**Figure 6G**). Furthermore, neutrophils involved in the swarms often changed their directionality from one cluster to another (**Figure 6F**). In mathematical terms, the average dynamic of the observed swarms was best described by a sigmoidal function (**Figure 6H**), suggesting that swarm formation undergoes an initial steady state, a growing phase and a plateau before its resolution. Moreover, we observed that the decreasing swarms showed a resolution period of ∼30 min.

To better visualize individual neutrophil behavior, as well as possible interactions with resident macrophages, we acquired high-magnification videos starting from 5 to 7 h p.v.. These videos confirmed that swarm formation occurs in proximity to SSM (**Figure 6I**; **Supplementary Movie 7**), with highly directed and skewed trajectories (**Figure 6J**), and the majority of the cells approaching the center of the swarm (**Figure 6K**). Moreover, using high-magnification 3D reconstruction and EM, we confirmed that neutrophils were located in close proximity to SSM clusters (**Figures 6L,M**). To investigate the involvement of SSM in the formation of swarms we quantified the accumulation of neutrophils in areas proximal or distal to SSM. Interestingly, the number of neutrophils fluctuated over time outside the SCS area (**Figure 6N**). By contrast, it constantly increased in areas rich in macrophages (**Figure 6O**) exhibiting the sigmoidal growth rate observed during swarm formation.

DISCUSSION

In this study, we investigated *in vivo* the behavior of neutrophils that are recruited to the draining LN following influenza vaccine administration. Neutrophil recruitment has been previously described in several infection models (22, 30, 44, 51, 61). However, despite the critical role of these cells in pathogen clearance and the initiation of the inflammatory response, their specific behavior upon vaccination remains poorly studied. In this work, we observed a rapid recruitment of activated and mature neutrophils in response to vaccination with an inactivated influenza virus. Although the role of neutrophils against influenza has been extensively studied in the lung (62), this is the first time that their behavior is characterized in the draining LN in the early response to influenza vaccine administration.

The way neutrophils enter the LN remains controversial. Different studies have suggested that neutrophils get recruited mainly via the HEV (44, 48). However, other authors have stated that neutrophils access the LN mainly via the lymphatic vessels (29–31). Our data suggested that influenza vaccination induces an initial recruitment of neutrophils via HEV, followed by a minor, secondary wave through the lymphatics that drain directly from the injection site to the sentinel LN. It is tempting to speculate that the type of recruitment might influence the function of the recruited cells. However, future experiments need to be performed to study differences in the behavior and the function of neutrophils that arrive through different routes. In addition, we found that a percentage of neutrophils downregulates the expression of CXCR4, a marker known to be involved in neutrophil mobilization from the bone marrow and trafficking through the circulation to the site of inflammation (63, 64). Moreover, consistently with neutrophils activation, we detected a downregulation of multiple cell surface receptors linked with leucocyte trafficking and accumulation (65, 66). By contrast, these receptors were expressed at high levels in resting neutrophils (67).

Neutrophil localization within the LN after pathogen challenge is tightly linked to their specific function. In a previous study, we observed that macrophages, located within the subcapsular sinus (SCS) and the medullary area of the LN, capture and retain influenza virus following vaccination. Interestingly, in both the areas, macrophages undergo necrosis-like cell death after viral capture that leads to their progressive decline (6). Our study demonstrated that neutrophils migrate toward the SCS progressively, probably

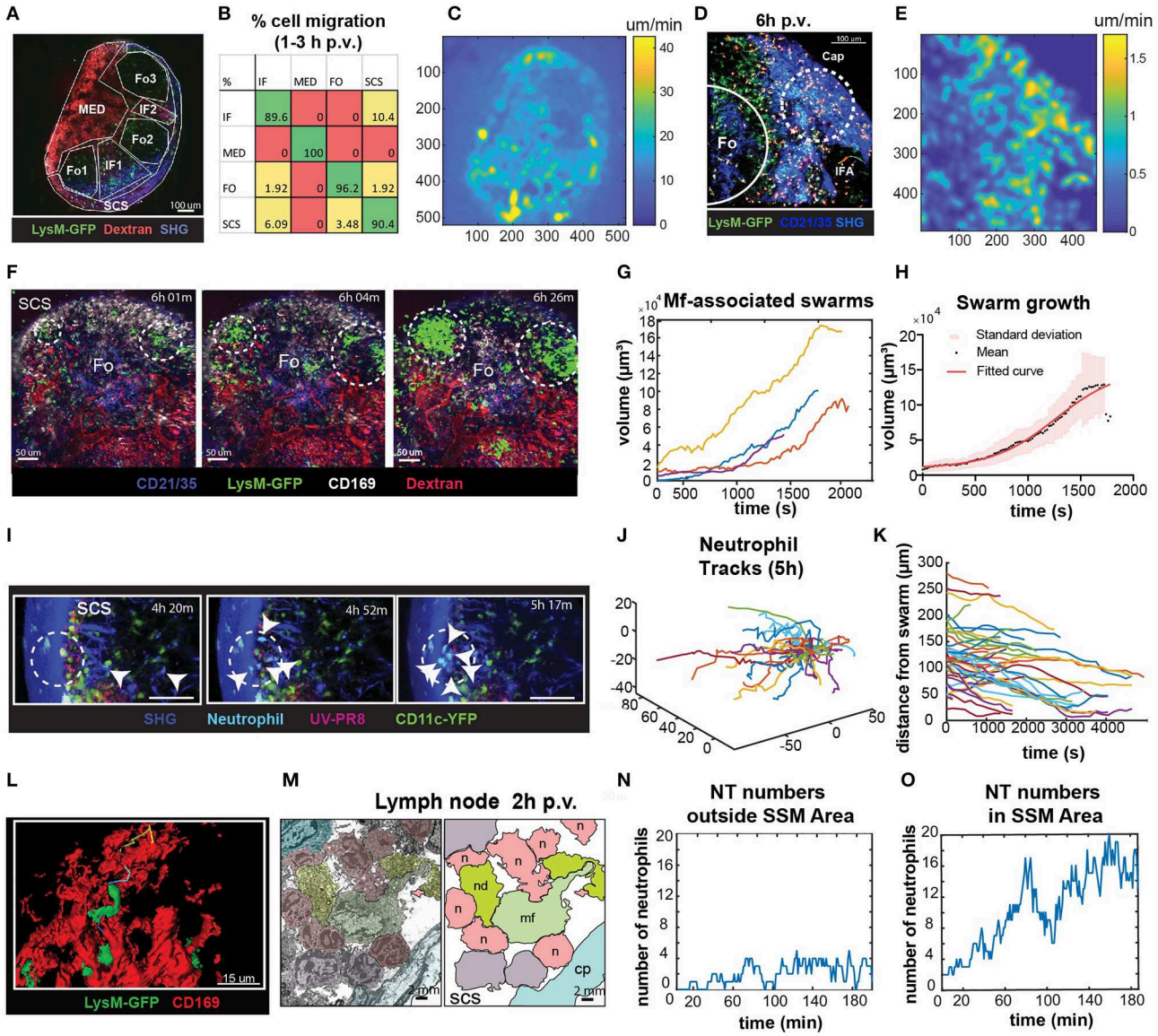

FIGURE 6 | Characterization of neutrophils swarm formation in the PLN after influenza vaccination. **(A)** Low magnification 2P-IVM micrograph showing the PLN of a LysM-GFP animal at 3 h p.v. Seven different areas are identified according to their anatomical structure and cell populations: SCS, follicles (Fo1-3), interfollicular areas (IF1-2), and medullary area (MED). **(B)** Transition matrix showing the migration of cells across different areas. The value at the i-th row and j-th column refers to the percentage of cells that migrated from the i-th to the j-th area. Values on the diagonal refer to the percentage of cells that remained in the same area. **(C)** Pixel velocity heatmap, showing hotspots with high motility. **(D)** 2P-IVM micrograph showing the IF and SCS areas at 6 h p.v. Cap refers to the collagen capsule. Dashed lines indicate hotspots toward which cells migrate with high motility. **(E)** Pixel velocity heatmap showing hotspots with high motility (yellow) **(E)**. Dashed lines indicate hotspots toward which cells migrate with high motility. **(F)** Sequence of micrographs at 6 h p.v. showing the formation of multiple LysM-GFP neutrophils swarms in the SCS in close proximity to CD169+ macrophages (white) **(G)** Swarm volumes over time observed at 6 h p.v.. Volumetric data built according to fluorescence intensity thresholding. **(H)** Sigmoid fit to previous swarm volume ($R = 0.652$) showing their averaged growth phase. **(I)** Sequence of micrographs with 25x magnification in the SCS showing CFP-expressing neutrophils initiating a swarm at 5 h p.v. **(J)** Trajectories of 5 h p.v. swarm plotted from the same origin **(K)** Time-course distances from the swarm center at 5 h p.v. **(L)** High magnification 3D reconstruction of LysM-GFP neutrophils interacting with CD169 macrophage network (red) in the SCS region. **(M)** Colored transmission electron micrograph (left) and schematic drawing (right) showing the interaction of different neutrophils (n) with a macrophage (mf) in the SCS of the LN at 2 h p.v.. **(N,O)** Number of neutrophils vs. time showing an oscillatory trend in an area without macrophages **(N)**, and an increasing trend indicative of swarming in an area associated with macrophages **(O)**.

in response to chemoatactic signals released by the necrotic macrophages, as suggested by other models based on infection (22, 48). Among the different signals released by the necrotic macrophages, IL-1α is one of the most potent (6). In this work, we have demonstrated that IL-1α and its receptor IL-1R are involved in the initial recruitment of neutrophils to the LN. Other

authors have previously confirmed the role of IL-1β and IL-1R in the recruitment of neutrophils to the infection site (33, 68, 69). However, we could not observe any significant secretion of IL-1β or activation of the inflammasome pathway in the LN following influenza vaccine administration (6). Therefore, we can conclude that the observed absence of neutrophil recruitment in the IL-1R-defective mice was associated to IL-1α released by macrophages.

Moreover, we confirmed that CXCL1, a mouse homolog of human IL-8, was also involved in the recruitment of neutrophils to the LN. The source of this chemokine needs to be further investigated but we speculate that DC and activated macrophages could be the main producers (70, 71). Indeed, the secretion of CXCL1 was almost abolished in mice lacking type-I interferon (IFN) receptors, suggesting an important role of LN macrophages and DC, the main producers of IFN, in this process. Thus, absence of IFN-I signaling in IFNARKO mice partially reduce the total number of CD169+ macrophages compared to the control, although it did not significantly impair the number of medullary macrophages. However, the specific elimination of macrophages reduced only partially the expression of CXCL1. Interestingly, our findings demonstrated that subcutaneous administration of IL1-α and CXCL1 induced the mobilization of neutrophils toward the LN. Nevertheless, we showed that CXCL1 induced the expression of CD69, a marker associated with the early activation, while IL-1α administration increased the expression of MHCII, suggesting a potential role of neutrophils in antigen presentation, as previously described in other models (40, 72). Neutrophils are sensitive to a vast array of chemoattractants that regulate their migration and infiltration to inflamed tissues. Indeed, Chou et al. (73), previously described this process as a cascade that require a multitude of chemokines, such as MIP-1α, MIP-1β, and MIP-2. Therefore, will be of interest to explore the complex nature of signals that mediate neutrophils recruitment post-influenza vaccination.

In the early phases of recruitment, we found that neutrophils exhibited significant differences, resulting in reduced speed, directionality, and displacement, while increased arrest coefficient. These findings suggest that the recruited neutrophils actively migrate and increase cell-to-cell interactions. Previous studies have associated the increase in the arresting of neutrophils with the oxidative burst (20) in which reactive oxygen species are generated. Antigen presentation might also influence the speed of neutrophils. Indeed, other authors have reported that neutrophils can serve as antigen presenting cells (APC) during influenza infection in mice (2, 74, 75). In support of the notion that neutrophils might act as APC in the context of influenza vaccination, we observed that they actively phagocytize influenza particles, which were previously associated with necrotic macrophages. Moreover, we could observe an increase in the expression of MHCII in these cells after exposure to IL-1α, which is released by the dying macrophages (6). However, it is not clear if the APC function of neutrophils might occur in the LN or, as suggested by other authors (76), in other immune-relevant organs, such as the spleen. In support of the former, we observed that neutrophils are able to transport influenza particles for long distances in the LN (77). This suggests that neutrophils can carry viral particles to specific areas as described for other infection models (78–80). Therefore the potential capacity of the neutrophils to transport viral particles to other organs as well as the capability of these cells to function as APC need to be further investigated.

Our findings supported that neutrophil behavior is a dynamic process, with significant differences observed already within the first 3 h p.v.. These findings were in agreement with previous *in vitro* studies in which the motility of neutrophils was found to change within minutes in response to both external (i.e., chemical gradients) and internal factors (i.e., directional memory) (81).

Among the different actions that occur within the first few hours after vaccination, we identified the formation of swarms, which is a process previously associated with tissue injury (49, 51). In this study, we showed that neutrophils swarms are formed in the SCS, co-localizing with the resident SSM population. The characterization of swarm dynamics showed consistent growth rates, suggesting that they are comparable to smaller transient swarms observed in other infection models (22). Regarding the factors that generate this behavior, tissue injury, neutrophil secondary cell death, and the release of the chemoattractant LTB4 have been previously proposed as triggers of swarm formation (51). Although LTB4 is mainly secreted by neutrophils, macrophages can also produce this molecule (51). These observations, along with our *in vivo* evidence of swarms association with SSM, suggest a close association between the two populations. In previous studies, swarm formation in the SCS was linked with the removal of resident SSM (24). We speculate that macrophage death contributes to the initiation, amplification, and stabilization of neutrophil swarming and recruitment via the release of different chemoattractants, such as IL-1α. However, the redundancy in the recruitment process of neutrophils, with the involvement of more than 30 chemokine receptors (36), makes the effect of a single molecule difficult to be distinguished from other cues that regulate neutrophil chemotaxis.

Regarding the swarm dynamics, a direct correlation between swarm size and tissue injury severity has previously been shown (82). Furthermore, the number of neutrophil secondary death is also proportional to the swarm size (51). It would be compelling to determine whether influenza vaccination induces the death of neutrophils in a way similar to the previously described macrophage death (6).

The quantification of the spatio-temporal migration and interaction patterns of cells from 2P-IVM data presents specific challenges. These arise from the difficulties both in cell tracking and in describing a complex biological system by means of numerical values. The difficulties in cell-tracking, arise from both the textureless appearance and the complex biomechanical properties of neutrophils, including high plasticity and formation of contacts. These problems are amplified by the high number of cells that need to be tracked. To facilitate individual tracking, the number of fluorescently-labeled cells can be reduced by performing an adoptive transfer of a limited number of fluorescently labeled cell to a non-fluorescent recipient animal. This justifies the differences in cell number between the experimental setup using LysM-GFP transgenic model or the adoptive transfer of CFP-neutrophils into wild type animals prior to imaging shown in **Figures 1**, **6**, respectively.

In this study, we described an alternative way to analyze cell motility in 2P-IVM videos when single cells cannot be tracked. Indeed, by computing pixel velocity, we identified the areas in the LN, called hotspots, in which cells were more active. The advantage of pixel-based measures with respect to track-based measures is that neither manual nor automatic single-cell tracking is required. Therefore, this allows the analysis of videos with a high number of cells.

The quantification of neutrophil behavior from 2P-IVM data is further challenged by the lack of mathematical models that make their motility patterns interpretable. Although optical probes can be used to transform a biological function into a light signal, their application for 2P-IVM remains challenging (83).

To address this issue, we developed a new method of analysis that brings two main advantages with respect to the previously used methods: capturing the time-varying motility of cells and making results interpretable. Indeed, the available methods to assess cell motility can lose information during the averaging process (81). Additionally, although several measures of cell motility were defined (84), the connection of their values to a biological meaning remains to be addressed by the investigator. When applied to our data, the standard track-based measures did not capture significant differences in neutrophil behavior. However, the new method of analysis, proposed in **Figure 5**, identified distinct actions, which changed over time, indicating clear differences in the functions of the analyzed cells. Although in this study we defined five distinct actions of neutrophils, alternative actions could be also defined in future studies, such as apoptosis or NETosis (78), amongst others.

The proposed method allowed to perform a dynamic *in situ* cytometric analysis as proposed in previous studies (53, 83) where distinct phenotypes of cells were identified in 2P-IVM data. However, a set of gates correlating phenotypes to actions were not defined previously. By contrast, our action-based model allowed to define a precise set of gates to interpret the results. It would be compelling to define an extended list of actions that neutrophils can perform or automatically unravel populations of cells expressing distinct phenotypes using data mining methods such as clustering algorithms (85, 86). Additionally, advanced computer vision methods can be applied to detect more complex behaviors, both on shorter and longer periods of time considering other parameters such as cell morphology, context, and space-time structures. This is in line with recent works that aim to recognize cellular motion phenotypes in *in vitro* cultures (87) or human actions using deep machine learning methods (88).

In conclusion, to analyze the complex dynamics of neutrophils in intravital imaging data, an interdisciplinary effort is required. By combining different imaging methodologies, molecular techniques, and pattern recognition methods, we identified distinct behaviors of neutrophils in the early response to influenza vaccination. These behaviors are the expression, of the biological mechanisms that follow influenza vaccination. In addition, we identified an interaction between neutrophil and macrophages, which might be important in terms of the capacity of the former to capture and present antigen.

METHODS

Mice

All animals were bred in-house or acquired from Janvier labs (C57BL/6). Mice were maintained under specific pathogen-free conditions at the Institute for Research in Biomedicine, Bellinzona and used in accordance with the Swiss Federal Veterinary Office guidelines. The following transgenic mice were used: LysM-GFP (89), IL-1R KO (90), TLR3 KO, Myd88 KO (91), CCR2 KO, IFNAR KO (92), CD169DTR (93), CD11c-YFP (94), CK6/ECFP (95), UBC-GFP (96). All strains were on C57BL/6 background. All animal experiments were performed in accordance with the Swiss Federal Veterinary Office guidelines and authorized by the relevant institutional committee (Commissione cantonale per gli esperimenti sugli animali, Ticino) of the Cantonal Veterinary with authorization numbers TI28/17, TI02/14, and TI07/13.

Virus Production Inactivation and Labeling

Influenza virus strain A/PR/8/34 was grown for 3 days in the allantoic cavity of 10-day embryonated chicken eggs. To remove cellular debris the allantoic fluid was harvested and centrifuged at 3,000 rpm for 30 min. Virus was subsequently purified twice in a discontinuous sucrose gradient at 25,000 rpm for 90 min. Virus stocks were quantified by tissue culture infective dose assay (TCID50). To be inactivated, viral suspensions were placed under the UV lamp at a distance of 15 cm for 15 min. For the labeling of UV-inactivated influenza virus, 50 mg/ml of DiD or DiO dye was added to the viral suspension and incubated for 20 min at RT. After that, virus was subsequently purified by centrifugation as mentioned before.

Antigen Administration and Injections

10^6 plaque-forming units (PFU) of inactivated virus per footpad in a final volume of 10 μL were injected into anesthetized mice at different time points prior to LN collection. Macrophage depletion from CD169DTR mice was established by intraperitoneal (i.p.) injection of 10 μg/kg of diphtheria toxin (Sigma-Aldrich) a day before vaccination. Recombinant murine IL-1α (1 μg/fp) and murine CXCL1 (0.5 μg/fp) were reconstituted in sterilized PBS and injected in a final volume of 10 μl 12 h before LN collection. For *in vivo* labeling of cells, mice received subcutaneous injection of 1 μg of fluorescently-labeled αCD21/35, αF4/80, and αCD169/footpad (Biolegend), 3 h before image acquisition. To label the blood vessel mice were injected intravenously with 70 kDa Rhodamin B isothiocyanate-Dextran or Fluorescein isothiocyanate-Dextran solution as described before (97).

Flow Cytometry

Neutrophil influx to the PLN was monitored using flow cytometry. PLN were collected, disrupted with tweezers, and digested for 10 min at 37°C in an enzyme mix composed of DNase I (0.28 mg/ml, Amresco), dispase (1 U/mL, Corning), and collagenase P (0.5 mg/mL, Roche) in calcium- and magnesium-free PBS (PBS-) followed by a stop solution composed of 2 mM EDTA (Sigma-Aldrich) and 2% heat-inactivated filter-sterilized

fetal calf serum (Thermo Fisher Scientific) in PBS- (Sigma-Aldrich). Fc receptors were blocked (αCD16/32, Biolegend) followed by surface staining and analyzed by flow cytometry on a LSRFortessaTM (BD Biosciences). Dead cells were excluded using ZombieAcqua fixable viability dye (Biolegend) and data were analyzed using FlowJo software (TriStar Inc).

Antibodies

In this study, cell suspension was isolated from harvested organs and immunostained with various combinations of the following fluorescence-conjugated antibodies: αB220 (RA3-6B2), αCD3 (17A2), αCD11b (M1/70), αCD69 (H1.2F3), αI-A/I-E (M5/114.15.2), αLy-6G (1A8), αCD21/CD35 (7E9), αF4/80 (BM8), αCD169 (3D6.112), αCD16/32 (90) (all from Biolegend).

Cytoplex Assay

The concentration of various cytokines and chemokine in the lymph was determined by LEGENDPlex assays (Mouse Proinflammatory Chemokine Panel and Mouse Inflammation Panel; Biolegend) according to manufacturer's instructions. Briefly, popliteal PLNs were collected and carefully disrupted in 75 μL ice-cold phosphate buffer, minimizing cell rupture. The suspension was centrifuged at 1,500 rpm for 5 min, and the supernatant was collected. Twenty-five microliter supernatant was used for the protocol following the manufacturer instructions. Samples were analyzed by flow cytometry on an LSRFortessa (BD Biosciences), and data were analyzed using LEGENDPlex software (BioLegend).

Immunohistology and Microscopy

Mice were euthanized, PLN harvested and fixed in 4% PFA at 4°C for 4–6 h. Organs were embedded in 4% low gelling agarose (Sigma-Aldrich) and 50 μm sections were cut with Leica VT1200S vibratome (Leica Microsystems), blocked with proper sera and stained with the indicated antibodies in 0.05% Tween-20 in 0.5% BSA PBS- for two days at 4°C shaking. More details are reported in the antibodies section. Immunofluorescence confocal microscopy was performed using a Leica TCS SP5 confocal microscope (Leica Microsystems). Micrographs were acquired in sequential scans and merged to obtain a multicolor image. Images were processed using Imaris software (Bitplane AG).

Electron Microscopy

PLN were collected and fixed in 2% formaldehyde 2.5% glutaraldehyde in 0.1 M sodium cacodylate buffer (pH 7.4) overnight at 4°C. LN were washed in 0.05 M maleate buffer (pH 5.15) and stained for 2 h in 1% uranyl acetate in maleate buffer. The samples were dehydrated by incubation for 15 min in ethanol water (60, 90, 100%) and embedded in Epon.

Intravital Two-Photon Microscopy

Deep tissue imaging was performed on a customized upright two-photon platform (TrimScope, LaVision BioTec). Two-photon probe excitation and tissue second-harmonic generation (SHG) were obtained with a set of two tunable Ti:sapphire lasers (Chamaleon Ultra I, Chamaleon Ultra II, Coherent) and an optical parametric oscillator that emits in the range of 1,010–1,340 nm (Chamaleon Compact OPO, Coherent), with output wavelength in the range of 690–1,080 nm.

Imaging was performed in the PLN as previously described (98).

Image Analysis and Data Processing

Cell detection, tracking and volumetric reconstruction from 4D 2P-IVM data were performed using Imaris (Oxford Instruments, v7.7.2). Raw data generated from Imaris were further processed and analyzed with a custom Matlab script.

Cell tracks were generated semi-automatically and curated to correct errors (i.e., jumps or non-detected cells). Tracks with a duration <5 points or 300 s were excluded from the analysis. Videos were stabilized using the drift correction functionality when needed, compensating for translational-drift only and by cropping the largest common area in the videos. Standard measures of cell motility were computed using Imaris. These include: Track duration (time interval between the first and the last time points in which a cell is tracked), Track Length (total length of the cell trajectory), Track Speed Mean (Track length/Track duration), Track Displacement (length of the vector from the first to the latest centroid position of the cell), Track Straightness (Track Displacement/Track Length), and Speed (instantaneous speed computed between adjacent time points).

Spectral Unmixing

An additional imaging channel, specific for the cells of interest was generated by classifying each pixel as foreground or background. This was achieved using the Coloc functionality of Imaris in combination with a custom supervised machine learning method for pixel classification implemented in Matlab as described by Pizzagalli and colleagues (99). This method trains a Supported Vector Machine (SVM) to classify pixels as background or background on the basis of examples provided by the user. A minimum of 20 and a maximum of 60 training points were provided for each video. To differentiate between background and foreground the following features were used: Local color, Gaussian-weighted average color in a neighborhood (sigma = 3, 7 μm).

Quantification of Cell Density in High Endothelial Venules (HEV) and Lymphatic Vessels (LV)

The density of neutrophils in a vessel presented in **Figure 1** is defined as the ratio of the number of cells inside a vessel and the volume of the vessel itself. The density of neutrophils in HEV was computed at different time points inside a selected HEV which was visible for the entire duration of the acquisition (3 h). HEV were labeled by the i.v. injection of 70 kDa Rhodamine B isothiocyanate-Dextran. Cells inside the HEV were manually counted every 300 s. The volume of the HEV was estimated as the volume of a cylinder, by measuring the average diameter in the xy plane and the average height along z and the length of the vessel.

The density of neutrophils in LV at the injection site were computed in a LV visible for the entire duration of the acquisition (4 h). Draining LV were labeled by the subcutaneous injection

of DiD-labeled virus and 70 kDa Rhodamine B isothiocyanate-Dextran. Cells were detected and counted automatically using the Spots function of Imaris. The volume of the LV was estimated via volumetric reconstruction using the Surfaces tool of Imaris.

Estimation of Distance of the Virus Particle With Respect to Cell Centroid

To confirm the internalization of the viral particles by neutrophils, the distance of the particles from the cell centroid was computed and compared to the cell radius. Cell radius was estimated via volumetric reconstruction of the cell surface and computed as the radius of a sphere having the same volume of the cell.

Pixel Velocity

The average velocity of pixels presented in **Figure 6A** was estimated via a custom Matlab script that computes optical flow as described in Karlsson and Bigun (60). Only the channel where the neutrophils were visible was used for optical flow estimation. To address the lack of texture of immune cells which leads to an aperture problem, Tikhonov regularization was used while computing the flow (Tikhonov constant = 40). Additionally, outliers were removed by Gaussian smoothing (sigma = 7) followed by the saturation of the bottom 1% and the top 1% of all pixel velocity values (set to the minimum and maximum values, respectively).

Action Recognition

Gating Strategy

We mapped a biological meaning (actions) to specific ranges of instantaneous motility measures. This allowed both to describe the dynamic behavior of neutrophils as a series of actions and provided a suggestion on the biological function of each neutrophil at different time points. However, the problem of identifying one action from a range of measures (gate) is an ill-posed problem which often arises when characterizing a complex biological system from experimental data (100). Indeed, not all the possible actions are known and several actions might exhibit similar motility measures leading to an undetermined solution. To solve this issue, we defined gating thresholds that minimize the overlap between distinct actions and we selected one action out of the multiple possible solutions, based on an arbitrary priority order. Although the gates used to detect actions are subjected to the bias of the investigator, these can be easily adapted according to the experimental settings and based on a priori knowledge.

Software Implementation

A custom Matlab script (**Supplementary Data File 1**) was used to automatically compute instantaneous motility measures and detect actions.

This script decomposes each track into track fragments (tracklets) with a fixed duration of 500 s (approximated to 17 time points with a sampling interval of 30 s). From a track with total duration Td $\geq$ 17 time points, $K = (\mathrm{Td} - 17) + 1$ tracklets were extracted by a sliding window. For the analysis of neutrophils actions in homeostatic conditions and due to the high speed of cells flowing in large blood vessels, the time window was reduced to five time points and the sampling interval of the microscope decreased to 20 s.

Then, the script computes the following measures on each tracklet. Displacement: distance between the initial and the final points of the tracks. Speed: track length/track duration. Straightness: displacement/track length.

Arrest coefficient is typically defined as the percentage of time in which a cell moves below a certain speed threshold. However, being the tracklets of short duration this results in a limited number of admissible percentages. Additionally, a sharp threshold may introduce artifacts. Therefore, we computed arrest coefficient by using a sigmoidal thresholding function defined as follows.

$$\mathrm{ac} = \frac{\sum_{i=1}^{k} 1 - \frac{1}{e^{1+s(k)-\tau}}}{\mathrm{ac}_0}$$

where $\tau = 2\ \mu$m/min is a speed threshold and $\mathrm{ac}_0 = \mathrm{k} - (\mathrm{k}/\mathrm{e}^{1-\tau})$ is the arrest coefficient of a cell having a constant speed of 0 μm/min.

Based on the aforementioned parameters, each tracklet was associated with one of the following actions:

"Arrested": Cell which does not move (i.e. interacting/adhering/death), exhibiting low speed, low directionality, low displacement, and high arrest coefficient.

"Patrolling": Cell which moves, covering a large area of tissue, with medium speed and directionality.

"Directed": Cell which moves toward a target exhibiting high speed and directionality (high displacement and low arrest coefficient).

"Flowing": Cell which flows inside the capillaries of blood vessels in the LN. A flowing cell exhibits extremely high speed and directionality.

Tracklet-to-action association was implemented by means of fixed thresholds corresponding to different gates defined in **Table 1**.

The detection of cells involved in a swarm (swarming) was achieved via a volumetric reconstruction. For the videos in **Figure 4** with adoptively transferred CK6/ECFP neutrophils, swarms were considered as surfaces with a minimum volume of $2^*10^3\ \mu\mathrm{m}^3$.

The number of cells in a swarm was estimated by dividing the swarm volume by the volume of a single cell (assumed to 1^*10^3 $\mu\mathrm{m}^3$ without spaces between cells).

Swarm Quantification

To quantify the size and the growth rate of swarms we defined both a cell density and an overall directionality criteria. More precisely, we detected swarms in regions where cells accumulated and where most trajectories pointed to. The "surfaces" functionality of Imaris was used to reconstruct the volume of swarms, selecting the marching cube algorithm with either a user-defined brightness threshold in low-magnification videos–**Figure 6C** or by manually defining a region of interest around the swarm in high magnification videos–**Figure 6I**.

TABLE 1 | Gating thresholds.

Evaluated on 500 s		Arrested	Patrolling	Directed	Flowing	Swarming
Speed (μm/min)	Min	0	2	6	10	–
	Max	7	8	25	300	–
Straightness (0..1)	Min	0	0.1	0.3	0.5	–
	Max	0.3	0.5	1	1	–
Arrest coefficient (0..1)	Min	0.7	0.1	0	0	–
	Max	1	0.8	0.2	0.2	–
Displacement (0..1)	Min	0	4	8	50	–
	Max	15	20	80	300	–
Volume (μm^3)	Min	–	–	–	–	2,000

Each action (row) is mapped to a specific range (min-max) of motility parameters (columns). Values refer to tracklets with a duration of 500 s.

Neutrophils involved in the swarm were manually tracked until the end of the videos or when they merged to emerging swarms.

Statistics

Results were expressed as mean ± standard deviation (SD). All statistical analyses were performed in Prism8 (Graphpad Software, La Jolla, USA). Means among two groups were compared with two-tailed *t*-test. Means among three or more groups were compared with one-way ANOVA with Dunn's multiple comparison post-test.

Software Availability and Usage

The source code of the program to quantify the actions of immune cells from their tracks, is provided in **Supplementary Data File 1**. This program requires the tracks of the cells to be exported from Imaris to an Excel file. After this has been done, it is possible to open the program in Matlab, enter the location of the Excel file, and executing the program. The plots counting the actions will be automatically created.

To facilitate this process, and to avoid the requirement of Matlab, the software will be further distributed as an open source plug-in for common imaging software at https://www.ltdb.info/tool and https://github.com/IRB-LTDB/.

DATA AVAILABILITY STATEMENT

The datasets generated for this study are available on request to the corresponding author.

ETHICS STATEMENT

All animal experiments were performed in accordance with the Swiss Federal Veterinary Office guidelines and authorized by the relevant institutional committee (Commissione cantonale per gli esperimenti sugli animali, Ticino) of the Cantonal Veterinary with authorization numbers TI28/17, TI02/14, and TI07/13.

AUTHOR CONTRIBUTIONS

SG directed the study. SG, DP, IL, and AP designed and performed experiments, analyzed and interpreted the results, and wrote the manuscript. RK supervised the computational aspects of data analysis. SG and MP-S performed 2P-IVM. YF and TV performed experiments.

FUNDING

This work was supported by the Swiss National Foundation (SNF) grants (176124), R'equipt (145038), and Ambizione (148183), the European Commission Marie Curie Reintegration Grant (612742), the Center for Computational Medicine in Cardiology (CCMC), and SystemsX.ch for a grant to DP (2013/124).

ACKNOWLEDGMENTS

We would like to thank David Jarrossay and Diego Morone for the provision of technical support, and Profs. Mariagrazia Uguccioni and Marcus Thelen for critical discussion of the manuscript.

SUPPLEMENTARY MATERIAL

The Supplementary Material for this article can be found online at: https://www.frontiersin.org/articles/10.3389/fimmu.2019.02621/full#supplementary-material

Supplementary Movie 1 | Recruitment of neutrophils from blood vessels. 4D 2P-IVM video acquired in the LN showing LysM-GFP neutrophils (green) recruited via blood vessels (labeled with i.v. injection of Rhodamin B isothiocyanate-Dextran–red, dashed line). Arrow indicates a hotspot where neutrophils accumulate during extravasation.

Supplementary Movie 2 | Recruitment of neutrophils from lymphatic vessels. 4D 2P-IVM video acquired in the site of injection, showing LysM-GFP neutrophils (green) recruited via lymphatic vessels (red) that draining to lymph node. UV-PR8 is labeled in FR (white) and collagen fibers are visible by second harmonic generation (SHG, blue).

Supplementary Movie 3 | Neutrophils phagocytize influenza virus particles. 4D 2P-IVM video acquired in the LN showing an interaction between LysM-GFP

neutrophils (green) and viral aggregates (UV-PR8-DiO, red). Lines indicate the tracks of neutrophils and viral aggregates, respectively.

Supplementary Movie 4 | Migration of neutrophils in the LN at 30, 75, and 135 min post-vaccination. Neutrophils (light-blue) adoptively transferred from a CK6/ECFP animal, migrate in the lymph node exhibiting different motility patterns over time. The vascular network is labeled via i.v. injection of Fluorescein isothiocyanate-Dextran (green), macrophages are labeled via CD169-PE antibody (red) while the collagen scaffold is visible via Second Harmonic Generation (SHG, blue).

Supplementary Movie 5 | Neutrophil migration in different areas of the LN. 4D 2P-IVM video acquired using a low magnification (10x) showing the migration of LysM-GFP neutrophils (green) in the different areas of the LN. Collagen scaffold is visible via Second Harmonic Generation (SHG, blue).

Supplementary Movie 6 | Swarm formation after vaccination. 4D 2P-IVM video showing the formation of multiple LysM-GFP neutrophils swarms (green) in the SCS in close proximity to CD169-AF647 macrophages (white). Blood vessels are labeled via i.v. dextran injection (red) and the LN scaffold is visible via Second Harmonic Generation (SHG, blue).

Supplementary Movie 7 | Swarm formation associated with dying macrophages. 4D 2P-IVM video showing swarm formation after vaccination. CFP-expressing neutrophils (light-blue) are adoptive transfer into CD11c-YFP (green) animal prior vaccine injection. UV-PR8 is labeled with DiD labeling dye (red). Dashed line indicates the subcapsular sinus area and arrows indicate recruited neutrophils.

Supplementary Movie 8 | Neutrophil migration in homeostasis. Neutrophils (light-blue) adoptively transferred from a CK6/ECFP animal flow within the blood vessels of the lymph node. Vascular network (labeled via i.v. injection of Fluorescein isothiocyanate-Dextran (green), macrophages are labeled via CD169-PE antibody (red) while the collagen scaffold is visible via Second Harmonic Generation (SHG, blue).

Supplementary Figure 1 | (A) Scanning electron micrograph showing an association between neutrophils (n) and HEV at 2 h post vaccination (p.v.). The lumen of the blood vessel is marked in red. **(B)** Flow cytometric analysis showing the recruitment of neutrophils (Ly6G+ CD11b+) at 12 h p.v.. Percentages of CD44+ **(C)**, CD62L **(D)** and CD49d+ **(E)** cells out of all neutrophils at 12 h p.v. compared with non-vaccinated controls. **(F)** Absolute numbers of CD169+ cells in the lymph node of DT treated CD169-DTR mice (left) and representative density dot plot showing the gating for CD169+CD11c intlow macrophage population (right). Quantification of CD169+ macrophages in CCR2KO **(G)** and IFNARKO mice **(H)**. **(I)** Total number of CD169+F4/80+ medullary macrophages in IFNARKO mice. **(J)** Schematic drawing (left) of an electron micrograph (right) showing neutrophils in the SCS phagocytizing UV-inactivated influenza virus at 2 h p.v..

Supplementary Figure 2 | (A) 2P-IVM micrograph showing the vascular structure of the popliteal lymph node and the tracks of neutrophils (white lines) prior to vaccination. Only neutrophils visible for at least 100 s and migrating within the lymph node are tracked. **(B,C)** Actions performed by the tracked neutrophils corresponding to distinct motility values shown in **(B)** mainly associated to flowing **(C)**.

REFERENCES

1. Alberts B, Johnson A, Lewis J, Raff M, Roberts K, Walter P. Chapter 24: Innate immunity. In: Bochicchio A. editor. *Molecular Biology of the Cell*. 6th ed. New York, NY: Garland Science (2002). p. 1298.
2. Leliefeld PHC, Koenderman L, Pillay J. How neutrophils shape adaptive immune responses. *Front Immunol.* (2015) 6:471. doi: 10.3389/fimmu.2015.00471
3. Hickman HD, Bennink JR, Yewdell JW. Caught in the act: intravital multiphoton microscopy of host-pathogen interactions. *Cell Host Microbe.* (2009) 5:13–21. doi: 10.1016/j.chom.2008.12.007
4. Medyukhina A, Timme S, Mokhtari Z, Figge MT. Image-based systems biology of infection. *Cytom A*. (2015) 87:462–470. doi: 10.1002/cyto.a.22638
5. Stein JV, Gonzalez SF, Gonzalez SF, Gonzalez SF. Dynamic intravital imaging of cell-cell interactions in the lymph node. *J Allergy Clin Immunol.* (2017) 139:12–20. doi: 10.1016/j.jaci.2016.11.008
6. Chatziandreou N, Farsakoglu Y, Palomino-Segura M, Lanzavecchia A, Carroll MC, Gonzalez Correspondence SF. Macrophage death following influenza vaccination initiates the inflammatory response that promotes dendritic cell function in the draining lymph node. *Cell Rep.* (2017) 18:2427–2440. doi: 10.1016/j.celrep.2017.02.026
7. Moseman EA, Iannacone M, Bosurgi L, Tonti E, Chevrier N, Tumanov A, et al. B cell maintenance of subcapsular sinus macrophages protects against a fatal viral infection independent of adaptive immunity. *Immunity.* (2012) 36:415–26. doi: 10.1016/j.immuni.2012.01.013
8. Carrasco YR, Batista FD. B cells acquire particulate antigen in a macrophage-rich area at the boundary between the follicle and the subcapsular sinus of the lymph node. *Immunity.* (2007) 27:160–71. doi: 10.1016/j.immuni.2007.06.007
9. Farsakoglu Y, Palomino-Segura M, Latino I, Zanaga S, Chatziandreou N, Pizzagalli DU, et al. Influenza vaccination induces NK-cell-mediated type-II IFN response that regulates humoral immunity in an IL-6-dependent manner. *Cell Rep.* (2019) 26:2307–15.e5. doi: 10.1016/j.celrep.2019.01.104
10. Iannacone M, Moseman EA, Tonti E, Bosurgi L, Junt T, Henrickson SE, et al. Subcapsular sinus macrophages prevent CNS invasion on peripheral infection with a neurotropic virus. *Nature.* (2010) 465:1079–83. doi: 10.1038/nature09118
11. Thomas SN, Rohner NA, Edwards EE. Implications of lymphatic transport to lymph nodes in immunity and immunotherapy. *Annu Rev Biomed Eng.* (2016) 18:207–33. doi: 10.1146/annurev-bioeng-101515-014413
12. Gonzalez SF, Lukacs-Kornek V, Kuligowski MP, Pitcher LA, Degn SE, Kim YA, et al. Capture of influenza by medullary dendritic cells via SIGN-R1 is essential for humoral immunity in draining lymph nodes. *Nat Immunol.* (2010) 11:427–34. doi: 10.1038/ni.1856
13. Förster R, Davalos-Misslitz AC, Rot A. CCR7 and its ligands: balancing immunity and tolerance. *Nat Rev Immunol.* (2008) 8:362–71. doi: 10.1038/nri2297
14. Muller WA. Mechanisms of leukocyte transendothelial migration. *Annu Rev Pathol Mech Dis.* (2011) 6:323–44. doi: 10.1146/annurev-pathol-011110-130224
15. Allen CDC, Cyster JG. Follicular dendritic cell networks of primary follicles and germinal centers: phenotype and function. *Semin Immunol.* (2008) 20:14–25. doi: 10.1016/j.smim.2007.12.001
16. Gunn MD, Ngo VN, Ansel KM, Ekland EH, Cyster JG, Williams LT. A B-cell-homing chemokine made in lymphoid follicles activates Burkitt's lymphoma receptor-1. *Nature.* (1998) 391:799–803. doi: 10.1038/35876
17. Gonzalez SF, Degn SE, Pitcher LA, Woodruff M, Heesters BA, Carroll MC. Trafficking of B cell antigen in lymph nodes. *Annu Rev Immunol.* (2011) 29:215–33. doi: 10.1146/annurev-immunol-031210-101255
18. Lian J, Luster AD. Chemokine-guided cell positioning in the lymph node orchestrates the generation of adaptive immune responses. *Curr Opin Cell Biol.* (2015) 36:1–6. doi: 10.1016/j.ceb.2015.05.003
19. Cyster JG. Chemokines and cell migration in secondary lymphoid organs. *Science.* (1999) 286:2098–102. doi: 10.1126/science.286.5447.2098
20. Förster R, Braun A, Worbs T. Lymph node homing of T cells and dendritic cells via afferent lymphatics. *Trends Immunol.* (2012) 33:271–80. doi: 10.1016/j.it.2012.02.007
21. Maletto BA, Ropolo AS, Alignani DO, Liscovsky MV, Ranocchia RP, Moron VG, et al. Presence of neutrophil-bearing antigen in lymphoid organs of immune mice. *Blood.* (2006) 108:3094–102. doi: 10.1182/blood-2006-04-016659
22. Chtanova T, Schaeffer M, Han SJ, van Dooren GG, Nollmann M, Herzmark P, et al. Dynamics of neutrophil migration in lymph nodes during infection. *Immunity.* (2008) 29:487–96. doi: 10.1016/j.immuni.2008.07.012

23. Petri B, Phillipson M, Kubes P. The physiology of leukocyte recruitment: an *in vivo* perspective. *J Immunol.* (2008) 180:6439–46. doi: 10.4049/jimmunol.180.10.6439
24. Kolaczkowska E, Kubes P. Neutrophil recruitment and function in health and inflammation. *Nat Rev Immunol.* (2013) 13:59–75 doi: 10.1038/nri3399
25. Mayadas TN, Cullere X, Lowell CA. The multifaceted functions of neutrophils. *Annu Rev Pathol Mech Dis.* (2013) 9:181–218. doi: 10.1146/annurev-pathol-020712-164023
26. Furze RC, Rankin SM. Neutrophil mobilization and clearance in the bone marrow. *Immunology.* (2008) 125:281–8. doi: 10.1111/j.1365-2567.2008.02950.x
27. Miyasaka M, Tanaka T. Lymphocyte trafficking across high endothelial venules: dogmas and enigmas. *Nat Rev Immunol.* (2004) 4:360–70. doi: 10.1038/nri1354
28. Gorlino CV, Ranocchia RP, Harman MF, García IA, Crespo MI, Morón G, et al. Neutrophils exhibit differential requirements for homing molecules in their lymphatic and blood trafficking into draining lymph nodes. *J Immunol.* (2014) 193:1966–74. doi: 10.4049/jimmunol.1301791
29. Arokiasamy S, Zakian C, Dilliway J, Wang W, Nourshargh S, Voisin MB. Endogenous TNFα orchestrates the trafficking of neutrophils into and within lymphatic vessels during acute inflammation. *Sci Rep.* (2017) 7:44189. doi: 10.1038/srep44189
30. Hampton HR, Bailey J, Tomura M, Brink R, Chtanova T. Microbe-dependent lymphatic migration of neutrophils modulates lymphocyte proliferation in lymph nodes. *Nat Commun.* (2015) 6:7139. doi: 10.1038/ncomms8139
31. Rigby DA, Ferguson DJP, Johnson LA, Jackson DG. Neutrophils rapidly transit inflamed lymphatic vessel endothelium via integrin-dependent proteolysis and lipoxin-induced junctional retraction. *J Leukoc Biol.* (2015) 98:897–912. doi: 10.1189/jlb.1HI0415-149R
32. Ley K, Laudanna C, Cybulsky MI, Nourshargh S. Getting to the site of inflammation: the leukocyte adhesion cascade updated. *Nat Rev Immunol.* (2007) 7:678–89. doi: 10.1038/nri2156
33. Miller LS, O'Connell RM, Gutierrez MA, Pietras EM, Shahangian A, Gross CE, et al. MyD88 mediates neutrophil recruitment initiated by IL-1R but not TLR2 activation in immunity against *Staphylococcus aureus*. *Immunity.* (2006) 24:79–91. doi: 10.1016/j.immuni.2005.11.011
34. Dinarello CA. Overview of the IL-1 family in innate inflammation and acquired immunity. *Immunol Rev.* (2018) 281:8–27. doi: 10.1111/imr.12621
35. Mantovani A, Dinarello CA, Molgora M, Garlanda C. Interleukin-1 and related cytokines in the regulation of inflammation and immunity. *Immunity.* (2019) 50:778–95. doi: 10.1016/j.immuni.2019.03.012
36. Lämmermann T. In the eye of the neutrophil swarm-navigation signals that bring neutrophils together in inflamed and infected tissues. *J Leukoc Biol.* (2016) 100:55–63. doi: 10.1189/jlb.1MR0915-403
37. Mantovani A, Cassatella MA, Costantini C, Jaillon S. Neutrophils in the activation and regulation of innate and adaptive immunity. *Nat Rev Immunol.* (2011) 11:519–31. doi: 10.1038/nri3024
38. Mócsai A. Diverse novel functions of neutrophils in immunity, infammation, and beyond. *J Exp Med.* (2013) 210:1289–99. doi: 10.1084/jem.20122220
39. Puga I, Cols M, Barra CM, He B, Cassis L, Gentile M, et al. B cell-helper neutrophils stimulate the diversification and production of immunoglobulin in the marginal zone of the spleen. *Nat Immunol.* (2012) 13:170–80. doi: 10.1038/ni.2194
40. Vono M, Lin A, Norrby-Teglund A, Koup RA, Liang F, Loré K. Neutrophils acquire the capacity for antigen presentation to memory CD4+ T cells *in vitro* and *ex vivo*. *Blood.* (2017) 129:1991–2001. doi: 10.1182/blood-2016-10-744441
41. Minns D, Smith KJ, Findlay EG. Orchestration of adaptive T cell responses by neutrophil granule contents. *Mediators Inflamm.* (2019) 2019:1–15. doi: 10.1155/2019/8968943
42. Duffy D, Perrin H, Abadie V, Benhabiles N, Boissonnas A, Liard C, et al. Neutrophils transport antigen from the dermis to the bone marrow, initiating a source of memory CD8+ T cells. *Immunity.* (2012) 37:917–29. doi: 10.1016/j.immuni.2012.07.015
43. Abdallah DSA, Egan CE, Butcher BA, Denkers EY. Mouse neutrophils are professional antigen-presenting cells programmed to instruct T h1 and T h17 T-cell differentiation. *Int Immunol.* (2011) 23:317–26. doi: 10.1093/intimm/dxr007
44. Bogoslowski A, Butcher EC, Kubes P. Neutrophils recruited through high endothelial venules of the lymph nodes via PNAd intercept disseminating *Staphylococcus aureus*. *Proc Natl Acad Sci USA.* (2018) 115:2449–54. doi: 10.1073/pnas.1715756115
45. Kienle K, Lämmermann T. Neutrophil swarming: an essential process of the neutrophil tissue response. *Immunol Rev.* (2016) 273:76–93. doi: 10.1111/imr.12458
46. Kreisel D, Nava RG, Li W, Zinselmeyer BH, Wang B, Lai J, et al. *In vivo* two-photon imaging reveals monocyte-dependent neutrophil extravasation during pulmonary inflammation. *Proc Natl Acad Sci USA.* (2010) 107:18073–8. doi: 10.1073/pnas.1008737107
47. Weninger W, Biro M, Jain R. Leukocyte migration in the interstitial space of non-lymphoid organs. *Nat Rev Immunol.* (2014) 14:232–46. doi: 10.1038/nri3641
48. Kamenyeva O, Boularan C, Kabat J, Cheung GYC, Kehrl JH. Neutrophil recruitment to lymph nodes limits local humoral response to *Staphylococcus aureus*. (2015) 11:e1004827. doi: 10.1371/journal.ppat.1004827
49. Ng LG, Qin JS, Roediger B, Wang Y, Jain R, Cavanagh LL, et al. Visualizing the neutrophil response to sterile tissue injury in mouse dermis reveals a three-phase cascade of events. *J Invest Dermatol.* (2011) 131:2058–68. doi: 10.1038/jid.2011.179
50. Shannon JG, Bosio CF, Hinnebusch BJ. Dermal neutrophil, macrophage and dendritic cell responses to *Yersinia pestis* transmitted by fleas. *PLoS Pathog.* (2015) 11:1–19. doi: 10.1371/journal.ppat.1004734
51. Lämmermann T, Afonso PV, Angermann BR, Wang JM, Kastenmüller W, Parent CA, et al. Neutrophil swarms require LTB4 and integrins at sites of cell death *in vivo*. *Nature.* (2013) 498:371–5. doi: 10.1038/nature12175
52. Figge MT, Murphy RF. Image-based systems biology. *Cytom A.* (2015) 87:459–61. doi: 10.1002/cyto.a.22663
53. Moreau HD, Lemaître F, Terriac E, Azar G, Piel M, Lennon-Dumenil A-M, et al. Dynamic *in situ* cytometry uncovers T cell receptor signaling during immunological synapses and kinapses *in vivo*. *Immunity.* (2012) 37:351–63. doi: 10.1016/j.immuni.2012.05.014
54. Mokhtari Z, Mech F, Zitzmann C, Hasenberg M, Gunzer M, Figge MT. Automated characterization and parameter-free classification of Cell tracks based on local migration behavior. *PLoS ONE.* (2013) 8:e80808. doi: 10.1371/journal.pone.0080808
55. Hyun YM, Choe YH, Park SA, Kim M. LFA-1 (CD11a/CD18) and Mac-1 (CD11b/CD18) distinctly regulate neutrophil extravasation through hotspots I and II. *Exp Mol Med.* (2019) 51:39. doi: 10.1038/s12276-019-0227-1
56. Pruenster M, Mudde L, Bombosi P, Dimitrova S, Zsak M, Middleton J, et al. The duffy antigen receptor for chemokines transports chemokines and supports their promigratory activity. *Nat Immunol.* (2009) 10:101–8. doi: 10.1038/ni.1675
57. Auffray C, Fogg D, Garfa M, Elain G, Join-Lambert O, Kayal S, et al. Monitoring of blood vessels and tissues by a population of monocytes with patrolling behavior. *Science.* (2007) 317:666–70. doi: 10.1126/science.1142883
58. Friedl P, Weigelin B. Interstitial leukocyte migration and immune function. *Nat Immunol.* (2008) 9:960–9. doi: 10.1038/ni.f.212
59. Lam P, Huttenlocher A. Interstitial leukocyte migration *in vivo*. *Curr Opin Cell Biol.* (2013) 25:650–8. doi: 10.1016/j.ceb.2013.05.007
60. Karlsson SM, Bigun J. Lip-motion events analysis and lip segmentation using optical flow. In: *2012 IEEE Computer Society Conference on Computer Vision and Pattern Recognition Workshops.* Providence, RI: IEEE (2012), p. 138–45. doi: 10.1109/CVPRW.2012.6239228
61. Lopez S, Marco AJ, Prats N, Czuprynski CJ. Critical role of neutrophils in eliminating listeria monocytogenes from the central nervous system during experimental murine listeriosis. *Infect Immun.* (2000) 68:4789–91. doi: 10.1128/IAI.68.8.4789-4791.2000
62. Ueki H, Wang IH, Fukuyama S, Katsura H, da Silva Lopes TJ, Neumann G, et al. *In vivo* imaging of the pathophysiological changes and neutrophil dynamics in influenza virus-infected mouse lungs. *Proc Natl Acad Sci USA.* (2018) 115:E6622–9. doi: 10.1073/pnas.1806265115

63. Martin C, Burdon PCE, Bridger G, Gutierrez-Ramos JC, Williams TJ, Rankin SM. Chemokines acting via CXCR2 and CXCR4 control the release of neutrophils from the bone marrow and their return following senescence. *Immunity.* (2003) 19:583–93. doi: 10.1016/S1074-7613(03)00263-2
64. Eash KJ, Means JM, White DW, Link DC, Mermod JJ, Dexter TM. CXCR4 is a key regulator of neutrophil release from the bone marrow under basal and stress granulopoiesis conditions. *Blood.* (2009) 113:4711–9. doi: 10.1182/blood-2008-09-177287
65. Khan AI, Kerfoot SM, Heit B, Liu L, Andonegui G, Ruffell B, et al. Role of CD44 and hyaluronan in neutrophil recruitment. *J Immunol.* (2004) 173:7594–601. doi: 10.4049/jimmunol.173.12.7594
66. Kishimoto TK, Jutila MA, Berg EL, Butcher EC. Neutrophil Mac-1 and MEL-14 adhesion proteins inversely regulated by chemotactic factors. *Science.* (1989) 245:1238–41. doi: 10.1126/science.2551036
67. Tsuda Y, Takahashi H, Kobayashi M, Hanafusa T, Herndon DN, Suzuki F. Three different neutrophil subsets exhibited in mice with different susceptibilities to infection by methicillin-resistant Staphylococcus aureus. *Immunity.* (2004) 21:215–26. doi: 10.1016/j.immuni.2004.07.006
68. Mayer-Barber KD, Yan B. Clash of the cytokine titans: counter-regulation of interleukin-1 and type I interferon-mediated inflammatory responses. *Cell Mol Immunol.* (2017) 14:22–35. doi: 10.1038/cmi.2016.25
69. Biondo C, Mancuso G, Midiri A, Signorino G, Domina M, Lanza Cariccio V, et al. The interleukin-1β/CXCL1/2/neutrophil axis mediates host protection against group B streptococcal infection. *Infect Immun.* (2014) 82:4508–17. doi: 10.1128/IAI.02104-14
70. De Filippo K, Henderson RB, Laschinger M, Hogg N. Neutrophil chemokines KC and macrophage-inflammatory protein-2 are newly synthesized by tissue macrophages using distinct TLR signaling pathways. *J Immunol.* (2008) 180:4308–15. doi: 10.4049/jimmunol.180.6.4308
71. Barry KC, Fontana MF, Portman JL, Dugan AS, Vance RE. IL-1α signaling initiates the inflammatory response to virulent legionella pneumophila *in vivo*. *J Immunol.* (2013) 190:6329–39. doi: 10.4049/jimmunol.1300100
72. Voisin M-B, Nourshargh S. Invited review neutrophil trafficking to lymphoid tissues: physiological and pathological implications. *J Pathol J Pathol.* (2019) 247:662–71. doi: 10.1002/path.5227
73. Chou RC, Kim ND, Sadik CD, Seung E, Lan Y, Byrne MH, et al. Lipid-cytokine-chemokine cascade drives neutrophil recruitment in a murine model of inflammatory arthritis. *Immunity.* (2010) 33:266–78. doi: 10.1016/j.immuni.2010.07.018
74. Hufford MM, Richardson G, Zhou H, Manicassamy B, García-Sastre A, Enelow RI, et al. Influenza-infected neutrophils within the infected lungs act as antigen presenting cells for anti-viral CD8+ T cells. *PLoS ONE.* (2012) 7:e46581. doi: 10.1371/journal.pone.0046581
75. Tate MD, Brooks AG, Reading PC, Mintern JD. Neutrophils sustain effective CD8 + T-cell responses in the respiratory tract following influenza infection. *Immunol Cell Biol.* (2012) 90:197–205. doi: 10.1038/icb.2011.26
76. Nourshargh S, Renshaw SA, Imhof BA. Reverse migration of neutrophils: where, when, how, and why? *Trends Immunol.* (2016) 37:273–86. doi: 10.1016/j.it.2016.03.006
77. Hashimoto Y, Moki T, Takizawa T, Shiratsuchi A, Nakanishi Y. Evidence for phagocytosis of influenza virus-infected, apoptotic cells by neutrophils and macrophages in mice. *J Immunol.* (2007) 178:2448–57. doi: 10.4049/jimmunol.178.4.2448
78. Naumenko V, Turk M, Jenne CN, Kim S-J. Neutrophils in viral infection. *Cell Tissue Res.* (2018) 371:505–16. doi: 10.1007/s00441-017-2763-0
79. Camp JV, Jonsson CB. A role for neutrophils in viral respiratory disease. *Front Immunol.* (2017) 8:550. doi: 10.3389/fimmu.2017.00550
80. Ratcliffe D, Migliorisi G, Cramer E. Translocation of influenza virus by migrating neutrophils. *Cell Mol Biol.* (1992) 38:63–70.
81. Hallett MB. editor. Biophysics of leukocytes: neutrophil chemotaxis, characteristics, and mechanisms. In: *The Neutrophil: Cellular Biochemistry and Physiology*. Boston, MA: CRC Press (1989).
82. Peters NC, Egen JG, Secundino N, Debrabant A, Kamhawi S, Lawyer P, et al. *In vivo* imaging reveals an essential role for neutrophils in Leishmaniasis transmitted by sand flies. *Science.* (2009) 321:970–4. doi: 10.1126/science.1159194.In
83. Bousso P, Moreau HD. Functional immunoimaging: the revolution continues. *Nat Rev Immunol.* (2012) 12:858–64. doi: 10.1038/nri3342
84. Beltman JB, Marée AFM, de Boer RJ, M Marée AF, de Boer RJ, Marée AFM, et al. Analysing immune cell migration. *Nat Rev Immunol.* (2009) 9:789–98. doi: 10.1038/nri2638
85. Wiwie C, Baumbach J, Röttger R. Comparing the performance of biomedical clustering methods. *Nat Methods.* (2015) 12:1033–8. doi: 10.1038/nmeth.3583
86. Pizzagalli DU, Gonzalez SF, Krause R. A trainable clustering algorithm based on shortest paths from density peaks. *Sci Adv.* (2019) 5:eaax3770. doi: 10.1126/sciadv.aax3770
87. Zhou FY, Ruiz-Puig C, Owen RP, White MJ, Rittscher J, Lu X. Motion sensing superpixels (MOSES) is a systematic computational framework to quantify and discover cellular motion phenotypes. *Elife.* (2019) 8:e40162. doi: 10.7554/eLife.40162
88. Zhang Y, Zhang Y, Zhang Z, Bao J, Song Y. Human activity recognition based on time series analysis using U-Net. *arXiv Preprint.* (2018)
89. Clausen BE, Burkhardt C, Reith W, Renkawitz R, Förster I. Conditional gene targeting in macrophages and granulocytes using LysMcre mice. *Transgenic Res.* (1999) 8:265–77. doi: 10.1023/A:1008942828960
90. Labow M, Shuster D, Zetterstrom M, Nunes P, Terry R, Cullinan EB, et al. Absence of IL-1 signaling and reduced inflammatory response in IL-1 type I receptor-deficient mice. *J Immunol.* (1997) 159:2452–61.
91. Hou B, Reizis B, DeFranco AL. Toll-like receptors activate innate and adaptive immunity by using dendritic cell-intrinsic and -extrinsic mechanisms. *Immunity.* (2008) 29:272–82. doi: 10.1016/j.immuni.2008.05.016
92. Muller U, Steinhoff U, Reis L, Hemmi S, Pavlovic J, Zinkernagel R, et al. Functional role of type I and type II interferons in antiviral defense. *Science.* (1994) 264:1918–21. doi: 10.1126/science.8009221
93. Miyake Y, Asano K, Kaise H, Uemura M, Nakayama M, Tanaka M. Critical role of macrophages in the marginal zone in the suppression of immune responses to apoptotic cell–associated antigens. *J Clin Invest.* (2007) 117:2268–78. doi: 10.1172/JCI31990
94. Lindquist RL, Shakhar G, Dudziak D, Wardemann H, Eisenreich T, Dustin ML, et al. Visualizing dendritic cell networks *in vivo*. *Nat Immunol.* (2004) 5:1243–50. doi: 10.1038/ni1139
95. Tran Cao HS, Reynoso J, Yang M, Kimura H, Kaushal S, Snyder CS, et al. Development of the transgenic cyan fluorescent protein (CFP)-expressing nude mouse for 'Technicolor' cancer imaging. *J Cell Biochem.* (2009) 107:328–34. doi: 10.1002/jcb.22128
96. Schaefer BC, Schaefer ML, Kappler JW, Marrack P, Kedl RM. Observation of antigen-dependent CD8+ T-Cell/ dendritic cell interactions *in vivo*. *Cell Immunol.* (2001) 214:110–22. doi: 10.1006/cimm.2001.1895
97. Palomino-Segura M, Gonzalez SF. Two-photon intravital imaging of leukocytes in the trachea during pneumococcal infection. *Methods Mol Biol.* (2019) 1968:183–94. doi: 10.1007/978-1-4939-9199-0_15
98. Miller MJ, Wei SH, Parker I, Cahalan MD. Two-photon imaging of lymphocyte motility and antigen response in intact lymph node. *Science.* (2002) 296:1869–73. doi: 10.1126/science.1070051
99. Pizzagalli DU, Thelen M, Gonzalez SF, Krause R. Semi-supervised machine learning facilitates cell colocalization and tracking in 2-photon microscopy. *BioRxiv*. (2019) doi: 10.1101/829838
100. Guzzi R, Colombo T, Paci P. Inverse problems in systems biology: a critical review. *Methods Mol Biol.* (2018) 1702:69–94. doi: 10.1007/978-1-4939-7456-6_6

Conflict of Interest: The authors declare that the research was conducted in the absence of any commercial or financial relationships that could be construed as a potential conflict of interest.

frontiers in Immunology

REVIEW
published: 26 November 2019
doi: 10.3389/fimmu.2019.02782

Live Intravital Imaging of Cellular Trafficking in the Cardiac Microvasculature—Beating the Odds

Dean Philip John Kavanagh and Neena Kalia*

Institute of Cardiovascular Sciences, College of Medical and Dental Sciences, University of Birmingham, Birmingham, United Kingdom

Although mortality rates from cardiovascular disease in the developed world are falling, the prevalence of cardiovascular disease (CVD) is not. Each year, the number of people either being diagnosed as suffering with CVD or undergoing a surgical procedure related to it, such as percutaneous coronary intervention, continues to increase. In order to ensure that we can effectively manage these diseases in the future, it is critical that we fully understand their basic physiology and their underlying causative factors. Over recent years, the important role of the cardiac microcirculation in both acute and chronic disorders of the heart has become clear. The recruitment of inflammatory cells into the cardiac microcirculation and their subsequent activation may contribute significantly to tissue damage, adverse remodeling, and poor outcomes during recovery. However, our basic understanding of the cardiac microcirculation is hampered by an historic inability to image the microvessels of the beating heart—something we have been able to achieve in other organs for over 100 years. This stems from a couple of clear and obvious difficulties related to imaging the heart—firstly, it has significant inherent contractile motion and is affected considerably by the movement of lungs. Secondly, it is located in an anatomically challenging position for microscopy. However, recent microscopic and technological developments have allowed us to overcome some of these challenges and to begin to answer some of the basic outstanding questions in cardiac microvascular physiology, particularly in relation to inflammatory cell recruitment. In this review, we will discuss some of the historic work that took place in the latter part of last century toward cardiac intravital, before moving onto the advanced work that has been performed since. This work, which has utilized technology such as spinning-disk confocal and multiphoton microscopy, has—along with some significant advancements in algorithms and software—unlocked our ability to image the "business end" of the cardiac vascular tree. This review will provide an overview of these techniques, as well as some practical pointers toward software and other tools that may be useful for other researchers who are considering utilizing this technique themselves.

Keywords: cardiac imaging, motion artifact detection, motion artifact removal, intravital imaging, microcirculation, ischaemia and reperfusion injury, cardiac microcirculation

OPEN ACCESS

Edited by:
Elzbieta Kolaczkowska, Jagiellonian University, Poland

Reviewed by:
Dianne Cooper, Queen Mary University of London, United Kingdom
Justin Deniset, University of Calgary, Canada

****Correspondence:***
Dean Philip John Kavanagh
d.kavanagh@bham.ac.uk

Specialty section:
This article was submitted to Inflammation, a section of the journal Frontiers in Immunology

Received: *21 August 2019*
Accepted: *13 November 2019*
Published: *26 November 2019*

Citation:
Kavanagh DPJ and Kalia N (2019) Live Intravital Imaging of Cellular Trafficking in the Cardiac Microvasculature—Beating the Odds. Front. Immunol. 10:2782. doi: 10.3389/fimmu.2019.02782

HEART DISEASE AND INFLAMMATION

In the United Kingdom, more than a quarter of all deaths are attributable to cardiovascular disease (CVD) and around 7.4 million people currently live with a heart or circulatory disease (1). While mortality is decreasing in developed countries, the number of people who are living with cardiovascular conditions is increasing; the number of patients in the UK who underwent percutaneous coronary interventions (PCI) in 2013 was seven times the number two decades earlier (2). Although there has been significant progress in the reduction of mortality rates from CVD, it is still the cause of death for almost 170,000 people every year– accounting for almost 28% of all mortality in the UK (3). In order to fully ensure that we can treat this disease properly in the next decade, it is critical that we fully understand the mechanisms that underlie this condition.

One of the key players in both acute and chronic heart conditions is inflammation. The role of inflammation in heart disease has become clearer in recent years. For many years, heart disease was considered to be a problem of hemodynamics, resulting simply from blockage or narrowing of blood vessels (4). It subsequently became apparent that a haemodynamic theory alone could not explain the manner in which heart failure (HF) progressed. This led those in the field at the time to suggest additional underlying mechanisms contributing to the development of HF. The "cytokine hypothesis," proposed in the early 1990s, suggested that it was in fact the release of cytokines during heart disease that drove the progression and pathology of this disorder (5). Since then, and particularly over the last 10 years, we have become increasingly aware of the importance of inflammation and the role leukocytes play in the progression of heart disease. Whether inflammation *causes* heart disease or vice-versa is a hotly debated topic, and probably varies on a patient-by-patient basis. Although circulating pro-inflammatory cytokine levels are raised in patients with HF and positively correlate with disease severity (6), this does not necessarily indicate that the inflammation is the predominant causative factor. Much of our understanding of the role of inflammation in heart disease is derived from animal models. For instance, animals over expressing TNFα have high levels of inflammatory infiltrate in their hearts and develop dilated cardiomyopathy; these mice have an exceptionally high mortality rate (∼25% at 6 months) (7). Interleukin-23p19$^{-/-}$ mice, who have an interleukin-23 deficiency (a cytokine important in the differentiation of CD4+ cells), show significantly increased inflammation, impaired scar formation, and adverse remodeling after MI (8). Consistent with this, using anti-inflammatory approaches has been shown to be beneficial in animal models of heart disease; administration of a TNFα antagonist attenuates the development of myocardial inflammation, fibrosis, and subsequent cell death in a model of streptozotocin-induced diabetic cardiomyopathy (9).

Exposure of cardiac endothelial cells to pro-inflammatory cytokines leads to the upregulation of adhesion molecules (10), which in turn, leads to the recruitment of inflammatory effector cells. These effector cells, which include neutrophils, monocytes, macrophages, and lymphocytes, can induce apoptotic, and phenotypic changes in cardiac endothelial cells via the release of cytokines, reactive oxygen species, or the engagement of counter-ligands on the endothelial cell surface (4). Endothelial cell phenotypic changes in this manner are not trivial—TGF-β and Ang-II can induce an endothelial-to-mesenchymal transition, shifting endothelial cells toward a fibroblast phenotype and leading to the development of cardiac fibrosis (11). It is clear, however, that some degree of inflammatory cell infiltrate is required for normal repair functions to take place following an ischaemic event or during the development of a chronic cardiac pathophysiological disease state (12). It is widely accepted and understood that inflammatory cells are often required for the resolution and repair of injured tissues. Indeed, that is also the case with the heart—for instance, monocytes/macrophages are essential for normal physiological healing of the heart following MI (13). However, what is important from a therapeutic point of view is that we are able to ensure that the inflammatory response to an insult is appropriately measured and does not overwhelm the local tissue environment. In particular, the main goal is to protect the local microvascular environment as it is within the microcirculation where the inflammation that is causative for HF is thought to predominantly occur (14).

THE IMPORTANCE OF THE CORONARY MICROCIRCULATION—THE "BUSINESS END" OF THE VASCULAR TREE

The potential role of the coronary microcirculation in pathologies of the heart has been known for some time. In 1967, Likoff et al. described a set of 15 patients who they considered to have coronary heart disease, but with patent coronary arteries (15). With remarkable foresight, Likoff et al. suggested that the coronary syndrome exhibited in these patients resulted from "abnormalities in the microcirculation" and that "an oxygen-diffusion impairment … at these levels could be responsible for the symptoms and signs of apparent myocardial ischemia" (15). Over the subsequent 50 years, our understanding of the importance of the microvasculature in coronary pathophysiology has improved significantly and we are now acutely aware of the importance of coronary microvascular dysfunction (CMVD). In 2013, CMVD was implicated as a primary causative factor for heart failure with preserved ejection fraction (HFpEF), shifting the causative emphasis away from left ventricular afterload excess (14). This suggestion is consistent with the idea that smaller vascular components are critical in determining the vascular resistance of the heart; ∼55% of the total vascular resistance in the heart originates in cardiac microvessels (16).

Understanding how the microvessels of the heart operate in health and disease is critical. The heart is supplied by two major coronary arteries—the left and right—which both originate from the early part of the ascending aorta. These arteries branch into smaller vessels which supply distinct anatomical regions of the heart. This branching initially occurs at the epicardium, before continuing into the myocardium where the vessels begin to form a tree-like network (17). Finally, in contrast with a number of other tissue beds, these vessels

develop into a non-tree like network with hairpin loops, T-, Y-, and H-shaped junctions (18). Interestingly, as a result of these connections, capillaries which are directly adjacent to each other may have completely opposite and counter-current flow profiles (19). Our understanding of microvascular perfusion in the cardiac microvasculature is further complicated by the contractile activity of the heart. Intramyocardial microvessels are subject to rhythmic compression during systole (20) with diameters decreasing by up to 20% (21). Furthermore, blood which enters the coronary arterioles during diastole can be squeezed out during systole, in some cases generating retrograde flow (22). Although one would assume similar physical forces to be applicable in the capillaries, the extent to which retrograde flow occurs in the terminal end of the microcirculation is currently unclear. This highly contorted structural design, in conjunction with the complexities of contraction-dependent retrograde and counter-current flow, makes *in vitro* or *in silico* modeling of the coronary microvasculature challenging. The ability to image the coronary microvasculature *in situ* is a critical step in helping us to understand the nature of pathophysiology that occurs in this bed.

Unfortunately, research investigation of the microcirculation in patients is difficult. Techniques such as positron emission tomography (PET) have allowed the identification of some cardiac specific haemodynamic parameters, such as myocardial blood flow (MBF; mL/min/g) and coronary flow reserve (CFR; MBF near maximal coronary vasodilation to basal MBF) (23). Single photon emission computed tomography (SPECT), magnetic resonance imaging (MRI), and ultrasound offer some structural information, but often without sufficient resolution to identify "true" microvasculature (24). While these are useful surrogate markers for coronary vascular dynamics, none of them are—in practical terms—suitable for clinicals or researchers to directly visualize the coronary microcirculation in patients (25). Compounding this situation, imaging the coronary microcirculation *in vivo* has also been considered, at least for the vast majority of the last 50 years, particularly challenging. This has led to some researchers referring to the cardiac microcirculation as a research "black box" (25). Not only is the heart in an anatomically challenging location in respect of imaging, the physiological motion inherent to the organ makes identification of the microvasculature difficult. Recent work has identified the size of the challenge facing scientists in regard cardiac motion. Of all of the major organs used for intravital microscopy, the heart has one of the highest maximal displacements under normal physiological conditions (up to 19.9 mm/s) (26); worse still, this displacement more than doubles when animals are on ventilation (47.8 mm/s) (26), an essential component during surgery for intravital imaging of the heart. As a result of this movement, without stabilization techniques, resolution at a single cell level is impossible—something which intravitalists have been able to achieve in other vascular beds for over a hundred years (27). This has led to the of significant deficits in our knowledge related to the coronary microcirculation and how this relates to cardiac diseases and pathophysiology (25). While many other tissue beds are readily available for intravital microscopy (28–33), the unique nature of the coronary microcirculation limits our ability to use these organs as surrogates for the study of this important vascular network.

IMAGING THE CORONARY MICROCIRCULATION—THE EARLY STUDIES

Experimental imaging studies of the microcirculation began to gather pace during the mid-to-late part of the 1900s. These studies could be categorized into three main categories: (1) those aimed at identifying the layout of the coronary microvascular network under normal physiological conditions and under conditions of hypoxia; (2) those examining the effect of cardiac contraction on the coronary microcirculation; and (3) studies seeking to understand the effects of myocardial ischemia reperfusion injury on the coronary microcirculation. In perhaps the first feasible example of cardiac intravital, Martini and Honig (34) performed microscopy on the beating heart of ventilated rats. In this preparation, the heart was exposed via an incision in the chest wall, covered with a glass slip, and illuminated via a point-strobe light driven into a ring condenser. While this model generated useable images, it did not control for movement. So poor was movement control, that the authors required "∼100–150 feet of film to provide 30–50 focused frames" (34).

Subsequent studies began to address this issue of stabilization. These studies all generally shared the same technical setup which was indicative of the time—images were captured using camera-based systems, with the tissue illuminated either by either epi- or trans-illumination. All of these preparations (and indeed, their modern counterparts) had to deal with two main physiological processes which induce movement—cardiac contraction and pulmonary inflation. In one of the first imaging studies of the beating canine heart, Tillmanns et al. used a number of adaptations to overcome the inherent difficulties with imaging the beating organ (35). Firstly, the authors considered epi-illumination—while easy to achieve—to be inefficient. As the ventricular wall is too thick for transillumination, light needed to be transmitted toward the microscope objective from a point *within* the heart muscle. This method of transillumination was achieved using what, even some 45 years later, might still be considered an elegant approach. Tillmanns et al. used a 20G needle, engineered to contain a quartz rod (which is conducive to light) with a mirrored end, with the terminal end modified to reflect light at 45°. Insertion of this under the superficial layer of the myocardium would lead to the transmission of light upwards and through the ventricular wall, making capture by light microscopy viable (35). In addition, to ensure that the microscope remained in focus with the surface of the beating heart, Tillmanns et al. designed what they termed a "focus keeper"—a floating, counterbalanced system that allowed the microscope objective to move in vertical synchronicity with the beating heart. This ensured that the objective always retained an identical z-distance from the tissue surface regardless of the movement of the heart itself. While controlling for movement in the XZ plane, it should be noted that this mechanism did

not specifically include mechanisms that compensated for lateral movement; rather, the application of the device with some downward force was expected to hold the heart in its lateral position (35). This group went on to further validate this method, publishing evidence of vascular patency and perfusion dynamics through imaging of the administration of FITC-conjugated dextran (19).

Following on from these initial studies, intravital microscopy of the heart continued to develop, with particular focus around the development of methods to improve tissue stability and resultant image quality. Originally, Nellis et al. attempted to mechanically (and relatively aggressively) fix a segment of the beating heart around a specific point, allowing them to image this area free from movement artifacts (36). However, they quickly found that aggressive mechanical fixation significantly impeded microvascular perfusion (36). Consequently, they slightly adapted their existing method to be more conservative in its approach to constraint. In this study, the authors designed two imaging techniques for the beating rabbit heart; (1) a free-motion imaging technique, where transillumination came from a light source underneath the tissue surface (thus, inside the ventricle) but with no mechanism to constrain the imaging site with relation to the light; (2) a fixed-position imaging technique, where the trans/epi-illumination also included a means for holding the tissue in positional synchronicity with the light source (37). In addition, the authors were one of the first groups to utilize electrocardiographic (ECG) gating to help minimize motion artifacts. However, rather than being used to trigger imaging, the ECG was linked to a stroboscopic light source. Using the QRS complex as a reference point, Nellis and colleagues were able to trigger rapid and short-lived (15–25 μs) illumination at the same point in the cardiac cycle (38). While the heart is moving relatively free at all times, only illuminating the surface at a particular point in the cardiac cycle gives a perception of stillness. Furthermore, slightly staggering the triggering delay from the QRS complex allowed the authors to give an impression of the heart moving in slow motion.

Pulmonary inflation proved a much more challenging issue to deal with; while the heart could be either physically constrained or movement compensated for, preventing the lungs from inflating is clearly an exceptionally difficult task in the context of most surgical setups. After many years, (39) identified high-frequency jet ventilation (HFJV) as a potential technique which could be used to mitigate some of this movement. HFJV is a relatively non-conventional mechanism of ventilation which is thought to be favorable in cohorts who are at risk of chronic lung injury (40). It maintains effective gas exchange, yet effectively reduces respiratory motion to almost nil, by working at very small tidal volumes and high respiratory rates (41). By applying this methodology to cardiac intravital imaging, the authors were able to ventilate the lungs, but with minimal physical displacement of the heart due to pulmonary movement. Cardiac displacement was further dampened by the positioning of 22G needles entering at the interventricular groove and exiting from the left ventricle (39) and tissue movement negated by the use of stroboscopic illumination. In a further technological advance, the authors designed a semi-automated electromagnetically controlled micromanipulator—termed the "*Wobbler*." This device could be registered manually with the location of the vasculature of interest at various points during the cardiac cycle. Once this information was known, an attached computer was able to move the micromanipulation arm in synchronicity with the vessel of interest. Using these techniques, the authors identified that around 75% of the total vascular resistance in the heart resides in vessels beneath 200 μm (39). Subsequent work from this group has used the same technique to successfully measure cardiac microvascular dynamics in response to α_1- and α_2-adrenergic stimulation (42) and the role of nitric oxide in the response to adenosine (43).

IN VITRO IMAGING OF THE HEART—THINKING OUTSIDE THE BOX

While the above approaches were relatively successful in achieving their goal of tissue stabilization, it is fair to say that they were not easily accessible to all laboratories. The development of the tools described were often complex and not always applicable across all use cases. In these situations, many users turned to the Langendorff heart, or isolated perfused heart, as a potential means for cardiac tissue imaging but with the ability to more easily control some of the movement aspects of the tissue.

The Langendorff model was first conceptualized by Langendorff (44), and since then has become a mainstay of the cardiovascular research community. However, unlike many other techniques which have their origins based in long history, the basic methodology for the Langendorff model remains largely unchanged since its original inception. For a more detailed and comprehensive description of the technique, the authors are directed to an excellent review covering this topic (45). However, to summarize—the heart is removed via careful dissection and the aorta is cannulated for the (retrograde) administration of a perfusion buffer. Administering this buffer against the normal physiological direction of flow closes the aortic valve and forces fluid to flow via the left and right main coronary arteries and into the resulting microvasculature. While the Langendorff model has some obvious disadvantages, there are some key advantages to consider: the model is straightforward, low cost, reproducible, and allows for the study of the heart in isolation.

In almost all use cases of the Langendorff model, the heart is perfused with Krebs-Henseleit buffer (KHB) (45). This buffer primarily relies on glucose as the primary metabolic substrate for the working heart. While this is sufficient to cover the energy needs of the tissue, perfusion with KHB (or other physiological buffers) does significantly limit the use of the Langendorff preparation for *in vitro* modeling of leukocyte trafficking using microscopic techniques. It should be noted that the Langendorff heart can be perfused with blood and interestingly, a number of studies have shown that doing this does significantly improve the function of the heart in this model (46–48). In smaller animals, the volumes of blood required for constant perfusion of this model may be prohibitive; perfusing one murine heart would require blood from many donors (49). In addition, blood from larger species is often unsuitable as their relatively larger

erythrocytes are less able to traverse murine capillaries (49). There are also potential questions about the validity of using these models for immune cell trafficking; studies have shown that blood collection in itself can result in leukocyte activation in the resulting isolate (50). In addition, oxygenation of isolated blood (a critical requirement) can often lead to cellular damage due to the formation of foam (51). Unfortunately, the relative expense and complication of using blood vs. KHB has meant that most researchers—unless they specifically require blood supplementation—favor KHB or other physiological buffers over perfusion with haematopoietic components. Some more complex options exist in order to facilitate blood perfusion (for example, parabiotic models); the reader is directed to other reviews where this is considered in more detail (49).

Very few studies have used the *ex vivo* perfused heart for imaging immune cell trafficking. It should be noted that it is not the case that there are a lack of *ex vivo* perfused heart models in which immune cells are administered; there are such models—but rather that these models do not undergo live imaging, instead relying on immunostaining or scanning electron microscopy methods on cut sections (52–54). Kuppat et al. used widefield fluorescence imaging, at the terminal end of their experiment and after the inducement of cardioplegia, to identify neutrophil trafficking in the microvasculature. Administration of labeled neutrophils and FITC-dextran (for vascular contrast) into the perfused *ex vivo* heart has been used to examine the role of angiotensin I converting enzyme (ACE) and nitric oxide in the attenuation of inflammation post ischemia-reperfusion injury (55). Neutrophil recruitment was markedly enhanced in guinea pig hearts following ischemia-reperfusion (IR) injury, a phenomena which could be reduced by administration of cilazaprilat (an ACE inhibitor) or enhanced by treatment with nitro-L-arginine (NOLAG) (55). The authors were also able to demonstrate some capillary plugging in this model—a phenomena where excessive leukocyte recruitment results in the blockage of capillaries and an ultimate failure of perfusion; often, when this occurs following IR injury, this is termed "no-reflow" (56).

Given the potential benefits of the Langendorff system, it remains surprising that to date this model has not been readily used to dynamically monitor the mechanisms of cellular trafficking in the perfused heart. What makes this perhaps more surprising is that the Langendorff model has been used extensively for *imaging* of the heart but outside of the context of immune cell trafficking. There are many examples of the model being used for other investigations, such as: imaging of sarcomere length during cardiac mechanics (57, 58); calcium handling and the identification of various types of calcium waves during health and disease (59–62); and the assessment of mitochondrial function using dyes which are sensitive to mitochondrial membrane potential ($\Delta\Psi m$) (63). Much of this imaging is actually performed live and used to generate image data for quantitative analysis; as such, the tools are readily available in most labs to adapt this model to examine cellular trafficking. Indeed, a combinatorial approach (for instance, imaging calcium transients alongside cellular recruitment) may help to yield more detailed information about the molecular events that occur in the context of immune cell recruitment. Given many labs will have access to heart tissue that is not suitable for intravital imaging but may be accessible for later *ex vivo* imaging, it may be worth considering the Langendorff model as a potential tool for investigating mechanisms of cell recruitment.

Other imaging models exist beyond than the Langendorff system, albeit somewhat less complex. For some experimental purposes, groups have found that imaging cardiac explants without any flow or contractile activity may provide some useful information about inflammatory processes. As a small part of a larger intravital study, Li et al. used cardiac explants to examine the behavior of neutrophils following IR injury (64). Hearts were isolated from LysM-GFP mice, in which neutrophils could be readily identified by their GFP^{hi} phenotype (64). Using two-photon microscopy, few neutrophils were identified in mice without IR injury; however, following IR injury, significantly increased numbers of neutrophils could be observed in the microvasculature. More importantly, even in the absence of any flow, these neutrophils could be observed crawling and transmigrating through the vessel wall into the tissue parenchyma (64). As an important methodological note, the authors were able to image the explanted heart for at least 6 h post reperfusion, likely due to the low phototoxicity and bleaching that is inherent with two-photon microscopy. However, the lack of flow and contraction in this model limits its translation to the whole organ.

CONFOCAL AND MULTIPHOTON INTRAVITAL IMAGING OF THE BEATING HEART—SEEING THINGS DIFFERENTLY

Cardiac intravital imaging advanced significantly with the introduction and uptake of more advanced imaging techniques such as laser scanning (raster scanning) confocal imaging, spinning disk confocal imaging, and multiphoton imaging. As understanding these techniques is key to garnering a full appreciation of how these new technologies have helped cardiac intravital reach the next level, we shall briefly touch on them from a technical stand point in this review an overview of the advantages and disadvantages of the methods discussed in this section is shown in **Table 1**. Should readers want further technical information about these techniques, there are excellent reviews to which one should refer (65–67). Examples of the types of images generated from cardiac intravital microscopy using these techniques are provided (**Figure 1**).

During regular widefield fluorescence imaging, the tissue is illuminated by a block of excitation light as it is focused in toward the plane of interest. As a result, not only does the excitation light excite the target focal plane, but also excites other focal planes above and beneath the target. These planes generate emission light, but as they are not in the same focal plane as the detector, they impact negatively on the resulting image and generally reduces image quality. Confocal imaging introduces a pinhole which rejects light that is not in the same focal plane as the detector. This significantly improves the image quality

TABLE 1 | Summary of the various options for cardiac intravital imaging.

	Disadvantages	Advantages
Imaging method		
Raster-scanning confocal	Inherently slower; requires advanced stabilization and/or gating mechanisms in order to use for cardiac IVM Prone to "tearing" artifacts due to the line-by-line nature of image formation	Identical illumination of each pixel (field uniformity) Well-established technique, more widely available, numerous vendors Better light transmission vs. spinning disk methods
Spinning disk confocal	Identical illumination of each pixel cannot be guaranteed (lack of field uniformity) Potentially increased background/non-focal plane light (due to pinhole crosstalk) Reduced light transmission vs. raster scanning methods	Generally much faster than raster scanning techniques Full field illumination; less prone to "tearing"-type artifacts (see **Figure 2**) Typically reduced laser powers are required; less photo-bleaching/-toxicity
Stabilizer attachment mechanism		
	Disadvantages	**Advantages**
Glue	Permanent; stabilizer cannot readily be manipulated once attached Requires care—excessive glue can block the field of view and removing it is difficult if placed incorrectly Potential for side effects from the application of glue	More straightforward than suction; not reliant on external equipment Quicker than suction stabilization techniques Firm bonding to the stabilizer
Suction	Requires monitoring to ensure seal is maintained Potential for tissue damage with high levels of suction Disturbance of tissue perfusion underneath the suction ring	Reversible and can be moved if positioned incorrectly Less impact on the tissue surface for post-imaging experiments
Gating		
	Disadvantages	**Advantages**
No gating	Highest potential for motion artifacts in resulting images Requires large numbers of frames to ensure sufficient data for analysis; inefficient data capture method Uses low exposure times and thus needs (relatively) stronger staining	Surgically more straightforward; ECG/respiratory readings not needed Technically more straightforward than gating mechanisms; less specialist knowledge required Quicker set up time
Retrospective	Requires large numbers of frames to ensure sufficient data for analysis; inefficient data capture method More technically challenging than not gating If pacing, potential for pacing to interfere with experimental outputs Requirement for post-capture processing	Better mechanism for abrogating motion artifacts than not gating Requires less complex/reactive equipment than prospective gating
Prospective	Most technically challenging gating option If pacing, potential for pacing to interfere with experimental outputs Requires non-trivial technical equipment to process a number of incoming input sources	Best mechanism for abrogating motion artifacts More efficient capture technique than retrospective gating or no gating Post-capture processing not required

There are a variety of options available to researchers who wish to begin experiments using cardiac intravital imaging. The above table summarizes some of the advantages and disadvantages of the various amendable options in this experimental model.

by rejecting out-of-focus light, reducing blur and improving resolution. There are two main methods relevant to this review: laser scanning and spinning disk. Although both are forms of confocal imaging, they should be considered very distinct in their methodologies. In the case of laser scanning confocal, this imaging is performed in a point-scanning mode; the microscope system has a single raster scanning beam which moves across the tissue to generate the resulting image pixel-by-pixel based on the returned signal at each point. Once reaching the end of the image, the scan head can either return to the start position and begin again (one-way) or reverse its direction (round trip). It may be immediately obvious that in a moving tissue, point-scanning methods may not be suitable for image capture. For the entire image frame to be captured in the exact same physical space, the tissue would need to remain entirely still for the duration of each raster scan duration. This—at least in the case of the heart—is impossible without complete cardioplegia; even with the most aggressive stabilization techniques, the heart retains some degree of contraction within the confines of the imaging window. Spinning disk confocal avoids some of these problems by generating multiple beams which illuminate the tissue simultaneously. These multiple beams are generated by placing a spinning disk (which contains up to 20,000 pinholes) in the emission light path. This disk runs at up to 10,000 rpm and illuminates the entire sample with these generated beams. The use of a second disk, running in sync with the first provides the pinhole effect that is critical to confocal imaging and allows for the generation of confocal quality imaging, but

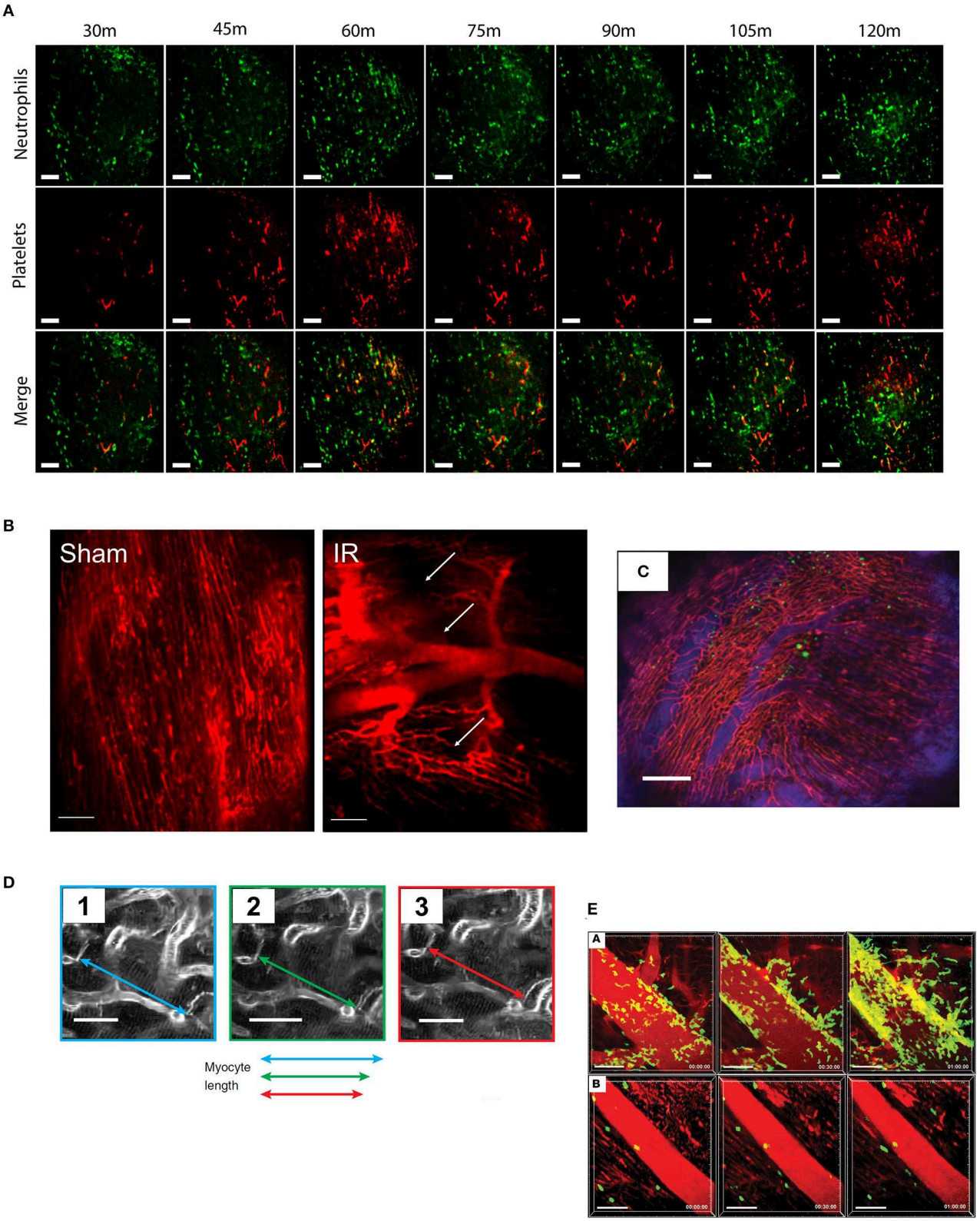

FIGURE 1 | Typical imaging results from cardiac intravital microscopy. As the technique has developed, so has the variety of parameters that can be assessed from cardiac intravital imaging. **(A)** Using fluorescently labeled antibodies, the recruitment of leukocytes (green, anti-Gr-1) and platelets (red, anti-CD41) to injured heart

(Continued)

FIGURE 1 | can be monitored. Importantly, particularly in models of acute inflammation where understanding of the chronology of cell recruitment is crucial, imaging can be taken from the same area over a period of time. Cell recruitment can be counted by simple identification, while thrombus formation can be analyzed by masking upon positive signal. Figures adapted from published figure (70) (scale bar: 100 μm). **(B)** Perfusion of the mouse with a vascular contrast agent allows researchers to identify viable areas of tissue perfusion and permits the calculation of functional capillary density. During IR injury, for example, there is a clear reduction in the amount of patent microvessels compared to an animal undergoing sham surgery. Areas of "no-reflow" are shown with white arrows. Figures adapted from published figure (68) (scale bar: 100 μm). **(C)** Using a combination of vascular contrast agents and cellular staining, cell trafficking in and out of vessels can be examined in depth. The range of fluorescent channels which can be examined is limited only by the availability of filters and dyes. In this example, GFP-labeled bone marrow cells can be seen in the heart, both inside and outside of the vascular space. Adapted from Lee et al. (69) (scale bar: 200 μm). **(D)** Advancements in stabilization (and synchronization) techniques have allowed for detailed physical measurements to be performed due to the near eradication of motion artifacts. For example, imaging the contraction of single cardiomyocytes is now possible using this technique. Adapted from published figure (70) (scale bars: 20 μm). **(E)** The use of genetically modified animal strains facilitates studies that examine trafficking without the need for antibody (or tracker)-based staining techniques. In this example, LysM-GFP positive neutrophils can been seen trafficking to the heart following IR injury (subpanel **A**), which can be inhibited by administration of a CXCL2 neutralizing antibody (subpanel **B**). Adapted from published figure (71) (scale bars: 50 μm).

without any loss of speed or image quality due to raster scanning methods. As a result, the raw (unprocessed) images derived from these techniques differ greatly (**Figure 2**). Raster scanning techniques tend to generate intravital imaging that has "tearing" artifacts, where imaging fields have intra-field artifacts due to movements during the travel of the scan head. On the other hand, spinning disk techniques tend to have inter-field artifacts, stemming from movements of the entire field between frames. In addition, in contrast to raster scanning techniques, field uniformity (identical stimulation at each pixel of the image) cannot be guaranteed. While this may be an issue for models that rely on pixel intensity (such as platelet recruitment), it can be mitigated by averaging frames across an imaging window (rather than analyzing still images). Spinning disk confocal is also prone to a phenomenon known as pinhole crosstalk. This results from out-of-plane/scattered emissions passing through an adjacent pinhole on the disk which is not in alignment with the pinhole the excitation light passed through (72). This effect leads to an increased background signal on spinning disk confocal microscopy when compared to laser scanning confocal. However, the speed advantages gained from employing spinning disk confocal has allowed some labs—including ours—to perform cardiac intravital without necessarily needing aggressive post-analysis image restoration techniques (68).

Multiphoton imaging is a further and more powerful form of confocal imaging that delivers focally limited imaging but without the need for a pinhole. In contrast with other microscopy techniques which use continuous wave laser/light sources, multiphoton microscopy uses pulsed lasers to generate a stream of infrared photons. As infrared photons have less energy than their non-infrared counterparts, the near simultaneous (within 1×10^{-18} s) absorption of two photons at the same fluorophore is required for excitation (as the wavelengths used are infrared, excitation wavelengths used for fluorophores are longer than they would be using confocal microscopy). In addition, as the beam is focused through the microscope optics, the photons become more and more crowded in space—thus increasing the chance that two photons may simultaneously interact with a single fluorophore. The net result of this combination of factors is that there is a small volume downstream of the objective—the focal plane, in this case—where the probability of two photons meeting a fluorophore near-simultaneously is sufficiently high enough that excitation can occur. It is this physical phenomenon

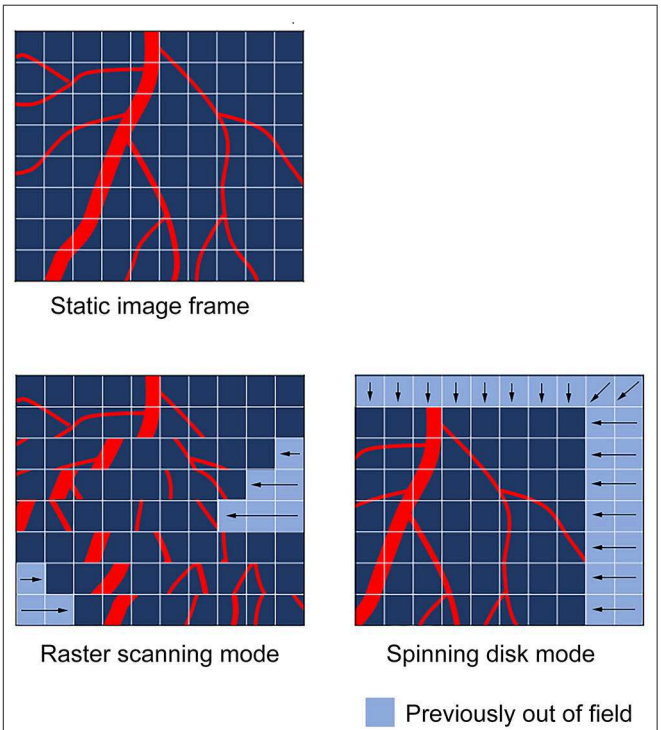

FIGURE 2 | Common artifacts observed during cardiac intravital in raster and spinning disc scanning modes. The type of motion artifacts observed during cardiac intravital are highly dependent on the nature of the scanning mode utilized to obtain the images. Raster scanning modes, which use a scan head to move across the tissue in a point-by-point fashion are subject to "tearing" artifacts, which result from the tissue moving while the scan head progresses across the tissue. This manifests in scanlines being positionally out-of-sync as the scan head moves in its secondary axis. In spinning disk mode, the scan head images the whole field of view during the imaging procedure. Thus, spinning disk imaging modes tend to cause whole-field image shifts.

that results in the excitation of fluorophores only within the focal plane—there is no out of focus excitation and it is this which delivers confocality without the need for a pinhole. Similar to laser scanning confocal, multiphoton microscopy operates in a point-scanning mode, working across the tissue in a pixel-by-pixel fashion. Again, similar to laser-scanning confocal, multiphoton imaging is highly sensitive to movement and requires a mixture of physical stabilization, a degree of

predictability in tissue movement (possibly including gating—discussed later), and post-acquisition image manipulation.

The first studies to effectively develop cardiac intravital using these imaging techniques to monitor immune cell trafficking in real-time were published at around the same time in 2012. The first of these studies, by Li et al. (64), used multiphoton microscopy to identify some of the basic characteristics of leukocyte trafficking within the heart, in real-time. This paper used two main approaches, combining elegant surgery, and an external stabilization device. For the first approach, the authors connected a donor heart into the circulation of a recipient mouse. To achieve heterotopic heart transplantation, they engrafted donor hearts into the right cervical region of recipient animals. In order to generate injury, some donor hearts had undergone cold (4°C) ischemia for 1 h prior to reconnection. To re-establish perfusion, the donor ascending aorta and pulmonary artery were connected to the recipient's right common carotid artery and right external jugular vein, respectively. Once successfully transplanted, the donor heart adopted a normal heartbeat in its ectopic position. In order to image this heart in position, the authors developed an imaging chamber consisting of a glass coverslip which was brought into contact with the heart using height-adjustment dials. The authors also applied a small ring of veterinary adhesive (cyanoacrylate based) in order to physically stabilize the heart against the chamber glass. By engrafting wild-type (WT) donor hearts onto either LysM-GFP mutant mice (whose neutrophils express high levels of GFP) or CX3CR1 GFP/GFP mutant mice (B6.129P-Cx3cr1^{tm1Litt}/J; whose monocytes express GFP), the authors were able to image the trafficking of exogenous (non-resident) neutrophils and monocytes to the heart during reperfusion (Q-dots were used as a vascular contrast medium). Using this technique, the authors identified minimal neutrophil recruitment in post-capillary venules during IR injury, but rather localized most recruitment activity to the walls of the larger coronary veins where they identified intraluminal crawling and congregation. In addition, monocyte recruitment to the microvasculature was also identified, although congregation of monocytes was not identified in this model (65). Perhaps one of the most interesting capabilities of this model is the ability to graft donor hearts from mutant mice; allowing researchers to investigate cardiac-specific mechanisms in the context of otherwise normal systemic physiology. The authors capitalized on this, using donor hearts from ICAM-1 mutants (B6.129S4-Icam1^{tm1Jcgr}/J); these mice do not express a functional form of ICAM-1 (73). Results from these hearts, alongside the use of Mac-1 blocking strategies, suggested a key role for Mac-1/ICAM-1 in intravascular crawling and transmigration of neutrophils. Subsequently, the authors adapted their original stabilization technique to stabilize the heart in its normal intrathoracic position. No neutrophil recruitment was noted in the absence of inflammation. Importantly, results from heart imaging in its normal position *in situ* correlated with the results obtained from heterotopic heart transplants. The authors noted that in this model, mice were able to tolerate this imaging procedure for at least three hours; this is important to note, as this preparation did not use pacing, or any special ventilation techniques (such as supplementation with medical air). The authors have subsequently used this imaging model in further sophisticated studies, including: the identification of a critical role for CCR2^{+} monocytes in driving neutrophil recruitment following ischemia (71) (imaging from this study is included in **Figure 1E**); showing evidence that tissue-resident macrophages promote or inhibit monocyte recruitment dependent on their CCR2 expression phenotype (74); and that ferroptosis (an iron-dependent form of cell death) is a key mediator of neutrophil recruitment in transplanted hearts through a TLR4/TRIF/Type I IFN signaling pathway (75).

Later in 2012, Lee et al. published (69) an alternative method for intravital imaging of the cardiac microcirculation, utilizing not only tissue stabilization but also cardiorespiratory gating. On the former point, the stabilization proposed by Lee and colleagues was significantly less intensive than in the work of Li et al. (64). The stabilizer in this study was essentially a small ring machined from stainless steel, with an outer and inner diameter of 3.6 and 2.2 mm, respectively. This ring had a small groove on the base, and was designed to be attached to the heart surface, using veterinary adhesive. The stabilizer was attached to an arm which itself was attached to a manipulator allowing it to be advanced or adjusted to the correct location on the surface of the heart. Due to the relatively small internal diameter of the ring, the initial design was specifically for use with "stick" objectives—extremely thin objective lenses that were designed to fit within the center of the machined ring (these objectives, manufactured by Olympus, are now hard to reasonably hard to obtain). The authors also published a modification that could be applied to the stabilizer that allowed for the use of standard diameter water-immersion lenses (in this study, the x20 XLUMPLANFL, which has a lens diameter of 5.2 mm at its base and 10.5 mm where it meets the base of the objective). These standard objectives still permitted the capture of high-quality multichannel imaging (an example from this method can be seen in **Figure 1C**). One of the useful aspects about using such a small stabilizer and the ability to manipulate the stabiliser's location, is that the heart can be positioned such that the only pressure the heart experiences is that of it contracting against the stabilizer. The authors suggest that this is "similar as the heart beating against the chest wall" (69). Although stabilization provided mechanical support to the beating heart, motion artifacts remained and physiological gating became necessary in order to circumvent these issues. This gating was designed to retain capture fields only during specific points of the cardiac and respiratory cycle. Initially, the authors had considered (and attempted) gating imaging on points in the cardiac cycle alone. However, the authors noted that gating on the cardiac cycle alone was insufficient as pulmonary movements were also significant contributors to the physical movement of the heart. In order to eliminate movement, the authors chose two points on both cycles in which to capture images. In the cardiac cycle, they chose a 15 ms window after the appearance of the *P* wave, as measured by electrocardiogram (ECG). In the pulmonary cycle, a window of 90 ms near the end of expiration was selected; as the animals were mechanically ventilated, the observers could be sure of the exact point in respiration at which imaging would be triggered. The net result was the generation of an optimal imaging window during

which image data could be retained. Using this information, the group designed an algorithm which could, in real-time, rebuild images using only line scans obtained during the optimal imaging window. Rebuilding these, the authors were able to generate captures in real-time, devoid of motion artifacts. In the initial paper, this model was tested, perhaps unsurprisingly, by examination of leukocyte recruitment following cardiac ischaemia-reperfusion injury. The authors labeled endogenous leukocytes by administration of Rhodamine 6G and noted leukocyte rolling in cardiac capillaries. The descriptions of leukocyte trafficking in this study were relatively preliminary and minimal analysis was performed on the trafficking described. Subsequent work from the group explored the addition of cardiac pacing as a means to gate imaging more reliably (76). The authors also suggested that this should also to allow for imaging to be better gated prospectively. A number of years later, the same group published an extensive methods paper, describing the various techniques they had developed to date in detail and distributing the 3D STL files in order for research groups to be able to print the stabilizers for themselves using 3D printing techniques (70). It is worth noting that others have since designed glue-dependent stabilizers that are relatively similar in design (77); but it is probably the case that are only so many ways that one can design a stabilizer for cardiac imaging—as the technique becomes more widespread, we would posit that significant differences in the overall design of stabilizers are unlikely.

We have also recently published work using a glue-based stabilizer for cardiac intravital microscopy (68). Although we have used a stabilizer that is similar in design to those used elsewhere in the literature, we have not used cardiopulmonary data to gate our imaging. Rather, we have used a combination of spinning disk confocal imaging, minimal exposure times, and high sensitivity detection in order to allow us to capture as many frames as possible during any given amount of time. The net result is that we have enough frames from which we can disregard those which are afflicted by motion artifacts, and retain those that are sufficiently clear (we have written software to help us achieve this, which we will come onto later). Using this technique, we have been able to examine the role that stem cells play in the downregulation of inflammatory injury following ischaemia-reperfusion injury. We have shown previously that haematopoietic stem cells (HSCs), in addition to their normal physiological role, are able to play an active role in the reduction of an acute inflammatory injury (78). Indeed, HSCs express a number of receptors for pro-inflammatory cytokines, such as the TNF receptors TNFR1 and TNFR2 (78), so it is contemplable that they may possess the ability to respond to inflammatory cytokines. Using spinning disk confocal imaging, we sought to identify the acute time course of neutrophil and platelet recruitment following the onset of reperfusion injury; and secondly, whether the administration of HSCs is able to affect the onset of this inflammatory response. By utilizing endogenous antibody labeling, we identified that both neutrophil and platelet recruitment is enhanced rapidly during reperfusion (a representative example of this imaging can be seen in **Figure 1A**). Furthermore, the administration of HSCs significantly reduced neutrophil and platelet accumulation during reperfusion. At the end of each experiment, we administered a vascular contrast agent to identify viable perfused microcirculation; as we could do this in the same animals, this allowed us to obtain additional functional data while not increasing the number of animals required for each group. Using this technique, we identified that IR injury is characterized with clear areas of microvascular no-reflow, evidenced by portions of cardiac microcirculation which do not take vascular contrast agent upon administration (a representative example of this imaging can be seen in **Figure 1B**).

Not all published methods rely on glue to affix stabilizers to the heart. Rather than rely on VetBond and other tissue adhesives, some groups have turned to negative pressures (suction) in order to affix their stabilizer devices to the tissue surface. Before suction stabilization was adopted as a means for imaging the heart, it had been used extensively as a means for imaging the lungs (79–81). Vinegoni et al. were the first to describe a suction based device for intravital imaging of the cardiac microvasculature (82). The device is small, similar to that described in Lee et al. (69); the internal chamber of the stabilization device has a diameter of 2 mm, while the outer diameter is 4.5 mm. The outer chamber is a hollow ring, which is attached to a vacuum regulator. This regulator provides gentle suction to the device and maintains the connection between the stabilizer and the tissue surface. The small diameter of the internal chamber does mean, again, that the user is highly dependent on access to micro-lens (or "stick") objectives. However, suction based techniques have a very clear advantage—it is much, much easier to remove a stabilizer that is being held on by suction than it is to remove one that is affixed to the heart with glue. As such, using suction-based stabilization techniques allow for the movement of the stabilizer unit to different parts of the heart and/or the possibility of recovery surgery in cardiac intravital imaging models. Again, in this study, the authors utilized cardiopulmonary gating in order to attempt to remove motion artifacts. Critically, the authors go to some lengths in this study to convince that the application of the suction stabilizer leaves no lasting effect on the cardiac tissue. As a result of application, the authors show no visible cardiac damage, no change to ECG traces, and no macro- or microvascular damage identified by Griffonia simplicifolia-I lectin administration (which labels endothelial cells) (82).

An elegant approach was devised by Jung et al. who created a small suction-assisted endoscope which could be advanced into the chest cavity and toward the heart with minimally invasive surgery (83). The aim of the endoscope was to transmit signal from the base of an imaging probe to the top, such that an objective lens could image the top of the probe as if it were imaging the surface of the heart. By attaching a number of rod lenses together, the authors were able to achieve this, generating a lens with a x1 magnification and a length of 20 mm. The bottom two-thirds of this lens was housed within a steel sleeve, and surrounded by an outer steel tube which acted as the suction tube. This suction tube was connected at its end to a rubber tube which provided the suction source (at a pressure of 50 mmHg), with the upper third of the imaging probe protruding through the suction tube. This entire construct is then held in place, and imaged through the tip of the imaging probe

with a high-numerical aperture objective. Validation data with the technique showed that application of suction through the construct virtually eliminated all movement, while the flow rate of cells through the microcirculation was not perturbed even at negative pressures as high as 150 mmHg (83). Furthermore, tissue damage was only observed at extreme levels of suction (300 mmHg) and no local inflammation was noted in areas where the suction was applied. One interesting aspect of this technique is that the authors were able to reproducibly (and with no evidence of damage) move the endoscope around the heart in order to image an area wider than a single field of view. This "wide-area scan" mode allows for individual captures to be tiled in a mosaic fashion, generating fields much larger than the initial limited field of view. In the publication associated with this work, the authors—using individual 250 μm fields of view—were able to construct an interlaced high resolution image of 1.2 mm by 1.2 mm (83). The authors went on to examine the recruitment of CX_3CR1^+ monocytes and neutrophils to the post ischaemic heart using both longitudinal (0, 1, or 6/7 days) and acute imaging (0, 5, or 30 min). Neutrophil recruitment increased acutely, with significantly enhanced neutrophil recruitment observed within 30 min [we have seen an identical observation using spinning disk confocal (68)]. Interestingly, neutrophil recruitment returns to baseline at 7 days post reperfusion. On the other hand, monocyte recruitment increases much more rapidly in reperfusion and precedes neutrophil recruitment, with a significant increase in monocyte presence as early as 5 min post reperfusion. Furthermore, this increase continues at 30 min and persists up to 6 days post-reperfusion. The authors also noted an increase in the number of monocytes flowing through the heart during reperfusion, but with a significant decrease in rolling during this period.

More recently, others have developed alternative suction stabilization techniques that do not depend on "stick" objectives or rod lenses. Matsuura et al. (84) have developed a suction-based stabilizer for use on rats that has a small central hole. In a slightly higher plane than the base of this central hole is an outlet for suction. Up from this is a notch onto which a larger cover slip sits, allowing the formation of a fully closed pressurized system once negative pressure is applied via suction through the outlet. The rat is positioned underneath the central hole of this stabilizer, and either side of the animal, two arms which protrude from the central portion of the stabilizer lock into two locking nuts which are located on metal breadboard and tightened to (a) lower the stabilizer in the z-plane onto the tissue, and (b) lock the stabilizer in place. With the coverslip in place between the tissue and the objective, water immersion objectives can be used with relative ease. Using a mixture of alignment and image processing techniques, the authors were able to monitor the trafficking of leukocytes in subsequent image frames, with frame to frame captures allowing for the calculation of leukocyte velocity and displacement. The authors were also able to identify an increase in leukocyte recruitment as a result of ischemia-reperfusion injury, which was induced via the insertion and inflation of a PCI balloon into a loop placed around the left anterior descending coronary artery. The authors further stated that leukocyte blockage of capillaries occurred within 1 h of reperfusion (84), consistent with results we have seen in our work (68).

NOTHING ALIVE IS TRULY STILL—ACQUISITION DATA PROCESSING AND ADAPTIVE FOCUSING MECHANISMS FOR IMAGING THE HEART

While stabilization techniques are able to eradicate the vast majority of tissue movement, it is impossible (unless the tissue is rendered cardioplegic) to prevent all movement of stabilized cardiac tissue. This is because even within the central imaging window of a cardiac stabilizer, the myocardium will continue to contract, regardless of much gross movement is reduced. Therefore, further compensatory techniques are required to eliminate these movement artifacts from resulting data. At present there are two main mechanisms by which this can be achieved; either by the use of software processing, or adaptively focused optics. On the latter, a number of techniques now exist which are set up to allow microscope optics to move in line with tissue movement. One of the earliest iterations of this approach used a high-speed (∼955fps) camera to detect movement of bright fluorescent particles in an imaging field, and subsequently moved the microscope objective accordingly to maintain these particles in the same initial location (85). This study was primarily for the movement of the objective in the *x,y* planes and not *z*. Additional work by the same authors later added the ability to also compensate for movement in the *z* plane, creating a system that could compensate for tissue movement in all three dimensions (86). Other solutions exist to help imaging setups mitigate against the movement of tissues in the axial plane. Spectral domain optical coherence tomography (OCT) has been used to rapidly measure the distance between a moving tissue and an imaging objective (87). When coupled with fast processing and piezoelectric control of objectives, this technique has been shown to be able to rapidly compensate for fast moving tissues in live animals.

Software processing is a much more accessible means for minimizing movement artifacts, from both a financial and a technical perspective. Software processing can be done either prospectively or retrospectively. Prospective image processing involves using information from the preparation and/or model to manipulate image capture in order to capture image frames that do not suffer from movement artifacts. In retrospective image processing, the image data is handled after it has been captured. In some cases, the data may be captured with a range of ancillary data such as ECG and respiratory cycles, while in others, image data may be captured alone and processed without the support of additional data sets. Image processing based on physiological parameters normally relies on either cardiac ECG gating, pulmonary gating, or a mixture of both. Such techniques aren't particularly new. In as far back as 1981, researchers were using the peak of the QRS complex as a timing reference for the triggering of an external stroboscopic light source (37). Although this is not technically a triggering of image capture (in this instance, the presence of light on a given image

frame allows the non-illuminated frames to be ignored), modern day equivalents are essentially more efficient versions of the same technique. Much of the work in this area has developed in the lab of Ralph Weissleder et a. who have published a number of studies [including an excellent and comprehensive methods paper (70)] which detail extensively how they have applied these techniques. For prospective image gating, the ECG and/or respiratory data must be processed and linked directly to the capture hardware in real-time. Windows are set in which tissue movement is likely to be minimal—in most cases this is normally defined as the entire QRS complex for the ECG, and either the P_{plat} or PEEP segment for pulmonary airway pressure (70, 88, 89). Although prospective gating strategies are more efficient in that they require the collection of less data (i.e., data likely to be spurious is rejected even before it is captured), they also require more expensive hardware and for capture systems to be compatible with fast triggering. However, one system—prospective sequential segmented microscopy (PSSM)—has been used as a method for generating motion-artifact free intravital imaging of the heart (76). In this technique, cardiac pacing is used to provide absolute definition of the cardiac cycle. Using this known pacing information, image capture can be accurately harmonized with an appropriate point in the cardiac cycle (in this study, pulmonary movement was minimized by either electronic triggering of the ventilator or pausing of its activity). In PSSM, the capture frequency and the pacemaker frequency are slightly offset. By doing this, it is possible to capture images from the heart during the entire cardiac cycle. This technique has been used to make determinations of cardiomyocyte activity at the single cell level; data from this technique shows it is possible to image the contractile activity of individual cardiomyocytes (76) (an example of the imagery underlying this technique is shown in **Figure 1D**).

It is much more common to see retrospective image processing techniques used in the context of cardiac intravital microscopy. While some of these techniques have been designed specifically with cardiac intravital in mind, others have been designed more generally for intravital microscopy. Others are simply general image processing techniques which can be applied to intravital microscopy. We will cover briefly the latter as they are the most generic and not cardiac specific. General image processing in the context of cardiac intravital most often takes the form of registration and alignment tools. Image registration is a technique to align or reposition images that have shifted in respect to one another. It is most often used in medical scanning, such as in CT and MRI scanning, but does have a use in intravital when handling images with reasonably manageable movement artifacts. Numerous plugins are available either for use in ImageJ/Fiji [we have found SPIM Registration to be a good tool in our hands (90)] or standalone [*elastix* is a well-established tool in this regard (91, 92)]. Some specific tools have been designed for registration of intravital microscopy data. *IMART* (Intravital Motion Artifact Reduction Tool) is a software tool designed specifically for the removal of motion artifacts (via registration) of intravital microscopy imaging (93). This image registration tool takes advantage of the fact that sequential frames in a time series are likely to be very similar to one another, while still being able to compensate for noise due to things like the introduction of cells, vascular dyes, and antibodies (93). *StabiTissue* is another tool that can perform similar functions and was also specifically designed for the purposes of intravital microscopy (94). Registration tools are useful, in particular when stabilization has been used and small amounts of residual movement remain. This is often the case, we have found, when using spinning-disk confocal imaging techniques for cardiac intravital imaging. Of course, registration tools are not particularly useful for line scanned images unless the image data has been processed by another tool first to repair distortions due to "during-scan" movement.

Retrospective image processing tools have two different tasks depending on the type of image data they are processing; for instance, line/raster scanned image data is very different to spinning disk confocal image data. The latter, providing it has been captured at a fast-enough speed, will contain full fields of valid image data. The former will contain image frames which will be made up of individual line scans that will be out of sync in the *x,y* plane. In order to process this data, the software must be able to return to the ECG/lung airway pressure data, connect this data with line scans, and reject line scan data which falls outside of the cardiac/pulmonary windows. Indeed, this is the approach that most studies have taken in this regard (69, 70, 88). While this means that the constructed image will be made of individual line scans with different temporal profiles, the image capture rate should be sufficient that the differences between them are relatively (and more importantly, biologically) insignificant. It is important, if it possible, for researchers to capture both ECG data and lung airway pressure—movement of the lungs is a clear contributor to the movement of the heart and a failure to take this into consideration can cause serious difficulties for cardiac intravital imaging—particularly for line-scanning techniques. However, not all techniques obtain respiratory or cardiac physiology data during capture. Indeed, we have found that cardiac intravital using spinning disk confocal does not require ECG or respiratory gating to generate useable imaging. In these cases, retrospective processing of image data sets without this information is required. In these cases, the most frequent approach used for this type of processing is frame rejection, where those with significant motion artifacts are removed from an image set. There are a number of tools available to allow researchers to achieve this, which work in a broadly similar fashion with some slight differences in how they achieve their goal of frame rejection.

Intravital_Microscopy_Toolbox is an ImageJ tool developed by Soulet et al. (95) which is designed to process an image stack and remove individual frames affected by motion artifacts. This software works by comparing each frame to a reference frame (or frames), and calculating a dissimilarity score. Using a cut-off value for this difference, the toolbox is able to remove frames which are considered to be too dissimilar to the reference frames. Along similar lines, we have developed a tool—termed *Tify*—which is able to process large image stacks and perform automated frame removal based on whether or not they meet given criteria (in terms of this review, this would be whether they contain motion artifacts or not) (96). However, rather

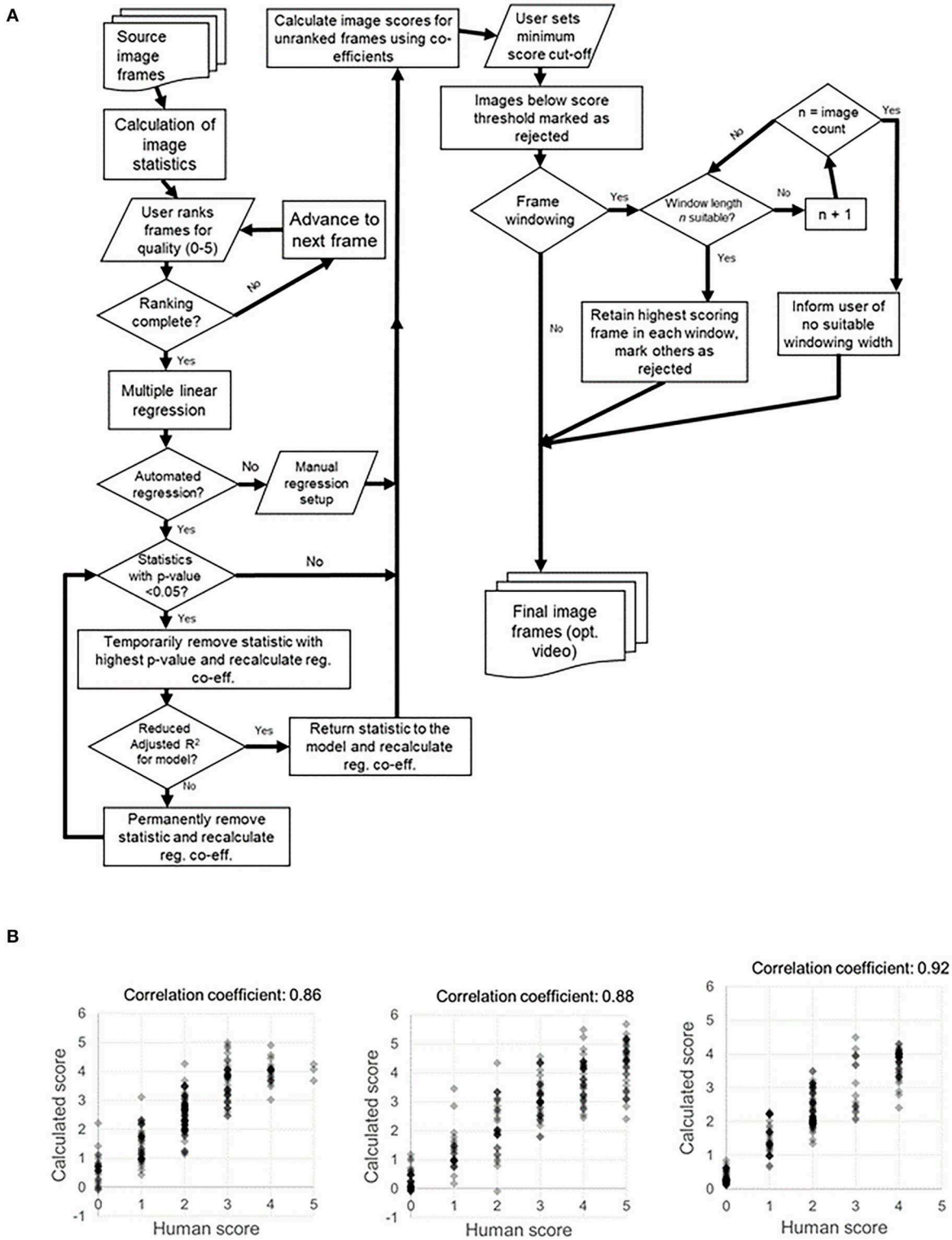

FIGURE 3 | Process map for *Tify* and example of human vs. computed image scoring for example sets of images. **(A)** Our image processing tool Tify has a set procedural pathway for processing video captures from spinning disk confocal imaging. This quality-based tool is able to exclude frames from a large image stack by exclusion based on quality scoring. Using a small subset of human scores, Tify is able to use regression to calculate estimated scores for frames which it has not seen and subsequently exclude them from final output videos. **(B)** Crucially, Tify is able to calculate scores which are proximal to human scores.

than use reference frames, *Tify* instead uses a small subset of human scoring, underlying image statistics (such as standard deviation, entropy, and skewness), and regression analysis to attempt to "quality score" all frames from an entire image stack (for an idea of the methodology involved, see **Figure 3**). To make this software more applicable for intravital microscopy, we built in two additional statistics which were specifically relevant to cardiac intravital imaging: sum pixel ramp and segment intensity deviation. Detailed descriptions on how these statistics are calculated is beyond the scope of this review, but detailed information is available in the published manuscript detailing *Tify* (96). On average, users needed to score around 20 frames in order for *Tify* to score the remaining frames in the image stack with high levels of accuracy. To test this accuracy, we asked users to attribute a quality score (0–5) to 200 frames of a video obtained from cardiac intravital imaging. We then provided Tify with the scores from the first 20 of these, and assessed the software's accuracy at calculating the rest; the correlation co-efficient between human scores and calculated scores was high (e.g., 0.76 ± 0.03 for one set) (96). This approach has some advantages—because the image scores for unseen frames are calculated formulaically, *Tify* does not need to have seen images in advance in order to score them—it simply needs to have a formula with which to calculate the scores from. Therefore, it is possible—for instance—that a user could carry out intravital microscopy on the heart, perform scoring on those images, and generate a formula that can be used for all subsequent cardiac intravital microscopy images that are processed through *Tify*. One of the other advantages to *Tify* that, at least to our knowledge, is not available in other post-acquisition software, is the ability to retain temporal relationships between the retained frames. Most methods of frame removal do not rely on a simple system of cut-off; that is, if an image is below a certain quality of score, then it is removed from the stack. When we designed *Tify*, it was important to us that the output from our program retained some temporal relationship—for instance, if our software had disposed of 20 s of consecutive frames (an extreme example) then the result would have a large temporal gap in the output. To avoid this, we built in a feature called Frame Windowing, which rather than being a frame rejection technique, should rather be considered as a frame selection technique. Users specify the size of a window in n frames, and the software identifies the highest quality frame from within that window. Once done, the software moves onto the next n frames, and so on until the end of the input file. The resulting output is $1/n$ times the size of the original file, but each frame has some degree of temporal link between them.

CONCLUDING REMARKS

For some time in the latter part of the 1970s and 1980s, it appeared as if cardiac intravital becoming a routine technique was an inevitability, given the pace of developments. It would be fair to comment that some of the techniques used in the 1980s were, even by todays technological standards, exceptionally elegant. However, the final leap toward using these techniques to monitor immune cell trafficking seemed to be lacking. It was not until the publications earlier this decade that allowed intravital microscopy of the heart to begin to gather pace again. As we approach the end of this decade, there are now a range of tools and approaches available to those who wish to explore intravital imaging of the cardiac microvasculature. We would put on record that such work is still challenging; the surgery required for exposure of the heart and induction of ischaemia is not trivial. However, the technological barriers that one used to face are no longer in the way. Using these new found techniques over the next decade, perhaps we may finally see an end to the days where the cardiac microcirculation is considered a research "black box."

AUTHOR CONTRIBUTIONS

DK and NK wrote and drafted the manuscript.

REFERENCES

1. British Heart Foundation. *Facts and Figures*. (2019). Available online at: https://www.bhf.org.uk/what-we-do/our-research/heart-statistics/heart-statistics-publications/cardiovascular-disease-statistics-2019 (accessed 30 July, 2019).
2. Bhatnagar P, Wickramasinghe K, Wilkins E, Townsend N. Trends in the epidemiology of cardiovascular disease in the UK. *Heart*. (2016) 102:1945–52. doi: 10.1136/heartjnl-2016-309573
3. British Heart Foundation. *2019 Statistics Compendium*. (2019). Available online at: https://www.bhf.org.uk/-/media/files/research/heart-statistics/bhf-statistics-compendium-2019-final.pdf?la=en (accessed 30 July 2019).
4. Van Linthout S, Tschöpe C. Inflammation - cause or consequence of heart failure or both? *Curr Heart Fail Rep*. (2017) 14:251–65. doi: 10.1007/s11897-017-0337-9
5. Seta Y, Shan K, Bozkurt B, Oral H, Mann DL. Basic mechanisms in heart failure: the cytokine hypothesis. *J Card Fail*. (1996) 2:243–9. doi: 10.1016/S1071-9164(96)80047-9
6. Torre-Amione G, Kapadia S, Benedict C, Oral H, Young JB, Mann DL. Proinflammatory cytokine levels in patients with depressed left ventricular ejection fraction: a report from the Studies of Left Ventricular Dysfunction. (SOLVD). *J Am Coll Cardiol*. (1996) 27:1201–6. doi: 10.1016/0735-1097(95)00589-7
7. Kubota T, Mctiernan CF, Frye CS, Slawson SE, Lemster BH, Koretsky AP, et al. Dilated cardiomyopathy in transgenic mice with cardiac-specific overexpression of tumor necrosis factor-alpha. *Circ Res*. (1997) 81:627–35. doi: 10.1161/01.RES.81.4.627
8. Savvatis K, Pappritz K, Becher PM, Lindner D, Zietsch C, Volk HD, et al. Interleukin-23 deficiency leads to impaired wound healing and adverse prognosis after myocardial infarction. *Circ Heart Fail*. (2014) 7:161–71. doi: 10.1161/CIRCHEARTFAILURE.113.000604
9. Westermann D, Van Linthout S, Dhayat S, Dhayat N, Schmidt A, Noutsias M, et al. Tumor necrosis factor-alpha antagonism protects from myocardial inflammation and fibrosis in experimental diabetic cardiomyopathy. *Basic Res Cardiol*. (2007) 102:500–7. doi: 10.1007/s00395-007-0673-0
10. Xie F, Fei X, Zhang MB, Zhang Y, Wang HW, Tang J, et al. Quantitative evaluation of hepatic microvascular perfusion after ischemia-reperfusion injury in rabbits by contrast-enhanced ultrasound perfusion imaging. *Ultrasound Med Biol*. (2018) 44:1053–62. doi: 10.1016/j.ultrasmedbio.2018.01.004
11. Zeisberg EM, Tarnavski O, Zeisberg M, Dorfman AL, Mcmullen JR, Gustafsson E, et al. Endothelial-to-mesenchymal transition contributes to cardiac fibrosis. *Nat Med*. (2007) 13:952–61. doi: 10.1038/nm1613
12. Zhang Y, Bauersachs J, Langer HF. Immune mechanisms in heart failure. *Eur J Heart Fail*. (2017) 19:1379–89. doi: 10.1002/ejhf.942

13. Frantz S, Hofmann U, Fraccarollo D, Schafer A, Kranepuhl S, Hagedorn I, et al. Monocytes/macrophages prevent healing defects and left ventricular thrombus formation after myocardial infarction. *FASEB J*. (2013) 27:871–81. doi: 10.1096/fj.12-214049
14. Paulus WJ, Tschöpe C. A novel paradigm for heart failure with preserved ejection fraction: comorbidities drive myocardial dysfunction and remodeling through coronary microvascular endothelial inflammation. *J Am College Cardiol*. (2013) 62:263–71. doi: 10.1016/j.jacc.2013.02.092
15. Likoff W, Segal BL, Kasparian H. Paradox of normal selective coronary arteriograms in patients considered to have unmistakable coronary heart disease. *N Engl J Med*. (1967) 276:1063–6. doi: 10.1056/NEJM196705112761904
16. Chilian WM. Microvascular pressures and resistances in the left ventricular subepicardium and subendocardium. *Circ Res*. (1991) 69:561–70. doi: 10.1161/01.RES.69.3.561
17. Matsumoto T, Kajiya F. Coronary microcirculation: physiology and mechanics. *Fluid Dyn Res*. (2005) 37:60–81. doi: 10.1016/j.fluiddyn.2004.02.005
18. Kassab GS, Rider CA, Tang NJ, Fung YC. Morphometry of pig coronary arterial trees. *Am J Physiol*. (1993) 265:H350–365. doi: 10.1152/ajpheart.1993.265.1.H350
19. Steinhausen M, Tillmanns H, Thederan H. Microcirculation of the epimyocardial layer of the heart. I A method for *in vivo* observation of the microcirculation of superficial ventricular myocardium of the heart and capillary flow pattern under normal and hypoxic conditions. *Pflugers Arch*. (1978) 378:9–14. doi: 10.1007/BF00581952
20. Yada T, Hiramatsu O, Kimura A, Goto M, Ogasawara Y, Tsujioka K, et al. In vivo observation of subendocardial microvessels of the beating porcine heart using a needle-probe videomicroscope with a CCD camera. *Circ Res*. (1993) 72:939–46. doi: 10.1161/01.RES.72.5.939
21. Toyota E, Fujimoto K, Ogasawara Y, Kajita T, Shigeto F, Matsumoto T, et al. Dynamic changes in three-dimensional architecture and vascular volume of transmural coronary microvasculature between diastolic- and systolic-arrested rat hearts. *Circulation*. (2002) 105:621–6. doi: 10.1161/hc0502.102964
22. Toyota E, Ogasawara Y, Hiramatsu O, Tachibana H, Kajiya F, Yamamori S, et al. Dynamics of flow velocities in endocardial and epicardial coronary arterioles. *Am J Physiol Heart Circulat Physiol*. (2005) 288:H1598–603. doi: 10.1152/ajpheart.01103.2003
23. Crea F, Camici PG, Bairey Merz CN. Coronary microvascular dysfunction: an update. *Eur Heart J*. (2014) 35:1101–11. doi: 10.1093/eurheartj/eht513
24. Pries AR, Habazettl H, Ambrosio G, Hansen PR, Kaski JC, Schachinger V, et al. A review of methods for assessment of coronary microvascular disease in both clinical and experimental settings. *Cardiovasc Res*. (2008) 80:165–74. doi: 10.1093/cvr/cvn136
25. Pries AR, Reglin B. Coronary microcirculatory pathophysiology: can we afford it to remain a black box? *Eur Heart J*. (2016) 38:478–88. doi: 10.1093/eurheartj/ehv760
26. Lee S, Courties G, Nahrendorf M, Weissleder R, Vinegoni C. Motion characterization scheme to minimize motion artifacts in intravital microscopy. *J Biomedi Opt*. (2017) 22:36005–36005. doi: 10.1117/1.JBO.22.3.036005
27. Wagner DD, Frenette PS. The vessel wall and its interactions. *Blood*. (2008) 111:5271–81. doi: 10.1182/blood-2008-01-078204
28. Marzi I. Intravital microscopy of the liver for investigation of microcirculation, leukocyte-endothelial interactions and macrophage function - Experimental results after liver transplantation. *Transplantationsmedizin*. (1994) 6:91–8.
29. Sumen C, Mempel TR, Mazo IB, Von Andrian UH. Intravital microscopy: visualizing immunity in context. *Immunity*. (2004) 21:315–29. doi: 10.1016/j.immuni.2004.08.006
30. Pittet MJ, Weissleder R. Intravital imaging. *Cell*. (2011) 147:983–91. doi: 10.1016/j.cell.2011.11.004
31. Kavanagh DP, Yemm AI, Alexander JS, Frampton J, Kalia N. Enhancing the adhesion of hematopoietic precursor cell integrins with hydrogen peroxide increases recruitment within murine gut. *Cell Transplant*. (2013) 22:1485–99. doi: 10.3727/096368912X653192
32. White RL, Nash G, Kavanagh DP, Savage CO, Kalia N. Modulating the adhesion of haematopoietic stem cells with chemokines to enhance their recruitment to the ischaemically injured murine kidney. *PLoS ONE*. (2013) 8:e66489. doi: 10.1371/journal.pone.0066489
33. Teo GS, Yang Z, Carman CV, Karp JM, Lin CP. Intravital imaging of mesenchymal stem cell trafficking and association with platelets and neutrophils. *Stem Cells*. (2015) 33:265–77. doi: 10.1002/stem.1848
34. Martini J, Honig CR. Direct measurement of intercapillary distance in beating rat heart in situ under various conditions of O 2 supply. *Microvasc Res*. (1969) 1:244–56. doi: 10.1016/0026-2862(69)90026-0
35. Tillmanns H, Ikeda S, Hansen H, Sarma JS, Fauvel JM, Bing RJ. Microcirculation in the ventricle of the dog and turtle. *Circ Res*. (1974) 34:561–9. doi: 10.1161/01.RES.34.4.561
36. Nellis SH, Leidtke AJ. Pressures and dimensions in the terminal vascular bed of the myocardium determined by a new free-motion technique. In: Tillmanns H, Kubler W, Zebe H, editors. *Microcirculation of the Heart: Theoretical and Clinical Problems*. Berlin: Springer-Verlag (1982). p. 61–73.
37. Nellis SH, Liedtke AJ, Whitesell L. Small coronary vessel pressure and diameter in an intact beating rabbit heart using fixed-position and free-motion techniques. *Circ Res*. (1981) 49:342–53. doi: 10.1161/01.RES.49.2.342
38. Chilian WM, Defily DV. Methodological approaches used for the study of the coronary microcirculation *in situ*. *J. Vascul Res*. (1991) 28:236–44. doi: 10.1159/000158868
39. Chilian WM, Eastham CL, Marcus ML. Microvascular distribution of coronary vascular resistance in beating left ventricle. *Am J Physiol*. (1986) 251:H779–788. doi: 10.1152/ajpheart.1986.251.4.H779
40. Yoder BA, Siler-Khodr T, Winter VT, Coalson JJ. High-frequency oscillatory ventilation: effects on lung function, mechanics, and airway cytokines in the immature baboon model for neonatal chronic lung disease. *Am J Respir Crit Care Med*. (2000) 162:1867–76. doi: 10.1164/ajrccm.162.5.9912145
41. Evans E, Biro P, Bedforth N. Jet ventilation. *BJA Educ*. (2007) 7:2–5. doi: 10.1093/bjaceaccp/mkl061
42. Jones CJ, Defily DV, Patterson JL, Chilian WM. Endothelium-dependent relaxation competes with alpha 1- and alpha 2-adrenergic constriction in the canine epicardial coronary microcirculation. *Circulation*. (1993) 87:1264–74. doi: 10.1161/01.CIR.87.4.1264
43. Jones CJ, Kuo L, Davis MJ, Defily DV, Chilian WM. Role of nitric oxide in the coronary microvascular responses to adenosine and increased metabolic demand. *Circulation*. (1995) 91:1807–13. doi: 10.1161/01.CIR.91.6.1807
44. Langendorff O. Untersuchungen am uberlebenden Saugethierherzen. *Pflugers Arch Ges Physiol Mensch Tiere*. (1895) 61:291–332. doi: 10.1007/BF01812150
45. Bell RM, Mocanu MM, Yellon DM. Retrograde heart perfusion: the Langendorff technique of isolated heart perfusion. *J Mol Cell Cardiol*. (2011) 50:940–50. doi: 10.1016/j.yjmcc.2011.02.018
46. Deng Q, Scicli AG, Lawton C, Silverman NA. Coronary flow reserve after ischemia and reperfusion of the isolated heart. Divergent results with crystalloid versus blood perfusion. *J Thorac Cardiovasc Surg*. (1995) 109:466–72. doi: 10.1016/S0022-5223(95)70277-6
47. Podesser BK, Hallstrom S, Schima H, Huber L, Weisser J, Kroner A, et al. The erythrocyte-perfused "working heart" model: hemodynamic and metabolic performance in comparison to crystalloid perfused hearts. *J Pharmacol Toxicol Methods*. (1999) 41:9–15. doi: 10.1016/S1056-8719(99)00018-0
48. Liao R, Podesser BK, Lim CC. The continuing evolution of the Langendorff and ejecting murine heart: new advances in cardiac phenotyping. *Am J Physiol Heart Circ Physiol*. (2012) 303:H156–167. doi: 10.1152/ajpheart.00333.2012
49. Sutherland FJ, Hearse DJ. The isolated blood and perfusion fluid perfused heart. *Pharmacol Res*. (2000) 41:613–27. doi: 10.1006/phrs.1999.0653
50. Cotter MJ, Norman KE, Hellewell PG, Ridger VC. A novel method for isolation of neutrophils from murine blood using negative immunomagnetic separation. *Am J Pathol*. (2001) 159:473–81. doi: 10.1016/S0002-9440(10)61719-1
51. Faria M, De Pinho MN. Extracorporeal blood oxygenation devices, membranes for. In: E Drioli, L Giorno, editors. *Encyclopedia of Membranes*. Berlin; Heidelberg: Springer Berlin Heidelberg (2015). p. 1–19. doi: 10.1007/978-3-642-40872-4_1468-1
52. Okazaki Y, Cao ZL, Ohtsubo S, Hamada M, Naito K, Rikitake K, et al. Leukocyte-depleted reperfusion after long cardioplegic arrest attenuates ischemia-reperfusion injury of the coronary endothelium and myocardium in rabbit hearts. *Eur J Cardiothorac Surg*. (2000) 18:90–7. doi: 10.1016/S1010-7940(00)00436-X

53. Takarabe K, Okazaki Y, Higuchi S, Murayama J, Natsuaki M, Itoh T. Nicorandil attenuates reperfusion injury after long cardioplegic arrest. *Asian Cardiovascul Thor Annals*. (2007) 15:204–9. doi: 10.1177/021849230701500306
54. Abicht JM, Sfriso R, Reichart B, Langin M, Gahle K, Puga Yung GL, et al. Multiple genetically modified GTKO/hCD46/HLA-E/hbeta2-mg porcine hearts are protected from complement activation and natural killer cell infiltration during *ex vivo* perfusion with human blood. *Xenotransplantation*. (2018) 25:e12390. doi: 10.1111/xen.12390
55. Kupatt C, Habazettl H, Zahler S, Weber C, Becker BF, Messmer K, et al. ACE-inhibition prevents postischemic coronary leukocyte adhesion and leukocyte-dependent reperfusion injury. *Cardiovascul Res*. (1997) 36:386–95. doi: 10.1016/S0008-6363(97)00191-0
56. Ragosta M, Camarano G, Kaul S, Powers ER, Sarembock IJ, Gimple LW. Microvascular integrity indicates myocellular viability in patients with recent myocardial infarction. New insights using myocardial contrast echocardiography. *Circulation*. (1994) 89:2562–9. doi: 10.1161/01.CIR.89.6.2562
57. Bub G, Camelliti P, Bollensdorff C, Stuckey DJ, Picton G, Burton RA, et al. Measurement and analysis of sarcomere length in rat cardiomyocytes in situ and *in vitro*. *Am J Physiol Heart Circ Physiol*. (2010) 298:H1616–25. doi: 10.1152/ajpheart.00481.2009
58. Botcherby EJ, Corbett A, Burton RA, Smith CW, Bollensdorff C, Booth MJ, et al. Fast measurement of sarcomere length and cell orientation in Langendorff-perfused hearts using remote focusing microscopy. *Circ Res*. (2013) 113:863–70. doi: 10.1161/CIRCRESAHA.113.301704
59. Minamikawa T, Cody SH, Williams DA. In situ visualization of spontaneous calcium waves within perfused whole rat heart by confocal imaging. *Am J Physiol*. (1997) 272:H236–243. doi: 10.1152/ajpheart.1997.272.1.H236
60. Hama T, Takahashi A, Ichihara A, Takamatsu T. Real time *in situ* confocal imaging of calcium wave in the perfused whole heart of the rat. *Cell Signal*. (1998) 10:331–7. doi: 10.1016/S0898-6568(97)00136-8
61. Kaneko T, Tanaka H, Oyamada M, Kawata S, Takamatsu T. Three distinct types of Ca²⁺ waves in langendorff-perfused rat heart revealed by real-time confocal microscopy. *Circul Res*. (2000) 86:1093–9. doi: 10.1161/01.RES.86.10.1093
62. Rubart M, Wang E, Dunn KW, Field LJ. Two-photon molecular excitation imaging of Ca2+ transients in Langendorff-perfused mouse hearts. *Am J Physiol Cell Physiol*. (2003) 284:C1654–68. doi: 10.1152/ajpcell.00469.2002
63. Matsumoto-Ida M, Akao M, Takeda T, Kato M, Kita T. Real-time 2-photon imaging of mitochondrial function in perfused rat hearts subjected to ischemia/reperfusion. *Circulation*. (2006) 114:1497–503. doi: 10.1161/CIRCULATIONAHA.106.628834
64. Li W, Nava RG, Bribriesco AC, Zinselmeyer BH, Spahn JH, Gelman AE, et al. Intravital 2-photon imaging of leukocyte trafficking in beating heart. *J Clin Invest*. (2012) 122:2499–508. doi: 10.1172/JCI62970
65. Ustione A, Piston DW. A simple introduction to multiphoton microscopy. *J Microsc*. (2011) 243:221–6. doi: 10.1111/j.1365-2818.2011.03532.x
66. Oreopoulos J, Berman R, Browne M. Spinning-disk confocal microscopy: present technology and future trends. *Methods Cell Biol*. (2014) 123:153–75. doi: 10.1016/B978-0-12-420138-5.00009-4
67. Bayguinov PO, Oakley DM, Shih CC, Geanon DJ, Joens MS, Fitzpatrick JJ. Modern laser scanning confocal microscopy. *Curr Protoc Cytom.* (2018) 85:e39. doi: 10.1002/cpcy.39
68. Kavanagh DPJ, Lokman A, Neag G, Colley A, Kalia N. Imaging the injured beating heart intravitally and the vasculoprotection afforded by haematopoietic stem cells. *Cardiovasc Res*. (2019) 115:1918–32. doi: 10.1093/cvr/cvz118
69. Lee S, Vinegoni C, Feruglio PF, Fexon L, Gorbatov R, Pivoravov M, et al. Real-time *in vivo* imaging of the beating mouse heart at microscopic resolution. *Nat Commun*. (2012) 3:1054. doi: 10.1038/ncomms2060
70. Vinegoni C, Aguirre AD, Lee S, Weissleder R. Imaging the beating heart in the mouse using intravital microscopy techniques. *Nat Protoc*. (2015) 10:1802–19. doi: 10.1038/nprot.2015.119
71. Li W, Hsiao HM, Higashikubo R, Saunders BT, Bharat A, Goldstein DR, et al. Heart-resident CCR2(+) macrophages promote neutrophil extravasation through TLR9/MyD88/CXCL5 signaling. *JCI Insight*. (2016) 1:e87315. doi: 10.1172/jci.insight.87315
72. Shimozawa T, Yamagata K, Kondo T, Hayashi S, Shitamukai A, Konno D, et al. Improving spinning disk confocal microscopy by preventing pinhole cross-talk for intravital imaging. *Proc Natl Acad Sci USA*. (2013) 110:3399–404. doi: 10.1073/pnas.1216696110
73. Xu H, Gonzalo JA, St Pierre Y, Williams IR, Kupper TS, Cotran RS, et al. Leukocytosis and resistance to septic shock in intercellular adhesion molecule 1-deficient mice. *J Exp Med*. (1994) 180:95–109. doi: 10.1084/jem.180.1.95
74. Bajpai G, Bredemeyer A, Li W, Zaitsev K, Koenig AL, Lokshina I, et al. Tissue resident CCR2- and CCR2+ cardiac macrophages differentially orchestrate monocyte recruitment and fate specification following myocardial injury. *Circ Res*. (2019) 124:263–78. doi: 10.1161/CIRCRESAHA.118.314028
75. Li W, Feng G, Gauthier JM, Lokshina I, Higashikubo R, Evans S, et al. Ferroptotic cell death and TLR4/Trif signaling initiate neutrophil recruitment after heart transplantation. *J Clin Invest*. (2019) 130:2293–304. doi: 10.1172/JCI126428
76. Aguirre AD, Vinegoni C, Sebas M, Weissleder R. Intravital imaging of cardiac function at the single-cell level. *Proc Natl Acad Sci USA*. (2014) 111:11257–62. doi: 10.1073/pnas.1401316111
77. Jones JS, Small DM, Nishimura N. *In vivo* calcium imaging of cardiomyocytes in the beating mouse heart with multiphoton microscopy. *Front Physiol*. (2018) 9:969. doi: 10.3389/fphys.2018.00969
78. Kavanagh DP, Yemm AI, Zhao Y, Frampton J, Kalia N. Mechanisms of adhesion and subsequent actions of a haematopoietic stem cell line, HPC-7, in the injured murine intestinal microcirculation *in vivo*. *PLoS ONE*. (2013) 8:e59150. doi: 10.1371/journal.pone.0059150
79. Kuhnle GE, Leipfinger FH, Goetz AE. Measurement of microhemodynamics in the ventilated rabbit lung by intravital fluorescence microscopy. *J Appl Physiol*. (1993) 74:1462–71. doi: 10.1152/jappl.1993.74.3.1462
80. Looney MR, Thornton EE, Sen D, Lamm WJ, Glenny RW, Krummel MF. Stabilized imaging of immune surveillance in the mouse lung. *Nat Methods*. (2011) 8:91–6. doi: 10.1038/nmeth.1543
81. Presson RGJr, Brown MB, Fisher AJ, Sandoval RM, Dunn KW, Lorenz KS, et al. Two-photon imaging within the murine thorax without respiratory and cardiac motion artifact. *Am J Pathol*. (2011) 179:75–82. doi: 10.1016/j.ajpath.2011.03.048
82. Vinegoni C, Lee S, Gorbatov R, Weissleder R. Motion compensation using a suctioning stabilizer for intravital microscopy. *Intravital*. (2012) 1:115–21. doi: 10.4161/intv.23017
83. Jung K, Kim P, Leuschner F, Gorbatov R, Kim JK, Ueno T, et al. Endoscopic time-lapse imaging of immune cells in infarcted mouse hearts. *Circ Res*. (2013) 112:891–9. doi: 10.1161/CIRCRESAHA.111.300484
84. Matsuura R, Miyagawa S, Fukushima S, Goto T, Harada A, Shimozaki Y, et al. Intravital imaging with two-photon microscopy reveals cellular dynamics in the ischeamia-reperfused rat heart. *Sci Rep*. (2018) 8:15991. doi: 10.1038/s41598-018-34295-w
85. Lee S, Nakamura Y, Yamane K, Toujo T, Takahashi S, Tanikawa Y, et al. Image stabilization for *in vivo* microscopy by high-speed visual feedback control. *IEEE Transac Robot*. (2008) 24:45–54. doi: 10.1109/TRO.2007.914847
86. Lee S, Ozaki T, Nakamura Y. *In vivo* microscope image stabilization through 3-D motion compensation using a contact-type sensor. In: *2008 IEEE/RSJ International Conference on Intelligent Robots and Systems*. Nice (2008). p. 1192–7.
87. Sherlock B, Warren S, Stone J, Neil M, Paterson C, Knight J, et al. Fibre-coupled multiphoton microscope with adaptive motion compensation. *Biomed Opt Exp*. (2015) 6:1876–84. doi: 10.1364/BOE.6.001876
88. Vinegoni C, Lee S, Feruglio PF, Marzola P, Nahrendorf M, Weissleder R. Sequential average segmented microscopy for high signal-to-noise ratio motion-artifact-free *in vivo* heart imaging. *Biomed Opt Exp*. (2013) 4:2095–106. doi: 10.1364/BOE.4.002095
89. Vinegoni C, Lee S, Aguirre AD, Weissleder R. New techniques for motion-artifact-free *in vivo* cardiac microscopy. *Front Physiol*. (2015) 6:147. doi: 10.3389/fphys.2015.00147
90. Preibisch S, Saalfeld S, Schindelin J, Tomancak P. Software for bead-based registration of selective plane illumination microscopy data. *Nat Methods*. (2010) 7:418–9. doi: 10.1038/nmeth0610-418
91. Klein S, Staring M, Murphy K, Viergever MA, Pluim JP. elastix: a toolbox for intensity-based medical image registration. *IEEE Trans Med Imag*. (2010) 29:196–205. doi: 10.1109/TMI.2009.2035616

92. Shamonin DP, Bron EE, Lelieveldt BP, Smits M, Klein S, Staring M, et al. Fast parallel image registration on CPU and GPU for diagnostic classification of Alzheimer's disease. *Front Neuroinform*. (2013) 7:50. doi: 10.3389/fninf.2013.00050
93. Dunn KW, Lorenz KS, Salama P, Delp EJ. IMART software for correction of motion artifacts in images collected in intravital microscopy. *Intravital*. (2014) 3:e28210–e28210. doi: 10.4161/intv.28210
94. Gómez-Conde I, Caetano SS, Tadokoro CE, Olivieri DN. Stabilizing 3D *in vivo* intravital microscopy images with an iteratively refined soft-tissue model for immunology experiments. *Comput Biol Med*. (2015) 64:246–60. doi: 10.1016/j.compbiomed.2015.07.001
95. Soulet D, Paré ACoste J, Lacroix S. Automated filtering of intrinsic movement artifacts during two-photon intravital microscopy. *PLoS ONE*. (2013) 8:e53942. doi: 10.1371/journal.pone.0053942
96. Kavanagh DPJ, Gallagher MT, Kalia N. Tify: a quality-based frame selection tool for improving the output of unstable biomedical imaging. *PLoS ONE*. (2019) 14:e0213162. doi: 10.1371/journal.pone.0213162

Conflict of Interest: The authors declare that the research was conducted in the absence of any commercial or financial relationships that could be construed as a potential conflict of interest.

frontiers in Immunology

METHODS
published: 29 November 2019
doi: 10.3389/fimmu.2019.02744

High Resolution Intravital Imaging of the Renal Immune Response to Injury and Infection in Mice

John Sedin[1], *Antoine Giraud*[1], *Svava E. Steiner*[2], *David Ahl*[1], *A. Erik G. Persson*[1], *Keira Melican*[2], *Agneta Richter-Dahlfors*[2] *and Mia Phillipson*[1]*

[1] Department of Medical Cell Biology, Uppsala University, Uppsala, Sweden, [2] Swedish Medical Nanoscience Center, Department of Neuroscience, Karolinska Institutet, Stockholm, Sweden

We developed an experimental set up that enables longitudinal studies of immune cell behavior *in situ* in the challenged as well as unchallenged kidney of anesthetized mice over several hours. Using highly controlled vacuum to stabilize the kidney, the superficial renal cortex could continuously be visualized with minimal disruption of the local microenvironment. No visible changes in blood flow or neutrophils and macrophages numbers were observed after several hours of visualizing the unchallenged kidney, indicating a stable tissue preparation without apparent tissue damage. Applying this set up to monocyte/macrophage ($CX_3CR1^{GFP/+}$) reporter mice, we observed the extensive network of stellate-shaped CX_3CR1 positive cells (previously identified as renal mononuclear phagocytes). The extended dendrites of the CX_3CR1 positive cells were found to bridge multiple capillaries and tubules and were constantly moving. Light induced sterile tissue injury resulted in rapid neutrophil accumulation to the site of injury. Similarly, microinfusion of uropathogenic *Escherichia coli* into a single nephron induced a rapid and massive recruitment of neutrophils to the site of infection, in addition to active bacterial clearance by neutrophils. In contrast, the kidney resident mononuclear phagocytes were observed to not increase in numbers or migrate toward the site of injury or infection. In conclusion, this model allows for longitudinal imaging of responses to localized kidney challenges in the mouse.

Keywords: intravital, renal infection, neutrophils, macrophages, mononuclear phagocytes, sterile injury

OPEN ACCESS

Edited by:
Connie Wong,
Monash University, Australia

Reviewed by:
Alexandre Boissonnas,
Institut National de la Santé et de la Recherche Médicale (INSERM), France
Gustavo B. Menezes,
Federal University of Minas Gerais, Brazil
David A. Hunstad,
Washington University in St. Louis, United States

***Correspondence:**
Mia Phillipson
mia.phillipson@mcb.uu.se

Specialty section:
This article was submitted to Antigen Presenting Cell Biology, a section of the journal Frontiers in Immunology

Received: *14 June 2019*
Accepted: *08 November 2019*
Published: *29 November 2019*

Citation:
Sedin J, Giraud A, Steiner SE, Ahl D, Persson AEG, Melican K, Richter-Dahlfors A and Phillipson M (2019) High Resolution Intravital Imaging of the Renal Immune Response to Injury and Infection in Mice. Front. Immunol. 10:2744. doi: 10.3389/fimmu.2019.02744

INTRODUCTION

The host immune response to injury and infections is both site- and situation-dependent, and is even influenced by the circadian rhythm, with variations in the mechanisms of leukocyte recruitment to different organs as well as to different infectious agents (1–3). In general, tissue resident immune cells acting as sentinels, rapidly detect changes of the microenvironment, and respond accordingly. This response includes macrophage phagocytosis and killing of the pathogens, but also production of chemokines and cytokines to activate and recruit other immune cells to the site. The first cells to be recruited from circulation to the site of infections are neutrophils, which are competent bacteria-killers via the production of reactive oxygen species and antibacterial products. In addition to their role in host defense, leukocytes contribution to tissue restoration following injury has recently been recognized (4–6).

In contrast to the urethra and the bladder, the kidney is typically considered sterile (7). However, urinary tract infections (UTI) are one of the most frequently reported bacterial infections, both in community and hospital settings (8). In some cases, the infection can spread from the urethra to the bladder and eventually further up into the kidney and, in the worst scenario, enter the blood circulation to cause urosepsis. During homeostasis, the urinary tract eliminates these microorganisms rapidly and efficiently by natural host defense mechanisms including physical (washing out, secretory IgA antibodies), chemical (pH, antibacterial peptides), and biological (immune cells) weapons (9). The healthy kidney contains at least five distinct populations of resident renal mononuclear phagocytes with overlapping dendritic and macrophage characteristics (10–12). These cells appear homogenously distributed throughout the kidney (13) and are derived either from the yolk sac during embryogenesis, or from hematopoietic stem cells by *de novo* recruitment of circulating monocytes (14). Activation of the resident renal mononuclear phagocytes is associated with the development and progression of kidney disease (15). However, the precis role of these numerous cells in maintaining and regulating kidney functions is not yet fully clarified. The sparse information regarding the function of resident renal mononuclear phagocytes can be partially attributed to the difficulties in studying them locally *in vivo* rather than as a whole population in an organ. Due to the high tissue density of the kidney, intravital imaging is limited to the superficial regions of the cortex and to the use of fluorescence, either from conjugated antibodies directed against specific surface markers or from genetically labeled cell populations which endogenously express fluorophores. Further, the correlation between levels of antibody-targeted surface molecules/fluorescently tagged gene and the phenotype of the cells needs to be confirmed. Overlapping expression of classical markers for dendritic cells and macrophages further contribute to confusion within the field regarding the action of these tissue resident populations.

Previously, we had developed a spatially-temporally controlled model of kidney infection in rats which allowed us to visually follow the progression of uropathogenic *Escherichia coli* (UPEC) kidney infection in real-time (16, 17). UPEC express a unique sub-set of virulence factors which allow them to colonize the urinary tract including adhesion pili and exotoxins (18). In this model, bacteria are microinfused into a single tubule of an exposed kidney in an anesthetized rat and followed with multiphoton microscopy. This work was one of the first to use intravital imaging to follow bacterial infection *in situ* and described a number of new phenomena including a rapid protective vascular coagulation response (17) and the role of bacterial virulence factors in host response kinetics (19). An aim had been to follow up on this work by detailing the early immune cell recruitment to UPEC infection, but a drawback in this model was the lack of tools available for rats, particularly a lack of fluorescently transgenic animals as are available in mouse models. In this current report, we describe an experimental set up that enables studies of immune cell behavior in the cortex of the mouse kidney, including transgenic animals, in both healthy animals and during injury and local bacterial infection in single nephron over several hours. Using this set up, the extended dendrites of the resident renal mononuclear phagocytes were found to bridge multiple capillaries and tubules and were in constant motion, apparently probing the environment of the healthy kidney. In addition, intravascular neutrophils were demonstrated to crawl within the microvasculature. Following both sterile injury and infection, the neutrophils rapidly accumulated in large numbers at the afflicted site, where they also were found to phagocytose bacteria. Neither sterile tissue injury nor bacterial infection however, did alter the mononuclear phagocytes network, which did not increase in number or migrated following the insult. In summary, this study demonstrates that a stable preparation for intravital microscopy of the mouse kidney cortex reveals distinct immune cell behavior *in situ* and can help to better understand their role and interactions.

MATERIALS AND METHODS

Animals

C57Bl/6J mice [30–35 g (Taconic, Denmark)], $CX_3CR1^{+/GFP}$ F1 hybrid mice [25–30 g (B6.129P-Cx3cr1tm1Litt/J, The Jackson Laboratory, (20)) and (C57Bl/6J, Taconic)] and $CX_3CR1^{+/CRE}$: Rosa-Tomato hybrid mice [25–30g ($Cx3cr1^{tm2.1(cre/ERT2)Jung}$ (21)) and $Gt(ROSA)26Sor^{tm14(CAG-tdTomato)Hze}$ (22)] were used. All animals had access to tap water and pelleted food *ad libitum* throughout the experimental study. The following antibodies were administered intravenously to visualize kidney resident mononuclear phagocytes, blood vessels, platelets and neutrophils, respectively: anti-mouse; F4/80, CD31 (PECAM-1), CD41, and Ly-6G (Gr-1). A detailed information about clone, suppliers, doses and conjugated fluorophores are presented in the **Supplementary Table 1**. The antibodies were administered approximately 30 min before start of experiments to optimize the staining of the target cells. All experiments were approved by the Regional Animal Ethics Committee in Uppsala, Sweden, under the ethical permit number C98/16.

Surgical Preparation, Tissue Stabilization, and Confocal Imaging (Figure 1A)

Mice were anesthetized by spontaneous inhalation of isoflurane (Abbott Scandinavia, Sweden) diluted 1.8–2.6% in a mixture of air and oxygen. The animals were immediately placed on a custom made table with a heating pad to control and maintain body temperature. The left jugular vein was catheterized with a PE-10 cannula for the injection of antibodies and saline (detailed information in **Supplementary Table 1**). Mice were then placed in the right, lateral decubitus position and a small incision into the left side of the abdominal cavity was made to expose the left kidney. To allow for real time imaging of the live kidney *in situ*, we constructed a modified version of the pancreatic vacuum window (23) with a 4 × 6 mm internal diameter. The window was covered with an imaging-grade 13 mm coverslip held in place with vacuum grease. The suction window (**Supplementary Figure 1**), attached to an in house constructed stand, was guided in position immediately above the kidney (**Figure 1A**). A low vacuum (8–16 mbar) was applied

before lowering the window in contact with the tissue. In each experiment the lowest vacuum needed for immobilization was used to prevent kidney damage. The table was then transferred to a line-scanning confocal microscope (Zeiss LSM 5 Live with Zeiss Zen 2009 software) and the objective (WPlanApo 40x/1.0 objective with 0.5x optical zoom) was lowered into the central region of the preparation to minimize any effects of suction transmitted to the edges of the tissue. A graphical description and pictures of the experimental setup are presented in **Figure 1A** and **Supplementary Figure 1**. For confocal fluorescence microscopy we used the Zeiss LSM 5 Live line-scanning microscope with simultaneous two-channel acquisition. This system is equipped with maintenance-free lasers of diode or solid-state type, 405 nm laser diode, 50 mW; 488 nm laser diode, 100 mW; diode-pumped solid-state laser 532 nm, 75 mW; laser diode 635 nm. Excitation filters, BP 415–480 for BV421 and eFluor450; BP 500–525 for GFP and Alexa 488; BP 550–615 or LP 505 for TRITC, BV605 and Alexa 555; LP 650 for BV650, Alexa 647 and eFluor660 combined with suitable beam splitters and lasers. Brightfield intravital microscopy was done using a with a X-Cite 120 PC fluorescence system (EXFO Photonic Solutions Inc, Canada).

Light Induced Tissue Injuries

Large injuries were induced by exposing the kidney to X-Cite 120 PC fluorescence system (EXFO Photonic Solutions Inc, Canada) at high intensity. Exposing the kidney to a short (10 s) burst of high intensity (50 mW) of the 405 nm excitation laser of the line-scanning confocal microscope induced a small scope in the renal cortex.

Bacterial Infection

The UPEC strain LT004 (16) which constitutively expresses GFP from a chromosomal insertion was used in infection experiments. Microinfusion was performed by adapting to mouse the method previously described for rat (16, 17, 24) Briefly, inoculum were grown overnight in Luria Broth (LB) with chloramphenicol (20 mg/μl) at 37°C. A 1:100 dilution of the overnight culture was then reinoculated into LB with chloramphenicol (20 mg/μl) and grown at 37°C to an OD600 of 0.6. The bacteria were then washed twice (5 min 5 kg) in NaCl (154 mM) and suspended in PBS to a final concentration of 1×10^9 CFU/ml. The final bacterial suspension used to microinfuse the kidney tubules were made by mixing the bacterial stock with the injection tracer solution in a 1:1 ratio, giving a final bacterial solution of 5×10^8 cfu ml^{-1}. The tracer solution was a mixture of 0.7 mg ml^{-1} Fast Green FCF (Fisher, Fair Lawn, NJ, USA) and 0.4 mg ml^{-1} Alexa Fluor 647 conjugated 10 kDa dextran.

Bacteria Infusion Into the Renal Tubule

Needles for the microinfusion were made from thin walled borosilicate glass capillaries of 1 mm outer diameter containing an inner filament (WPI TW100F-4) by pulling the capillary in opposite directions with an in house constructed micropipette puller. The tip of the needle was cut off at the desired tip diameter of 8–10 μm using a Dumont 5/45 forceps and sanded to a 30° tip angle. Before using the micropipette, the pipette was function tested by injecting air in 1 M hydrochloric acid, injection pressure 20 psi. After the test the tip was gently dried with a soft tissue.

Pipette Filling

The capillary was mounted to the nozzle of a pneumatic PicoPump (WPI PV820) on the hold pressure port with the vent port connected to an industrial vacuum line. Using a Leitz micromanipulator and holder to hold the pipette the tip was lowered into the bacterial suspension and filled from the tip using vacuum pressure.

Microinfusion (Figure 1B)

The capillary was mounted to the nozzle of the PV820 on the eject pressure port with the vent port connected to the atmosphere. Using the hold pressure gauge the hold pressure was set to 2 psi. Under stereoscopic microscope observation (96x), using a Leitz micromanipulator and pipette holder, the bacterial suspension was injected for ∼10 min into one renal tubule in mouse, prepared as described for confocal imaging (described above). The rate of infusion averaged 49 ± 23 nl min-1 (n = 7), which corresponded to delivery of about 5×10^5 cfu. In sham-infected animals sterile PBS mixed with tracer solution was infused into the renal tubules. Observation was performed with a PlanApo 20x/0.8 objective with 0.6 up to 0.8x optical zoom in the confocal microscope described above.

RESULTS

The Experimental Setup Allows Maintained Kidney Integrity

The superficial renal cortex was continuously visualized for several hours in anesthetized mice under an upright laser-scanning confocal microscope using the experimental setup described in **Figure 1A** and **Supplementary Figure 1**. The kidney was stabilized within the peritoneal cavity by means of an in-house constructed vacuum stabilized observation window (23) to avoid the use of a kidney cup that can alter circulation, accelerate dehydration, and drop in organ temperature. Further, the use of an upright microscope facilitate long *in vivo* observations with maintained peripheral circulation, as it allows for the organ of interest to be situated at the level of the heart to avoid development of edema. To minimize the disruption of renal tissue integrity and microcirculation by the stabilizing holding arm, the size of the window was enlarged compared to the original design (23) to spread the low, negative gas pressure over a larger surface area (**Supplementary Figure 1**). Using this approach, auto-fluorescent proximal tubule and CD31 stained blood vessels with visible blood flow could be detected over time to a depth up to 100 μm (**Supplementary Video 1**). No visible major changes in blood flow were detected after 5 h post operation (**Supplementary Video 2**). Administration of anti-mouse Ly-6G antibodies intravenously revealed the presence of neutrophils interacting with capillary endothelium (**Figure 2** and **Supplementary Video 3**), demonstrating that in our setting neutrophils normally scan the vasculature of the renal cortex in the unchallenged kidney. Repeated imaging over a period of

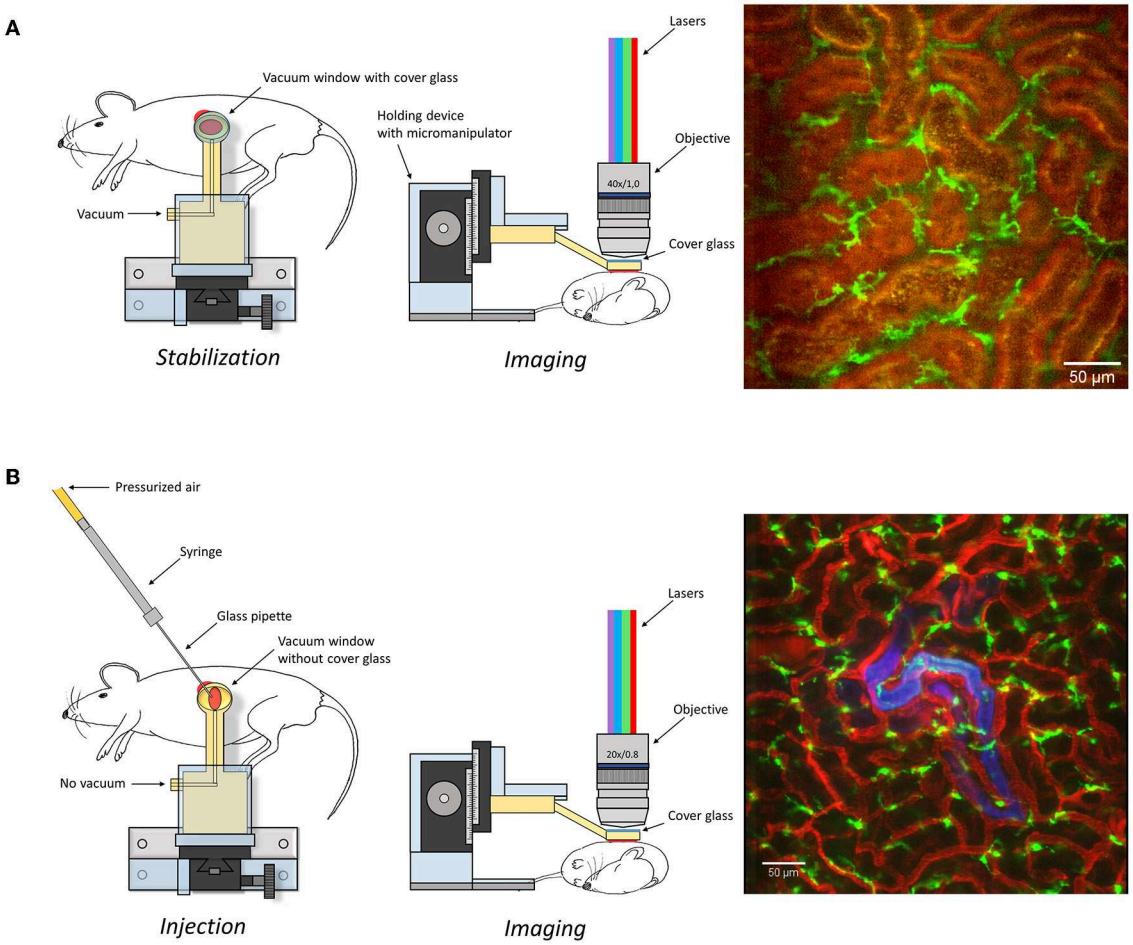

FIGURE 1 | Graphical depiction of the experimental set-up described in the manuscript to expose **(A)** or microinfuse **(B)** and image the kidney. An image captured under these settings is presented as an example on right of the graphical description. Scale bar represents 50 µm. Additional information is available in **Supplementary Figure 1** and **Supplementary Video 1**.

more than 2 h of the intact live kidney did not show any clear increase in the number of visible detected neutrophils (**Figure 2**) or the number of adherent and/or crawling neutrophils. Thus, this experimental setup allows for visualization of the kidney cortex in the anesthetized mouse without concomitant obvious or dramatic neutrophil activation and recruitment hours after exposure.

Renal Network of Probing Mononuclear Phagocytes

The CX_3CR1 chemokine receptor is a commonly used marker for macrophages, monocytes and some dendritic cells. Using a transgenic mouse strain expressing the green fluorescent protein under the regulatory signal governing the expression of CX_3CR1 (20) we monitored the distribution and behavior of these cells in the kidney. Confocal microscopy of $CX_3CR1^{+/GFP}$ mouse kidney *in situ* in anesthetized mice revealed an extensive network of stellate-shaped CX_3CR1 positive cells in the interstitium of the superficial renal cortex (**Figure 3** and **Supplementary Video 4**). As previously described, most of these cells, also called renal mononuclear phagocytes (rMoPhs) (25), demonstrated transcapillary and transtubular connections with their multiple dendrites bridging several tubules and capillaries (**Figure 3** and **Supplementary Videos 4**, **5**) (13, 26). Further, *in vivo* visualization verified that the majority of the CX_3CR1 positive cells located in the cortex were also positive for the pan-macrophage marker F4/80 (**Figure 4**), confirming previous observations (13, 27). These were situated in close proximity to the tubular capillaries (**Figure 3** and **Supplementary Videos 4**, **5**). Time laps recording experiments over 1 h showed dendritic activity of these cells, and they seemed to be constantly probing and sampling the vasculature as well as the tubules (**Figure 5** and **Supplementary Video 6**). These observations confirm previously reported observations by other groups and further validate that our experimental does not seem to alter the rMoPhs network (13, 26).

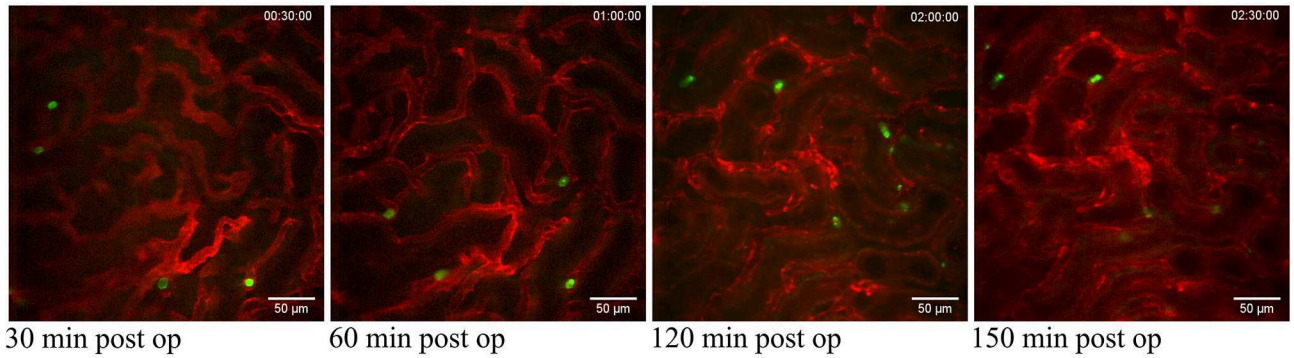

FIGURE 2 | Neutrophils scanning capillaries within the superficial cortex in the unchallenged kidney. Confocal snapshots of the unchallenged kidney in a live C57BL/6J mouse taken at 30, 60, 120, and 150 min post-operation from the **Supplementary Video 3**. Capillaries are visualized in red (anti-CD31- mAb Alexa Fluor 555) and circulating neutrophils in green (anti-Ly6G-mAb Alexa Fluor 488). Scale bars are 50 µm and pictures are representative of 5 experiments. WPlanApo 40x/1.0 objective with 0.5 zoom was used.

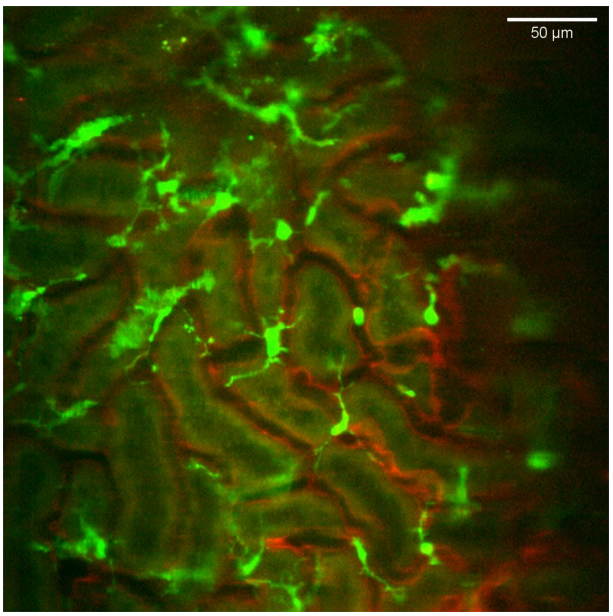

FIGURE 3 | Distribution and stellar shape of CX_3CR1 positive mononuclear phagocytes in the renal cortex. Confocal snapshot from the **Supplementary Video 4**. Blood vessels in red (eFluor 450 conjugated anti-CD31 mAb) and mononuclear phagocytes in green (CX_3CR1-GFP). The scale bar indicates 50 µm. Recorded through a WPlanApo 40x/1.0 objective with 0.5 zoom. Additional 3 dimensional observations are presented in **Supplementary Video 5**.

Recruitment of Neutrophils to Renal Sterile Injury or Bacterial Infections

To explore if our experimental setting did not altered the immune reactivity of the exposed mouse kidney, we tried to visualize the recruitment of circulating neutrophils to injury site. A superficial injury on the kidney was induced by over exposing it to intense light sources from a fluorescence illumination system or a high intensity 405 nm laser that, respectively, can induce a large or a small burn injury in the cortex. The light induced damages led to a rapid and massive accumulation of neutrophils to damaged area (**Figure 6A** and **Supplementary Video 7**). In the case of smaller local laser-induced damage, neutrophils recruited from circulation were also detected in close proximity of the injury (**Supplementary Figure 2**). The large network of rMoPhs was not affected by the sterile injuries. Indeed no obvious changes were observed in the pattern of the CX_3CR1 positive cell network at the site of neutrophil accumulation (**Figure 6B** and **Supplementary Video 8**). This observation corroborates the description of CX_3CR1 positive cells acting merely as sentinels activated upon injury to release chemokines that rapidly trigger the recruitment of neutrophils at the early stage of bacterial infections (15, 28).

To observe the immune cell reaction induced by an infectious stimulus, we injected 10^5 cfu of a fluorescent uropathogenic *Escherichia coli* strain (UPEC) directly into a single renal tubule adapting a method developed in the rat to the mouse [**Figure 1B**, (16)]. Observation of the infected site over several hours revealed the dynamics of bacterial growth and tubule colonization as well as neutrophils moving to the infected site (**Figure 7A** and **Supplementary Video 9**). The presented experimental setting do thus maintain the abilities to detect and signal a local infection that lead to neutrophil chemotaxis toward to infected regions in the kidney cortex. While neutrophils were observed close to the infected site at the late time points, the CX_3CR1 positive cells network appeared similar compared to prior to when the bacteria were injected (**Figure 7B** and **Supplementary Video 10**). This observed relative passivity of macrophages compared to neutrophils in phagocytosis during infection in the upper urinary tract agrees with results present in the literature (29). Interestingly sham-infusion of PBS alone in a tubule did not induce neutrophil recruitment, implicating the bacteria as the attracting inflammatory agent and showing that tubuli puncture *per se* was not sufficient to trigger a massive neutrophil response. Moreover, the setting allowed for real time visualization of bacterial clearance by neutrophils as we could observe that the GFP signal originating

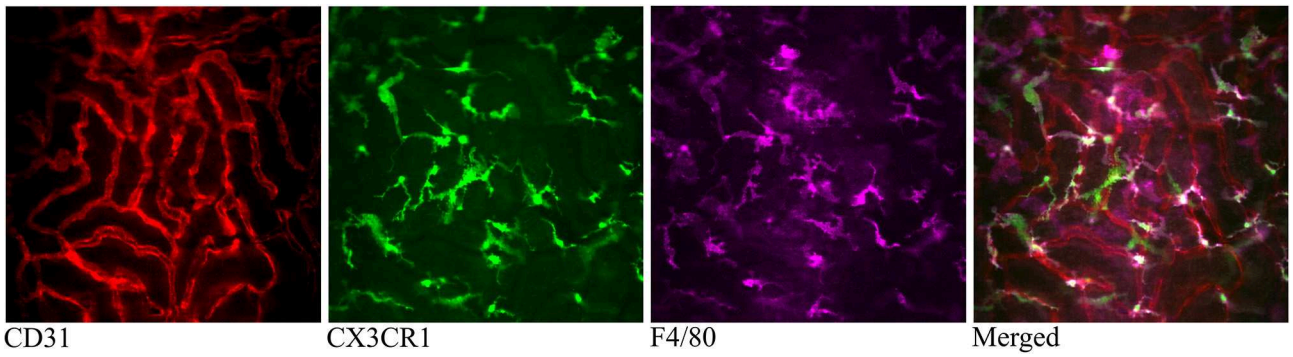

FIGURE 4 | Confocal snapshot of the live kidney in a $CX_3CR1^{+/GFP}$ mouse taken 30 min after intravenously administered anti-F4/80-mAb-Alexa Fluor 647. Capillaries are displayed in red (anti- CD31-mAb eFluor 450), mononuclear phagocytes in green (CX_3CR1-GFP) and in magenta (anti-F4/80- mAb Alexa Fluor 647). Double positive cells appear bright in the merged figure. All scale bars represent 50 μm. WPlanApo 40 x/1.0 objective with 0.5 zoom was used.

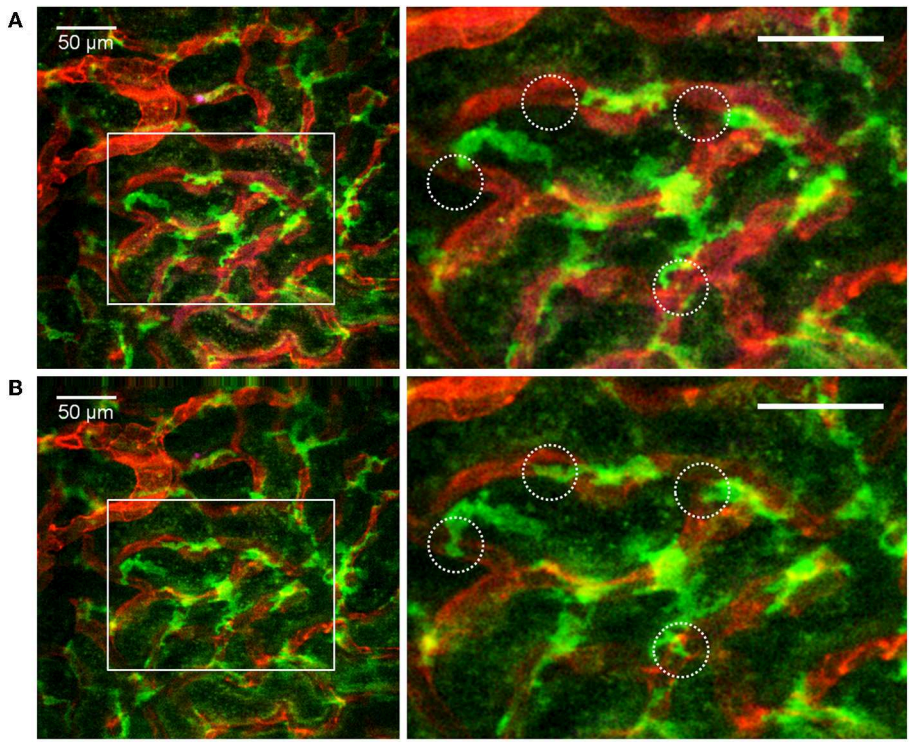

FIGURE 5 | Distribution and dendritic activity of $F4/80^+$ mononuclear phagocytes in the renal cortex. Confocal snapshot at different time points from the **Supplementary Video 6**. **(A,B)** Show of perivascular $F4/80^+$ mononuclear phagocytes sampling the renal capillaries. Capillaries are displayed in red (anti-CD31-mAb Alexa Fluor 555) and mononuclear phagocytes in green (anti-F4/80-mAb Alexa Fluor 647). Boxed areas highlight several active cells with extension and retraction of dendrites (circles). Scale bar 50 μm. WPlanApo 40x/1.0 objective with 0.5 zoom was used.

from infecting bacteria decreased and finally disappeared in parallel to neutrophils becoming GFP-positive (**Figure 8** and **Supplementary Video 11**).

The correlating rat model of UPEC infection has previously shown that upon UPEC infection in a single renal tubule, coagulation is triggered in the local peri-tubular capillaries (17, 30). This coagulatory response observed several hours after infection has been shown to be protective by isolating the infection site and preventing bacterial translocation into the blood stream and a progression to urosepsis (17). In the mouse setting, some experiments were carried out with circulation tracers. These reporters allowed monitoring the quality of blood flow during observation. Light injury induced important perturbation in the circulation, as reveled by the accumulation of platelets in the capillaries surrounding the damaged area (**Figure 6B** and **Supplementary Video 7**). Tubule infusion in the

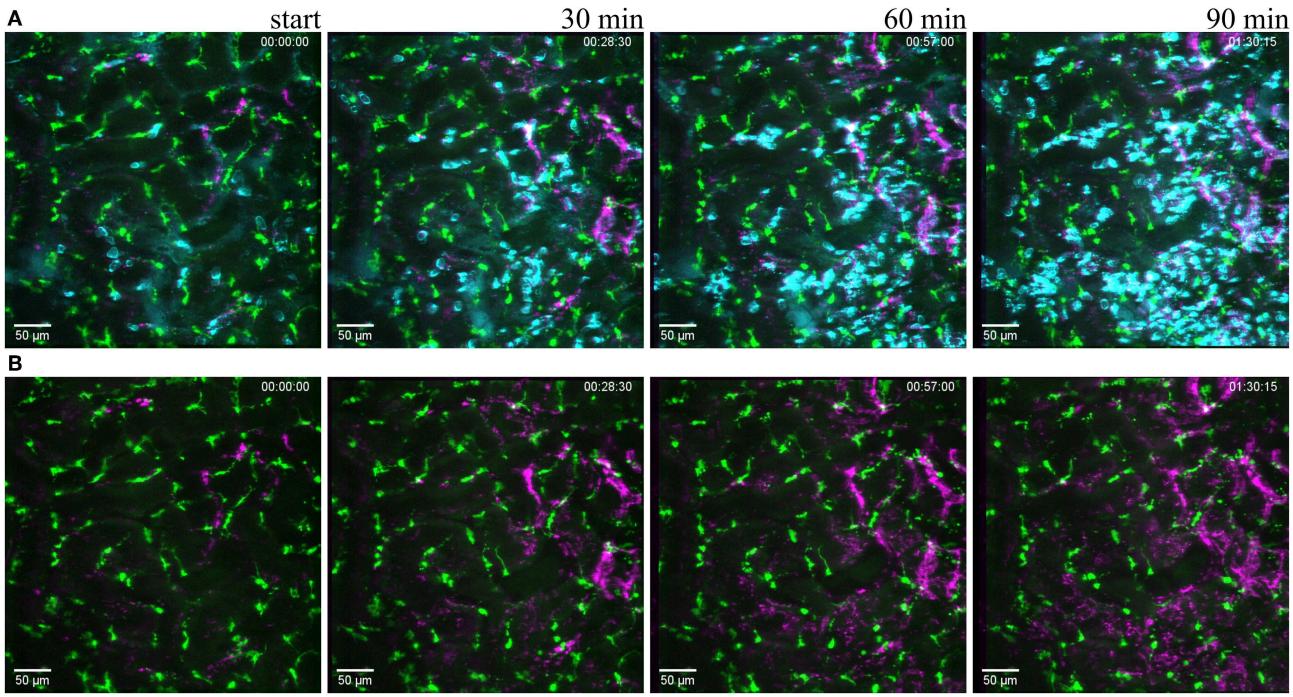

FIGURE 6 | Reaction to light induced sterile injury. Snapshot at 0, 30, 60, and 90 min of **Supplementary Video 7** from $CX_3CR1^{+/GFP}$ mouse kidney after over exposure under a fluorescence lamp at maximum intensity to induce large area damage. Recorded through a PlanApo 20x/0.8 objective with 0.8 zoom. Scale bar 50 µm. (**A** related to **Supplementary Video 7**) Mononuclear phagocytes displayed in green (CR_3CR1-GFP), neutrophils in cyan (anti-Ly6G-mAb Brilliant Violet 421) and platelets in magenta (anti CD41-mAb Brilliant Violet 605) to visualize blood flow. (**B** related to **Supplementary Video 8**) Same picture as in **(A)** without the neutrophil fluorescence for a better observation of the CR_3CR1-GFP cells and platelet accumulation.

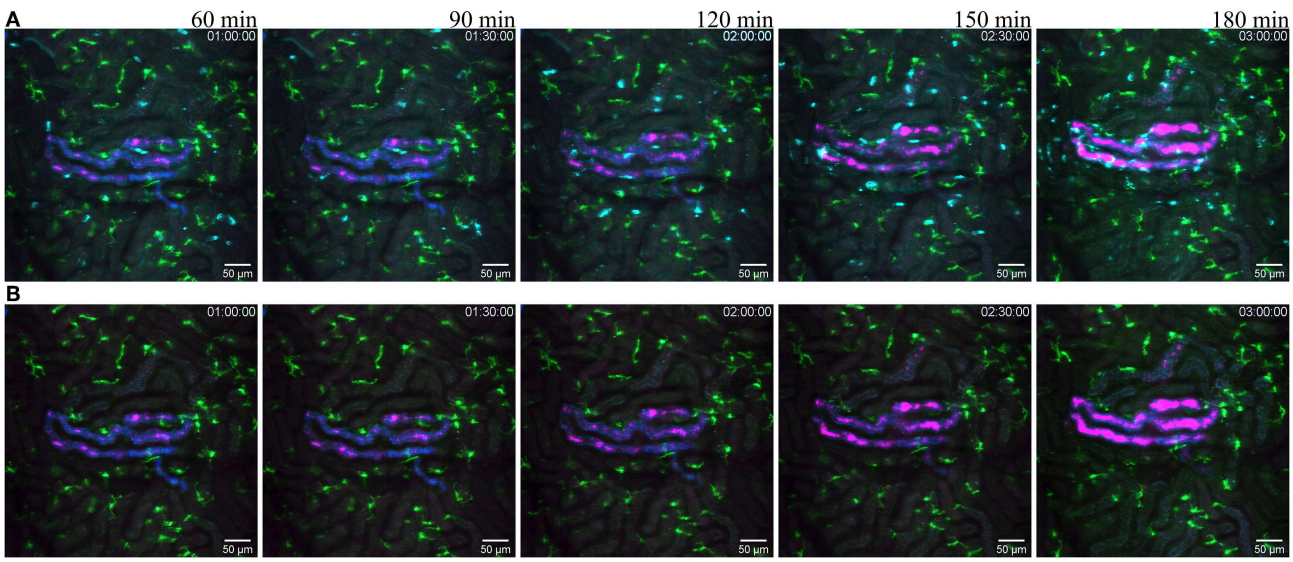

FIGURE 7 | Reaction to infected tubule. (**A** related to **Supplementary Video 9**) snapshot taken at 60, 90, 120, 150, and 180 min post infection of one tubule with the UPEC strain (GFP displayed in magenta) in a of a $CX_3CR1^{+/CRE}$:Rosa-Tomato mouse recorded through a PlanApo 20x/0.8 objective with 0.7 zoom. The injected bacterial solution contains an injection tracer (blue, Alexa Fluor 647 conjugated dextran) to visualize injected tubule. Neutrophils are shown in cyan (anti-Ly6G mAb Brilliant Violet 421). CX_3CR1 positive cells are displayed in green (tdTomato). (**B** related to **Supplementary Video 10**) Same picture as in **(A)** without the neutrophil fluorescence for a better observation of the CR_3CR1-GFP cells and bacterial growth.

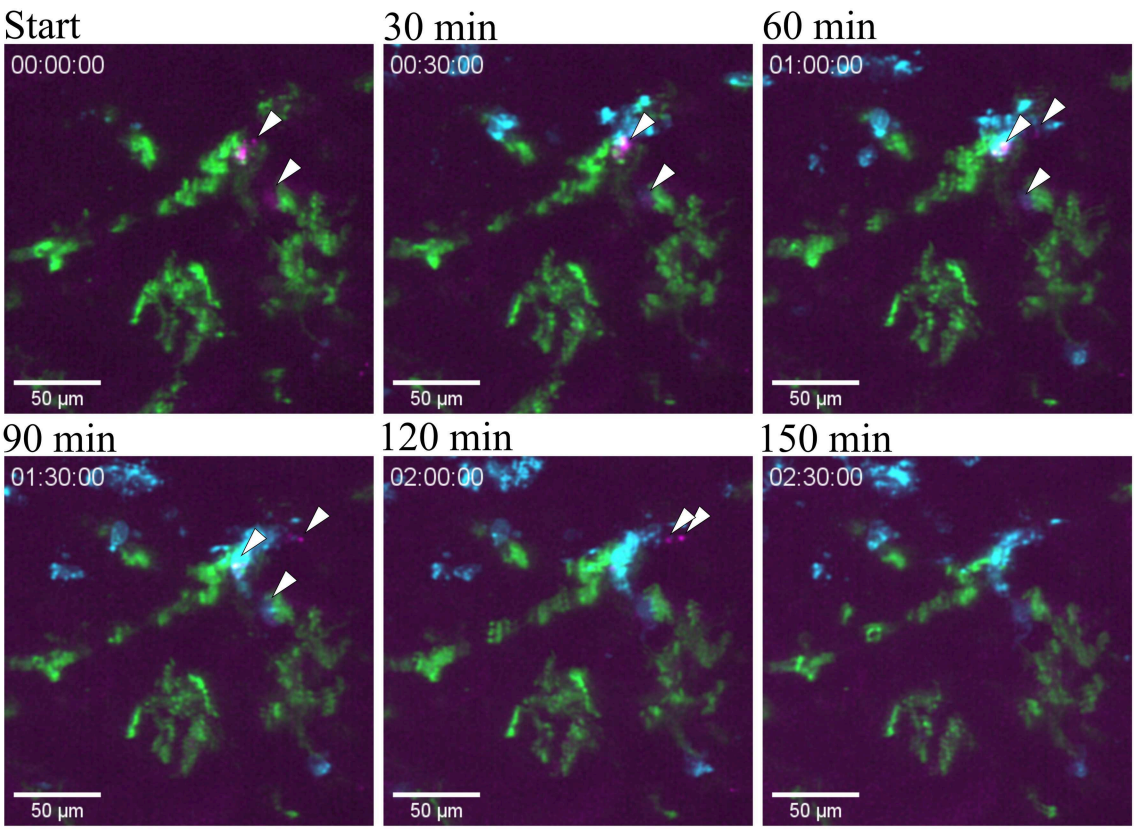

FIGURE 8 | Bacterial clearance. Snapshots taken from **Supplementary Video 10** at different time point post infection of one tubule infused with the UPEC strain (GFP) in a of a $CX_3CR1^{+/CRE}$:Rosa-Tomato mouse showing the clearing of bacteria by neutrophil in red (Ly6G mAb-BV421). CX_3CR1 positive cells are displayed in green (tdTomato) and UPEC in magenta (GFP). PlanApo 20x/0.8 objective with 0.6 zoom.

mouse is a delicate manipulation to perform. Going through the kidney capsule can be difficult and can lead to either perforation of capillaries or bacterial leakage. Only few infusions had been successfully performed and the very limited number of observations could neither allow us to conclude if this clotting around infected tubules is or isn't also a protective mechanism in the mouse. However, trials that resulted in bacterial leakage or local bleeding, both with UPEC or PBS, lead to an observable perturbation in blood flow quality in the capillaries as the circulation tracer was not displaced by passing erythrocytes as revealed by capillaries segments emitting intense fluorescent signal from the circulation tracer (**Supplementary Video 12**). The presented model may thus be used to investigate local coagulation in capillaries surrounding an infected tubule as has been done in the rat model (17).

DISCUSSION

This study demonstrates means to longitudinally study the behavior of resident and recruited immune cells in kidney cortex under basal conditions as well as during localized tissue injury and infection *in vivo* in the mouse. This model offers many genetic tools to visualize and decipher immune cell behavior and interaction by direct visualization. Using this approach, we could observe the numerous stellate-shaped CX_3CR1^+ and $F4/80^+$ resident renal mononuclear phagocytes, which were found scattered throughout the kidney, where they exerted a probing behavior as their extended dendrites spanned several tubules and capillaries, and were in motion. Further, neutrophil scanning of the kidney vasculature was observed under basal conditions, and massive neutrophil accumulation was detected following light-induced sterile injury or bacterial infection, whereas the structure of the renal mononuclear phagocytes network was not affected by either challenge.

The development of experimental models to study biological events in the living animal is both difficult and time consuming. Great care must be taken no to disturb the function and integrity of the organ studied. As the kidney is a very delicate organ that is highly dependent on an intact blood flow, it is a demanding organ to study *in vivo*. By carefully applying a gentle controlled negative pressure (vacuum) to the outer surface of the kidney, the vacuum suction window provided both stabilization and optimal tissue preparation for imaging. Using bright and photostable fluorophores, e.g., Alexa Fluor dyes, the risk of phototoxicity was minimized. Further, a multi-photon microscope would improve the z-resolution and further

reducing the risk of phototoxicity, making it possible to image even deeper into the tissue. Importantly, this method enables imaging *in situ* and does not involve removal of the organ from the animal, allowing for the study of infection with the vasculature, nervous, and immune systems intact. Further, with this method we were able to image beyond 5 h post-op, which is probably close to the time limit a mouse can be kept anesthetized under our experimental conditions without severely affecting the blood pressure.

Animal models of inflammation has together with intravital microscopy been instrumental for increasing the understanding of the mechanisms underlying the leukocyte recruitment from circulation to tissue, as well as leukocyte effector function at different inflamed sites. While the high density of renal tissue impedes traditional bright field imaging of its vasculature and immune cells, high-speed confocal microscopy of fluorescently marked cells, and/or structures enables visualization of blood flow and cell-cell interactions to limited depth in living animals. Intravital microscopy is inevitable associated with both circulatory and respiratory movements, which highlights the importance of reliable models where these cells can be visualized during minimal organ stress. By utilizing a modified version of the technique presented by Looney et al. (23), we have established a method for real-time analysis of the renal microenvironment which is a powerful tool to learn more about the renal resident immune cells during homeostasis as well as during the pathology of bacterial infections *in vivo*. The present technique provides access to the intact microcirculation and microanatomy of the mouse kidney, with the combination of easy to use, high resolution, great stability and with maintenance of normal immune cell reactivity.

In the healthy kidney, numerous mononuclear phagocytes are scattered throughout the renal tissue. The mononuclear phagocytes can be divided into several subpopulations dependent on their expression levels of macrophage- and dendritic cell markers (F4/80, CD11b, and CD11c, respectively). Recent gene array data combined with antibodies directed against CD64 and MerTK (efferocytosis receptor) indicate that the majority of these cells are macrophages, and not dendritic cells as previously believed (11, 31). In addition to their distinct identities, their diverse effector functions remains to be fully established. Clodronate-depletion removes actively phagocytosing cells and resulted in lower plasma creatinine levels following kidney injury, demonstrating that these macrophages aggravate acute kidney injury (32). However, when the renal mononuclear phagocytes are depleted to a larger extent using the CD11b-diphtera toxin receptor model, protection against ischemia-reperfusion injuries is not observed (33), which indicates that some of the renal mononuclear phagocytes have important functions in tissue recovery.

The role of both neutrophils and renal mononuclear phagocytes in bacterial infections has previously been described (9, 15, 29). Using a model of repeated transurethral installation of *E. coli* (UPEC) into the bladder, flow cytometry following kidney homogenization demonstrated that renal neutrophil- but not macrophage numbers were increased 3 h following bacterial instillation, while the total number of dendritic cells and macrophages decreased over time (29). Further, the mononuclear phagocytes were shown to upregulate CXCL2 in response to infection, and thereby contributed to the recruitment of neutrophils. The method developed in the current manuscript enabled tracking of local immune cell behavior over time in the renal cortex of unaffected kidneys or following sterile injury or bacterial infections. We observed that neutrophils of the healthy kidney displayed a normal behavior, as they were sporadically scanning the inside of the blood vessels, and, in response to injury and infection, rapidly accumulate in large numbers at the affected site. The renal mononuclear phagocytes of healthy kidneys were as expected actively scanning their local microenvironment with their dendrites spanning several tubules and capillaries, but, in contrast to neutrophils, did not migrate toward adjacent sterile injury or bacterial infection within the observation time. This is in contrast to what is described for the sterile injury of the liver (34), where F4/80$^+$ cells originating from the peritoneal cavity accumulated as early as 1 h following insult. Cells of the innate immune system are classically viewed as first responders to invasion and damage, where they contribute in different ways to restore tissue homeostasis. It is clear that their ability to detect and respond to environmental signals differ between challenges as well as affected sites (3, 35).

In summary, we established a model that enables longitudinal and precise imaging of the superficial kidney cortex for hours in mouse without impacting the circulation and immune cell potential. This model allowed us to visualize the behavior of neutrophils and resident mononuclear phagocytes submitted to localize aseptic as well as septic challenges.

DATA AVAILABILITY STATEMENT

All datasets generated for this study are included in the article/**Supplementary Material**.

ETHICS STATEMENT

The animal study was reviewed and approved by Regional Animal Ethics Committee in Uppsala, Sweden.

AUTHOR CONTRIBUTIONS

JS, AG, and DA conducted all the experiments. JS, AG, SS, KM, DA, AP, ARD, and MP designed the study, analyzed the data, interpreted the results. JS, AG, KM, and MP wrote the manuscript. All authors contributed to the editing of the manuscript, read and approved the final version before submission.

FUNDING

The work was supported by the Swedish Foundation for Strategic Research (Stiftelsen för Strategisk Forskning, SSF), Swedish Research Council (2018-02552), Ragnar Söderberg

foundation, Knut and Alice Wallenberg foundation, Novo Nordisk Foundation, the Erling-Persson Family Foundation, Getinge AB, and Swedish Medical Nanoscience Center (www.medicalnanoscience.se) at Karolinska Institutet.

SUPPLEMENTARY MATERIAL

The Supplementary Material for this article can be found online at: https://www.frontiersin.org/articles/10.3389/fimmu.2019.02744/full#supplementary-material

Supplementary Video 1 related to **Figure 1A |** 3D projection of a z-stack taken with a WPlanApo 40x/1.0 objective with 0.5 zoom showing autofluorescent tubules in green and labeled blood vessels in red (Alexa Fluor 555 conjugated anti-CD31 mAb). The stack (depth 83 μm) was exported to video at 12 fps using ImageJ.

Supplementary Video 2 | Visualization of blood flow. Live imaging of the kidney of a $CX_3CR1^{+/GFP}$ mouse 5 h after surgery taken with a WPlanApo 40x/1.0 objective with 0.5 zoom. Blood flow was imaged by i.v. injection of TRITC dextran 500 kDa as contrast agent that allow the observation of erythrocytes as black (not stained) dots. Sequence was recorded at a rate of 2 fps for 150 s and then exported to video at 12 fps using ImageJ. GFP fluorescence from the CX_3CR1 positive cells not displayed.

Supplementary Video 3 related to **Figure 2 |** Neutrophils scanning capillaries within the superficial cortex in the unchallenged kidney of a C57Bl/6J mouse with a WPlanApo 40x/1.0 objective with 0.5 zoom. Blood vessels are labeled with Alexa Fluor 555 conjugated anti-CD31 mAb (red) and neutrophils are seen in green (Alexa Fluor 488 conjugated anti-Ly6G mAb). Elapsed time is shown at the low right. The time lapse was recorded directly after surgery at 0.3 fps and exported to video at 24 fps using ImageJ. The scale bar indicates 50 μm.

Supplementary Videos 4, 5 related to **Figure 3 |** Video 4 Distribution of CX_3CR1 positive mononuclear phagocytes in the renal cortex of $CX_3CR1^{+/GFP}$ mouse. Blood vessels are in red (eFluor 450 conjugated anti-CD31 mAb) and mononuclear phagocytes in green (CX_3CR1-GFP). Elapsed time is shown at the low right. The time lapse was recorded at 6 fps with a WPlanApo 40x/1.0 objective with 0.5 zoom and exported to video at 24 fps using ImageJ. The scale bar indicates 50 μm. Video 5: 3D projection of a z-stack (depth 86.74 μm) taken on the same mouse with a WPlanApo 40x/1.0 objective with 0.5 zoom showing blood vessels in red (eFluor 450 conjugated anti-CD31 mAb), CX_3CR1 positive cells in green (GFP) and neutrophils in cyan (Alexa Fluor 555 conjugated anti-Ly6G mAb).

Supplementary Video 6 related to **Figure 5 |** Distribution and dendritic activity of $F4/80^+$ mononuclear phagocytes in the renal cortex of a C57Bl/6J mouse. Blood vessels are displayed in red (Alexa Fluor 555 conjugated anti-CD31 mAb) and mononuclear phagocytes in green (AF647 anti-F4/80 mAb) and neutrophils in magenta (Alexa Fluor 488 conjugated anti-Ly6G mAb). Elapsed time is shown at the low right. The time lapse was recorded at 0.3 fps with a WPlanApo 40x/1.0 objective with 0.5 zoom and exported to video at 24 fps using ImageJ. The scale bar indicates 50 μm.

Supplemental Video 7 related to **Figure 6A |** Recruitment of neutrophils to light induced sterile injury. The $CX_3CR1^{+/GFP}$ mouse kidney following exposure under a fluorescence lamp at maximum intensity to induce a large damaged area. Mononuclear phagocytes are displayed in green (GFP), neutrophils in cyan (Brilliant Violett 421 conjugated anti-Ly6G-mAb) and platelets in magenta (Brilliant Violett 605 conjugated anti CD41) to visualize blood flow. Elapsed time is shown at the low right. Twenty stacks (depth: 51.7 μm) were recorded with 5 min intervals with a PlanApo 20x/0.8 objective with 0.8 zoom and exported to video at 9 fps using ImageJ (3D-Projection). The scale bar indicates 50 μm.

Supplementary Video 8 related to **Figure 6B |** Light-induced sterile injury, same video as **Supplementary Video 7** related to **Figure 5A** without the neutrophil fluorescence to better visualize the behavior of CX_3CR1 positive cells and blood flow. The $CX_3CR1^{+/GFP}$ mouse kidney following exposure under a fluorescence lamp at maximum intensity to induce a large damaged area. Mononuclear phagocytes are displayed in green (GFP) and platelets in magenta (Brilliant Violett 605 conjugated anti CD41) to visualize blood flow. Elapsed time is shown at the low right. Twenty stacks were recorded with 5 min intervals with a PlanApo 20x/0.8 objective with 0.8 zoom and exported to video at 9 fps using ImageJ. The scale bar indicates 50 μm.

Supplementary Video 9 related to **Figure 7A |** Recruitment of neutrophils to an infected tubule. Live imaging of the kidney area surrounding one tubule infected with the UPEC strain from 90 to 155 min post infection. Bacteria are displayed in magenta (GFP), mononuclear phagocytes in green (tdTomato) and neutrophils in cyan (Brilliant Violett 421 conjugated anti-Ly6G mAb). Elapsed time is shown at the upper right. Fourteen stacks (depth: 53.5 μm) were recorded with 5 min intervals with a PlanApo 20x/0.8 objective with 0.7 zoom and exported to video at 9 fps using ImageJ (3D-Projection). The scale bar indicates 50 μm.

Supplementary Video 10 related to **Figure 7B |** Live imaging of the kidney area surrounding one tubule infected with the UPEC strain from 90 to 155 min post infection. This is the same video as **Supplemental Video 9** related to **Figure 7A** without the neutrophil fluorescence to better visualize the behavior of CX_3CR1 positive cells around the infected tubule. Bacteria are displayed in magenta (GFP) and mononuclear phagocytes in green (tdTomato). Elapsed time is shown at the upper right. Fourteen stacks (depth: 53.5 μm) were recorded with 5 min intervals with a PlanApo 20x/0.8 objective with 0.7 zoom and exported to video at 9 fps using ImageJ (3D-Projection). The scale bar indicates 50 μm.

Supplementary Video 11 related to **Figure 8 |** Bacterial clearance by neutrophils in close vicinity of CX_3CR1 positive cells. UPEC strain is displayed in magenta (GFP), neutrophils in cyan (eFluor 660 conjugated anti-Ly6G mAb) and CX_3CR1 positive cells in green (tdTomato). Elapsed time is shown at the upper left corner. Thirty five stacks (depth: 83.2 μm) were recorded with 5 min intervals with a PlanApo 20x/0.8 objective with 0.6 zoom and exported to video at 9 fps. The scale bar indicates 50 μm.

Supplementary Video 12 | Live imaging with a WPlanApo 40x/1.0 objective with 0.5 zoom of the kidney of a $CX_3CR1^{+/GFP}$ mouse where one tubule was infused with PBS and one with the UPEC strain, recorded 3.5 h after infection. The i.v. injection of TRITC dextran 500 kDa as contrast agent allow for blood flow assessment as the circulating erythrocytes replace the dectran and appear as black (not stained) dots. Seconds 0:00 to 0:03 present the untouched surrounding area, 0:04 to 0:21 the UPEC infected tubule and 0:21 to 0:25 the PBS infused tubule. Sequences were recorded at a rate of 2 fps for 150 s and then exported to video at 12 fps using ImageJ.

Figure S1 | Post-surgery pictures of the experimental setting taken before transferring the animal to the microscope **(A)** or before tubule micro infusion **(C)** and of the respective stabilizing window used **(B,D)**.

Figure S2 | Confocal tile scan of a live kidney 60 min post laser-induced tissue damage. Exposing the kidney to a short (10 s) burst of high intensity 405 nm laser (50 mW) induced a small scope of approximately 0.1 mm^2 in the renal cortex. Within 60 min the area surrounding the scope was infiltrated with Ly-6G positive neutrophils (magenta). Mononuclear phagocytes displayed in green (anti-F4/80-mAb), renal capillaries in red (anti-CD31-mAb) and neutrophils in magenta (anti-Ly6G-mAb). The scope is outlined by white arrows. The scale bar indicates 100 μm.

REFERENCES

1. Maas SL, Soehnlein O, Viola JR. Organ-specific mechanisms of transendothelial neutrophil migration in the lung, liver, kidney, and aorta. *Front Immunol.* (2018) 9:2739. doi: 10.3389/fimmu.2018.02739
2. Pick R, He W, Chen C-S, Scheiermann C. Time-of-Day-Dependent Trafficking And Function Of Leukocyte Subsets. *Trends Immunol.* (2019) 40:524–37. doi: 10.1016/j.it.2019.03.010
3. Rankin LC, Artis D. Beyond host defense: emerging functions of the immune system in regulating complex tissue physiology. *Cell.* (2018) 173:554–67. doi: 10.1016/j.cell.2018.03.013

4. Christoffersson G, Phillipson M. The neutrophil: one cell on many missions or many cells with different agendas? *Cell Tissue Res.* (2018) 371:415–23. doi: 10.1007/s00441-017-2780-z
5. Davies LC, Jenkins SJ, Allen JE, Taylor PR. Tissue-resident macrophages. *Nat Immunol.* (2013) 14:986–95. doi: 10.1038/ni.2705
6. Theret M, Mounier R, Rossi F. The origins and non-canonical functions of macrophages in development and regeneration. *Development.* (2019) 146:dev156000. doi: 10.1242/dev.156000
7. Hilt EE, McKinley K, Pearce MM, Rosenfeld AB, Zilliox MJ, Mueller ER, et al. Urine is not sterile: use of enhanced urine culture techniques to detect resident bacterial flora in the adult female bladder. *J Clin Microbiol.* (2014) 52:871–6. doi: 10.1128/JCM.02876-13
8. Flores-Mireles AL, Walker JN, Caparon M, Hultgren SJ. Urinary tract infections: epidemiology, mechanisms of infection and treatment options. *Nat Rev Microbiol.* (2015) 13:269–84. doi: 10.1038/nrmicro3432
9. Abraham SN, Miao Y. The nature of immune responses to urinary tract infections. *Nat Rev Immunol.* (2015) 15:655–63. doi: 10.1038/nri3887
10. Alikhan MA, Ricardo SD. Mononuclear phagocyte system in kidney disease and repair. *Nephrology.* (2013) 18:81–91. doi: 10.1111/nep.12014
11. George JF, Lever JM, Agarwal A. Mononuclear phagocyte subpopulations in the mouse kidney. *Am J Physiol Ren Physiol.* (2017) 312:F640–6. doi: 10.1152/ajprenal.00369.2016
12. Kawakami T, Lichtnekert J, Thompson LJ, Karna P, Bouabe H, Hohl TM, et al. Resident renal mononuclear phagocytes comprise five discrete populations with distinct phenotypes and functions. *J Immunol.* (2013) 191:3358–72. doi: 10.4049/jimmunol.1300342
13. Soos TJ, Sims TN, Barisoni L, Lin K, Littman DR, Dustin ML, et al. CX_3CR1+ interstitial dendritic cells form a contiguous network throughout the entire kidney. *Kidney Int.* (2006) 70:591–6. doi: 10.1038/sj.ki.5001567
14. Ginhoux F, Jung S. Monocytes and macrophages: developmental pathways and tissue homeostasis. *Nat Rev Immunol.* (2014) 14:392–404. doi: 10.1038/nri3671
15. Weisheit CK, Engel DR, Kurts C. Dendritic cells and macrophages: sentinels in the kidney. *Clin J Am Soc Nephrol.* (2015) 10:1841–51. doi: 10.2215/CJN.07100714
16. Månsson LE, Melican K, Boekel J, Sandoval RM, Hautefort I, Tanner GA, et al. Real-time studies of the progression of bacterial infections and immediate tissue responses in live animals. *Cell Microbiol.* (2007) 9:413–24. doi: 10.1111/j.1462-5822.2006.00799.x
17. Melican K, Boekel J, Månsson LE, Sandoval RM, Tanner GA, Källskog Ö, et al. Bacterial infection-mediated mucosal signalling induces local renal ischaemia as a defence against sepsis. *Cell Microbiol.* (2008) 10:1987–98. doi: 10.1111/j.1462-5822.2008.01182.x
18. Terlizzi ME, Gribaudo G, Maffei ME. UroPathogenic *Escherichia coli* (UPEC) infections: virulence factors, bladder responses, antibiotic, and non-antibiotic antimicrobial strategies. *Front Microbiol.* (2017) 8:1566. doi: 10.3389/fmicb.2017.01566
19. Melican K, Sandoval RM, Kader A, Josefsson L, Tanner GA, Molitoris BA, et al. Uropathogenic *Escherichia coli* P and Type 1 fimbriae act in synergy in a living host to facilitate renal colonization leading to nephron obstruction. *PLOS Pathog.* (2011) 7:e1001298. doi: 10.1371/journal.ppat.1001298
20. Jung S, Aliberti J, Graemmel P, Sunshine MJ, Kreutzberg GW, Sher A, et al. Analysis of fractalkine receptor CX_3CR1 function by targeted deletion and green fluorescent protein reporter gene insertion. *Mol Cell Biol.* (2000) 20:4106–14. doi: 10.1128/MCB.20.11.4106-4114.2000
21. Yona S, Kim K-W, Wolf Y, Mildner A, Varol D, Breker M, et al. Fate mapping reveals origins and dynamics of monocytes and tissue macrophages under homeostasis. *Immunity.* (2013) 38:79–91. doi: 10.1016/j.immuni.2012.12.001
22. Madisen L, Zwingman TA, Sunkin SM, Oh SW, Zariwala HA, Gu H, et al. A robust and high-throughput Cre reporting and characterization system for the whole mouse brain. *Nat Neurosci.* (2010) 13:133–40. doi: 10.1038/nn.2467
23. Looney MR, Thornton EE, Sen D, Lamm WJ, Glenny RW, Krummel MF. Stabilized imaging of immune surveillance in the mouse lung. *Nat Methods.* (2011) 8:91–6. doi: 10.1038/nmeth.1543
24. Choong FX, Sandoval RM, Molitoris BA, Richter-Dahlfors A. Chapter three - multiphoton microscopy applied for real-time intravital imaging of bacterial infections *in vivo*. In: Conn PM, editor. *Methods in Enzymology Imaging and Spectroscopic Analysis of Living Cells*. New York, NY: Academic Press (2012). p. 35–61.
25. Nelson PJ, Rees AJ, Griffin MD, Hughes J, Kurts C, Duffield J. The renal mononuclear phagocytic system. *J Am Soc Nephrol.* (2012) 23:194–203. doi: 10.1681/ASN.2011070680
26. Snelgrove SL, Kausman JY, Lo C, Lo C, Ooi JD, Coates PT, et al. Renal dendritic cells adopt a pro-inflammatory phenotype in obstructive uropathy to activate T cells but do not directly contribute to fibrosis. *Am J Pathol.* (2012) 180:91–103. doi: 10.1016/j.ajpath.2011.09.039
27. Kitching AR, Ooi JD. Renal dendritic cells: the long and winding road. *J Am Soc Nephrol.* (2018) 29:4–7. doi: 10.1681/ASN.2017101145
28. Schiwon M, Weisheit C, Franken L, Gutweiler S, Dixit A, Meyer-Schwesinger C, et al. Crosstalk between sentinel and helper macrophages permits neutrophil migration into infected uroepithelium. *Cell.* (2014) 156:456–68. doi: 10.1016/j.cell.2014.01.006
29. Tittel AP, Heuser C, Ohliger C, Knolle PA, Engel DR, Kurts C. Kidney dendritic cells induce innate immunity against bacterial pyelonephritis. *J Am Soc Nephrol.* (2011) 22:1435–41. doi: 10.1681/ASN.2010101072
30. Schulz A, Chuquimia OD, Antypas H, Steiner SE, Sandoval RM, Tanner GA, et al. Protective vascular coagulation in response to bacterial infection of the kidney is regulated by bacterial lipid A and host CD147. *Pathog Dis.* (2018) 76:fty087. doi: 10.1093/femsle/fty087
31. Gautier EL, Shay T, Miller J, Greter M, Jakubzick C, Ivanov S, et al. Gene-expression profiles and transcriptional regulatory pathways that underlie the identity and diversity of mouse tissue macrophages. *Nat Immunol.* (2012) 13:1118–28. doi: 10.1038/ni.2419
32. Day Y-J, Huang L, Ye H, Linden J, Okusa MD. Renal ischemia-reperfusion injury and adenosine 2A receptor-mediated tissue protection: role of macrophages. *Am J Physiol Ren Physiol.* (2005) 288:F722–31. doi: 10.1152/ajprenal.00378.2004
33. Ferenbach DA, Sheldrake TA, Dhaliwal K, Kipari TMJ, Marson LP, Kluth DC, et al. Macrophage/monocyte depletion by clodronate, but not diphtheria toxin, improves renal ischemia/reperfusion injury in mice. *Kidney Int.* (2012) 82:928–33. doi: 10.1038/ki.2012.207
34. Wang J, Kubes P. A reservoir of mature cavity macrophages that can rapidly invade visceral organs to affect tissue repair. *Cell.* (2016) 165:668–78. doi: 10.1016/j.cell.2016.03.009
35. Mujal AM, Krummel MF. Immunity as a continuum of archetypes. *Science.* (2019) 364:28–9. doi: 10.1126/science.aau8694

Conflict of Interest: The authors declare that the research was conducted in the absence of any commercial or financial relationships that could be construed as a potential conflict of interest.

frontiers in Immunology

ORIGINAL RESEARCH
published: 08 January 2020
doi: 10.3389/fimmu.2019.02988

Optimization of *In vivo* Imaging Provides a First Look at Mouse Model of Non-Alcoholic Fatty Liver Disease (NAFLD) Using Intravital Microscopy

Rachelle P. Davis[1,2], *Bas G. J. Surewaard*[1,2,3], *Madison Turk*[1,2], *Agostina Carestia*[1,2], *Woo-Yong Lee*[2,3], *Björn Petri*[1,2], *Stefan J. Urbanski*[4], *Carla S. Coffin*[1,5] *and Craig N. Jenne*[1,2]*

[1] Department of Microbiology, Immunology, and Infectious Diseases, University of Calgary, Calgary, AB, Canada, [2] Snyder Institute for Chronic Diseases, University of Calgary, Calgary, AB, Canada, [3] Department of Physiology and Pharmacology, University of Calgary, Calgary, AB, Canada, [4] Department of Pathology and Laboratory Medicine, University of Calgary, Calgary, AB, Canada, [5] Department of Medicine, Cumming School of Medicine, University of Calgary, Calgary, AB, Canada

OPEN ACCESS

Edited by:
Valentin A. Pavlov, Northwell Health, United States

Reviewed by:
Giovanni Tarantino, University of Naples Federico II, Italy
Dimitrios Davalos, Cleveland Clinic Lerner College of Medicine, Case Western Reserve University, United States

***Correspondence:**
Craig N. Jenne
cnjenne@ucalgary.ca

Specialty section:
This article was submitted to Inflammation, a section of the journal Frontiers in Immunology

Received: *03 July 2019*
Accepted: *05 December 2019*
Published: *08 January 2020*

Citation:
Davis RP, Surewaard BGJ, Turk M, Carestia A, Lee W-Y, Petri B, Urbanski SJ, Coffin CS and Jenne CN (2020) Optimization of In vivo Imaging Provides a First Look at Mouse Model of Non-Alcoholic Fatty Liver Disease (NAFLD) Using Intravital Microscopy. Front. Immunol. 10:2988. doi: 10.3389/fimmu.2019.02988

Non-alcoholic fatty liver disease is a spectrum of liver pathology ranging from simple steatosis to steatohepatitis and can progress to diseases associated with poor outcomes including cirrhosis and hepatocellular carcinoma (HCC). NAFLD research has typically focused on the pathophysiology associated with lipid metabolism, using traditional measures such as histology and serum transaminase assessment; these methods have provided key information regarding NAFLD progression. Although valuable, these techniques are limited in providing further insight into the mechanistic details of inflammation associated with NAFLD. Intravital microscopy (IVM) is an advanced tool that allows for real-time visualization of cellular behavior and interaction in a living animal. Extensive IVM imaging has been conducted in liver, but, in the context of NAFLD, this technique has been regularly avoided due to significant tissue autofluorescence, a phenomenon that is exacerbated with steatosis. Here, we demonstrate that, using multiple imaging platforms and optimization techniques to minimize autofluorescence, IVM in fatty liver is possible. Successful fatty liver intravital imaging provides details on cell trafficking, recruitment, function, and behavior in addition to information about blood flow and vessel dynamics, information which was previously difficult to obtain. As more than 30% of the global population is overweight/obese, there is a significant proportion of the population at risk for NAFLD and complications due to NAFLD (liver decompensation, cirrhosis, HCC). IVM has the potential to elucidate the poorly understood mechanisms surrounding liver inflammation and NAFLD progression and possesses the potential to identify key processes that may be targeted for future therapeutic interventions in NAFLD patients.

Keywords: intravital imaging, fatty liver, NAFLD, mice, technique

INTRODUCTION

Non-alcoholic fatty liver disease (NAFLD) is characterized by a spectrum of pathologies ranging from simple hepatocyte steatosis to non-alcoholic steatohepatitis (NASH) (1). Individuals with NAFLD, and especially those with NASH, are at risk of progression to more significant liver disease such as cirrhosis and hepatocellular carcinoma (2). Typically, NAFLD is associated with a body mass index (BMI) $>$ 35, diabetes, dyslipidemia, and the metabolic syndrome (3). It is estimated that 30% of the North American population is overweight or obese, suggesting a significant proportion of the population is at risk for NAFLD (4). In the United States, NAFLD/NASH has become the leading cause of end-stage liver disease requiring liver transplantation (5). Due to the significant burden of NAFLD/NASH, to both society and to the health care system, there is an urgent need to develop improved pre-clinical animal models for the testing of new therapies as well as improving our understanding of mechanisms of disease pathogenesis. Although the methionine-choline deficient diet (MCD) is a common mouse model of NASH, in many ways it does not accurately recapitulate the chronic microenvironment remodeling that occurs in humans with NAFLD (6). Specifically, MCD models of NAFLD try to replicate disease using a short 2 to 3 week time frame. It is thought this rather "acute" model of liver disease does not accurately recapitulate the chronic tissue remodeling that occurs over a period of decades in humans. Considering this, we have implemented a 20 week high fat diet (HFD) for mice that better models the clinical course of NAFLD development (7).

Although first utilized in the middle of the nineteenth century (8–10), intravital microscopy (IVM) has, over the past two decades, moved to the forefront for tracking cell behavior in real-time, in living animals (11–15). This approach provides remarkable insight into in cell dynamics and *in vivo* disease progression within intact tissues. One of the most studied organs by IVM is the liver. In addition to having a central role in metabolism and protein synthesis, the liver is also an important front-line immune tissue. The liver is crucial for pathogen clearance from the circulation, immunosurveillance, and is a common site for both primary and metastatic cancers (11, 16–19). In fact, more than 800 papers have been published using IVM in the liver (20). Although mouse models of disease have proven extremely useful for studying immune cell interactions in infection and tissue repair (21–23), there remains a distinct gap in the IVM literature with regards to mouse models of NAFLD. The primary reason for this paucity of studies is the notoriously difficult and unique issues involved with imaging a fatty liver. The liver is known to possess a relatively strong profile of autofluorescence, which is greatly exacerbated in conditions of lipid accumulation (24). Due to this significant imaging obstacle, fluorescent IVM of NAFLD in a mouse model has, in the past, been consistently avoided.

Autofluorescence in the liver originates from several sources and can have variable excitation and emission profiles. For example, vitamin A is naturally fluorescent and is found in relatively high concentration in hepatic stellate cells within the liver (25). Similarly, nicotinamide adenine dinucleotide (NADH) fluorescence is common within hepatocytes in the liver (25). Other sources of autofluorescence include metabolites and fatty acids (26). Many of these endogenous emission signals are present in the 400–500 nm range, and thus, the liver exhibits naturally high fluorescence using UV and 488 nm excitation lasers in particular (27). Importantly, this natural autofluorescence is enhanced by the lipid accumulation and metabolic stress that are hallmark in NAFLD. Following significant optimization, and in consideration of the biophotonics of liver imaging, we have developed a successful multicolour IVM approach that enables the study of this tissue in NAFLD mice. This article explains in detail the differences between imaging of fatty liver and healthy controls and delineates the methodological approach to successful image acquisition based on some of the different microscope platforms available.

MATERIALS AND METHODS

Mice and Model of NAFLD

C57Bl/6 mice were purchased from Jackson Laboratories (Bar Harbor, ME). Animals were housed in a pathogen-free environment at the University of Calgary. All experimental protocols were approved by the University of Calgary Animal Care Committee and were in compliance with guidelines from the Canadian Council for Animal Care (AC16-0040; AC18-0050). NAFLD mice were fed a high fat, high sucrose diet obtained from Dyets Inc (Bethlehem, PA) *ad libitum* for 20 weeks beginning at 6 weeks of age. Diet was a custom formula containing 40% fat, 40% sucrose, 20% protein. Control mice were fed standard mouse chow and housed in the same facility to ensure comparable microbiome.

Antibodies and Reagents

Conjugated antibodies used for *in vivo* imaging are as follows: PE-conjugated anti-CD49b (platelets), Alexa Fluor (AF) 647-conjugated anti-F4/80 (Kupffer cells), Brilliant Violet (BV) 421-conjugated anti-Ly6G (neutrophils), and PerCP/Cy5.5-conjugated anti-CD8a. All antibodies were purchased from Biolegend Inc. (San Diego, CA, USA). Antibodies were administered at a dose of 1–3 μg/animal intravenously (i.v.) 10 min prior to imaging. Polystyrene beads (Fluoresbrite YG microspheres 1.0 μm, Polysciences Inc., Washington, PA, USA) were injected intravenously during image acquisition to track blood flow and to measure Kupffer cell function. Rhodamine-conjugated dextran was used as vascular contrast agent for visualization of liver sinusoids; injected intravenously 10 min prior to imaging.

Intravital Microscopy

Surgical preparation of animals for intravital microscopy of the mouse liver was performed as previously described (28). After general anesthesia (10 mg/kg xylazine hydrochloride and 200 mg/kg ketamine hydrochloride), an i.v. catheter was inserted in the tail vein to administer fluorescently labeled antibodies or additional anesthetic directly into the bloodstream. For surgery, a laparotomy was performed, and the abdominal skin and peritoneum were removed to expose the liver. The falciform

ligament was cut after securing the sternum away from the liver using a suture. The mouse was moved to a heated stage, to maintain body temperature throughout image acquisition, and placed on its right side. Using a wet cotton swab, the stomach was manipulated to maneuver the liver into place on a glass coverslip. The gastrointestinal tract was moved away from the liver and secured by wrapping in wet gauze. One layer of wet tissue was placed on the liver to preserve physiological conditions, prevent drying, and diminish movement. Imaging was performed using an inverted Leica SP8 resonance-scanning microscope (Leica Microsystems) with a 25× water-immersion objective lens. For spinning-disk microscopy an inverted microscope (IX81; Olympus) was used, equipped with a focus drive (Olympus), a motorized stage (Applied Scientific Instrumentation), and fitted with a motorized objective turret equipped with 20×/0.70 UPLANSAPO objective lenses coupled to a confocal light path (WaveFx; Quorum Technologies) based on a modified CSU-10 head (Yokogawa Electric Corporation).

IVM Analysis

For vessel diameter, sinusoids were manually measured using the LasX software ruler. Each FOV had 10 sinusoidal measurements to accurately represent the entire FOV. For cell/particle quantification, random fields of view (FOV) were chosen and the number of events were counted for a given frame. For blood flow velocity, sinusoids between 80 and 120 μm of length were identified and the velocity of fluorescent beads passing through these sinusoids was measured. For each bead, a time measurement in seconds to traverse the measured distance was recorded. Distance was divided by time, and the measurements were repeated in a minimum of five sinusoids/FOV.

$$Blood\ Flow\ Velocity\ (\frac{\mu m}{s}) = \frac{distance\ bead\ traveled\ in\ \mu m}{time\ required\ to\ travese\ measure\ distance}$$

To calculate flow rate, sinusoidal measurements of vascular diameter allowed for the calculation of the sinusoidal cross-section area. Blood velocity (from the bead calculations) was applied to determine the overall flow rate in $\mu m^3/s$.

$$Blood\ Flow\ Rate\ \left(\frac{\mu m^3}{s}\right) = \pi * sinusoidal\ radius\ (\mu m)^2 * blood\ flow\ velocity\ (\frac{\mu m}{s})$$

Cell behaviors as visualized by IVM were characterized as either stationary (cells that move <1 cell diameter in 3 min of imaging) or crawling (cells interacting with the endothelium and traversing >1 cell diameter in 3 min).

Histology and Alanine Aminotransferase (ALT) Measurements

Following euthanasia, liver samples were collected and fixed in formalin. Paraffin embedding was performed, and 4.0 μm sections were stained with hematoxylin and eosin (H&E). All mouse slides were assessed by a blinded hepatopathologist to determine the degree of steatosis, the presence of inflammation and hepatocyte ballooning. Blood was collected via cardiac puncture using a 1:10 dilution of 4% sodium citrate (Sigma Aldrich), and then centrifuged at 1,000 × g for 10 min to obtain plasma. Blood plasma samples were sent to Calgary Lab Services (CLS, Calgary, Canada) and ALT measurements were performed to assess degree of liver tissue damage.

Progressive Emission Filter Scan (Lambda Scan)

Marked autofluorescence can be observed in tissues depending on the excitation/emission spectra used. To assemble a complete fluorescence profile of the liver, the Lambda Scan feature of LasX software (Leica microsystems) was utilized. Fixed excitation wavelength lasers were used, one at a time, and emission filters positioned in front of HyD detectors were set to function as 50 nm-wide band pass filters. Scanning was performed using 20 nm step-wise advancements of the emission filter via automated algorithm; settings were as follows: for the 405 nm excitation laser (50% power), emission filters scanned from 425 to 775 nm; for the 488 nm excitation laser (10% power), emission filters scanned from 510 to 760 nm; for the 552 nm excitation laser (10% power), emission filters scanned from 560 to 770 nm; and for the 638 nm excitation laser (5% power), emission filters scanned from 645 to 775 nm. Snapshots for individual excitation wavelengths were captured at each 20 nm interval within the scan range.

Statistical Analysis

With the exception of velocity measurements, a Student's *T*-test was used to determine statistical significance in all instances. For comparison of velocity measurements, a One-way ANOVA with Tukey post-test was used. All reported measurements represent the mean of 5 FOV/animal. $N = 5$ animals/group, $^{*}p < 0.05$, $^{**}p < 0.01$, $^{***}p < 0.001$.

RESULTS

20 Week HFD Generates a Reproducible NAFLD Phenotype With Elevated Autofluorescence

To determine the liver phenotype following HFD for 20 weeks, animal body mass, liver damage, and lipid accumulation was assessed in mice fed HFD and in age-matched controls. Mice on HFD had significantly increased body mass compared to age-matched control animals (**Figure 1A**). Plasma ALT levels indicated significant hepatic damage in HFD mice compared to controls (**Figure 1B**) and histological analysis of the liver revealed marked lipid deposition within hepatocytes of HFD mice, whereas minimal steatosis was observed in controls (**Figure 1C**). Overall, mice fed an HFD show a consistent NAFLD phenotype, involving weight gain, steatosis, and elevated ALT levels validating the selected mouse model of NAFLD. The steatosis observed in mice fed HFD resulted in significant liver autofluorescence in a wide range of wavelengths when imaged by IVM (**Figure 1D**). Even in the absence of added fluorescent labels

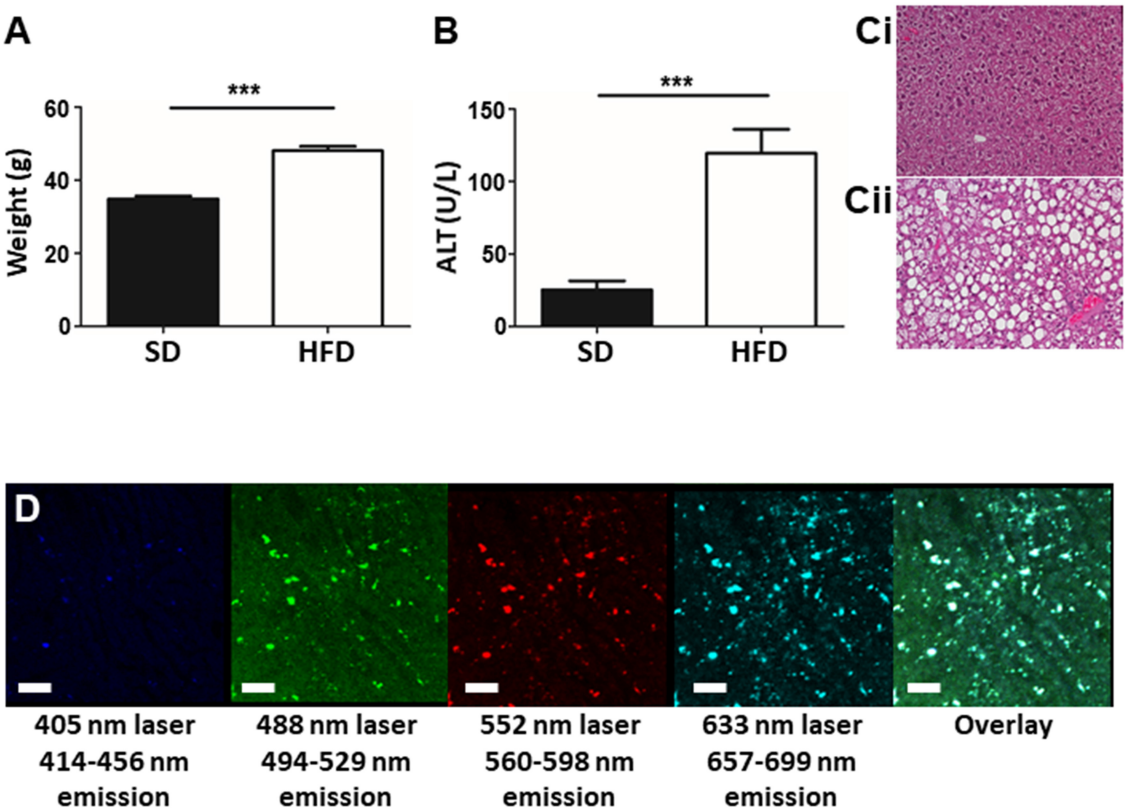

FIGURE 1 | Establishment of a mouse model of NAFLD. Animals were fed either SD or HFD for 20 w and animal weight **(A)** and plasma ALT levels **(B)** were measured. Histology of the mouse liver reveals normal tissue architecture in animals fed SD **(Ci)**, whereas, animals fed HFD **(Cii)** display pronounced steatosis and hepatocyte ballooning. IVM imaging of unstained liver (i.e., no exogenous fluorophores or dyes added) shows an overall autofluorescence dotted by focal intense spots of fluorescence (white spots in the overlay image) (scale bar = 100 μm) **(D)**. ***$p < 0.001$.

or dyes, strong background autofluorescence dotted with foci of high intensity signal are seen throughout the liver, in multiple emission wavelengths.

Lambda Scanning for Autofluorescent Profile Mapping

As illustrated in **Figure 1D**, lipid dense tissues demonstrate significant autofluorescence when visualized by confocal microscopy. To better map the specific wavelengths of light attributed to this autofluorescent signal a spectral scan was performed. A spectral scan involves imaging a given tissue with a fixed excitation wavelength and a narrow, step-wise shifting emission filter. In a scan, a single excitation laser is used, and fluorescence is captured for each of a series of sequential detection filter ranges. For example, fluorescence is captured through a series of sequential, overlapping 50 nm gates (400–450, 420–470, 440–490 nm, etc.) With this approach, we mapped the complete autofluorescent signature of the liver for each excitation laser (**Supplemental Figure 1**).

Mapping the autofluorescence profile in this manner is informative regarding which specific fluorophores should be avoided (emission overlap with regions of high autofluorescence), and which fluorophores may be better options. With respect to the Leica SP8 imaging platform, spectral mapping can be done through an automatic feature, the Lambda Scan, where both the emission detector bandwidth and number of imaging steps can be specified. Lambda scanning was performed on NAFLD mice to map the full autofluorescence profile. Results show substantial autofluorescence between 450 and 520 nm when excited by the 405 nm laser and between 550 and 650 nm when excited by the 488 nm laser. Additionally, discrete, punctate autofluorescence can been seen in most imaging windows. We utilized this spectral scan to choose antibodies: those that have a higher Stokes shift (maximal separation of excitation and emission spectra of a given fluorophore) and are excited outside of the 488/552 nm range to avoid the autofluorescent characteristics of fatty liver.

IVM Image Acquisition: Optimization for NAFLD and Microscope Platform

To minimize the autofluorescence phenomenon, and to ensure it was possible to identify and track multiple cell populations within a fatty liver, we employed several optimization strategies. First, microscope settings were selected to utilize sequential scanning. This approach involves cycling each excitation laser on and off in a sequence, to minimize the collection of non-specific light (background) from sub-optimal excitation (i.e., excite with

single wavelengths sequentially as opposed to multiple excitation wavelengths simultaneously). Often, multiple laser lines are switched on together, allowing for simultaneous excitation and visualization of multiple fluorophores by different optical detectors. Although this approach supports rapid imaging of samples, it can generate unwanted fluorescence through off-peak excitation of fluorescent compounds or molecules. For example, molecules that are normally not excited by a 488 nm laser may be excited by a 405 nm laser and bleed into photodetectors used to image fluorophores excited by the 488 nm laser. In this case, ensuring the 405 nm laser is off when imaging with the 488 nm laser will limit excitation and bleed through of unintended fluorescent signals.

Additionally, the use of a tunable Spectral Detector emission filter located before the optical detectors [photomultiplier tubes (PMTs) or hybrid gapless detectors (HyDs)] allowed us to narrow the wavelength range of the captured emission fluorescence (**Figure 2A**). This process allows us to maximize detection of desired emission spectra while "cropping-out" non-specific autofluorescence spectral overlap signal. Although narrowing the emission filter captures less light, this is outweighed by the advantage of excluding background and spectral overlap from other fluorophores.

To compensate for the loss of collected fluorescent signal resulting from the use of narrow emission filters, other settings required adjustment to compensate. The resonance scanning confocal microscope (RSM) platform used in these experiments was equipped with a mix of PMTs and HyDs for signal detection. Whereas, PMTs are excellent at imaging bright fluorophores or fluorophores with emissions below 400 nm or above 750 nm, they often require high excitation laser power and substantial signal amplification (gain) at the detector (**Supplemental Table 1**). In contrast, HyD-based detectors are significantly more sensitive, allowing for detection of dimmer signals with less electronic amplification (thus less signal noise), ideal for imaging through narrow wavelength emission filters. Additionally, using an RSM allowed for the adjustments to be made to the optical pinhole diameter, increasing photon capture. Normally, a smaller pinhole allows for the capture of less out-of-focus light rendering a higher resolution image; however, opening the pinhole slightly maximizes light capture with minimal sacrifice of image resolution. Pinhole adjustments are possible and straightforward on most scanning confocal imaging platforms. In contrast, although possible, adjusting the pinhole diameter on most spinning-disk microscope platforms is not simple and often requires additional hardware installation (29). Optimal imaging of the autofluorescent liver requires balance of all these settings; therefore, careful consideration of fluorophore combinations is needed in order to acquire the best image possible with minimal background.

The livers of mice fed a SD can be effectually and clearly imaged utilizing conventional settings (**Supplemental Table 2**) on an RSM (**Figure 2Bi**); however, imaging of cellular targets labeled with fluorophore-conjugated antibodies is nearly impossible in the liver of mice fed an HFD (**Figure 2Bii**). Although application of sequential imaging, narrow emission filters, and optimized pinhole can enhance imaging of livers in SD mice (**Figure 2Biii**), this approach is more critical in HFD mice where specific fluorophore signals that could not previously be separated from autofluorescence are now imaged as discrete, discernable markers (**Figure 2Biv**). This approach not only allowed for clear visualization of specific labels, but also highlighted anatomical changes in the liver with lipid deposits now easily identifiable as dark circular structures located between the liver sinusoids (outlined in white, **Figure 2Bv**).

Following optimization of fatty liver imaging on an RSM platform, we next compared image quality to that obtained on a spinning-disk microscope (fixed pinhole diameter, non-tunable emission detectors, camera-based images as compared to PMT/HyD-based imaging on RSM). It should be noted that although our spinning-disk microscope utilizes multiple excitation laser wavelengths, these laser lines are not identical to the RSM platform (491, 561, and 642 nm for SDM vs. 405, 488, 552, and 638 nm for RSM). This makes use of the identical labeling antibodies difficult, and thus comparison of specific markers is not optimal; however, general comparison of background fluorescence and the separation of signal from noise/background is possible. Imaging healthy livers (SD) using a spinning-disk microscope yields clear images, capable of discerning multiple fluorescent markers and tracking several cell types in real-time (**Figure 2Ci**). This imaging is very comparable to what is captured in SD mice using the optimized RSM protocol (**Figure 2Bii**). Importantly, when imaging the liver of mice fed a HFD, spinning-disk microscopy demonstrates limitations (**Figure 2Cii**). Due to the fixed (glass) band-pass filters located in front of the image capture CCD camera, it is difficult to optimize imaging windows to enhance signal collection while limiting non-specific spectral bleed-through. In much the same fashion as the non-optimized RSM (**Figure 2Bii**), spinning-disk microscopy of liver in HFD animals captures numerous patches of generalized autofluorescence and a punctate pattern of high intensity signal in multiple channels (appearing as white spots). In contrast, optimized RSM of HFD livers reduces the diffuse autofluorescence and eliminates the high intensity autofluorescent areas (**Figure 2Biv**), allowing for tracking of several cell types within this diseased liver.

IVM to Visualize Liver Physiology and Cell Tracking

The greatest advantage of IVM over other techniques (histology, FACS, etc.) is the ability to assess intact tissues under physiological conditions. Intravenous delivery of fluorophore-conjugated albumin rapidly highlights the vasculature, permitting the identification, and tracing of the living network of liver sinusoids and venules. The use of this vascular contrast agent in mice fed SD illustrates a dense honeycomb of liver sinusoids that converge on larger draining venules (**Figure 3Ai**). This vasculature is interwoven with clear columns of hepatocytes separating the sinusoids (**Figure 3Aiii**). In contrast, the liver vasculature of mice fed a HFD (**Figures 3Aii,iv**) demonstrates a restricted and convoluted network that bends and wraps around the hepatocyte lipid deposits (dark circular voids in **Figure 3Aiv**) associated with

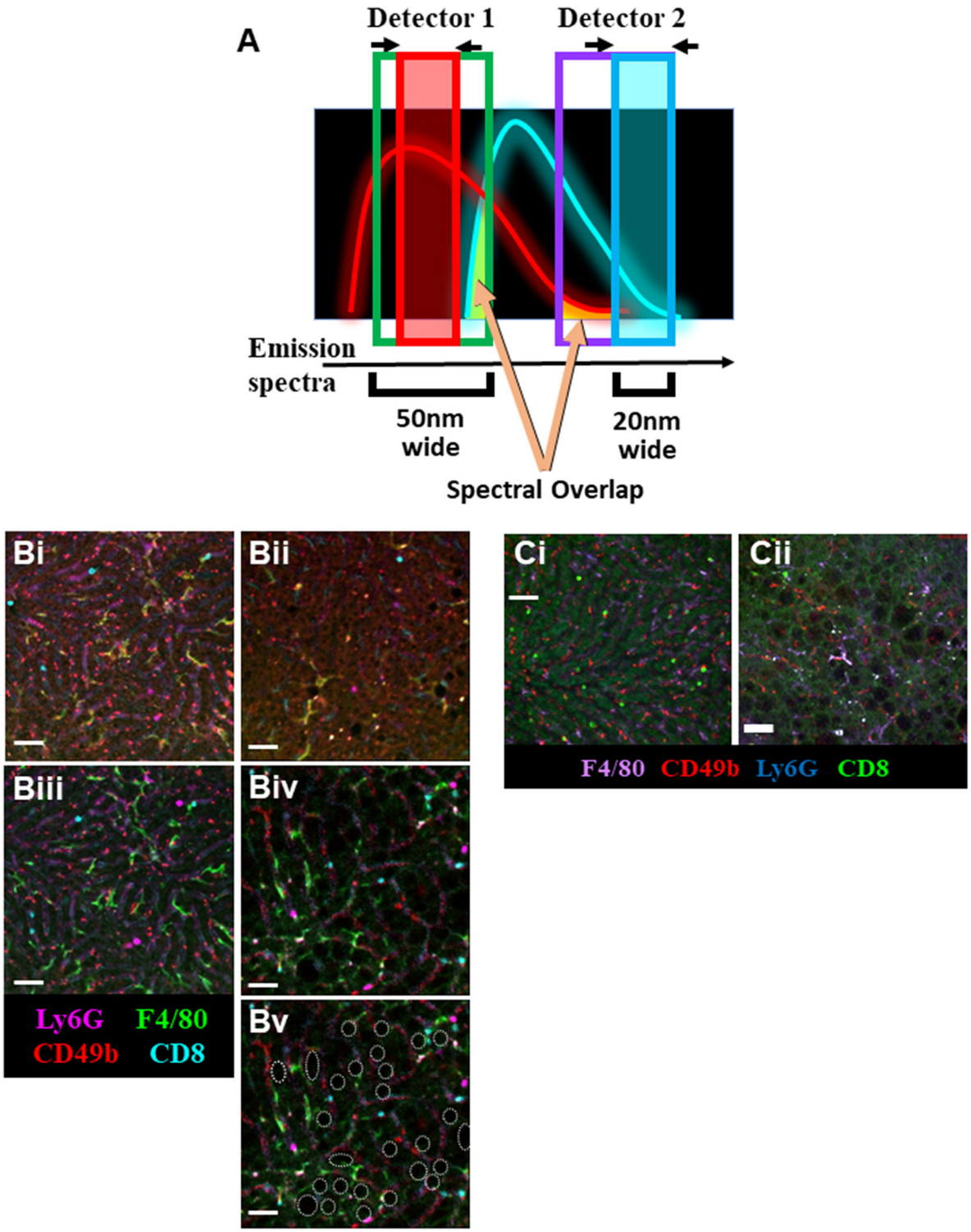

FIGURE 2 | Optimization of IVM of murine NAFLD. **(A)** Schematic representation of the imaging strategy utilizing narrower emission filters (red and blue boxes) that have been shifted away from peak fluorophore emission to limit the collection of non-specific spectral overlap (yellow shading). IVM of liver using resonant scanning confocal microscopy with conventional filter settings in animals fed SD **(Bi)** or HFD **(Bii)**. RSC imaging of livers from mice fed SD **(Biii)** or HFD **(Biv)** using optimized (narrowed filters, off-peak fluorescence collection, sequential excitation) imaging parameters yields substantially less background autofluorescence and allows for clear visualization of multiple labeled immune cell populations. Cell populations were labeled with i.v. fluorophore-conjugated antibodies 10 min prior to imaging (scale bar = 50 μm). Additionally, lipid deposits are visible in the liver of mice fed HFD (**Bv**, white outlines; same FOV as **Biv**). IVM of liver using spinning disk microscopy in animals fed SD **(Ci)** or HFD **(Cii)**. Animals were i.v. injected with fluorophore-conjugated antibodies 10 min prior to imaging (scale bar = 50 μm).

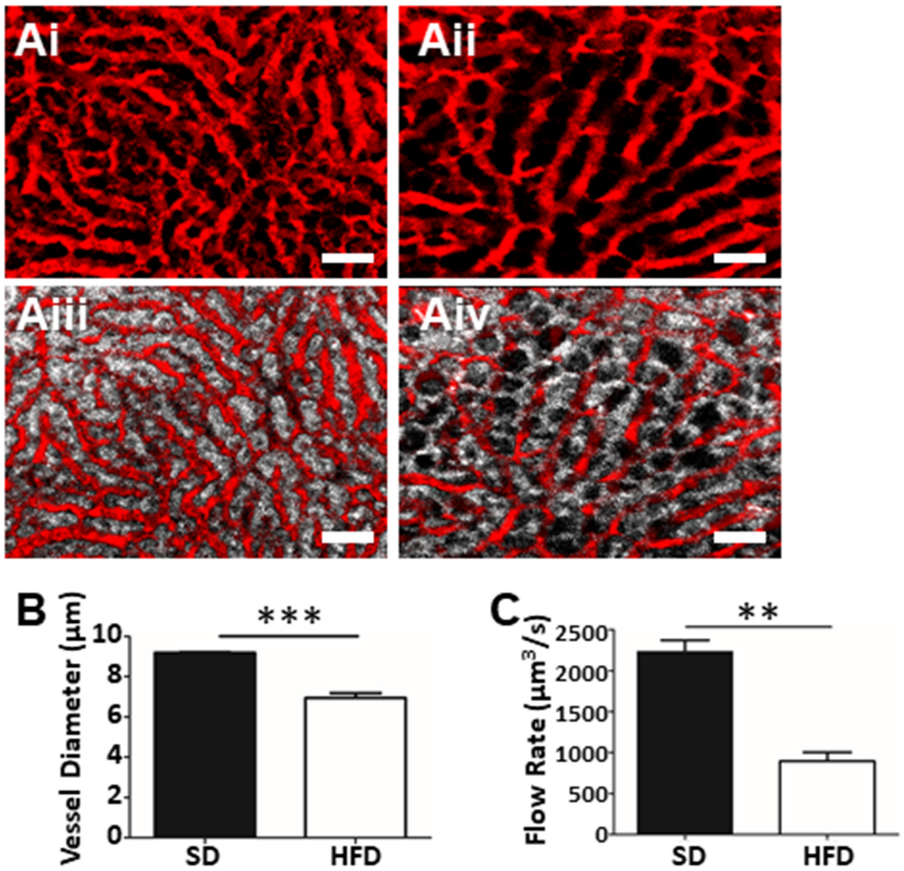

FIGURE 3 | Assessment of fatty liver physiology using IVM. Mapping of liver vasculature in mice fed SD **(Ai)** or HFD **(Aii)** using an i.v. injection of FITC-conjugated albumin (red). Overlay of hepatocyte fluorescence with vascular contrast agent (SD, **Aiii**; HFD, **Aiv**) (scale bar = 50 μm). **(B)** Mean liver sinusoidal diameter as measured by IVM (values represent vascular diameter in μm, mean of >10 sinusoids/FOV; 5 FOV/animal, $n = 3$ animals per group). Mean sinusoidal blood flow rate as determined by IVM **(C)**. Rate was calculated by measuring the sinusoidal cross-sectional area and blood velocity (as determined by velocity of i.v. injected fluorescent beads) and values are reported as $\mu m^3/s$. ***$p < 0.001$; **$p < 0.01$.

the steatosis seen in NAFLD. Direct measurement of the images allowed us to determine vascular diameter (**Figure 3B**). Assessment of multiple vessels per field of view (FOV), and multiple FOVs per animal provided an overall picture of vascular physiology and demonstrates statistically narrower liver sinusoids in the HFD mice. Furthermore, by introducing fluorescently-conjugated antibodies to label platelets, or i.v. injection of fluorescent polystyrene beads (1 μm in diameter), we were able to determine the blood flow velocity within the liver sinusoids. Combining this velocity, with vascular diameters allows for the calculation the overall hepatic blood flow (**Figure 3C**). Not surprisingly, given the restriction in vascular diameter, animals fed HFD demonstrated significantly reduced blood flow through the hepatic sinusoids when compared to blood flow in the livers of healthy mice.

IVM is not restricted to assessing vascular function and blood flow dynamics in the liver. Intravenous introduction of fluorophore-conjugated antibodies against specific cell surface markers, or the use of mice expressing fluorescent reporter proteins, allows specific cell populations to be labeled and tracked in real-time. Through the addition of anti-Ly6G (labels neutrophils), anti-F4/80 (labels macrophage), anti-CD8 (labels cytotoxic T cells), and anti-CD49b (labels platelets and NK cells) we were able to visualize and track multiple cell populations in simultaneously in the living animal (**Figure 4A**) (14, 17, 21, 23). With this approach we directly enumerated the number of cells visible per FOV (**Figures 4B,C**) and characterized cellular behavior (**Figures 4D,E**). For example, tracking of neutrophils within the liver vasculature revealed significantly more stationary cells than crawling cells in the fatty liver (**Figure 4D**). This observation is consistent with what has been observed in livers of healthy mice where few actively crawling cells are seen (13, 30).

Moreover, as these images and associated videos are collected in real time, we are able measure the velocity of the crawling cells and the velocity of circulating fluorescent beads (**Figure 4E**). In this instance, we have determined that neutrophils move significantly faster than CD8+ T cells but are significantly slower than objects (beads) observed freely circulating in the bloodstream. One of the primary immune functions of the liver is to filter circulating pathogens from the blood; a process that

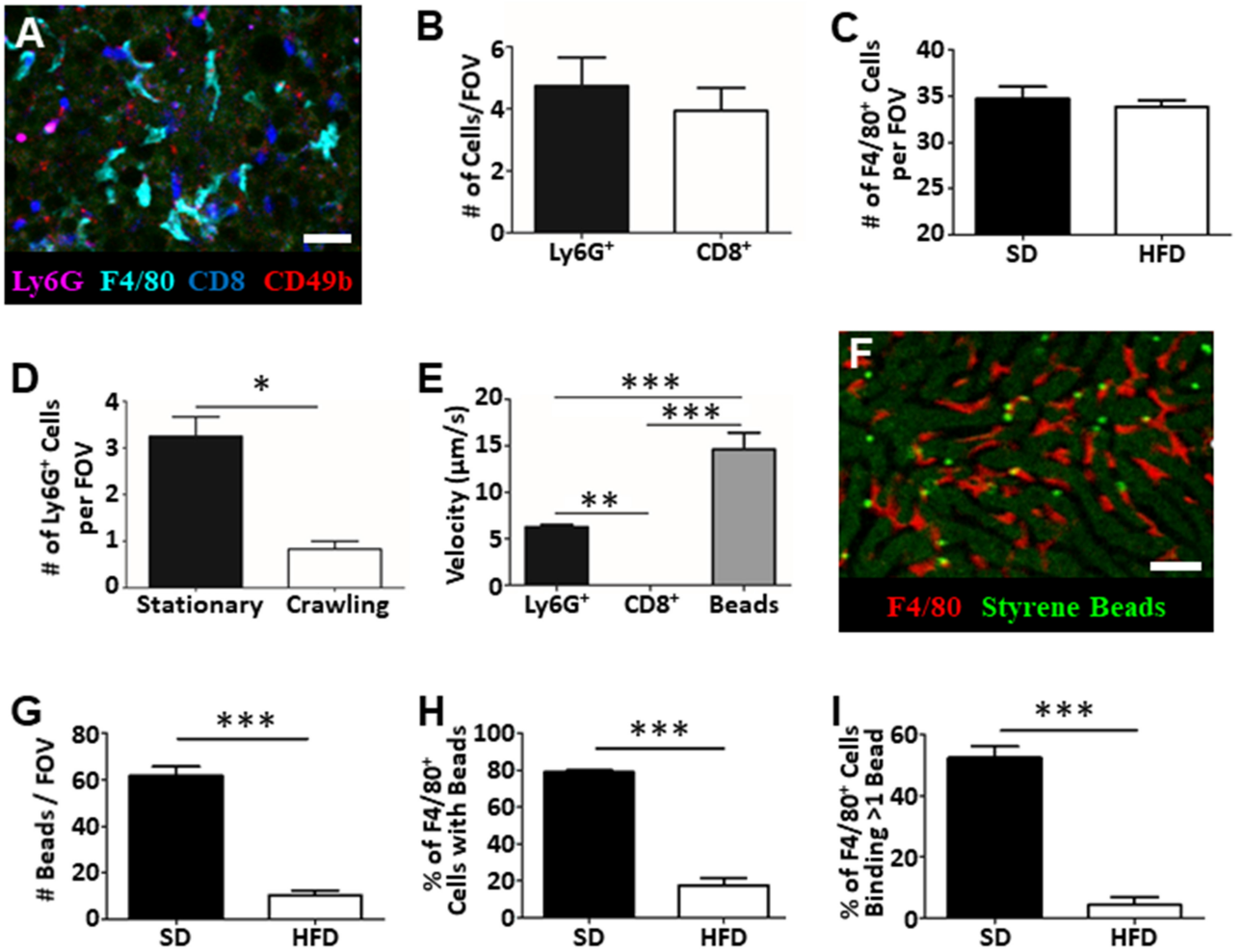

FIGURE 4 | Tracking of immune cell behavior and function in fatty liver by IVM. Fluorescent antibody labeling of multiple immune cell populations enables tracking of cell behavior and function by IVM **(A)**. Cells were labeled by i.v. injection fluorophore-conjugated antibodies 10 min prior to imaging. Scale bar = 50 μm. **(B)** Quantification of the number of neutrophils (Ly6G+) and cytotoxic T cells (CD8+) by IVM in the livers of mice fed HFD (values represent the number of cells/FOV; minimum of 5 FOV/animal; $n = 3$ animals). **(C)** Quantification of the number of macrophage (F4/80+) by IVM in the livers of mice fed SD or HFD (values represent the number of cells/FOV; minimum of 5 FOV/animal; $n = 3$ animals per group). **(D)** IVM assessment of neutrophil behavior in the livers of mice HFD; 5 FOV/animal; $n = 3$ animals. **(E)** Determination of neutrophil (Ly6G+), cytotoxic T cell (CD8+) or intravascular bead velocity in the livers of mice fed HFD (values represent mean object velocity in μm/s from 5 FOV/animal; $n = 3$ animals). **(F)** Representative image obtained by IVM of sterile bead capture (bright green) by liver macrophage (F4/80+; red). Scale bar = 50 μm. **(G)** Quantification of bead capture in the liver (values represent the number of beads/FOV; minimum of 5 FOV/animal; $n = 3$ animals). **(H)** Determination of the fraction of macrophage that have captured a minimum of 1 bead (values represent the % of macrophages binding beads/FOV; minimum of 5 FOV/animal; $n = 3$ animals). **(I)** Determination of fraction of macrophage that have bound multiple beads (values represent the % of macrophages binding multiple beads/FOV; minimum of 5 FOV/animal; $n = 3$ animals). $^{***}p < 0.001$; $^{**}p < 0.01$; $^{*}p < 0.05$.

is largely mediated by the liver-resident macrophage population, the Kupffer cells (KC) (31, 32). Through the introduction of small (1 μm), sterile, fluorescent polystyrene beads into the circulation, we were able to visualize KC binding and capture of the circulating microspheres (**Figure 4F**). Comparison of target capture in healthy mice and mice fed an HFD demonstrated a reduced capacity for pathogen clearance in the fatty liver (**Figure 4G**) as reflected by a significant reduction in bead capture. Importantly, because we were able to directly visualize these immune responses, we determined that the observed deficiency in bead capture stems from both a reduced number of KCs "catching" beads (**Figure 4H**) and, a reduced capacity, on a per cell basis, to capture multiple targets (**Figure 4I**). These basic analyses demonstrate the power of IVM to assess liver physiology and immune function within a living, intact tissue and offer the ability to shed light on key processes (immune cell recruitment, cell behavior, cell-cell interactions, vascular tone, and blood flow) associated with disease progression and liver dysfunction within the context of fatty liver disease.

DISCUSSION

In the current study, we demonstrate how IVM can be used to study liver physiology and immune cell behavior in a murine

model of NAFLD in animals receiving long-term HFD. To our knowledge, this technique for imaging NAFLD has not been reported to date. Optimization of multi-color imaging provides a new approach to study NAFLD in a living animal in real-time. Although many different murine models of NAFLD exist, each with their own advantages/disadvantages, the model chosen for this study involves a 20 week HFD. This model not only recapitulates the key clinical features of NAFLD (based on histology and serology), but also allows adequate time for critical immune and tissue reprogramming (macrophage phenotypes, T cell subsets) and remodeling (vascular structure, fibrosis). This reprogramming is critically important when one considers the diverse population of liver resident immune cell populations and phenotypes (Kupffer cells, *i*NKT cells, NK cells, etc.). We believe this chronic model is a more accurate depiction of human disease progression, a condition that takes decades to develop in patients, affording time for immune cell populations to reprogram to respond to increased hepatocyte stress and tissue remodeling.

For more than two decades, IVM has been used to study liver biology and immune responses. Utilizing technologies ranging from white light microscopy to epifluorescence, confocal microscopy (spinning disk, laser scanning, resonant scanning) and multiphoton microscopy, we have gained much knowledge of liver physiology, inflammation, tissue repair, and host-pathogen interactions (23, 33–38). Although these approaches have generated a wealth of information by mapping cell behaviors, cell-cell interactions and generating detailed 3D renderings of liver anatomy, most studies have only looked at healthy livers or at tissues following acute challenge (infection, sterile injury). Liver conditions such as NAFLD, where there is substantial accumulation of lipid within the liver and critical changes in mitochondrial physiology (39, 40), often alter the fluorescent properties of the liver tissue itself. Although this has little impact on techniques such as white light microscopy, the impact on fluorescent imaging is far more significant. As we have demonstrated, NAFLD results in increased autofluorescence within the diseased liver, which makes the tracking of fluorescently labeled targets quite difficult with standard imaging approaches. Through the use of advanced microscope technologies, technologies that in recent years have become accessible and available to many research institutions, and careful optimization of intravital imaging parameters, it is now possible to track multiple populations of individual immune cells within a mouse model of NAFLD. It should be noted that imaging strategies described herein have been optimized on a Leica SP8 microscope. Although overall optimization approaches are applicable across multiple platforms, specific settings (laser power, detector sensitivity/exposure time, pinholes, etc.) will likely have to be empirically determined on each individual imaging platform for best performance.

This new imaging capability opens important doors in the area of NAFLD research, allowing us to address a myriad of different questions that are simply not possible with other techniques; How does a fatty liver respond to pathogen challenge? How do resident immune cells respond to potential pharmacological therapeutics in a fatty liver? How do leukocyte populations interact with each other and with the liver parenchyma? By visualizing tissue physiology, blood flow, pathogen interactions, and cell behaviors within intact living tissues, in real-time, these questions can now be answered. For example, multiple studies have noted an increase in macrophage or decrease in CD4+ T cell populations in the liver during the development of NAFLD but these studies have not completely determined how these cell populations interact within the liver microenvironment nor have they fully mapped how these populations contribute to disease progression (41–43). Given the central role the immune system plays in the progression of liver disease, results in this context will be critical to advance understanding of disease pathogenesis as well as therapeutic interventions for patients with NAFLD.

Due to the elevated autofluorescence found in a fatty liver, accurate real-time imaging has been difficult to achieve (24). RSM provides an attractive platform due its wide range of possible image acquisition settings, highlighting the effectiveness of this technology as a suitable platform for IVM imaging in NAFLD. Further, features such as the Lambda Scan can provide additional detail on spectral regions of fluorescence that can be avoided prior to the development of labeling panels and further image optimization. In fact, this approach of spectral Lambda Scanning and emission filter shifting/optimization could be applied to various types of tissue known to exhibit significant autofluorescence to gain the same insight, and image quality (**Supplemental Figure 2**). The experimental approaches and data presented in this study provides detailed step-by-step information to optimize IVM imaging in any tissue with marked background fluorescence and provides important considerations to be included in model development by microscopists in both beginner and advanced stages of training. Importantly, IVM is not limited to RSM or spinning-disk microscopy. Additional imaging platforms including widefield fluorescence and two-photon microscopy each have their own advantages and disadvantages with respect to IVM of the liver. For example, two-photon imaging does not require a pinhole, typically results in reduced photodamage, generates less out-of-focus fluorescence and often has higher sensitivity for some fluorophores (20). We did not explore the feasibility of this platform in the imaging of fatty liver in the current work. A recent study has suggested application of this platform for imaging fixed murine fatty liver tissue samples is possible (44); however, an extensive workup of autofluorescence profiles, optimization for imaging multiple cell populations, and application to live animals remains to be completed.

Although this study has demonstrated the power of IVM, there are limitations that should be acknowledged. First, IVM can be restricted in the number of cell types that can be labeled at one time. Typically, the number of colors used is anywhere from one to five, but some studies have visualized up to eight markers in a single liver. This limitation in the number of markers that can be imaged means that observations are often simplified and cannot distinguish specific cell subsets in the same way flow cytometry can. Additionally, many markers used for flow cytometry simply are not bright enough *in vivo* or are based on intracellular targets requiring cell permeabilization prior to labeling making these markers not suitable for IVM. Furthermore, this study did not include the use of multiphoton

imaging, a technique that has become increasingly common due to its longer wavelengths allowing for greater tissue penetration and often less autofluorescence.

The obesity epidemic is staggeringly prominent in North America, and NAFLD is quickly becoming the number one indication for liver transplant (45, 46). Considering this, it becomes imperative to delineate the mechanisms associated with the inflammatory progression of NAFLD and provide new techniques to intimately examine the liver microenvironment in the context of NAFLD. We believe the data presented here provides critical new avenues for NAFLD research and represents an exciting new platform for exploration and discovery, especially in the context of immunity. Further experiments using IVM in a mouse model of NAFLD can expose crucial differences in leukocyte trafficking and behavior that may be altered in a NAFLD setting and can provide greater detail into immune mediated fibrosis and functional immune differences that may exist within NAFLD.

DATA AVAILABILITY STATEMENT

The datasets generated for this study are available on request to the corresponding author.

ETHICS STATEMENT

The animal study was reviewed and approved by University of Calgary Animal Care Committee in compliance with guidelines from the Canadian Council for Animal Care.

AUTHOR CONTRIBUTIONS

RD and CJ designed the experiments and wrote the manuscript. CC contributed to experimental design and revised the manuscript. BS, AC, W-YL, and BP contributed to imaging and microscope optimization. MT contributed to imaging and manuscript revision. SU characterized liver pathology and verified the mouse model of NALFD.

FUNDING

This work was supported with grants from the Canadian Foundation for Innovation (CFI), the Natural Sciences and Engineering Research Council of Canada (NSERC), and the Canadian Institutes of Health Research (CIHR). RD was supported by a studentship from the Canadian Liver Foundation (CLF) and the University of Calgary Faculty of Graduate Studies Indigenous Graduate Award. BS was supported by Canadian Institutes for Health Research (CIHR). MT was supported by a University of Calgary Eyes High Doctoral Scholarship and a Natural Sciences and Engineering Research Council of Canada (NSERC) Alexander Graham Bell Canada Graduate Scholarship. AC was funded by the Beverley Phillips Rising Star Post-doctoral Fellowship and the University of Calgary and the Cumming School of Medicine Post-doctoral Scholar Program. BP was supported by the Snyder Mouse Phenomics Resources Laboratory funded by the Snyder Institute for Chronic Diseases at the University of Calgary. CJ was supported by the Canada Research Chair Program (CRC).

ACKNOWLEDGMENTS

The authors thank Dr. Mark Swain for his assistance with model design and assessment.

SUPPLEMENTARY MATERIAL

The Supplementary Material for this article can be found online at: https://www.frontiersin.org/articles/10.3389/fimmu.2019.02988/full#supplementary-material

REFERENCES

1. Lau JKC, Zhang X, Yu J. Animal models of non-alcoholic fatty liver disease: current perspectives and recent advances. *J Pathol.* (2017) 241:36–44. doi: 10.1002/path.4829
2. Dowman JK, Tomlinson JW, Newsome PN. Pathogenesis of non-alcoholic fatty liver disease. *QJM.* (2010) 103:71–83. doi: 10.1093/qjmed/hcp158
3. Buzzetti E, Pinzani M, Tsochatzis EA. The multiple-hit pathogenesis of non-alcoholic fatty liver disease (NAFLD). *Metabolism.* (2016) 65:1038–48. doi: 10.1016/j.metabol.2015.12.012
4. Shields M, Carroll MD, Ogden CL. Adult obesity prevalence in Canada and the United States. *NCHS Data Brief.* (2011) 56:1–8.
5. Benedict M, Zhang X. Non-alcoholic fatty liver disease: an expanded review. *World J Hepatol.* (2017) 9:715–32. doi: 10.4254/wjh.v9.i16.715
6. Van Herck MA, Vonghia L, Francque SM. Animal models of nonalcoholic fatty liver disease—a starter's guide. *Nutrients.* (2017) 9:1–13. doi: 10.3390/nu9101072
7. Stephenson K, Kennedy L, Hargrove L, Demieville J, Thomson J, Alpini G, et al. Updates on dietary models of nonalcoholic fatty liver disease: current studies and insights. *Gene Expr.* (2018) 18:5–17. doi: 10.3727/105221617X15093707969658
8. Julius cohnheim (1839-1884) experimental pathologist. *JAMA.* (1968) 206:1561–1562. doi: 10.1001/jama.206.7.1561
9. Hall M. *A Critical and Experimental Essay on the Circulation of the Blood.* London: R. B. Seeley and W. Burnside (1831).
10. Waller A. LVIII. Microscopic observation on the perforation of the capillaries by the corpuscles of the blood, and on the origin of mucus and pus-globules. *London Edinburgh Dublin Philos Mag J Sci.* (1846) 29:397–405. doi: 10.1080/14786444608645527
11. Guidotti LG, Inverso D, Sironi L, Di Lucia P, Fioravanti J, Ganzer L, et al. Immunosurveillance of the liver by intravascular effector CD8+ T cells. *Cell.* (2015) 161:486–500. doi: 10.1016/j.cell.2015.03.005
12. Geissmann F, Cameron TO, Sidobre S, Manlongat N, Kronenberg M, Briskin MJ, et al. Intravascular immune surveillance by CXCR6+ NKT cells patrolling liver sinusoids. *PLoS Biol.* (2005) 3:e113. doi: 10.1371/journal.pbio.0030113
13. McDonald B, Kubes P. Innate immune cell trafficking and function during sterile inflammation of the liver. *Gastroenterology.* (2016) 151:1087–95. doi: 10.1053/j.gastro.2016.09.048
14. McDonald B, Davis RP, Kim SJ, Tse M, Esmon CT, Kolaczkowska E, et al. Platelets and neutrophil extracellular traps collaborate to promote intravascular coagulation during sepsis in mice. *Blood.* (2017) 129:1357–67. doi: 10.1182/blood-2016-09-741298

15. Kolaczkowska E, Jenne CN, Surewaard BGJ, Thanabalasuriar A, Lee W-Y, Sanz M-J, et al. Molecular mechanisms of NET formation and degradation revealed by intravital imaging in the liver vasculature. *Nat Commun.* (2015) 6:6673. doi: 10.1038/ncomms7673
16. Surewaard BGJ, Thanabalasuriar A, Zheng Z, Tkaczyk C, Cohen TS, Bardoel BW, et al. α-toxin induces platelet aggregation and liver injury during *Staphylococcus aureus* sepsis. *Cell Host Microbe.* (2018) 24:271–284.e3. doi: 10.1016/j.chom.2018.06.017
17. Huang L-R, Wohlleber D, Reisinger F, Jenne CN, Cheng R-L, Abdullah Z, et al. Intrahepatic myeloid-cell aggregates enable local proliferation of CD8+ T cells and successful immunotherapy against chronic viral liver infection. *Nat Immunol.* (2013) 14:574–83. doi: 10.1038/ni.2573
18. Ghouri YA, Mian I, Rowe JH. Review of hepatocellular carcinoma: epidemiology, etiology, and carcinogenesis. *J Carcinog.* (2017) 16:1–8. doi: 10.4103/jcar.JCar_9_16
19. McDonald B, Spicer J, Giannais B, Fallavollita L, Brodt P, Ferri LE. Systemic inflammation increases cancer cell adhesion to hepatic sinusoids by neutrophil mediated mechanisms. *Int J Cancer.* (2009) 125:1298–305. doi: 10.1002/ijc.24409
20. Marques PE, Oliveira AG, Chang L, Paula-Neto HA, Menezes GB. Understanding liver immunology using intravital microscopy. *J Hepatol.* (2015) 63:733–42. doi: 10.1016/j.jhep.2015.05.027
21. Jenne CN, Wong CHY, Zemp FJ, McDonald B, Rahman MM, Forsyth PA, et al. Neutrophils recruited to sites of infection protect from virus challenge by releasing neutrophil extracellular traps. *Cell Host Microbe.* (2013) 13:169–80. doi: 10.1016/j.chom.2013.01.005
22. Wang J, Kubes P. A reservoir of mature cavity macrophages that can rapidly invade visceral organs to affect tissue repair. *Cell.* (2016) 165:668–78. doi: 10.1016/j.cell.2016.03.009
23. Dal-Secco D, Wang J, Zeng Z, Kolaczkowska E, Wong CHY, Petri B, et al. A dynamic spectrum of monocytes arising from the *in situ* reprogramming of CCR2 + monocytes at a site of sterile injury. *J Exp Med.* (2015) 212:447–56. doi: 10.1084/jem.20141539
24. Diao S, Hong G, Antaris AL, Blackburn JL, Cheng K, Cheng Z, et al. Biological imaging without autofluorescence in the second near-infrared region. *Nano Res.* (2015) 8:3027–34. doi: 10.1007/s12274-015-0808-9
25. Burkhardt M, Vollmar B, Menger MD. *In vivo* analysis of hepatic NADH fluorescence. Methodological approach to exclude Ito-cell vitamin A-derived autofluorescence. *AdvExpMedBiol.* (1998) 454:83–9. doi: 10.1007/978-1-4615-4863-8_10
26. Croce AC, Ferrigno A, Di Pasqua LG, Berardo C, Mannucci B, Bottiroli G, et al. Fluorescing fatty acids in rat fatty liver models. *J Biophotonics.* (2017) 10:905–10. doi: 10.1002/jbio.201600195
27. Croce AC, Ferrigno A, Vairetti M, Bertone R. Autofluorescence properties of isolated rat hepatocytes under different metabolic conditions. *Photochem Photobiol Sci.* (2004) 3:920–6. doi: 10.1039/b407358d
28. Heymann F, Niemietz PM, Peusquens J, Ergen C, Kohlhepp M, Mossanen JC, et al. Long term intravital multiphoton microscopy imaging of immune cells in healthy and diseased liver using CXCR6.Gfp reporter mice. *J Vis Exp.* (2015) 2015:10–5. doi: 10.3791/52607
29. Jonkman J, Brown CM. Any way you slice it—a comparison of confocal microscopy techniques. *J Biomol Tech.* (2015) 26:54–65. doi: 10.7171/jbt.15-2602-003
30. Menezes GB, Lee W-Y, Zhou H, Waterhouse CCM, Cara DC, Kubes P. Selective down-regulation of neutrophil Mac-1 in endotoxemic hepatic microcirculation via IL-10. *J Immunol.* (2009) 183:7557–68. doi: 10.4049/jimmunol.0901786
31. Zeng Z, Surewaard BGJ, Wong CHY, Geoghegan JA, Jenne CN, Kubes P. CRIg functions as a macrophage pattern recognition receptor to directly bind and capture blood-borne gram-positive bacteria. *Cell Host Microbe.* (2016) 20:99–106. doi: 10.1016/j.chom.2016.06.002
32. Helmy KY, Katschke KJ, Gorgani NN, Kljavin NM, Elliott JM, Diehl L, et al. CRIg: a macrophage complement receptor required for phagocytosis of circulating pathogens. *Cell.* (2006) 124:915–27. doi: 10.1016/j.cell.2005.12.039
33. Kubes P, Payne D, Woodman RC. Molecular mechanisms of leukocyte recruitment in postischemic liver microcirculation. *Am J Physiol Gastrointest Liver Physiol.* (2002) 283:G139–47. doi: 10.1152/ajpgi.00058.2002
34. Bonder CS, Norman MU, Swain MG, Zbytnuik LD, Yamanouchi J, Santamaria P, et al. Rules of recruitment for Th1 and Th2 lymphocytes in inflamed liver: a role for alpha-4 integrin and vascular adhesion protein-1. *Immunity.* (2005) 23:153–63. doi: 10.1016/j.immuni.2005.06.007
35. Piergiovanni M, Bianchi E, Capitani G, Li Piani I, Ganzer L, Guidotti LG, et al. Microcirculation in the murine liver: a computational fluid dynamic model based on 3D reconstruction from *in vivo* microscopy. *J Biomech.* (2017) 63:125–34. doi: 10.1016/j.jbiomech.2017.08.011
36. Frevert U, Engelmann S, Zougbédé S, Stange J, Ng B, Matuschewski K, et al. Intravital observation of plasmodium berghei sporozoite infection of the liver. *PLoS Biol.* (2005) 3:1034–46. doi: 10.1371/journal.pbio.0030192
37. Sturm A, Amino R, Van De Sand C, Regen T, Retzlaff S, Rennenberg A, et al. Manipulation of host hepatocytes by the malaria parasite for delivery into liver sinusoids. *Science.* (2006) 313:1287–90. doi: 10.1126/science.1129720
38. McAvoy EF, McDonald B, Parsons SA, Wong CH, Landmann R, Kubes P. The role of CD14 in neutrophil recruitment within the liver microcirculation during endotoxemia. *J Immunol.* (2011) 186:2592–601. doi: 10.4049/jimmunol.1002248
39. Auger C, Alhasawi A, Contavadoo M, Appanna VD. Dysfunctional mitochondrial bioenergetics and the pathogenesis of hepatic disorders. *Front Cell Dev Biol.* (2015) 3:40. doi: 10.3389/fcell.2015.00040
40. Grattagliano I, Montezinho LP, Oliveira PJ, Frühbeck G, Gómez-Ambrosi J, Montecucco F, et al. Targeting mitochondria to oppose the progression of nonalcoholic fatty liver disease. *Biochem Pharmacol.* (2019) 160:34–45. doi: 10.1016/j.bcp.2018.11.020
41. Tacke F. Targeting hepatic macrophages to treat liver diseases. *J Hepatol.* (2017) 66:1300–12. doi: 10.1016/j.jhep.2017.02.026
42. CD4+ T Cell loss drives NAFLD progression to hepatocellular carcinoma. *Cancer Discov.* (2016) 6:OF8. doi: 10.1158/2159-8290.CD-RW2016-046
43. Paquissi FC. Immune imbalances in non-alcoholic fatty liver disease: From general biomarkers and neutrophils to interleukin-17 axis activation and new therapeutic targets. *Front Immunol.* (2016) 7:1–13. doi: 10.3389/fimmu.2016.00490
44. Shao T, Liu T, Liu H, Zhang M, Shen Y, Gao A, et al. Identification of fatty liver disease at diverse stages using two-photon absorption of triphenylamine-based BODIPY analogues. *J Mater Chem B.* (2019) 7:3704–9. doi: 10.1039/C9TB00421A
45. Jayakumar S. Liver transplantation for non-alcoholic fatty liver disease—a review. *AME Med J.* (2018) 3:29. doi: 10.21037/amj.2018.01.16
46. Ofosu A, Ramai D, Reddy M. Non-alcoholic fatty liver disease: controlling an emerging epidemic, challenges, and future directions. *Ann Gastroenterol.* (2018) 31:288–95. doi: 10.20524/aog.2018.0240

Conflict of Interest: The authors declare that the research was conducted in the absence of any commercial or financial relationships that could be construed as a potential conflict of interest.

frontiers in Immunology

ORIGINAL RESEARCH
published: 15 January 2020
doi: 10.3389/fimmu.2019.03021

Reduced Neutrophil Extracellular Trap (NET) Formation During Systemic Inflammation in Mice With Menkes Disease and Wilson Disease: Copper Requirement for NET Release

*Iwona Cichon[1], Weronika Ortmann[1], Aleksandra Bednarz[2], Malgorzata Lenartowicz[2] and Elzbieta Kolaczkowska[1]**

[1] Department of Experimental Hematology, Institute of Zoology and Biomedical Research, Jagiellonian University, Kraków, Poland, [2] Department of Genetics and Evolutionism, Institute of Zoology and Biomedical Research, Jagiellonian University, Kraków, Poland

OPEN ACCESS

Edited by:
Robson Coutinho-Silva, Federal University of Rio de Janeiro, Brazil

Reviewed by:
Cassiano Felippe Gonçalves-De-Albuquerque, Universidade Federal Do Estado Do Rio De Janeiro, Brazil
Markus Sperandio, Ludwig Maximilian University of Munich, Germany

***Correspondence:**
Elzbieta Kolaczkowska
ela.kolaczkowska@uj.edu.pl

Specialty section:
This article was submitted to Inflammation, a section of the journal Frontiers in Immunology

Received: 01 August 2019
Accepted: 10 December 2019
Published: 15 January 2020

Citation:
Cichon I, Ortmann W, Bednarz A, Lenartowicz M and Kolaczkowska E (2020) Reduced Neutrophil Extracellular Trap (NET) Formation During Systemic Inflammation in Mice With Menkes Disease and Wilson Disease: Copper Requirement for NET Release. Front. Immunol. 10:3021. doi: 10.3389/fimmu.2019.03021

Neutrophil extracellular traps (NETs) contribute to pathological disorders, and their release was directly linked to numerous diseases. With intravital microscopy (IVM), we showed previously that NETs also contribute to the pathology of systemic inflammation and are strongly deposited in liver sinusoids. Over a decade since NET discovery, still not much is known about the metabolic or microenvironmental aspects of their formation. Copper is a vital trace element essential for many biological processes, albeit its excess is potentially cytotoxic; thus, copper levels are tightly controlled by factors such as copper transporting ATPases, ATP7A, and ATP7B. By employing IVM, we studied the impact of copper on NET formation during endotoxemia in liver vasculature on two mice models of copper excess or deficiency, Wilson (ATP7B mutants) and Menkes (ATP7A mutants) diseases, respectively. Here, we show that respective ATP7 mutations lead to diminished NET release during systemic inflammation despite unaltered intrinsic capacity of neutrophils to cast NETs as tested *ex vivo*. In Menkes disease mice, the *in vivo* effect is mostly due to diminished neutrophil infiltration of the liver as unmutated mice with a subchronic copper deficiency release even more NETs than their controls during endotoxemia, whereas in Wilson disease mice, excess copper directly diminishes the capacity to release NETs, and this was further confirmed by *ex vivo* studies on isolated neutrophils co-cultured with exogenous copper and a copper-chelating agent. Taken together, the study extends our understanding on how microenvironmental factors affect NET release by showing that copper is not a prerequisite for NET release but its excess affects the trap casting by neutrophils.

Keywords: endotoxemia, sepsis, neutrophils, neutrophil extracellular traps, trace elements, copper, Menkes disease, Wilson disease

INTRODUCTION

The capacity to cast neutrophil extracellular traps (NETs) by neutrophils was described 15 years ago, yet not all aspects or mechanisms of their release were revealed thus far (1). NETs are still being studied mostly using isolated neutrophils, but it seems critical to follow their release *in vivo* where NET formation might be affected by additional factors such as the presence of other cell populations (specific to the organ as well as other leukocytes) and microenvironment conditions such as local plasma content. In particular, the immunometabolic requirements for NET release are still ambiguous, including requirement for some macro- and micronutrients. Thus, far, only zinc dependency of NETs was reported (2), whereas impact of iron was inconclusive as various chelating agents were either stimulating or inhibiting NET formation (3, 4). NETs are structures released by highly activated neutrophils whose backbone consists of DNA decorated with nuclear histones and granular proteins such as antimicrobials (e.g., defensins) and proteases (e.g., neutrophil elastase, NE), but also cytoplasmic and cytoskeletal proteins (1, 5). While originally NETs were believed to be beneficial for the host defense via their capacity to capture and immobilize pathogens (1, 6), it was subsequently recognized that they can also cause bystander damage or contribute to disease outbreak or relapses (7–9). This "Dr. Jekyll and Mr. Hyde phenotype" can be attributed to early and late stages of inflammation, respectively. One of conditions in which release of NETs goes from beneficial [early blood bacterial trapping (10)] to detrimental [delayed organ damage (7)] is sepsis and endotoxemia (6). As systemic inflammation is associated with high mortality, independently of the causative pathogen or just the presence of lipopolysaccharide (LPS)/endotoxin (11), this calls for new therapeutic strategies but first requires gaining detailed knowledge on the mechanisms of NET release. Recent studies have shown liver dysfunction as an early event in systemic inflammation (12), and intravital microscopy revealed that during sepsis or endotoxemia, NETs are released robustly into liver sinusoids of mice (6, 7, 10). Beyond systemic inflammation, there are multiple conditions in which liver is strongly affected, and some of them are connected with excess/deficiency of microelements (13–16).

Metal ions play an essential role in many biological processes acting as chemical catalyzers, structure stabilizers, gene regulators, and signaling molecules (17). This also includes immune processes as metal ions are essential for both leukocytes and pathogens (18) and transition metals/trace elements important in immunity include Fe, Zn, Mn, and Cu (18, 19). Interestingly, when PMA (a phorbol ester) was used to induce NETs, neutrophils contained void vacuoles with visibly reduced concentrations of Ca, Fe, Zn, and Cu but NETs themselves did not contain Cu although they did Ca, Fe, P, and S (20).

At the cellular level, copper serves as a cofactor in multiple proteins due to its redox ability (19, 21, 22). Its uptake (both dietary and peripheral distribution) occurs via membrane copper transporters, including CTR1 (23). Copper is important for the immune system function as macrophage and lymphocyte activities are diminished when it is deficient (24). As to neutrophils, their maturation is altered in copper-deficient individuals. In humans, neutropenia accompanying copper deficiency results from arrest of maturation of neutrophils (promyelocytes/metamyelocytes ratio is altered) (25) but most probably also from their impaired release from the bone marrow and decreased life span of circulating ones (26). Furthermore, anti-neutrophil antibodies were detected in the serum of copper-deficient patients, suggesting a possible reason for (partial) depletion of neutrophils (27). On the other hand, the excess of copper is highly toxic because this element is a potent inducer of reactive free radicals that can cause oxidative damage to proteins, lipids, and nucleic acids (21). Therefore, numerous mechanisms were developed to control copper levels, and they include P-type ATPases (ATP7A and ATP7B), which are involved in copper efflux and intracellular sequestration (21, 28). Mutations in *Atp7a* gene result in depletion of copper in the liver due to impaired intestinal copper intake while *Atp7b* mutations lead to systemic accumulation of copper due to impaired excretion by the liver (14, 16, 28–30). Therefore, we undertook the current study to verify the impact of copper excess and deficiency on NET release into liver sinusoids during systemic inflammatory reaction. The facts that directly prompted us to the investigation were the following: (i) neutrophil status is affected by the lack of copper (26), (ii) copper is released during NET formation (20), (iii) excess of copper affects the liver (31), (iv) NETs are strongly deposited in the liver during systemic inflammation (7, 10), and (v) deficiency of other trace elements was shown to affect NET release (2, 3). Since we aimed to primarily study NETs *in situ* in the liver vasculature, where they are formed during systemic inflammation, we used two mouse models of human genetic disorders in which copper homeostasis is disrupted, Menkes disease and Wilson disease. In addition, liver is one of the organs that is mostly affected by genetic copper excess (Wilson disease) (14) or marginal copper deficiency (leading to non-alcoholic fatty liver disease, NAFLD) (32).

Wilson disease patients present with progressive liver damage as well as neurological disorders and psychiatric symptoms (31). In toxic milk mice (tx-J) that serve as the disease model, the gene encoding ATP7B is affected. This protein serves as a copper-transporting molecule that, at high intracellular copper concentrations, effluxes its excess. Thus, if ATP7B is malfunctioning, this process is impaired as well as subsequent copper excretion into the bile, which results in copper accumulation in the liver, brain, and, to a lower extent, in other tissues (29, 30). By 6 months of age, copper concentration can be over 50-fold more than that of a normal adult animal (33).

On the other hand, mutations in the human *ATP7A* gene lead to a neurological disorder called Menkes disease, which usually results in mortality at 3–5 years of age in its classical form (16). The mouse ATP7A protein is encoded by the X-linked *Atp7a* gene, and among its several reported mutations in mice, one ($Atp7a^{mo\text{-}ms}$) results in the *mottled* phenotype resembling Menkes disease and affects mosaic mutant males (15, 34). In these mice, similarly to patients with Menkes disease, copper accumulates in the small intestine (trapped in enterocytes) and kidneys, while liver, brain, and heart display its deficiency (34). Additionally, as in the classical form of Menkes disease, the mosaic mutation of *Atp7a* leads to early death on about day 16.

The phenotype can be partially reversed by regular s.c. copper (II) chloride injections since the second day of life till day 45 (34, 35). Mice still display symptoms of Menkes disease, and their copper levels are decreased.

With the application of intravital microscopy, herein we reveal that NET formation in the vasculature of endotoxemic liver is impaired in mice with genetic mutations leading to either deficiency or excess of copper. The two mutations affect *Atp7a* and *Atp7b*, respectively, and we demonstrate that the products of both genes are expressed by some neutrophils. Polymorphonuclear leukocytes of animals with Wilson disease (Atp7btx-J/J) casted less NETs despite more profound infiltration of the liver. *Ex vivo* studies confirmed that copper concentration beyond its serum levels inhibits NET formation and in higher concentration kills the cells. On the other hand, in Menkes disease mice ($Atp7a^{mo\text{-}ms}$), weaker NET formation correlated with lower neutrophil numbers. However, in mice with subchronic copper deficiency (inbred mice treated for 8 days with a copper chelator), despite decreased neutrophil counts, NET formation was even increased. This indicates that copper might not be required for NET casting or even interfere with it whereas in *Atp7a* mutants, additional traits are present and we discuss them. Taken together, we demonstrate that while copper does not seem to be a prerequisite for NET formation, its high levels affect this process and directly kill neutrophils.

MATERIALS AND METHODS

Mice

All animals were maintained in the Animal Unit of the Institute of Zoology and Biomedical Research, Jagiellonian University. Mice were housed under standardized conditions of temperature (21–22°C) and illumination (12 h light/12 h darkness) with free access to tap water and pelleted food (Labofeed H diet, Kcynia, Poland). As a reference inbred strain, age-matched C57Bl/6J male mice were used. They were purchased from Charles River (Germany) via AnimaLab (Poland). All experimental animal protocols were approved by the Local Ethical Committee No. II in Kraków (293/2017 and 293A/2018) and were in compliance with the EU Animal Care Guidelines. Main murine strains used in experiments were *Atp7a* mosaic mutant mice and *Atp7b* toxic milk mice and their respective littermates.

Atp7a Mosaic Mutant Mice (The Menkes Disease Model)

Mice were bred in the Department of Genetics and Evolutionism, Jagiellonian University, and derived from a closed outbred colony. In the present study we used mosaic mutant males, which exhibit lethal phenotype about day 16 after birth and age-matched wild type males. Mosaic missense mutation ($^{ms}/^{-}$) consists of G to C nucleotide change in the exon 15 of *Atp7a* gene resulting in an arginine to proline substitution in the 6th highly conserved transmembrane domain of ATP7A protein (15). Mosaic mutant males ($^{ms}/^{-}$) were obtained by mating heterozygous ($^{ms}/^{+}$) females with normal ($^{+}/^{-}$) males. To rescue the otherwise lethal phenotype, mice were receiving subcutaneous injections of 50 µl of 0.01% $CuCl_2$ solution (5 µg Cu/g body weight) every 2 days from day 2 to day 45 after birth. Very few pups survive. In the present study, we used 3-month-old males that could still survive without further copper supplementation and reach maturity (36).

Atp7b Toxic Milk Mice (The Wilson Disease Model)

The mutant C3HeB/FeJ Atp7btx-J/J and control C3HeB/FeJ mice were purchased from The Jackson Laboratory (Bar Harbor, ME, USA) and bred in the Department of Genetics and Evolutionism, Jagiellonian University. The tx-J mutants have a genetic defect that originated due to a G to A base substitution at the position 2,135 in the exon 8 of the *Atp7b* gene; this caused a Gly712Asp missense mutation in the second putative membrane-spanning domain of the ATP7B protein (37). Homozygous mutants (tx-J/tx-J) were obtained by mating heterozygous (tx-J/+) females with heterozygous (tx-J/+) males, and tail biopsy was obtained from each mouse to check for *Atp7b* mutation. Experiments were performed on 7/8-month-old male mice. The age was adjusted in such a way that a 6-month point of very high copper concentration was reached (33).

Antibodies and Dyes for IVM

For intravital microscopy, the following antibodies were used, Alexa Fluor 647 anti-neutrophil elastase (clone G-2, Santa Cruz Biotechnology), Brilliant Violet 421 anti-Ly6G (1A8, BioLegend), PE anti-F4/80 (clone BM8, eBioscience), or Alexa Fluor 488 anti-F4/80 (clone BM8, Invitrogen), and PE anti-CD49b (clone HMα2, BioLegend). Sytox green (the DNA dye) was purchased from Invitrogen. All antibodies were injected i.v. via the jugular vein ∼20 min prior to intravital imaging. Sytox green was administrated during imaging as it stains DNA instantly.

Induction of Systemic Inflammation/Endotoxemia

Mice (C3HeB/FeJ Atp7btx-J/J, C3HeB/FeJ, $Atp7^{amo\text{-}ms}$, outbreds, C57Bl/6J) were i.p. injected with 1 mg/kg b.w. LPS (*Escherichia coli* serotype 0111:B4; Sigma-Aldrich), and they were subjected to intravital imaging 24 h post LPS injection. Some animals were left untreated. In some experiments, prior to endotoxemia induction, C57Bl/6J were injected i.p. with 5 mg/kg b.w of copper chelator tetrathiomolybdate (TTM, Sigma-Aldrich) every 24 h for 8 days.

Preparation of the Mouse Liver for Intravital Microscopy

Mice were anesthetized with a mixture of ketamine hydrochloride (200 mg/kg b.w.; Biowet Pulawy) and xylazine hydrochloride (10 mg/kg b.w.; aniMedica). After anesthesia, cannulation of the right jugular vein was performed for the supply of the anesthetics and for injection of antibodies or other reagents. Preparation of the liver for intravital imaging was performed as previously described by Kolaczkowska et al. (7). Briefly, a midline incision followed by a lateral incision along the costal margin to the midaxillary line was performed to expose the liver. The mouse was placed in a right lateral position, and ligaments attaching the liver to the diaphragm and the stomach were cut, thus allowing the liver to be externalized

onto an imaging board covered with a saline-soaked kimwipe tissue. Then, a coverglass was placed on the left liver lobe and the space underneath the coverglass was filled with saline (it was constantly refilled to keep the tissue moist). The animal positioned on the imaging board was subsequently placed under the upright microscope.

Spinning Disk Confocal Intravital Microscopy

The mouse liver was visualized with a ZEISS Axio Examiner.Z1 upright microscope equipped with a metal halide light source (AMH-200-F6S; Andor, Oxford Instruments) with motorized 6 position excitation filter wheel and laser-free confocal spinning disk device (DSD2; Andor, Oxford Instruments) with ZEISS EC Plan-NEOFLUAR 10×/0.3 and/or ZEISS EC Plan-NEOFLUAR 20×/0.5 air objective. Four excitation filters were used (DAPI: 390/40 nm; GFP: 482/18 nm; RFP: 561/14 nm; Cy5: 640/14 nm) and visualized with the appropriate emission filters (DAPI: 452/45 nm, exposure time 500 ms; GFP: 525/45 nm, exposure time 500 ms; RFP: 609/54 nm, exposure time 500 ms; Cy5: 676/29 nm, exposure time 250 ms). The 5.5 megapixel sCMOS camera (Zyla 5.5; Andor, Oxford Instruments) was used for fluorescence detection. An iQ 3.6.1 acquisition software (Andor, Oxford Instruments) was used to drive the microscope.

NET Formation Analyses

Fluorescence imaging of NET components was performed with intravital immunofluorescence analysis. NETs were visualized by co-staining of neutrophil elastase (anti-NE antibodies; 1.6 μg) and extracellular DNA (Sytox green; 0,1 mM in saline). NETs were quantified with SD-IVM using previously published methodology (7, 38). In brief, images were acquired as *z* stacks of *xy* planes (1 mm intervals) from the bottom to the top of sinusoids in each field of view using a 20× objective lens, and saved as extended focus images in tiff format. Images from individual color channels were exported and analyzed in ImageJ software (NIH). The intensity of elastase staining was analyzed so that differences in background fluorescence between experiments and antibody lots could be accounted for and background autofluorescence could be eliminated, contrast was adjusted to minimize autofluorescent background staining, and a minimum brightness threshold was set to yield only positive staining. The same contrast and threshold values were applied to all images from all mice strains and groups within the experiment. Thresholded images were converted to binary (black and white), and the area per field of view (FOV) covered by positive fluorescence staining (black) was calculated with ImageJ software. Data are expressed as the percentage of area in each FOV covered by positive fluorescence staining. In *ex vivo* studies on isolated neutrophils, the cells were incubated on coverglasses, and then subsequently immunocytostained for the presence of NETs (as described below). NETs stained on coverglasses were visualized using the same microscope. Briefly, in ImageJ, images were converted to a grayscale (8-bit type) and thresholded to black and white to estimate the positive signal of extDNA/NET (black).

Neutrophil, Kupffer Cell, and Platelet Counts

Neutrophils were visualized with anti-mouse Ly6G antibodies (0.4 μg/mouse), Kupffer cells (KCs) were stained with anti-F4/80 antibodies (0.4 μg for PE or 3 μg for Alexa Fluor 488/mouse), and platelets were stained with anti-CD49b antibodies (0.6 μg/mouse). Neutrophils and KCs were counted per 20× FOV, minimum 4 FOV from each mouse. The area covered by platelets was estimated as described previously (7, 38) and above for NETs, on images acquired as *z* stacks of *xy* planes (1 mm intervals) from the bottom to the top of sinusoids and is expressed as the percentage of area in each FOV covered by positive fluorescence staining.

3D Reconstruction of Liver Cross-Sections

Overview of mouse livers was established on a side view of a 3D reconstruction (IMARIS software, Bitplane, Oxford Instruments) of a series of optical cross-sections (*z* stacks). In brief, a series of *z* stacks through the liver was performed with a z-step of 1 μm approximately through 50 *z* planes. Then, liver structure was reconstructed with IMARIS software with DAPI, RFP, and Cy5 channels, for neutrophils, KCs, and neutrophil elastase, respectively. Additionally, on some acquired *z* stacks, red signal (KC staining) was made semi-transparent to expose the blue signal (neutrophil staining) present inside.

Isolation of Mouse Neutrophils From the Bone Marrow

Bone marrow neutrophils were isolated as described previously (39). Briefly, mice were euthanized and the femurs and tibias were removed. The ends of the bones were resected and the bone marrow was removed by flushing with 10 ml of ice-cold HBSS(−) (w/o Ca^{2+} and Mg^{2+}; Lonza Bioscience). The bone marrow was then suspended by drawing it through a 20-gauge needle. Marrow cells were then pelleted in a centrifuge (1,300 rpm, 4°C, 6 min) and after that resuspended in 5 ml of 0.2% NaCl for about 30 s for hypotonic lysis of the red blood cells followed by the addition of 5 ml of 1.6% NaCl. After immediate centrifugation (1,400 rpm, 4°C, 7 min), the cell suspension was placed over a discontinuous Percoll gradient (GE Healthcare) consisting of 78, 69, and 52% layers diluted in HBSS(−). The cell suspension was spun at 2,600 rpm, 4°C, for 30 min. Neutrophils localized to a band between the 78 and 69% layers were collected with a transfer pipette and washed in HBSS(−) (1,500 rpm, 4°C, 6 min), and the cell pellet was suspended in HBSS(+) (HBSS with Ca^{2+} and Mg^{2+}) (Lonza Bioscience).

Ex vivo Neutrophil Viability, Counts, and Adhesion

The purity of isolated neutrophils was over 99%, and neutrophil viability was over 98% in each experiment. To estimate viability, cells were stained with Trypan blue dye (Sigma-Aldrich) and counted in the Bürker hemocytometer. The numbers and purity were assessed by Türk solution (0.01% crystal violet in 3% acetic acid) staining. The viability was double-checked with PrestoBlue® (Invitrogen) assay, which yielded the same results.

The ability of the cells to adhere to cell culture plate after LPS (75 μg/ml) stimulation was tested using the crystal violet test (CV). After incubation, supernatants with non-adherent cells were removed, whereas adhering cells were fixed with absolute methanol (RT, 10 min). After fixation, methanol was removed and crystal violet solution (25 mg in 5 ml 20% methanol; Avantor) was added to each well (RT, 5 min). Following incubation, the plate was gently washed in running tap water and air-dried. To recover crystal violet, 100 μl of 100% methanol was added to each well and the plate was agitated for 10 min. The optical density (O.D.) was measured in a spectrofluorometer (Infinite 200 Pro, Tecan, Austria, Gmbh) at 570 nm.

Ex vivo Evaluation of Reactive Oxygen Species/Respiratory Burst

Content of reactive oxygen species (ROS) in LPS-stimulated neutrophils was measured by two methods, NBT test, and fluorescent DCF-DA assay. In the latter test, the cell-permeable fluorogenic probe 2′,7′-Dichlorofluorescin Diacetate (DCF-DA; Sigma-Aldrich) was added to each well at a final concentration of 25 μM, 30 min after neutrophil stimulation with LPS (75 μg/ml). For the positive control, 1 mM H_2O_2 was used. After 30 min of incubation (37°C, 5% CO_2) the plate was centrifuged (3,000 rpm, 5 min, RT) and cell pellets were rinsed in 100 μl of PBS. Then, the fluorescence intensity was measured in a spectrofluorometer (Infinite 200 Pro, Tecan, Austria, Gmbh) at 485(20)/535(25) nm. The respiratory burst was measured with nitroblue tetrazolium assay (NBT). Briefly, neutrophils were stimulated with LPS (75 μg/ml) and 1 h before the end of the incubation period, NBT solution (10 mg/ml in dH_2O; Sigma Aldrich, St. Louis, MO) was added to each well and incubated for 1 h (37°C, 5% CO_2). Following the incubation, supernatants were removed and the cells were fixed with absolute methanol for 15 min. They were subsequently washed twice with 70% methanol, air-dried, and solubilized (in 120 μl of 2 M potassium hydroxide and 140 μl of dimethyl sulfoxide) to release formazan deposits. The O.D. was measured in a spectrofluorometer (Infinite 200 Pro, Tecan, Austria, Gmbh) at 595 nm.

Ex vivo Studies on NET Release by Neutrophils

Neutrophils suspended in HBSS(+) were seeded in wells of either 96- or 24-well plates (Nest; Thermo Scientific, respectively). They were let to adhere for 30 min and then were stimulated for 6 h with LPS (75 μg/ml), various concentrations of copper (II) chloride (Cu 0.25, 0.5, 1, 2, 3, 130, and 200 μg per ml; Sigma-Aldrich), copper chelator tetrathiomolybdate (TTM 10 μM), or a mixture of Cu and TTM. In some experiments, phorbol 12-myristate 13-acetate (PMA, 50 nM/3 h; Sigma-Aldrich) was used as a positive control for NET formation. After incubation, cell viability was verified with PrestoBlue®. Alternatively, immediately after incubation, the cells were carefully fixed in sequence of 1, 2, and 3% paraformaldehyde in PBS for 2, 10, and 20 min, respectively, to not disrupt formed NETs and washed in PBS. Neutrophils seeded in 24-well plates were used for immunocytochemistry.

Immunocytochemical Staining of NETs, CTR1, and ATP7A/B in Neutrophils

After incubation with stimulants, neutrophils were immediately fixed in paraformaldehyde as described above. Extracellular staining [for citrullinated histones H3 (citH3) and extracellular DNA (extDNA)]: prior to staining, coverglasses were washed two times for 5 min in PBS, and then incubated in blocking solution (3% BSA in PBS) (BSA, bovine serum albumin, Sigma-Aldrich) for 45 min at RT. Subsequently, coverglasses were soaked with rabbit polyclonal anti-histone H3 (citrulline R2 + R8 + R17) antibodies diluted 1:200 in 1% BSA/PBS (Abcam) and incubated overnight at 4°C in a humid chamber. The slides were then washed in PBS and incubated with Cy3-conjugated goat anti-rabbit IgG (H+L) antibody (diluted 1:300 in PBS/1% BSA, Jackson Immunoresearch) for 1 h at RT. At the end of the procedure, Sytox green was added to stain for extDNA (5 μM). After washing in PBS the coverglasses were mounted with VECTASHIELD Mounting Medium (Vector Laboratories). Intracellular staining (CTR1, ATP7A, ATP7B): prior to staining, cells seeded on coverglasses were permeabilized by bathing in TBS (Triton X-100, $Na_2HPO_4 \times 12H_2O$, $Na_2HPO_4 \times 1H_2O$, BSA, NaCl, dH_2O) for 5 min. Non-specific antibody binding was blocked by incubation with 3% BSA/PBS for 45 min. Subsequently, the cells were labeled with rabbit polyclonal antibodies anti-ATP7A (diluted 1:100; Abcam) or anti-ATP7B (diluted 1:100; GeneWay) or rabbit polyclonal anti-SLC31A/CTR1 (diluted 1:250; Novus Biologicals) and incubated overnight at 4°C in a humid chamber. The slides were then washed in PBS and incubated with the secondary antibody goat anti-rabbit IgG–H&L (Cy3) (diluted 1:100) for 1 h at RT. After the coverglasses were washed in PBS, they were mounted with VECTASHIELD Mounting Medium. Fluorescent signal was detected with a ZEISS Axio Examiner.Z1 upright microscope equipped with confocal spinning disk device DSD2.

Measurement of Copper Content in Livers and Plasma

The level of copper in livers obtained from mutants and the wild-genotype control male mice was measured by atomic absorption spectrophotometry (AAS). The liver samples were weighed and digested in 2 ml of boiling Suprapur-grade nitric acid (Sigma-Aldrich). After being cooled down to RT, each sample was suspended in 10 ml of deionized water. Reference material samples were prepared in a similar manner. The copper concentration was measured using the graphite furnace AAS technique (AAnalyst 800, Perkin-Elmer). Moreover, three samples of nitric acid were used as blanks. In addition, three samples of a standard reference material, Cu = 189 ± 4 mg/kg, were analyzed for normalization of the obtained data.

Biochemical Assessment of Liver Injury

Blood was collected by cardiac puncture into a heparinized syringe. Samples were centrifuged at 1,200 *g* for 10 min for the retrieval of plasma.

Subsequently, mice were euthanized and their livers were collected and homogenized. Samples were analyzed for ALT activity as per the manufacturer's protocol (Sigma-Aldrich).

Statistics

All data are presented as mean values ± SD. Data were compared either by unpaired two-tailed Student's *t* test or one-way analysis of variance with Bonferroni multiple

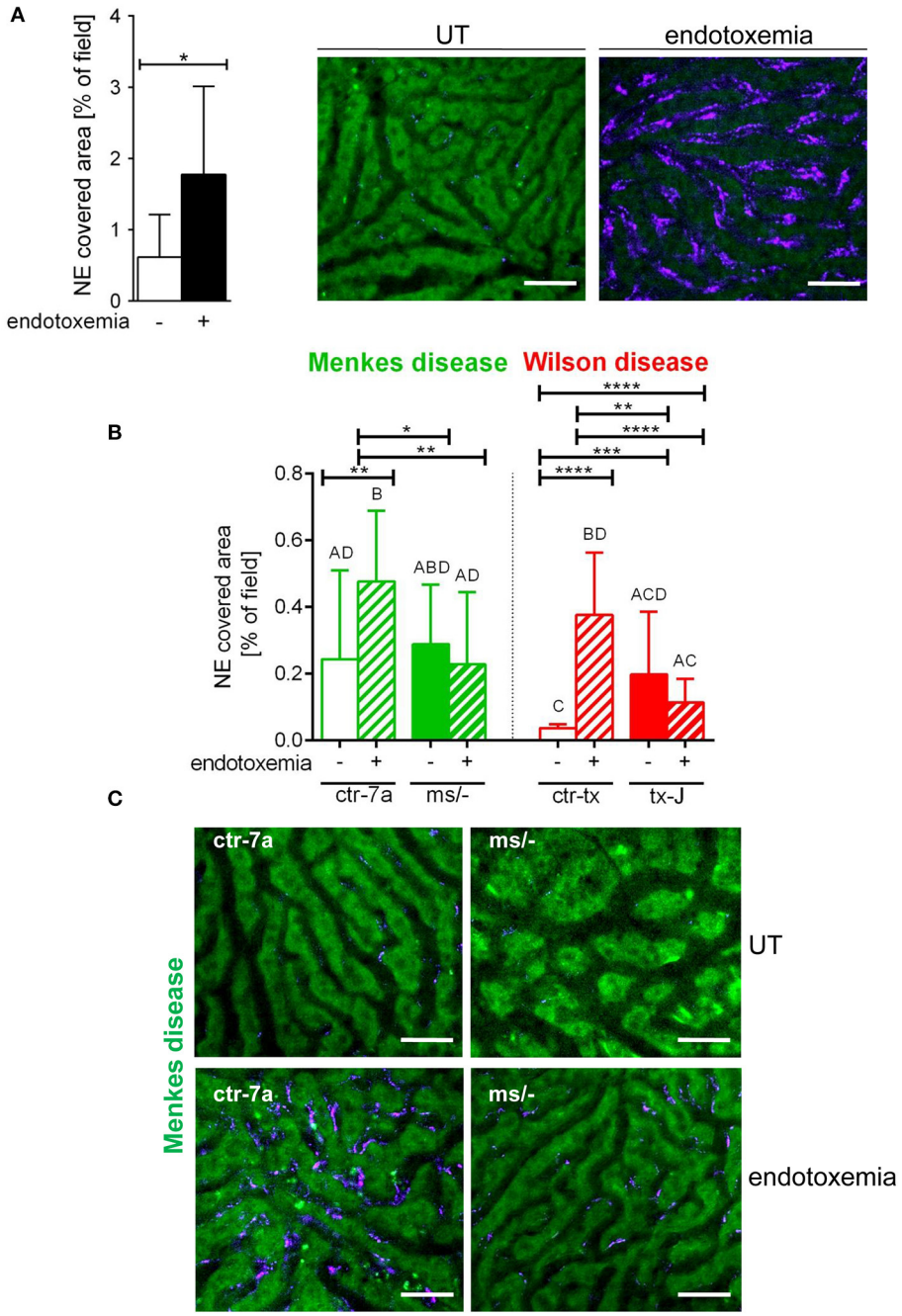

FIGURE 1 | Deposition of neutrophil extracellular traps (NETs) in liver sinusoids during endotoxemia in C57Bl/6J mice **(A)** and in animals with Wilson (tx-J) and Menkes ($^{ms/-}$) diseases and their respective controls — ctr-tx and ctr-7a **(B,C)**. NET formation was quantified as the percentage of area covered by neutrophil elastase (NE) in each analyzed field of view (FOV) (mice $n = 3$/group). Asterisks indicate significant differences using unpaired two-tailed Student's *t* test (*$P \leq 0.05$, **$P \leq 0.01$, ***$P \leq 0.001$, ****$P \leq 0.0001$) in **(A,B)** or one-way ANOVA (*post hoc* Bonferroni) test in **(B)**; different letters indicate statistically significant differences between groups. Representative pictures of NE deposition in livers of C57Bl/6J mice are presented in **(A)** and of Menkes disease mice and their littermates in **(C)** (images of Wilson disease mice and their controls are presented in **Supplementary Figure 1**). On images, autofluorescent hepatocytes (green) can be observed, and between them, sinusoids are seen as black areas. In the latter structures, NE signal is deposited along endothelium (violet). UT, untreated. The scale bar indicates 50 μm.

comparisons *post hoc* test. Statistical significance was set at $P < 0.05$.

RESULTS

NET Release by Neutrophils in Septic Mice With Menkes and Wilson Diseases

NETs are hardly present in the vasculature of untreated mice (6, 7, 10), and it was also the case in this study (**Figure 1** and **Supplementary Figure 1**). During systemic inflammation, all parameters were studied 24 h post LPS administration. *In vivo* NET release was thus far studied mainly in C57Bl/6J mice (7, 10, 40), and for this reason, we compared the release of the traps by *Atp7a/b* mutants and their unmutated counterparts to the above inbred strain (**Figures 1A–C**). Littermates of the mutant mice — outbred (ctr-7a) for $^{ms/-}$ animals with Menkes disease and C3HeB/FeJ (ctr-tx) for tx-J mice with Wilson disease — did produce NETs upon endotoxemia, but, significantly <C57Bl/6J mice (**Figure 1A** vs. **Figure 1B**). To detect NETs in the liver, mice were injected with fluorescent Sytox green to stain extDNA and Alexa Fluor 647 labeled antibodies directed against neutrophil elastase. Overlaying signals of the nuclear and granular components of neutrophils laying along sinusoid walls were considered indicative of NETs as previously published (6, 7, 10). Accordingly, **Figure 2** presents exemplary images of NETs formed in liver sinusoids of $^{ms/-}$ and tx-J mice and their counterpart controls. To quantify NET release, the area covered by neutrophil elastase was estimated with ImageJ as described previously (6, 7, 10). Importantly, in both Menkes and Wilson disease endotoxemic mice, NET formation was significantly lower in comparison to their respective unmutated controls with provoked inflammation (**Figure 1C**, **Supplementary Figure 1**, and **Supplementary Movies 1**, **2**). In fact, upon LPS stimulation, no increase in NET release was observed in either of the mutants when compared to their healthy counterparts.

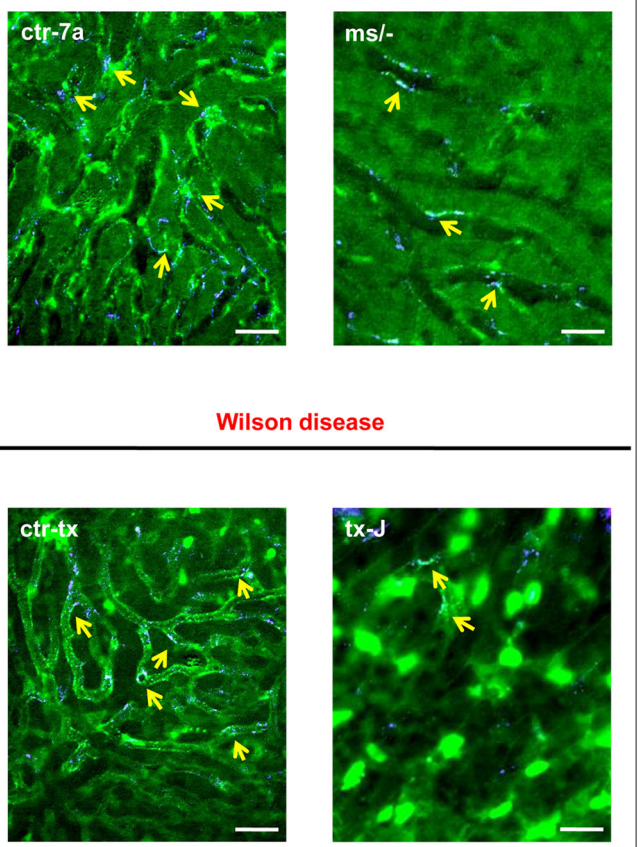

FIGURE 2 | Detection of NET components in the liver vasculature of endotoxemic Wilson (tx-J) and Menkes ($^{ms/-}$) disease mice and their respective controls (ctr-tx and ctr-7a). On images, autofluorescent hepatocytes (dim green) as well as Sytox green^{+} extracellular DNA (bright green) and NE signal (violet) are seen. Overlay of extDNA and NE is indicative of NETs (yellow arrows). The scale bar indicates 50 μm.

Neutrophil Influx Into Livers of Septic Mice With Menkes and Wilson Diseases

In the course of endotoxemia, accumulation of neutrophils in the liver is observed (7), and this phenomenon was also captured herein in livers of LPS-treated C57Bl/6J (not shown), and ctr-7a and ctr-tx mice (**Figures 3A,B**). However, in the case of Menkes disease mice, neutrophil numbers were as low as in ctr-7a untreated animals even after LPS administration. $^{ms/-}$ animals are in general characterized by low numbers of neutrophils as there are abnormalities in their maturation (25). On the contrary, neutrophil numbers in livers of tx-J mice with systemic inflammation were even higher than in endotoxemic ctr-tx animals (**Figures 3A,B**, **4C** and **Supplementary Movies 1**, **2**). On 3D *z* stacks performed through the liver, we also noticed that in Wilson disease mice, partially engulfed neutrophils were present in multiple KCs (**Figure 4D**). Although some neutrophils could also be spotted inside liver macrophages in Menkes disease mice, such events were rare.

KC Counts in Menkes and Wilson Disease Mice During Endotoxemia

KCs constitute the largest population of resident macrophages in the body, and their primary function is to protect the liver from bacterial infections (41). As numbers of KCs might be strain-specific (42), we firstly verified their numbers in healthy mice and observed more KCs in C3HeB/FeJ (ctr-tx) than in outbred (ctr-7a) mice (**Figure 4A** and **Supplementary Figure 2**). However, Menkes mutants had more KCs than ctr-7a and Wilson disease animals. In the course of systemic inflammation, an increase in counts of KCs was observed, in both ctr-7a (statistically significant) and mutated $^{ms/-}$ animals (tendency) (**Figure 4A**). This was not a case either for ctr-tx or tx-J mice, and furthermore, these animals had significantly less KCs present in their liver sinusoids 24 h post endotoxemia induction (**Figures 4A,C**).

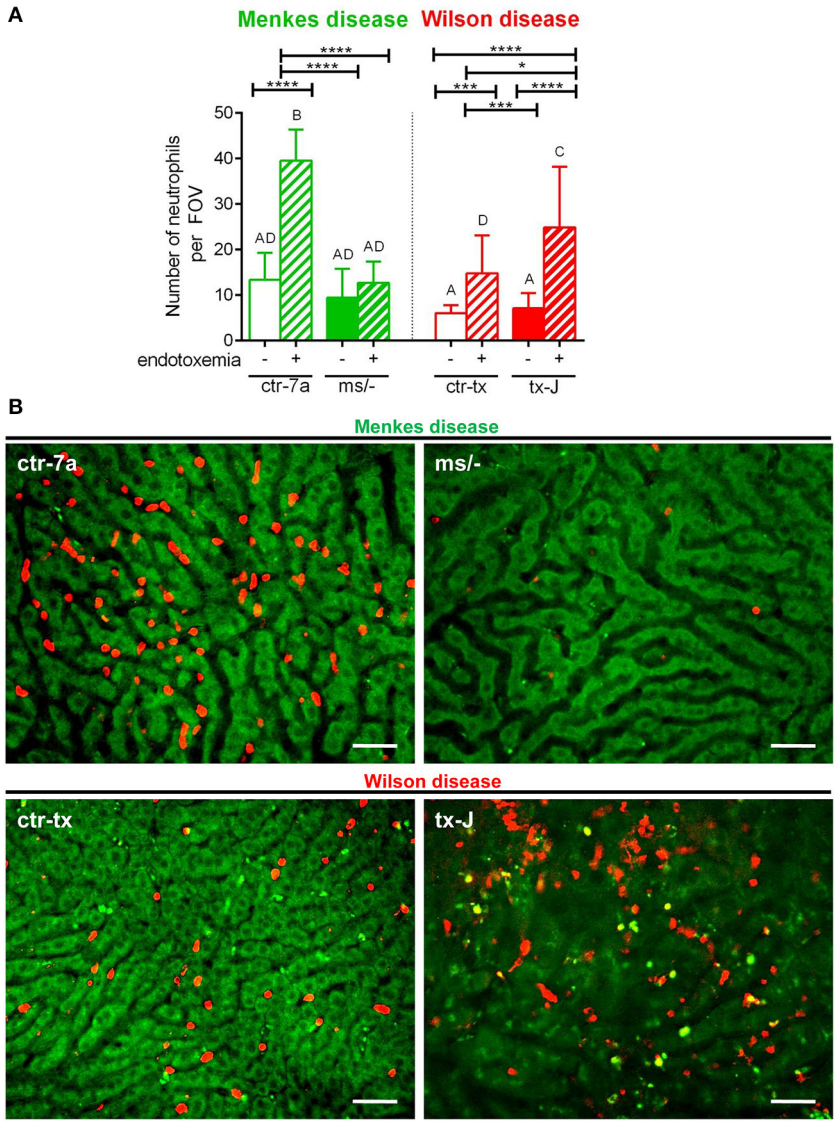

FIGURE 3 | The presence of neutrophils in livers of Wilson (tx-J) and Menkes ($^{ms/-}$) disease mice and their respective controls (ctr-tx and ctr-7a) with systemic inflammation. Neutrophils were counted per field of view (FOV; $n = 3$/group) **(A)**. Asterisks indicate significant differences using unpaired two-tailed Student's *t* test (*$P \leq 0.05$, ***$P \leq 0.001$, ****$P \leq 0.0001$) and one-way ANOVA (*post hoc* Bonferroni) test (different letters indicate statistically significant differences between groups). Representative images revealing neutrophil deposition in liver sinusoids are presented in **(B)**. On images, autofluorescent hepatocytes (green) can be observed, and between them, sinusoids are seen as black areas. In the latter structures, neutrophils are deposited (false red color; Brilliant Violet 421 anti-Ly6G antibody). The scale bar indicates 50 μm.

Platelet Accumulation in Sinusoids of Mice With Wilson and Menkes Diseases

Platelets are pivotal during systemic inflammation as they are important for a cross-talk between KCs and pathogens (43), and they might be important for NET formation (44), and contribute to NET pathology (10). We detected less platelets in sinusoids of ctr-tx (C3HeB/FeJ) mice than the outbreds, which is in line with reported variations between some murine strains (45). However, there were no differences between the control animals and their respective mutants (**Figure 4B**). According to ANOVA, there were no significant differences in platelet accumulation in liver sinusoids of Wilson disease mice (tx-J) and their littermates, although *t* test showed weaker platelet accumulation upon endotoxemia. The same pattern was observed for Menkes disease mice (**Figure 4B**).

Functional Characteristics of Neutrophils Isolated From Mutant Mice

To verify if reduced NET formation detected during systemic inflammation in either $^{ms/-}$ or tx-J mice resulted from intrinsic restrains of neutrophils or rather the microenvironment, basic parameters of neutrophils were evaluated (**Figure 5**).

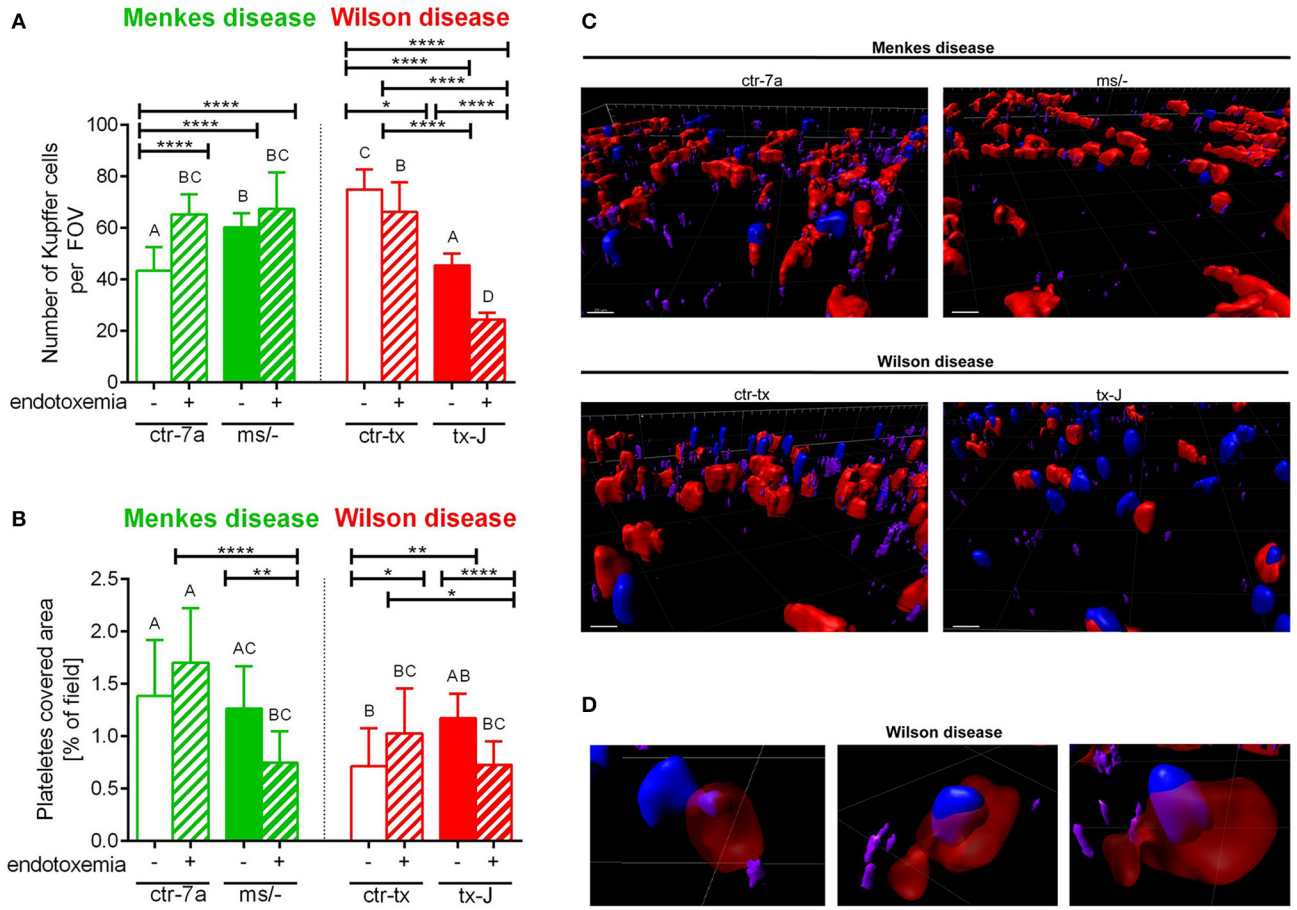

FIGURE 4 | The presence of Kupffer cells **(A)** and platelets **(B)** in livers of Wilson (tx-J) and Menkes ($^{ms/-}$) disease mice and their respective controls (ctr-tx and ctr-7a) with endotoxemia. Kupffer cells were counted per field of view (FOV), and area covered by platelets is expressed in percentage (as calculated by ImageJ) (mice $n = 3$/group). Asterisks indicate significant differences using unpaired two-tailed Student's *t* test ($^{*}P \leq 0.05$, $^{**}P \leq 0.01$, $^{****}P \leq 0.0001$) and one-way ANOVA (*post hoc* Bonferroni) test (different letters indicate statistically significant differences between groups). A series of optical cross-sections (*z* stacks) were made through inflamed livers. Exemplary images of *z* stacks made through the liver of Menkes disease and Wilson disease mice and their respective controls are shown in **(C)**. Kupffer cells are marked in red, neutrophils in blue, and neutrophil elastase in violet. In endotoxemic mice with Wilson disease, neutrophils present (partially or fully) inside some Kupffer cells were observed **(D)**. The scale bar indicates 20 μm.

The viability of neutrophils isolated from all mutant and control strains was similar (data not shown) and so was their ability to adhere (**Figure 5B**). The only difference was stronger adhesion of neutrophils from mice on C3HeB/FeJ background (both ctr-tx and tx-J) detected 3 h after cell seeding, suggesting that this was due to genetic factors (data now shown). However, after 6 h, there were neither intergroup nor interstrain differences in neutrophil adhesion (**Figure 5B**). We also did not detect differences in the capacity to perform respiratory burst/release ROS between Menkes disease mice and their genetically unaltered littermates (**Figure 5C** and **Supplementary Figure 3**). However, mice on the outbred background (both ctr-7a and $^{ms/-}$) started producing more ROS after several hours (6 vs. 1–3 h; **Supplementary Figure 3B** vs. **Supplementary Figure 3A**, **Figure 5C**, respectively), whereas a reversed pattern was observed in mice on the C3HeB/FeJ background. Importantly, we detected that neutrophils isolated from both mutant strains could form NETs upon LPS stimulation *ex vivo* although they released less NETs than their unmutated controls (**Figure 5A**).

Phenotype of Copper Chelator Treated Mice

Some C57Bl/6J mice were treated with a Cu chelator for eight constitutive days and then treated with LPS to induce 24-h systemic inflammation. In these animals, liver sinusoids were layered with significantly more NETs than in their saline-treated counterparts (**Figure 6**). Albeit the numbers of KCs (**Figure 6C**) and platelets (**Figure 6D**) were unchanged in these mice, significantly less neutrophils infiltrated liver sinusoids (**Figure 6B**).

Copper Levels in Mice With Wilson and Menkes Diseases

Copper levels were estimated by AAS. Despite Cu injections into mice with Menkes disease ($^{ms/-}$), to keep them alive, their copper

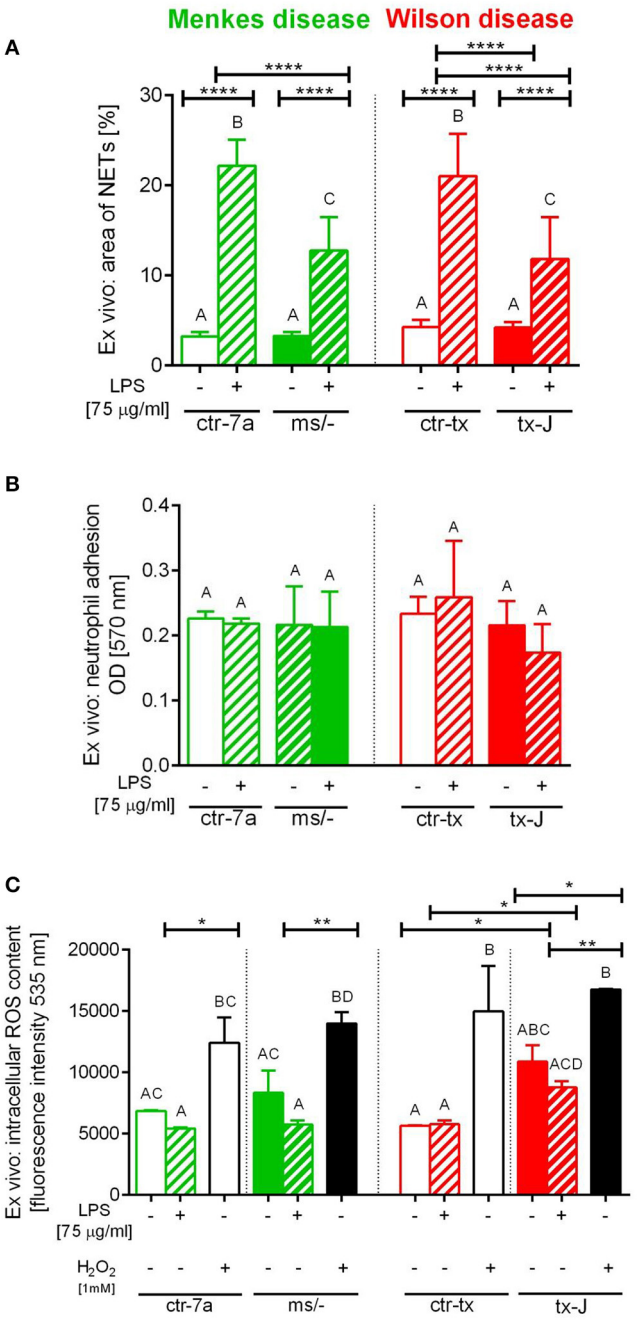

FIGURE 5 | *Ex vivo* studies on isolated bone marrow neutrophils of Wilson (tx-J) and Menkes ($^{ms/-}$) disease mice and their respective controls (ctr-tx and ctr-7a) evaluating their capacity to form NETs **(A)**, adhere **(B)**, and release reactive oxygen species (ROS; **C**). NET formation and capacity to adhere were evaluated 6 h after stimulation with LPS, and the content of ROS was measured after the first hour (DCF-DA test). In **(C)**, white/black bars represent responses of cells treated with H_2O_2 (positive control)—data for neutrophils from control mice (white bars) and mutants (black bars). Asterisks indicate significant differences using unpaired two-tailed Student's *t* test (*$P \leq 0.05$, **$P \leq 0.01$, ****$P \leq 0.0001$) and one-way ANOVA (*post hoc* Bonferroni) test (different letters indicate statistically significant differences between groups).

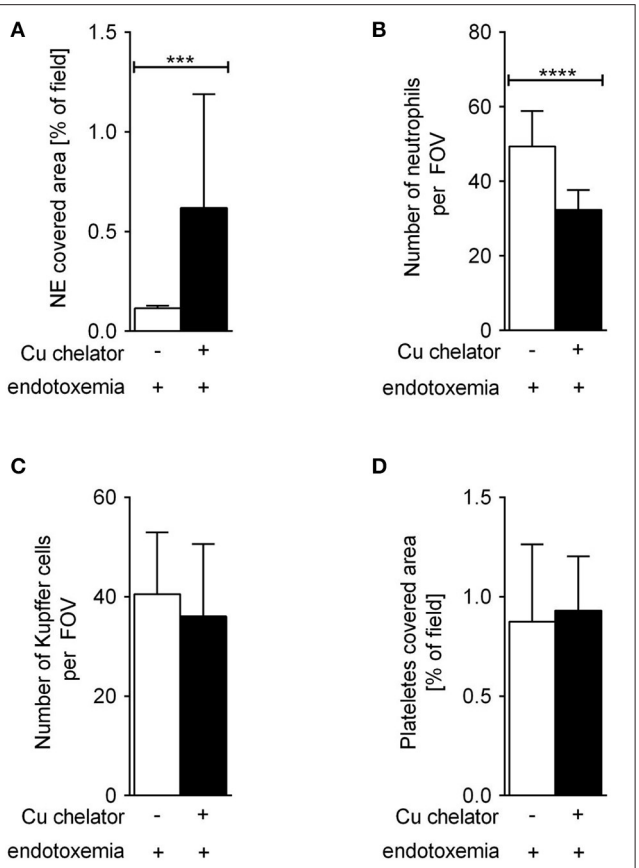

FIGURE 6 | The impact of subchronic copper deficiency on NET formation **(A)**, neutrophil numbers **(B)**, Kupffer cell counts **(C)**, and platelet covered area **(D)** in C57Bl/6J mice. Copper chelator (Cu chelator) was administered for 8 days and then LPS-systemic inflammation was induced. NET covered area and cell counts were performed 24 h later. Asterisks indicate significant differences using unpaired two-tailed Student's *t* test (***$P \leq 0.001$, ****$P \leq 0.0001$).

levels were still diminished in both the liver and (especially) the plasma (**Figure 7A**). As anticipated, we detected significant copper accumulation in livers of mice with Wilson disease (tx-J), higher by ∼50-fold than in ctr-tx animals (**Figure 7A**). However, plasma copper levels were not increased in tx-J mice. In spite of being a disease of copper intracellular overload, the total serum copper is usually low/reduced in the circulation of individuals with the Wilson disease, mice or human, but it might increase in time (30, 46). This is in contrast to copper levels in the liver and the GI tract where its high accumulation impacts cells, including infiltrating leukocytes.

Liver Damage in Mice With Wilson Disease vs. Menkes Disease

Alanine aminotransferase (ALT) can be found in the blood and some organs, although in greatest abundance in the liver, and its increased levels/activity are indicative of liver damage (7). Activity of ALT was unchanged in Menkes disease mice as

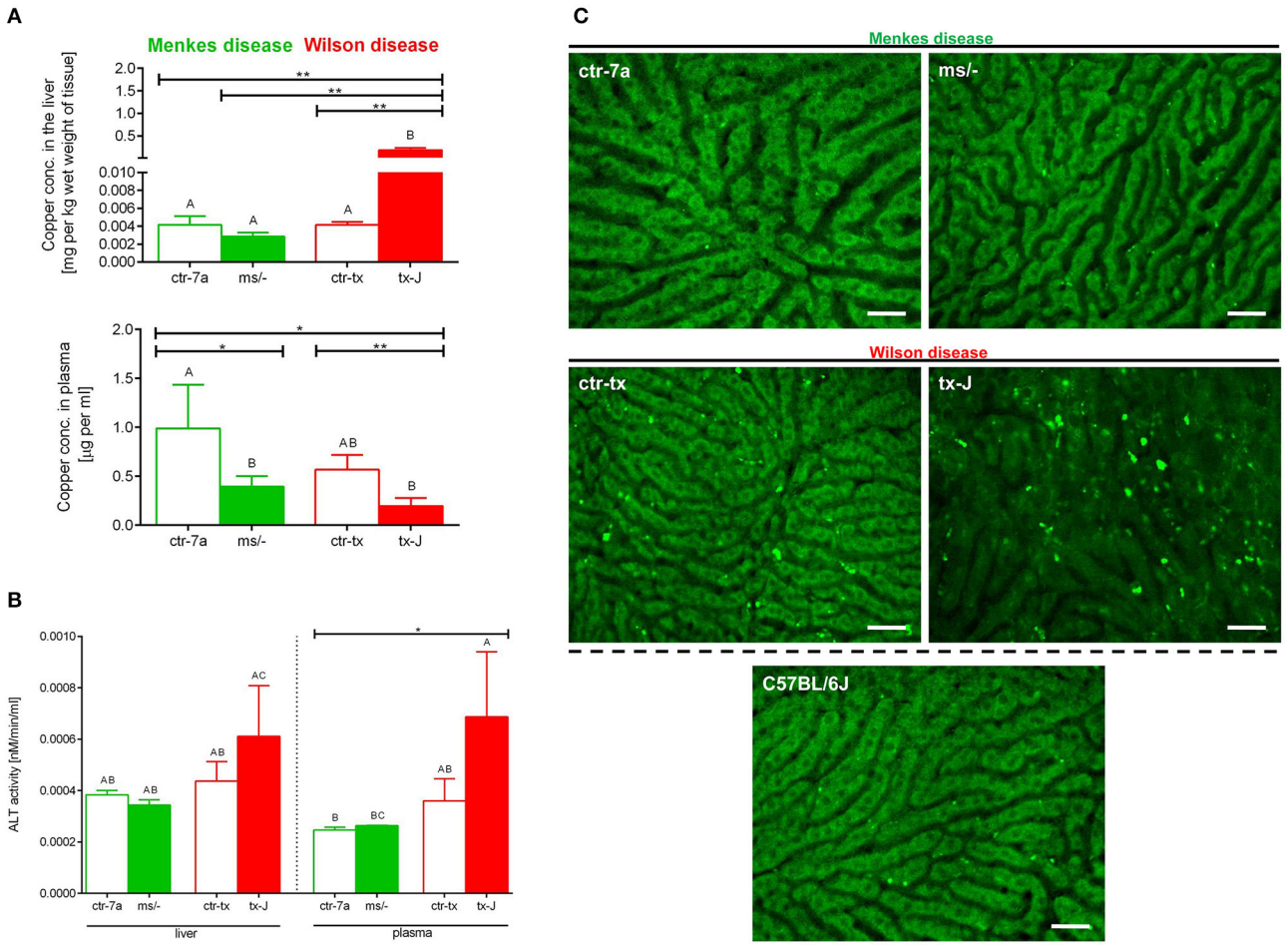

FIGURE 7 | Liver and plasma copper accumulation **(A)** and alanine transaminase (ALT; **B**) levels estimated in mice with Wilson (tx-J) and Menkes ($^{ms/-}$) diseases and their respective controls (ctr-tx and ctr-7a). Asterisks indicate significant differences using unpaired two-tailed Student's *t* test (*$P \leq 0.05$, **$P \leq 0.01$) and one-way ANOVA (*post hoc* Bonferroni) test (different letters indicate statistically significant differences between groups). Condition of hepatocytes, visibility of sinusoids, and deposition of autofluorescent aggregates is shown on representative images of livers in **(C)**; images of mice with Wilson and Menkes diseases are shown along with their controls and C57Bl/6J mice. No additional staining was performed, and only autofluorescent hepatocytes (green) were recorded in the GFP channel. Between the hepatocytes, sinusoids (black ducts) can be observed. The scale bar indicates 50 µm.

measured in their liver homogenates and plasma (**Figure 7B**). Conversely, there was a tendency to increased ALT activity in both liver tissue and plasma of mice with Wilson disease, but the differences did not reach statistical significance (**Figure 7B**). The data corresponded with the architecture of liver sinusoids; i.e., while livers appeared to emit a homogeneous autofluorescent signal in Menkes disease mice, sinusoids were well-visible and hepatocyte nuclei were clearly observable; in Wilson disease mice, all these parameters were altered (**Figure 7C**, representative images; **Supplementary Movies 1**, **2**). Hepatocyte morphology was disturbed, their nuclei were hardly evident, and sinusoids were less visible and less of them appeared on average in FOVs. Moreover, numerous green autofluorescent corpuscles were observed (**Figure 7C** and **Supplementary Movies 1**, **2**). It should be stressed that some autofluorescent aggregates, although much less frequent, were also detected in controls of Wilson disease mice (ctr-tx).

Expression of CTR1, ATP7A, and ATP7B in Neutrophils

One of the cellular copper transporters is high-affinity copper uptake protein 1 (CTR1), and its expression was detected in both resting neutrophils and those incubated with copper (0.5, 1, and 2 µg/ml) whereas the signal was stronger (more dispersed) in cells cultured without it (**Supplementary Figure 4**). This is in agreement with CTR1 expression in other organs of mice exposed to either copper-rich or -deficient diets (47). Nevertheless, the expression of CTR1 was detected only on up to 5% of cells (data not shown), which suggests that other copper transporter(s) must also be operating in neutrophils. In line with this, divalent metal transporter 1 (DMT1) was shown to be upregulated on inflammatory neutrophils (42). Also the presence of ATP7A and ATP7B proteins was detected in some neutrophils (~5%) either resting or incubated with copper (**Supplementary Figure 4**). ATP7A expression seemed dispersed between the trans-Golgi

network and through the cytoplasm, independently of the presence of exogenous copper (**Supplementary Figure 4**). This is in line with ATP7A shuttling copper between the Golgi apparatus and the cell membrane to maintain its proper concentration (21). However, while ATP7B expression was also diffused throughout the cytosol in resting cells, it was more confined to Golgi apparatus in the presence of copper (**Supplementary Figure 4**).

Ex vivo Studies: Viability of Neutrophils and Formation of NETs in the Presence of Exogenous Copper

Isolated neutrophils, when treated with various concentrations of copper, revealed high sensitivity to this element. Decreased viability of the cells was observed from concentration 1 μg/ml onwards when Cu was the only exogenous factor (**Figure 8A**; –LPS). When higher concentrations of copper were added to neutrophil cultures (up to 200 μg/ml), 100% mortality was observed (not shown). When neutrophils were additionally incubated with LPS, exogenous copper was less toxic (**Figure 8A**; +LPS). Copper chelator (TTM) rescued neutrophil viability in all concentrations of copper tested; here, shown for 1 μg/ml (**Figure 8B**; –LPS). Both LPS (**Supplementary Figure 5**) and PMA (not shown) alone induced NET formation while copper alone did not induce NET formation (**Supplementary Figure 5**). When NET release was induced by LPS in the presence of copper, it did not affect NET release in concentrations up to 1 μg/ml, and neither did copper chelator (**Figure 9A**). Furthermore, the chelator restored NET formation by neutrophils incubated with 1 μg/ml of copper (**Figures 9A,B**).

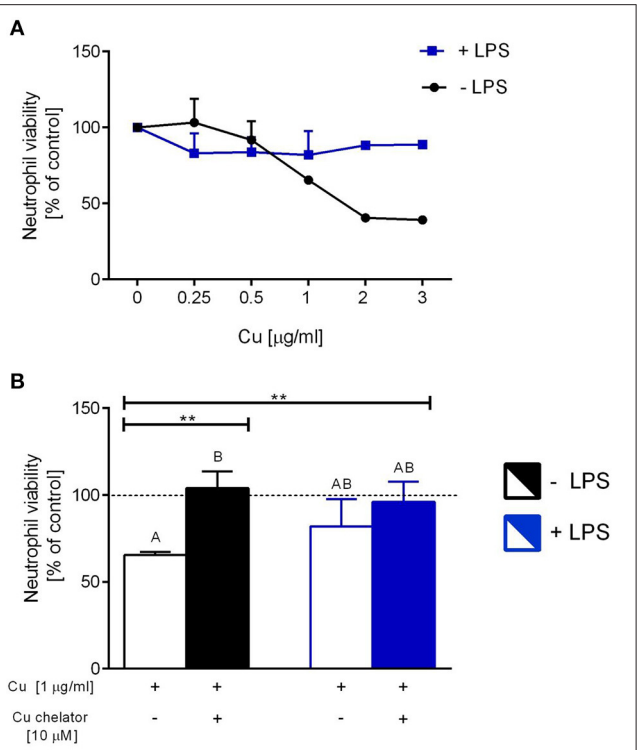

FIGURE 8 | The impact of exogenous copper of neutrophil viability **(A)**, and counteraction of copper effects by its chelating agent **(B)** in *ex vivo* conditions. Neutrophils isolated from the bone marrow of C57Bl/6J mice were incubated with various copper concentrations in the presence (+LPS) or absence (–LPS) of lipopolysaccharide **(A)**. Cell viability reversed by the Cu chelator **(B)**. The dotted line **(B)** indicates values for untreated neutrophils (Cu concentration "0" in **A**). Asterisks indicate significant differences using unpaired two-tailed Student's *t* test (**$P \leq 0.01$) and one-way ANOVA (*post hoc* Bonferroni) test (different letters indicate statistically significant differences between groups).

DISCUSSION

Sepsis is one of the leading causes of death (48) and also patients with endotoxemia are at risk of increased mortality (11). Moreover, endotoxemia occurs in many patients with sepsis, but also in many clinical settings that are non-infectious in nature. A severe form of systemic inflammation is characterized by (multi)organ failure and although liver is not the most commonly affected organ, when it is, this becomes a grave complication and leads to its acute failure (12). Moreover, LPS plays a prominent role in liver injury in rodents and human individuals (49). We furthermore confirmed these findings in mouse models of bacterial and LPS-induced systemic inflammation and we were able to correlate them with NET formation and their inadequate removal, proteolytic activity of neutrophil elastase, and microcoagulation connected with platelet deposition (7, 10). While knowledge on direct NET inducers is rather vast, we still do not know much about microenvironmental factors that are critical for casting the traps. Involvement of some trace elements in NET formation was studied previously, and it was shown that formation of PMA-induced NETs is zinc dependent (2), but impact of iron is less clear as various iron-chelating agents were shown to either stimulate or inhibit NET formation (3, 4). Moreover, influx of calcium ions was shown to proceed NET release in numerous models (50). All the above elements were shown to be released (themselves or as a part of protein complexes) during NET formation, and the traps were also decorated with them (20). Also copper is present in neutrophils and was localized both in their cytoplasm and nucleus, and it is released from them in response to at least some of the NET inducers (PMA) (20, 51).

Herein we report that in mice with either phenotype, of high (Wilson disease) and low (Menkes disease) copper levels in the liver, NET formation during endotoxemia was impaired whereas NET release during this condition is one of the hallmarks of the human reaction to LPS and has been proposed to serve as its promising blood biomarker (6, 52). The fact that less NETs were formed in inflamed livers of Menkes mice correlates with hardly occurring neutrophil infiltration and impaired neutropoiesis is most probably directly responsible for this phenomenon. Of note, we also show that respective controls of Wilson/Menkes disease mice produce significantly less NETs than C57Bl/6J mice, with C3HeB/FeJ mice displaying the weakest capacity to cast NETs. Thus, these data further extend previous findings on murine strain differences in respect to the efficiency of NET formation (53). In animals with Wilson disease (*Atp7b* mutants), indeed very high accumulation of copper was

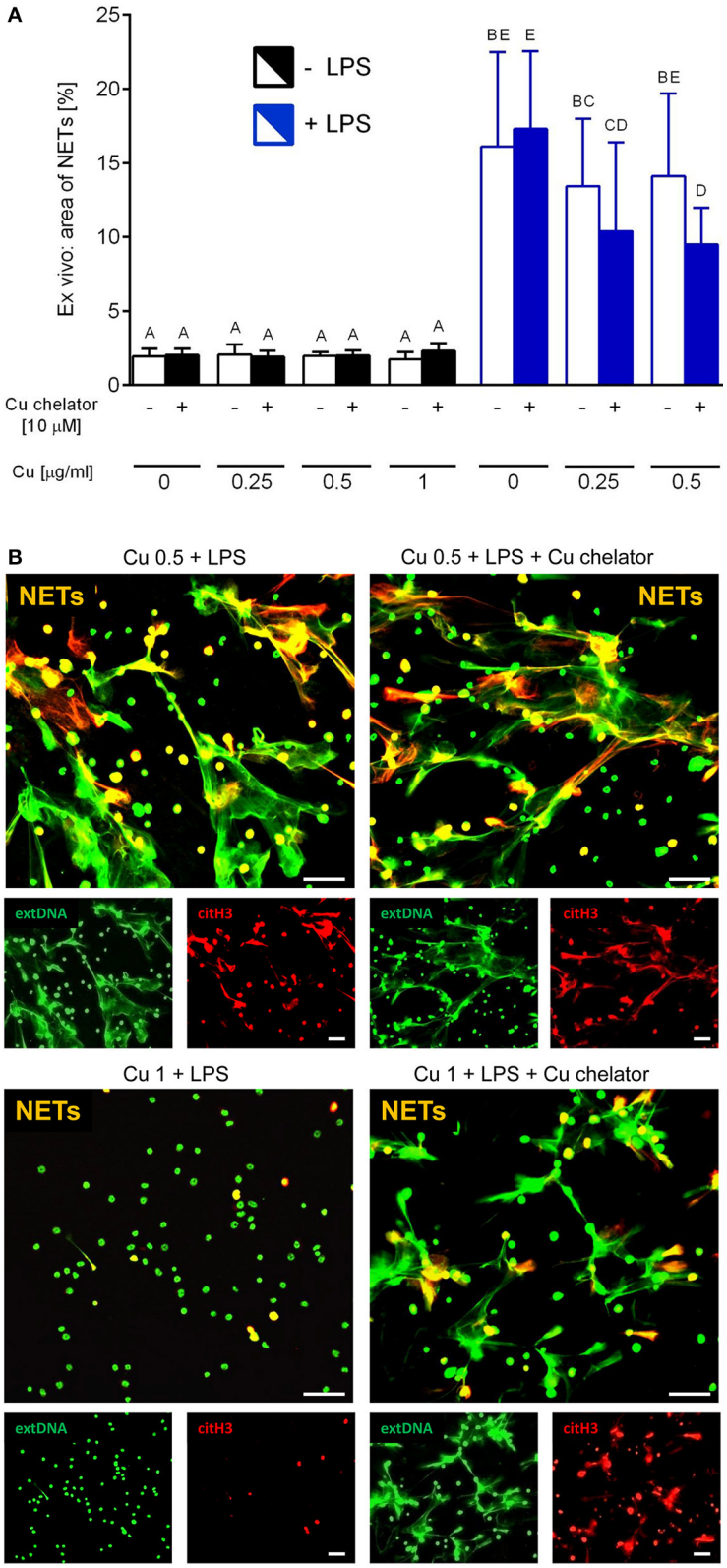

FIGURE 9 | Neutrophil extracellular trap (NET) formation in the presence of exogenous copper. Neutrophils were either incubated with LPS (+LPS), various concentrations of copper (Cu), or left alone. Additionally, some cells were stimulated with LPS and/or copper chelator when co-cultured with the varying concentrations

(Continued)

FIGURE 9 | of copper. In all groups, neutrophil capacity to form NETs was quantified **(A)**. Different letters indicate statistically significant differences between groups using one-way ANOVA (*post hoc* Bonferroni). Representative images of NETs formed by LPS in the presence of copper with or w/o copper chelator are shown in **(B)**. Extracellular DNA (extDNA) is shown in green and citrullinated histone H3 (citH3) is shown in red. To visualize co-localization of NET components, the images from each channel were overlaid (NETs, overlay; orange). The scale bar indicates 50 μm.

observed in the organ and accordingly liver was injured. In particular, the appearance of the organ revealed with intravital microscopy was striking as sinusoids were hardly visible, and hepatocytes were enlarged and their nuclei were barely evident, a phenotype coinciding with hematoxylin-stained liver sections (33). Moreover, numerous autofluorescent bodies could be detected. Autofluorescence and its distribution in the liver is an intrinsic parameter that can provide real-time information on the morphology and functional properties of this organ (54). When liver is malfunctioning, autofluorescence is more prominent and rather than by NAD(P)H, it is emitted by collagen and vitamin A (54).

In damaged (non-infectious) liver, NET formation is very weak as we showed previously for sterile thermal liver injury and further compared it to systemic bacterial infection (55). However, although very few NETs were observed during systemic inflammation in Wilson mice, at the same time, a larger number of neutrophils infiltrated the liver than in endotoxemic control (ctr-tx) animals. This indicates that the cells were not prone to cast NETs. To verify it further, we performed an *ex vivo* experiment in which we incubated neutrophils isolated from bone marrow with various copper concentrations. Our first observation was that neutrophils were very sensitive to copper and they remained fully viable only in copper (II) chloride concentrations of up to 0.5 μg/ml. This is in line with the fact that ∼0.5 μg/ml is an average serum concentration of copper in healthy C57Bl/6J mice (56) and mice on the C3HeB/FeJ background (**Figure 7A**; ctr-tx). However, in the presence of LPS, neutrophils were less sensitive to copper. This might be connected to the fact that neutrophils activated by pro-inflammatory factors such as LPS have a prolonged life span and delayed apoptosis (57). Moreover, one of the effects of transition metals, including copper, on cells is induction of apoptosis. In fact, Cu-induced hepatotoxicity and neurotoxicity, occurring also during Wilson disease, is connected to its pro-apoptotic action (58).

Neutrophils primed *ex vivo* to cast NETs by LPS were releasing their similar quantities in the presence of exogenous copper within the physiological range (0.25–0.5 μg/ml) and copper-chelating agent only slightly (if at all) decreased the process. However, at the copper concentrations that were toxic to neutrophils (>1 μg/ml) significantly less NETs were released and the copper chelator restored this phenomenon. This indicates that indeed high copper concentrations prevent the release of NETs or it directly echoes low numbers of live neutrophils.

To verify if neutrophils themselves are equipped with the machinery to control intracellular copper levels, we studied cellular expression of some of its regulators. We revealed that at least some neutrophils express the copper transporter — CTR1, and moreover some of them express both ATP7A and ATP7B (up to 5% of neutrophils). While expression of ATP7A is anticipated in most cell types (21), ATP7B expression was so far only reported in hepatocytes and KCs (33). To the best of our knowledge, expression of ATP7 isoforms was not studied in neutrophils so far. Since neutrophils from Wilson disease mice lack functional ATP7B, they might still be able to efflux excessive copper via ATP7A. But our studies indicate that only to a certain point beyond which the cells first decrease their activity (weaker NET release at 1 μg/ml) and then die (>1 μg/ml). In fact, the latter concentration is the one observed in the serum of ATP7B-deficient mice at the age of 28 weeks and older (30). Interestingly, transplantation of only hepatocytes of ATP7B-deficient mice into spleens of their control littermates increases serum copper levels by 60% (59). Overall, the above studies indicate that the production of neutrophils is not diminished by high copper concentrations (serum and liver), and during systemic inflammation, these cells infiltrate liver even stronger than in genetically wild type mice. This might suggest that higher numbers of neutrophils are recruited to the liver to compensate for lower neutrophil activity.

In Wilson disease mice, also lower numbers of KCs and platelets were detected than in their control counterparts. KCs are macrophages of the liver that are central to both the hepatic and systemic response to infection (60). As they normally express ATP7B to regulate their copper levels, they are as overloaded with the element as hepatocytes (33), which most probably results in their death. In fact, KCs cooperate with platelets during the early stages of systemic inflammation as platelets facilitate a cross-talk between KCs and pathogens/their derivatives (43). Because numbers of KCs are lower in Wilson disease mice, platelet counts might be diminished as they adhere to KCs in the course of endotoxemia (43). Even more importantly, during ongoing sepsis, profound platelet aggregation occurs within and around NETs, and it is significantly diminished when they are removed or not formed (10). We propose the above factors to be responsible for weak platelet deposition in inflamed livers of Wilson disease mice. Interestingly, we also noticed neutrophils present inside numerous KCs of Wilson disease mice. This might suggest that more neutrophils die while present in the copper overloaded liver and they are engulfed by liver macrophages. Additionally or alternatively, due to low numbers of KCs, dying neutrophils are not properly removed, which results in their accumulation in the organ.

In mice with the Menkes disease (*Atp7a* mutants) phenotype, also significantly less NETs were detected in the course of endotoxemia. However, in contrast to tx-J animals, in these mice, significantly less neutrophils were infiltrating the liver and it is known that copper deficiency impairs their maturation in the bone marrow (25). As mentioned above, KCs are important for the initiation of systemic inflammation as together with

platelets they activate a proper inflammatory response that leads to neutrophil infiltration (43). During systemic reaction, their numbers might slightly increase (60–62), and this was also observed in mice with Menkes disease. However, although copper deficiency does not seem to impact numbers of KCs, it is known to affect some macrophage activities (e.g., their capacity to perform respiratory burst) (63). Moreover, reduced superoxide anion production was also observed in neutrophils of copper deficient individuals (64). Therefore, lower levels of NETs released during endotoxemia in *Atp7a* mutant mice might have also resulted from weaker production of ROS. However, NET formation was shown to be ROS(NOX)-independent in multiple settings including sepsis, and so was NET release induced by complement receptors, TLR2/TLR4 ligands or TLR4-activated platelets (7, 40, 65). In fact, physiological NET triggers (pathogens and their derivatives, and cytokines) seem to act in a ROS-independent manner (66). Therefore, weaker NET release probably rather results from low neutrophil numbers. The Menkes disease mice also had lower platelet counts present in inflamed livers. Alteration in platelet capacity to adhere and form plug/thrombus was shown previously in copper-deficient animals (67, 68) but what we observed in the current study might simply result from less NETs being cast as they form a platform for platelet adhesion in LPS-induced systemic inflammation (10).

To verify if copper deficiency results in a weaker NET formation, we kept C57Bl/6J mice, with unaltered ATPase expression, on daily copper chelator injections for 8 days to mimic a semi-chronic copper deprivation. To our surprise, during endotoxemia, much stronger NET release was detected in the livers of these animals than in their saline-treated controls. Similarly as in *Atp7a* mutants, less neutrophils were present in liver sinusoids but the numbers of KCs and platelets were unchanged. These results imply that indeed copper deficiency directly affects neutrophil numbers but the impact on NET formation is more complex. In our *ex vivo* experiments, copper chelator alone (when no exogenous copper was added) was not impacting NET formation (even in higher concentrations than show here), suggesting that copper is not essential for the release of NETs. The fundamental difference between mice with subchronic copper deficiency and *Atp7a* mutated animals is high accumulation of copper in the intestines of the latter animals (35). It is because copper has been shown to affect microbiota diversity in the gut of mice (69) and microbiota content (both qualitative and quantitative) is critical for proper aging of neutrophils and their removal as well as for casting NETs (70). Furthermore, antibiotic therapy was shown to affect ATP7A expression in the colon of mice (71). Therefore, depending on the status of microbiota, diverse numbers of aged neutrophils might be available in mice with subchronic copper deficiency and *Atp7a* mutants, while it is the aged neutrophil phenotype that exhibits enhanced NET formation under inflammatory conditions (70). Although we are unaware of studies on microbiota composition in Menkes disease-affected humans or mice, it is known to be altered in Wilson disease patients (72). Therefore, verification of microbiota changes in Menkes patients and in Wilson and Menkes mice could shed light on this issue.

In conclusion, with the application of intravital microscopy, we revealed that in both *in vivo* phenotypes of inappropriate copper distribution/levels and efflux in the body, resulting from altered genotypes, NET formation is decreased during systemic inflammation. This implies that at early stages of the reaction, affected individuals are less armed to capture pathogens and indeed some Wilson disease patients are more prone to sepsis (73). Overall, the study reveals that the requirement for different microelements for NET formation considerably varies as unlike zinc, low or negligible levels of copper do not interfere with NET formation or might even enhance it. In contrast, high copper concentrations (beyond 1 μg/ml) inhibit NET release, but this is mostly due to the cytotoxicity toward neutrophils.

DATA AVAILABILITY STATEMENT

The datasets generated for this study are available on request to the corresponding author.

ETHICS STATEMENT

All protocols were approved by the Local Ethical Committee No. II in Krakow (Permission Nos. 293/2017 and 293A/2018).

AUTHOR CONTRIBUTIONS

IC acquired data (performed all intravital microscopy, *ex vivo* studies, immunocytochemistry, biochemical tests), performed all analyses, and participated in interpretation of data. WO acquired data (some *ex vivo* studies, immunocytochemistry). ML and AB provided mice, ATP7Bα, and CTR1α, and secured ASS analyses. EK provided study conception and design, participated in analyses and interpretation of data, and wrote the manuscript.

FUNDING

This study was supported by grants [Nos. 2018/29/B/NZ6/00713 and 2014/15/B/NZ6/02519 (EK)] from the National Science Center, Poland (NCN).

SUPPLEMENTARY MATERIAL

The Supplementary Material for this article can be found online at: https://www.frontiersin.org/articles/10.3389/fimmu.2019.03021/full#supplementary-material

Supplementary Movie 1 | Menkes disease mice ($^{ms/-}$) and their controls (ctr-7a) with 24-h endotoxemia. Neutrophils were labeled with Brilliant Violet 421 anti-Ly6G antibody (blue), neutrophil elastase with Alexa Fluor 647 anti-NE (violet) and platelets with PE anti-CD49b (red). Autofluorescent hepatocytes are green. The scale bar indicates 50 μm.

Supplementary Movie 2 | Wilson disease mice (tx-J) and their controls (ctr-tx) with 24-h endotoxemia. Neutrophils were labeled with Brilliant Violet 421 anti-Ly6G antibody (blue), neutrophil elastase with Alexa Fluor 647 anti-NE (violet), Kupffer cells with Alexa Fluor 488 anti-F4/80 (bright green) and platelets with PE anti-CD49b (red). Autofluorescent hepatocytes are green (dim green). The scale bar indicates 50 μm.

REFERENCES

1. Brinkmann V, Reichard U, Goosmann C, Fauler B, Uhlemann Y, Weiss DS, et al. Neutrophil extracellular traps kill bacteria. *Science.* (2004) 303:1532–5. doi: 10.1126/science.1092385
2. Hasan R, Rink L, Haase H. Zinc signals in neutrophil granulocytes are required for the formation of neutrophil extracellular traps. *Innate Immu.* (2013) 19:253–64. doi: 10.1177/1753425912458815
3. Vollger L, Akong-Moore K, Cox L, Goldmann O, Wang Y, Schafer ST, et al. Iron-chelating agent desferrioxamine stimulates formation of neutrophil extracellular traps (NETs) in human blood-derived neutrophils. *Biosci Rep.* (2016) 36:e00333. doi: 10.1042/BSR20160031
4. Kono M, Saigo K, Yamamoto S, Shirai K, Iwamoto S, Uematsu T, et al. Iron-chelating agent, deferasirox, inhibits neutrophil activation and extracellular trap formation. *Clin Exp Pharmacol Physiol.* (2016) 43:915–20. doi: 10.1111/1440-1681.12612
5. Urban CF, Ermert D, Schmid M, Abu-Abed U, Goosmann C, Nacken W, et al. Neutrophil extracellular traps contain calprotectin, a cytosolic protein complex involved in host defense against *Candida albicans. PLoS Pathog.* (2009) 5:e1000639. doi: 10.1371/journal.ppat.1000639
6. McDonald B, Urrutia R, Yipp BG, Jenne CN, Kubes P. Intravascular neutrophil extracellular traps capture bacteria from the bloodstream during sepsis. *Cell Host Microbe.* (2012) 12:324–33. doi: 10.1016/j.chom.2012.06.011
7. Kolaczkowska E, Jenne CN, Surewaard BG, Thanabalasuriar A, Lee WY, Sanz MJ, et al. Molecular mechanisms of NET formation and degradation revealed by intravital imaging in the liver vasculature. *Nat Commun.* (2015) 6:6673. doi: 10.1038/ncomms7673
8. Kolaczkowska E, Kubes P. Neutrophil recruitment and function in health and inflammation. *Nat Rev Immunol.* (2013) 13:159–75. doi: 10.1038/nri3399
9. Jorch SK, Kubes P. An emerging role for neutrophil extracellular traps in noninfectious disease. *Nat Med.* (2017) 23:279–87. doi: 10.1038/nm.4294
10. McDonald B, Davis RP, Kim SJ, Tse M, Esmon CT, Kolaczkowska E, et al. Platelets and neutrophil extracellular traps collaborate to promote intravascular coagulation during sepsis in mice. *Blood.* (2017) 129:1357–67. doi: 10.1182/blood-2016-09-741298
11. Ronco C, Piccinni P, Rosner HM. *Endotoxemia and Endotoxin Shock Disease, Diagnosis and Therapy*. Basel: Karger (2010).
12. Wang D, Yin Y, Yao Y. Advances in sepsis-associated liver dysfunction. *Burns Trauma.* (2014) 2:97–105. doi: 10.4103/2321-3868.132689
13. Le A, Shibata NM, French SW, Kim K, Kharbanda KK, Islam MS, et al. Characterization of timed changes in hepatic copper concentrations, methionine metabolism, gene expression, and global DNA methylation in the Jackson toxic milk mouse model of Wilson disease. *Int J Mol Sci.* (2014) 15:8004–23. doi: 10.3390/ijms15058004
14. Przybylkowski A, Gromadzka G, Wawer A, Bulska E, Jablonka-Salach K, Grygorowicz T, et al. Neurochemical and behavioral characteristics of toxic milk mice: an animal model of Wilson's disease. *Neurochem Res.* (2013) 38:2037–45. doi: 10.1007/s11064-013-1111-3
15. Lenartowicz M, Grzmil P, Shoukier M, Starzynski R, Marciniak M, Lipinski P. Mutation in the CPC motif-containing 6th transmembrane domain affects intracellular localization, trafficking and copper transport efficiency of ATP7A protein in mosaic mutant mice–an animal model of Menkes disease. *Metallomics.* (2012) 4:197–204. doi: 10.1039/C1MT00134E
16. Moller LB, Mogensen M, Horn N. Molecular diagnosis of Menkes disease: genotype-phenotype correlation. *Biochimie.* (2009) 91:1273–7. doi: 10.1016/j.biochi.2009.05.011
17. Bhattacharjee A, Chakraborty K, Shukla A. Cellular copper homeostasis: current concepts on its interplay with glutathione homeostasis and its implication in physiology and human diseases. *Metallomics.* (2017) 9:1376–88. doi: 10.1039/C7MT00066A
18. Fu Y, Chang FM, Giedroc DP. Copper transport and trafficking at the host-bacterial pathogen interface. *Acc Chem Res.* (2014) 47:3605–13. doi: 10.1021/ar500300n
19. Samanovic MI, Ding C, Thiele DJ, Darwin KH. Copper in microbial pathogenesis: meddling with the metal. *Cell Host Microbe.* (2012) 11:106–15. doi: 10.1016/j.chom.2012.01.009
20. De Samber B, Niemiec MJ, Laforce B, Garrevoet J, Vergucht E, De Rycke R, et al. Probing intracellular element concentration changes during neutrophil extracellular trap formation using synchrotron radiation based X-ray fluorescence. *PLoS ONE.* (2016) 11:e0165604. doi: 10.1371/journal.pone.0165604
21. La Fontaine S, Mercer JF. Trafficking of the copper-ATPases, ATP7A and ATP7B: role in copper homeostasis. *Arch Biochem Biophys.* (2007) 463:149–67. doi: 10.1016/j.abb.2007.04.021
22. Kardos J, Heja L, Simon A, Jablonkai I, Kovacs R, Jemnitz K. Copper signalling: causes and consequences. *Cell Commun Signal.* (2018) 16:71. doi: 10.1186/s12964-018-0277-3
23. Ren F, Logeman BL, Zhang X, Liu Y, Thiele DJ, Yuan P. X-ray structures of the high-affinity copper transporter Ctr1. *Nat Commun.* (2019) 10:1386. doi: 10.1038/s41467-019-09376-7
24. Hopkins RG, Failla ML. Chronic intake of a marginally low copper diet impairs *in vitro* activities of lymphocytes and neutrophils from male rats despite minimal impact on conventional indicators of copper status. *J Nutr.* (1995) 125:2658–68. doi: 10.1093/jn/125.10.2658
25. Hirase N, Abe Y, Sadamura S, Yufu Y, Muta K, Umemura T, et al. Anemia and neutropenia in a case of copper deficiency: role of copper in normal hematopoiesis. *Acta Haematol.* (1992) 87:195–7. doi: 10.1159/000204758
26. Percival SS. Neutropenia caused by copper deficiency: possible mechanisms of action. *Nutr Rev.* (1995) 53:59–66. doi: 10.1111/j.1753-4887.1995.tb01503.x
27. Higuchi S, Higashi A, Nakamura T, Yanabe Y, Matsuda I. Anti-neutrophil antibodies in patients with nutritional copper deficiency. *Eur J Pediatr.* (1991) 150:327–30. doi: 10.1007/BF01955933
28. Hartwig C, Zlatic SA, Wallin M, Vrailas-Mortimer A, Fahrni CJ, Faundez V. Trafficking mechanisms of P-type ATPase copper transporters. *Curr Opin Cell Biol.* (2019) 59:24–33. doi: 10.1016/j.ceb.2019.02.009
29. La Fontaine S, Theophilos MB, Firth SD, Gould R, Parton RG, Mercer JF. Effect of the toxic milk mutation (tx) on the function and intracellular localization of Wnd, the murine homologue of the Wilson copper ATPase. *Hum Mol Genet.* (2001) 10:361–70. doi: 10.1093/hmg/10.4.361
30. Huster D, Finegold MJ, Morgan CT, Burkhead JL, Nixon R, Vanderwerf SM, et al. Consequences of copper accumulation in the livers of the Atp7b$^{-/-}$ (Wilson disease gene) knockout mice. *Am J Pathol.* (2006) 168:423–34. doi: 10.2353/ajpath.2006.050312
31. Czlonkowska A, Litwin T, Dusek P, Ferenci P, Lutsenko S, Medici V, et al. Wilson disease. *Nat Rev Dis Primers.* (2018) 4:21. doi: 10.1038/s41572-018-0018-3
32. Morrell A, Tallino S, Yu L, Burkhead JL. The role of insufficient copper in lipid synthesis and fatty-liver disease. *IUBMB Life.* (2017) 69:263–70. doi: 10.1002/iub.1613
33. Jonczy A, Lipinski P, Ogorek M, Starzynski RR, Krzysztofik D, Bednarz A, et al. Functional iron deficiency in toxic milk mutant mice (tx-J) despite high hepatic ferroportin: a critical role of decreased GPI-ceruloplasmin expression in liver macrophages. *Metallomics.* (2019) 11:1079–92. doi: 10.1039/C9MT00035F
34. Lenartowicz M, Starzynski RR, Jonczy A, Staron R, Antoniuk J, Krzeptowski W, et al. Copper therapy reduces intravascular hemolysis and derepresses ferroportin in mice with mosaic mutation (Atp7a(mo-ms)): An implication for copper-mediated regulation of the Slc40a1 gene expression. *Biochim Biophys Acta Mol Basis Dis.* (2017) 1863:1410–21. doi: 10.1016/j.bbadis.2017.02.020
35. Lenartowicz M, Windak R, Tylko G, Kowal M, Styrna J. Effects of copper supplementation on the structure and content of elements in kidneys of mosaic mutant mice. *Biol Trace Elem Res.* (2010) 136:204–20. doi: 10.1007/s12011-009-8533-4
36. Flurkey K, Currer JM, Harrison DE. The mouse in aging research. In: *The Mouse in Biomedical Research. 2nd Edn.* Fox JG, et al. editors. Burlington, MA: American College Laboratory Animal Medicine Elsevier. (2007). p. 637–672.
37. Coronado V, Nanji M, Cox DW. The Jackson toxic milk mouse as a model for copper loading. *Mamm Genome.* (2001) 12:793–5. doi: 10.1007/s00335-001-3021-y
38. Jenne CN, Wong CH, Zemp FJ, McDonald B, Rahman MM, Forsyth PA, et al. Neutrophils recruited to sites of infection protect from virus challenge by releasing neutrophil extracellular traps. *Cell Host Microbe.* (2013) 13:169–80. doi: 10.1016/j.chom.2013.01.005

39. Heit B, Liu L, Colarusso P, Puri KD, Kubes P. PI3K accelerates, but is not required for, neutrophil chemotaxis to fMLP. *J Cell Sci.* (2008) 121:205–14. doi: 10.1242/jcs.020412
40. Yipp BG, Petri B, Salina D, Jenne CN, Scott BN, Zbytnuik LD, et al. Infection-induced NETosis is a dynamic process involving neutrophil multitasking *in vivo*. *Nat Med.* (2012) 18:1386–93. doi: 10.1038/nm.2847
41. Heymann F, Tacke F. Immunology in the liver–from homeostasis to disease. *Nat Rev Gastroenterol Hepatol.* (2016) 13:88–110. doi: 10.1038/nrgastro.2015.200
42. Lefebvre T, Millot S, Richard E, Blouin JM, Lalanne M, Lamrissi-Garcia I, et al. Genetic background influences hepcidin response to iron imbalance in a mouse model of hemolytic anemia (Congenital erythropoietic porphyria). *Biochem Biophys Res Commun.* (2019) 520:297–303. doi: 10.1016/j.bbrc.2019.09.141
43. Wong CH, Jenne CN, Petri B, Chrobok NL, Kubes P. Nucleation of platelets with blood-borne pathogens on Kupffer cells precedes other innate immunity and contributes to bacterial clearance. *Nat Immunol.* (2013) 14:785–92. doi: 10.1038/ni.2631
44. Clark SR, Ma AC, Tavener SA, McDonald B, Goodarzi Z, Kelly MM, et al. Platelet TLR4 activates neutrophil extracellular traps to ensnare bacteria in septic blood. *Nat Med.* (2007) 13:463–9. doi: 10.1038/nm1565
45. Barrios M, Rodriguez-Acosta A, Gil A, Salazar AM, Taylor P, Sanchez EE, et al. Comparative hemostatic parameters in BALB/c, C57BL/6 and C3H/He mice. *Thromb Res.* (2009) 124:338–43. doi: 10.1016/j.thromres.2008.11.001
46. Patil M, Sheth KA, Krishnamurthy AC, Devarbhavi H. A review and current perspective on Wilson disease. *J Clin Exp Hepatol.* (2013) 3:321–36. doi: 10.1016/j.jceh.2013.06.002
47. Kuo YM, Gybina AA, Pyatskowit JW, Gitschier J, Prohaska JR. Copper transport protein (Ctr1) levels in mice are tissue specific and dependent on copper status. *J Nutr.* (2006) 136:21–6. doi: 10.1093/jn/136.1.21
48. Angus DC, van der Poll T. Severe sepsis and septic shock. *N Engl J Med.* (2013) 369:840–51. doi: 10.1056/NEJMra1208623
49. Jirillo E, Caccavo D, Magrone T, Piccigallo E, Amati L, Lembo A, et al. The role of the liver in the response to LPS: experimental and clinical findings. *J Endotoxin Res.* (2002) 8:319–27. doi: 10.1179/096805102125000641
50. Francis RJ, Butler RE, Stewart GR. Mycobacterium tuberculosis ESAT-6 is a leukocidin causing Ca2+ influx, necrosis and neutrophil extracellular trap formation. *Cell Death Dis.* (2014) 5:e1474. doi: 10.1038/cddis.2014.394
51. Niemiec MJ, De Samber B, Garrevoet J, Vergucht E, Vekemans B, De Rycke R, et al. Trace element landscape of resting and activated human neutrophils on the sub-micrometer level. *Metallomics.* (2015) 7:996–1010. doi: 10.1039/C4MT00346B
52. Paues Goranson S, Thalin C, Lundstrom A, Hallstrom L, Lasselin J, Wallen H, et al. Circulating H3Cit is elevated in a human model of endotoxemia and can be detected bound to microvesicles. *Sci Rep.* (2018) 8:12641. doi: 10.1038/s41598-018-31013-4
53. Ermert D, Urban CF, Laube B, Goosmann C, Zychlinsky A, Brinkmann V. Mouse neutrophil extracellular traps in microbial infections. *J Innate Immun.* (2009) 1:181–93. doi: 10.1159/000205281
54. Croce AC, De Simone U, Freitas I, Boncompagni E, Neri D, Cillo U, et al. Human liver autofluorescence: an intrinsic tissue parameter discriminating normal and diseased conditions. *Lasers Surg Med.* (2010) 42:371–8. doi: 10.1002/lsm.20923
55. Slaba I, Wang J, Kolaczkowska E, McDonald B, Lee WY, Kubes P. Imaging the dynamic platelet-neutrophil response in sterile liver injury and repair in mice. *Hepatology.* (2015) 62:1593–605. doi: 10.1002/hep.28003
56. Pousset D, Piller V, Bureaud N, Piller F. High levels of ceruloplasmin in the serum of transgenic mice developing hepatocellular carcinoma. *Eur J Biochem.* (2001) 268:1491–9. doi: 10.1046/j.1432-1327.2001.02015.x
57. Colotta F, Re F, Polentarutti N, Sozzani S, Mantovani A. Modulation of granulocyte survival and programmed cell death by cytokines and bacterial products. *Blood.* (1992) 80:2012–20. doi: 10.1182/blood.V80.8.2012.2012
58. Rana SV. Metals and apoptosis: recent developments. *J Trace Elem Med Biol.* (2008) 22:262–84. doi: 10.1016/j.jtemb.2008.08.002
59. Shi Z, Liang XL, Lu BX, Pan SY, Chen X, Tang QQ, et al. Diminution of toxic copper accumulation in toxic milk mice modeling Wilson disease by embryonic hepatocyte intrasplenic transplantation. *World J Gastroenterol.* (2005) 11:3691–5. doi: 10.3748/wjg.v11.i24.3691
60. Dixon LJ, Barnes M, Tang H, Pritchard MT, Nagy LE. Kupffer cells in the liver. *Compr Physiol.* (2013) 3:785–97. doi: 10.1002/cphy.c120026
61. Hutchins NA, Wang F, Wang Y, Chung CS, Ayala A. Kupffer cells potentiate liver sinusoidal endothelial cell injury in sepsis by ligating programmed cell death ligand-1. *J Leukoc Biol.* (2013) 94:963–70. doi: 10.1189/jlb.0113051
62. Zigmond E, Samia-Grinberg S, Pasmanik-Chor M, Brazowski E, Shibolet O, Halpern Z, et al. Infiltrating monocyte-derived macrophages and resident kupffer cells display different ontogeny and functions in acute liver injury. *J Immunol.* (2014) 193:344–53. doi: 10.4049/jimmunol.1400574
63. Babu U, Failla ML. Respiratory burst and candidacidal activity of peritoneal macrophages are impaired in copper-deficient rats. *J Nutr.* (1990) 120:1692–9. doi: 10.1093/jn/120.12.1692
64. Babu U, Failla ML. Copper status and function of neutrophils are reversibly depressed in marginally and severely copper-deficient rats. *J Nutr.* (1990) 120:1700–9. doi: 10.1093/jn/120.12.1700
65. Pilsczek FH, Salina D, Poon KK, Fahey C, Yipp BG, Sibley CD, et al. A novel mechanism of rapid nuclear neutrophil extracellular trap formation in response to *Staphylococcus aureus*. *J Immunol.* (2010) 185:7413–25. doi: 10.4049/jimmunol.1000675
66. Tatsiy O, McDonald PP. Physiological stimuli induce PAD4-dependent, ROS-independent NETosis, with early and late events controlled by discrete signaling pathways. *Front Immunol.* (2018) 9:2036. doi: 10.3389/fimmu.2018.02036
67. Lominadze DG, Saari JT, Miller FN, Catalfamo JL, Justus DE, Schuschke DA. Platelet aggregation and adhesion during dietary copper deficiency in rats. *Thromb Haemost.* (1996) 75:630–4. doi: 10.1055/s-0038-1650334
68. Schuschke DA, Saari JT, Nuss JW, Miller FN. Platelet thrombus formation and hemostasis are delayed in the microcirculation of copper-deficient rats. *J Nutr.* (1994) 124:1258–64. doi: 10.1093/jn/124.8.1258
69. Zhai Q, Li T, Yu L, Xiao Y, Feng S, Wu J, et al. Effects of subchronic oral toxic metal exposure on the intestinal microbiota of mice. *Sci Bull.* (2017) 62:831–40. doi: 10.1016/j.scib.2017.01.031
70. Zhang D, Chen G, Manwani D, Mortha A, Xu C, Faith JJ, et al. Neutrophil ageing is regulated by the microbiome. *Nature.* (2015) 525:528–32. doi: 10.1038/nature15367
71. Miller KA, Vicentini FA, Hirota SA, Sharkey KA, Wieser ME. Antibiotic treatment affects the expression levels of copper transporters and the isotopic composition of copper in the colon of mice. *Proc Natl Acad Sci USA.* (2019) 116:5955–60. doi: 10.1073/pnas.1814047116
72. Geng H, Shu S, Dong J, Li H, Xu C, Han Y, et al. Association study of gut flora in Wilson's disease through high-throughput sequencing. *Medicine.* (2018) 97:e11743. doi: 10.1097/MD.0000000000011743
73. Gow PJ, Smallwood RA, Angus PW, Smith AL, Wall AJ, Sewell RB. Diagnosis of Wilson's disease: an experience over three decades. *Gut.* (2000) 46:415–9. doi: 10.1136/gut.46.3.415

Conflict of Interest: The authors declare that the research was conducted in the absence of any commercial or financial relationships that could be construed as a potential conflict of interest.

frontiers in Immunology

REVIEW
published: 31 January 2020
doi: 10.3389/fimmu.2020.00078

Imaging Platelet Processes and Function—Current and Emerging Approaches for Imaging *in vitro* and *in vivo*

Samantha J. Montague[1], *Yean J. Lim*[1,2], *Woei M. Lee*[1,2] *and Elizabeth E. Gardiner*[1]*

[1] ACRF Department of Cancer Biology and Therapeutics, The John Curtin School of Medical Research, The Australian National University, Canberra, ACT, Australia, [2] Research School of Electrical, Energy and Materials Engineering, The Australian National University, Canberra, ACT, Australia

OPEN ACCESS

Edited by:
Elzbieta Kolaczkowska, Jagiellonian University, Poland

Reviewed by:
Heyu Ni, University of Toronto, Canada
Kellie Machlus, Brigham and Women's Hospital and Harvard Medical School, United States

***Correspondence:**
Elizabeth E. Gardiner
elizabeth.gardiner@anu.edu.au

Specialty section:
This article was submitted to Inflammation, a section of the journal Frontiers in Immunology

Received: *23 November 2019*
Accepted: *13 January 2020*
Published: *31 January 2020*

Citation:
Montague SJ, Lim YJ, Lee WM and Gardiner EE (2020) Imaging Platelet Processes and Function—Current and Emerging Approaches for Imaging in vitro and in vivo. Front. Immunol. 11:78. doi: 10.3389/fimmu.2020.00078

Platelets are small anucleate cells that are essential for many biological processes including hemostasis, thrombosis, inflammation, innate immunity, tumor metastasis, and wound healing. Platelets circulate in the blood and in order to perform all of their biological roles, platelets must be able to arrest their movement at an appropriate site and time. Our knowledge of how platelets achieve this has expanded as our ability to visualize and quantify discreet platelet events has improved. Platelets are exquisitely sensitive to changes in blood flow parameters and so the visualization of rapid intricate platelet processes under conditions found in flowing blood provides a substantial challenge to the platelet imaging field. The platelet's size (~2 μm), rapid activation (milliseconds), and unsuitability for genetic manipulation, means that appropriate imaging tools are limited. However, with the application of modern imaging systems to study platelet function, our understanding of molecular events mediating platelet adhesion from a single-cell perspective, to platelet recruitment and activation, leading to thrombus (clot) formation has expanded dramatically. This review will discuss current platelet imaging techniques *in vitro* and *in vivo*, describing how the advancements in imaging have helped answer/expand on platelet biology with a particular focus on hemostasis. We will focus on platelet aggregation and thrombus formation, and how platelet imaging has enhanced our understanding of key events, highlighting the knowledge gained through the application of imaging modalities to experimental models *in vitro* and *in vivo*. Furthermore, we will review the limitations of current imaging techniques, and questions in thrombosis research that remain to be addressed. Finally, we will speculate how the same imaging advancements might be applied to the imaging of other vascular cell biological functions and visualization of dynamic cell-cell interactions.

Keywords: platelet, thrombosis, microscopy-brightfield, polarized light, interference, scanning electron, microscope, receptors

INTRODUCTION

Imaging and Platelets

Platelets are minute disk-shaped cells that are produced from megakaryocytes and have prominent roles in hemostasis. Platelets contain many granules that hold growth factors, chemokines, and other platelet-activating molecules and proteins and have an open canalicular system (OCS) important for protein transport. Furthermore, platelets also have a plethora of membrane surface receptors that are vital for platelet activation and thus, function, and for interactions with other immune cells including leukocytes (1, 2), malaria-infected red cells (3) and adaptive immune cells (4–6).

Excellent historical accounts of the first visual observations of platelets have been extensively reviewed (7, 8). Notable observations were made by Max Shultze (9) and Bizzozero (10), both pioneers of cell biology who adapted existing oil immersion microscopes within moist chambers to visualize blood "particles" and describe them as another blood component distinct from leukocytes and erythrocytes. Bizzozero also described how platelets had a physiological role in stopping hemorrhages (bleeds) in vessels (10).

Since the development of rudimentary immersion lenses, a number of improved and unique optics and laser technologies have emerged. These modern imaging tools are designed to observe diverse molecular and morphological changes of cells and/or dynamic interactions within a network of living cells *in vitro* and *in vivo*. For analyses of blood cell function, applications have largely focused on immune and red blood cell (RBC) biology as these cells are $>5\,\mu m$ in diameter and are well-suited for most commercial micro-imaging tools, where imaging in three dimensions at high spatial resolution is achievable.

Platelets, on the other hand, have received less focus, due to both being small in size (around 2–3 μm) and with the potential to be rapidly activated. The biophysical properties of platelets are distinct in their sensitivity to changes in blood fluid shear force, thus capturing platelet events at physiological flow rates requires high performance imaging systems as platelets are highly susceptible to motion blurring. Thus, platelet imaging under physiological flow conditions tests the limitation of spatial-temporal imaging resolution where sub-platelet structures are not visible (11).

Platelets, the Infantry of the Blood

Platelets circulate in the blood in a resting, quiescent state, with circulating levels maintained at a constant level within the normal range 150–400 $\times$ 10^9 platelets per liter of blood in healthy people (12). Human platelets circulate for between 7 and 10 days and are selectively removed by resident cells of the liver or spleen for clearance unless they are consumed as part of a hemostatic response (13). Although platelets do not contain a nucleus (therefore no DNA), they contain RNA, ribosomes, mitochondria, and a number of storage organelles and granules, which are dynamically regulated during normal platelet function (14, 15).

Granules

Platelet alpha, dense, gamma, and lambda granules contain chemokines (platelet factor 4; PF4, CXCL7), growth factors (vascular endothelial growth factor; VEGF, platelet-derived growth factor; PDGF), coagulation proteins and platelet-activating molecules (ADP, Factor V, Factor XIII, fibrinogen, and von Willebrand Factor; VWF) as well as lysosomes/proteolytic enzymes (16–18). Release of platelet granular contents helps stabilize platelet aggregates, enhance further platelet recruitment, and amplifying wound repair and immunological and inflammatory processes (15, 19–21). Often these granule contents can be used to indicate and quantify platelet activation.

Adheso-Signaling Receptors

Platelets have a host of membrane-associated receptors that engage with one or more counter-receptors or plasma/extracellular matrix proteins. Of major importance, glycoprotein (GP) Ib-IX-V, which binds VWF as well as P-selectin, Factors XI and XII, leukocyte integrin αMβ2, collagen, thrombin and kininogen, and GPVI, which binds collagen, fibrin and laminin (22), initiate platelet adhesion events. These receptors act in concert (23) to translate cues from the surrounding vascular environment to mediate molecular signaling pathways that lead to platelet activation, platelet adhesion as well as mediating interactions with other cells (24, 25). The goal is for platelets to adhere and seal the damaged vessel area, thus maintaining hemostasis (26). Platelet receptor engagement triggers phosphorylation and activation of intracellular molecules (Src family kinases, phosphoinositol-3 kinase and protein kinase C), degranulation, and the rearrangement of the cytoskeleton causing platelet shape change (27). Ultimately, these activation steps result in the activation of the platelet-specific integrin αIIbβ3, which non-covalently binds dimeric plasma fibrinogen as well as potentially other plasma proteins (fibronectin, cadherins, VWF) thus bridging adjacent platelets (28).

As platelets also contain an OCS, receptor engagement and cytoskeletal rearrangement coordinates the exposure of this specialized internal membrane network that is important for protein transport (29) and amplification of prothrombotic responses. The cytoskeletal rearrangement enables platelet receptors to cluster (30, 31) which amplifies signaling events and helps stabilize platelet contact points. Activated platelet membranes become negatively charged through the exposure of phosphatidylserine and this mediates procoagulant (thrombin generating) capacity (32). Phosphatidylserine exposure can also occur in pathophysiological settings such as on exposure of murine platelets to antiplatelet autoantibodies (33). An additional consequence of receptor activation is the metalloproteolytic shedding of the ligand-binding ectodomains of GPIbα (the ligand-binding portion of GPIb-IX-V) and GPVI receptors. Through this metalloproteolytic process, thrombus propagation may be controlled and limited (34, 35).

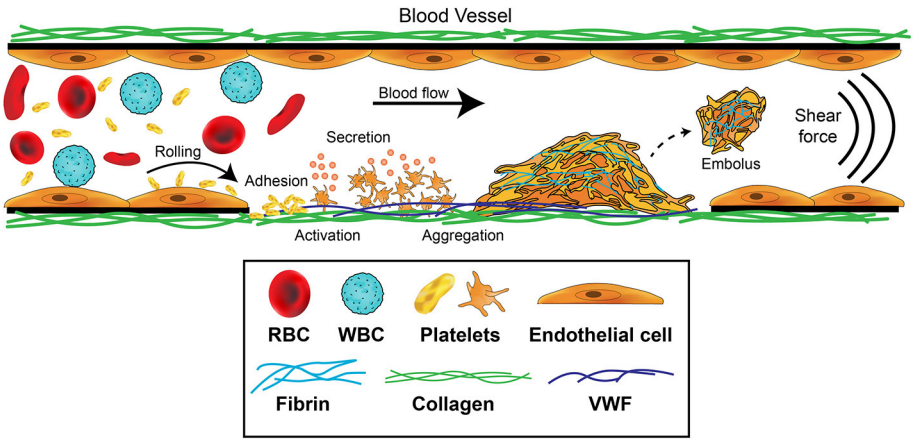

FIGURE 1 | Platelet contributions to thrombus formation. Platelets circulate in the blood stream in a quiescent (resting) state. When exposed extracellular matrix proteins such as von Willebrand Factor (VWF) or collagen are detected at the site of injury, platelets are induced to roll, and then adhere. The GPIb-IX-V complex and GPVI receptors on platelets orchestrate this adhesion and activation process. Adherent platelets become activated, expose P-selectin and phosphatidylserine, and secrete secondary mediators such as ADP and thromboxane. This promotes platelet recruitment and activation of αIIbβ3 which mediates platelet aggregation by binding plasma fibrinogen. Coagulation is also activated resulting in fibrin formation following thrombin cleavage of fibrinogen, leading to the consolidation of the platelet aggregate into a thrombus and healing of the damaged area. Fibrinolytic processes eventually dissolve the formed thrombus, causing the thrombus to embolize. Thrombosis occurs when there is increased coagulation and exaggerated thrombus formation and/or reduction of fibrinolytic processes, potentially leading to occlusion of the blood vessel.

The Process of Thrombus Formation

Thrombosis is an exaggerated and generally undesired form of hemostasis where there is uncontrolled platelet adhesion and aggregation, leading to increased thrombin formation, and fibrin generation (36). Large thrombi (blood clots) may occlude blood vessels or undergo embolization, where the thrombi break apart and pieces move to occlude smaller vessels causing strokes and myocardial infarction (37). Arterial thrombosis usually is triggered by rupture of a collagen- and tissue factor-rich stenotic plaque at relatively high (1,000–5,000 s^{-1}) wall shear rates, which are sufficient to unfold VWF and activate platelets. Venous thrombosis occurs at very low or static (0–200 s^{-1}) shear rates with contributions from the vascular bed and inflammatory cells (38). Together, acute venous and arterial thrombosis accounts for the most common causes of death in developed countries (39–41).

Platelet aggregation leading to thrombus formation is a multistep adhesion process (**Figure 1**) involving distinct receptors and adhesive ligands, with the contribution of individual receptor-ligand interactions to the aggregation process dependent on the prevailing blood flow conditions (42, 43). Platelets normally circulate in a quiescent, latent form but initially roll, then adhere at sites of endothelial injury, where matrix proteins such as collagen, VWF or laminin are exposed. If the rheological conditions are altered such that non-laminar disrupted flow is present, platelet activation is also immediately triggered (36, 44, 45). Engagement of GPIbα by the A1 domain of VWF under a shear force is critical for generation of ligand–receptor signals (46, 47). Intracellular signals then trigger platelets to change shape and flatten, cluster receptors, undergo calcium flux, generate reactive oxygen species and begin to degranulate. These steps serve to stabilize the adherent platelet, amplify the platelet activation, and enhance recruitment of additional platelets to the aggregate. Platelets are able to form stable adhesion contacts at all shear rates found throughout the vasculature (48) and activation can occur directly in flowing blood—within regions of a flowing blood column that can impart either intermittent or sustained elevated shear exposure in the absence of blood vessel wall contact (49).

Development of high-speed imaging approaches have enabled many laboratories to evaluate and quantify this process *in vitro* and our understanding of how receptors, vascular constituents, rheology and secondary messengers released from platelets contribute to this process has expanded. Nonetheless, important additional contributions of RBCs and leukocytes as well as contributions from specific vascular beds, coagulation processes and blood rheology considerations are generally missing from experiments *in vitro*, meaning that many aspects of this system remain to be well-defined.

Imaging Platelet Function *in vitro* to Advance Our Understanding of Thrombosis

In the modern era, platelet function can be readily imaged *in vitro* using advanced light-based microscopy systems with phase contrast or fluorescence capabilities (**Table 1**). In many cases, the isolation of human platelets from anticoagulated blood is desirable to reduce cellular autofluorescence (68) and allow clearer visualization of platelets. Platelet isolation is rapidly achieved using low speed centrifugation (110 *g*), to obtain a preparation of platelet-rich plasma (PRP; platelets plus all plasma proteins) with minimal numbers of RBCs and leukocytes. Removal of microparticles can be achieved by ultracentrifugation of isolated plasma at >100,000 *g* and used for platelet resuspension. Using selected anticoagulants and wash

TABLE 1 | Imaging techniques and applications for platelet research *in vitro*.

Imaging method	Key points	Resolution	Platelet/cell imaging applications	Limitations	References
Conventional/ Bright-field/Widefield	Uses visible light or high intensity light sources to illuminate a sample	*L* = 200–300 nm *Ax* = 500–800 nm	Thrombus formation >Microfluidics Large platelet aggregates	Low resolution Not suitable for single cell evaluation Limited by wavelength of light and NA of objective lens	(50)
Confocal/CLSM	Uses light to illuminate a sample through a pinhole to improve optical resolution Uses spatial filtering to block out-of-focus light	L = >200 nm (reflection) >250 nm (fluorescence)	Thrombus formation Platelet spreading >Surface receptor information Healthy controls vs. patients differences > wild type mice vs. knock out mice differences	Fluorescence label Surface area and receptors data Minimal information on cytoskeleton	(50–52)
QPM/DHM	Generates quantitative measurements from shifts in phase	L = >270 nm	Volumetric measurements of thrombus formation	No receptor profile details Requires complex post-image analysis	(53–56)
CLEM/3D cryoEM	Approaching atomic level analysis of ultrastructural changes, adhesion, and granule secretion	L = < 1 nm	Platelet secretion; Megakaryocyte positioning in sinusoids and platelet production (applied in intravital setting)	Samples need to be mounted on a grid; precise solvent requirements	(57–60)
STED	Confocal excitation beam overlaid by a depletion beam to inhibit fluorescence emission at target area of interest	L = 50–60 nm	Platelet protein distribution when co-incubated with cancer cells Platelet protein storage	Deconvolution required Need specific STED dyes Decreased scan step size + increased acquisition time	(61–64)
SMLM SIM PALM (d) STORM PAINT	Illumination that relies on single molecule switching by stochastic excitation Switching on/off of a fluorescent molecule or through excitation	L = >20 nm *Ax* = >50 nm	Platelet cytoskeleton proteins Actin nodules/tubulin Megakaryocyte structure and function Synapses Platelet receptor co-localization and receptor clustering	Computer power/software and storage Vast number of data points Post-data analysis and complex image reconstruction Specific photoswitchable and activatable fluorescence labels	(31, 65–67)

A non-exhaustive list of imaging techniques used to study platelet spreading, function, receptor profiles, and platelet protein/cytoskeletal protein organization in vitro. Rows highlighted in blue are examples of microscopy approaches that operate at nanoscopic/super resolution limits of diffraction. L, Laterally; Ax, Axially; NA, numerical aperture; CLSM, Confocal Laser Scanning Microscopy; QPM, Quantitative Phase Microscopy; DHM, Digital Holographic Microscopy; CLEM, Correlative light-electron microscopy; cryoEM, Cryogenic Electron Microscopy; SPIM, Selective Plane Illumination Microscopy; STED, Stimulated Emission Depletion; SMLM, Single-Molecule Localization Microscopy; SIM, Structured Illumination Microscopy; PALM, Photo-Activated Localization Microscopy; STORM, Stochastic Optical Reconstruction Microscopy; PAINT, Point Accumulation for Imaging Nanoscale Topography.

buffers that control pH well, plasma proteins can be "washed" away from platelets to generate a washed platelet preparation that is free of all plasma components. This fractionation and preparation is ideal for single platelet imaging and spreading. In summary, the single cell imaging techniques have utility to examine specific surface receptors, platelet cytoskeletal changes, interactions with immobilized ligands such as collagen and fibrinogen, or platelet-cell interactions. Washed platelets, PRP and anticoagulated whole blood can be also used in microfluidic-based systems to examine thrombus formation under conditions found in flowing blood.

Micro-Imaging Platelets in a Dish

Platelets can quickly change from a rounded, non-adherent form to adhere and undergo rapid shape change (flatten) when exposed to purified immobilized ligands such as extracellular matrix proteins collagen and laminin and adhesive proteins, including fibrinogen and VWF. This "spreading" effect can lead to the formation of filopodia and lamellipodia with subsequent ability to actively mobilize, which requires cytoskeletal protein rearrangement, including polymerization of actin, and other cytoskeletal proteins (69). Platelet adhesion and extent of spreading (area covered) can be quantified.

Widefield microscopy, including phase contrast, total internal reflection fluorescence (TIRF) (70, 71), reflectance interference contrast (RIC) (72), differential interference contrast (DIC) (73) and confocal microscopy with fluorescence capabilities (74) have enabled visualization of activation events in real time including clustering of platelet receptors and cytoskeleton rearrangement following platelet contact with immobilized ligands. Washed platelets are usually resuspended in permeabilizing buffer containing fluorescently-tagged antibodies or probes targeting actin and tubulin (51, 75, 76), and allowed to spread at 37°C for 30–120 min on microscope slides coated with an immobilized ligand to visualize changes in cytoskeletal rearrangement (**Figure 2B**). Actin-mediated cytoskeletal rearrangements allow the formation of filopodia

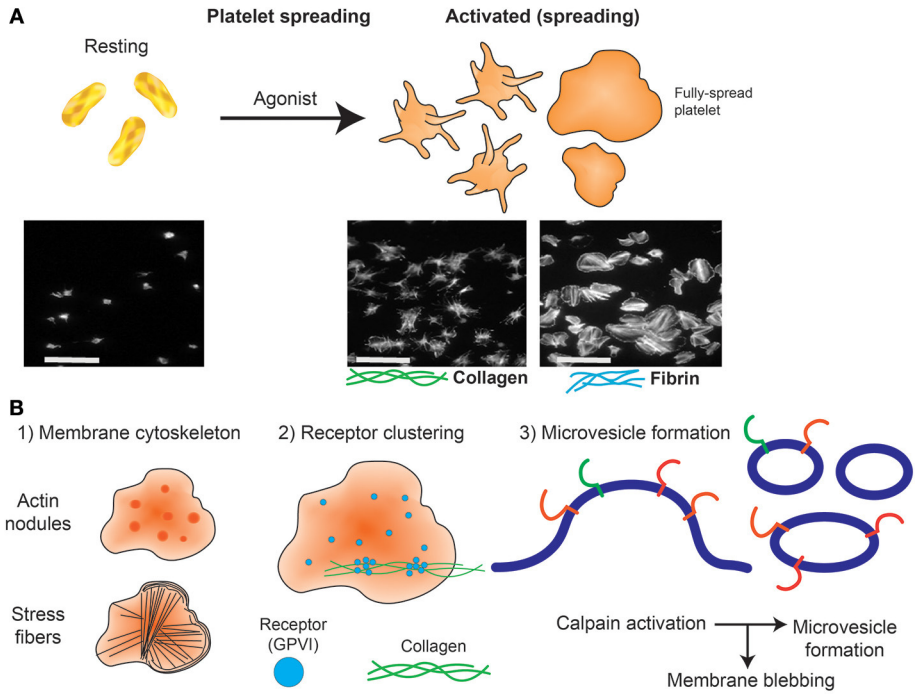

FIGURE 2 | Platelet spreading. **(A)** Under resting conditions platelets normally are non-adherent. Upon exposure to an activating agonist, platelets change shape by reorganizing cytoskeletal elements, leading to the formation of filopodia, followed by lamellipodia and an increase in surface area. When platelets are exposed to immobilized ligands in experiments *in vitro*, this shape change is known as platelet spreading. Light microscopy images shows actin arrangement and morphology of phalloidin-treated platelets exposed to non-coated coverslips (left) or coverslips pre-coated with collagen (middle) or fibrin (right). Images were taken using an inverted bright-field fluorescence microscope. Scale bar = 20 μm. **(B)** Schematic of processes that can be imaged during platelet spreading *in vitro* include (1) Cytoskeletal protein rearrangement, such as formation of actin nodules, microtubule organization and generation of stress fibers; (2) super resolution microscopy (dSTORM, SIM) can capture GPVI clustering (purple dots) and alignment along collagen fibers (green lines); (3) microvesicle formation can be imaged using optical systems that provide resolution below 150 nm; discrete cytoskeletal rearrangement occurs alongside calpain-dependent processes, where calcium-sensitive proteases detach membrane proteins, allowing membrane blebbing required for microvesicle release from platelets and megakaryocytes.

and then lamellipodia and microscopy has identified differential contributions of each of these structures to a forming thrombus (77). Live cell imaging has demonstrated roles for GTPase proteins including Cdc24, RAC1, and RhoA (78). Widefield microscopy has also been valuable in assessing megakaryocyte (platelet parental cell) function, including studying roles of receptors, cytokines and growth factors in pro-platelet formation (79–81).

Widefield microscopy imaging together with the availability of genetic data has helped identify and characterize platelet defects in patients with syndromes including Scott syndrome (82), Wiskott-Aldrich syndrome (65), and Filamin A disorders (83, 84). These syndromes are challenging to detect or evaluate using conventional platelet function testing due to associated thrombocytopenia (low platelet count). Of note, platelet spreading assays, which are not affected by low platelet count, can help define bleeding phenotypes in patient samples that are negative for an aggregation defect (85). The combination of biological optical microimaging with genomic information has opened up new avenues to test and evaluate these rare conditions that are not limited by low platelet counts but are still constrained by the limits of optical diffraction (86, 87).

Nanoscale Imaging of Single Platelets

Initial ultra-high resolution imaging studies of the platelet cytoskeleton and membrane glycoproteins were assessed using electron microscopy (EM) (88–90). EM is a highly specialized and time-consuming technique that provides excellently detailed nanometer scale level imaging resolution of platelet ultrastructure including intracellular organelles, cytoskeletal components, and storage granules that is beyond the resolution limits of conventional light microscopy. EM has been used to describe platelet dysfunction disorders, such as Gray Platelet syndrome, the rare congenital autosomal recessive bleeding disorder caused by an absence or deficiency in alpha granules (91, 92).

Scanning and transmission EM protocols generally require multiple washing of small portions of sample and can also integrate immunolabeling and negative staining techniques. Transmission EM requires thin tissue sections through which electrons can pass generating a projection image of the interior of cells, structure and organization of protein molecules and cytoskeletal filaments, and the arrangement of protein in cell membranes (by freeze-fracture). Scanning EM provides a wealth of information about surface topography, atomic composition and distribution of immunolabels. A limitation of EM samples

obtained from platelets from patients and thrombi are they often become unviable at the time of processing and this imposes limitations on the types of biological questions that can be pursued.

The emergence of super resolution microscopy and other nanoscopy techniques (93–95) have overcome several limitations of traditional light-based approaches to achieve nanometer resolution. Unlike EM techniques, these samples can be prepared using regular biochemical processes that preserve biological functions. Amongst many nanoscopic techniques, Structured Illumination Microscopy (SIM) and Single Molecule Localization Microscopy (SMLM) approaches (61) have provided unique insights into cytoskeletal protein clusters of actin nodules (65), tubulin and actin stress fibers (96, 97), and cytoskeletal rearrangement during platelet activation (98, 99). These approaches also have greatly improved knowledge of surface receptor co-localizations. For example, the platelet receptor GPVI has been shown to dimerize and cluster along collagen fibers (**Figure 2**) and is co-localized with integrin α2β1 (31). It will be interesting to apply these high resolution techniques to determine whether other receptor-ligand interactions, such as GPIb-IX-V on immobilized VWF, also demonstrate dynamic movement, and whether GPVI clusters in this way on fibrin(ogen) or other immobilized GPVI ligands. The consequences of receptor clustering on platelet aggregate formation and stability, and whether clustered receptors are protected from proteolytic cleavage by metalloproteinases such as A Disintegrin And Metalloproteinase (ADAM) 10 (100) are additional research questions that can now be addressed.

SIM imaging approaches are well-suited to evaluate platelet-specific defects in individuals and or genetically modified animals with congenital deficiencies in protein expression. For example, SIM has been applied to study spreading behavior and changes in cytoskeletal rearrangement in platelets with cytoskeletal protein deficiency; such as ARPC1-deficiency, where reduced actin-related protein 2/3 complex (Arp2/3) led to aberrant platelet spreading (66) and Wiskott-Aldrich syndrome protein (WASp) deficient platelets from patients and WASp knockout mice resulted in reduced actin nodule formation (65). With the expanding implementation of SIM in other microscopy methods (e.g., TIRF microscopy), we anticipate SIM to have increased applications in high to super-resolution imaging of platelet and thrombus behavior (101).

High resolution microscopy has also been valuable in assessing megakaryocyte (platelet parental cell) function, including studying roles of receptors, cytokines, and growth factors in pro-platelet formation (57, 80, 81). However, these imaging techniques have been developed for a static system, which does not permit implementation of fluid shear stress, a crucial physiological driver of platelet production. The next frontier, therefore, is to couple these imaging processes to microfluidic systems, and examine platelet and megakaryocyte processes under conditions found in flowing blood.

Brown et al. used electron tomography coupled with intravital correlative light-electron microscopy (CLEM) to capture thrombopoiesis events in real time and calculate megakaryocyte membrane parameters during this process of platelet production. They identified that mass fusion between internal and external membranes allows megakaryocytes to extend multiple protrusions rather than proplatelets into the marrow sinusoidal vessel space (58).

MICROFLUIDICS IMAGING OF PLATELETS: RECAPITULATING THROMBUS FORMATION *IN VITRO*

Laboratory Research and Extending to the Clinical Sector

Microfluidic devices and flow-based systems provide good avenues to study these concepts in combination, thus allowing coagulation, platelet function, and roles of shear to be studied simultaneously, using small quantities of blood (**Table 1**). Simple single channel microfluidic systems generally uses glass capillary tubes (optically clear) or conduits made using a mask to produce channels usually of 50–100 μm thick channels in polydimethylsiloxane (PDMS) which are mounted on glass coverslips (102). The channels or capillaries are coated with an adhesive ligand (103, 104). A syringe pump either pulls or pushes antibody- or fluorescently labeled blood, PRP or washed platelets in the presence of anticoagulant (generally trisodium citrate and PPACK), through the channel at constant shear rates which are determined by the velocity of the flow and viscosity values that are appropriate for the sample being evaluated. If the contribution of coagulation to the hemostatic process is to be assessed, then the sample must be carefully recalcified to overcome the anticoagulant (105, 106). The whole process is captured using a high-resolution objective lens with a high-speed photodetector or high-sensitivity camera (usually confocal or widefield/fluorescence). Altering channel geometrics can help study platelet aggregation/thrombus formation in conditions recapitulating pathological vessel geometries, stenotic vessels, and vessel areas where stagnation points and shear gradients may occur (107, 108). Microfluidic platforms have been reviewed in detail elsewhere (109, 110).

Many laboratories have used microfluidic systems to monitor thrombus formation, demonstrate the effects of fluid shear stress and define molecular events involved (110–114). Microfluidic studies have assessed thrombus formation in healthy donors (50, 115) and patients afflicted with von Willebrand disease, hemophilia, or thrombocytopenia (114, 116), and used to tease out points of difference between immobilized ligands. De Witt and colleagues ranked 52 different adhesive surfaces for thrombus formation at arterial and venous shear rates (104) and others have studied thrombus formation in blood from mice with genetically engineered deficiencies in platelet receptors or signaling proteins (50). At this time, the only commonly used clinical device that incorporates an element of shear stress to evaluate platelet function is the platelet function analyser (PFA)-100 or PFA-200 which assess time to occlusion of collagen/epinephrine or collagen/ADP coated cartridges by a sample of citrated whole blood. Values in healthy donor samples for time to occlusion are extremely broad and data are unreliable in samples where the hematocrit or platelet count is low (117).

Taken together, findings have led to the consensus that increasing shear stress promotes binding of platelet GPIbα

and/or αIIbβ3 to VWF, promoting activation and platelet aggregation (112, 118–120). Exposure to fluid shear stress or immobilization on a solid support matrix modulates VWF tertiary structure, inducing the molecule to unfold and expose sites within the A1 domain of VWF that directly bind to the GPIbα subunit of GPIb-IX-V. This generates signaling events that trigger platelet aggregation (46, 47). Therefore, the effect of pulsatile flow compared to constant flow on thrombus formation will be an important aspect in future studies, especially in the context of platelet activation in mechanical circulatory support devices, such as left ventricular assist devices (LVADs) and extracorporeal membrane oxygenation (ECMO) circuits (34, 108).

Recent studies have also assessed platelet receptor roles in thrombus growth and stability, with GPVI being a key potential player, through its interaction with fibrin in a growing thrombus (121, 122). Targeting of GPVI, a specific receptor found only on platelets and megakaryocytes, provides a good target for anti-platelet therapy without associated bleeding risks (123, 124). Microfluidic systems are therefore a useful tool to examine new GPVI antagonists on reducing thrombus growth and stability. ACT017, a humanized antibody fragment against GPVI, is an example of one of these targets tested with *in vitro* microfluidic systems and has progressed through Phase 1 trials (121, 125, 126).

Recapitulating a Blood Vessel in a Microfluidics System

Microfluidic imaging systems of whole blood exposed to shear have also provided insight into the contribution of RBCs to thrombus propagation, especially at venous shear rates (121, 127). RBCs are the most abundant blood cell type and are heavily glycosylated. They circulate through the central lumen of the vessel and serve to marginate platelets away from the lumen center and toward the vessel wall. RBCs are the major contributor to blood viscosity, and hence, to vascular fluid shear stress (128–130), which in turn impacts on platelet activity. Therefore, it is important to consider the contribution of RBCs in the design of all microfluidic imaging experiments, particularly when using RBC-free PRPs, or washed platelets. This is typically partially compensated by altering the shear stress in the microfluidic chamber.

Some efforts have been made to grow endothelial cells in microfluidic channels to evaluate endothelial cell contribution to platelet activation and recruitment for forming thrombi (48). Whilst challenging, the seeding, culturing and maintenance of viable endothelial cells to mimic a blood vessel environment in a microfluidic channel formed with a 3D collagen-based hydrogel has been successfully developed (131, 132). However, imaging in thick non-homogeneous cellular network requires good laser scanning microscopy techniques, i.e., intravital microscopy, that will be covered in greater detail in later sections.

Real Time Microfluidics Quantitative Imaging of Platelets

Thrombus surface area coverage, height and volume are commonly measured in microfluidic devices, but this often requires the use of fluorescently labeled antibodies or probes with variable affinities and efficiencies of binding to the platelet membrane. This approach is not always well-suited for live imaging quantification as these reagents can potentially interfere with normal platelet processes and receptor function. Additionally, laser microscopy increases the risk of photobleaching which, together with phototoxicity, are highly confounding variables during live measurement (133). Further, volumetric quantification is routinely conducted using total fluorescence intensity, which is ultimately limited by the dynamic range of the photodetectors and prone to signal saturation. Other quantitation mechanisms include generalized scoring of thrombi or using the integrated density of the fluorescence signal per field of view (50, 104, 134). These have allowed robust quantitation and comparisons of patient thrombi formed compared to healthy controls, but are not yet standardized approaches, meaning comparison of data across microfluidic systems and between laboratories is not always straightforward (135). Furthermore, most approaches require setting signal thresholds, which can introduce the potential for operator bias and impact on quantitation in real-time.

Although microfluidic systems have advanced the field, these systems do not perform well if coagulation is permitted to proceed. In anticoagulated microfluidic systems the physical properties of thrombi formed do not include the contribution of thrombin activation.

Imaging Hemostasis and Thrombosis Processes *in vivo*

Whilst imaging of thrombus formation *in vitro* has helped to quantify the contribution of platelet receptors, ligands, and other parameters to thrombus formation, imaging *in vivo* still remains the premier research tool as it permits assessment of thrombus formation in its native microenvironment, which considers contributions from coagulopathy, other blood cells and processes (for example neutrophil extracellular traps) and the endothelium (**Table 2**). Injury to a blood vessel may be induced using a precisely-guided laser, ligation of a blood vessel, topical application of ferric chloride, or by mechanical or electrolytic injury (150, 151). The selected mode of thrombosis-inducing injury very much depends on the vascular bed being examined and the experimental question being addressed as relative contributions of the surrounding endothelium, transitory leukocytes, and RBCs and the coagulation and complement pathways vary significantly with the mode of injury.

The development of rapid (spinning disk) laser scanning confocal microscopes (152) has enabled sufficient speed to capture transient events in flowing blood. Using laser scanning microscopy, there is sufficient depth penetration to image thrombus formation in mice using laser-induced injury models (136, 153). For example, Falati et al. have assessed the roles of platelet, tissue factor and fibrin in the formation of thrombi in mice after laser-induced endothelial injury (136). However, there is still limited depth which laser confocal microscopy can achieve due to high optical scattering (154). Since then, the inclusion of ultrafast laser systems for multiphoton microscope has open up

TABLE 2 | Imaging techniques and applications for platelet research *in vivo*.

Imaging method	Key points	Platelet/cell imaging applications	Limitations	References
Confocal scanning	Point scanning microscopy Emitted light selected through a pinhole	Intravital imaging Thrombus formation in mice	Acquisition speed Photobleaching	(136, 137)
1 photon	Excitation with 1 photon laser and illumination of focus and out of focus planes Pinhole distinguishes signal from out of focus plane	Thrombopoiesis (platelet generation)	Limited depth	(80)
2 photon	2 photon laser excitation in focal plane only	Skin Tumor imaging Platelet biogenesis	Limited depth (up to 1 mm) Specialist set up / "in house set ups"	(138)
Spinning disk	Scans sample at multiple points with a CCD camera	Platelet recruitment to injury sites in organs Thrombus formation Platelet-endothelial interactions	Cross-talk between pin holes Limited depth	(139–141)
Multiview SPIM/SIM view	Light-sheet system with switching between 4 pathways	Zebrafish heart development	Limited applications for larger organisms so far Ongoing development for fast 3D scanning	(142, 143)
SHG	2 photons scattered by molecule and emit 1 photon of half excitation wavelength	Collagen/myosin visualization Zebrafish embryos Tumors	Limited to number of structural proteins (unless adding to fluorescence microscopy) Depth limitation	(95, 144, 145)
THG	3 photons scattered by molecule and generate 1 photon of a third of excitation wavelength	Extracellular matrix proteins Tumors	Vessel width limits Excitation power required	(95, 146)
CARS	Non-linear optical process with 3 laser beams (pump, Stokes and probe) Beams interact to generate coherent signal	Tumor imaging/blood flow measurements	New/limited applications so far Complex set up Lacks information on phase	(147–149)

A non-exhaustive list of imaging techniques used to study platelet generation, function, and roles in thrombus formation in vivo and details of new imaging approaches and current limitations. SPIM, Selective Plane Illumination Microscopy; SIM, Structured Illumination Microscopy; DSLM, Digital Scanned laser Lightsheet fluorescence Microscopy; SHG, Second-Harmonic Generation microscopy; THG, Third Harmonic Generation microscopy; CARS, Coherent Anti-Stokes Raman Scattering microscopy.

new opportunities to reach from several hundred micrometers up to 1 millimeter in depth, which expands the hemostasis research questions that can be asked using blood vessels of animals *in vivo* (155). Indeed, the use of the term "intravital microscopy" is now synonymous with the use of multiphoton microscopes across biology.

Intravital Microscopy Systems

Intravital microscopy systems are now routine to study disease models because of the ability to capture cellular activities in its microenvironment. These instruments use an ultrafast laser system that achieves a reduction of light scattering in tissue and therefore increases depth of imaging. In addition, video rate intravital microscopy offers real-time monitoring so as to record rapid and dynamic events for accurate quantification of events at sub-cellular size scale (156, 157).

Intravital microscopy for thrombosis studies usually requires injection of fluorescently labeled platelets or fluorophore-conjugated antibodies to target a platelet receptor or protein of interest (150, 151). Mice that have been genetically altered to be deficient in a protein or genetically engineered to express reporter-tagged proteins in a cell-specific manner, such as GFP, YFP, and mCherry also have great utility (150, 158–160). Several reports have now used intravital imaging to investigate megakaryocyte-derived structures entering bone marrow sinusoids (161, 162) and platelet production.

Hemostasis and Thrombus Formation in Its Natural Microenvironment

The development of mice expressing multiple reporters, such as the colorful "confetti" mice reduces the reliance on antibody labeling of cells. For platelet studies, the R26R-Confetti mice were used to study migrating mechanoscavenging platelets that collect bacteria (74). Studies using transgenic mice expressing LifeAct-GFP have also revealed details of platelet actin cytoskeletal structure and nodules (65, 163). When pairing these fluorescent transgenic mice with an intravital microscope, it becomes possible to delve deep underneath dense tissue and potentially observe megakaryopoiesis and changes in ploidy and proplatelet formation and release into the blood stream (87, 164). Fluorescently-labeled platelets have enabled studies of platelet migration and platelet interactions with other blood cells, in a number of physiology scenarios, including inflammation (139), infection (165), and cancer (166).

Key thrombus formation studies *in vivo* have aimed to define the evolution of a thrombus by examining initial steps of platelet activation, signaling and recruitment, and how different extents of platelet activation can affect the stability of the formed thrombus. Stalker and colleagues visualized platelet recruitment following endothelial damage to a cremaster muscle microcirculation, and identified that platelets formed a thrombus with at least 2 distinct zones. The inner core zone contained tightly packed degranulated platelets (as measured by P-selectin

expression), which was co-localized with fibrin (167, 168), and had evidence of active thrombin (167, 169). The outer shell zone consisted of loosely-packed platelets, with reduced P-selectin expression and undetectable levels of fibrin. Other intravital laser-induced thrombosis studies have examined roles for tissue factor, thrombin generation (170), platelet receptors GPIbα (171, 172), GPVI (173, 174), protease-activated receptor 4 (175, 176), $P2Y_{12}$ (177, 178), and αIIbβ3 (153, 179, 180). Roles for plasma proteins, such as VWF and fibrinogen (170) fibronectin (181, 182) vitronectin (183) and neutrophil extracellular traps (165) and signaling molecules (184) in platelet activation and accumulation following damage to the endothelium have been defined using intravital imaging systems (150). Thrombi properties vary with the nature of the blood cellular composition and vascular bed as well as the extent of the induced injury, and therefore both factors will determine the response and level of the associated inflammation. This remains a major consideration in the choice of *in vivo* model and imaging modality.

Limitations of Imaging in Living Organs

A common challenge in intravital imaging is the maintenance of a comparable extent of injury within an animal and across a series of experiments in different batches of animals. This is dependent on consistent laser power, diameter of the laser beam, and depth of the blood vessel. This is especially difficult in confocal systems that often use dual laser sources (i.e., one for imaging and another to induce injury) that require considerable co-alignment in all 3 planar directions to achieve accurate and consistent laser injury. It is possible to use the laser for imaging to also induce laser injury (157) for example in multiphoton imaging, the high-energy near-infrared and infrared pulsed laser allows one to perform laser ablation at a localized section in tissue at a specified depth. To further extend the imaging depth achievable, longer infrared wavelength lasers for triple photon absorption are available and would be a great advantage to platelet researchers but can be limited to the range of excitable fluorophores (185).

The ideal system would allow consistent imaging of platelet recruitment and thrombus formation with minimal photobleaching at any chosen imaging depth. While there are numerous commercial multiphoton intravital microscopes available, the ability to achieve high speed, signal and depth drive many laboratories to build their own systems, which are adapted to the laboratory specifications and requirements (186). However, subtle differences and non-standard configurations mean that experimental conditions cannot be fully duplicated between laboratories.

While the implementation of fluorophores and fluorescent probes are an established method for visualization *in vivo* and *in vitro*, they face various limitations that can impact on the biological application studied or imaged, including interference with receptor signaling, cytotoxicity, and target specificity (**Table 2**). Thus, the heavy reliance on these biochemical tools can create significant issues with imaging *in vivo* (187, 188). Label-free intravital imaging offers an exciting option to reduce this issue and will allow imaging of platelets and their structures in their physiological environment. A label-free imaging approach will also reduce or remove phototoxicity and photobleaching complications and allow imaging of true dynamic events leading to platelet activation and thrombus formation.

Other potential intravital imaging techniques using multiphoton effects include second and third harmonic generation (SHG, THG) microscopy and Raman scattering (Coherent Anti-stokes Raman scattering; CARS). Many of these modalities have been established in other cell biology systems, and could be applied to intravital mouse thrombosis models (**Table 2**). SHG microscopy is a non-linear imaging technique, where light scattered over non-centrosymmetric molecules (including the extracellular matrix protein collagen) produces a photon at half the incident wavelength (95). THG microscopy involves non-linear light scattering originating from polarization of an excited volume, including at water-lipid/water-protein interfaces. Thus this approach is relevant to the imaging of molecular events at platelet and cell membranes (146). Raman/CARS microscopy detects signal from inelastic photon scattering upon interaction with matter (95), and would have utility in measuring thrombus volume.

An additional task that all high resolution imaging approaches bring is in the handling and processing of extremely large data files, the necessity to improve contrast and resolution, remove out of focus signal and correct for animal movement (e.g., breathing) that uses image registration (156). In addition to motion, images can be enhanced by going through image deconvolution processes (189, 190). For traditional deconvolution (except for blind deconvolution), it is necessary to first obtain an image of the ideal point spread function of the imaging system. Once the ideal point spread function is determined (191), one can then identify a suitable deconvolution mask to sharpen the images. A mismatch of the ideal point spread function of the system will introduce unnecessary image defects in deconvolved images (192). Upon imaging, it is crucial for imaging specialists to use image registration and deconvolution to improve final images and remove artifacts prior to quantification, in order to reduce errors (193).

Beyond Fluorescence Imaging: Quantitative Imaging Without Fluorescence Labeling *in vitro*

Reflectance Interference Contrast Microscopy (RICM) (46, 72) is one of the first non-label quantitative imaging approaches that uses interference to examine how platelets interact with an immobilized substrate. Although, this approach is sensitive to several nanometers above the coverslip glass, it is limited to measure signals from a small thickness (∼100 nanometers) of a single platelet and cannot be used to quantify volumetric information of platelet aggregates or thrombus.

Current standardized microfluidic imaging systems with label-free imaging approaches exploits the refractive index of platelets as its endogenous label. Since there is no nucleus in a platelet, the refractive index of platelets is likely to be stable, providing an opportunity to capture high amounts of quantitative data. Quantitative phase microscopy (QPM) provides measurements of cell depth by monitoring changes in refractive index, which shifts the phase of the incident light wave (53). QPM not only allows non-invasive and label-free imaging

of cells, it eliminates the risk of photo-bleaching and reduces optical distortion of samples (54). QPM has been implemented to quantify the volume, mass, and density of platelet aggregates and thrombi formed on collagen-coated microfluidic channels in the presence or absence of tissue factor when exposed to venous shear rates (73). Digital holographic microscopy (DHM), a form of holographic QPM, has been applied to imaging blood samples, and quantify platelet aggregates formed at low (100 s^{-1}) shear (194). More recently, DHM was used to quantitatively measure changes in volume of platelet aggregates over time when exposed to different shear rates (**Figure 3**). A stability index was developed by monitoring the reduction in thrombi volume after the established thrombi field was exposed to elevated (7,000 s^{-1} and 12,000 s^{-1}) shear rates using physiological buffered solution (55). The use of QPM with microfluidic systems permits acquisition of accurate values for thrombus height, area and volume without the requirement of fluorescence labeling and the potential to provide a new means of assessing platelet function in clinical samples.

Due to the ease and simplicity of sample handling, QPM techniques can aid predictive models of thrombus formation, contraction, and stability across a range of shear rates and are ideal modalities for development for point-of-care devices to assess platelet function and thrombosis and bleeding risk in at risk patients. These imaging approaches can address research questions targeting mechanisms involved in the regulation of thrombus size, for example the respective roles of metalloproteinases (34, 198) or tetraspanins (199, 200) in modulating thrombus size and stability. However, as QPM techniques rely on phase information in transmitted light, they can often be limited by strongly scattering media. For instance, RBCs are strong scattering agents, akin to tiny polymer lenses, and obscure the visualization of platelets during thrombus formation.

Integrating High Speed Imaging Into Microfluidic Systems

There is a wealth of molecular tools, platelet-reactive surfaces, microfluidic devices and imaging modalities that sit within research spaces, each approach with specific strengths and weaknesses. Ideally the acquisition of data will be performed under agreed standardized experimental conditions, permitting comparison and integration of findings into current models of thrombus formation under flow.

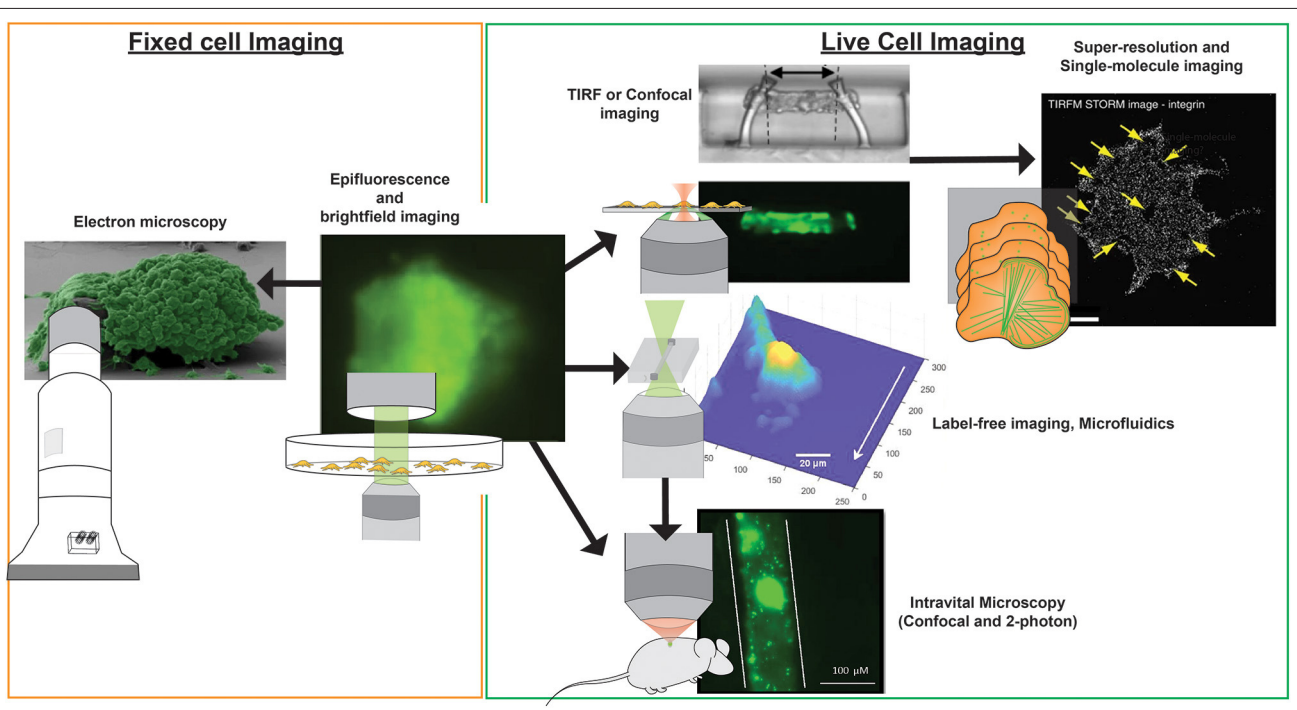

FIGURE 3 | Imaging modalities for visualizing platelets. Multiple imaging modalities can be used for platelet imaging depending on the process to be imaged and imaging environment. Epifluorescence and bright-field imaging are most commonly used for general assessment of thrombus size and the biochemical composition of platelets (195). Electron microscopy allows resolving fine physical structures of single or an aggregate of platelets but is limited to fixed samples (195). Where imaging of functional platelets is required, *in vitro* imaging using TIRF or confocal microscopy could reveal dynamic events of single platelet activity and thrombosis (196), with the option of employing super-resolution and single-molecule imaging techniques for nanometer resolution of fluorescently-tagged biomolecules (65). To recapitulate more physiological conditions, the use of microfluidics and label-free microscopy can provide physiological flow conditions and reduce the risk of phototoxicity incurred by photobleaching, respectively. Finally, *in vivo* platelet imaging has been realized by confocal and 2-photon microscopy, the latter which provides greater tissue penetration and less phototoxicity, but with a higher equipment cost (197). Microscopy images were obtained from https://doi.org/10.1038/s41467-019-09150-9, https://doi.org/10.1038/s41467-019-10067-6, https://doi.org/10.1038/ncomms8254, and https://doi.org/10.1371/journal.pone.0071447, under the Creative Commons license (CC BY 4.0, https://creativecommons.org/licenses/by/4.0/). Images were cropped and figure letters were removed for clarity.

In vitro Imaging Cytometry

Conventional flow cytometry requires a narrow stream of fluorescently labeled cells in suspension to enter a single weakly focused laser beam. This allows direct single point excitation of fluorescence from each cell passing through the focused laser beam. This approach is devoid of any spatial information with regards to the cell that has been detected and devoid of any morphological information for the detected cell.

Imaging flow cytometry (IFC) aims to incorporate high speed imaging into a flow cytometry system either through a high speed camera system or improved laser scanning methods (201). Although progress in the field of IFC has achieved imaging speed of several hundred imaging frames per second (202), the resolvable image resolutions and imaging depth of these IFC systems can detect platelet/cell aggregates (203, 204) and changes at the platelet membrane (205), but still cannot resolve sub-platelet structures owing to trade-offs between sensitivity, speed, and resolution of the sensor (206).

Currently there are no standardized methods available in the clinical hematology laboratory to evaluate platelet function under vascular fluid shear conditions. Hence, an imaging flow cytometry system that can evaluate platelet function in a standardized way in samples from people with platelet counts below 100×10^9/L would be an asset to clinical hematology. Real time assessment by point-of-care/clinical lab-based imaging flow cytometry devices using microfluidics could help address these issues. For example, information on platelet function in acquired thrombocytopenia at initial presentation and then after therapy could inform on platelet quality particularly if platelet count has not been normalized. Further, monitoring platelet function and thrombotic risk could help guide clinical decisions on patient-specific antiplatelet/anticoagulant therapy to help reduce thrombotic events.

In vivo Imaging Cytometry

The concept of *in vivo* IFC systems was developed to count, characterize, and image biological cells flowing in a living organism (in this case a mouse) at different time points, thus providing longitudinal information of biological events. The *in vivo* flow cytometer was first used to quantify the circulation lifetime of different tumor cells and monitor apoptotic cells in circulation (166, 207, 208) with single cell sensitivity. However, existing *in vivo* IFC approaches are limited by technological challenges that restrict 2D regions of interest to superficial layers of tissue, preventing the experimental interrogation of cellular and molecular events in major blood vessels. Application of laser scanning technology and laser beam shaping, have circumvented this limitation to achieve single cell analysis *in vivo*. For instance, a recent study used multiphoton microscopy techniques to expand the field of *in vivo* imaging tools and visualize calcium fluxes of 10,000 neurons over millimeter ranges (209).

More Than One Imaging Microscope: Multimodal Imaging

Until now, almost all platelet imaging has been conducted exclusively using a single type of microscope system i.e., spinning disk confocal and structured illumination microscopy. While it is convenient to adopt existing imaging protocols for platelet imaging, there are inherent challenges in imaging platelets due to the complex nature of the platelet-platelet aggregation process. Label-free imaging modalities such as photoacoustic imaging (210) and optical coherence tomography (211) can be combined with an existing multiphoton microscopy system to achieve both structural and fluorescence imaging (212).

CONCLUDING REMARKS

Many brilliant advances in imaging techniques for analyses using *in vivo* and *in vitro* approaches have helped build substantial understanding of roles of receptors, molecular signaling, and the relative contributions of RBCs, leukocytes and platelets to thrombosis and hemostasis as well as other vascular processes. These research-based approaches have been critical for exploration of new means to develop and evaluate novel therapeutics that ultimately improve patient hematology healthcare. The next stage will be to bring one or more of these imaging modalities into the clinical space in an appropriate format and with a well-characterized and standardized ability to evaluate and quantify platelet function in patients at risk of thrombosis, or with unexplained bleeding, or a low platelet count where assessment of platelet function is precluded from using standard hematology laboratory approaches. It is hoped that these tools will also be useful to assess anticoagulant and antiplatelet effectiveness and for stratifying patients who are at risk of thrombosis or bleeding.

AUTHOR CONTRIBUTIONS

All authors listed have made a substantial, direct and intellectual contribution to the work, and approved it for publication.

FUNDING

We received funding support from the National Health and Medical Research Council of Australia and the Australian Research Council.

REFERENCES

1. Weyrich AS, Zimmerman GA. Platelets: signaling cells in the immune continuum. *Trends Immunol.* (2004) 25:489. doi: 10.1016/j.it.2004.07.003
2. Rossaint J, Margraf A, Zarbock A. Role of platelets in leukocyte recruitment and resolution of inflammation. *Front Immunol.* (2018) 9:2712. doi: 10.3389/fimmu.2018.02712
3. Kho S, Barber BE, Johar E, Andries B, Poespoprodjo JR, Kenangalem E, et al. Platelets kill circulating parasites of all major Plasmodium species

in human malaria. *Blood.* (2018) 132:1332–44. doi: 10.1182/blood-2018-05-849307
4. Semple JW, Italiano JE, Freedman J. Platelets and the immune continuum. *Nat Rev Immunol.* (2011) 11:264–74. doi: 10.1038/nri2956
5. Iannacone M. Platelet-mediated modulation of adaptive immunity. *Sem Immunol.* (2016) 28:555–60. doi: 10.1016/j.smim.2016.10.008
6. Xu XR, Zhang D, Oswald BE, Carrim N, Wang X, Hou Y, et al. Platelets are versatile cells: new discoveries in hemostasis, thrombosis, immune responses, tumor metastasis and beyond. *Crit Rev Clin Lab Sci.* (2016) 53:409–30. doi: 10.1080/10408363.2016.1200008
7. Mazzarello P, Calligaro AL, Calligaro A. Giulio Bizzozero: a pioneer of cell biology. *Nat Rev Mol Cell Biol.* (2001) 2:776–81. doi: 10.1038/35096085
8. Berndt MC, Metharom P, Andrews RK. A brief history of blood platelets: a personal view. In: *Platelets in Thrombotic and Non-Thrombotic Disorders: Pathophysiology, Pharmacology and Therapeutics: an Update.* P Gresele, NS Kleiman, JA Lopez and CP Page, editors. Cham: Springer International Publishing (2017). p. 3–9. doi: 10.1007/978-3-319-47462-5_1
9. Schultze, M. Ein heizbarer Objecttisch und seine Verwendung bei Untersuchungen des Blutes. *Archiv f. mikrosk. Anatomie.* (1865) 1:1–42. doi: 10.1007/BF02961404
10. Bizzozero G. Su di un nuovo elemento morfologico del sangue dei mammiferi e della sua importanza nella trombosi e nella coagulazione. *L'Osservatore.* (1881) 17:785–7.
11. Ivanciu L, Stalker TJ. Spatiotemporal regulation of coagulation and platelet activation during the hemostatic response *in vivo*. *J. Thrombosis Haemostasis.* (2015) 13:1949–59. doi: 10.1111/jth.13145
12. Daly ME. Determinants of platelet count in humans. *Haematologica.* (2011) 96:10–3. doi: 10.3324/haematol.2010.035287
13. Quach ME, Chen W, Li R. Mechanisms of platelet clearance and translation to improve platelet storage. *Blood.* (2018) 131:1512–21. doi: 10.1182/blood-2017-08-743229
14. Van Holten TC, Bleijerveld OB, Wijten P, De Groot PG, Heck AJR, Barendrecht AD, et al. Quantitative proteomics analysis reveals similar release profiles following specific PAR-1 or PAR-4 stimulation of platelets. *Cardiovasc Res.* (2014) 103:140–6. doi: 10.1093/cvr/cvu113
15. Golebiewska EM, Poole AW. Platelet secretion: From haemostasis to wound healing and beyond. *Blood Rev.* (2015) 29:153–62. doi: 10.1016/j.blre.2014.10.003
16. Zufferey A, Schvartz D, Nolli S, Reny JL, Sanchez JC, Fontana P. Characterization of the platelet granule proteome: evidence of the presence of MHC1 in alpha-granules. *J Proteom.* (2014) 101:130–40. doi: 10.1016/j.jprot.2014.02.008
17. Pagel O, Walter E, Jurk K, Zahedi RP. Taking the stock of granule cargo: platelet releasate proteomics. *Platelets.* (2017) 28:119–28. doi: 10.1080/09537104.2016.1254762
18. Yadav S, Storrie B. The cellular basis of platelet secretion: Emerging structure/function relationships. *Platelets.* (2017) 28:108–18. doi: 10.1080/09537104.2016.1257786
19. Elzey BD, Tian J, Jensen RJ, Swanson AK, Lees JR, Lentz SR, et al. Platelet-mediated modulation of adaptive immunity. A communication link between innate and adaptive immune compartments. *Immunity.* (2003) 19:9–19. doi: 10.1016/S1074-7613(03)00177-8
20. Nurden AT. The biology of the platelet with special reference to inflammation, wound healing and immunity. *Front Biosci.* (2018) 23:726–51. doi: 10.2741/4613
21. Weller CD, Gardiner EE, Arthur JF, Southey M, Andrews RK. Autologous platelet-rich plasma for healing chronic venous leg ulcers: clinical efficacy and potential mechanisms. *Int Wound J.* (2019) 16:788–92. doi: 10.1111/iwj.13098
22. Gardiner EE, Andrews RK. Platelet Adhesion. In: *Platelets in Thrombotic and Non-Thrombotic Disorders: Pathophysiology, Pharmacology and Therapeutics: An Update.* Gresele P, Kleiman NS, Lopez JA, and Page CP, editors. Cham: Springer International Publishing (2017). p. 309–19. doi: 10.1007/978-3-319-47462-5_23
23. Arthur JF, Gardiner EE, Matzaris M, Taylor SG, Wijeyewickrema L, Ozaki Y, et al. Glycoprotein VI is associated with GPIb-IX-V on the membrane of resting and activated platelets. *Thromb Haemost.* (2005) 93:716–23. doi: 10.1160/TH04-09-0584
24. Gardiner EE, Andrews RK. Platelet receptor expression and shedding: glycoprotein Ib-IX-V and glycoprotein VI. *Transf Med Rev.* (2014) 28:56–60. doi: 10.1016/j.tmrv.2014.03.001
25. Mezger M, Nording H, Sauter R, Graf T, Heim C, Von Bubnoff N, et al. Platelets and immune responses during thromboinflammation. *Front Immunol.* (2019) 10:1731. doi: 10.3389/fimmu.2019.01731
26. Brass LF, Diamond SL, Stalker TJ. Platelets and hemostasis: a new perspective on an old subject. *Blood Adv.* (2016) 1:5–9. doi: 10.1182/bloodadvances.2016000059
27. Senis YA, Mazharian A, Mori J. Src family kinases: at the forefront of platelet activation. *Blood.* (2014) 124:2013–24. doi: 10.1182/blood-2014-01-453134
28. Dunne E, Spring CM, Reheman A, Jin W, Berndt MC, Newman DK, et al. Cadherin 6 has a functional role in platelet aggregation and thrombus formation. *Arterioscler Thromb Vasc Biol.* (2012) 32:1724–31. doi: 10.1161/ATVBAHA.112.250464
29. Selvadurai MV, Hamilton JR. Structure and function of the open canalicular system – the platelet's specialized internal membrane network. *Platelets.* (2018) 29:319–25. doi: 10.1080/09537104.2018.1431388
30. Kasirer-Friede A, Ware J, Leng L, Marchese P, Ruggeri ZM, Shattil SJ. Lateral clustering of platelet GP Ib-IX complexes leads to up-regulation of the adhesive function of integrin alpha IIbbeta 3. *J Biol Chem.* (2002) 277:11949–56. doi: 10.1074/jbc.M108727200
31. Poulter NS, Pollitt AY, Owen DM, Gardiner EE, Andrews RK, Shimizu H, et al. Clustering of glycoprotein VI (GPVI) dimers upon adhesion to collagen as a mechanism to regulate GPVI signaling in platelets. *J Thromb Haemost.* (2017) 15:549–64. doi: 10.1111/jth.13613
32. Choo HJ, Kholmukhamedov A, Zhou C, Jobe S. Inner mitochondrial membrane disruption links apoptotic and agonist-initiated phosphatidylserine externalization in platelets. *Arterioscler Thromb Vasc Biol.* (2017) 37:1503–12. doi: 10.1161/ATVBAHA.117.309473
33. Li C, Piran S, Chen P, Lang S, Zarpellon A, Jin JW, et al. The maternal immune response to fetal platelet GPIbα causes frequent miscarriage in mice that can be prevented by intravenous IgG and anti-FcRn therapies. *J Clin Invest.* (2011) 121:4537–47. doi: 10.1172/JCI57850
34. Gardiner EE. Proteolytic processing of platelet receptors. *Res Pract Thromb Haemost.* (2018) 2:240–50. doi: 10.1002/rth2.12096
35. Montague SJ, Andrews RK, Gardiner EE. Mechanisms of receptor shedding in platelets. *Blood.* (2018) 132:2535–45. doi: 10.1182/blood-2018-03-742668
36. Furie B, Furie BC. Mechanisms of thrombus formation. *New Engl J Med.* (2008) 359:938–49. doi: 10.1056/NEJMra0801082
37. Spronk HMH, Padro T, Siland JE, Prochaska JH, Winters J, Van Der Wal AC, et al. Atherothrombosis and thromboembolism: position paper from the second maastricht consensus conference on thrombosis. *Thromb Haemost.* (2018) 118:229–50. doi: 10.1160/TH17-07-0492
38. Jackson SP. Arterial thrombosis-insidious, unpredictable and deadly. *Nat Med.* (2011) 17:1423–36. doi: 10.1038/nm.2515
39. Mackman N. Triggers, targets and treatments for thrombosis. *Nature.* (2008) 451:914–8. doi: 10.1038/nature06797
40. Mcfadyen JD, Jackson SP. Differentiating haemostasis from thrombosis for therapeutic benefit. *Thromb Haemostas.* (2013) 110:859–67. doi: 10.1160/TH13-05-0379
41. Mozaffarian D, Benjamin EJ, Go AS, Arnett DK, Blaha MJ, Cushman M, et al. Executive summary: Heart disease and stroke statistics—2016 update: a report from the American heart association. *Circulation.* (2016) 133:447–54. doi: 10.1161/CIR.0000000000000366
42. Berndt MC, Metharom P, Andrews RK. Primary haemostasis: newer insights. *Haemophilia.* (2014) 20:15–22. doi: 10.1111/hae.12427
43. Wang Y, Gallant RC, Ni H. Extracellular matrix proteins in the regulation of thrombus formation. *Curr Opin Hematol.* (2016) 23:280–7. doi: 10.1097/MOH.0000000000000237
44. Kroll MH, Hellums JD, Mcintire LV, Schafer AI, Moake JL. Platelets and shear stress *Blood.* (1996) 88:1525–41. doi: 10.1182/blood.V88.5.1525.bloodjournal8851525
45. Hansen CE, Qiu Y, Mccarty OJT, Lam WA. Platelet mechanotransduction. *Ann Rev Biomed Eng.* (2018) 20:253–75. doi: 10.1146/annurev-bioeng-062117-121215

46. Ruggeri ZM, Orje JN, Habermann R, Federici AB, Reininger AJ. Activation-independent platelet adhesion and aggregation under elevated shear stress. *Blood.* (2006) 108:1903–10. doi: 10.1182/blood-2006-04-011551
47. Gardiner EE, Arthur JF, Shen Y, Karunakaran D, Moore LA, Am Esch JS. II, et al. GPIba-selective activation of platelets induces platelet signaling events comparable to GPVI activation events. *Platelets.* (2010) 21:244–52. doi: 10.3109/09537101003695339
48. Coenen DM, Mastenbroek TG, Cosemans JMEM. Platelet interaction with activated endothelium: mechanistic insights from microfluidics. *Blood.* (2017) 130:2819–28. doi: 10.1182/blood-2017-04-780825
49. Slepian MJ, Sheriff J, Hutchinson M, Tran P, Bajaj N, Garcia JGN, et al. Shear-mediated platelet activation in the free flow: perspectives on the emerging spectrum of cell mechanobiological mechanisms mediating cardiovascular implant thrombosis. *J Biomech.* (2017) 50:20–5. doi: 10.1016/j.jbiomech.2016.11.016
50. Van Geffen JP, Brouns SLN, Batista J, Mckinney H, Kempster C, Nagy M, et al. High-throughput elucidation of thrombus formation reveals sources of platelet function variability. *Haematologica.* (2019) 104:1256–67. doi: 10.3324/haematol.2018.198853
51. Cardo L, Thomas SG, Mazharian A, Pikramenou Z, Rappoport JZ, Hannon MJ, et al. Accessible synthetic probes for staining actin inside platelets and megakaryocytes by employing Lifeact peptide. *Chembiochem.* (2015) 16:1680–8. doi: 10.1002/cbic.201500120
52. Celi A, Merrill-Skoloff G, Gross P, Falati S, Sim DS, Flaumenhaft R, et al. Thrombus formation: direct real-time observation and digital analysis of thrombus assembly in a living mouse by confocal and widefield intravital microscopy. *J Thromb Haemost.* (2003) 1:60–8. doi: 10.1046/j.1538-7836.2003.t01-1-00033.x
53. Park Y, Depeursinge C, Popescu G. Quantitative phase imaging in biomedicine. *Nat Photonics.* (2018) 12:578–89. doi: 10.1038/s41566-018-0253-x
54. Lee K, Kim K, Jung J, Heo J, Cho S, Lee S, et al. Quantitative phase imaging techniques for the study of cell pathophysiology: from principles to applications. *Sensors.* (2013) 13:4170–91. doi: 10.3390/s130404170
55. He X, Montague SJ, Tao X, Gardiner EE, Lee WM. Quantifying embolism: label-free volumetric mapping of thrombus structure and kinesis in a microfluidic system with optical holography. *Adv Biosyst.* (2018) 2:1800089. doi: 10.1002/adbi.201800089
56. Ma Y, Guo S, Pan Y, Fan R, Smith ZJ, Lane S, et al. Quantitative phase microscopy with enhanced contrast and improved resolution through ultra-oblique illumination (UO-QPM). *J Biophotonics.* (2019) 12:e201900011. doi: 10.1002/jbio.201900011
57. Scandola C, Erhardt M, Rinckel J-Y, Proamer F, Gachet C, Eckly A. Use of electron microscopy to study megakaryocytes. *Platelets.* (2020) 5:1–10. doi: 10.1080/09537104.2019.1708885
58. Brown E, Carlin LM, Nerlov C, Lo Celso C, Poole AW. Multiple membrane extrusion sites drive megakaryocyte migration into bone marrow blood vessels. *Life Sci Alliance.* (2018) 1:e201800061. doi: 10.26508/lsa.201800061
59. Eckly A, Rinckel J-Y, Proamer F, Gachet C. High-resolution 3D imaging of megakaryocytes using focused ion beam-scanning electron microscopy. *Methods Mol Biol.* (2018) 1812:217–31. doi: 10.1007/978-1-4939-8585-2_13
60. Engberts KB, Seinen C, Geerts WJC, Heijnen HFG. Electron tomography and correlative approaches in platelet studies. *Methods Mol Biol.* (2018) 1812:55–79. doi: 10.1007/978-1-4939-8585-2_4
61. Schermelleh L, Ferrand A, Huser T, Eggeling C, Sauer M, Biehlmaier O, et al. Super-resolution microscopy demystified. *Nat Cell Biol.* (2019) 21:72–84. doi: 10.1038/s41556-018-0251-8
62. Rönnlund D, Xu L, Perols A, Gad AKB, Eriksson Karlström A, Auer G, et al. Multicolor fluorescence nanoscopy by photobleaching: concept, verification, and its application to resolve selective storage of proteins in platelets. *ACS Nano.* (2014) 8:4358–65. doi: 10.1021/nn406113m
63. Vicidomini G, Bianchini P, Diaspro A. STED super-resolved microscopy. *Nat Methods.* (2018) 15:173. doi: 10.1038/nmeth.4593
64. Bergstrand J, Xu L, Miao X, Li N, Oktem O, Franzen B, et al. Super-resolution microscopy can identify specific protein distribution patterns in platelets incubated with cancer cells. *Nanoscale.* (2019) 11:10023–33. doi: 10.1039/C9NR01967G
65. Poulter NS, Pollitt Y, Davies A, Malinova D, Nash GB, Hannon MJ, et al. Platelet actin nodules are podosome-like structures dependent on Wiskott–Aldrich syndrome protein and ARP2/3 complex. *Nat Commun.* (2015) 6:7254. doi: 10.1038/ncomms8254
66. Kahr WHA, Pluthero FG, Elkadri A, Warner N, Drobac M, Chen CH, et al. Loss of the Arp2/3 complex component ARPC1B causes platelet abnormalities and predisposes to inflammatory disease. *Nat Commun.* (2017) 8:14816. doi: 10.1038/ncomms14816
67. Miklosi AG, Del Favero G, Marko D, Harkany T, Lubec G. Resolution matters: correlating quantitative proteomics and nanoscale-precision microscopy for reconstructing synapse identity. *Proteomics.* (2018) 18:1800139. doi: 10.1002/pmic.201800139
68. Yakimov BP, Gogoleva MA, Semenov AN, Rodionov SA, Novoselova MV, Gayer AV, et al. Label-free characterization of white blood cells using fluorescence lifetime imaging and flow-cytometry: molecular heterogeneity and erythrophagocytosis [Invited]. *Biomed Opt Exp.* (2019) 10:4220–36. doi: 10.1364/BOE.10.004220
69. Sorrentino S, Studt JD, Medalia O, Tanuj Sapra K. Roll, adhere, spread and contract: structural mechanics of platelet function. *Eur J Cell Biol.* (2015) 94:129–38. doi: 10.1016/j.ejcb.2015.01.001
70. Mattheyses AL, Simon SM, Rappoport JZ. Imaging with total internal reflection fluorescence microscopy for the cell biologist. *J Cell Sci.* (2010) 123:3621–8. doi: 10.1242/jcs.056218
71. Jiang Y, Fu H, Springer TA, Wong WP. Electrostatic steering enables flow-activated von Willebrand Factor to bind platelet glycoprotein, revealed by single-molecule stretching and imaging. *J Mol Biol.* (2019) 431:1380–96. doi: 10.1016/j.jmb.2019.02.014
72. Lee D, Fong KP, King MR, Brass LF, Hammer DA. Differential dynamics of platelet contact and spreading. *Biophys J.* (2012) 102:472–82. doi: 10.1016/j.bpj.2011.10.056
73. Baker-Groberg SM, Phillips KG, Mccarty OJ. Quantification of volume, mass, and density of thrombus formation using brightfield and differential interference contrast microscopy. *J Biomed Opt.* (2013) 18:16014. doi: 10.1117/1.JBO.18.1.016014
74. Gaertner F, Ahmad Z, Rosenberger G, Fan S, Nicolai L, Busch B, et al. Migrating platelets are mechano-scavengers that collect and bundle bacteria. *Cell.* (2017) 171:1368–82.e1323. doi: 10.1016/j.cell.2017.11.001
75. Riedl J, Crevenna AH, Kessenbrock K, Yu JH, Neukirchen D, Bista M, et al. Lifeact: a versatile marker to visualize F-actin. *Nat Methods.* (2008) 5:605–7. doi: 10.1038/nmeth.1220
76. Melak M, Plessner M, Grosse R. Actin visualization at a glance. *J Cell Sci.* (2017) 130:525–30. doi: 10.1242/jcs.189068
77. Schurr Y, Sperr A, Volz J, Beck S, Reil L, Kusch C, et al. Platelet lamellipodia formation is not required for thrombus formation and stability. *Blood.* (2019) 39:S1–S92. doi: 10.1055/s-0039-1680096
78. Aslan JE, Mccarty OJT. Rho GTPases in platelet function. *J Thromb Haemostasis.* (2013) 11:35–46. doi: 10.1111/jth.12051
79. Thon JN, Montalvo A, Patel-Hett S, Devine MT, Richardson JL, Ehrlicher A, et al. Cytoskeletal mechanics of proplatelet maturation and platelet release. *J Cell Biol.* (2010) 191:861–74. doi: 10.1083/jcb.201006102
80. Nishimura S, Nagasaki M, Kunishima S, Sawaguchi A, Sakata A, Sakaguchi H, et al. IL-1α induces thrombopoiesis through megakaryocyte rupture in response to acute platelet needs. *J Cell Biol.* (2015) 209:453–66. doi: 10.1083/jcb.201410052
81. Machlus KR, Wu SK, Stumpo DJ, Soussou TS, Paul DS, Campbell RA, et al. Synthesis and dephosphorylation of MARCKS in the late stages of megakaryocyte maturation drive proplatelet formation. *Blood.* (2016) 127:1468–80. doi: 10.1182/blood-2015-08-663146
82. Wielders SJ, Broers J, Ten Cate H, Collins PW, Bevers EM, Lindhout T. Absence of platelet-dependent fibrin formation in a patient with Scott syndrome. *Thromb Haemost.* (2009) 102:76–82. doi: 10.1160/TH08-11-0719
83. Nurden P, Debili N, Coupry I, Bryckaert M, Youlyouz-Marfak I, Solé G, et al. Thrombocytopenia resulting from mutations in filamin A can be expressed as an isolated syndrome. *Blood.* (2011) 118:5928–37. doi: 10.1182/blood-2011-07-365601
84. Watson SP, Lowe GC, Lordkipanidzé M, Morgan NV, Consortium TG. Genotyping and phenotyping of platelet function disorders.

J Thromb Haemostasis. (2013) 11:351–63. doi: 10.1111/jth.12199
85. Khan AO, Maclachlan A, Lowe GC, Nicolson PLR, Al Ghaithi R, Thomas SG, et al. High-throughput platelet spreading analysis: a tool for the diagnosis of platelet- based bleeding disorders. *Haematologica*. (2019) 2019:225912. doi: 10.3324/haematol.2019.225912
86. Biasetti J, Sampath K, Cortez A, Azhir A, Gilad AA, Kickler TS, et al. Space and time resolved detection of platelet activation and von Willebrand Factor conformational changes in deep suspensions. *Int J Biomed Imaging.* (2017) 2017:8318906. doi: 10.1155/2017/8318906
87. Schulze H, Stegner D. Imaging platelet biogenesis *in vivo*. *Res Pract Thromb Haemost.* (2018) 2:461–8. doi: 10.1002/rth2.12112
88. Fox JEB, Boyles JK. The membrane skeleton – A distinct structure that regulates the function of cells. *Bioessays.* (1988) 8:14–8. doi: 10.1002/bies.950080105
89. Hartwig JH. Mechanisms of actin rearrangements mediating platelet activation. *J Cell Biol.* (1992) 118:1421–42. doi: 10.1083/jcb.118.6.1421
90. Nurden AT, Phillips DR, George JN. Platelet membrane glycoproteins: historical perspectives. *J Thromb Haemost.* (2006) 4:3–9. doi: 10.1111/j.1538-7836.2005.01549.x
91. Raccuglia G. Gray platelet syndrome: a variety of qualitative platelet disorder. *Am J Med.* (1971) 51:818–28. doi: 10.1016/0002-9343(71)90311-1
92. Nurden AT, Nurden P. The gray platelet syndrome: clinical spectrum of the disease. *Blood Rev.* (2007) 21:21–36. doi: 10.1016/j.blre.2005.12.003
93. Huang B, Bates M, Zhuang X. Super-resolution fluorescence microscopy. *Ann Rev Biochem.* (2009) 78:993–1016. doi: 10.1146/annurev.biochem.77.061906.092014
94. Wu Y, Chandris P, Winter PW, Kim EY, Jaumouillé V, Kumar A, et al. Simultaneous multiview capture and fusion improves spatial resolution in wide-field and light-sheet microscopy. *Optica.* (2016) 3:897–910. doi: 10.1364/OPTICA.3.000897
95. Follain G, Mercier L, Osmani N, Harlepp S, Goetz JG. Seeing is believing - multi-scale spatio-temporal imaging towards *in vivo* cell biology. *J Cell Sci.* (2017) 130:23–38. doi: 10.1242/jcs.189001
96. Lickert S, Sorrentino S, Studt J-D, Medalia O, Vogel V, Schoen I. Morphometric analysis of spread platelets identifies integrin α(IIb)β(3)-specific contractile phenotype. *Sci Rep.* (2018) 8:5428–8. doi: 10.1038/s41598-018-23684-w
97. Mayr S, Hauser F, Peterbauer A, Tauscher A, Naderer C, Axmann M, et al. Localization microscopy of actin cytoskeleton in human platelets. *Int J Mol Sci.* (2018) 19:1150. doi: 10.3390/ijms19041150
98. Cuenca-Zamora EJ, Ferrer-Marín F, Rivera J, Teruel-Montoya R. Tubulin in platelets: when the shape matters. *Int J Mol Sci.* (2019) 20:3484. doi: 10.3390/ijms20143484
99. Zuidscherwoude M, Green HLH, Thomas SG. Formin proteins in megakaryocytes and platelets: regulation of actin and microtubule dynamics. *Platelets.* (2019) 30:23–30. doi: 10.1080/09537104.2018.1481937
100. Gardiner EE, Arthur JF, Kahn ML, Berndt MC, Andrews RK. Regulation of platelet membrane levels of glycoprotein VI by a platelet-derived metalloproteinase. *Blood.* (2004) 104:3611–7. doi: 10.1182/blood-2004-04-1549
101. Guo M, Chandris P, Giannini JP, Trexler AJ, Fischer R, Chen J, et al. Single-shot super-resolution total internal reflection fluorescence microscopy. *Nat Methods.* (2018) 15:425–8. doi: 10.1038/s41592-018-0004-4
102. Hastings SM, Griffin MT, Ku DN. Hemodynamic studies of platelet thrombosis using microfluidics. *Platelets.* (2017) 28:427–33. doi: 10.1080/09537104.2017.1316483
103. Westein E, De Witt S, Lamers M, Cosemans JM, Heemskerk JW. Monitoring in vitro thrombus formation with novel microfluidic devices. *Platelets.* (2012) 23:501–9. doi: 10.3109/09537104.2012.709653
104. De Witt SM, Swieringa F, Cavill R, Lamers MME, Van Kruchten R, Mastenbroek T, et al. Identification of platelet function defects by multi-parameter assessment of thrombus formation. *Nat Commun.* (2014) 5:4257. doi: 10.1038/ncomms5257
105. Swieringa F, Baaten CC, Verdoold R, Mastenbroek TG, Rijnveld N, Van Der Laan KO, et al. Platelet control of fibrin distribution and microelasticity in thrombus formation under flow. *Arterioscler Thromb Vasc Biol.* (2016) 36:692–9. doi: 10.1161/ATVBAHA.115.306537
106. Nagy M, Heemskerk JWM, Swieringa F. Use of microfluidics to assess the platelet-based control of coagulation. *Platelets.* (2017) 28:441–8. doi: 10.1080/09537104.2017.1293809
107. Casa LDC, Ku DN. Geometric design of microfluidic chambers: platelet adhesion versus accumulation. *Biomed Microdev.* (2014) 16:115–26. doi: 10.1007/s10544-013-9811-7
108. Lui M, Gardiner EE, Arthur JF, Pinar I, Lee WM, Ryan K, et al. Novel stenotic microchannels to study thrombus formation in shear gradients: influence of shear forces and human platelet-related factors. *Int J Mol Sci.* (2019) 20:2967. doi: 10.3390/ijms20122967
109. Zilberman-Rudenko J, Mccarty OJT. Utility and development of microfluidic platforms for platelet research. *Platelets.* (2017) 28:425–6. doi: 10.1080/09537104.2017.1325187
110. Herbig BA, Yu X, Diamond SL. Using microfluidic devices to study thrombosis in pathological blood flows. *Biomicrofluidics.* (2018) 12:042201. doi: 10.1063/1.5021769
111. Branchford BR, Ng CJ, Neeves KB, Di Paola J. Microfluidic technology as an emerging clinical tool to evaluate thrombosis and hemostasis. *Thromb Res.* (2015) 136:13–9. doi: 10.1016/j.thromres.2015.05.012
112. Sakariassen KS, Orning L, Turitto VT. The impact of blood shear rate on arterial thrombus formation. *Fut Sci.* (2015) 1:FSO30. doi: 10.4155/fso.15.28
113. Zhang C, Neelamegham S. Application of microfluidic devices in studies of thrombosis and hemostasis. *Platelets.* (2017) 28:434–40. doi: 10.1080/09537104.2017.1319047
114. Brouns SLN, Van Geffen JP, Heemskerk JWM. High-throughput measurement of human platelet aggregation under flow: application in hemostasis and beyond. *Platelets.* (2018) 29:662–9. doi: 10.1080/09537104.2018.1447660
115. Baaten CCFMJ, Swieringa F, Misztal T, Mastenbroek TG, Feijge MAH, Heemskerk JWM. Platelet heterogeneity in activation-induced glycoprotein shedding: functional effects. *Blood Adv.* (2018) 2:2320–31. doi: 10.1182/bloodadvances.2017011544
116. Schoeman RM, Lehmann M, Neeves KB. Flow chamber and microfluidic approaches for measuring thrombus formation in genetic bleeding disorders. *Platelets.* (2017) 28:463–71. doi: 10.1080/09537104.2017.1306042
117. Harrison P. The role of PFA-100® testing in the investigation and management of haemostatic defects in children and adults. *Br J Haematol.* (2005) 130:3–10. doi: 10.1111/j.1365-2141.2005.05511.x
118. Maxwell MJ, Westein E, Nesbitt WS, Giuliano S, Dopheide SM, Jackson SP. Identification of a 2-stage platelet aggregation process mediating shear-dependent thrombus formation. *Blood.* (2007) 109:566–76. doi: 10.1182/blood-2006-07-028282
119. Nesbitt WS, Westein E, Tovar-Lopez FJ, Tolouei E, Mitchell A, Fu J, et al. A shear gradient–dependent platelet aggregation mechanism drives thrombus formation. *Nat Med.* (2009) 15:665. doi: 10.1038/nm.1955
120. Xu E-R, Von Bülow S, Chen P-C, Lenting PJ, Kolšek K, Aponte-Santamaría C, et al. Structure and dynamics of the platelet integrin-binding C4 domain of von Willebrand factor. *Blood.* (2019) 133:366–76. doi: 10.1182/blood-2018-04-843615
121. Lehmann M, Schoeman RM, Krohl PJ, Wallbank AM, Samaniuk JR, Jandrot-Perrus M, et al. Platelets drive thrombus propagation in a hematocrit and glycoprotein vi-dependent manner in an *in vitro* venous thrombosis model. *Arterioscler Thromb Vasc Biol.* (2018) 38:1052–62. doi: 10.1161/ATVBAHA.118.310731
122. Loyau S, Ho-Tin-Noé B, Bourrienne MC, Boulaftali Y, Jandrot-Perrus M. Microfluidic modeling of thrombolysis. *Arterioscler Thromb Vasc Biol.* (2018) 38:2626–37. doi: 10.1161/ATVBAHA.118.311178
123. Chatterjee M, Gawaz M. Clinical significance of receptor shedding-platelet GPVI as an emerging diagnostic and therapeutic tool. *Platelets.* (2017) 28:362–71. doi: 10.1080/09537104.2016.1227062
124. Denorme F, Rondina MT. Targeting glycoprotein VI for thromboembolic disorders. *Arterioscler Thromb Vasc Biol.* (2019) 39:839–40. doi: 10.1161/ATVBAHA.119.312621
125. Lebozec K, Jandrot-Perrus M, Avenard G, Favre-Bulle O, Billiald P. Design, development and characterization of ACT017, a humanized Fab that blocks platelet's glycoprotein VI function without causing bleeding risks. *MAbs.* (2017) 9:945–58. doi: 10.1080/19420862.2017.1336592

126. Voors-Pette C, Lebozec K, Dogterom P, Jullien L, Billiald P, Ferlan P, et al. Safety and tolerability, pharmacokinetics, and pharmacodynamics of ACT017, an antiplatelet GPVI (Glycoprotein VI) Fab. *Arterioscler Thromb Vasc Biol.* (2019) 39:956–64. doi: 10.1161/ATVBAHA.118.312314
127. Byrnes JR, Wolberg AS. Red blood cells in thrombosis. *Blood.* (2017) 130:1795–9. doi: 10.1182/blood-2017-03-745349
128. Pries AR, Neuhaus D, Gaehtgens P. Blood viscosity in tube flow: dependence on diameter and hematocrit. *Am J Physiol.* (1992) 263:H1770–8. doi: 10.1152/ajpheart.1992.263.6.H1770
129. Fogelson AL, Neeves KB. Fluid mechanics of blood clot formation. *Annu Rev Fluid Mech.* (2015) 47:377–403. doi: 10.1146/annurev-fluid-010814-014513
130. Lanotte L, Mauer J, Mendez S, Fedosov DA, Fromental J-M, Claveria V, et al. Red cells' dynamic morphologies govern blood shear thinning under microcirculatory flow conditions. *Proc Natl Acad Sci USA*. (2016) 113:13289–94. doi: 10.1073/pnas.1608074113
131. Zheng Y, Chen J, Craven M, Choi NW, Totorica S, Diaz-Santana A, et al. *In vitro* microvessels for the study of angiogenesis and thrombosis. *Proc Natl. Acad Sci USA*. (2012) 109:9342–7. doi: 10.1073/pnas.1201240109
132. Morgan JP, Delnero PF, Zheng Y, Verbridge SS, Chen J, Craven M, et al. Formation of microvascular networks *in vitro*. *Nat Protoc.* (2013) 8:1820–36. doi: 10.1038/nprot.2013.110
133. Dobrucki JW, Feret D, Noatynska A. Scattering of exciting light by live cells in fluorescence confocal imaging: phototoxic effects and relevance for FRAP studies. *Biophys J.* (2007) 93:1778–86. doi: 10.1529/biophysj.106.096636
134. Pugh N, Bihan D, Perry DJ, Farndale RW. Dynamic analysis of platelet deposition to resolve platelet adhesion receptor activity in whole blood at arterial shear rate. *Platelets.* (2015) 26:216–9. doi: 10.3109/09537104.2014.893289
135. Mangin PH, Gardiner EE, Nesbitt WS, Kerrigan SW, Korin N, Lam W, et al. *In vitro* flow based systems to study platelet function and thrombus formation: recommendations for standardization: communication from the SSC on Biorheology of the ISTH. *J Thromb Haemost.* (2020) doi: 10.1111/jth.14717. [Epub ahead of print].
136. Falati S, Gross P, Merrill-Skoloff G, Furie BC, Furie B. Real-time *in vivo* imaging of platelets, tissue factor and fibrin during arterial thrombus formation in the mouse. *Nat Med.* (2002) 8:1175–80. doi: 10.1038/nm782
137. Welsh JD, Stalker TJ, Voronov R, Muthard RW, Tomaiuolo M, Diamond SL, et al. A systems approach to hemostasis: 1. The interdependence of thrombus architecture and agonist movements in the gaps between platelets. *Blood.* (2014) 124:1808–15. doi: 10.1182/blood-2014-01-550335
138. Dütting S, Gaits-Iacovoni F, Stegner D, Popp M, Antkowiak A, Van Eeuwijk JMM, et al. A Cdc42/RhoA regulatory circuit downstream of glycoprotein Ib guides transendothelial platelet biogenesis. *Nat Commun.* (2017) 8:15838. doi: 10.1038/ncomms15838
139. Jenne CN, Wong CHY, Petri B, Kubes P. The Use of Spinning-Disk Confocal Microscopy for the Intravital Analysis of Platelet Dynamics in Response to Systemic and Local Inflammation. *PLoS ONE.* (2011) 6:e25109. doi: 10.1371/journal.pone.0025109
140. Nishimura S, Manabe I, Nagasaki M, Seo K, Yamashita H, Hosoya Y, et al. *In vivo* imaging in mice reveals local cell dynamics and inflammation in obese adipose tissue. *J Clin Invest.* (2008) 118:710–21. doi: 10.1172/JCI33328
141. Takizawa H, Nishimura S, Takayama N, Oda A, Nishikii H, Morita Y, et al. Lnk regulates integrin alphaIIbbeta3 outside-in signaling in mouse platelets, leading to stabilization of thrombus development *in vivo*. *J Clin Invest.* (2010) 120:179–90. doi: 10.1172/JCI39503
142. Mickoleit M, Schmid B, Weber M, Fahrbach FO, Hombach S, Reischauer S, et al. High-resolution reconstruction of the beating zebrafish heart. *Nat Methods.* (2014) 11:919. doi: 10.1038/nmeth.3037
143. Glaser AK, Chen Y, Yin C, Wei L, Barner LA, Reder NP, et al. Multidirectional digital scanned light-sheet microscopy enables uniform fluorescence excitation and contrast-enhanced imaging. *Sci Rep.* (2018) 8:13878. doi: 10.1038/s41598-018-32367-5
144. Levental KR, Yu H, Kass L, Lakins JN, Egeblad M, Erler JT, et al. Matrix crosslinking forces tumor progression by enhancing integrin signaling. *Cell.* (2009) 139:891–906. doi: 10.1016/j.cell.2009.10.027
145. Chen X, Nadiarynkh O, Plotnikov S, Campagnola PJ. Second harmonic generation microscopy for quantitative analysis of collagen fibrillar structure. *Nat Protoc.* (2012) 7:654–69. doi: 10.1038/nprot.2012.009
146. Weigelin B, Bakker GJ, Friedl P. Third harmonic generation microscopy of cells and tissue organization. *J Cell Sci.* (2016) 129:245–55. doi: 10.1242/jcs.152272
147. Tolles WM, Nibler JW, Mcdonald JR, Harvey AB. A review of the theory and application of coherent anti-stokes raman spectroscopy (CARS). *Appl Spectrosc.* (1977) 31:253–71. doi: 10.1366/000370277774463625
148. Tu H, Boppart SA. Coherent anti-Stokes Raman scattering microscopy: overcoming technical barriers for clinical translation. *J Biophoton.* (2014) 7:9–22. doi: 10.1002/jbio.201300031
149. Lee M, Downes A, Chau Y-Y, Serrels B, Hastie N, Elfick A, et al. *In vivo* imaging of the tumor and its associated microenvironment using combined CARS / 2-photon microscopy. *Intravital.* (2015) 4:e1055430. doi: 10.1080/21659087.2015.1055430
150. Westrick RJ, Winn ME, Eitzman DT. Murine models of vascular thrombosis. *Arterioscler Thromb Vasc Biol.* (2007) 27:2079–93. doi: 10.1161/ATVBAHA.107.142810
151. Jagadeeswaran P, Cooley BC, Gross PL, Mackman N. Animal models of thrombosis from zebrafish to nonhuman primates: Use in the elucidation of new pathologic pathways and the development of antithrombotic drugs. *Circ Res.* (2016) 118:1363–79. doi: 10.1161/CIRCRESAHA.115.306823
152. Oreopoulos J, Berman R, Browne M. Spinning-disk confocal microscopy: present technology and future trends. In: *Methods in Cell Biology*. Waters JC and Wittman T, editor. Cambridge, MA: Academic Press (2014). p. 153–75. doi: 10.1016/B978-0-12-420138-5.00009-4
153. Rosen ED, Raymond S, Zollman A, Noria F, Sandoval-Cooper M, Shulman A, et al. Laser-induced noninvasive vascular injury models in mice generate platelet- and coagulation-dependent thrombi. *Am J Pathol.* (2001) 158:1613–22. doi: 10.1016/S0002-9440(10)64117-X
154. Ntziachristos V. Going deeper than microscopy: the optical imaging frontier in biology. *Nat Methods.* (2010) 7:603–14. doi: 10.1038/nmeth.1483
155. Wu Z, Rademakers T, Kiessling F, Vogt M, Westein E, Weber C, et al. Multi-photon microscopy in cardiovascular research. *Methods.* (2017) 130:79–89. doi: 10.1016/j.ymeth.2017.04.013
156. Li YX, Gautam V, Brüstle A, Cockburn IA, Daria VR, Gillespie C, et al. Flexible polygon-mirror based laser scanning microscope platform for multiphoton in-vivo imaging. *J Biophoton.* (2017) 10:1526–37. doi: 10.1002/jbio.201600289
157. Li YX, Montague SJ, Brustle A, He XF, Gillespie C, Gaus K, et al. High contrast imaging and flexible photomanipulation for quantitative in vivo multiphoton imaging with polygon scanning microscope. *J Biophoton.* (2018) 11:e201700341. doi: 10.1002/jbio.201700341
158. Kamocka MM, Mu J, Liu X, Chen N, Zollman A, Sturonas-Brown B, et al. Two-photon intravital imaging of thrombus development. *J Biomed Opt.* (2010) 15:016020–016020. doi: 10.1117/1.3322676
159. Abe T, Fujimori T. Reporter mouse lines for fluorescence imaging. *Dev Growth Differ.* (2013) 55:390–405. doi: 10.1111/dgd.12062
160. Yuan Y, Alwis I, Wu MCL, Kaplan Z, Ashworth K, Bark D Jr, et al. Neutrophil macroaggregates promote widespread pulmonary thrombosis after gut ischemia. *Sci Transl Med.* (2017) 9:eaam5861. doi: 10.1126/scitranslmed.aam5861
161. Junt T, Schulze H, Chen Z, Massberg S, Goerge T, Krueger A, et al. Dynamic visualization of thrombopoiesis within bone marrow. *Science.* (2007) 317:1767–70. doi: 10.1126/science.1146304
162. Kowata S, Isogai S, Murai K, Ito S, Tohyama K, Ema M, et al. Platelet demand modulates the type of intravascular protrusion of megakaryocytes in bone marrow. *Thromb Haemost.* (2014) 112:743–56. doi: 10.1160/TH14-02-0123
163. Thomas SG, Poulter NS, Bem D, Finney B, Machesky LM, Watson SP. The actin binding proteins cortactin and HS1 are dispensable for platelet actin nodule and megakaryocyte podosome formation. *Platelets.* (2017) 28:372–9. doi: 10.1080/09537104.2016.1235688
164. Stegner D, Vaneeuwijk JMM, Angay O, Gorelashvili MG, Semeniak D, Pinnecker J, et al. Thrombopoiesis is spatially regulated by the bone marrow vasculature. *Nat. Commun.* (2017) 8:127–127. doi: 10.1038/s41467-017-00201-7
165. Mcdonald B, Davis RP, Kim S-J, Tse M, Esmon CT, Kolaczkowska E, et al. Platelets and neutrophil extracellular traps collaborate to promote

intravascular coagulation during sepsis in mice. *Blood*. (2017) 129:1357–67. doi: 10.1182/blood-2016-09-741298
166. Turk M, Naumenko V, Mahoney DJ, Jenne CN. Tracking cell recruitment and behavior within the tumor microenvironment using advanced intravital imaging approaches. *Cells*. (2018) 7. doi: 10.3390/cells7070069
167. Stalker TJ, Traxler EA, Wu J, Wannemacher KM, Cermignano SL, Voronov R, et al. Hierarchical organization in the hemostatic response and its relationship to the platelet-signaling network. *Blood*. (2013) 121:1875–85. doi: 10.1182/blood-2012-09-457739
168. Tomaiuolo M, Matzko CN, Poventud-Fuentes I, Weisel JW, Brass LF, Stalker TJ. Interrelationships between structure and function during the hemostatic response to injury. *Proc Natl Acad Sci USA*. (2019) 116:2243–52. doi: 10.1073/pnas.1813642116
169. Welsh JD, Poventud-Fuentes I, Sampietro S, Diamond SL, Stalker TJ, Brass LF. Hierarchical organization of the hemostatic response to penetrating injuries in the mouse macrovasculature. *J Thromb Haemos.* (2017) 15:526–37. doi: 10.1111/jth.13600
170. Dubois C, Panicot-Dubois L, Gainor JF, Furie BC, Furie B. Thrombin-initiated platelet activation in vivo is vWF independent during thrombus formation in a laser injury model. *J Clin Invest.* (2007) 117:953–60. doi: 10.1172/JCI30537
171. Brill A, Fuchs TA, Chauhan AK, Yang JJ, De Meyer SF, Köllnberger M, et al. von Willebrand factor-mediated platelet adhesion is critical for deep vein thrombosis in mouse models. *Blood*. (2011) 117:1400–7. doi: 10.1182/blood-2010-05-287623
172. Wang Y, Gao H, Shi C, Erhardt PW, Pavlovsky AA, Simon DI. Leukocyte integrin Mac-1 regulates thrombosis via interaction with platelet GPIbα. *Nat Commun.* (2017) 8:15559. doi: 10.1038/ncomms15559
173. Munnix ICA, Strehl A, Kuijpers MJE, Auger JM, Meijden PEJVD, Zandvoort M, et al. The glycoprotein VI-phospholipase Cγ2 signaling pathway controls thrombus formation induced by collagen and tissue factor *in vitro* and *in vivo*. *Arterioscler Thromb Vasc Biol.* (2005) 25:2673–78. doi: 10.1161/01.ATV.0000193568.71980.4a
174. Mangin P, Yap CL, Nonne C, Sturgeon SA, Goncalves I, Yuan Y, et al. Thrombin overcomes the thrombosis defect associated with platelet GPVI/FcRγ deficiency. *Blood*. (2006) 107:4346–53. doi: 10.1182/blood-2005-10-4244
175. Vandendries ER, Hamilton JR, Coughlin SR, Furie B, Furie BC. Par4 is required for platelet thrombus propagation but not fibrin generation in a mouse model of thrombosis. *Proc Natl Acad Sci USA*. (2007) 104:288–92. doi: 10.1073/pnas.0610188104
176. French SL, Hamilton JR. Protease-activated receptor 4: from structure to function and back again. *Br J Pharmacol.* (2016) 173:2952–65. doi: 10.1111/bph.13455
177. Andre P, Delaney SM, Larocca T, Vincent D, Deguzman F, Jurek M, et al. P2Y12 regulates platelet adhesion/activation, thrombus growth, and thrombus stability in injured arteries. *J Clin Invest.* (2003) 112:398–406. doi: 10.1172/JCI17864
178. Zhang Y, Ye J, Hu L, Zhang S, Zhang SH, Li Y, et al. Increased platelet activation and thrombosis in transgenic mice expressing constitutively active P2Y12. *J Thromb Haemost.* (2012) 10:2149–57. doi: 10.1111/j.1538-7836.2012.04894.x
179. He L, Pappan LK, Grenache DG, Li Z, Tollefsen DM, Santoro SA, et al. The contributions of the alpha 2 beta 1 integrin to vascular thrombosis *in vivo*. *Blood.* (2003) 102:3652–7. doi: 10.1182/blood-2003-04-1323
180. Shen B, Zhao X, O'brien KA, Stojanovic-Terpo A, Delaney MK, Kim K, et al. A directional switch of integrin signalling and a new anti-thrombotic strategy. *Nature*. (2013) 503, 131–135. doi: 10.1038/nature12613
181. Ni H, Yuen PS, Papalia JM, Trevithick JE, Sakai T, Fassler R, et al. Plasma fibronectin promotes thrombus growth and stability in injured arterioles. *Proc Natl Acad Sci USA*. (2003) 100:2415–9. doi: 10.1073/pnas.2628067100
182. Chauhan AK, Kisucka J, Cozzi MR, Walsh MT, Moretti FA, Battiston M, et al. Prothrombotic effects of fibronectin isoforms containing the EDA domain. *Arterioscler Thromb Vasc Biol.* (2008) 28:296–301. doi: 10.1161/ATVBAHA.107.149146
183. Reheman A, Gross P, Yang H, Chen P, Allen D, Leytin V, et al. Vitronectin stabilizes thrombi and vessel occlusion but plays a dual role in platelet aggregation. *J Thromb Haemost.* (2005) 3:875–83. doi: 10.1111/j.1538-7836.2005.01217.x
184. Nonne C, Lenain N, Hechler B, Mangin P, Cazenave JP, Gachet C, et al. Importance of platelet phospholipase Cgamma2 signaling in arterial thrombosis as a function of lesion severity. *Arterioscler Thromb Vasc Biol.* (2005) 25:1293–8. doi: 10.1161/01.ATV.0000163184.02484.69
185. Guesmi K, Abdeladim L, Tozer S, Mahou P, Kumamoto T, Jurkus K, et al. Dual-color deep-tissue three-photon microscopy with a multiband infrared laser. *Light*. (2018) 7:12. doi: 10.1038/s41377-018-0012-2
186. Power RM, Huisken J. Putting advanced microscopy in the hands of biologists. *Nat Methods*. (2019) 16:1069–73. doi: 10.1038/s41592-019-0618-1
187. Progatzky F, Dallman MJ, Lo Celso C. From seeing to believing: labelling strategies for *in vivo* cell-tracking experiments. *Interface Focus.* (2013) 3:20130001. doi: 10.1098/rsfs.2013.0001
188. Bedford R, Tiede C, Hughes R, Curd A, Mcpherson MJ, Peckham M, et al. Alternative reagents to antibodies in imaging applications. *Biophys Rev*. (2017) 9:299–308. doi: 10.1007/s12551-017-0278-2
189. Wallace W, Schaefer LH, Swedlow JR. A working person's guide to deconvolution in light microscopy. *BioTechniques*. (2001) 31:1076–97. doi: 10.2144/01315bi01
190. He T, Sun Y, Qi J, Hu J, Huang H. Image deconvolution for confocal laser scanning microscopy using constrained total variation with a gradient field. *Appl Opt.* (2019) 58:3754–66. doi: 10.1364/AO.58.003754
191. Cole RW, Jinadasa T, Brown CM. Measuring and interpreting point spread functions to determine confocal microscope resolution and ensure quality control. *Nat Protoc.* (2011) 6:1929–41. doi: 10.1038/nprot.2011.407
192. Mcnally JG, Karpova T, Cooper J, Conchello JA. Three-dimensional imaging by deconvolution microscopy. *Methods.* (1999) 19:373–85. doi: 10.1006/meth.1999.0873
193. Dunn KW, Lorenz KS, Salama P, Delp EJ. IMART software for correction of motion artifacts in images collected in intravital microscopy. *Intravital.* (2014) 3:e28210. doi: 10.4161/intv.28210
194. Boudejltia KZ, Ribeiro De Sousa D, Uzureau P, Yourassowsky C, Perez-Morga D, Courbebaisse G, et al. Quantitative analysis of platelets aggregates in 3D by digital holographic microscopy. *Biomed Opt Exp.* (2015) 6:3556–63. doi: 10.1364/BOE.6.003556
195. Ting LH, Feghhi S, Taparia N, Smith AO, Karchin A, Lim E, et al. Contractile forces in platelet aggregates under microfluidic shear gradients reflect platelet inhibition and bleeding risk. *Nat Commun.* (2019) 10:1204. doi: 10.1038/s41467-019-09150-9
196. Chen Z, Lu J, Zhang C, Hsia I, Yu X, Marecki L, et al. Microclot array elastometry for integrated measurement of thrombus formation and clot biomechanics under fluid shear. *Nat Commun.* (2019) 10:2051. doi: 10.1038/s41467-019-10067-6
197. Faraday N, Schunke K, Saleem S, Fu J, Wang B, Zhang J, et al. Cathepsin G-dependent modulation of platelet thrombus formation *in vivo* by blood neutrophils. *PLoS ONE.* (2013) 8. doi: 10.1371/journal.pone.0071447
198. Mastenbroek TG, Feijge MAH, Kremers RMW, Bosch MTJVD, Swieringa F, Cosemans JMEM. Platelet-associated matrix metalloproteinases regulate thrombus formation and exert local collagenolytic activity. *Arterioscler Thromb Vasc Biol.* (2015) 35:2554–61. doi: 10.1161/ATVBAHA.115.306153
199. Haining EJ, Matthews AL, Noy PJ, Romanska HM, Harris HJ, Pike J, et al. Tetraspanin Tspan9 regulates platelet collagen receptor GPVI lateral diffusion and activation. *Platelets.* (2017) 28:629–42. doi: 10.1080/09537104.2016.1254175
200. Matthews AL, Koo CZ, Szyroka J, Harrison N, Kanhere A, Tomlinson MG. Regulation of leukocytes by TspanC8 tetraspanins and the "Molecular Scissor" ADAM10. *Front Immunol.* (2018) 9:1451. doi: 10.3389/fimmu.2018.01451
201. Tuchin VV, Tárnok A, Zharov VP. *In vivo* flow cytometry: a horizon of opportunities. *Cytometry Part A.* (2011) 79:737–45. doi: 10.1002/cyto.a.21143
202. Doan M, Vorobjev I, Rees P, Filby A, Wolkenhauer O, Goldfeld AE, et al. Diagnostic potential of imaging flow cytometry. *Trends Biotechnol.* (2018) 36:649–52. doi: 10.1016/j.tibtech.2017.12.008
203. Hui H, Fuller K, Erber WN, Linden MD. Measurement of monocyte-platelet aggregates by imaging flow cytometry. *Cytometry.* (2015) 87:273–8. doi: 10.1002/cyto.a.22587

204. Hui H, Fuller KA, Erber WN, Linden MD. Imaging flow cytometry in the assessment of leukocyte-platelet aggregates. *Methods.* (2017) 112:46–54. doi: 10.1016/j.ymeth.2016.10.002
205. Reddy EC, Wang H, Christensen H, Mcmillan-Ward E, Israels SJ, Bang KWA, et al. Analysis of procoagulant phosphatidylserine-exposing platelets by imaging flow cytometry. *Res Pract Thromb Haemost.* (2018) 2:736–50. doi: 10.1002/rth2.12144
206. Han Y, Gu Y, Zhang AC, Lo YH. Imaging technologies for flow cytometry. *Lab Chip.* (2016) 16:4639–47. doi: 10.1039/C6LC01063F
207. He W, Wang H, Hartmann LC, Cheng JX, Low PS. *In vivo* quantitation of rare circulating tumor cells by multiphoton intravital flow cytometry. *Proc Natl Acad Sci USA.* (2007) 104:11760–5. doi: 10.1073/pnas.0703875104
208. Tan X, Patil R, Bartosik P, Runnels JM, Lin CP, Niedre M. *In vivo* flow cytometry of extremely rare circulating cells. *Sci Rep.* (2019) 9:3366. doi: 10.1038/s41598-019-40143-2
209. Weisenburger S, Tejera F, Demas J, Chen B, Manley J, Sparks FT, et al. Volumetric Ca2+ imaging in the mouse brain using hybrid multiplexed sculpted light microscopy. *Cell.* (2019) 177:1050–66.e1014. doi: 10.1016/j.cell.2019.03.011
210. Galanzha EI, Shashkov EV, Tuchin VV, Zharov VP. *In vivo* multispectral, multiparameter, photoacoustic lymph flow cytometry with natural cell focusing, label-free detection and multicolor nanoparticle probes. *Cytometry.* (2008) 73:884–94. doi: 10.1002/cyto.a.20587
211. Yu Y, Yu M, Liu J, Ding N, Huang J, Wan D, et al. *In vivo* monitoring of thrombosis in mice by optical coherence tomography. *J Biophotonics.* (2019) 12:e201900105. doi: 10.1002/jbio.201900105
212. Tang S, Krasieva TB, Chen Z, Tromberg BJ. Combined multiphoton microscopy and optical coherence tomography using a 12-fs broadband source. *J Biomed Opt.* (2006) 11:020502. doi: 10.1364/BIO.2006.TuH4

Conflict of Interest: The authors declare that the research was conducted in the absence of any commercial or financial relationships that could be construed as a potential conflict of interest.

frontiers in Immunology

REVIEW
published: 04 February 2020
doi: 10.3389/fimmu.2020.00092

Intravital Microscopy of the Beating Murine Heart to Understand Cardiac Leukocyte Dynamics

*Nathaniel H. Allan-Rahill[1], Michael R. E. Lamont[1], William M. Chilian[2], Nozomi Nishimura[1] and David M. Small[1]**

[1] Nancy E. and Peter C. Meinig School of Biomedical Engineering, Cornell University, Ithaca, NY, United States, [2] Department of Integrative Medical Sciences, Northeast Ohio Medical University, Rootstown, OH, United States

Cardiovascular disease is the leading cause of worldwide mortality. Intravital microscopy has provided unprecedented insight into leukocyte biology by enabling the visualization of dynamic responses within living organ systems at the cell-scale. The heart presents a uniquely dynamic microenvironment driven by periodic, synchronous electrical conduction leading to rhythmic contractions of cardiomyocytes, and phasic coronary blood flow. In addition to functions shared throughout the body, immune cells have specific functions in the heart including tissue-resident macrophage-facilitated electrical conduction and rapid monocyte infiltration upon injury. Leukocyte responses to cardiac pathologies, including myocardial infarction and heart failure, have been well-studied using standard techniques, however, certain questions related to spatiotemporal relationships remain unanswered. Intravital imaging techniques could greatly benefit our understanding of the complexities of *in vivo* leukocyte behavior within cardiac tissue, but these techniques have been challenging to apply. Different approaches have been developed including high frame rate imaging of the beating heart, explantation models, micro-endoscopy, and mechanical stabilization coupled with various acquisition schemes to overcome challenges specific to the heart. The field of cardiac science has only begun to benefit from intravital microscopy techniques. The current focused review presents an overview of leukocyte responses in the heart, recent developments in intravital microscopy for the murine heart, and a discussion of future developments and applications for cardiovascular immunology.

Keywords: intravital microscopy, cardiovascular, heart, multiphoton microscopy, leukocyte

OPEN ACCESS

Edited by:
Connie Wong,
Monash University, Australia

Reviewed by:
Justin Deniset,
University of Calgary, Canada
Raluca Aura Niesner,
Freie Universität Berlin, Germany
Junichi Kikuta,
Osaka University, Japan

***Correspondence:**
David M. Small
dms542@cornell.edu

Specialty section:
This article was submitted to Inflammation, a section of the journal Frontiers in Immunology

Received: *22 October 2019*
Accepted: *14 January 2020*
Published: *04 February 2020*

Citation:
Allan-Rahill NH, Lamont MRE, Chilian WM, Nishimura N and Small DM (2020) Intravital Microscopy of the Beating Murine Heart to Understand Cardiac Leukocyte Dynamics. Front. Immunol. 11:92. doi: 10.3389/fimmu.2020.00092

INTRODUCTION

The primary function of the heart is to pump blood throughout the body via the circulatory system, delivering oxygen and nutrients to the tissues, and removing carbon dioxide and waste simultaneously. The heart is composed of four chambers, each separated by uni-directional valves, that synchronously work to cycle blood through the systemic and pulmonary circulation. The function of the heart relies on the action of contractile cells, known as cardiomyocytes, specialized conducting cells that facilitate coordinating rhythmic contraction, extracellular matrix that provide mechanical support, as well as veins, arteries, and microvasculature to supply blood to the working muscle. Importantly, the heart vascular network, known as the coronary circulation, maintains perfusion of myocardial tissue with hemodynamics that are out-of-phase to the systemic circulation (1).

Almost all diseases of the heart involve an immune response with a high degree of spatial and temporal regulation that is orchestrated by functionally varied leukocyte populations. This dynamic nature of leukocytes, coupled with the fact that contractile motion at the cell and tissue level is an essential function of the heart, present a unique and challenging environment to study the immune system. Given that the heart is highly specialized and metabolically active, containing the highest oxygen consumption rate per unit of tissue in the human body (2), it is highly susceptible to insults that decrease its function. These include myocardial infarction, a condition that is caused by the partial blockage of blood supply to the myocardium, and chronic heart failure, which is a slow and progressive pathology that weakens the pumping ability of the heart. Diseases of the heart are the most common cause of death in the United States and the majority of populations worldwide (3). Furthermore, the incidence of heart disease continues to increase at an alarming rate despite significant advancements in therapies and techniques (4). Although an inflammatory component has long been recognized as a contributing factor in these diseases, the coupling between the dynamics of the inflammatory cell populations and heart function remains unexplored.

Common techniques to study the cellular basis of cardiac disease in experimental models typically capture a static point in time (e.g., post-mortem immunohistology) or use reduced preparations (e.g., *ex vivo* perfused heart, cell dissociation or isolation and analysis such as flow cytometry). These approaches have led to enormous progress in our fundamental understanding of leukocyte biology in the heart over the past century. However, these approaches fail to capture simultaneous and interacting processes at the cell-scale. The study of leukocyte dynamics in the majority of organ systems, including brain (5–7), kidney (8–10) skin (11, 12), and many more (13–17), have greatly benefitted from intravital microscopy imaging approaches by providing invaluable insight into the fundamental behavior and function of these cells during normal and diseased states. The field of cardiovascular science has started to overcome the barriers of applying intravital microscopy to the heart, a critical step in understanding the pathophysiological basis of these devastating cardiovascular diseases.

The purpose of this review is to provide an overview of leukocyte responses in the heart, outline the advances in the application of intravital multiphoton microscopy to the rodent heart, and highlight its application to investigate specific questions about leukocyte biology within the heart.

IMMUNE CELL POPULATIONS OF THE HEART

The heart of a healthy adult mouse contains the full repertoire of leukocyte populations including mononuclear phagocytes, dendritic cells, neutrophils, T cells, and B cells (18). These leukocyte classes differ in their regional location in the steady-state heart (19), likely due to specific interactions with both cardiomyocytes (20) and non-cardiomyocyte resident cells including endothelial cells (21), smooth muscle cells, and fibroblasts (22), all of which are sources of cytokines, chemokines, and growth factors.

The predominant immune cell population in the heart during healthy conditions is the tissue resident macrophages, accounting for 5–10% of non-myocytes in the heart (23–25). Resident macrophages are found primarily near endothelial cells and within the interstitium between cardiomyocytes (26). Fate mapping studies have shown that cardiac macrophages arise from embryonic progenitors before the start of definitive hematopoiesis and then self-renew through local proliferation with minimal input from blood derived monocytes (26, 27). C-C chemokine receptor type 2 (CCR2) expression is low in the cardiac resident population of macrophages, however a small population of CCR2+ cardiac macrophages, and lymphocyte antigen 6C (Ly6C)+ macrophages exist in the myocardium and are thought to be derived from circulating precursors (27, 28). Histological studies demonstrate that resident macrophages have a spindle-like morphology and associate closely with cardiomyocytes and endothelial cells (20, 25). To maintain homeostasis, these cells survey the local microenvironment and can phagocytose dying or senescent cells (23). Mice expressing green fluorescent protein (GFP) under the control of the Cx3C chemokine receptor (Cx3Cr1) promotor are commonly used to identify monocytes and resident mononuclear phagocytes including cardiac resident macrophage populations (25, 29). In other organs such as the brain, these $Cx3Cr1^{+/GFP}$ mice were used to discover that Cx3Cr1+ cells are actively moving their processes in the normal state and respond within minutes to injury (30–32). Tissue resident cardiac macrophages have recently been discovered to have tissue-specific functions in both health and disease that are not only essential for a coordinated response to injury, but also vital for healthy, steady-state cardiac physiology. Hulsmans et al. (20) demonstrated that resident macrophages are denser in the atrioventricular node, where they actively couple to cardiomyocytes to facilitate electrical conduction through connexin-43-containing gap junctions. Inducible transgenic ablation of these resident macrophages resulted in atrioventricular block, demonstrating a previously unknown, tissue specific function of macrophages. Intravascular patrolling monocytes that are Cx3Cr1+ were observed in the mouse heart during steady-state conditions (33), and are thought to rapidly infiltrate during inflammatory conditions, as has been described in other tissues (34, 35). Mast cells, dendritic cells, B cells, and regulatory T cells are found sparsely in normal cardiac tissue, while neutrophils and monocytes are not observed in myocardial tissue unless within the coronary circulation or in response to a stimulus (19, 27).

The heart is susceptible to a wide range of injuries, both acute and chronic in their nature, that initiate leukocyte responses that aim to repair. Acute myocardial infarction occurs due to an occluded or ruptured coronary artery causing ischemia to a region of the heart that would otherwise be perfused. This event initiates a coordinated immune response that can be divided into inflammatory and reparative phases which differ in leukocyte composition and phenotype (18). The inflammatory phase occurs shortly after ischemia and involves the degranulation of resident

mast cells (21), the release of cytokines and chemokines including interleukin (IL)-1, IL-6, tumor necrosis factor-alpha (TNF-α), and CC-chemokine ligand 2 (CCL2) from resident macrophages and cardiomyocytes (36–38), hematopoietic growth factors from fibroblasts (39), and activation of endothelial cells to upregulate adhesion molecules (40, 41). Together these factors recruit neutrophils and monocytes from the circulation and hematopoietic stem and progenitor cell populations from the bone marrow (23, 42, 43). Within the infarcted heart, neutrophils and monocytes remove dead and dying cells by efferocytosis (44) and the release of proteolytic enzymes to facilitate digestion of dead tissue (45, 46). These actions further enhance inflammation by the production of cytokines including TNF-α, IL-1, and IL-6 (36, 47–49). Neutrophil numbers diminish ∼3–4 days post-infarction in the mouse, whereas monocytes continue to accumulate in the infarct for several days thereafter, where they differentiate into macrophages and express $Ly6C^{Low}$ (50). The presence of neutrophils is essential for the transition to the reparative phase since the release of neutrophil gelatinase-associate lipocalin promotes a reparative macrophage polarization (51). The reparative phase is further characterized by a decreased production of inflammatory cytokines and growth factors (52), accumulation of mast cells (53), and a transition of cardiac macrophages to a reparative phenotype that secrete transforming growth factor-beta (TGF-β) and vascular endothelial growth factor (VEGF) to promote fibrosis and angiogenesis (52, 54). Interestingly, some reports suggest mast cells do not influence levels of inflammation following infarction, however are more important for restoring cardiac contractility by regulating calcium sensitization of cardiomyocyte myofilaments (53).

Immune cell dynamics in chronic and adaptive pathologies of the heart such as heart failure, are amenable to intravital imaging approaches, since these changes can be far more subtle than the rapid and intense reaction caused by acute cardiac pathologies such as myocardial infarction. Heart failure is broadly defined as a condition in which the heart muscle is unable to pump enough blood to meet the body's nutrition and oxygen demands. If the heart muscle is too weak, the fraction of blood pumped out from the left ventricle can drop below 30–35%, a condition known as heart failure with reduced ejection fraction. On the other hand, heart failure with preserved ejection fraction (HFpEF) occurs when there is a deficiency in the relaxation and filling capacity of the heart chambers (diastolic dysfunction) while maintaining a normal ejection fraction (55, 56). HFpEF is increasing in incidence with a mortality rate equal to other cardiac pathologies (57–59) and an absence of any evidence-based therapies. The etiology and risk factors are broad and unclear, and there are limited experimental animal models that recapitulate the pathology (60), making it difficult to study leukocyte function. Tissue biopsies of human HFpEF patients show that cardiac macrophages (61) and blood monocytes (62) increase, and an animal model of diastolic dysfunction and aged mice demonstrate this increase is due to monocyte recruitment and increased hematopoiesis from bone marrow and spleen (61). In an animal model of pressure overload induced by transaortic constriction (TAC) that mimics aspects of HFpEF but eventually develop a reduced ejection fraction, Nevers et al. demonstrated T-cell recruitment, increased lymphocytes and macrophages in the myocardium, and increased endothelial cell expression of adhesion molecules VCAM1, ICAM1, and E-selectin (63). Wnt-mediated neutrophil recruitment facilitates cardiac dysfunction during heart failure, which has been demonstrated by improved cardiac function following neutrophil depletion in the TAC model (64). However, the behavior and localization of these neutrophils within the microcirculation or myocardium that are responsible for this damage are unknown. Furthermore, the TAC model has been criticized as a surrogate model of HFpEF due to the acute effects of aortic constriction. More recently, Hulsmans et al. used a mouse model of diastolic dysfunction and aged mice (18–30 months old) to demonstrate that increased myocardial macrophages result from monocyte recruitment and increased hematopoiesis (61). Understanding of the relationship between the ejection fraction, the blood delivered to the rest of the body and the local blood flow within the heart itself, is also limited in heart failure models.

A major advantage of using intravital microscopy to study cardiac disease, is the ability to visualize fast and dynamic behaviors of leukocyte sub-types that can influence tissue repair. Such interactions have been described in other tissues, including neutrophil mediated dismantling of damaged vessels and the creation of channels for regrowth in liver (65), and patrolling monocyte mediated neutrophil activation (10) and effector CD4+ T cell antigen recognition (9) in the inflamed kidney. It is possible that similar actions occur within the heart, yet this remains unknown. Specific cellular interactions that could be investigated with cardiac intravital microscopy include the neutrophil-induced promotion of reparative macrophage polarization following infarction (51), and neutrophil-dependent induction of hypertrophy (64).

INTRAVITAL IMAGING OF LEUKOCYTES IN THE HEART: PREVIOUS APPROACHES

Approaches to imaging the rodent heart at cell resolution need to consider three separate aspects—surgical access, image acquisition, and pre- or post-processing of images. Previous approaches to imaging leukocytes in the heart at cell resolution used varied strategies to address these three aspects, and are summarized in **Tables 1**, **2**.

One of the first approaches to imaging leukocyte populations in the mouse heart used heterotopic heart explantation with the primary application to study leukocyte recruitment into the inflamed heart (66). Heterotopic heart models are advantageous for discriminating between infiltrating leukocyte and resident cell dynamics, because the leukocyte populations of the recipient animal were labeled through transgenic techniques, whilst the donor heart remains unlabeled. Therefore, labeled leukocyte populations following transplantation are indicative of infiltrating cells and are not tissue resident cells. This technique involves transplanting a donor heart into the right cervical position of a recipient mouse, connecting the right common carotid artery to the donor ascending aorta, and

TABLE 1 | Surgical and stabilization approaches in the heart.

	Surgical access	Stabilization	Advantages	Limitations	References
Heterotopic heart explantation	• Right cervical or abdominal transplantation of donor heart with circulatory integration	• Stabilization chamber	• Investigating graft and host cell interactions	• Abnormal hemodynamics, low temporal resolution	(66–68)
Micro-endoscopy	• 2–3 mm intercostal incision	• Suction probe	• Reduced motion artifact • Repeat longitudinal imaging	• Reduced lateral and axial resolution due to GRIN lens	(33)
Passive stabilization	• Left thoracotomy	• 3D-printed or machined circular probe with tissue adhesive	• High spatial and temporal resolution • Wide fields of view	• Motion artifact limits visualization of single-cycle dynamics	(69–76)*

**Matsuura et al. (69) achieved passive stabilization in a rat model by retracting the anterior thoracic wall and placing a suction-assisted stabilization chamber.*

TABLE 2 | Imaging and reconstruction approaches in the intravital heart.

	Image acquisition	Advantages	Limitations	References
Image gating	• Laser scanning microscopy • 1–16 fps • Z-stack • External pacing of cardiac and respiratory cycles • Prospective or retrospective gating	• High spatial and temporal resolution • Wide field of view	• External control of cardiac and respiratory cycles may induce abnormalities • Restricted to stable portions of cardiac cycle	(70, 71, 73, 77)
Free running	• Laser scanning microscopy • 15–30 fps • Single z-plane	• Capture fast dynamic events	• Motion artifact limits quantification of beat-to-beat dynamics • Restricted to single z-plane	(33, 69, 70, 72)
Cardiorespiratory reconstruction	• Laser scanning microscopy • 30 fps • Z-stack • Nearest neighbor cardio-respiratory phase-space reconstruction	• High spatial and temporal resolution • Wide field of view • Image volumes visualized across full cardiac and respiratory cycles • No external pacing	• Inability to visualize beat-to-beat dynamics	(74–76)

right external jugular vein to the donor pulmonary artery. Optical access is gained by placing the mouse within a stabilization chamber allowing a coverglass to be lowered onto the heterotopic heart (**Figure 1A**). Image acquisition used video-rate scanning with 15-frame averaging, and Z-stack imaging that was partially synchronized with the heart rhythm. This method produced images of neutrophils and macrophages at baseline and following ischemia-reperfusion induced either by transplantation or coronary artery ligation. Imaging demonstrated recruitment of neutrophils to the heart, their extravasation from coronary veins, and their infiltration of the myocardium where they form large clusters (**Figure 3A**). In combination with transgenic cell ablation studies (diphtheria toxin receptor targeted expression), this technique has been used to demonstrate that tissue-resident, CCR2-expressing cardiac macrophages promote monocyte recruitment after transplantation (67). The same authors also present intravital imaging of neutrophils flowing, rolling, and crawling within coronary vessels of the murine heart in its native intrathoracic position during baseline and inflamed conditions. Intra-abdominal heart transplantation using a similar technique has also been used to image trafficking of donor dendritic cells following transplantation, finding that they migrate out of donor tissue and that this behavior is Cx3Cr1-dependent (68). While the heterotopic heart presents a unique system to study leukocyte dynamics in the context of transplant-induced ischemia-reperfusion and acute and chronic rejection, it remains restricted to these applications since the heterotopic heart does not contribute to the hemodynamics of the recipient despite perfusion of the donor coronary circulation and beating of the heart. Understanding cardiac leukocyte dynamics during healthy, steady-state conditions requires imaging of the heart within the natural intrathoracic location. More recently, a similar stabilization device enabled imaging the native heart within the intrathoracic position of rats (69). This technique involves removing the anterior chest wall and applying a circular stabilizer affixed with a cover glass and suction ring to reduce motion. Using a clever ischemia reperfusion model that was deployed during intravital imaging, the authors showed the accumulation of transplanted, GFP+, bone-marrow derived leukocytes that occlude capillaries following reperfusion.

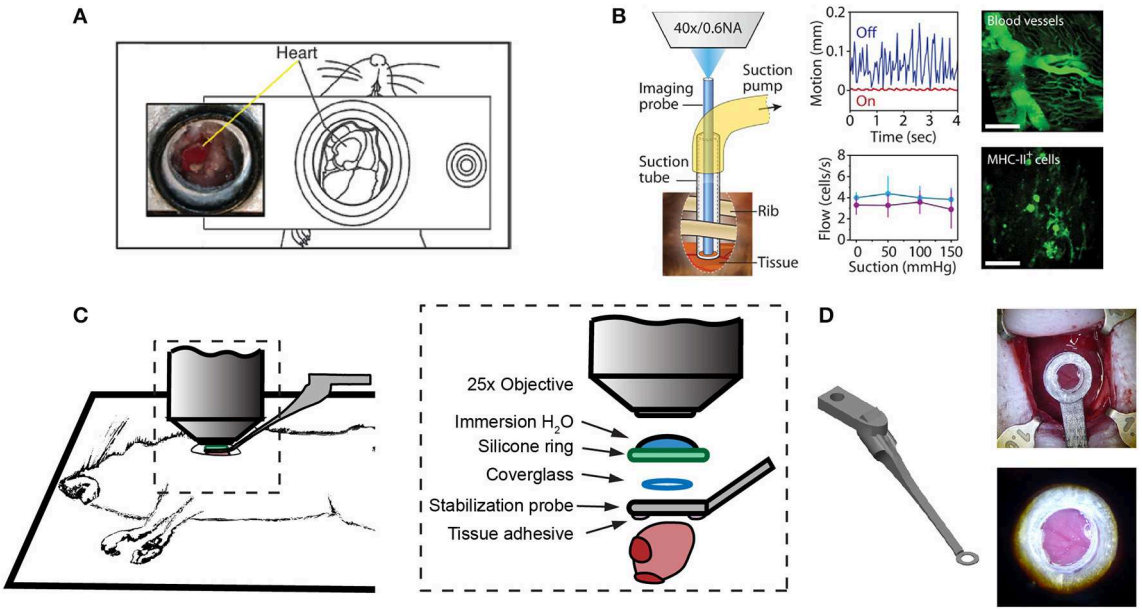

FIGURE 1 | Surgical approaches for intravital microscopy of the beating mouse heart. **(A)** The cervical explanted heart model provides the benefits of studying cardiac graft vs. host interaction [image adapted from Li et al. (66) with permission]. **(B)** Endoscopic, suction-stabilized imaging provides a less invasive approach and enables time-lapse imaging that reduces motion and appears to leave major histocompatibility complex class-II (MHC-II) + immune cell numbers unchanged [image reproduced from Jung et al. (33) with permission]. **(C)** Intrathoracic approaches enable a wider field of view of the freely beating heart in mechanically ventilated animals. Optical access to the heart is gained by a left thoracotomy in the anesthetized mouse. **(D)** Passive tissue stabilization is achieved by a 3D printed stainless steel probe (left) with a coverglass and reservoir for water immersion of the microscope objective. Tissue adhesive is applied to the underside of the stabilization probe prior to attachment to the left ventricle. Photographs show the probe attached to the heart (top right) and a view of the heart surface with visible coronary vessels in the window (bottom right). Image adapted from Jones et al. (78).

Less invasive approaches are achievable through the use of suction-assisted, micro-endoscope, optical probes (33). A benefit of this technique is the local stabilization of the myocardial tissue that significantly reduces motion artifact and therefore eliminates the need for retrospective image processing. This technique utilizes a gradient refractive index (GRIN) lens within suction tubing, an assembly that is sufficiently small (2–3 mm) to be inserted through an incision in the intercostal space, thereby making repeat longitudinal imaging achievable (**Figure 1B**). To counter the small field of view typically achievable with micro-endoscopic lenses, the lens can be moved within the suction tubing via a translation stage to image multiple regions. Using repeated imaging over 6 days in $Cx3Cr1^{+/GFP}$ mice to track monocytes and $LysM^{+/GFP}$ mice to track neutrophils, Jung et al. provided evidence that following acute myocardial infarction, recruited monocytes come first from the vascular reservoir and then later from the spleen. Although this technique allows repeat imaging which is advantageous for studies of long-term leukocyte infiltration, the use of GRIN lenses results in a reduction in image resolution and imaging depth due to low numerical aperture (NA) and is not well-suited for studying leukocyte dynamics that involve fine cellular features. Image resolution and achievable depth rely on many factors including acquisition speed and fluorescence excitation source (multiphoton or single photon excitation), however the approximate lateral and axial resolution of GRIN lenses are 1 and 12 μm, respectively, with ≤0.6 NA objectives, compared to sub-micron resolution with approximately 1.0 NA objectives (79–81). GRIN lens imaging depth has been reported to be ∼95 μm in brain tissue compared to ∼1,000 μm without (82–85), but was not specified in heart. Typically, ∼100–200 μm depth of imaging is achieved with a traditional objective in the heart (78).

Passive tissue stabilization that sufficiently reduces cardiac and respiration-induced motion in the axial direction can be used in tracking leukocyte dynamics on short-time scales with relatively wide fields of view. This has been demonstrated by Lee et al. using rhodamine-6G to label leukocytes (70). Passive tissue stabilization involves the application of a stabilizing ring that is bonded to the surface of the heart (**Figures 1C,D**). Image capture typically requires gating image acquisition by synchronizing with the stable portion of the cardiac cycle (diastole) (71). To eliminate motion from breathing, many studies transiently pause ventilator-induced respiration (70). Externally pacing the heart also simplifies timing image acquisition. If adequate stabilization is achieved with tissue stabilization devices so that axial motion of the cardiac contraction remains less than the axial dimension of the structure of interest (cell or capillary), then free-running images can be used to capture very short time-scale dynamics that occur over one heart beat. In our experience, cardiac contraction induced axial motion is often greater than the structure of interest, and severe suppression of motion might suggest inadequate ventricular function. Furthermore, transiently stopping ventilation of the animal, and externally pacing the heart can exert aberrant effects on the animal and heart

function. Using similar passive motion stabilizers, prospective and retrospective image gating methods have been incorporated to image with high resolution (71) however, image gating fails to capture the dynamics of the heart at its peak contraction (systole). Recently, Kavanagh et al. have applied passive tissue stabilization of the beating heart without gating strategies, using fluorophore-conjugated antibodies to visualize neutrophils and platelets following ischemia-reperfusion injury (72).

MOTION WITHIN MOTION—CAPTURING A MOVING CELL WITHIN A MOVING ORGAN

Motion is a defining characteristic of leukocytes, blood flow, and most importantly, the heart. The progress of cardiac leukocyte biology requires techniques to quantitatively assess leukocyte characteristics including polarized morphology, spatially-dependent speeds, and transmigration ideally with minimal artifacts and invasiveness.

Intravital microscopy of the beating mouse heart has primarily relied on multiphoton microscopy, specifically 2-photon excitation fluorescence (2PEF) microscopy, because it provides fluorescence imaging with microscopic resolution at depth in intact tissues (86). In contrast to confocal microscopy, which utilizes continues-wave (non-pulsed) laser wavelengths at which single photons can excite fluorescence, 2PEF microscopy uses photons with approximately half the energy of the confocal microscope lasers and approximately double the excitation wavelength. Therefore, it requires the nearly simultaneous (within $\sim 10^{-16}$ s) interaction of two photons with a fluorescent molecule to excite fluorescence (87). The emitted fluorescence signal then scales as the square of the excitation intensity, rather than proportionally as with confocal or wide-field fluorescence microscopy, resulting in a signal primarily emitted from the beam focus where intensity is highest. An image is reconstructed by scanning this focus in the sample, measuring the amount of emitted fluorescence, and assigning that value to the image pixel corresponding to the focus position. Scattering of the emitted light does not blur the reconstructed image because all the light is known to have originated from the focus point. To achieve the higher intensities required for two-photon microscopy, the excitation laser is pulsed, and because the gaps in time between pulses are relatively long, the average power remains low. These characteristics greatly increase the signal-to-noise ratio, restrict excitation to a narrow focal volume, and minimize harmful energy deposition in the tissue. Confocal microscopy can also be used *in vivo*, but because it relies on rejection of scattered and out-of-focus light, the signal decays rapidly with depth. A further advantage of using longer wavelengths is reduced light scattering which also increases imaging depth compared to confocal microscopy.

An important consideration is that leukocyte behavior varies with time, especially during inflammatory conditions. Therefore, different imaging approaches are best at capturing the intravital dynamics depending on whether the activity is faster or slower than the speed of tissue motion. For example, leukocyte crawling, extravasating, and migration through myocardial tissue typically occurs at speeds of ∼7–10 μm/min (66). Since this is slower than tissue motion during systole, ∼9 mm/s (5.4×10^5 μm/min), and the leukocytes remain in the field of view over multiple heartbeats, imaging can be gated to limit acquisition during stable portions of the cardiac cycle (**Figure 2A**). However, fast leukocyte dynamics, such as intravascular flow, must account for three-dimensional movement of the tissue throughout the cardiac cycle which requires additional approaches.

It is possible to achieve capture of cell dynamics throughout the whole cardiac cycle without the need for external pacing, gating strategies, or breath holds, by using passive tissue stabilization, mechanical ventilation, and fast resonant scanning acquisition coupled with cardiorespiratory-cycle dependent image reconstruction algorithms (78). **Figures 2B–F** demonstrates reconstruction methods to achieve high quality volumetric images of cardiac dynamics at the microscale. Bidirectional raster scanning at a single depth relative to the microscope (Z-position) is achieved by scanning the beam focus using slow galvanometric scanning for the Y-axis, and fast resonant scanning for the X-axis, which enables the acquisition of frames at ∼30 frames/s. X, Y, Z position refers to the microscope stage position and not to the orientation of the cardiac tissue since the heart is actively beating and therefore moving through the imaged region. The two primary sources of motion within acquired imaging frames are the cardiac muscle contraction and respiratory motion of the lungs pushing on the heart. Therefore, the electrocardiogram (ECG) and lung pressure are simultaneously recorded and used to index image frames according to where they occurred in the cardiac and respiratory cycles. Raster scanning of the beam focus generates a line of pixels at a specific Y-axis galvanometer position and Z-axis stage height (a single Y, Z position) at a known time relative to the cardiac and respiratory cycles. By selecting line segments that occur at a particular portion of the cardiac and respiratory cycles, image volumes can be reconstructed at any desired point during the cardiac cycle by using, for each Y, Z position in the reconstructed volume, the line scan which occurred at the requested cardiac phase. A limiting factor of this method is not all points within cardio-respiratory phase space will be sampled, which can result in missing segments within reconstructed image volumes. By using lines that are *nearest* to the desired point in cardio-respiratory phase space, complete volumetric reconstruction can be achieved. We find that ∼3 s of image acquisition per imaging plane is sufficient to enable detailed volumetric reconstructions across the cardiac cycle.

Reconstruction methods are advantageous for tracking leukocyte dynamics that occur over slower, minute time scales, including neutrophil infiltration of explanted heart tissue [**Figure 3A**; (66)] and high resolution images of Cx3Cr1+ resident macrophage morphological changes in response to laser induced focal injury or following infarction (**Figures 3B,C**). Faster leukocyte activities including rolling and migratory behaviors can also be captured with free-running image acquisition without cardio-respiratory phase dependent reconstruction (**Figure 3D**). However, axial displacement due to cardiac and respiratory induced motion causes the transient disappearance of selected cells, therefore restricting the ability to capture sequential heartbeat (beat-to-beat) dynamics.

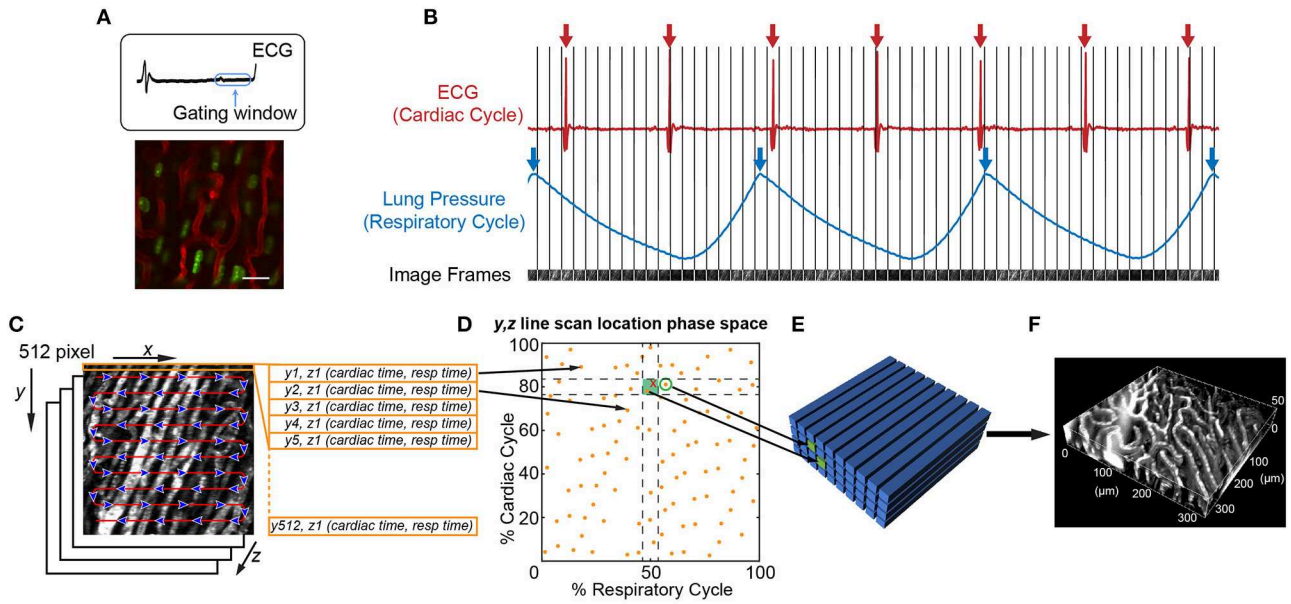

FIGURE 2 | Image acquisition and reconstruction techniques for the beating mouse heart *in vivo*. **(A)** Heart structure is relatively stable during diastole allowing acquisition of full image frames with no motion artifact [image adapted from Lee et al. (70) with permission]. **(B–F)** Line-by-line reconstruction enables volumetric reconstructions at any point within the cardiac or respiratory cycles. **(B)** Simultaneous recording of the electrocardiogram (ECG) and lung pressure during imaging produces image frames at a single Z-plane that are captured at various points in the cardiac and respiratory cycles. The R-wave peak of the ECG (red arrows) and inspiratory peak of the lung pressure (blue arrows) are defined as the start and end of the cardiac cycle and respiratory cycle, respectively. **(C)** Each 512 × 512 pixel image frame is produced by raster scanning the excitation laser in the X-direction, therefore each line has a defined position in Y, a depth in Z, and a time it was captured with respect to the cardiac cycle (cardiac time) and respiratory cycle (respiratory time). **(D)** Each Y, Z line in the image is associated with a phase in the cardiac and respiratory cycles (yellow spots). An image volume is reconstructed using image lines for each Y, Z position that occur at a specified part of respiratory and cardiac cycles (green shaded box). **(E)** The closest Y, Z position (green circle) to a requested point in cardio-respiratory phase space that is absent (red cross) can be used to completely fill a three-dimensional volume. **(F)** Reconstructed vasculature of the beating mouse heart during diastole. Vasculature is fluorescently labeled with a Texas Red dye conjugated to a 70 kDa dextran. Scale bar in A represents 20 μm.

THE FUTURE OF INTRAVITAL MICROSCOPY FOR CARDIAC LEUKOCYTE DYNAMICS

Active Motion Compensation

Passive stabilization in combination with different acquisition and reconstruction methods, often with gating (either during imaging or at reconstruction), enables structural imaging and some measurements (70, 71, 78, 88). However, since all reconstruction methods rely on assembling image data from multiple cardiac and/or respiratory cycles, reconstructed images cannot be used to measure or visualize any process that occurs faster than the number of cycles required to generate the reconstruction, such as non-adherent leukocyte and red blood cell motion within vessels. Dynamics that change from heartbeat to heartbeat such as arrhythmic, electrical conduction irregularities in individual cells, also cannot be visualized with current reconstructions. One solution that does not involve altering the natural physiology beyond surgical access and application of an imaging window is active motion compensation, which involves moving the focal plane in synchrony with the heart motion.

The key challenge in active motion compensation is generating a feedback signal that indicates the motion of the tissue. With an appropriate feedback signal, the motion of the tissue can be matched by moving either the focal plane of the microscope, such as the microscope objective using actuators for fast motion, or moving the mouse using the microscope stage for slower motion. The feasibility of these methods was shown in early approaches using stroboscopic illumination of epicardial microvessels in combination to image, and a computer-controlled electromechanical micromanipulator that moved a micropipette in synchrony with the heart to capture phasic changes in microvascular pressure in the left ventricle of cats (89). To generate a feedback signal, image-based motion compensation methods use the alignment of successive images. In cardiac imaging, a separate camera capable of faster frame rates must be used to image a fiducial such as a fluorescent bead implanted within an imageable volume. However, this method has only been successful in correcting for in-plane motion (90) while axial movements (toward and away from the microscope objective) pose a particular challenge in cardiac imaging because such movements cause biological structures to come into and out of focus. Contact-based motion compensation methods have been proposed which use cantilever probes or strain gauges to detect three dimensional motion however, there have been no reports of successful *in vivo* imaging using laser scanning microscopy through a single cardiac cycle using this method (77).

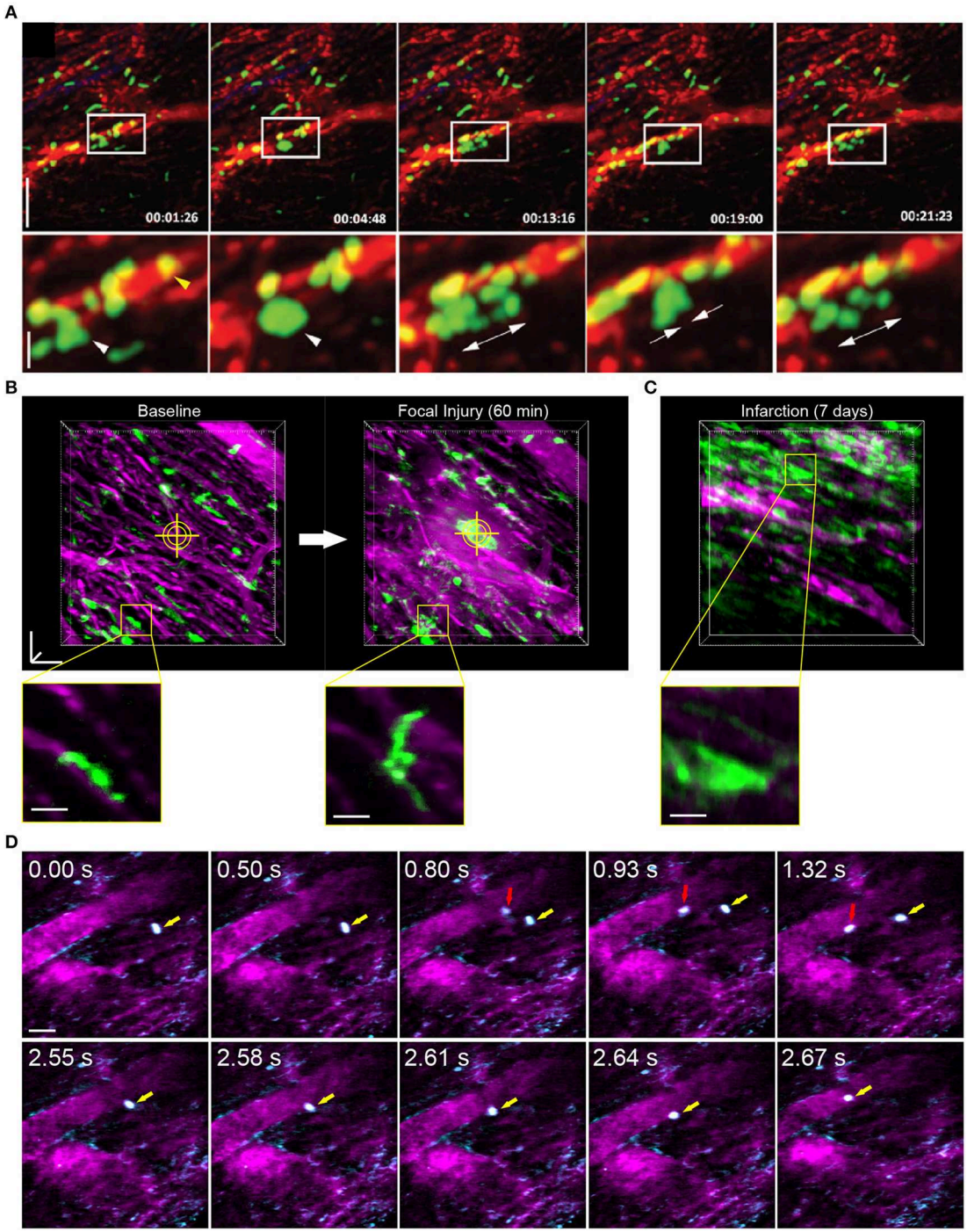

FIGURE 3 | Leukocyte dynamics in the mouse heart using intravital multiphoton microscopy. **(A)** Intravital multiphoton imaging of explanted heart tissue after heterotopic cardiac transplantation into LysM$^{+/GFP}$ mice shows neutrophil (green) infiltration from the host through vasculature labeled with non-targeted 655 nm Q-dots in red [image adapted from Li et al. (66) with permission]. Time stamp is h:min:s and scale bar is 60 μm (top) and 20 μm (bottom). **(B)** Intravital multiphoton microscopy with cardiorespiratory-dependent image reconstruction of Cx3Cr1$^{+/GFP}$ mice hearts enables visualization of acute morphological changes of resident cardiac macrophages (green) in response to focal, laser-irradiation injury (yellow cross-hairs) over 1 h. Images are perspective Z-projections over 50 μm in depth and insets are single Z-slice of the region outlined in yellow, from 80% of the cardiac cycle and 50% of the respiratory cycle. **(C)** Intravital imaging shows increased number of macrophages in the heart following myocardial infarction compared to baseline. Vasculature is fluorescently labeled with Texas Red dextran (**B–D**, magenta). **(D)** Free-running intravital multiphoton microscopy captures intravascular rolling (red arrow) and crawling (yellow arrow) behavior of leukocytes labeled with rhodamine-6G (cyan) within vessels (magenta, Texas Red dextran). **(B–D)** Scale bars represent 50 μm, except insets in **(B)** that are 20 μm. Images captured with an Olympus XLPlan N 25 × 1.05 NA objective. All animal procedures were approved by the Institutional Animal Care and Use Committee of Cornell University.

Early studies using stroboscopic illumination have measured diameter changes over 100 heat beats in small coronary vessels of the rabbit heart (91). A third motion compensation strategy takes advantage of angular changes in the reflection of a positioning laser off the surface of the tissue to measure (92) and correct for axial motion in applications such as imaging in rodent spinal cord (93). Reflective positioning offers advantages over contact-based and image-based methods as it is simple, sensitive, and does not rely on additional physical probing of the animal. The application of reflective motion compensation to cardiac imaging is a promising direction that could enable single-cycle measurements of cell trafficking and electrical activity.

Deeper Imaging

The current maximum 2PEF imaging depth within the mouse heart is ∼200 μm, limiting visualization to functions within the epicardial layer. Although this provides a good first step to studying immune cell dynamics in the heart, there are both structural and functional differences within deeper layers of the heart. Structurally, specialized conduction fibers, known as Purkinje fibers, are located in the subendocardial space, and larger coronary arteries lie deeper within the mouse myocardium. Given the recent discovery that resident macrophages facilitate electrical conduction in the heart (20), and that atherosclerosis occurs within larger coronary arteries, deeper imaging within 300 μm from the epicardial surface would enable the study of leukocyte function and behavior within these contexts.

Recent advancements in mid-infrared laser sources now make deeper imaging feasible using three-photon microscopy (94). By utilizing three excitation photons to excite a single emission photon, excitation sources with longer wavelengths can be used, and these longer wavelengths penetrate deeper into tissue and scatter much less than 2PEF wavelengths. However, the probability of three-photon interaction is low, so achieving a usable amount of fluorescence requires a higher excitation photon density or peak power. New short-pulse laser sources can now reach such peak powers at sufficient repetition rates for imaging, and provide longer wavelengths, which enable greater imaging depth (84, 94). Laser sources based on photonic crystal fibers emitting around 1,700 nm have been developed specifically for deep imaging applications (95), as well as commercially available excitation sources with turn-key optical parametric amplifiers that can be tuned from 1 to 2 μm. While able to provide more than adequate power and pulse repetition rates for three-photon imaging of slow dynamics, excitation sources in these higher wavelength ranges typically operate at a lower repetition rate (frequency of photon pulse) which presents a challenge for cardiac imaging which relies on very fast raster scanning. A resonant scanner sweeps across the focal plane so quickly that some pixels will fall between two laser pulses resulting in no signal. Current laser sources are not far off, as only 12–15 MHz is needed to guarantee at least a single pulse to acquire a 512 × 512 image at 30 fps. Continued advancements in laser technology to produce high repetition rate sources in the mid-infrared range would alleviate this problem.

Deeper imaging is also impaired by sample-dependent optical aberrations. The use of an adaptive optical element such a deformable mirror can greatly improve multiphoton microscope performance (96–98). By pre-compensating for system and sample aberrations in the excitation beam wavefront, an improved focus is achieved resulting in higher intensities and better spatial confinement. This allows for deeper penetration with greater image contrast and resolution.

Chronic Implantable Window

Other organ systems have benefitted from chronic implantable windows to enable time-lapse imaging, making it possible to follow the same regions at the micro-scale during disease progression. This includes the cranial window (5, 6, 99, 100), dorsal skinfold chamber (101, 102), abdominal window for intestine, liver and spleen (103–105), a modified abdominal window for kidney (106, 107), and a fixation plate with micro-endoscope for femur bone marrow (108). Chronic imaging of the mouse heart would allow unprecedented visualization of pathophysiological processes in diseases of the heart, including the ability to monitor angiogenesis and fibrosis post-infarction within the full inflammatory milieu of leukocyte populations. Currently, time-lapse imaging over multiple imaging sessions for the mouse heart involves repeated surgeries for opening and closing an incision. Recently, chronic intravital imaging of the lung was achieved through a permanent window attached to a superficial portion of lung (109). This demonstrates the ability to chronically access the thoracic cavity and suggests accessing the anatomically deeper heart is feasible.

CONCLUSIONS

With continued advancements in technology to access and image the murine heart, we are sure to make strides toward increasing our understanding of leukocyte dynamics during diseases of the heart. Targeting the immune system with therapies has proven to be successful in other diseases, especially immunotherapies for cancer (110). However, applying similar types of therapies to the varied diseases of the heart first requires an understanding of leukocyte behavior within the true *in vivo* environment which can be improved with intravital, multiphoton microscopy.

AUTHOR CONTRIBUTIONS

DS conceived the idea for the review, performed literature search, and wrote the manuscript. NA-R wrote the active motion compensation section. ML wrote the deeper imaging section. NN and WC provided direction for the manuscript. All authors contributed to reviewing and editing the final manuscript.

FUNDING

This research was funded by the American Heart Association (17POST33680127 to DS), National Institutes of Health (5R21EB024694-03 to NN), and the National Science Foundation (DBI-1707312).

REFERENCES

1. Goodwill AG, Dick GM, Kiel AM, Tune JD. Regulation of coronary blood flow. *Compr Physiol.* (2017) 7:321–82. doi: 10.1002/cphy.c160016
2. Klabunde RE. Myocardial oxygen demand. In: Taylor C, editor. *Cardiovascular Physiology Concepts*. 2nd ed. Baltimore, MD: Lippincott Williams & Wilkins (2011), p. 182–6.
3. GBD 2017 Causes of Death Collaborators. Global, regional, and national age-sex-specific mortality for 282 causes of death in 195 countries and territories, 1980-2017: a systematic analysis for the Global Burden of Disease Study 2017. *Lancet.* (2018) 392:1736–88. doi: 10.1016/S0140-6736(18)32203-7
4. Benjamin EJ, Muntner P, Alonso A, Bittencourt MS, Callaway CW, Carson AP, et al. Heart disease and stroke statistics-2019 update: a report from the American Heart Association. *Circulation.* (2019) 139:e56–528. doi: 10.1161/CIR.0000000000000659
5. Ahn SJ, Anrather J, Nishimura N, Schaffer CB. Diverse inflammatory response after cerebral microbleeds includes coordinated microglial migration and proliferation. *Stroke.* (2018) 49:1719–26. doi: 10.1161/STROKEAHA.117.020461
6. Cruz Hernandez JC, Bracko O, Kersbergen CJ, Muse V, Haft-Javaherian M, Berg M, et al. Neutrophil adhesion in brain capillaries reduces cortical blood flow and impairs memory function in Alzheimer's disease mouse models. *Nat Neurosci.* (2019) 22:413–20. doi: 10.1038/s41593-018-0329-4
7. Garre JM, Silva HM, Lafaille JJ, Yang G. CX3CR1^{+} monocytes modulate learning and learning-dependent dendritic spine remodeling via TNF-alpha. *Nat Med.* (2017) 23:714–22. doi: 10.1038/nm.4340
8. Devi S, Li A, Westhorpe CL, Lo CY, Abeynaike LD, Snelgrove SL, et al. Multiphoton imaging reveals a new leukocyte recruitment paradigm in the glomerulus. *Nat Med.* (2013) 19:107–12. doi: 10.1038/nm.3024
9. Westhorpe CLV, Norman MU, Hall P, Snelgrove SL, Finsterbusch M, Li A, et al. Effector CD4^{+} T cells recognize intravascular antigen presented by patrolling monocytes. *Nat Commun.* (2018) 9:747–22. doi: 10.1038/s41467-018-03181-4
10. Finsterbusch M, Hall P, Li A, Devi S, Westhorpe CL, Kitching AR, et al. Patrolling monocytes promote intravascular neutrophil activation and glomerular injury in the acutely inflamed glomerulus. *Proc Natl Acad Sci USA.* (2016) 113:E5172–81. doi: 10.1073/pnas.1606253113
11. Gaylo-Moynihan A, Prizant H, Popović M, Fernandes NRJ, Anderson CS, Chiou KK, et al. Programming of distinct chemokine-dependent and -independent search strategies for Th1 and Th2 cells optimizes function at inflamed sites. *Immunity.* (2019) 51:298–309.e6. doi: 10.1016/j.immuni.2019.06.026
12. Sumaria N, Roediger B, Ng LG, Qin J, Pinto R, Cavanagh LL, et al. Cutaneous immunosurveillance by self-renewing dermal gammadelta T cells. *J Exp Med.* (2011) 208:505–18. doi: 10.1084/jem.20101824
13. Park C, Hwang IY, Kehrl JH. The use of intravital two-photon and thick section confocal imaging to analyze B lymphocyte trafficking in lymph nodes and spleen. *Methods Mol Biol.* (2018) 1707:193–205. doi: 10.1007/978-1-4939-7474-0_14
14. Sumen C, Mempel TR, Mazo IB, von Andrian UH. Intravital microscopy: visualizing immunity in context. *Immunity.* (2004) 21:315–29. doi: 10.1016/j.immuni.2004.08.006
15. Lutz SE, Smith JR, Kim DH, Olson CVL, Ellefsen K, Bates JM, et al. Caveolin1 is required for Th1 cell infiltration, but not tight junction remodeling, at the blood-brain barrier in autoimmune neuroinflammation. *Cell Rep.* (2017) 21:2104–17. doi: 10.1016/j.celrep.2017.10.094
16. Swanson PA II, Hart GT, Russo MV, Nayak D, Yazew T, Pena M, et al. CD8^{+} T cells induce fatal brainstem pathology during cerebral malaria via luminal antigen-specific engagement of brain vasculature. *PLoS Pathog.* (2016) 12:e1006022. doi: 10.1371/journal.ppat.1006022
17. Tsujikawa A, Ogura Y. Evaluation of leukocyte-endothelial interactions in retinal diseases. *Ophthalmologica.* (2012) 227:68–79. doi: 10.1159/000332080
18. Swirski FK, Nahrendorf M. Cardioimmunology: the immune system in cardiac homeostasis and disease. *Nat Rev Immunol.* (2018) 18:733–44. doi: 10.1038/s41577-018-0065-8
19. Epelman S, Liu PP, Mann DL. Role of innate and adaptive immune mechanisms in cardiac injury and repair. *Nat Rev Immunol.* (2015) 15:117–29. doi: 10.1038/nri3800
20. Hulsmans M, Clauss S, Xiao L, Aguirre AD, King KR, Hanley A, et al. Macrophages facilitate electrical conduction in the heart. *Cell.* (2017) 169:510–22.e20. doi: 10.1016/j.cell.2017.03.050
21. Frangogiannis NG, Lindsey ML, Michael LH, Youker KA, Bressler RB, Mendoza LH, et al. Resident cardiac mast cells degranulate and release preformed TNF-alpha, initiating the cytokine cascade in experimental canine myocardial ischemia/reperfusion. *Circulation.* (1998) 98:699–710. doi: 10.1161/01.CIR.98.7.699
22. Wu L, Ong S, Talor MV, Barin JG, Baldeviano GC, Kass DA, et al. Cardiac fibroblasts mediate IL-17A-driven inflammatory dilated cardiomyopathy. *J Exp Med.* (2014) 211:1449–64. doi: 10.1084/jem.20132126
23. Heidt T, Courties G, Dutta P, Sager HB, Sebas M, Iwamoto Y, et al. Differential contribution of monocytes to heart macrophages in steady-state and after myocardial infarction. *Circ Res.* (2014) 115:284–95. doi: 10.1161/CIRCRESAHA.115.303567
24. Pinto AR, Ilinykh A, Ivey MJ, Kuwabara JT, D'Antoni ML, Debuque R, et al. Revisiting cardiac cellular composition. *Circ Res.* (2016) 118:400–9. doi: 10.1161/CIRCRESAHA.115.307778
25. Pinto AR, Paolicelli R, Salimova E, Gospocic J, Slonimsky E, Bilbao-Cortes D, et al. An abundant tissue macrophage population in the adult murine heart with a distinct alternatively-activated macrophage profile. *PLoS ONE.* (2012) 7:e36814. doi: 10.1371/journal.pone.0036814
26. Leid J, Carrelha J, Boukarabila H, Epelman S, Jacobsen SE, Lavine KJ. Primitive embryonic macrophages are required for coronary development and maturation. *Circ Res.* (2016) 118:1498–511. doi: 10.1161/CIRCRESAHA.115.308270
27. Epelman S, Lavine KJ, Beaudin AE, Sojka DK, Carrero JA, Calderon B, et al. Embryonic and adult-derived resident cardiac macrophages are maintained through distinct mechanisms at steady state and during inflammation. *Immunity.* (2014) 40:91–104. doi: 10.1016/j.immuni.2013.11.019
28. Bajpai G, Schneider C, Wong N, Bredemeyer A, Hulsmans M, Nahrendorf M, et al. The human heart contains distinct macrophage subsets with divergent origins and functions. *Nat Med.* (2018) 24:1234–45. doi: 10.1038/s41591-018-0059-x
29. Jung S, Aliberti J, Graemmel P, Sunshine MJ, Kreutzberg GW, Sher A, et al. Analysis of fractalkine receptor CX_3CR1 function by targeted deletion and green fluorescent protein reporter gene insertion. *Mol Cell Biol.* (2000) 20:4106–14. doi: 10.1128/MCB.20.11.4106-4114.2000
30. Nimmerjahn A, Kirchhoff F, Helmchen F. Resting microglial cells are highly dynamic surveillants of brain parenchyma *in vivo*. *Science.* (2005) 308:1314–8. doi: 10.1126/science.1110647
31. Davalos D, Grutzendler J, Yang G, Kim JV, Zuo Y, Jung S, et al. ATP mediates rapid microglial response to local brain injury *in vivo*. *Nat Neurosci.* (2005) 8:752–8. doi: 10.1038/nn1472
32. Rosidi NL, Zhou J, Pattanaik S, Wang P, Jin W, Brophy M, et al. Cortical microhemorrhages cause local inflammation but do not trigger widespread dendrite degeneration. *PLoS ONE.* (2011) 6:e26612. doi: 10.1371/journal.pone.0026612
33. Jung K, Kim P, Leuschner F, Gorbatov R, Kim JK, Ueno T, et al. Endoscopic time-lapse imaging of immune cells in infarcted mouse hearts. *Circ Res.* (2013) 112:891–9. doi: 10.1161/CIRCRESAHA.111.300484
34. Auffray C, Fogg D, Garfa M, Elain G, Join-Lambert O, Kayal S, et al. Monitoring of blood vessels and tissues by a population of monocytes with patrolling behavior. *Science.* (2007) 317:666–70. doi: 10.1126/science.1142883
35. Li L, Huang L, Sung SS, Vergis AL, Rosin DL, Rose CE Jr, et al. The chemokine receptors CCR2 and CX3CR1 mediate monocyte/macrophage trafficking in kidney ischemia-reperfusion injury. *Kidney Int.* (2008) 74:1526–37. doi: 10.1038/ki.2008.500
36. Gwechenberger M, Mendoza LH, Youker KA, Frangogiannis NG, Smith CW, Michael LH, et al. Cardiac myocytes produce interleukin-6 in culture and in viable border zone of reperfused infarctions. *Circulation.* (1999) 99:546–51. doi: 10.1161/01.CIR.99.4.546
37. Frangogiannis NG. Chemokines in the ischemic myocardium: from inflammation to fibrosis. *Inflamm Res.* (2004) 53:585–95. doi: 10.1007/s00011-004-1298-5
38. Frangogiannis NG, Dewald O, Xia Y, Ren G, Haudek S, Leucker T, et al. Critical role of monocyte chemoattractant protein-1/CC chemokine ligand

2 in the pathogenesis of ischemic cardiomyopathy. *Circulation.* (2007) 115:584–92. doi: 10.1161/CIRCULATIONAHA.106.646091
39. Anzai A, Choi JL, He S, Fenn AM, Nairz M, Rattik S, et al. The infarcted myocardium solicits GM-CSF for the detrimental oversupply of inflammatory leukocytes. *J Exp Med.* (2017) 214:3293–310. doi: 10.1084/jem.20170689
40. Moccetti F, Brown E, Xie A, Packwood W, Qi Y, Ruggeri Z, et al. Myocardial infarction produces sustained proinflammatory endothelial activation in remote arteries. *J Am Coll Cardiol.* (2018) 72:1015–26. doi: 10.1016/j.jacc.2018.06.044
41. Lee WW, Marinelli B, van der Laan AM, Sena BF, Gorbatov R, Leuschner F, et al. PET/MRI of inflammation in myocardial infarction. *J Am Coll Cardiol.* (2012) 59:153–63. doi: 10.1016/j.jacc.2011.08.066
42. Swirski FK, Nahrendorf M. Leukocyte behavior in atherosclerosis, myocardial infarction, and heart failure. *Science.* (2013) 339:161–6. doi: 10.1126/science.1230719
43. Swirski FK, Nahrendorf M, Etzrodt M, Wildgruber M, Cortez-Retamozo V, Panizzi P, et al. Identification of splenic reservoir monocytes and their deployment to inflammatory sites. *Science.* (2009) 325:612–6. doi: 10.1126/science.1175202
44. Wan E, Yeap XY, Dehn S, Terry R, Novak M, Zhang S, et al. Enhanced efferocytosis of apoptotic cardiomyocytes through myeloid-epithelial-reproductive tyrosine kinase links acute inflammation resolution to cardiac repair after infarction. *Circ Res.* (2013) 113:1004–12. doi: 10.1161/CIRCRESAHA.113.301198
45. Frangogiannis NG, Smith CW, Entman ML. The inflammatory response in myocardial infarction. *Cardiovasc Res.* (2002) 53:31–47. doi: 10.1016/S0008-6363(01)00434-5
46. Creemers E, Cleutjens J, Smits J, Heymans S, Moons L, Collen D, et al. Disruption of the plasminogen gene in mice abolishes wound healing after myocardial infarction. *Am J Pathol.* (2000) 156:1865–73. doi: 10.1016/S0002-9440(10)65060-2
47. Herskowitz A, Choi S, Ansari AA, Wesselingh S. Cytokine mRNA expression in postischemic/reperfused myocardium. *Am J Pathol.* (1995) 146:419–28.
48. Kurrelmeyer KM, Michael LH, Baumgarten G, Taffet GE, Peschon JJ, Sivasubramanian N, et al. Endogenous tumor necrosis factor protects the adult cardiac myocyte against ischemic-induced apoptosis in a murine model of acute myocardial infarction. *Proc Natl Acad Sci USA.* (2000) 97:5456–61. doi: 10.1073/pnas.070036297
49. Hirschl MM, Gwechenberger M, Binder T, Binder M, Graf S, Stefenelli T, et al. Assessment of myocardial injury by serum tumour necrosis factor alpha measurements in acute myocardial infarction. *Eur Heart J.* (1996) 17:1852–9. doi: 10.1093/oxfordjournals.eurheartj.a014803
50. Prabhu SD, Frangogiannis NG. The biological basis for cardiac repair after myocardial infarction: from inflammation to fibrosis. *Circ Res.* (2016) 119:91–112. doi: 10.1161/CIRCRESAHA.116.303577
51. Horckmans M, Ring L, Duchene J, Santovito D, Schloss MJ, Drechsler M, et al. Neutrophils orchestrate post-myocardial infarction healing by polarizing macrophages towards a reparative phenotype. *Eur Heart J.* (2017) 38:187–97. doi: 10.1093/eurheartj/ehw002
52. Hilgendorf I, Gerhardt LM, Tan TC, Winter C, Holderried TA, Chousterman BG, et al. Ly-6Chigh monocytes depend on Nr4a1 to balance both inflammatory and reparative phases in the infarcted myocardium. *Circ Res.* (2014) 114:1611–22. doi: 10.1161/CIRCRESAHA.114.303204
53. Ngkelo A, Richart A, Kirk JA, Bonnin P, Vilar J, Lemitre M, et al. Mast cells regulate myofilament calcium sensitization and heart function after myocardial infarction. *J Exp Med.* (2016) 213:1353–74. doi: 10.1084/jem.20160081
54. Dace DS, Apte RS. Effect of senescence on macrophage polarization and angiogenesis. *Rejuvenation Res.* (2008) 11:177–85. doi: 10.1089/rej.2007.0614
55. Gazewood JD, Turner PL. Heart failure with preserved ejection fraction: diagnosis and management. *Am Fam Physician.* (2017) 96:582–8.
56. Tannenbaum S, Sayer GT. Advances in the pathophysiology and treatment of heart failure with preserved ejection fraction. *Curr Opin Cardiol.* (2015) 30:250–8. doi: 10.1097/HCO.0000000000000163
57. Steinberg BA, Zhao X, Heidenreich PA, Peterson ED, Bhatt DL, Cannon CP, et al. Trends in patients hospitalized with heart failure and preserved left ventricular ejection fraction: prevalence, therapies, and outcomes. *Circulation.* (2012) 126:65–75. doi: 10.1161/CIRCULATIONAHA.111.080770
58. Owan TE, Hodge DO, Herges RM, Jacobsen SJ, Roger VL, Redfield MM. Trends in prevalence and outcome of heart failure with preserved ejection fraction. *N Engl J Med.* (2006) 355:251–9. doi: 10.1056/NEJMoa052256
59. Bhatia RS, Tu JV, Lee DS, Austin PC, Fang J, Haouzi A, et al. Outcome of heart failure with preserved ejection fraction in a population-based study. *N Engl J Med.* (2006) 355:260–9. doi: 10.1056/NEJMoa051530
60. Sharma K, Kass DA. Heart failure with preserved ejection fraction: mechanisms, clinical features, and therapies. *Circ Res.* (2014) 115:79–96. doi: 10.1161/CIRCRESAHA.115.302922
61. Hulsmans M, Sager HB, Roh JD, Valero-Munoz M, Houstis NE, Iwamoto Y, et al. Cardiac macrophages promote diastolic dysfunction. *J Exp Med.* (2018) 215:423–40. doi: 10.1084/jem.20171274
62. Glezeva N, Voon V, Watson C, Horgan S, McDonald K, Ledwidge M, et al. Exaggerated inflammation and monocytosis associate with diastolic dysfunction in heart failure with preserved ejection fraction: evidence of M2 macrophage activation in disease pathogenesis. *J Card Fail.* (2015) 21:167–77. doi: 10.1016/j.cardfail.2014.11.004
63. Nevers T, Salvador AM, Grodecki-Pena A, Knapp A, Velazquez F, Aronovitz M, et al. Left ventricular T-cell recruitment contributes to the pathogenesis of heart failure. *Circ Heart Fail.* (2015) 8:776–87. doi: 10.1161/CIRCHEARTFAILURE.115.002225
64. Wang Y, Sano S, Oshima K, Sano M, Watanabe Y, Katanasaka Y, et al. Wnt5a-mediated neutrophil recruitment has an obligatory role in pressure overload-induced cardiac dysfunction. *Circulation.* (2019) 140:487–99. doi: 10.1161/CIRCULATIONAHA.118.038820
65. Wang J, Hossain M, Thanabalasuriar A, Gunzer M, Meininger C, Kubes P. Visualizing the function and fate of neutrophils in sterile injury and repair. *Science.* (2017) 358:111–6. doi: 10.1126/science.aam9690
66. Li W, Nava RG, Bribriesco AC, Zinselmeyer BH, Spahn JH, Gelman AE, et al. Intravital 2-photon imaging of leukocyte trafficking in beating heart. *J Clin Invest.* (2012) 122:2499–508. doi: 10.1172/JCI62970
67. Bajpai G, Bredemeyer A, Li W, Zaitsev K, Koenig AL, Lokshina I, et al. Tissue resident CCR2- and CCR2+ cardiac macrophages differentially orchestrate monocyte recruitment and fate specification following myocardial injury. *Circ Res.* (2019) 124:263–78. doi: 10.1161/CIRCRESAHA.118.314028
68. Ueno T, Kim P, McGrath MM, Yeung MY, Shimizu T, Jung K, et al. Live images of donor dendritic cells trafficking via CX3CR1 pathway. *Front Immunol.* (2016) 7:412. doi: 10.3389/fimmu.2016.00412
69. Matsuura R, Miyagawa S, Fukushima S, Goto T, Harada A, Shimozaki Y, et al. Intravital imaging with two-photon microscopy reveals cellular dynamics in the ischeamia-reperfused rat heart. *Sci Rep.* (2018) 8:15991. doi: 10.1038/s41598-018-34295-w
70. Lee S, Vinegoni C, Feruglio PF, Fexon L, Gorbatov R, Pivoravov M, et al. Real-time *in vivo* imaging of the beating mouse heart at microscopic resolution. *Nat Commun.* (2012) 3:1054. doi: 10.1038/ncomms2060
71. Aguirre AD, Vinegoni C, Sebas M, Weissleder R. Intravital imaging of cardiac function at the single-cell level. *Proc Natl Acad Sci USA.* (2014) 111:11257–62. doi: 10.1073/pnas.1401316111
72. Kavanagh DPJ, Lokman AB, Neag G, Colley A, Kalia N. Imaging the injured beating heart intravitally and the vasculoprotection afforded by haematopoietic stem cells. *Cardiovasc Res.* (2019) 115:1918–32. doi: 10.1093/cvr/cvz118
73. Vinegoni C, Aguirre AD, Lee S, Weissleder R. Imaging the beating heart in the mouse using intravital microscopy techniques. *Nat Protoc.* (2015) 10:1802–19. doi: 10.1038/nprot.2015.119
74. Small DM, Lamont MRE, Allan-Rahill NH, Nishimura N. *In vivo* multiphoton microscopy of the beating mouse heart in health and disease. In: *Biophotonics Congress: Optics in the Life Sciences.* Tucson, AZ: OSA Publishing (2019).
75. Small DM, Allan-Rahill NH, Lamont MRE, Djakpa S, Marvarakumari GJ, Zhu Y, et al. Intravital multiphoton microscopy reveals increased capillary patrolling by leukocytes and cardiomyocyte dysfunction in high fat diet induced hypertrophy. In: *Basic Cardiovascular Sciences 2019 Scientific Sessions*. Boston, MA: American Heart Association (2019).
76. Allan-Rahill NH, Small DM, Lamont MRE, Djakpa S, Marvarakumari GJ, Zhu Y, et al. Automated analysis of displacement from intravital multiphoton

microscopy in mouse ventricle. In: *Basic Cardiovascular Sciences 2019 Scientific Sessions*. Boston, MA: American Heart Association (2019).
77. Vinegoni C, Lee S, Aguirre AD, Weissleder R. New techniques for motion-artifact-free *in vivo* cardiac microscopy. *Front Physiol.* (2015) 6:147. doi: 10.3389/fphys.2015.00147
78. Jones JS, Small DM, Nishimura N. *In vivo* calcium imaging of cardiomyocytes in the beating mouse heart with multiphoton microscopy. *Front Physiol.* (2018) 9:969. doi: 10.3389/fphys.2018.00969
79. Barretto RP, Messerschmidt B, Schnitzer MJ. *In vivo* fluorescence imaging with high-resolution microlenses. *Nat Methods.* (2009) 6:511–2. doi: 10.1038/nmeth.1339
80. Flusberg BA, Jung JC, Cocker ED, Anderson EP, Schnitzer MJ. *In vivo* brain imaging using a portable 3.9 gram two-photon fluorescence microendoscope. *Opt Lett.* (2005) 30:2272–4. doi: 10.1364/OL.30.002272
81. Engelbrecht CJ, Johnston RS, Seibel EJ, Helmchen F. Ultra-compact fiber-optic two-photon microscope for functional fluorescence imaging *in vivo*. *Opt Express.* (2008) 16:5556–64. doi: 10.1364/OE.16.005556
82. Levene MJ, Dombeck DA, Kasischke KA, Molloy RP, Webb WW. *In vivo* multiphoton microscopy of deep brain tissue. *J Neurophysiol.* (2004) 91:1908–12. doi: 10.1152/jn.01007.2003
83. Huland DM, Brown CM, Howard SS, Ouzounov DG, Pavlova I, Wang K, et al. *In vivo* imaging of unstained tissues using long gradient index lens multiphoton endoscopic systems. *Biomed Opt Express.* (2012) 3:1077–85. doi: 10.1364/BOE.3.001077
84. Kobat D, Horton NG, Xu C. *In vivo* two-photon microscopy to 1.6-mm depth in mouse cortex. *J Biomed Opt.* (2011) 16:106014. doi: 10.1117/1.3646209
85. Kobat D, Durst ME, Nishimura N, Wong AW, Schaffer CB, Xu C. Deep tissue multiphoton microscopy using longer wavelength excitation. *Opt Express.* (2009) 17:13354–64. doi: 10.1364/OE.17.013354
86. Helmchen F, Denk W. Deep tissue two-photon microscopy. *Nat Methods.* (2005) 2:932–40. doi: 10.1038/nmeth818
87. Zipfel WR, Williams RM, Webb WW. Nonlinear magic: multiphoton microscopy in the biosciences. *Nat Biotechnol.* (2003) 21:1369–77. doi: 10.1038/nbt899
88. Lee S, Vinegoni C, Sebas M, Weissleder R. Automated motion artifact removal for intravital microscopy, without a priori information. *Sci Rep.* (2014) 4:4507. doi: 10.1038/srep04507
89. Chilian WM, Eastham CL, Marcus ML. Microvascular distribution of coronary vascular resistance in beating left ventricle. *Am J Physiol.* (1986) 251(4 Pt 2):H779–88. doi: 10.1152/ajpheart.1986.251.4.H779
90. Lee S, Nakamura Y, Yamane K, Toujo T, Takahashi S, Tanikawa Y, et al. Image stabilization for *in vivo* microscopy by high-speed visual feedback control. *IEEE Trans Robot.* (2008) 24:45–54. doi: 10.1109/TRO.2007.914847
91. Nellis SH, Liedtke AJ, Whitesell L. Small coronary vessel pressure and diameter in an intact beating rabbit heart using fixed-position and free-motion techniques. *Circ Res.* (1981) 49:342–53. doi: 10.1161/01.RES.49.2.342
92. Lee S, Courties G, Nahrendorf M, Weissleder R, Vinegoni C. Motion characterization scheme to minimize motion artifacts in intravital microscopy. *J Biomed Opt.* (2017) 22:36005. doi: 10.1117/1.JBO.22.3.036005
93. Laffray S, Pages S, Dufour H, De Koninck P, De Koninck Y, Cote D. Adaptive movement compensation for *in vivo* imaging of fast cellular dynamics within a moving tissue. *PLoS ONE.* (2011) 6:e19928. doi: 10.1371/journal.pone.0019928
94. Horton NG, Wang K, Kobat D, Clark CG, Wise FW, Schaffer CB, et al. three-photon microscopy of subcortical structures within an intact mouse brain. *Nat Photonics.* (2013) 7. doi: 10.1038/nphoton.2012.336
95. Xu C, Wise FW. Recent advances in fiber lasers for nonlinear microscopy. *Nat Photonics.* (2013) 7. doi: 10.1038/nphoton.2013.284
96. Debarre D, Botcherby EJ, Watanabe T, Srinivas S, Booth MJ, Wilson T. Image-based adaptive optics for two-photon microscopy. *Opt Lett.* (2009) 34:2495–7. doi: 10.1364/OL.34.002495
97. Ji N, Sato TR, Betzig E. Characterization and adaptive optical correction of aberrations during *in vivo* imaging in the mouse cortex. *Proc Natl Acad Sci USA.* (2012) 109:22–7. doi: 10.1073/pnas.1109202108
98. Ji N. Adaptive optical fluorescence microscopy. *Nat Methods.* (2017) 14:374–80. doi: 10.1038/nmeth.4218
99. Nishimura N, Schaffer CB, Friedman B, Lyden PD, Kleinfeld D. Penetrating arterioles are a bottleneck in the perfusion of neocortex. *Proc Natl Acad Sci USA.* (2007) 104:365–70. doi: 10.1073/pnas.0609551104
100. Nishimura N, Schaffer CB, Friedman B, Tsai PS, Lyden PD, Kleinfeld D. Targeted insult to subsurface cortical blood vessels using ultrashort laser pulses: three models of stroke. *Nat Methods.* (2006) 3:99–108. doi: 10.1038/nmeth844
101. Danielczok JG, Terriac E, Hertz L, Petkova-Kirova P, Lautenschlager F, Laschke MW, et al. Red blood cell passage of small capillaries is associated with transient $Ca2^{+}$-mediated adaptations. *Front Physiol.* (2017) 8:979. doi: 10.3389/fphys.2017.00979
102. Frueh FS, Spater T, Lindenblatt N, Calcagni M, Giovanoli P, Scheuer C, et al. Adipose tissue-derived microvascular fragments improve vascularization, lymphangiogenesis, and integration of dermal skin substitutes. *J Invest Dermatol.* (2017) 137:217–27. doi: 10.1016/j.jid.2016.08.010
103. Ritsma L, Steller EJ, Beerling E, Loomans CJ, Zomer A, Gerlach C, et al. Intravital microscopy through an abdominal imaging window reveals a pre-micrometastasis stage during liver metastasis. *Sci Transl Med.* (2012) 4:158ra45. doi: 10.1126/scitranslmed.3004394
104. Ritsma L, Steller EJ, Ellenbroek SI, Kranenburg O, Borel Rinkes IH, van Rheenen J. Surgical implantation of an abdominal imaging window for intravital microscopy. *Nat Protoc.* (2013) 8:583–94. doi: 10.1038/nprot.2013.026
105. Rakhilin N, Garrett A, Eom CY, Chavez KR, Small DM, Daniel AR, et al. An intravital window to image the colon in real time. *Nat Commun.* (2019) 10:5647. doi: 10.1038/s41467-019-13699-w
106. Schiessl IM, Grill A, Fremter K, Steppan D, Hellmuth MK, Castrop H. Renal interstitial platelet-derived growth factor receptor-beta cells support proximal tubular regeneration. *J Am Soc Nephrol.* (2018) 29:1383–96. doi: 10.1681/ASN.2017101069
107. Schiessl IM, Fremter K, Burford JL, Castrop H, Peti-Peterdi J. Long-term cell fate tracking of individual renal cells using serial intravital microscopy. *Methods Mol Biol.* (2019). doi: 10.1007/7651_2019_232. [Epub ahead of print].
108. Reismann D, Stefanowski J, Gunther R, Rakhymzhan A, Matthys R, Nutzi R, et al. Longitudinal intravital imaging of the femoral bone marrow reveals plasticity within marrow vasculature. *Nat Commun.* (2017) 8:2153. doi: 10.1038/s41467-017-01538-9
109. Entenberg D, Voiculescu S, Guo P, Borriello L, Wang Y, Karagiannis GS, et al. A permanent window for the murine lung enables high-resolution imaging of cancer metastasis. *Nat Methods.* (2018) 15:73–80. doi: 10.1038/nmeth.4511
110. O'Donnell JS, Teng MWL, Smyth MJ. Cancer immunoediting and resistance to T cell-based immunotherapy. *Nat Rev Clin Oncol.* (2019) 16:151–67. doi: 10.1038/s41571-018-0142-8

Conflict of Interest: The authors declare that the research was conducted in the absence of any commercial or financial relationships that could be construed as a potential conflict of interest.

frontiers in Immunology

ORIGINAL RESEARCH
published: 21 February 2020
doi: 10.3389/fimmu.2020.00039

Multiphoton Intravital Microscopy of Mandibular Draining Lymph Nodes: A Mouse Model to Study Corneal Immune Responses

Maria J. Lopez[1,2], *Yashar Seyed-Razavi*[1,2†], *Takefumi Yamaguchi*[1†], *Gustavo Ortiz*[1], *Victor G. Sendra*[1,2], *Deshea L. Harris*[1,2], *Arsia Jamali*[1,2] *and Pedram Hamrah*[1,2,3,4,5*]

[1] *Department of Ophthalmology, Center for Translational Ocular Immunology, Tufts Medical Center, Tufts University School of Medicine, Boston, MA, United States,* [2] *Department of Ophthalmology, Harvard Medical School, Schepens Eye Research Institute/Massachusetts Eye and Ear Infirmary, Boston, MA, United States,* [3] *Program in Immunology, School of Graduate Biomedical Sciences, Tufts University, Boston, MA, United States,* [4] *Cornea Service, Department of Ophthalmology, Tufts New England Eye Center, Tufts Medical Center, Tufts University School of Medicine, Boston, MA, United States,* [5] *Cornea Service, Department of Ophthalmology, Massachusetts Eye & Ear Infirmary, Harvard Medical School, Boston, MA, United States*

OPEN ACCESS

Edited by:
Connie Wong, Monash University, Australia

Reviewed by:
Jens Volker Stein, Université de Fribourg, Switzerland
Daniel Carr, University of Oklahoma Health Sciences Center, United States

***Correspondence:**
Pedram Hamrah
pedram.hamrah@tufts.edu

[†]These authors share second authorship

Specialty section:
This article was submitted to Antigen Presenting Cell Biology, a section of the journal Frontiers in Immunology

Received: *26 July 2019*
Accepted: *08 January 2020*
Published: *21 February 2020*

Citation:
Lopez MJ, Seyed-Razavi Y, Yamaguchi T, Ortiz G, Sendra VG, Harris DL, Jamali A and Hamrah P (2020) Multiphoton Intravital Microscopy of Mandibular Draining Lymph Nodes: A Mouse Model to Study Corneal Immune Responses. Front. Immunol. 11:39. doi: 10.3389/fimmu.2020.00039

Multiphoton intravital microscopy (MP-IVM) is a powerful tool to image cells *in vivo*. Its application in immunology research has opened new horizons, allowing intravital imaging of leukocytes at the single-cell level. A transparent cornea is vital to retain vision. As an immune privileged site, a rapid innate response to foreign antigens is crucial in clearing opportunistic bacterial and viral pathogens, and minimizing collateral structural damage to the cornea. Furthermore, dissecting the mechanisms and preventing the immunological rejection process after corneal transplantation is imperative to retain sight. Therefore, understanding the underlying mechanisms behind corneal immunity, specifically the process of antigen presentation and adaptive immunity in the mandibular draining lymph nodes (dLNs) *in vivo*, is crucial. Attempts of intravital imaging of mandibular dLNs have yielded little success to date, due to breathing artifacts and the location that is difficult to access. Herein, we present the first MP-IVM mouse model of the mandibular dLNs, utilizing transgenic mice in which $CD11c^+$ cells are fluorescently labeled. Furthermore, we demonstrate that CD11c-YFP^+ cells are localized mainly in the parafollicular cortex (T cell zone) and subcapsular area and are sparsely distributed in the follicular region (B cell zone) of mandibular dLNs during steady state. A significant increase in host CD11c-YFP^+ cell density is noted at 14 and 21 days following allogeneic corneal transplantation, compared to steady state ($p < 0.05$). Moreover, allogeneic corneal transplantation results in increased host-derived CD11c-YFP^+ cell mean speed and displacement in mandibular dLNs, compared to steady state ($p < 0.001$). The meandering index, an index for directionality, is significantly increased after allogeneic corneal transplantation at both 14 and 21 days, compared to steady state ($p < 0.001$). Taken together, our study demonstrates the necessary methodology required for intravital multiphoton

imaging of the mandibular dLNs, allowing visualization of spatiotemporal kinetics of immune cells *in vivo*, and provides a window into the corneal immune reflex arc. This technique will be a powerful tool to investigate the pathogenesis of ocular immune and inflammatory diseases.

Keywords: intravital imaging, multiphoton microscopy, corneal transplantation, mandibular draining lymph nodes, antigen presenting cells, kinetics, dendritic cells

INTRODUCTION

As a window to the foreign world, the immune privileged status of the cornea is crucial in maintaining transparency and vision in the face of constant exposure to the external environment (1–4). Following damage to the epithelial layer, a rapid, specific, and selective immune response is mounted against foreign antigens, including opportunistic bacterial and viral pathogens, as chronic keratitis can lead to structural alterations of the corneal stroma that may result in opacity, corneal scarring, and ultimately vision impairment (5).

Before the discovery of resident bone marrow-derived leukocytes, the cornea was long believed to be a collagenous tissue devoid of leukocytes. However, it is now acknowledged that the steady state mammalian cornea contains a heterogeneous populations of resident corneal leukocytes, including professional antigen-presenting cells (APCs), such as conventional dendritic cells (cDCs) and macrophages (6–8). cDCs are unique in their nature to prime T cells and induce antigen-specific immune responses or immunological tolerance in draining lymph nodes (dLNs) (9–11). Interestingly, in the ocular tissues, evidence suggests that antigens can also directly drain into the mandibular dLNs (12–14). Therefore, the investigation of the process of antigen presentation by corneal cDCs in the mandibular dLNs will provide understanding of underlying mechanisms behind corneal immunity, specifically the process of antigen presentation and adaptive immunity. Thus, we sought to study APCs in the mandibular dLNs *in vivo*, where the physiological conditions such as tissue oxygenation and temperature, and therefore tissue environment, are preserved.

Multiphoton intravital microscopy (MP-IVM) has significant advantages over other types of microscopy. It allows long-term imaging of biological processes, with minimal toxicity and photobleaching (15–17), and achieves high-contrast images at the cellular level in thick, non-transparent specimens with less potential photo-damage (18, 19). Furthermore, a distinct advantage of MP-IVM is that it provides high spatiotemporal resolution, allowing for cellular analysis of leukocytes, such as cDCs (20, 21), T cells, and B cells in their native anatomical context (22–24). Furthermore, interaction between different leukocytes during steady state and in pathological conditions have been described with MP-IVM (25–28).

MP-IVM has been widely used to image inguinal and popliteal LNs for lymphocyte trafficking in *in vivo* and *ex vivo* settings (20, 22, 23, 25, 29–31). However, to date, studies of the mandibular dLNs have only been attempted in *ex vivo* and *in vitro* studies (12, 27, 32, 33). Possible reasons why MP-IVM of the mandibular dLNs have as of yet been largely missing may be the difficultly in exposing the tissue and inability to properly stabilize it, leading to artifacts arising from breathing and pulsations from the beating heart. In the current study, we present for the first time, to our knowledge, the necessary steps to provide stable long-term MP-IVM imaging of the mandibular dLNs and reveal CD11c-YFP$^+$ cell kinetics during steady state and following allogeneic corneal transplantation.

METHODS

Animals

Six- to 8-week old male transgenic mice expressing yellow fluorescent protein (YFP) under the control of the CD11c promoter (C57BL/6 background; a kind gift of Dr. Michel C. Nussenzweig from Rockefeller University; called CD11c-YFP mice) (20) and transgenic T-Red mice selectively expressing DsRed in T cells (C57BL/6 background; a kind gift of Dr. Ulrich H. von Andrian, Harvard Medical School) (34) were bred in house. CD11c-YFP mice were used as recipients in our murine model of corneal transplantation. Age- and sex-matched wild-type (WT) BALB/c mice (Charles River Laboratory, Wilmington, MA, United States) served as corneal donors. The Schepens Eye Research Institute and Tufts Medical Center Animal Care and Use Committees approved the protocol. We treated all animals according to the ARVO Statement for the Use of Animals in Ophthalmic and Vision Research.

Corneal Transplantation

To study the behavior of immune cells in diseased states of the cornea, we used a murine model of corneal allotransplantation (allogeneic) as previously described (35). Briefly, BALB/c mice were used as corneal donors; a 2.0-mm trephine was used to delimitate the donor button, which was excised with Vannas scissors (2 mm cutting edge; Fine Science Tools, Foster City, CA, United States) and transplanted into anesthetized CD11c-YFP transgenic mice. The host bed was prepared by excising 1.5 mm of the central cornea, previously demarcated using a 1.5 mm trephine. The donor cornea was secured to the host bed with eight interrupted 11-0 Nylon sutures (A9016N Surgical Specialties, Wyomissing, PA, United States). At the end of the procedure, antibiotic ointment (Erythromycin Ophthalmic Ointment USP, 0.5%, Bausch & Lomb Inc., Tampa, FL, United States) was applied to the cornea to reduce the risk of infections, and the eyelids were closed by performing a tarsorrhaphy for 3–5 days with 8-0 Nylon sutures (AA-0122 Surgical Specialties). The corneal sutures were removed 7 days after transplantation, and animals underwent MP-IVM after 14 and 21 days postoperatively.

Multiphoton Intravital Microscopy

We used a custom-made multiphoton intravital microscope Ultima Pro Multiphoton Microscopy System, Bruker Technology, WI, United States) equipped with two Mai Tai Titanium-Sapphire lasers (Newport Spectra-Physics, Irvine, United States) for simultaneous coaxial illumination. One of the lasers was set at 850 nm wavelength (to visualize YFP^+ cells) or 760 nm wavelength (to visualize $DsRed^+$ cells), and the other laser was set at 900 nm wavelength for second harmonic generation to visualize the dLN capsule in a completely separated channel, a convenient tool to analyze the anatomical distribution of the cells within the dLN. Image acquisition was performed using Prairie View Software (Bruker Technology). A 20× water immersion objective (NA: 0.95, Olympus, XLUMPlanFL N, Tokyo, Japan) was used to capture images of the mandibular dLNs with volumes of 70 × 596 × 596 μm at 3 μm Z-steps with 30 s intervals over 30 min.

Immunohistochemistry and Confocal Microscopy

Mandibular dLNs of CD11c-YFP mice were excised, fixed in 4% paraformaldehyde at room temperature (RT) for 30 min, and, after freezing in liquid nitrogen, were embedded in optimal cutting temperature media (Tissue-Tek; Sakura Finetek USA, Inc, Torrance, CA, United States). Sixty-micrometer frozen sections were then blocked in 2% bovine serum albumin containing 1% anti-CD16/CD32 Fc block (Bio X Cell, West Lebanon, NH, United States) for 90 min at RT and were stained with fluorophore-conjugated antibodies against CD3 and CD45R/B220 (both BioLegend, San Diego, CA, United States) for 60 min. After washing, samples were imaged via a FV10-ASW confocal microscope (Olympus).

Flow Cytometry

Mandibular dLNs of CD11c-YFP mice were excised, and single cells were obtained by mechanically passing the samples through a 40 μm strainer (Thermo Fisher Scientific, Waltham, MA, United States). Single-cell suspensions were then blocked in FACS buffer containing 1% anti-CD16/CD32 Fc block (Bio X Cell) and were stained with a viability marker (LIVE/DEAD Fixable Blue Dead Cell Stain kit, Thermo Fisher Scientific) for 30 min at RT. Next, samples were stained with fluorophore-conjugated antibodies against CD45, CD11c, dendritic cell inhibitory receptor 2 (DCIR2), CD68, CD3, or respective isotype controls (all BioLegend, or BD Biosciences, San Jose, CA, United States) for 45 min at RT to yield fluorescence minus one stainings. After washing, samples underwent flow cytometric acquisition using a BD LSR II flow cytometer (BD Biosciences). Postacquisition data analysis was performed using FlowJo v9 software (FlowJo LLC, Ashland, OR, United States).

Image Analysis

Images were exported from the multiphoton microscope to reconstruct 3D and 4D videos and to analyze the images with Imaris (Bitplane, Zurich, Switzerland). $CD11c\text{-}YFP^+$ cells were counted, and densities calculated (cell number divided by the volume of the analyzed area of the dLN). Cell 3D instantaneous velocity, mean speed, displacement, and meandering index were obtained. Cell mean speed was defined as the mean speed of a cell over the entire measurement period (μm/min). Cell displacement was defined as the distance between first and last imaging point (μm). Meandering index, a measure for the directionality of cell migration, was defined as the ratio of the cell displacement and the cell's total path length (30). In all measurements of 3D instantaneous velocity, mean speed, displacement, and meandering index, tracks shorter than 2 min were excluded from analysis.

Statistical Analysis

Results are presented as mean ± standard error of the mean (SEM). Three MP-IVM stacks/time series or confocal micrographs were analyzed from three different animals/condition and statistical significance determined by either *t*-test or one-way ANOVA with Tukey *post-hoc* (Prism Graphpad software, San Diego, CA, United States). Differences between groups were considered significant at $p < 0.05$.

RESULTS

Components Necessary for Intravital Microscopy of the Mandibular dLNs

To isolate the mandibular dLNs for MP-IVM, we utilized a custom-built microscope stage with a metallic base to provide support for the magnetic pieces of the stage (**Figure 1A**). A piece of modeling clay was used to secure the skin flap created during the microsurgical preparation and to support the mouse head laterally. A wooden spatula was used to keep dLNs slightly elevated above the surrounding tissues during intravital imaging, while nerves, blood, and lymphatic vessels were retained intact. A pedestal composed of three to four small magnets served as support for positioning a heating system unit on top of a dLN chosen for imaging, and the height of this stand was adjusted by adding or removing magnetic pieces according to the size of the mouse. A heating system/glass coverslip unit was used to regulate the dLN temperature during imaging and was made of polyethylene tubing (Intramedic, Sparks, MD, United States, Cat. No. 427420), looped to fit an 18-mm circle glass coverslip (VWR Cat. No. 48380046). One end of the tube was connected to a peristaltic pump (Masterflex L/S, Cole-Parmer, Vernon Hills, IL, United States), and the other end was immersed in a hot water bath. During image acquisition, hot water was continuously pumped through this system, maintaining the temperature of the surgical area at desired 37 ± 1°C. The fully assembled stage setup, without and with a mouse, are represented in **Figures 1B,C**.

Microsurgical Preparation of Mandibular Draining Lymph Nodes for Multiphoton Intravital Microscopy

Mice were initially anesthetized with an intraperitoneal (i.p.) injection of ketamine HCl (100 mg/kg), xylazine (20 mg/kg), and acepromazine (3 mg/kg), resulting in up to 70 min of deep anesthesia. The proper plane of anesthesia was assessed every 30–60 min, and supplemental doses of ketamine

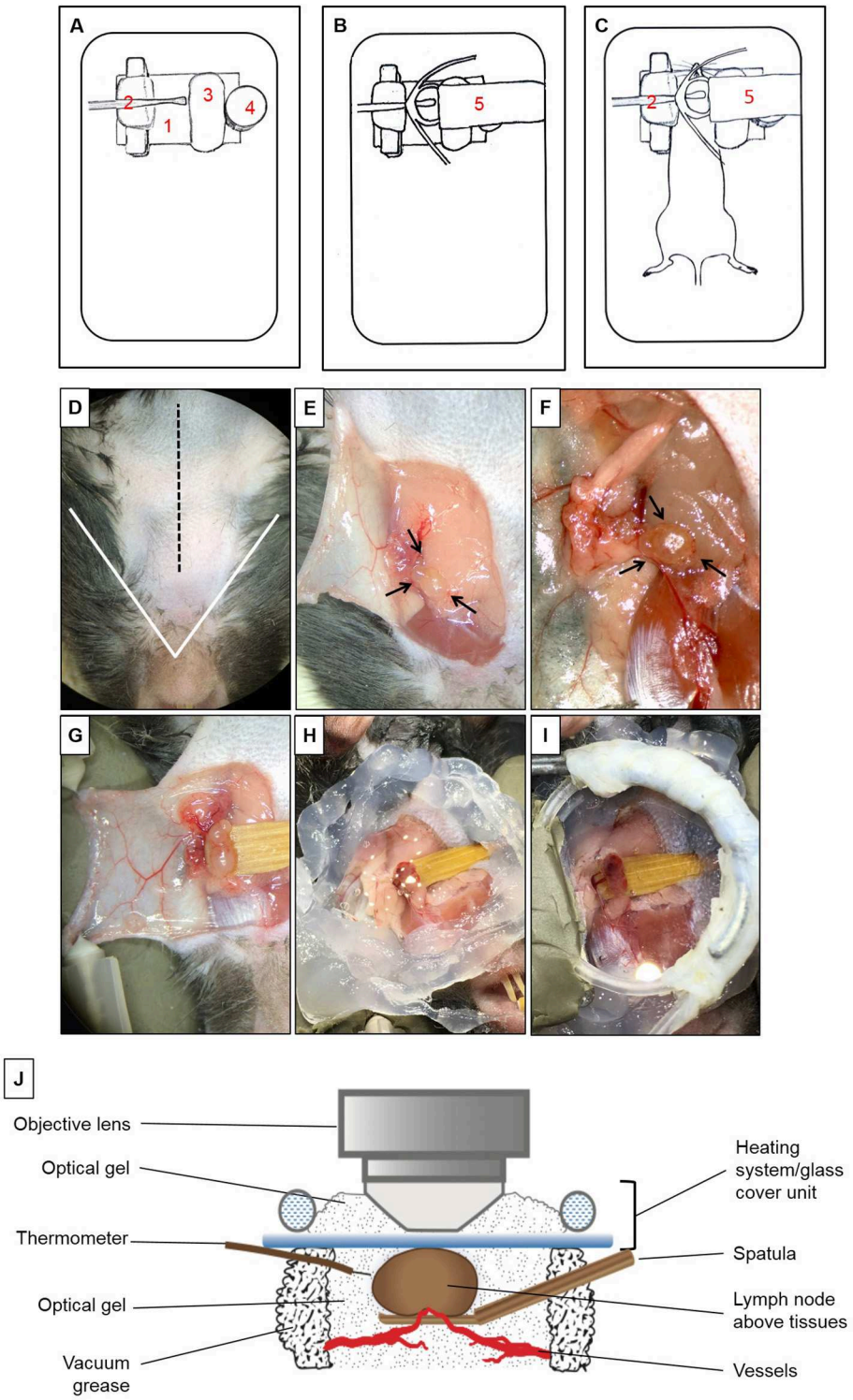

FIGURE 1 | Multiphoton intravital microscopy setup. **(A–C)** Microscope stage setup for imaging of mandibular draining lymph nodes (dLNs) with multiphoton intravital microscopy (MP-IVM). **(A)** Partially assembled stage: (1) Metallic flat base to be used as support for the magnetic parts of the stage. (2) Spatula to keep the dLN slightly elevated above surrounding tissues with keeping nerves, blood, and lymphatic vessels intact. (3) Skin flap holder. (4) Magnetic pedestal for positioning of heating system. **(B)** Fully assembled stage: (5) Heating tubing system positioned on top of magnetic stand. This tube is connected to a peristaltic pump on one end, and the other end is immersed in a hot water bath to create a continuous source of heat around the dLN during intravital imaging. Below the tubing circle, a glass coverslip functions as the roof of a chamber in which the dLN is maintained moist and at the physiological temperature during imaging. **(C)** Positioning of anesthetized

(Continued)

FIGURE 1 | mouse on the completely assembled stage. **(D–I)** Microsurgical preparation of the mandibular dLN. **(D)** Ventral view of the surgical area (mouse's head toward the surgeon). The area above the white triangle represents *the regio intermandibularis.* The dotted black midline represents the area where an approximately 15 mm skin incision is made. **(E)** The skin flap is separated, exposing the ipsilateral mandibular dLNs (black arrows) and is secured with two 30G needles (shown in **D**) to keep the dLNs exposed at all times. **(F)** After microdissection, one of the dLNs is carefully liberated from surrounding tissues (arrows). **(G)** A wooden spatula is positioned underneath the dLN to slightly elevate it above surrounding tissues. Proper blood flow to the dLN can be surveyed with any necessary adjustments made at this step. **(H)** Vacuum grease is applied around the dLN to create the walls of a chamber and filled with optical gel. **(I)** Heating system/glass coverslip unit is positioned onto the grease surrounding the dLN, creating a sealed chamber containing the dLN and optical gel. **(J)** Schematic diagram of the dLN and MP-IVM imaging chamber highlighting the components of the chamber, positioning of the heating system/glass coverslip unit, and the thermometer. Through this unit, warm water recirculates at a constant rate to keep the chamber at desired 37 ± 1°C. This chamber is filled with optical gel to keep the moisture and adequate temperature around the dLN during imaging with MP-IVM. A thermometer is located inside the chamber to control the temperature during imaging.

(100 mg/kg) were given as required, alternating between ketamine/xylazine/acepromazine and ketamine. The fur on the ventral side of the neck was shaved, and 0.08 ml Bupivacaine 0.25% (Hospira, Inc., Lake Forest, IL, United States) was injected subcutaneously to minimize local pain/distress during the procedure. A 15-mm midline skin incision was made (**Figure 1D**). A skin flap was separated from the superficial cervical fascia to expose the ipsilateral mandibular dLNs (**Figure 1E**). This skin flap was fixed to the stage to keep the surgical area around the dLNs gently exposed (**Figures 1F,G**). Under a dissection microscope, the adipose tissue around one of the dLNs was removed without damaging the dLN vasculature (**Figure 1F**). To avoid artifacts due to minor movement of the dLN from breathing and heartbeats, a small wooden spatula was placed underneath the dLN to keep it slightly elevated and out of contact with surrounding tissues (**Figure 1G** and **Supplementary Video 1**). Special attention was paid to preserve blood circulation of the dLN when elevating the spatula. Vacuum grease (Dow Corning, Midland, MI, United States) was applied around the dLN and optical gel (Genteal gel, Novartis, Fort Worth, TX, United States) then applied on the dLN to maintain moisture during imaging (**Figure 1H**). The heating system/glass coverslip unit was then mounted on the grease, creating a sealed chamber over the dLN area (**Figures 1I,J**), and contact between the glass coverslip and the surface of the dLN. The heating system/glass coverslip unit allowed temperature regulation of the dLN with warm water circulated in a continuous motion with a peristaltic pump and water bath. The temperature of the surgical area inside the chamber, in close proximity to the dLN, was monitored throughout imaging with a dual input digital thermometer (Model HH12B, Omega Engineering, Norwalk, CT, United States; **Figure 1J**) and adjusted to 37 ± 1°C. During surgical preparation, the mouse body temperature was regulated with disposable hand warmers and foil.

Multiphoton Intravital Microscopy of the Mouse Mandibular Draining Lymph Nodes

Once the dLN was properly prepared and a sealed chamber over the dLN was achieved, the animal was carefully placed under the microscope; the objective lens was positioned above the glass coverslip and dLN (**Figure 1J**). Optical gel was used to create an interphase between the objective lens and the glass coverslip. Through the eyepieces of the microscope, we could visualize the dLN under epifluorescence illumination before scanning, to ensure that the objective lens is in the correct position above the dLN. During image acquisition, the mouse body temperature was regulated with disposable hand warmers (HeatMax Inc., Dalton, GA, United States) and foil. The pulse rate, oxygen saturation, respiratory rate, and body temperature of the mouse were continuously monitored utilizing a MouseOx Plus monitor (Starr Life Sciences, Oakmont, PA, United States).

Characterization of YFP$^+$ Cells in the Mandibular Draining Lymph Nodes of CD11c-YFP Mice During Steady State

To assess the phenotype of YFP$^+$ cells in the mandibular dLNs of transgenic CD11c-YFP mice, we analyzed coexpression of various immune cell markers on YFP$^+$ cells during steady state, using fluorescence minus one staining followed by flow cytometry. We initially gated out debris, dead cells, and doublets, using forward and side scatters and a viability marker. As shown in **Figure 2**, YFP$^+$ cells in the mandibular dLNs were mainly cDCs, as they coexpressed CD45 (pan-leukocyte marker), CD11c (cDC marker), and DRIC2 (cDC marker), with a small population (17.5%) coexpressing the macrophage marker CD68 and a minor fraction constituting T cells (CD3$^+$; 13.5%). Thus, our flow cytometry evaluation indicated that YFP$^+$ cells in the mandibular dLNs of CD11c-YFP mice were predominantly cDCs and, to lesser extent, macrophages or T cells.

Multiphoton Intravital Imaging of Naïve CD11c-YFP$^+$ Cells of the Mandibular Draining Lymph Nodes

Little is known about the dynamics of cDCs in mandibular dLNs in an *in vivo* setting. Therefore, we first sought to investigate CD11c-YFP$^+$ cells kinetics during steady state mandibular dLNs. The collagenous capsule of the dLN was visualized using second harmonics, allowing delimitation of the subcapsular, parafollicular (T cell areas), and follicular areas (B cell areas) of the dLN (**Figures 3A,B** and **Supplementary Video 2**). We found that steady state CD11c-YFP$^+$ cells are predominantly oval in shape, with some showing an elongated dendritiform shape (**Figure 3C** and **Supplementary Video 3**). The CD11c-YFP$^+$ cells were distributed mostly in the subcapsular area (**Figures 3A,D**; 5,123.66 ± 487.31 cells/mm^3) but also in the parafollicular cortex or T cell areas (4,677.87 ± 903.54 cells/mm^3), and sparsely in the follicular B cell areas (1,958.33 ± 193.72 cells/mm^3). We next performed confocal microscopy of mandibular dLNs of CD11c-YFP mice, stained with CD3 (T cell marker) and CD45R/B220 (B cell marker) to unequivocally

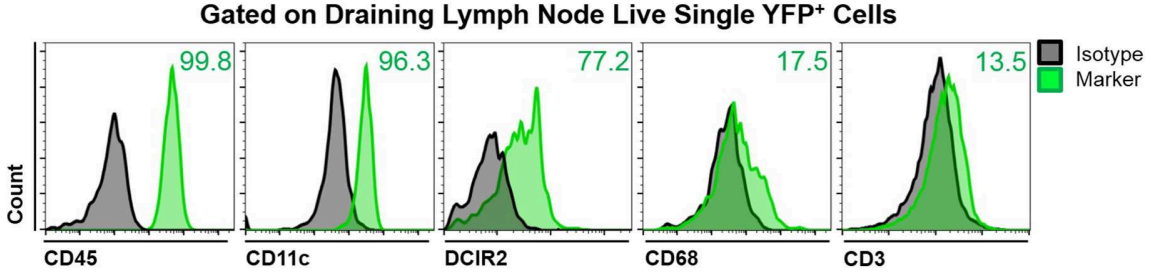

FIGURE 2 | Characterization of YFP$^+$ cells in mandibular draining lymph nodes of CD11c-YFP mice during steady state. Representative flow cytometric histograms showing coexpression of CD45 (pan-leukocyte marker), CD11c (cDC marker), DCIR2 (cDC marker), CD68 (macrophage marker), or CD3 (T cell marker) on live single YFP$^+$ cells. Gray histograms represent fluorescence minus one isotype control staining and green histograms show coexpression of the indicated marker. Plots are representative of three independent experiments.

distinguish parafollicular and follicular areas (**Figure 3E**). As presented in **Figure 3F**, confocal microscopy confirmed our MP-IVM findings, showing higher densities of CD11c-YFP$^+$ cells in the parafollicular area (5,572.97 ± 875.02 cells/mm^3) compared to follicular area (3,089.19 ± 641.43 cells/mm^3; $p = 0.02$). Longitudinal analysis revealed static CD11c-YFP$^+$ cells, exhibiting neither cell displacement nor dendrite extension, and motile CD11c-YFP$^+$ cells with sampling motion (**Supplementary Videos 3, 4**). The average CD11c-YFP$^+$ cells' mean speed during steady state was 3.58 ± 0.09 μm/min, where cells with smallest dimensions exhibited the most motility (**Supplementary Video 4**).

Corneal Allotransplantation Resulted in a Significant Increase in Host-Derived CD11c-YFP$^+$ Cells Kinetics in the Mandibular Draining Lymph Nodes

To study the behavior of activated host cDCs in mandibular dLNs, we analyzed kinetics of CD11c-YFP$^+$ cells at 14 and 21 days after corneal allotransplantation (allogeneic), as previously described (35). CD11c-YFP$^+$ cell density in the mandibular dLNs increased significantly 14 days after corneal allotransplantation, compared to steady state (20,745.67 ± 2,050.87 vs. 10,307.56 ± 1,103.13 cells/mm^3, $p = 0.002$; **Figure 4**). Cells agglomerated into the T cell areas (parafollicular cortex) and the majority acquired an oval shape; a few still conserved the dendritiform shape, with dendrites' probing movements more than real cell body movements (**Supplementary Videos 3**, **5**). Analysis of cell motility revealed that host-derived CD11c-YFP$^+$ cells exhibited increased mean speed and displacement (**Figure 5**). CD11c-YFP$^+$ cells acquired higher speeds at day 14 following allotransplantation, compared to steady state (7.90 ± 0.19 vs. 3.58 ± 0.09 μm/min, respectively, $p < 0.001$; **Figures 5A,C–E** and **Supplementary Video 6**). Increased cell displacement and mean speed changes were maintained at 21 days after corneal allotransplantation (7.40 ± 0.17 μm/min; **Supplementary Video 7**).

We next aimed to investigate the meandering index of CD11c-YFP$^+$ cells, defined as the ratio of the net displacement of a cell (from start to finish points in a straight line) and the total path length that the cell moved from the beginning to end (30). Interestingly, we found meandering indices of CD11c-YFP$^+$ cells increased with time, 0.37 ± 0.01 at 14 and 0.53 ± 0.01 at 21 days postallotransplantation compared to steady state (0.26 ± 0.02, $p = 0.001$; **Figures 5B–E**). This indicates that CD11c-YFP$^+$ cells exhibited a more directional migration pattern following transplantation compared to the random movement in the naïve mandibular dLNs.

T Cells Demonstrate Distinct Kinetics Compared to CD11c-YFP$^+$ Cells in the Mandibular Draining Lymph Nodes

To assess if our model would allow studying other immune cells as well, we next evaluated the kinetics of T cells in the mandibular dLNs during steady state (**Supplementary Video 8**). As shown in **Figure 6A**, we observed DsRed$^+$ T cells (in red) in clusters in the dLN with collagen visualized by second harmonic generation (in blue). **Figure 6B** illustrates T cell displacement in the dLN during steady state. We observed brisk T cell meanderings in the mandibular dLNs with 3D instantaneous velocity of 6.08 ± 0.09 μm/min. We observed that, compared with CD11c-YFP$^+$ cells (3.58 ± 0.09 μm/min), DsRed$^+$ T cells displayed higher mean speed (12.67 ± 0.27 μm/min, $p < 0.001$; **Figure 6C**) and directionality, as well as a higher meandering index of DsRed$^+$ T cells (0.51 ± 0.01) compared with CD11c-YFP$^+$ cells (0.26 ± 0.02, $p < 0.001$; **Figure 6D**). Thus, our findings suggest that our model can be utilized to study kinetics of various immune cells in the mandibular dLNs.

DISCUSSION

Corneal immune responses have previously been widely studied in *ex vivo* settings. These studies have provided valuable insights about immune responses to foreign antigens. However, to understand the complexity of the corneal immune arc and the underlying cellular mechanisms involved in antigen presentation process to prime T cells and evoke an immune response, it is essential to study it in an *in vivo* context. During *in vivo* assessment, physiological parameters such as proper tissue oxygenation and temperature must be preserved, allowing cells to behave similarly to a physiological state. Herein, we present, to

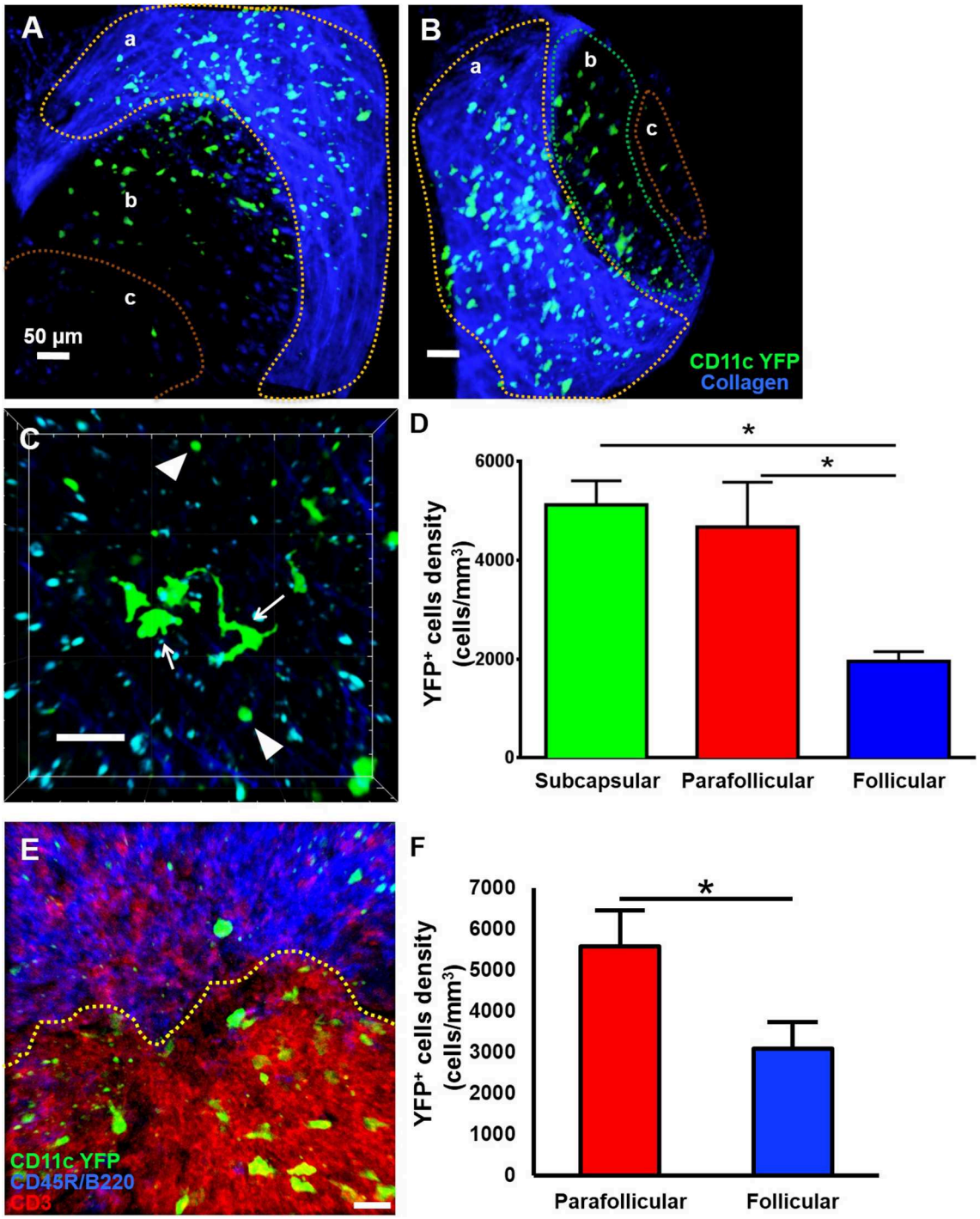

FIGURE 3 | Anatomical distribution of CD11c-YFP$^+$ cells in mandibular draining lymph nodes during steady state. **(A–D)** Representative multiphoton intravital microscopy images of a mandibular draining lymph node (dLN) during steady state. **(A)** Maximum projection of a mandibular dLN in which three areas can be identified: (a) subcapsular area delimitated by the second harmonic generation (blue; capsule's collagen fibers), (b) parafollicular cortex or T cell areas, and (c) follicular cortex or B cell areas. CD11c-YFP$^+$ cells (green cells) are distributed predominantly in the subcapsular area, but also in the follicular and parafollicular areas. **(B)** Oblique view of the same dLN, in which the extent of the dLN's capsule (blue) can be appreciated. **(C)** Magnified parafollicular cortex of the dLN, showing different YFP$^+$ cDC morphology and sizes. White arrows point to cells with dendritiform projections; arrow heads indicate round shaped, smaller cDCs. **(D)** Quantitative analysis of CD11c-YFP$^+$ cell densities among the three areas of the dLNs during steady state (pooled from three independent experiments with a total of $n = 3$ mice). **(E,F)** Confocal microscopy of a mandibular dLN during steady state. **(E)** Representative confocal micrograph of a 60 µm section of a dLN of a CD11c-YFP mouse during steady state, showing distribution of CD11c-YFP$^+$ cells (green) among parafollicular cortex or T cell area (CD3, red) and follicular cortex or B cell area (CD45R/B220, blue). **(F)** Quantification of CD11c-YFP$^+$ cells in the parafollicular and follicular areas (pooled from three independent experiments with a total of $n = 3$ mice). Bars: Mean ± SEM, one-way ANOVA with Tukey *post-hoc* (for **D**) and *t*-test (for **F**), $^*p < 0.05$, scale bars: 50 µm.

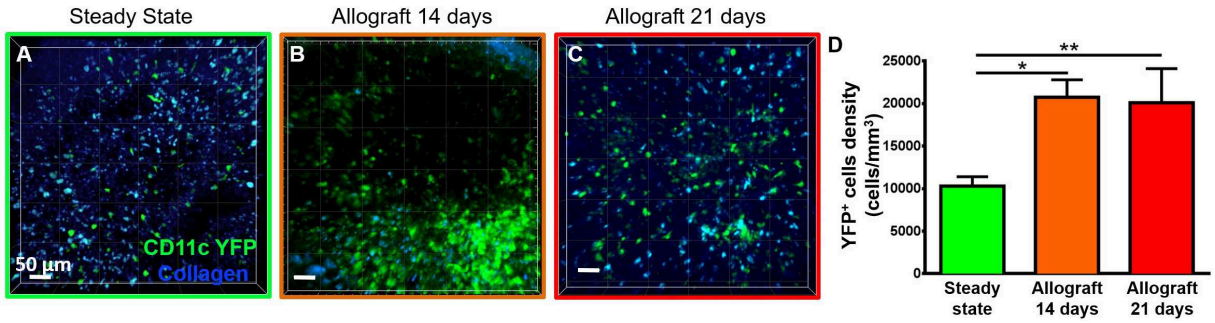

FIGURE 4 | Density of CD11c-YFP$^+$ cells in mandibular draining lymph nodes. **(A–C)** Representative multiphoton intravital microscopy images of mandibular draining lymph nodes (dLNs) during **(A)** steady state and **(B)** 14 and **(C)** 21 days after corneal allotransplantation reveal an increase in the number of host-derived CD11c-YFP$^+$ cells (green cells). **(D)** Quantitative analysis of host CD11c-YFP$^+$ cells density in dLNs (pooled from three independent experiments with a total of $n = 3$ mice/group). Bars: Mean ± SEM, one-way ANOVA with Tukey *post-hoc*, $*p < 0.05$, $**p < 0.01$, scale bars: 50 µm.

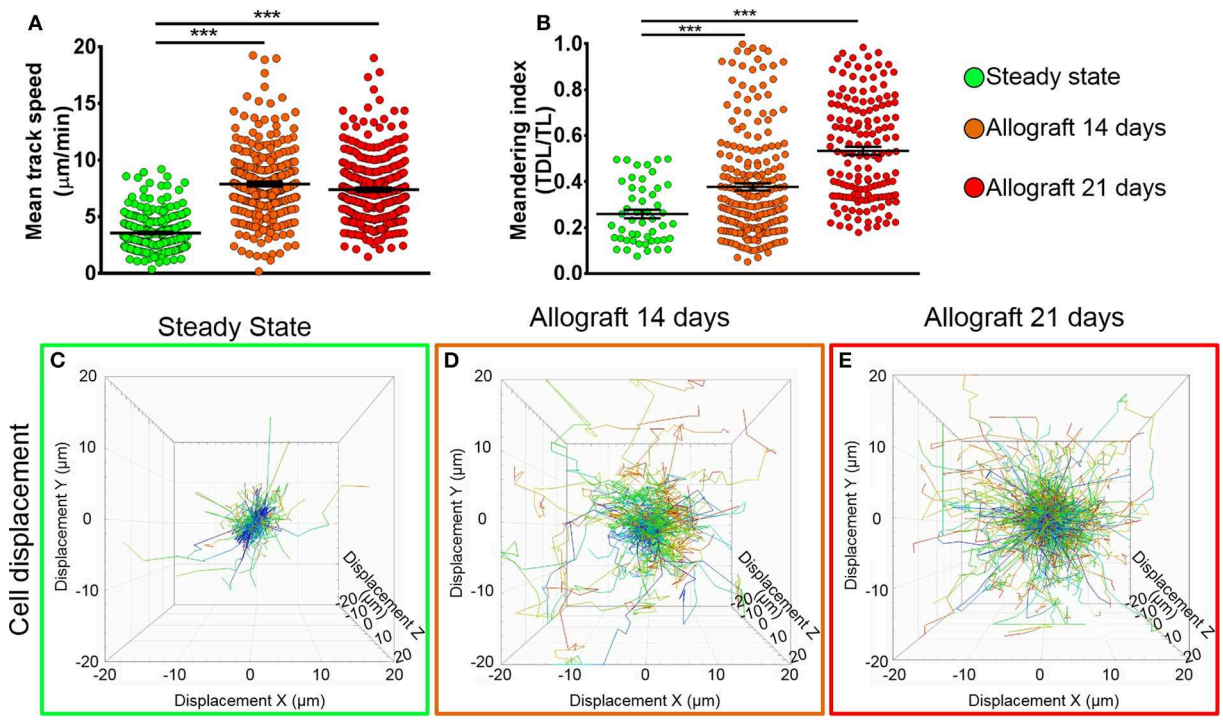

FIGURE 5 | Kinetics of CD11c-YFP$^+$ cells in mandibular draining lymph nodes. **(A,B)** Quantitative analysis of **(A)** mean speed and **(B)** meandering indices (track displacement length divided by track length) of host CD11c-YFP$^+$ cells during steady state, 14, and 21 days after corneal allotransplantation (pooled from three independent experiments with a total of $n = 3$ mice/group). **(C–E)** Representative cell displacement lengths normalized to a starting point. Bars: Mean ± SEM, one-way ANOVA with Tukey *post-hoc*, $***p < 0.001$.

our knowledge, the first model for *in vivo* imaging of the corneal dLNs utilizing MP-IVM.

MP-IVM has been proven to be a reliable method to visualize and analyze innate and adaptive immune responses at a single-cell level. The more accessible inguinal and popliteal LNs have been widely studied via MP-IVM. The first report of *in vivo* imaging of the inguinal dLNs was in 2003, where Miller et al. described and quantified the migratory behavior of adoptively transferred fluorescently labeled T cells in mice (22). One year later, Mempel et al. described a mouse model to image popliteal dLNs utilizing MP-IVM (25). These reports reveal the feasibility and reproducibility of MP-IVM in imaging superficial dLNs. Contrary to these dLNs, *in vivo* imaging of mandibular dLNs is challenging due to its anatomical proximity to lungs and heart. Thus, respiratory movement and heartbeats are powerful mechanical artifacts that hinder a proper stabilization of the dLN for appropriate image acquisition at a microscopic level over time, since a few micrometers tissue movement can turn into uninterpretable 3D images (36). We have overcome this problem by stabilizing the mandibular dLN in two steps: careful

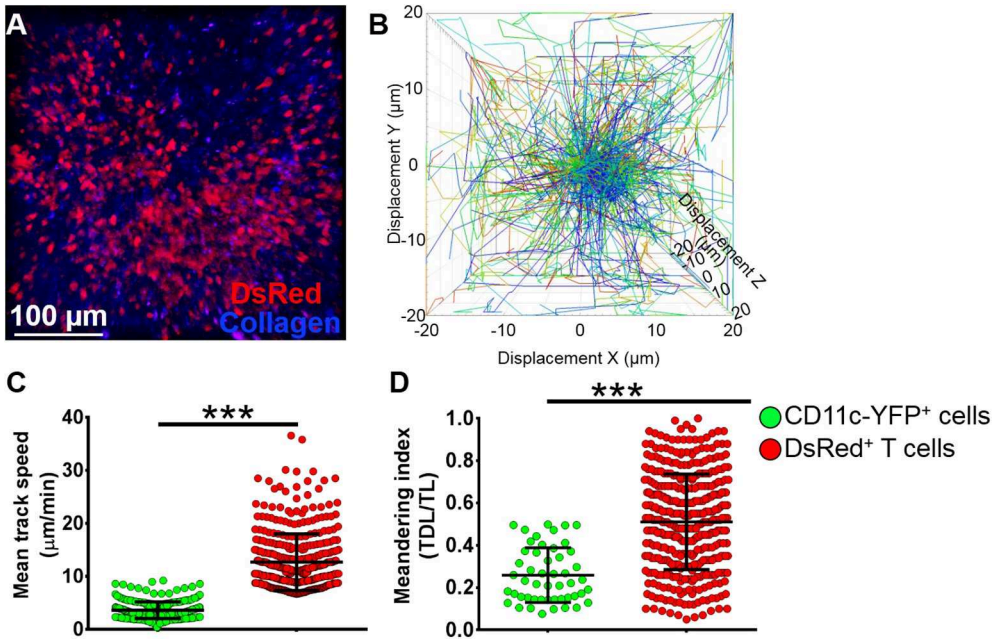

FIGURE 6 | Kinetics of T cells in mandibular draining lymph nodes. **(A)** Representative multiphoton intravital microscopy image of a mandibular draining lymph nodes (dLNs) of a transgenic T-Red mouse during the steady state showing DsRed$^+$ T cells (red) and collagen (blue). **(B)** Representative cell displacement lengths normalized to a starting point. **(C,D)** Comparison of cell mean speed **(C)** and meandering indices **(D)** between CD11c-YFP$^+$ and DsRed$^+$ T cells in the dLNs during steady state (pooled from three independent experiments with a total of $n = 3$ mice/group). Bars: Mean ± SEM, *t*-test, $^{***}p < 0.001$, scale bar: 100 µm.

microdissection of the tissue around the dLN and slightly elevating the dLN from/above the surrounding structures using a spatula. This in turn means imaging is not affected by heartbeats or breathing artifacts. During this step, it is crucial to ensure that the blood flow to the dLN is not interrupted by either severing or stretching of the feeding vessels while elevating the dLN. This is to ensure proper tissue oxygenation and maintaining proper physiological temperature (37 ± 1°C). Temperature is a critical aspect in analyzing cell dynamics: if proper temperature is not achieved or if it is not constant during the entire image acquisition, interstitial cell motility will be affected (23, 30), with no dendrite movement or "probing;" hence, dynamic analysis will not be reliable. We achieved a proper temperature, ensuring that a sealed chamber around the dLN was made with vacuum grease and was filled with optical gel. The function of this gel is to keep the dLN moist and at a physiological temperature. The ceiling of this chamber was formed by a glass coverslip and a heating tubing system through which hot water circulated at a constant rate. With this heating system, we tried attempted to mimic the physiological conditions of proper temperature for an adequate interstitial cell movement.

Through utilizing a custom-made stage, appropriate microdissection, a sealed chamber, and constant physiological temperature regulation, we have been able to perform longitudinal MP-IVM of the mandibular dLNs. We demonstrate that the mean speed and movement directionality of host-derived CD11c-YFP$^+$ cells increase significantly after corneal allotransplantation as compared with steady state. Furthermore, after 14 days, CD11c-YFP$^+$ cells tend to agglomerate in the parafollicular cortex of dLNs. This is in line with a previous report from Lindquist et al. who described the spatiotemporal characteristics of dendritic cell networks in normal inguinal dLNs of live mice (20). In these studies, the authors explained how steady state cDCs are entangled in an extensive cell network while they are probing T cells, but that after activation, these cells become more motile and distribute into the sessile network to be readily accessible to migrating T cells. Similarly, with our model of *in vivo* imaging of corneal dLNs, we are able to visualize the distribution of CD11c-YFP$^+$ cells in all three regions of the mandibular dLNs. During steady state, CD11c-YFP$^+$ cells are either static with some dendrite probing or exhibit a low mean speed with random movement throughout the dLNs parenchyma.

Previous studies have shown that corneal trauma results in secretion of proinflammatory cytokines, leading to activation of APCs, enhanced expression of maturation markers, including major histocompatibility complex II and costimulatory molecules, CD80 and CD86, subsequently resulting in their mobilization to dLNs (8, 37, 38). In the current study, we assessed the density and kinetics of CD11c-YFP$^+$ cells in the mandibular dLNs following corneal transplantation. We observed that following corneal allotransplantation, density and motility of host CD11c-YFP$^+$ cells increase significantly, with cell movement becoming more directional. The change in directionality may be indicative of CD11c-YFP$^+$ cells movements toward T cells in the parafollicular areas of the dLNs to prime them and elicit T cell responses. Although we demonstrate alterations in the density and motility of CD11c-YFP$^+$ cells, as a subpopulation of APCs in the mandibular dLNs following corneal transplantation, our study is limited in revealing

potential association between alterations in cell kinetics and functions of these cells. Thus, further studies are necessary to examine the correlation between kinetics and functionality of APCs during steady state and following transplantation.

In the current study, T cells in the mandibular dLNs showed a mean track speed of 12.67 μm/min and 3D instantaneous velocity of 6.08 μm/min. In line with our findings, Miller et al. observed that average T cell speed in inguinal dLNs ranges between of 10.2 and 11.5 μm/min in live mice (22), and Mempel et al. reported mean 3D velocity of 8.4 μm/min for T cells in popliteal dLNs (23, 25). Furthermore, consistent with our findings, a study on kinetics of CD11c-YFP$^+$ cells in the inguinal dLNs suggest that cDCs move more slowly compared to T cells with their median speed ranging between 1 and 4 μm/min depending on the dLN area (20). Indeed, MP-IVM has been used to study cell-to-cell interactions, a crucial step in understanding immune responses. In 2004, Mempel et al. could distinguish three stages of T cell activation mediated by DCs in popliteal dLNs over time (transient encounters, followed by stable contacts, and finally high motility and proliferation of T cells) (25). MP-IVM can be also used to study immune cells in peripheral tissues. For instance, in 2011, Celli et al. using a murine ear skin graft model and MP-IVM, showed that activation of graft-reactive CD8$^+$ T cells occurs in the dLNs, and this T cell cross-priming is mediated by host's APCs that had previously infiltrated the graft (28). Furthermore, the study provided insight into molecular mechanisms involved in skin graft rejection. In a more recent report, Kitano et al. characterized the dynamic interaction of different cDC subsets in the skin dLNs, providing *in vivo* evidence of the differential role of migratory and resident cDCs in cytotoxic T cell generation within the dLNs (21). With our model of *in vivo* imaging of the corneal dLNs and utilizing different combinations of transgenic mice (for example, mice expressing fluorescent proteins subpopulations of T cells), one would be able to study the process of antigen presentation in inflamed and pathological states of the cornea, such as after corneal transplantation, and may be able to characterize the dynamics and molecular mechanisms involved in corneal graft rejection to provide insights that may lead to the development of immunomodulatory therapies to prevent immunological transplant rejections.

DATA AVAILABILITY STATEMENT

The datasets generated for this study are available on request to the corresponding author.

ETHICS STATEMENT

The animal study was reviewed and approved by Schepens Eye Research Institute Animal Care and Use Committee and Tufts Medical Center Animal Care and Use Committee.

AUTHOR CONTRIBUTIONS

ML, TY, and PH designed the research. ML, TY, AJ, VS, and GO performed the research. ML, YS-R, TY, AJ, GO, DH, and PH analyzed the data. ML, YS-R, AJ, VS, DH, and PH wrote the paper.

FUNDING

This study was supported by grants NIH R21-EY025393 (PH), NIH K08-EY020575 (PH), NIH R01-EY022695 (PH), Research to Prevent Blindness Career Development Award (PH), Research to Prevent Blindness Challenge Grant, Fight for Sight Grant-in-Aid (PH), Massachusetts Lions Eye Research Fund, Inc. (PH), Tufts Medical Center Institutional Support (PH), Bausch Lomb Ocular Surface Research Award (TY), and Uehara Foundation Fellowhip (TY).

ACKNOWLEDGMENTS

We are grateful to Dr. Michel C. Nussenzweig from Rockefeller University for his kind gift of CD11c-YFP mice and Dr. Ulrich H. von Andrian from Harvard Medical School for kindly providing transgenic T-Red mice.

SUPPLEMENTARY MATERIAL

The Supplementary Material for this article can be found online at: https://www.frontiersin.org/articles/10.3389/fimmu.2020.00039/full#supplementary-material

Supplementary Video 1 | After careful microdissection of tissue surrounding the dLN, and without damaging feeding vessels, the dLN is positioned on a wooden spatula, and slightly elevated above surrounding structures. In this video, the dLN has been slightly repositioned to show intact vasculature, uninterrupted blood flow, and heart pounding or breathing movements that would otherwise impede imaging are not observed.

Supplementary Video 2 | Mandibular dLN of a CD11c-YFP mouse during steady state. Z-stack of optical sections rendered into 3D data set. The dLN capsule's collagen fibers can be observed through the second harmonic generation (blue). Located underneath the collagen capsule are the CD11c-YFP$^+$ cells (green) in the subcapsular area (a). Toward the center, is located the parafollicular area or T cell zone (b) and the follicular area or B cell zone (c), where CD11c-YFP$^+$ cells are still present, but sparsely. Scale bar: 50 μm.

Supplementary Video 3 | Zoomed parafollicular cortex of a mandibular dLN of a CD11c-YFP mouse during steady state. Z-stack of optical sections rendered into 3D data set. Different cell morphologies and sizes of CD11c-YFP$^+$ cells can be appreciated (green). Scale bar: 50 μm.

Supplementary Video 4 | Time-lapse video of the parafollicular area of a mandibular dLN of a CD11c-YFP mouse during steady state. CD11c-YFP$^+$ cells (green) are distributed throughout the dLN parenchyma. The majority of them show static cell bodies, with dendrite movement or "probing." The smaller cells are more motile, showing random movements with larger displacements. Scale bar: 50 μm.

Supplementary Video 5 | Time-lapse video of the parafollicular area of a mandibular dLN of a CD11c-YFP mouse during steady state. Zoomed to appreciate CD11c-YFP$^+$ cells dendrites' "probing" and movement of the smaller cells through the dLN parenchyma. Compared with the larger ones, the smaller cells are more motile, interacting and making close contacts with each other. Scale bar: 50 μm.

Supplementary Video 6 | Time-lapse video of the parafollicular area of an ipsilateral mandibular dLN 14 days after corneal allotransplantation to a

CD11c-YFP mouse. CD11c-YFP$^+$ cells (green) are distributed throughout the dLN parenchyma, some of them clustered in the inferior right corner. Scale bar: 50 μm.

Supplementary Video 7 | Time-lapse video of the parafollicular area of an ipsilateral mandibular dLN 21 days after corneal allotransplantation to a CD11c-YFP mouse. CD11c-YFP$^+$ cells (green) are distributed throughout the dLN parenchyma, most of them have lost their dendritiform shape, and have become oval, representing smaller and more motile. Scale bar: 50 μm.

Supplementary Video 8 | Time-lapse video of the parafollicular area of a mandibular dLN of a transgenic T-Red mouse with DsRed$^+$ T cells during steady state. T cells (red) show random rapid movements with large displacements. Scale bar: 50 μm.

REFERENCES

1. Medawar PB. Immunological tolerance. *Nature*. (1961) 189:14–7. doi: 10.1038/189014a0
2. Streilein JW. Ocular immune privilege: the eye takes a dim but practical view of immunity and inflammation. *J Leukoc Biol*. (2003) 74:179–85. doi: 10.1189/jlb.1102574
3. Forrester JV, Xu H. Good news-bad news: the Yin and Yang of immune privilege in the eye. *Front Immunol*. (2012) 3:338. doi: 10.3389/fimmu.2012.00338
4. Pearlman E, Sun Y, Roy S, Karmakar M, Hise AG, Szczotka-Flynn L, et al. Host defense at the ocular surface. *Int Rev Immunol*. (2013) 32:4–18. doi: 10.3109/08830185.2012.749400
5. Benhar I, London A, Schwartz M. The privileged immunity of immune privileged organs: the case of the eye. *Front Immunol*. (2012) 3:296. doi: 10.3389/fimmu.2012.00296
6. Hamrah P, Liu Y, Zhang Q, Dana MR. The corneal stroma is endowed with a significant number of resident dendritic cells. *Invest Ophthalmol Vis Sci*. (2003) 44:581–9. doi: 10.1167/iovs.02-0838
7. Hamrah P, Zhang Q, Liu Y, Dana MR. Novel characterization of MHC class II-negative population of resident corneal Langerhans cell-type dendritic cells. *Invest Ophthalmol Vis Sci*. (2002) 43:639–46.
8. Hamrah P, Liu Y, Zhang Q, Dana MR. Alterations in corneal stromal dendritic cell phenotype and distribution in inflammation. *Arch Ophthalmol*. (2003) 121:1132–40. doi: 10.1001/archopht.121.8.1132
9. Banchereau J, Briere F, Caux C, Davoust J, Lebecque S, Liu YJ, et al. Immunobiology of dendritic cells. *Annu Rev Immunol*. (2000) 18:767–811. doi: 10.1146/annurev.immunol.18.1.767
10. Guermonprez P, Valladeau J, Zitvogel L, Théry C, Amigorena S. Antigen presentation and T cell stimulation by dendritic cells. *Annu Rev Immunol*. (2002) 20:621–67. doi: 10.1146/annurev.immunol.20.100301.064828
11. Liu YJ. Dendritic cell subsets and lineages, and their functions in innate and adaptive immunity. *Cell*. (2001) 106:259–62. doi: 10.1016/S0092-8674(01)00456-1
12. Egan RM, Yorkey C, Black R, Loh WK, Stevens JL, Woodward JG, et al. Peptide-specific T cell clonal expansion *in vivo* following immunization in the eye, an immune-privileged site. *J Immunol*. (1996) 157: 2262–71.
13. Perez VL, Biuckians AJ, Streilein JW. *In-vivo* impaired T helper 1 cell development in submandibular lymph nodes due to IL-12 deficiency following antigen injection into the anterior chamber of the eye. *Ocul Immunol Inflamm*. (2000) 8:9–24. doi: 10.1076/0927-3948(200003)8:1;1-S;FT009
14. Boonman ZF, van Mierlo GJ, Fransen MF, Franken KL, Offringa R, Melief CJ, et al. Intraocular tumor antigen drains specifically to submandibular lymph nodes, resulting in an abortive cytotoxic T cell reaction. *J Immunol*. (2004) 172:1567–74. doi: 10.4049/jimmunol.172.3.1567
15. Germain RN, Miller MJ, Dustin ML, Nussenzweig MC. Dynamic imaging of the immune system: progress, pitfalls and promise. *Nat Rev Immunol*. (2006) 6:497–507. doi: 10.1038/nri1884
16. Cahalan MD, Parker I, Wei SH, Miller MJ. Two-photon tissue imaging: seeing the immune system in a fresh light. *Nat Rev Immunol*. (2002) 2:872–80. doi: 10.1038/nri935
17. Denk W, Strickler JH, Webb WW. Two-photon laser scanning fluorescence microscopy. *Science*. (1990) 248:73–6. doi: 10.1126/science.2321027
18. Hoover EE, Squier JA. Advances in multiphoton microscopy technology. *Nat Photonics*. (2013) 7:93–101. doi: 10.1038/nphoton.2012.361
19. So PT, Dong CY, Masters BR, Berland KM. Two-photon excitation fluorescence microscopy. *Annu Rev Biomed Eng*. (2000) 2:399–429. doi: 10.1146/annurev.bioeng.2.1.399
20. Lindquist RL, Shakhar G, Dudziak D, Wardemann H, Eisenreich T, Dustin ML, et al. Visualizing dendritic cell networks *in vivo*. *Nat Immunol*. (2004) 5:1243–50. doi: 10.1038/ni1139
21. Kitano M, Yamazaki C, Takumi A, Ikeno T, Hemmi H, Takahashi N, et al. Imaging of the cross-presenting dendritic cell subsets in the skin-draining lymph node. *Proc Natl Acad Sci USA*. (2016) 113:1044–9. doi: 10.1073/pnas.1513607113
22. Miller MJ, Wei SH, Cahalan MD, Parker I. Autonomous T cell trafficking examined *in vivo* with intravital two-photon microscopy. *Proc Natl Acad Sci USA*. (2003) 100:2604–9. doi: 10.1073/pnas.2628040100
23. Miller MJ, Wei SH, Parker I, Cahalan MD. Two-photon imaging of lymphocyte motility and antigen response in intact lymph node. *Science*. (2002) 296:1869–73. doi: 10.1126/science.1070051
24. Murooka TT, Mempel TR. Multiphoton intravital microscopy to study lymphocyte motility in lymph nodes. *Methods Mol Biol*. (2012) 757:247–57. doi: 10.1007/978-1-61779-166-6_16
25. Mempel TR, Henrickson SE, Von Andrian UH. T-cell priming by dendritic cells in lymph nodes occurs in three distinct phases. *Nature*. (2004) 427:154–9. doi: 10.1038/nature02238
26. Bousso P, Robey E. Dynamics of CD8+ T cell priming by dendritic cells in intact lymph nodes. *Nat Immunol*. (2003) 4:579–85. doi: 10.1038/ni928
27. Miller MJ, Hejazi AS, Wei SH, Cahalan MD, Parker I. T cell repertoire scanning is promoted by dynamic dendritic cell behavior and random T cell motility in the lymph node. *Proc Natl Acad Sci USA*. (2004) 101:998–1003. doi: 10.1073/pnas.0306407101
28. Celli S, Albert ML, Bousso P. Visualizing the innate and adaptive immune responses underlying allograft rejection by two-photon microscopy. *Nat Med*. (2011) 17:744–9. doi: 10.1038/nm.2376
29. Henrickson SE, Mempel TR, Mazo IB, Liu B, Artyomov MN, Zheng H, et al. *In vivo* imaging of T cell priming. *Sci Signal*. (2008) 1:pt2. doi: 10.1126/stke.112pt2
30. Halin C, Mora JR, Sumen C, von Andrian UH. *In vivo* imaging of lymphocyte trafficking. *Annu Rev Cell Dev Biol*. (2005) 21:581–603. doi: 10.1146/annurev.cellbio.21.122303.133159
31. von Andrian UH. Intravital microscopy of the peripheral lymph node microcirculation in mice. *Microcirculation*. (1996) 3:287–300. doi: 10.3109/10739689609148303
32. Camelo S, Shanley A, Voon AS, McMenamin PG. The distribution of antigen in lymphoid tissues following its injection into the anterior chamber of the rat eye. *J Immunol*. (2004) 172:5388–95. doi: 10.4049/jimmunol.172.9.5388
33. Okada S, Albrecht RM, Aharinejad S, Schraufnagel DE. Structural aspects of the lymphocyte traffic in rat submandibular lymph node. *Microsc Microanal*. (2002) 8:116–33. doi: 10.1017/S1431927601020049
34. Mempel TR, Pittet MJ, Khazaie K, Weninger W, Weissleder R, von Boehmer H., et al. Regulatory T cells reversibly suppress cytotoxic T cell function independent of effector differentiation. *Immunity*. (2006) 25:129–41. doi: 10.1016/j.immuni.2006.04.015
35. Yamagami S, Miyazaki D, Ono SJ, Dana MR. Differential chemokine gene expression in corneal transplant rejection. *Invest Ophthalmol Vis Sci*. (1999) 40:2892–7.

36. Mempel TR, Scimone ML, Mora JR, von Andrian UH. *In vivo* imaging of leukocyte trafficking in blood vessels and tissues. *Curr Opin Immunol.* (2004) 16:406–17. doi: 10.1016/j.coi.2004.05.018
37. Yamagami S, Hamrah P, Miyamoto K, Miyazaki D, Dekaris I, Dawson T, et al. CCR5 chemokine receptor mediates recruitment of MHC class II-positive Langerhans cells in the mouse corneal epithelium. *Invest Ophthalmol Vis Sci.* (2005) 46:1201–7. doi: 10.1167/iovs.04-0658
38. Chen W, Lin H, Dong N, Sanae T, Liu Z, Yoshitomi T. Cauterization of central cornea induces recruitment of major histocompatibility complex class II+ Langerhans cells from limbal basal epithelium. *Cornea*. (2010) 29:73–9. doi: 10.1097/ICO.0b013e3181ac9f92

Conflict of Interest: The authors declare that the research was conducted in the absence of any commercial or financial relationships that could be construed as a potential conflict of interest.

frontiers in Immunology

ORIGINAL RESEARCH
published: 07 May 2020
doi: 10.3389/fimmu.2020.00742

Intravital Multiphoton Microscopy of the Ocular Surface: Alterations in Conventional Dendritic Cell Morphology and Kinetics in Dry Eye Disease

Arsia Jamali[1,2†], Yashar Seyed-Razavi[1,2†], Cecilia Chao[1,2], Gustavo Ortiz[1,2], Brendan Kenyon[1,2,3], Tomas Blanco[1,2], Deshea L. Harris[1,2] and Pedram Hamrah[1,2,3,4]*

[1] Center for Translational Ocular Immunology, Tufts Medical Center, Tufts University School of Medicine, Boston, MA, United States, [2] Department of Ophthalmology, Tufts Medical Center, Tufts University School of Medicine, Boston, MA, United States, [3] Program in Neuroscience, School of Graduate Biomedical Sciences, Tufts University, Boston, MA, United States, [4] Program in Immunology, School of Graduate Biomedical Sciences, Tufts University, Boston, MA, United States

OPEN ACCESS

Edited by:
Connie Wong,
Monash University, Australia

Reviewed by:
Janos Nemeth,
Semmelweis University, Hungary
Björn Petri,
University of Calgary, Canada

***Correspondence:**
Pedram Hamrah
pedram.hamrah@tufts.edu;
p_hamrah@yahoo.com

[†]These authors share first authorship

Specialty section:
This article was submitted to Antigen Presenting Cell Biology, a section of the journal Frontiers in Immunology

Received: 07 August 2019
Accepted: 01 April 2020
Published: 07 May 2020

Citation:
Jamali A, Seyed-Razavi Y, Chao C, Ortiz G, Kenyon B, Blanco T, Harris DL and Hamrah P (2020) Intravital Multiphoton Microscopy of the Ocular Surface: Alterations in Conventional Dendritic Cell Morphology and Kinetics in Dry Eye Disease. Front. Immunol. 11:742. doi: 10.3389/fimmu.2020.00742

Dry eye disease (DED) is a multifactorial disease of the ocular surface, characterized by loss of tear film homeostasis and ocular symptoms, in which neurosensory abnormalities have recently been shown to play an etiological role. Although the role of inflammation has been widely studied in DED, the kinetics of immune cells of the ocular surface in this complex disease are hereto unclear. Herein, we utilized intravital multiphoton imaging on transgenic mice to investigate the 3D morphology and kinetics of conventional dendritic cells (cDCs) and the role of ocular surface sensory nerves in regulating them in both the naïve state and experimental DED. Mice with DED had significantly lower tear secretion ($p < 0.01$), greater corneal fluorescein staining ($p < 0.001$), and higher cDC density in the ocular surface ($p < 0.05$), compared to naïve mice. cDCs in DED mice showed morphological alterations in the limbus, exhibiting smaller surface area ($p < 0.001$) and volume ($p < 0.001$) compared to naïve mice. Furthermore, corneal cDCs showed greater sphericity in DED mice compared to naïve mice ($p < 0.01$). In addition, limbal cDCs displayed significantly increased migratory kinetics in DED, including mean track speed, 3D instantaneous velocity, track length, and displacement, compared to naïve mice (all $p < 0.05$). In mice with DED, cDCs showed a higher meandering index in the limbus compared to central cornea ($p < 0.05$). In DED, cDCs were less frequently found in contact with nerves in the limbus, peripheral, and central cornea ($p < 0.05$). cDCs in contact with nerves demonstrated a larger surface area ($p < 0.001$) and volume ($p < 0.001$), however, they exhibited less sphericity ($p < 0.05$) as compared to cDCs not in contact with nerves in naïve mice. Importantly, cDCs in contact with nerves during DED had a decreased track length, displacement, mean track speed, and 3D instantaneous velocity compared to those not in contact with nerves (all $p < 0.05$). Taken together, we present *in vivo* evidence of altered cDC kinetics and 3D morphology

in DED. Furthermore, apparent neuronal contact significantly alters cDC kinetics and morphological characteristics, suggesting that ocular surface nerves may play a direct role in mediating immune responses in DED.

Keywords: intravital imaging, multiphoton microscopy, conventional dendritic cells, ocular surface, dry eye disease, cornea, limbus, sensory nerves

INTRODUCTION

Dry eye disease (DED) is one of the most common causes of clinical ophthalmic visits, since it is accompanied by ocular discomfort and results in diminished quality of life (1). It is estimated that more than 16 million adults in the United States suffer from DED, with an estimated prevalence of 3.0% in men and 7.8% in women, imposing a significant public health and economic burden (2, 3). DED is "a multifactorial disease of the ocular surface characterized by a loss of homeostasis of the tear film, and accompanied by ocular symptoms, in which tear film instability and hyperosmolarity, ocular surface inflammation and damage, and neurosensory abnormalities play etiological roles" (1). It can arise due to desiccating stress, systemic conditions, medications, and neurosensory abnormalities (1).

The ocular surface is composed of the avascular cornea, neighboring conjunctiva, eyelids, tear film, and secretory glands, including lacrimal and meibomian glands. The ocular surface functions as a physical and immunological barrier to the external environment, such as foreign particles and opportunistic pathogens while allowing light to penetrate into the eye by maintaining the health of the ocular surface and tear film stability. The cornea is densely innervated by sensory nerves supplied by the ophthalmic division of the trigeminal nerve, sympathetic fibers derived from the superior cervical ganglion, and parasympathetic fibers that originate from the ciliary ganglion (4, 5). Sensory nerves enter the peripheral cornea in a radial pattern and travel parallel to the corneal surface toward the corneal center. The nerve fibers in the stroma comprise the stromal nerve plexus and the branches beneath the basal epithelial cell layer form a dense nerve plexus, termed the subbasal nerve plexus (4, 6). In addition to its dense innervation, the cornea is an immune privileged tissue and also hosts antigen-presenting cells (APCs), including epithelial and stromal conventional dendritic cells (cDCs) and stromal macrophages during steady state (7–12).

Involved in both initiation and progression of the DED, inflammation is considered a key process in the pathogenesis of DED (13–16). The inflammatory microenvironment in the ocular surface during DED facilitates maturation of ocular surface APCs and their subsequent egress to the draining lymph nodes, where they prime naïve $CD4^+$ T cells toward effector T helper (Th)1 and Th17 cells (17–19). Through the efferent arm of the immune response, effector T cells migrate to the ocular surface, where they exacerbate inflammation via further tissue damage. In addition, DED-associated inflammation further exacerbates the destructive milieu in the ocular surface, leading to decreased goblet cell density, altered tear composition, and increased surface irregularity, generating focal points for accelerated tear thinning, and consequently promoting squamous metaplasia in an interferon gamma (IFN-γ)-mediated manner (20, 21). Furthermore, inflammation directly stimulates corneal nociceptor nerve terminals (22, 23). Persistent ocular surface inflammation then results in nerve fiber damage, which in turn perpetuates the disease (24). In this regard, it has been shown that desiccating stress leads to diminished corneal subbasal and intraepithelial nerve density, altered nerve morphology, decreased cornea sensitivity, and pain (25–30). Damage and malfunction of the corneal sensory nerves can lead to decreased blink reflex and tear production, which further augments the disease (31–33).

Although the role of inflammation in the pathogenesis of DED is well studied (14–17, 34), our knowledge on the kinetics of corneal immune cells and the potential role of nerves in affecting immune cell migration during the course of DED is limited. In this study, we investigate the effects of desiccating stress-induced DED on alterations in the three-dimensional (3D) morphology and kinetics of cDCs, as well as their relation to nerves. Utilizing intravital multiphoton microscopy (IV-MPM) of the ocular surface of transgenic mice with fluorescent-tagged cDCs and nerves, we demonstrate that cDCs are more spherical and more motile during DED. In addition, we demonstrate how contact with nerves impacts these morphological and kinetic alterations of cDCs during DED.

MATERIALS AND METHODS

Mice

Wild-type female C57BL/6 mice were purchased from Charles River (Charles River Laboratories, Wilmington, MA, United States). $Thy1^{YFP}$ mice [B6.Cg-Tg (Thy1-YFP)16Jrs/J] were obtained from the Jackson Laboratory (Bar Harbor, ME, United States) as heterozygous and bred to homozygous with repeated matings between male and female mice with high copies of the transgenes for yellow fluorescent protein (YFP). This was required in order to obtain mice with higher fluorescence for IV-MPM. $CD11c^{EYFP}$ mice were a generous gift from Dr. Michel C. Nussenzweig from Rockefeller University (35). $CD11c^{YFP} \times Thy1^{YFP}$ mice were generated by crossing homozygous $Thy1^{YFP}$ with homozygous $CD11c^{EYFP}$ repeatedly until both the nerves and cDCs were colocalized with YFP in the cornea. Primer sets used for quantitative PCR for genotyping included the following: Thy1-YFP forward 5-GCCCTGGCCCACCCTCGTGACCACCTTCG-3, Thy1-YFP reverse 5- CCTGATGCCGTTCTTCTGCTTGTCGGGCA-3, CD11c-EYFP forward 5-TGCTGGTTGTTGTGCTGTCTCATC-3, and CD11c-EYFP reverse 5-GGGGGTGTTCTGCTGGTAG TGGTC-3.

The Thy1-YFP mice express YFP under the control of regulatory elements of the Thy1 gene and thus label neuronal populations, primarily sensory and motor neurons. The CD11c-YFP mice carry the EYFP transgene under the control of the CD11c promoter (35). Thus, our $CD11c^{YFP} \times Thy1^{YFP}$ mice allow visualization of both $CD11c^{+}$ cDCs and $Thy1^{+}$ neurons in the same animals. Because females are more prone to DED and female mice develop more severe clinical disease than age-matched males (36), in this study, only 6- to 8-week-old female mice were used in all experiments. Mice were housed at Tufts Department of Lab Animal Medicine and were treated in accordance with the Association of Research and Vision in Ophthalmology (ARVO) statement for the Use of Animals in Ophthalmology and Vision Research. All experiments were performed after the review and approval from the Institutional Animal Care and Use Committee (IACUC number B2018-47) at Tufts University and Tufts Medical Center, Boston, MA, United States.

Murine Model of Dry Eye Disease

At the age of 6–8 weeks, $CD11c^{YFP} \times Thy1^{YFP}$ mice were either housed in a low-humidity, temperature-regulated custom-made controlled environment chamber (Percival Scientific Inc, Perry, IA, United States) for 4 weeks to develop desiccating stress-induced evaporative DED, or were kept under standard housing with a humidity of 50–60% and a temperature of 21–23°C to serve as naïve controls (37). Using the controlled environment chamber, we exposed the animals to a humidity of 15%, and air circulation of 15 L/min, at 21–23°C temperature using the INTELLIS Ultra Control System and Desiccant dryer 50 cfm leading to desiccating stress. The chamber is sealed, avoiding the direct exchange of air between the outside and the inside, and is connected to a desiccant, which introduces air with low humidity inside the chamber. Inside the chamber, three sensors are located in order to monitor the humidity, airflow, and temperature. Sensors are connected to a router in order to automatically monitor the parameters. In order to maximize exposure, mice were housed in custom-designed fenestrated cages (Ancare Corp. Bellmore, NY, United States). The cages were built with vents at each side to maximize the airflow through them in order to achieve greater desiccating stress on the ocular surface.

Clinical Evaluation

Corneal fluorescein staining (CFS) was performed and scored according to the National Eye Institute (NEI) scale (38). In brief, CFS was graded in five corneal regions, each ranging from 0 to 3, and the sum of the scores of all regions was measured (range, 0–15). Tear secretion was assessed by measuring the wetted length of a phenol red thread (Zone-Quick; Hilco Vision Headquarters, Plainville, MA, United States), which was placed in the lateral canthus of anesthetized mice for 30 sec (39, 40).

Ocular Surface Intravital Multiphoton Microscopy

Animals were anesthetized, and body and ocular surface temperatures were tightly regulated as previously described (41, 42). For central corneal IV-MPM, following intraperitoneal injection of ketamine (100 mg/kg), xylazine (20 mg/kg), and acepromazine (3 mg/kg) mixture, mice were placed on a custom and tiltable stereotactic stage to focus on the cornea and limbus. Proper depth of anesthesia was assessed every 30–60 min with supplemental doses of ketamine alone (100 mg/kg). Topical proparacaine hydrochloride (0.5%) and Genteal ophthalmic lubricant gel (Alcon, Fort Worth, TX, United States) were applied to the examined eye and a 5-0 non-absorbable silk suture (Surgical Specialities Corporation, Reading, PA, United States) was placed around the eye to prevent eye closure, blinking, and nystagmus while allowing the normal flow of blood to the eye. To maintain ocular surface temperature and moisture, a sealed chamber was created around the exposed portion of the eye using high vacuum grease (Dow Corning, Midland, MI, United States) and plastics placed on the grease as previously described (41). Genteal gel was added to the chamber, and hot water circulated through the tubing and chamber assembly to maintain a temperature range within 2°C of the physiological ocular surface temperature (34°C; range, 33-35°C). The IV-MPM setup and surgical mouse preparation for imaging the limbus and peripheral cornea are described elsewhere (42).

An Ultima Multiphoton Microscope System (Bruker, Fitchburg, WI, United States) equipped with two MaiTai Ti/Sapphire DeepSee lasers (Newport Spectra-Physics, Irvine, CA, United States), allowing for simultaneous coaxial 850 and 900 nm illumination to achieve two-photon excitation and second harmonic generation, was utilized for all experiments. Using a 20×-1.0 NA (Olympus XLUMPLFLN, Tokyo, Japan) water immersion objective, scans of the ocular surface were taken every 30–60 sec over a period of up to an hour with 512×512 resolution and twofold line averaging, as previously described (41).

Image Analysis and Processing

3D measurements of cell morphology and cell motility were calculated using Imaris (Bitplane, Zurich, Switzerland) as previously described (41). In short, 3D cell analysis was performed to elucidate 3D cell surface area (μm^2), volume (μm^3), and sphericity (range, 0–1) by creating a surface object using the surface tool. Careful consideration and manual confirmation of each cell surface was performed to ensure that created surfaces were representative of the morphology of individual cells. Image stacks were converted into four-dimensional (4D) movies, semi-automated tracking of cell motility was performed, and cell bodies were tracked over time and were manually confirmed at each frame to determine total track length (total track distance of a cell, μm) and displacement length (distance from the initial position of a cell in the track to the last, as a straight line, μm), 3D instantaneous velocity (velocity of a cell between two consecutive frames, μm/min), mean track speed (average speed of a cell over length of imaging, μm/min), and meandering index, which provides a measure of the deviation from a straight line of a migratory cell (a value of 1 indicating that the track is a straight line) (43). Static cells with a displacement of <10 μm were excluded from meandering index analysis (41). In order to elucidate the effect of cDC contact with nerves on cDC morphological and kinetic parameters, each cell in

all videos from all areas of limbus, peripheral, and central cornea was assessed by two independent investigators using 3D and 4D reconstructed videos to evaluate the presence of contact or lack of contact with nerves (interobserver agreement kappa = 0.83). All cells in the assessed videos were categorized as either with or without contact with nerves, unless the investigators did not agree on the presence or lack of contact with nerves. In such cases, the examined cells were excluded from further analysis on the effect of nerve contact on cDC morphology and kinetics.

Confocal Microscopy

In order to assess if we can observe cDCs in contact with nerves in the limbus and cornea of wild-type C57BL/6 and $CD11c^{YFP} \times Thy1^{YFP}$ mice, the corneas and limbus of wild-type C57BL/6 and $CD11c^{YFP} \times Thy1^{YFP}$ mice were excised; samples from wild-type mice were fixed in chilled acetone for 15 min, washed, blocked for 30 min at room temperature (RT) with 3% bovine serum albumin (BSA) containing 1% anti-CD16/CD32 Fc receptor mAb (Bio X Cell, West Lebanon, NH, United States), and were then incubated with a combination of primary fluorophore-conjugated antibodies against Thy1, CD45, F4/80 (all Biolegend, San Diego, CA, United States), and CD11c (eBioscience, San Diego, CA, United States) for 90 min at RT. After washing for three times, samples were mounted with mounting media containing 4′,6-diamidino-2-phenylindole (DAPI; Vector Laboratories, Inc., Burlingame, CA, United States) and were visualized by a Leica SP8 confocal microscope (Leica Microsystems Inc., Buffalo Grove, IL, United States). Samples from $CD11c^{YFP} \times Thy1^{YFP}$ mice were freshly mounted and underwent confocal microscopy. After acquisition, the epithelium was digitally removed, and 3D videos were reconstructed using Imaris.

Flow Cytometry

The bone marrow of $CD11c^{YFP} \times Thy1^{YFP}$ double-transgenic mice were harvested and strained using a 70 μm nylon mesh to yield single-cell suspension. Red blood cells were removed by incubating the single cells in ammonium-chloride-potassium lysing buffer for 1 min at RT. Samples were then washed, blocked and stained in fluorescence-activated cell sorting buffer containing 1% anti-CD16/CD32 Fc receptor mAb (Bio X Cell) and LIVE/DEAD Fixable Blue Dead Cell Stain (Thermo Fisher Scientific, Waltham, MA, United States) at RT for 20 min. Next, single cell suspensions were labeled with fluorophore-conjugated antibodies against CD45, CX3CR1, CD11c, CD11b, CD68, and PDCA-1, or appropriate conjugated isotype controls, for 60 min at RT (all Biolegend or eBioscience). Following a wash, samples underwent flow cytometric analysis using a BD LSR II Flow Cytometer (BD Biosciences). The acquired data were analyzed by FlowJo v10 (FlowJo, LLC, Ashland, OR, United States). Debris, dead cells, and doublets were excluded using forward and side scatters and a live/dead cell marker (**Supplementary Figure S1**).

Statistical Analysis

Results are presented as mean ± standard error of the mean (SEM). To compare cDC morphological and kinetic characteristics between groups, at least three IV-MPM videos, each taken from an individual mouse, were pooled. To determine the differences in cDC density, morphological and kinetic parameters between experimental DED and naïve groups, as well as between cDCs in contact and not in contact with nerves, *t* test was employed. To assess regional differences in the density, morphology, and kinetic parameters of cDCs (in three regions of limbus, peripheral, and central cornea), ANOVA with Tukey *post hoc* test was used (Prism GraphPad Software, La Jolla, CA, United States). Differences between groups were considered significant if $p < 0.05$.

RESULTS

Clinical Assessment of Dry Eye Disease Severity

Clinical assessment revealed that mice exposed to desiccating stress developed clinical signs of DED, with a significantly higher CFS (13.8 ± 0.3) compared to naïve controls (0.5 ± 0.2, $p < 0.001$; n = 5–6/group; **Figures 1A,B**). Furthermore, the mice exposed to desiccating stress showed lower tear volume (3.4 ± 0.92 mm) in comparison to naïve mice (8.8 ± 0.5 mm, $p = 0.005$; n = 6–12/group; **Figure 1C**).

Alterations in Dendritic Cell Density and 3D Morphology in Dry Eye Disease

We initially aimed to characterize the identity of YFP^+ cells in $CD11c^{YFP} \times Thy1^{YFP}$ mice. Thus, we performed flow cytometry on the bone marrow of these transgenic mice. As depicted in **Supplementary Figure S1**, we initially gated out debris and dead cells (**Supplementary Figure S1**A), doublets (**Supplementary Figure S1**B), and gated on YFP^+ cells (**Supplementary Figure S1**C). Next, using fluorescent minus one controls, we observed that YFP^+ cells in the bone marrow of $CD11c^{YFP} \times Thy1^{YFP}$ mice were in fact cDCs, as they expressed the pan-leukocyte marker, CD45, myeloid markers, CD11b and CX3CR1, dendritic cell marker, CD11c; but were majorly negative for plasmacytoid dendritic cell marker, PDCA-1, as well as macrophage marker, CD68 (**Supplementary Figure S1**D).

Having established the identity of YFP^+ cells in $CD11c^{YFP} \times Thy1^{YFP}$ mice, we next examined if desiccating stress-induced DED affects the density of YFP^+ cDCs in the limbus, peripheral, and central cornea, using IV-MPM (**Figure 2A**). A higher density of YFP^+ cDCs was found in both the limbus and peripheral cornea in the DED group (limbus, 437.5 ± 45.1 cells/mm^2; peripheral cornea, 243.8 ± 32.9 cells/mm^2) compared to naïve controls (limbus, 260.4 ± 30.9 cells/mm^2, $p = 0.013$; peripheral cornea, 127.5 ± 23.2 cells/mm^2, $p = 0.021$; **Figure 2B**). However, despite a 2.4-fold increase, the density of cDCs in the central cornea did not reach statistical significance (137.5 ± 33.1 cells/mm^2 in DED vs. 58.3 ± 4.2 cells/mm^2 in naïve mice, $p = 0.076$; **Figure 2B**). Furthermore, as expected, in both naïve mice and mice with DED, we observed higher densities of cDCs in the limbus compared with that in the peripheral ($p = 0.027$ and $p = 0.009$, respectively) and central corneas ($p = 0.003$ and $p < 0.001$, respectively).

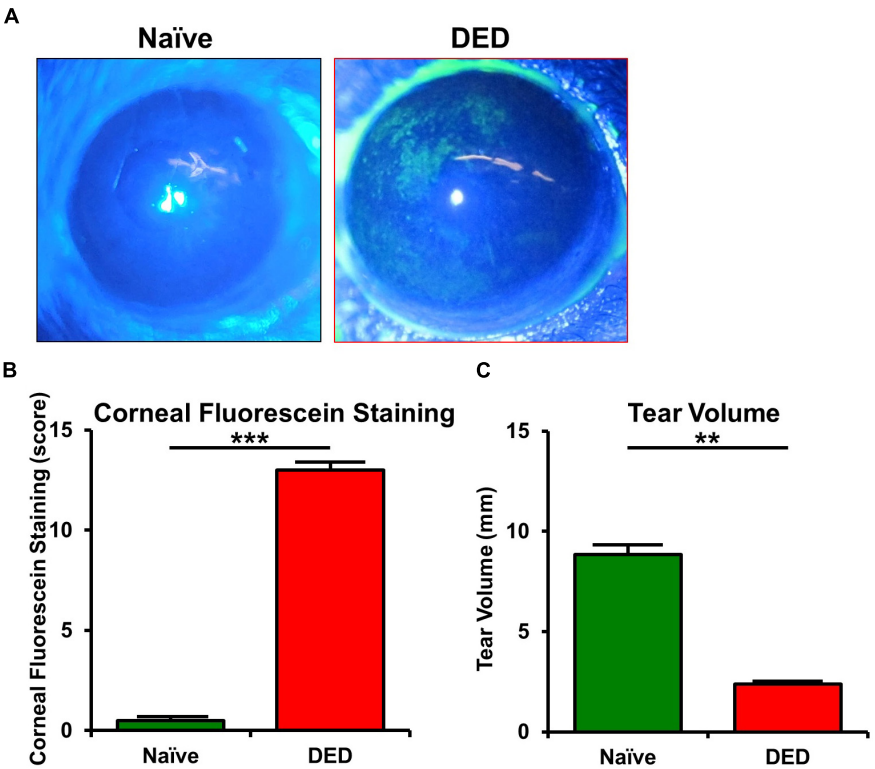

FIGURE 1 | Ocular surface findings in desiccating stress-induced dry eye disease. **(A)** Representative corneal fluorescein staining images. **(B)** Quantification of fluorescein staining scores revealed a significant increase in corneal staining in mice exposed to desiccating stress compared to naïve controls (n = 5–6/group). **(C)** Tear volume using phenol red thread test showed a significant decrease in tear volume in mice exposed to desiccating stress compared to naïve controls (n = 6–12/group). Results are presented as mean ± SEM, t test, $^{**}p < 0.01$, $^{***}p < 0.001$.

We next compared the 3D morphological parameters of cDCs in DED to naïve mice. As shown in **Figure 2C**, cDCs in the limbus and peripheral cornea of DED mice were smaller, with lower 3D cell surface area compared to that of naïve mice (limbus, 1,127.2 ± 55.0 vs. 1,761.9 ± 104.1 μm^2, $p < 0.001$; peripheral cornea, 1,279.0 ± 129.8 vs. 1,875.5 ± 148.5 μm^2, $p = 0.005$), but there was no difference in the central cornea between the groups (DED, 1,616.5 ± 128.4 vs. naïve mice, 2,049.8 ± 242.8 μm^2, $p = 0.088$; **Figure 2C**). cDC volume in the limbus was also lower in DED compared to that in the naïve group (1,880.8 ± 184.3 vs. 3,371.5 ± 186.3 μm^3, $p < 0.001$; **Figure 2D**) but not in the peripheral cornea (2,375.4 ± 324.0 vs. 3,038.9 ± 306.5 μm^3, $p = 0.184$) and central cornea (3,530.7 ± 391.6 vs. 3,750.1 ± 510.4 μm^2, $p = 0.744$; **Figure 2D**). Furthermore, assessment of cDC sphericity in DED exhibited higher sphericity in the peripheral (0.66 ± 0.02 vs. 0.54 ± 0.01, $p < 0.001$) and central corneas (0.68 ± 0.01 vs. 0.59 ± 0.03, $p = 0.002$), but not in the limbus (0.63 ± 0.01 vs. 0.62 ± 0.01, $p = 0.432$) compared to naïve controls (**Figure 2E**). Assessing the potential regional differences in the morphology of cDCs, we noticed that it is only during DED that limbal cDCs exhibited less 3D cell surface area ($p = 0.035$; **Supplementary Figure S2**A) and volume ($p = 0.002$; **Supplementary Figure S2**B) compared to central corneal cDCs. However, we did not observe significant regional differences in the sphericity of cDCs during DED (**Supplementary Figure S2**C).

Taken together, our results highlight that DED significantly alters cDC morphology in the limbus and cornea, with more prominent alterations in the limbus and peripheral cornea.

Alterations in cDC Kinetics in Dry Eye Disease

Having observed alterations in the morphological properties of cDCs in DED, we next investigated if the *in vivo* ocular surface cDC kinetics are altered in DED. Thus, we performed IV-MPM and analyzed kinetics of cDCs in the limbus/peripheral corneas of naïve mice (**Supplementary Video S1**) and mice with DED (**Supplementary Video S2**), as well as in the central cornea in naïve controls (**Supplementary Video S3**) and following induction of DED by desiccating stress (**Supplementary Video S4**). Representative IV-MPM still images of cDC migration in the limbus and cornea of naïve and DED mice are shown in **Figure 3A**. We observed that the track length of cDCs in the limbus was significantly increased in DED (80.73 ± 3.79 μm) compared to naïve mice (69.24 ± 2.53 μm, $p = 0.033$; **Figures 3B,D**). The difference was also present in the central cornea (115.60 ± 8.53 vs. 35.13 ± 5.60 μm, $p < 0.001$) and in the peripheral cornea (92.39 ± 6.85 vs. 59.51 ± 5.45 μm, $p < 0.001$;

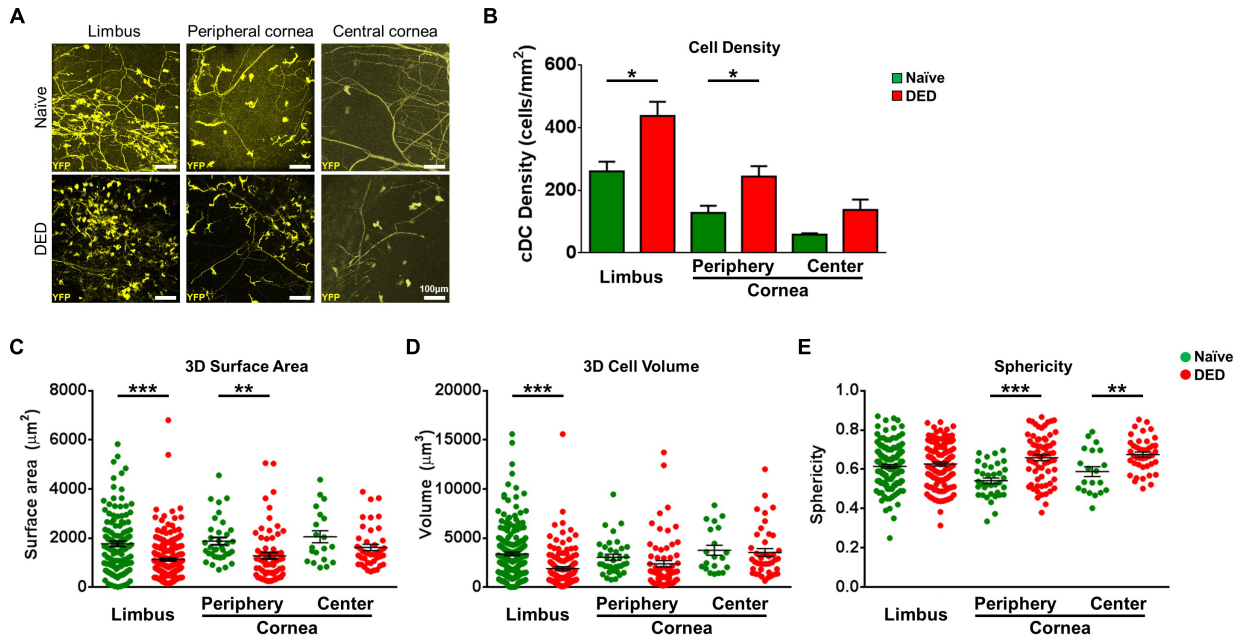

FIGURE 2 | Morphological features of conventional dendritic cells. **(A)** Representative intravital multiphoton microscopy (IV-MPM) images of ocular surface conventional dendritic cells (cDCs) in naïve mice and after exposure to desiccating stress-induced dry eye disease (DED). **(B)** Quantification of the density of YPF^{+} cDCs highlighting an increase in cDCs in the limbus and cornea in DED (n = 3–5/group). **(C–E)** 3D Morphological analyses of YPF^{+} cDCs in naïve and after exposure to desiccating stress, pooled from at least three mice/group, including **(C)** 3D cell surface area, **(D)** 3D cell volume, and **(E)** sphericity. Scale bars: 100 μm. Results are presented as mean ± SEM, t test, *$p < 0.05$, **$p < 0.01$, and ***$p < 0.001$.

Figures 3C,D). Interestingly, we also noted a significantly longer displacement in cDCs in DED compared to naïve mice in the limbus (8.87 ± 0.68 vs. 6.63 ± 0.32 μm, $p = 0.028$) as well as central cornea (11.09 ± 1.68 vs. 4.59 ± 0.44 μm, $p = 0.007$). However, cDC displacement was comparable in the peripheral corneas of naïve (5.18 ± 0.44 μm) and DED mice (7.65 ± 1.33 μm, $p = 0.080$; **Figure 3E**).

Analysis of velocity revealed significant differences in 3D instantaneous velocity of ocular surface cDCs in DED compared to the naïve setting (**Figure 3F**). This increase was noted in cDCs within the limbus (1.70 ± 0.02 vs. 1.52 ± 0.01 μm/min, $p < 0.001$), peripheral (1.49 ± 0.02 vs. 1.35 ± 0.02 μm/min, $p < 0.001$), and central cornea (2.02 ± 0.04 vs. 1.14 ± 0.03 μm/min, $p < 0.001$) compared to naïve. Similarly, we observed a greater mean track speed of cDCs in DED compared to naïve mice in the limbus (2.69 ± 0.11 vs. 2.35 ± 0.05 μm/min, $p = 0.036$), peripheral (3.04 ± 0.18 vs. 2.12 ± 0.09 μm/min, $p < 0.001$), and central cornea (3.24 ± 0.20 vs. 1.60 ± 0.14 μm/min, $p < 0.001$; **Figure 3G**). Thus, our findings show that, while in naïve mice cDCs show minor motility, following exposure to desiccating stress, their kinetic features are altered, exhibiting higher kinesis with a faster speed.

To further assess the directionality of the movements of cDCs in the ocular surface, we measured meandering indices of cDCs in the limbus and cornea during DED, since during the steady state, the motility is limited. We noted a significant regional difference in the meandering index of limbal cDCs (0.30 ± 0.03) compared with cDCs in the central cornea (0.17 ± 0.04, $p = 0.044$; **Figure 3H**) in mice with DED. However, we did not observe a significant difference between peripheral (0.20 ± 0.03) and central corneal cDCs ($p = 0.979$; **Figure 3H**).

We also evaluated the regional differences in the kinetics of cDCs in the limbus, peripheral, and central cornea. We observed that in naïve mice, cDCs in the limbus traveled over longer tracks compared with cDCs in the central cornea ($p = 0.008$; **Supplementary Figure S2**D). However, in mice with DED, cDCs in the central cornea moved over longer tracks compared with cDCs in the limbus ($p < 0.001$; **Supplementary Figure S2**D). No significant differences were observed in the displacement of cDCs in the limbus, peripheral, and central cornea (**Supplementary Figure S2**E). In naïve mice, cDCs in the limbus showed higher 3D instantaneous velocity compared with cDCs in the peripheral ($p < 0.001$; **Supplementary Figure S2**F) and central cornea ($p < 0.001$; **Supplementary Figure S2**F). Furthermore, peripheral corneal cDCs migrated with a higher 3D instantaneous velocity compared with cDCs in the central cornea ($p = 0.007$; **Supplementary Figure S2**F). In mice with DED, cDCs in the central cornea exhibited higher 3D instantaneous velocity compared with cDCs in the limbus ($p < 0.001$; **Supplementary Figure S2**F) and peripheral cornea ($p < 0.001$; **Supplementary Figure S2**F). However, we did not detect significant differences in mean track speed of cDCs in the limbus, peripheral, and central corneas (**Supplementary Figure S2**G). In summary, we observed that during DED, cDCs exhibited altered migratory kinetics, with the highest pace in the peripheral and central cornea.

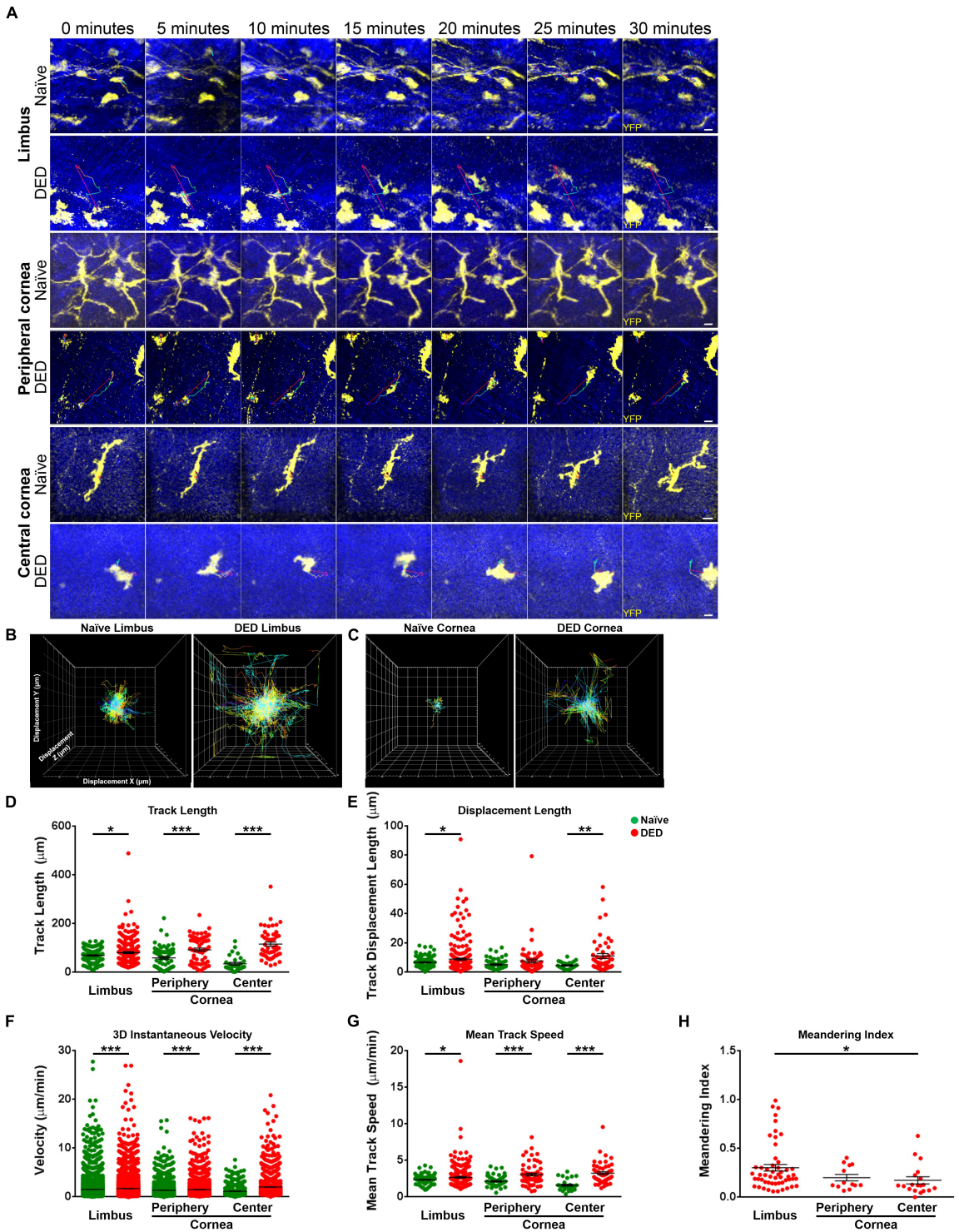

FIGURE 3 | Kinetics of conventional dendritic cells. **(A)** Representative still images of YFP$^+$ conventional dendritic cells (cDCs) in the limbus (top panels), peripheral (middle panels), and central corneas (bottom panels). The thin colored lines represent cell tracks based on the time scale. **(B,C)** Representative displacement tracks of YFP$^+$ cDCs with centered alignment in the **(B)** limbus and **(C)** cornea in naïve state and after exposure to desiccating stress-induced dry eye disease (DED) reveal altered displacement and directionality of cDCs after exposure to desiccating stress. **(D,E)** Kinetic characteristics including **(D)** track length, **(E)** displacement length, **(F)** 3D instantaneous velocity, **(G)** mean track speed, and **(H)** and meandering indices of YFP$^+$ cDC tracks, pooled from at least three mice/group. Scale bars: 10 μm. Results are presented as mean ± SEM, *t* test, $^*p < 0.05$, $^{**}p < 0.01$, and $^{***}p < 0.001$.

The Impact of Nerve Contact on Alterations in Morphology and Kinetics of cDCs

Associations between nerves and immune cells at the ocular surface have recently been reported (12, 44). Desiccating stress-induced DED has been noted to lead to morphological and functional ocular surface nerve alterations (25–28). Accordingly, we sought to investigate if the morphology and kinetic properties of cDCs in the ocular surface change when they were in contact with nerves in both DED and the naïve setting. In order to assess if we can visualize cDCs with and without contact with nerves, we initially performed confocal microscopy on whole-mounted limbus/cornea of wild-type mice during steady state. As presented in **Figure 4A**, we could detect cDCs, judged by expression of CD45 and CD11c, in contact with Thy1-expressing nerves (white arrows) as well as without contact with $Thy1^+$ nerves (red arrow). Noteworthy, we observed that $CD11c^+$ cells in contact (**Supplementary Figure S3**, white arrows) and without contact with nerves (**Supplementary Figure S3**, red arrows) do not costain with F4/80, confirming their identity as cDCs. Next, to assess if we can observe cDCs in contact with nerves in the limbus and cornea of $CD11c^{YFP} \times Thy1^{YFP}$ mice, we performed confocal microscopy on fresh corneal samples of double-transgenic naïve mice. As represented in **Figure 4B**, we identified cDCs, which were with contact (**Figure 4B** and **Supplementary Figures S4A,B**, white arrows; **Supplementary Video S5**) or without contact (**Figure 4B** and **Supplementary Figures S4C,D**, red arrows; **Supplementary Video S6**) with YFP^+ nerves. Notably, in confocal micrographs, cDCs could be differentiated from $Thy1^+$ nerves based on their morphology and presence of DAPI-stained nucleus (**Supplementary Figures S4B,D**; arrows). Next, we analyzed the frequency of cDCs with nerve contact (**Figure 4C**, white arrow; **Supplementary Video S7**) and without nerve contact (**Figure 4C**, red arrow; **Supplementary Video S8**) in naïve and DED mice via IV-MPM. We observed that, while 78.1 ± 3.6% of cDCs in the limbus were in contact with nerves during steady state, in mice with DED, only 47.9 ± 6.3% of cDCs in the limbus were in contact with nerves ($p = 0.013$; $n = 3$–5/group; **Supplementary Figure S5**). Notably, we observed a comparable reduction in the frequency of cDCs in contact with nerves in mice with DED in the peripheral and central cornea in mice with DED compared with naïve mice ($p = 0.026$ and $p < 0.001$, respectively; **Supplementary Figure S5**). Next, we analyzed 3D morphological parameters of cDCs in with and without nerve contact in naïve and DED mice using IV-MPM. Our analysis revealed that in naïve mice, cDCs in contact with nerves were significantly larger in terms of 3D cell surface area (2,359.0 ± 177.7 vs. 1,481.7 ± 90.0 μm^2, $p < 0.001$; **Figure 4D**) and volume (4,522.9 ± 422.8 vs. 2,466.0 ± 175.7 μm^3, $p < 0.001$; **Figure 4E**), but less spherical (0.57 ± 0.01 vs. 0.61 ± 0.01, $p = 0.043$; **Figure 4F**), compared to cDCs that are not in contact with nerves. Similarly, in the DED group, cDCs that were in contact with nerves had a greater 3D cell surface area compared to those not in contact with nerves (1,747.2 ± 193.9 vs. 1,255.0 ± 60.7 μm^2, $p = 0.004$; **Figure 4D**). However, there were no significant differences in volume and sphericity of cDCs with and without nerve contact in DED (volume, 2,860.4 ± 293.7 vs. 2,308.9 ± 138.1 μm^3, $p = 0.129$; sphericity, 0.66 ± 0.02 vs. 0.66 ± 0.01, $p = 0.985$, respectively; **Figures 4E,F**).

We next sought to investigate the effect of contact with nerves on cDC kinetics. As depicted in **Figures 5A,B**, we observed that cDCs in contact with nerves showed less motility in comparison with cDCs without apparent contact with nerves in both naïve (**Figure 5A**) and DED mice (**Figure 5B**). There were no significant differences in the track length (79.99 ± 4.20 vs. 68.41 ± 3.62 μm, $p = 0.102$; **Figure 5C**) of cDCs with and without nerve contact in the naïve setting. However, cDCs that are in contact with nerves showed a lower displacement (3.15 ± 0.36 vs. 5.62 ± 0.43 μm, $p = 0.004$; **Figure 5D**), 3D instantaneous velocity (0.83 ± 0.01 vs. 1.05 ± 0.01 μm/min, $p < 0.001$; **Figure 5E**), and mean track speed (1.60 ± 0.07 vs. 1.93 ± 0.06 μm/min, $p = 0.005$; **Figure 5F**) compared to cDCs not in contact with nerves. Interestingly, cDCs in contact with nerves showed a shorter track length (65.57 ± 4.24 vs. 81.64 ± 3.99 μm, $p = 0.012$; **Figure 5C**), less displacement (7.46 ± 0.78 vs. 9.96 ± 0.73 μm, $p = 0.030$; **Figure 5D**), lower 3D instantaneous velocity (1.39 ± 0.02 vs. 1.56 ± 0.01 μm/min, $p < 0.001$; **Figure 5E**), and mean track speed (2.24 ± 0.13 vs. 2.61 ± 0.09 μm/min, $p = 0.017$; **Figure 5F**) compared to cDCs not in contact with nerves in the DED setting. Finally, analysis of meandering index for cDCs in mice with DED revealed no significant difference in directionality between cDCs in contact and those not in contact with nerves (0.26 ± 0.05 vs. 0.29 ± 0.03, $p = 0.65$; **Figure 5G**). Thus, our results suggest that contact with nerves alters the aforementioned changes in the morphological properties and kinetics of cDCs in DED.

DISCUSSION

Through the use of IV-MPM on double-transgenic mice, we presented detailed alterations in the 3D morphology and kinetics of ocular surface cDCs following desiccating stress-induced DED and cDC-nerves interplay in this process. Multiple properties of IV-MPM, including its non-invasive nature, small focal point, second harmonic generation, and limited phototoxicity allow for real-time assessment of single cDC dynamics with high spatial and temporal resolution *in vivo*, without requiring antibodies and dyes for visualization. Using the strengths of IV-MPM, we showed that following exposure to desiccating stress, cDCs are increased in the ocular surface and exhibit remarkable alterations in their morphology and migratory characteristics. In fact, while during the steady state cDCs possess an elongated shape with long dendrites and are relatively static, they adopt a more migratory state (45) in DED, with less surface area and volume and more sphericity and migratory kinetics. Furthermore, we revealed that during DED, a significant fraction of cDCs lose their contact with nerves, which significantly alters their kinetics and 3D morphological parameters, suggesting the importance of neuroimmune interplay in the course of DED.

Several murine models have been developed to investigate DED. These include a wide range of genetic modifications, surgical techniques, and medical interventions to decrease tear production or secretion. Among less invasive approaches,

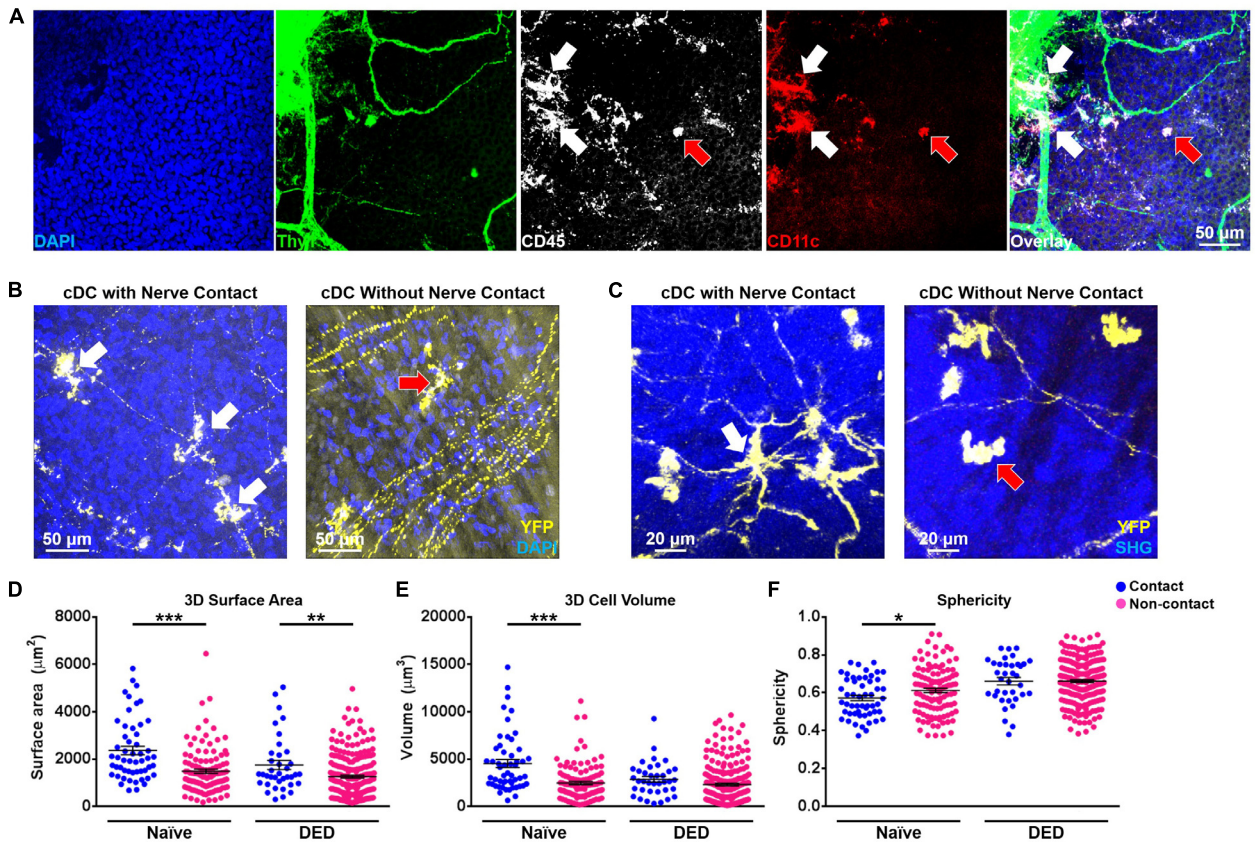

FIGURE 4 | Morphological features of conventional dendritic cells based on their relation with nerves. **(A)** Representative confocal micrograph of corneal/limbal whole mount of a naïve wild-type mouse stained with Thy1, CD45, CD11c, and 4′,6-diamidino-2-phenylindole (DAPI) showing $CD45^+$ $CD11c^+$ conventional dendritic cells (cDCs) in contact (white arrows) and without contact (red arrow) with $Thy1^+$ nerves. **(B)** Representative confocal micrograph of corneal/limbal whole-mount of a naïve $CD11c^{YFP}$ × $Thy1^{YFP}$ mouse mounted with DAPI showing YFP^+ cDCs in contact (white arrows) and without contact (red arrow) with YFP^+ nerves. **(C)** Representative intravital multiphoton microscopy (IV-MPM) images of peripheral corneal cDCs in contact (left panel, white arrow) and without contact (right panel, red arrow) with nerves in $CD11c^{YFP}$ × $Thy1^{YFP}$ mice after exposure to desiccating stress-induced dry eye disease (DED). **(D–F)** Morphological characteristics including **(D)** 3D cell surface area, **(E)** 3D cell volume, and **(F)** sphericity of cDCs in contact and without contact with nerves, pooled from at least three mice/group. Scale bars: 50 µm in **(A,B)** and 20 µm in **(C)**. Results are presented as mean ± SEM, *t* test. SHG, Second harmonic generation. $^*p < 0.05$, $^{**}p < 0.01$, and $^{***}p < 0.001$.

inducing lacrimal gland insufficiency and atrophy by administrating agents such as parasympatholytic molecule scopolamine or imposing desiccating stress on the ocular surface by placing laboratory animals in controlled environment with low humidity and high flow rate are commonly used (37, 46–48). In order to avoid potential effects of surgical procedures, genetic modifications, and systemic medications on immune cells as well as potential off-target systemic effects of such manipulations, in this study, we aimed to induce DED solely by exposing the mice to environmental desiccating stress via a controlled environment chamber, as a model of desiccation-induced DED (37).

During steady state, cDCs reside among the basal layers of the epithelium as well as in the anterior stroma in the cornea (7, 49–51). We previously reported that during steady state, populations of corneal immune cells including cDCs are mainly static, only exhibiting centroid movement with minor displacement, suggestive of environmental sampling (41). In line with the prior report, we observed that cDCs are less motile in the naïve setting; however, greater track length, 3D instantaneous velocity, and mean track speed reaching ∼3 µm/min in the cornea are noted in cDCs following DED. Although there is paucity of similar studies in the literature to directly compare our findings, in a report investigating migration in the peripheral cornea and limbus following intrastromal suture-induced inflammation, auto-fluorescent immune cells were noted to have a mean speed of 9.5 µm/min, with a maximum speed of 54.0 µm/min (52). We previously reported that after thermal cautery burn, $CD11c^+$ and $MHC\text{-}II^+$ APCs have a mean speed of approximately 1.9 and 3.0 µm/min in the cornea, respectively (41). The differences between reports might be explained by the differences in the type of examined cells and the nature of inflammatory response in the cornea since, herein, we investigated DED as a subacute to chronic inflammatory state, while previous reports assessed acute corneal inflammation (41). Furthermore, we noted regional differences in the morphology and kinetics of cDCs. We observed that, in particular during DED, cDCs in the limbus harbor less

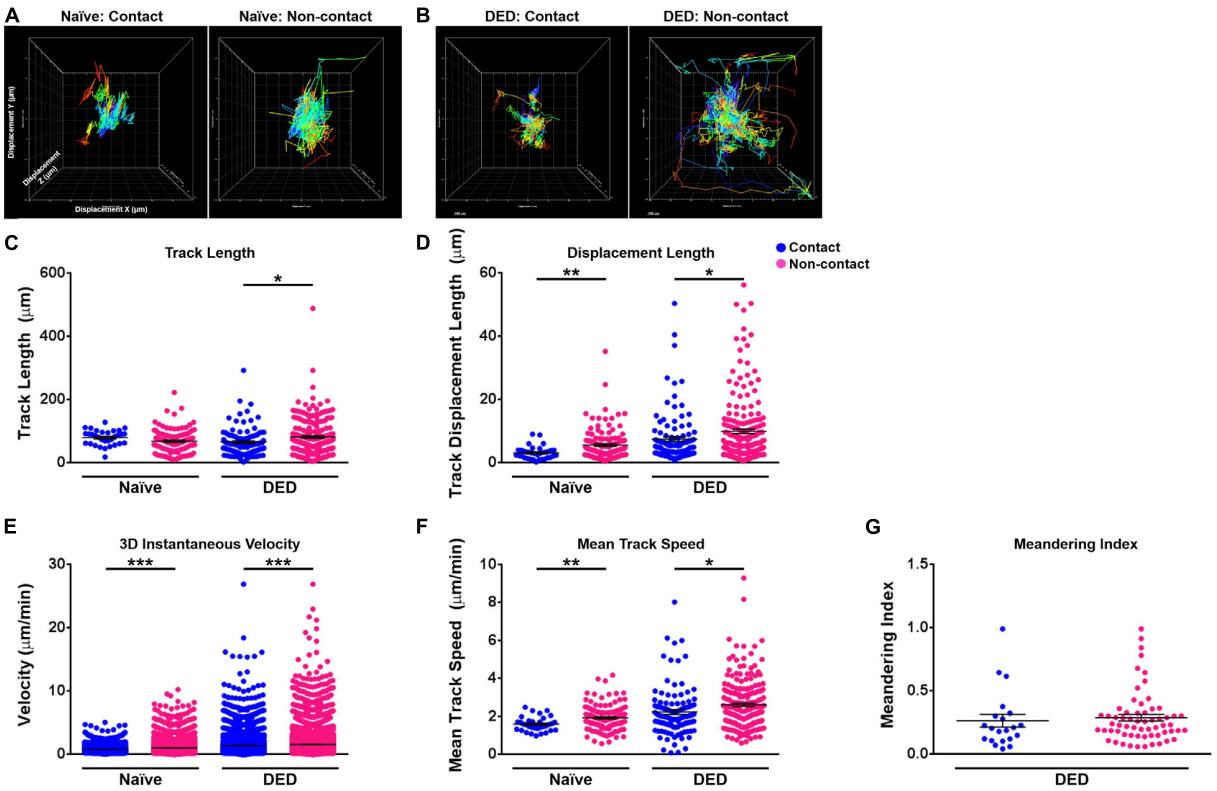

FIGURE 5 | Kinetics of conventional dendritic cells according to their relation with nerves. **(A,B)** Representative displacement tracks of YFP$^+$ conventional dendritic cells (cDCs) with and without nerve contact in **(A)** naïve and **(B)** dry eye disease (DED) mice with centered alignment shows reduced alterations in cDCs with nerve contact. **(C–G)** Kinetic characteristics including **(C)** track length, **(D)** displacement length, **(E)** 3D instantaneous velocity, **(F)** mean track speed, and **(G)** meandering indices of YFP$^+$ cDC tracks in contact or not in contact with nerves, pooled from at least three mice/group. Results are presented as mean ± SEM, *t* test, $^*p < 0.05$, $^{**}p < 0.01$, and $^{***}p < 0.001$.

surface area and volume and travel with lower 3D instantaneous velocity compared to central corneal cDCs. This maybe at least in part explained by some cDCs, which undergo morphological alterations that facilitate adhesion and extravasation from blood vessels or egress to draining lymph nodes in the limbal area.

Resident immune cells in the cornea are considered long-lived, since even after 6 months following transfer of bone marrow cells or bone marrow-derived hematopoietic stem cells to irradiated mice, not all immune cells in the cornea are replaced (53, 54). Transferred cells initially reach the limbus and later migrate to peripheral and subsequently to central corneas (53, 54); however, it is not yet clear if during the steady state, the resident immune cells of the cornea slowly self-regenerate through mitosis, arise from tissue resident precursors, or are recruited from the circulating blood (49, 53, 54). Nevertheless, upon inflammatory stimuli and increase in chemokines/cytokines in the cornea, cDCs are increased in the cornea, at least in part through recruitment from the blood (50, 51, 55). In this study, we observed that cDCs displayed longer track lengths in DED in the limbus, and exhibited a higher meandering index in the limbus compared with the corneal areas; thus, in line with prior studies, it might be postulated that cDCs recruited from the blood stream enter the tissue in the limbus, where they migrate to the peripheral and then the central cornea due to chemotactic gradients in the cornea during DED. However, in the cornea, cDCs did not show a preferential movement direction judged by centered displacement plots and meandering indices. This finding might be explained by the fact that desiccating stress, as the stimulus for inflammation, affects the cornea relatively evenly; thus, cDCs were not directed toward a specific location in the cornea. Additional investigation of immune cell kinetics at various time points following exposure to desiccating stress is required to elucidate a correlation between kinetics of cDCs and DED progression.

Association of immune cells and nerves has been reported in various peripheral and lymphoid tissues (56–61). In the cornea, the most densely innervated tissue of the body, cDCs and macrophages have been shown to reside in close proximity to the nerves in both humans and rodents (12, 44, 62–65). Although, during steady state, the immune cells display a close association with nerves in the cornea, it is shown that macrophages dissociate from nerves following corneal insults (12). Although the impact of this dissociation on the initiation or propagation of immune response, and the mechanisms associated with this warrant further in depth studies, it may be postulated that, upon receiving a danger signal directly from the microenvironment or through

nerves, immune cells dissociate from nerves to freely surveil the tissue, take up antigens, and transfer them to draining lymph nodes. Secretory factors, such as cytokines, chemokines, and neurotransmitters, may play a role in the dissociation of immune cells from the nerves. In this regard, it has been shown that neurotransmitters, such as beta-endorphin, which are released by immune cells, may decrease the association of immune cells with dorsal nerve ganglion cells *in vitro* (66). In line with these observations, we demonstrate that cDCs in contact with nerves were larger, less spherical, and less motile compared to cDCs not in contact with nerves in naïve mice. However, although cDCs generally became smaller, more spherical, and motile in DED, cDCs in contact with nerves were still larger and less motile than other cDCs. These observations suggest that preservation of contact with nerves may prevent the morphological and kinetic alterations of cDCs in DED.

There is a growing body of evidence suggesting that the nervous system contributes to the control of local inflammation. Various studies have found that neurotransmitters and neuropeptides, such as substance P (SP), calcitonin gene-related peptide (CGRP), vasoactive intestinal polypeptide, secretoneurin, nerve-growth factor (NGF), and neuropeptide Y, are able to directly modulate the immune response in peripheral tissues (67–74). In this regard, the release of two key neuropeptides, CGRP and SP, by sensory nerves induces neurogenic inflammation (61, 75). These neuropeptides directly act on vascular endothelial and smooth muscle cells to enable vasodilation, increase capillary permeability, and stimulate leukocyte extravasation (76, 77) and thus play an important role in progression of DED (23, 78, 79). Despite the progress on neural control of inflammation, previous studies have focused on non-contact-mediated mechanisms through which nerves may regulate immune cells, whereas our study suggests the potential presence of additional contact-mediated mechanisms for neuroimmune interactions, since we observed differences in multiple parameters between cDCs with and without nerve contact. Notably, while cDC contact with nerves dampened cDC motility, it did not reduce cDC movement to naïve levels. This may be, in part, explained by the potential damage or dysfunction of nerves at the ocular surface as a result of DED or by the inflammatory microenvironment, impacting the immunomodulatory effect that nerves may have on cDCs.

It should also be noted that the corneal epithelial cells that provide support to the terminal nerve fibers extending toward the ocular surface (80) may also influence cDC–nerve association (44). Furthermore, it has previously been shown that morphology, thickness, and migration patterns of corneal epithelial cells may be altered in various corneal conditions (81–83). In particular, DED is associated with increased corneal epithelial cell turnover and thickness (84), likely due to an increase in the proliferation and migration of limbal epithelial stem cells via a natural centripetal migratory movement as a result of increased desquamation in DED (81, 85, 86). Therefore, the investigation of neuro-immune–epithelial interaction in steady state and disease states, such as in DED, may provide crucial information as to the impact of epithelial cells on neuro-immune crosstalk or vice versa. Considering that the prevalence of DED increases with age (3) and, conversely, corneal nerve density and sensitivity is decreased during aging (28), another avenue for future studies is to investigate the effect of aging on trafficking of immune cells and on neuro-immune interactions in the cornea.

Considering that the cornea is an avascular tissue, systemic administration of large molecules, such as antibodies, does not allow labeling of the corneal structures (87–89). Similarly, subconjunctival injection of antibodies generally does not lead to proper labeling of all corneal structures, such as the epithelium (90), in which a subset of immune cells reside. Moreover, intact corneal epithelium, as the most anterior layer of the cornea, does not allow for penetration of large molecules (90–92). Thus, to assess cDCs and nerves, in this study, we took benefit of transgenic mice with fluorescently labeled cDCs and nerves. However, this approach harbors several shortcomings. One of the limitations is that not all ocular surface nerves express Thy1 and hence YFP; thereby, we may have underestimated the number of cDCs in contact with nerves and falsely classified them to the non-contact group, which may have decreased the power of our comparisons. While this may indeed be the case, our results demonstrate significant differences in morphology and kinetics between cells in contact and not in contact with nerves. Furthermore, we determined the contact between corneal nerves and cDCs based on fluorescence signal detected by IV-MPM using Imaris, which enabled us to assess the spatial relation of each cell with surrounding nerves in 3D. Nevertheless, fluorescence signal may not reflect true contact. Therefore, future studies, utilizing alternative methodologies, such as transmission electron microscopy or *in vitro* co-cultures, are needed to confirm our findings. Another potential limitation of our study is the complicated process of preparing the mice for imaging, including application of local anesthetic drops, lubricant, and suture placement around the eye, all of which may potentially affect corneal nerve function and immune cell behavior. However, in this study, our control naïve mice also underwent a similar procedure for imaging, which limits potential inaccuracy of our findings. The presence of Thy1-YFP^+ myeloid-derived cells, capable of secreting NGF following inflammation within the cornea, has previously been reported (93, 94). To address possible limitation of inclusion of these cells among the YFP^+ cells in our $CD11c^{YFP} \times Thy1^{YFP}$ double-transgenic mice, we performed flow cytometric analysis on YFP^+ cells and found that the majority of them align with a cDC phenotype. Therefore, the inclusion of Thy1-YFP^+ cells in our analyses is likely negligible. Furthermore, in our transgenic $CD11c^{YFP} \times Thy1^{YFP}$ mice, both cDCs and nerves are labeled with a similar fluorescent protein. Although we could differentiate the YFP^+ cDCs from YFP^+ neuronal axons in the limbus and the cornea based on their morphology and presence/lack of movement, the application of transgenic mice with differential labeling of cDCs and nerves or alternative approaches to co-label cDCs or corneal nerves would be necessary to further elucidate fine alterations in the morphology of cDCs and nerves and studying potential membrane exchange between these structures in future studies. Nevertheless, we hope that the current study will stimulate further studies in this area.

Further studies are warranted to assess if removal from a desiccating stress environment after development of DED can lead to restoration of morphological and kinetic alterations of cDCs to the naïve setting, and if this is the case, how long is needed for such a recovery. Moreover, additional studies into the mechanisms of neuro-immune interactions at the ocular surface in disease and naïve states are warranted to categorically demonstrate the immunomodulatory role of ocular surface nerves as indicated by the novel intravital kinetic data presented herein. In summary, in this study, using IV-MPM, we illustrated that cDCs undergo morphological alterations and display increased migratory characteristics during DED that is, in part, ameliorated by corneal nerves. Taken together, we present *in vivo* evidence indicating that sensory nerves of the ocular surface may play an important role in modulating ocular surface immune cells in health and disease.

DATA AVAILABILITY STATEMENT

The datasets generated for this study are available on request to the corresponding author.

ETHICS STATEMENT

The animal study was reviewed and approved by Tufts University, Tufts Medical Center Institutional Animal Care and Use Committee (IACUC).

AUTHOR CONTRIBUTIONS

AJ, YS-R, and PH designed the research. AJ, YS-R, CC, GO, BK, TB, and DH performed the research. AJ, YS-R, CC, GO, TB, DH, and PH analyzed the data. AJ, YS-R, CC, GO, BK, TB, DH, and PH prepared the manuscript.

FUNDING

This work was supported by grants NIH R01-EY022695 (PH) and NIH R01-EY029602 (PH).

ACKNOWLEDGMENTS

The authors would like to express their gratitude to Dr. Michel C. Nussenzweig (Rockefeller University, New York, NY, United States) for the CD11c^{EYFP} mice, as a generous gift. Furthermore, the authors would like to acknowledge Allen Parmelee and Stephen Kwok for technical assistance at Tufts University of School of Medicine flow cytometry core facility.

SUPPLEMENTARY MATERIAL

The Supplementary Material for this article can be found online at: https://www.frontiersin.org/articles/10.3389/fimmu.2020.00742/full#supplementary-material

FIGURE S1 | Flow cytometric characterization of YFP$^+$ cells in CD11c^{YFP} × Thy1^{YFP} mice. **(A–C)** Sequential gating strategy to select live single YFP$^+$ cells among bone marrow cell suspension of a naïve CD11c^{YFP} × Thy1^{YFP} mouse. **(A)** Gating out dead cells and debris and **(B)** doublets, and **(C)** gating on YFP$^+$ cells. **(D)** Fluorescent minus one histograms for CD45, CD11b, CX3CR1, CD11b, PDCA-1, and CD68 on YFP$^+$ cells. The experiment was repeated 3 times.

FIGURE S2 | Regional differences in the morphology and kinetics of conventional dendritic cells (cDCs) in the limbus, peripheral, and central cornea. **(A–C)** Morphologic characteristics including 3D cell surface area **(A)**, 3D cell volume **(B)**, and sphericity **(C)** of YFP$^+$ cDCs in naïve and DED conditions. **(D–G)** Kinetic characteristics including track length **(D)**, displacement length **(E)**, 3D instantaneous velocity **(F)**, and mean track speed **(G)** of YFP$^+$ cDCs in transgenic CD11c^{YFP} × Thy1^{YFP} mice in naïve and DED conditions. Data is pooled from at least 3 mice/group. Results are presented as mean ± SEM, ANOVA with Tukey *post hoc*, $^*p < 0.05$, $^{**}p < 0.01$, and $^{***}p < 0.001$.

FIGURE S3 | Conventional dendritic cells in the cornea reside with or without contact with nerves. Representative confocal micrograph of corneal/limbal whole-mount of a naïve wild-type mouse stained with Thy1, CD11c, F4/80, and DAPI showing CD11c$^+$ F4/80^{neg} conventional dendritic cells can be found in contact (white arrows) or without contact (red arrows) with Thy1$^+$ nerves. The experiment was repeated 3 times. Scale bar: 50 μm.

FIGURE S4 | Morphologic differentiation of conventional dendritic cells and nerves in the cornea of transgenic CD11c^{YFP} × Thy1^{YFP} mice. Representative confocal micrograph of freshly excised corneal/limbal sample from a naïve CD11c^{YFP} × Thy1^{YFP} mouse mounted with DAPI. conventional dendritic cells (cDCs) exhibit a distinct morphology compared with nerves. **(A)** Representative maximum intensity projection of whole-mounted tissue, depicting cDCs in contact with nerves (white arrows). **(B)** Respective section on the level of nucleus shows presence of nucleus in the YFP$^+$ cDCs (white arrows). **(C)** Representative maximum intensity projection of whole-mounted tissue, illustrating cDCs without contact with nerves (red arrow). **(D)** Respective section on the level of nucleus shows presence of nucleus in the YFP$^+$ cDC (red arrow). The experiment was repeated 3 times. Scale bars: 50 μm.

FIGURE S5 | Frequency of conventional dendritic cells in contact with nerves in the limbus and cornea of transgenic CD11c^{YFP} × Thy1^{YFP} mice. Quantification of relative frequency of YFP$^+$ conventional dendritic cells in contact with nerves in the limbus, peripheral, and central cornea in naïve mice and following exposure to desiccating stress (n = 3–5/group). Results are presented as mean ± SEM, t-test, $^*p < 0.05$, $^{***}p < 0.001$.

VIDEO S1 | Kinetics of conventional dendritic cells in the limbus of a naïve mouse. Representative intravital multi-photon microscopy movie of the limbus of a CD11c^{YFP} × Thy1^{YFP} transgenic mouse in naïve setting. As shown, conventional dendritic cells exhibited subtle locomotion over short tracks. Yellow: YFP, yellow fluorescent protein; Blue: SHG, second harmonic generation delineating collagen. White arrows points to cells with apparent movement. Scale bar: 50 μm.

VIDEO S2 | Kinetics of conventional dendritic cells in the limbus of a mouse with dry eye disease. Representative intravital multi-photon microscopy movie of the limbus of a CD11c^{YFP} × Thy1^{YFP} transgenic mouse under exposure to desiccating stress. As shown, conventional dendritic cells displaced over longer tracks with a higher mean speed. Yellow: YFP, yellow fluorescent protein; Blue: SHG, second harmonic generation delineating collagen. White arrows points to cells with apparent movement. Scale bar: 50 μm.

VIDEO S3 | Kinetics of conventional dendritic cells in the central cornea of a naïve mouse. Representative intravital multi-photon microscopy movie of the central cornea of a CD11c^{YFP} × Thy1^{YFP} transgenic mouse in naïve setting. As shown, conventional dendritic cells exhibited subtle locomotion over short tracks. Yellow; YFP, yellow fluorescent protein; Blue: SHG, second harmonic generation delineating collagen. Scale bar: 50 μm.

VIDEO S4 | Kinetics of conventional dendritic cells in the central cornea of a mouse with dry eye disease. Representative intravital multi-photon microscopy movie of the central cornea of a CD11c^{YFP} × Thy1^{YFP} transgenic mouse under exposure to desiccating stress. As shown, conventional dendritic cells displaced over longer tracks with a higher mean speed. Yellow: YFP, yellow fluorescent protein; Blue: SHG, second harmonic generation delineating collagen. White arrows points to cells with apparent movement. Scale bar: 50 μm.

VIDEO S5 | Confocal micrograph of conventional dendritic cells in contact with nerves. Representative 3D reconstructed video of confocal micrograph of a $CD11c^{YFP} \times Thy1^{YFP}$ transgenic mouse, indicating conventional dendritic cells (cDCs), containing nucleus, in contact with nerve. cDCs and nerves express YFP and are hence illustrated in yellow. Note the dendrite of the cDCs in contact with corneal nerves. Yellow: YFP, yellow fluorescent protein; Blue: DAPI, indicating nucleus. Scale bar: 50–60 μm.

VIDEO S6 | Confocal micrograph of conventional dendritic cells without nerve contact. Representative 3D reconstructed video of confocal micrograph of a $CD11c^{YFP} \times Thy1^{YFP}$ transgenic mouse, indicating a conventional dendritic cell (cDC), containing nucleus, without nerve contact. cDCs and nerves express YFP and are hence illustrated in yellow. Note that the cDC is not in contact with corneal nerves. Yellow: YFP, yellow fluorescent protein; Blue: DAPI, indicating nucleus. Scale bar: 50 μm.

VIDEO S7 | Intravital multiphoton microscopy of conventional dendritic cells in contact with nerves. Representative intravital multi-photon microscopy image of a $CD11c^{YFP} \times Thy1^{YFP}$ transgenic mouse, indicating conventional dendritic cells (cDCs) in contact with nerve. cDCs and nerves express YFP and are hence illustrated in yellow. Note the dendrite of the cDC in contact with corneal nerves. Yellow; YFP, yellow fluorescent protein; Blue: SHG, second harmonic generation delineating collagen. Scale bar: 20 μm.

VIDEO S8 | Intravital multiphoton microscopy of conventional dendritic cells without nerve contact. Representative intravital multi-photon microscopy image of a $CD11c^{YFP} \times Thy1^{YFP}$ transgenic mouse, indicating conventional dendritic cells (cDCs) without nerve contact. CDcs and nerves express YFP and are hence illustrated in yellow. Note that the cDC highlighted by the arrow is not in contact with corneal nerves. Yellow: YFP, yellow fluorescent protein; Blue: SHG, second harmonic generation delineating collagen. Scale bar: 20 μm.

REFERENCES

1. Craig JP, Nichols KK, Akpek EK, Caffery B, Dua HS, Joo CK, et al. TFOS DEWS II definition and classification report. *Ocul Surf*. (2017) 15:276–83. doi: 10.1016/j.jtos.2017.05.008
2. Stapleton F, Alves M, Bunya VY, Jalbert I, Lekhanont K, Malet F, et al. TFOS DEWS II epidemiology report. *Ocul Surf*. (2017) 15:334–65. doi: 10.1016/j.jtos.2017.05.003
3. Dana R, Bradley JL, Guerin A, Pivneva I, Stillman IÖ, Evans AM, et al. Estimated prevalence and incidence of Dry Eye disease based on coding analysis of a large, all-age United States health care system. *Am J Ophthalmol*. (2019) 202:47–54. doi: 10.1016/j.ajo.2019.01.026
4. Muller LJ, Marfurt CF, Kruse F, Tervo TM. Corneal nerves: structure, contents and function. *Exp Eye Res*. (2003) 76:521–42. doi: 10.1016/s0014-4835(03)00050-2
5. Al-Aqaba MA, Fares U, Suleman H, Lowe J, Dua HS. Architecture and distribution of human corneal nerves. *Br J Ophthalmol*. (2010) 94:784–9. doi: 10.1136/bjo.2009.173799
6. Oliveira-Soto L, Efron N. Morphology of corneal nerves using confocal microscopy. *Cornea*. (2001) 20:374–84. doi: 10.1046/j.1475-1313.2003.00106.x
7. Hamrah P, Zhang Q, Liu Y, Dana MR. Novel characterization of MHC class II-negative population of resident corneal Langerhans cell-type dendritic cells. *Invest Ophthalmol Vis Sci*. (2002) 43:639–46.
8. Brissette-Storkus CS, Reynolds SM, Lepisto AJ, Hendricks RL. Identification of a novel macrophage population in the normal mouse corneal stroma. *Invest Ophthalmol Vis Sci*. (2002) 43:2264–71.
9. Hamrah P, Liu Y, Zhang Q, Dana MR. The corneal stroma is endowed with a significant number of resident dendritic cells. *Invest Ophthalmol Vis Sci*. (2003) 44:581–9. doi: 10.1167/iovs.02-0838
10. Chinnery HR, Ruitenberg MJ, Plant GW, Pearlman E, Jung S, McMenamin PG. The chemokine receptor CX3CR1 mediates homing of MHC class II-positive cells to the normal mouse corneal epithelium. *Invest Ophthalmol Vis Sci*. (2007) 48:1568–74. doi: 10.1167/iovs.06-0746
11. Hattori T, Chauhan SK, Lee H, Ueno H, Dana R, Kaplan DH, et al. Characterization of Langerin-expressing dendritic cell subsets in the normal cornea. *Invest Ophthalmol Vis Sci*. (2011) 52:4598–604. doi: 10.1167/iovs.10-6741
12. Seyed-Razavi Y, Chinnery HR, McMenamin P. G. A novel association between resident tissue macrophages and nerves in the peripheral stroma of the murine cornea. *Invest Ophthalmol Vis Sci*. (2014) 55:1313–20. doi: 10.1167/iovs.13-12995
13. Johnson ME, Murphy PJ. Changes in the tear film and ocular surface from dry eye syndrome. *Prog Retin Eye Res*. (2004) 23:449–74. doi: 10.1016/j.preteyeres.2004.04.003
14. Calonge M, Enríquez-de-Salamanca A, Diebold Y, González-García MJ, Reinoso R, Herreras JM, et al. Dry eye disease as an inflammatory disorder. *Ocul Immunol Inflamm*. (2010) 18:244–53. doi: 10.3109/09273941003721926
15. No authors listed. Research in dry eye: report of the research subcommittee of the International Dry Eye Workshop. (2007). *Ocul Surf*. (2007) 5:179–93. doi: 10.1016/s1542-0124(12)70086-1
16. Stern ME, Schaumburg CS, Pflugfelder SC. Dry eye as a mucosal autoimmune disease. *Int Rev Immunol*. (2013) 32:19–41. doi: 10.3109/08830185.2012.748052
17. Barabino S, Chen Y, Chauhan S, Dana R. Ocular surface immunity: homeostatic mechanisms and their disruption in dry eye disease. *Prog Retin Eye Res*. (2012) 31:271–85. doi: 10.1016/j.preteyeres.2012.02.003
18. Gandhi NB, Su Z, Zhang X, Volpe EA, Pelegrino FS, Rahman SA, et al. Dendritic cell-derived thrombospondin-1 is critical for the generation of the ocular surface Th17 response to desiccating stress. *J Leukoc Biol*. (2013) 94:1293–301. doi: 10.1189/jlb.1012524
19. Pflugfelder SC, Corrales RM, de Paiva CS. T helper cytokines in dry eye disease. *Exp Eye Res*. (2013) 117:118–25. doi: 10.1016/j.exer.2013.08.013
20. De Paiva CS, Villarreal AL, Corrales RM, Rahman HT, Chang VY, Farley WJ, et al. Dry eye-induced conjunctival epithelial squamous metaplasia is modulated by interferon-gamma. *Invest Ophthalmol Vis Sci*. (2007) 48:2553–60. doi: 10.1167/iovs.07-0069
21. Rivas L, Oroza MA, Perez-Esteban A, Murube-del-Castillo J. Morphological changes in ocular surface in dry eyes and other disorders by impression cytology. *Graefes Arch Clin Exp Ophthalmol*. (1992) 230:329–34. doi: 10.1007/bf00165940
22. Belmonte C, Aracil A, Acosta MC, Luna C, Gallar J. Nerves and sensations from the eye surface. *Ocul Surf*. (2004) 2:248–53. doi: 10.1016/s1542-0124(12)70112-x
23. Mantelli F, Massaro-Giordano M, Macchi I, Lambiase A, Bonini S. The cellular mechanisms of dry eye: from pathogenesis to treatment. *J Cell Physiol*. (2013) 228:2253–6. doi: 10.1002/jcp.24398
24. Belmonte C, Nichols JJ, Cox SM, Brock JA, Begley CG, Bereiter DA, et al. TFOS DEWS II pain and sensation report. *Ocul Surf*. (2017) 15:404–37. doi: 10.1016/j.jtos.2017.05.002
25. Benitez del Castillo JM, Wasfy MA, Fernandez C, Garcia-Sanchez J. An in vivo confocal masked study on corneal epithelium and subbasal nerves in patients with dry eye. *Invest Ophthalmol Vis Sci*. (2004) 45:3030–5. doi: 10.1167/iovs.04-0251
26. Bourcier T, Acosta MC, Borderie V, Borrás F, Gallar J, Bury T, et al. Decreased corneal sensitivity in patients with dry eye. *Invest Ophthalmol Vis Sci*. (2005) 46:2341–5. doi: 10.1167/iovs.04-1426
27. Simsek C, Kojima T, Dogru M, Tsubota K. Alterations of murine subbasal corneal nerves after environmental Dry Eye stress. *Invest Ophthalmol Vis Sci*. (2018) 59:1986–95. doi: 10.1167/iovs.17-23743
28. Stepp MA, Pal-Ghosh S, Tadvalkar G, Williams A, Pflugfelder SC, de Paiva CS. Reduced intraepithelial corneal nerve density and sensitivity accompany desiccating stress and aging in C57BL/6 mice. *Exp Eye Res*. (2018) 169:91–8. doi: 10.1016/j.exer.2018.01.024
29. Dieckmann G, Goyal S, Hamrah P. Neuropathic corneal pain: approaches for management. *Ophthalmology*. (2017) 124:S34–47. doi: 10.1016/j.ophtha.2017.08.004
30. Galor A, Moein HR, Lee C, Rodriguez A, Felix ER, Sarantopoulos KD, et al. Neuropathic pain and dry eye. *Ocul Surf*. (2018) 16:31–44. doi: 10.1016/j.jtos.2017.10.001

31. Baudouin C, Aragona P, Messmer EM, Tomlinson A, Calonge M, Boboridis KG, et al. Role of hyperosmolarity in the pathogenesis and management of dry eye disease: proceedings of the OCEAN group meeting. *Ocul Surf*. (2013) 11:246–58. doi: 10.1016/j.jtos.2013.07.003
32. Yagci A, Gurdal C. The role and treatment of inflammation in dry eye disease. *Int Ophthalmol*. (2014) 34:1291–301. doi: 10.1007/s10792-014-9969-x
33. Cruzat A, Qazi Y, Hamrah P. In vivo confocal microscopy of corneal nerves in health and disease. *Ocul Surf*. (2017) 15:15–47. doi: 10.1016/j.jtos.2016.09.004
34. McKay TB, Seyed-Razavi Y, Ghezzi CE, Dieckmann G, Nieland TJF, Cairns DM, et al. Corneal pain and experimental model development. *Prog Retin Eye Res*. (2018) 71:88–113. doi: 10.1016/j.preteyeres.2018.11.005
35. Lindquist RL, Shakhar G, Dudziak D, Wardemann H, Eisenreich T, Dustin ML, et al. Visualizing dendritic cell networks in vivo. *Nat Immunol*. (2004) 5:1243–50. doi: 10.1038/ni1139
36. de Paiva CS. Effects of aging in Dry Eye. *Int Ophthalmol Clin*. (2017) 57:47–64. doi: 10.1097/iio.0000000000000170
37. Barabino S, Shen L, Chen L, Rashid S, Rolando M, Dana MR. The controlled-environment chamber: a new mouse model of dry eye. *Invest Ophthalmol Vis Sci*. (2005) 46:2766–71. doi: 10.1167/iovs.04-1326
38. Lemp MA. Report of the National Eye Institute/industry workshop on clinical trials in Dry Eyes. *CLAO J*. (1995) 21:221–32.
39. Kilic S, Kulualp K. Tear production rate in a mouse model of Dry Eye according to the phenol red thread and endodontic absorbent paper point tear tests. *Comp Med*. (2016) 66:367–72.
40. Dursun D, Wang M, Monroy D, Li DQ, Lokeshwar BL, Stern ME, et al. A mouse model of keratoconjunctivitis sicca. *Invest Ophthalmol Vis Sci*. (2002) 43:632–8.
41. Seyed-Razavi Y, Lopez MJ, Mantopoulos D, Zheng L, Massberg S, Sendra VG, et al. Kinetics of corneal leukocytes by intravital multiphoton microscopy. *FASEB J*. (2019) 33:2199–211. doi: 10.1096/fj.201800684RR
42. Jamali A, Harris DL, Blanco T, Lopez MJ, Hamrah P. Resident plasmacytoid dendritic cells patrol vessels in the naïve limbus and conjunctiva. *Ocul Surf*. (2020) 18:277–85. doi: 10.1016/j.jtos.2020.02.005
43. Sumen C, Mempel TR, Mazo IB, von Andrian UH. Intravital microscopy: visualizing immunity in context. *Immunity*. (2004) 21:315–29. doi: 10.1016/j.immuni.2004.08.006
44. Gao N, Lee P, Yu FS. Intraepithelial dendritic cells and sensory nerves are structurally associated and functional interdependent in the cornea. *Sci Rep*. (2016) 6:36414. doi: 10.1038/srep36414
45. Lammermann T, Germain RN. The multiple faces of leukocyte interstitial migration. *Semin Immunopathol*. (2014) 36:227–51. doi: 10.1007/s00281-014-0418-8
46. Guzman M, Keitelman I, Sabbione F, Trevani AS, Giordano MN, Galletti JG. Desiccating stress-induced disruption of ocular surface immune tolerance drives dry eye disease. *Clin Exp Immunol*. (2016) 184:248–56. doi: 10.1111/cei.12759
47. De Paiva CS, Chotikavanich S, Pangelinan SB, Pitcher JD III, Fang B, Zheng X, et al. IL-17 disrupts corneal barrier following desiccating stress. *Mucosal Immunol*. (2009) 2:243–53. doi: 10.1038/mi.2009.5
48. Barbosa FL, Xiao Y, Bian F, Coursey TG, Ko BY, Clevers H, et al. Goblet cells contribute to ocular surface immune tolerance-implications for Dry Eye disease. *Int J Mol Sci*. (2017) 18:978. doi: 10.3390/ijms18050978
49. Chen W, Hara K, Tian Q, Zhao K, Yoshitomi T. Existence of small slow-cycling Langerhans cells in the limbal basal epithelium that express ABCG2. *Exp Eye Res*. (2007) 84:626–34. doi: 10.1016/j.exer.2006.11.006
50. Hamrah P, Huq SO, Liu Y, Zhang Q, Dana MR. Corneal immunity is mediated by heterogeneous population of antigen-presenting cells. *J Leukoc Biol*. (2003) 74:172–8. doi: 10.1189/jlb.1102544
51. Hamrah P, Liu Y, Zhang Q, Dana MR. Alterations in corneal stromal dendritic cell phenotype and distribution in inflammation. *Arch Ophthalmol*. (2003) 121:1132–40. doi: 10.1001/archopht.121.8.1132
52. Steven P, Bock F, Huttmann G, Cursiefen C. Intravital two-photon microscopy of immune cell dynamics in corneal lymphatic vessels. *PLoS One*. (2011) 6:e26253. doi: 10.1371/journal.pone.0026253
53. Chinnery HR, Humphries T, Clare A, Dixon AE, Howes K, Moran CB, et al. Turnover of bone marrow-derived cells in the irradiated mouse cornea. *Immunology*. (2008) 125:541–8. doi: 10.1111/j.1365-2567.2008.02868.x
54. Nakamura T, Ishikawa F, Sonoda KH, Hisatomi T, Qiao H, Yamada J, et al. Characterization and distribution of bone marrow-derived cells in mouse cornea. *Invest Ophthalmol Vis Sci*. (2005) 46:497–503. doi: 10.1167/iovs.04-1154
55. Lopez MJ, Seyed-Razavi Y, Jamali A, Harris DL, Hamrah P. The chemokine receptor CXCR4 mediates recruitment of CD11c+ conventional dendritic cells into the inflamed murine cornea. *Invest Ophthalmol Vis Sci*. (2018) 59:5671–81. doi: 10.1167/iovs.18-25084
56. Veres TZ, Shevchenko M, Krasteva G, Spies E, Prenzler F, Rochlitzer S, et al. Dendritic cell-nerve clusters are sites of T cell proliferation in allergic airway inflammation. *Am J Pathol*. (2009) 174:808–17. doi: 10.2353/ajpath.2009.080800
57. Hu D, Nicholls PK, Claus M, Wu Y, Shi Z, Greene WK, et al. Immunofluorescence characterization of innervation and nerve-immune cell interactions in mouse lymph nodes. *Eur J Histochem*. (2019) 63:3059. doi: 10.4081/ejh.2019.3059
58. Al-Shalan HAM, Hu D, Nicholls PK, Greene WK, Ma B. Immunofluorescent characterization of innervation and nerve-immune cell neighborhood in mouse thymus. *Cell Tissue Res*. (2019) 378:239–54. doi: 10.1007/s00441-019-03052-4
59. Veres TZ, Rochlitzer S, Shevchenko M, Fuchs B, Prenzler F, Nassenstein C, et al. Spatial interactions between dendritic cells and sensory nerves in allergic airway inflammation. *Am J Respir Cell Mol Biol*. (2007) 37:553–61. doi: 10.1165/rcmb.2007-0087OC
60. Heuss ND, Pierson MJ, Montaniel KR, McPherson SW, Lehmann U, Hussong SA, et al. Retinal dendritic cell recruitment, but not function, was inhibited in MyD88 and TRIF deficient mice. *J Neuroinflamm*. (2014) 11:143. doi: 10.1186/s12974-014-0143-1
61. Chiu IM, von Hehn CA, Woolf CJ. Neurogenic inflammation and the peripheral nervous system in host defense and immunopathology. *Nat Neurosci*. (2012) 15:1063–7. doi: 10.1038/nn.3144
62. Patel DV, McGhee CN. Mapping of the normal human corneal sub-Basal nerve plexus by in vivo laser scanning confocal microscopy. *Invest Ophthalmol Vis Sci*. (2005) 46:4485–8. doi: 10.1167/iovs.05-0794
63. Zhivov A, Stave J, Vollmar B, Guthoff R. In vivo confocal microscopic evaluation of Langerhans cell density and distribution in the normal human corneal epithelium. *Graefes Arch Clin Exp Ophthalmol*. (2005) 243:1056–61. doi: 10.1007/s00417-004-1075-8
64. Cruzat A, Witkin D, Baniasadi N, Zheng L, Ciolino JB, Jurkunas UV, et al. Inflammation and the nervous system: the connection in the cornea in patients with infectious keratitis. *Invest Ophthalmol Vis Sci*. (2011) 52:5136–43. doi: 10.1167/iovs.10-7048
65. Leppin K, Behrendt AK, Reichard M, Stachs O, Guthoff RF, Baltrusch S, et al. Diabetes mellitus leads to accumulation of dendritic cells and nerve fiber damage of the subbasal nerve plexus in the cornea. *Invest Ophthalmol Vis Sci*. (2014) 55:3603–15. doi: 10.1167/iovs.14-14307
66. Hua S, Hermanussen S, Tang L, Monteith GR, Cabot PJ. The neural cell adhesion molecule antibody blocks cold water swim stress-induced analgesia and cell adhesion between lymphocytes and cultured dorsal root ganglion neurons. *Anesth Analg*. (2006) 103:1558–64. doi: 10.1213/01.ane.0000243410.61451.c1
67. Sasaoka A, Ishimoto I, Kuwayama Y, Sakiyama T, Manabe R, Shiosaka S, et al. Overall distribution of substance P nerves in the rat cornea and their three-dimensional profiles. *Invest Ophthalmol Vis Sci*. (1984) 25:351–6.
68. Dunzendorfer S, Kaser A, Meierhofer C, Tilg H, Wiedermann CJ. Cutting edge: peripheral neuropeptides attract immature and arrest mature blood-derived dendritic cells. *J Immunol*. (2001) 166:2167–72. doi: 10.4049/jimmunol.166.4.2167
69. Seiffert K, Granstein RD. Neuroendocrine regulation of skin dendritic cells. *Ann N Y Acad Sci*. (2006) 1088:195–206. doi: 10.1196/annals.1366.011
70. Szliter EA, Lighvani S, Barrett RP, Hazlett LD. Vasoactive intestinal peptide balances pro- and anti-inflammatory cytokines in the *Pseudomonas aeruginosa*-infected cornea and protects against corneal perforation. *J Immunol*. (2007) 178:1105–14. doi: 10.4049/jimmunol.178.2.1105
71. Souza-Moreira L, Campos-Salinas J, Caro M, Gonzalez-Rey E. Neuropeptides as pleiotropic modulators of the immune response. *Neuroendocrinology*. (2011) 94:89–100. doi: 10.1159/000328636

72. Oh JY, Choi H, Lee RH, Roddy GW, Ylöstalo JH, Wawrousek E, et al. Identification of the HSPB4/TLR2/NF-kappaB axis in macrophage as a therapeutic target for sterile inflammation of the cornea. *EMBO Mol Med*. (2012) 4:435–48. doi: 10.1002/emmm.201200221
73. Lambrecht BN. Immunologists getting nervous: neuropeptides, dendritic cells and T cell activation. *Respir Res*. (2001) 2:133–8. doi: 10.1186/rr49
74. Troger J, Kieselbach G, Teuchner B, Kralinger M, Nguyen QA, Haas G, et al. Peptidergic nerves in the eye, their source and potential pathophysiological relevance. *Brain Res Rev*. (2007) 53:39–62. doi: 10.1016/j.brainresrev.2006.06.002
75. Godinho-Silva C, Cardoso F, Veiga-Fernandes H. Neuro-immune cell units: a new paradigm in physiology. *Ann Rev Immunol*. (2019) 37:19–46. doi: 10.1146/annurev-immunol-042718-041812
76. McCormack DG, Mak JC, Coupe MO, Barnes PJ. Calcitonin gene-related peptide vasodilation of human pulmonary vessels. *J Appl Physiol (1985)*. (1989) 67:1265–70. doi: 10.1152/jappl.1989.67.3.1265
77. Springer J, Geppetti P, Fischer A, Groneberg DA. Calcitonin gene-related peptide as inflammatory mediator. *Pulm Pharmacol Ther*. (2003) 16:121–30. doi: 10.1016/S1094-5539(03)00049-X
78. Beuerman RW, Stern ME. Neurogenic inflammation: a first line of defense for the ocular surface. *Ocul Surf*. (2005) 3:S203–6. doi: 10.1016/s1542-0124(12)70256-2
79. Mantelli F, Micera A, Sacchetti M, Bonini S. Neurogenic inflammation of the ocular surface. *Curr Opin Allergy Clin Immunol*. (2010) 10:498–504. doi: 10.1097/ACI.0b013e32833e16cc
80. Stepp MA, Tadvalkar G, Hakh R, Pal-Ghosh S. Corneal epithelial cells function as surrogate Schwann cells for their sensory nerves. *Glia*. (2017) 65:851–63. doi: 10.1002/glia.23102
81. Lemp MA, Mathers WD. Corneal epithelial cell movement in humans. *Eye (Lond)*. (1989) 3(Pt 4):438–45. doi: 10.1038/eye.1989.65
82. Walczysko P, Rajnicek AM, Collinson JM. Contact-mediated control of radial migration of corneal epithelial cells. *Mol Vis*. (2016) 22:990–1004.
83. Lu F, Simpson T, Sorbara L, Fonn D. Malleability of the ocular surface in response to mechanical stress induced by orthokeratology contact lenses. *Cornea*. (2008) 27:133–41. doi: 10.1097/ICO.0b013e318158b4b5
84. Fabiani C, Barabino S, Rashid S, Dana MR. Corneal epithelial proliferation and thickness in a mouse model of dry eye. *Exp Eye Res*. (2009) 89:166–71. doi: 10.1016/j.exer.2009.03.003
85. Nagasaki T, Zhao J. Centripetal movement of corneal epithelial cells in the normal adult mouse. *Invest Ophthalmol Vis Sci*. (2003) 44:558–66. doi: 10.1167/iovs.02-0705
86. Di Girolamo N, Bobba S, Raviraj V, Delic NC, Slapetova I, Nicovich PR, et al. Tracing the fate of limbal epithelial progenitor cells in the murine cornea. *Stem Cells*. (2015) 33:157–69. doi: 10.1002/stem.1769
87. Howes EL, Cruse VK, Kwok MT. Mononuclear cells in the corneal response to endotoxin. *Invest Ophthalmol Vis Sci*. (1982) 22:494–501.
88. BenEzra D, Maftzir G, Hochberg E, Anteby I, Lorberboum-Galski H. Ocular distribution of the chimeric protein IL2-PE40. *Curr Eye Res*. (1995) 14:153–8. doi: 10.3109/02713689508999927
89. Kim YC, Chiang B, Wu X, Prausnitz MR. Ocular delivery of macromolecules. *J Control Release*. (2014) 190:172–81. doi: 10.1016/j.jconrel.2014.06.043
90. Dastjerdi MH, Sadrai Z, Saban DR, Zhang Q, Dana R. Corneal penetration of topical and subconjunctival bevacizumab. *Invest Ophthalmol Vis Sci*. (2011) 52:8718–23. doi: 10.1167/iovs.11-7871
91. Thiel MA, Coster DJ, Standfield SD, Brereton HM, Mavrangelos C, Zola H, et al. Penetration of engineered antibody fragments into the eye. *Clin Exp Immunol*. (2002) 128:67–74. doi: 10.1046/j.1365-2249.2002.01808.x
92. Mantelli F, Mauris J, Argueso P. The ocular surface epithelial barrier and other mechanisms of mucosal protection: from allergy to infectious diseases. *Curr Opin Allergy Clin Immunol*. (2013) 13:563–8. doi: 10.1097/ACI.0b013e3283645899
93. Sarkar J, Chaudhary S, Namavari A, Ozturk O, Chang JH, Yco L, et al. Corneal neurotoxicity due to topical benzalkonium chloride. *Invest Ophthalmol Vis Sci*. (2012) 53:1792–802. doi: 10.1167/iovs.11-8775
94. Sarkar J, Chaudhary S, Jassim SH, Ozturk O, Chamon W, Ganesh B, et al. CD11b+GR1+ myeloid cells secrete NGF and promote trigeminal ganglion neurite growth: implications for corneal nerve regeneration. *Invest Ophthalmol Vis Sci*. (2013) 54:5920–36. doi: 10.1167/iovs.13-12237

Conflict of Interest: The authors declare that the research was conducted in the absence of any commercial or financial relationships that could be construed as a potential conflict of interest.

frontiers in Immunology

ORIGINAL RESEARCH
published: 12 August 2020
doi: 10.3389/fimmu.2020.01713

Effect of Dry Eye Disease on the Kinetics of Lacrimal Gland Dendritic Cells as Visualized by Intravital Multi-Photon Microscopy

Gustavo Ortiz[1,2†], *Cecilia Chao*[1,2†], *Arsia Jamali*[1,2], *Yashar Seyed-Razavi*[1,2], *Brendan Kenyon*[1,2,3], *Deshea L. Harris*[1,2], *Driss Zoukhri*[2,4] *and Pedram Hamrah*[1,2,3,5*]

[1] Center for Translational Ocular Immunology, Tufts Medical Center, Tufts University School of Medicine, Boston, MA, United States, [2] Department of Ophthalmology, Tufts Medical Center, Tufts University School of Medicine, Boston, MA, United States, [3] Program in Neuroscience, Graduate School of Biomedical Sciences, Tufts University, Boston, MA, United States, [4] Department of Comprehensive Care, Tufts University School of Dental Medicine, Boston, MA, United States, [5] Program in Immunology, Graduate School of Biomedical Sciences, Tufts University, Boston, MA, United States

OPEN ACCESS

Edited by:
Elzbieta Kolaczkowska, Jagiellonian University, Poland

Reviewed by:
Mihaela Gadjeva, Harvard Medical School, United States
Geeta K. Vemuganti, University of Hyderabad, India
Tetsuya Kawakita, Kitasato Institute Hospital, Japan

***Correspondence:**
Pedram Hamrah
pedram.hamrah@tufts.edu

[†] *These authors have contributed equally to this work*

Specialty section:
This article was submitted to Antigen Presenting Cell Biology, a section of the journal Frontiers in Immunology

Received: *27 July 2019*
Accepted: *26 June 2020*
Published: *12 August 2020*

Citation:
Ortiz G, Chao C, Jamali A, Seyed-Razavi Y, Kenyon B, Harris DL, Zoukhri D and Hamrah P (2020) Effect of Dry Eye Disease on the Kinetics of Lacrimal Gland Dendritic Cells as Visualized by Intravital Multi-Photon Microscopy. Front. Immunol. 11:1713. doi: 10.3389/fimmu.2020.01713

The lacrimal gland (LG) is the main source of the tear film aqueous layer and its dysfunction results in dry eye disease (DED), a chronic immune-mediated disorder of the ocular surface. The desiccating stress (DS) murine model that mimics human DED, results in LG dysfunction, immune cell infiltration, and consequently insufficient tear production. To date, the immune cell kinetics in DED are poorly understood. The purpose of this study was to develop a murine model of intravital multi-photon microscopy (IV-MPM) for the LG, and to investigate the migratory kinetics and 3D morphological properties of conventional dendritic cells (cDCs), the professional antigen presenting cells of the ocular surface, in DED. Mice were placed in a controlled environmental chamber with low humidity and increased airflow rate for 2 and 4 weeks to induce DED, while control naïve transgenic mice were housed under standard conditions. DED mice had significantly decreased tear secretion and increased fluorescein staining ($p < 0.01$) compared to naïve controls. Histological analysis of the LG exhibited infiltrating mononuclear and polymorphonuclear cells ($p < 0.05$), as well as increased LG swelling ($p < 0.001$) in DED mice compared to controls. Immunofluorescence staining revealed increased density of cDCs in DED mice ($p < 0.001$). IV-MPM of the LG demonstrated increased density of cDCs in the LGs of DED mice, compared with controls ($p < 0.001$). cDCs were more spherical in DED at both time points compared to controls ($p < 0.001$); however, differences in surface area were found at 2 weeks in DED compared with naïve controls ($p < 0.001$). Similarly, 3D cell volume was significantly lower at 2 weeks in DED vs. the naïve controls ($p < 0.001$). 3D instantaneous velocity and mean track speed were significantly higher in DED compared to naïve mice ($p < 0.001$). Finally, the meandering index, an index for directionality, was significant increased at 4 weeks after DED compared with controls and 2 weeks of DED ($p < 0.001$). Our IV-MPM study sheds light into the 3D morphological alterations and cDC kinetics in the LG during DED.

While in naïve LGs, cDCs exhibit a more dendritic morphology and are less motile, they became more spherical with enhanced motility during DED. This study shows that IV-MPM represents a robust tool to study immune cell trafficking and kinetics in the LG, which might elucidate cellular alterations in immunological diseases, such as DED.

Keywords: conventional dendritic cell, lacrimal gland, dry eye disease (DED), intravital multiphoton microscopy, kinetics

INTRODUCTION

Dry eye disease (DED) is a significant public health concern affecting ∼16 million adults in the United States alone (1, 2). DED is defined as "a multifactorial disease of the ocular surface characterized by a loss of homeostasis of the tear film, and accompanied by ocular symptoms, in which tear instability and hyperosmolarity, ocular surface inflammation and damage, and neurosensory abnormalities play an etiological role" (3). The lacrimal gland is the main source of the aqueous layer of the tear film, which is crucial to protect the cornea and conjunctiva from desiccation, infection and inflammation, thus preserving corneal transparency (4, 5).

Tear secretion is finely regulated by the lacrimal functional unit (LFU). The LFU is defined as the conjunction of lacrimal glands (main and accessory), the ocular surface and the communicating innervation (6). Importantly, this innervation is responsible for the maintenance of the tear film through baseline and reflex tearing. Like any neural reflex, this can be broken into an afferent and efferent arm. The sensory nerves within the cornea represent the afferent arm, detecting changes in the tear film osmolarity or mechanical stimuli, necessitating lacrimation. These signals are relayed to the LG through the parasympathetic nerves via the efferent arm, resulting in lacrimation. Thus, the homeostasis of the ocular surface and tear film stability can be compromised if any component of the LFU is damaged or dysfunctional, predisposing development of DED (7). Desiccating stress (DS) induced by housing animals in a low humidity controlled environment leads to recruitment of immune cells and enlarged secretory vesicles in the LG, suggesting that increased DS at the ocular surface may induce inflammation within the LG (8). Recently, a study showed that DED induced by DS affects sensory nerve density, morphology and function within the cornea (9). This study revealed that DED reduces the sensitivity of corneal nerves, suggesting that the afferent arm of the LFU may become dysfunctional. Furthermore, previous studies have shown that inflammation and neuropathic pain are common sequelae following spinal cord injury (10). Conversely, intact nerves can control inflammation within peripheral tissues by signaling to immune cells, preventing excessive damage to host tissues (11). Thus, there is a precedent for the notion that nerve dysfunction or loss of homeostatic signaling could lead to inflammation. We therefore hypothesize that compromised corneal sensory nerves on the ocular surface (afferent pathways of the LFU) may, in addition to decreased tear secretion, directly lead to LG inflammation.

Conventional dendritic cells (cDCs) are professional antigen presenting cells (APCs), responsible for the sensing of foreign antigens. cDCs are able to engulf, process, and present antigens from peripheral tissues to T cells within the draining lymph nodes. As such, cDCs link the innate and adaptive immune responses, and are critically involved in the initiation of immune responses (12). This holds true in the case of immune-mediated diseases as well, since cDCs have been shown to play a central role in the pathogenesis of DED (13). Contrary to long-held notions of corneal immune privilege, the cornea is not devoid of immune cells, and resident populations of cDCs have been identified in both the cornea (14, 15) and LG (16). DS has been shown to result in increased density of corneal cDCs (17) and decreased density of corneal nerve fibers (9). More recently, our group and others have shown that there is an inverse correlation between cDC and nerve density in the cornea (18–20). Moreover, our group has shown that greater corneal cDC motility was found during thermal cautery-induced acute corneal inflammation (21). However, the impact of DS-induced DED on cDC motility and kinetic properties in the LG, has not been investigated to date.

Intravital multiphoton microscopy (IV-MPM) enables studying the kinetics and 3-dimentional (3D) morphology of immune cells and cell-to-cell interaction *in vivo* over time (22, 23). By providing second harmonic generation, it also allows collagen delineation in the tissue (24). Thus, it has been widely used to study immune cells behaviors within solid tissues, including lymph nodes (25–27), bone marrow (28), cornea (21), skin (29), and the gastrointestinal tract (30). However, to date, IV-MPM has not been used to examine immune cell populations in the LG. Therefore, the purpose of this study was to first develop a novel IV-MPM model with proper regulation of temperature and tissue stability to study immune cell kinetics of the lacrimal glands, second to assess the 3D morphology of cDCs, and third to study cell kinetics of cDCs during DED.

MATERIALS AND METHODS

Mice

Thy1-YFP mice (B6.Cg-Tg [Thy1-YFP]16Jrs/J) were obtained from the Jackson Laboratory (Bar Harbor, ME) as heterozygous and bred to homozygous with repeated matings between male and female mice with high copies of the transgenes for YFP for Thy1-YFP. This was required in order to obtain mice with higher fluorescence for IV-MPM. CD11c-EYFP mice were a generous gift from Dr. Michel C. Nussenzweig from Rockefeller University (27). Thy-1 x CD11c-EYFP mice were generated

by crossing homozygous Thy1-YFP with homozygous CD11c-EYFP repeatedly until the both the nerves and DCs were co-localized with YFP in the cornea. Primer sets used for qPCR for genotyping: Thy1-YFP forward 5′- GCCCTGGCCCACCCTC GTGACCACCTTCG-3′ and reverse 5′- CCTGATGCCGTT CTTCTGCTTGTCGGGCA-3′, and CD11c-EYFP forward 5′- TGCTGGTTGTTGTGCTGTCTCATC-3′ and reverse 5′- GGG GGT GTT CTG CTG GTA GTG GTC-3′.

$Thy1^{YFP}$ mice express YFP under the control of regulatory elements of the Thy1 gene, and thus label neuronal populations, primarily sensory and motor neurons. The $CD11c^{YFP}$ mice carry EYFP transgene under the control of the CD11c promoter (27). Thus, our $CD11c^{YFP} \times Thy1^{YFP}$ mice allow visualization of both $CD11c^{+}$ cDCs and $Thy1^{+}$ neurons in the same animals. C57BL/6N wild-type (WT) female mice were obtained from Charles River Laboratories, Inc. (Wilmington, MA). Because female gender is a risk factor of DED and female C57BL/6N mice develop greater corneal barrier disruption than age-matched males (31), in this study only 6- to 8-week old female mice were used in all experiments. Mice were housed at Tufts Department of Lab Animal Medicine and were treated in accordance with the Association of Research and Vision in Ophthalmology (ARVO) statement for the Use of Animals in Ophthalmology and Vision Research. All experiments were performed after the review and approval from the Institutional Animal Care and Use Committee (IACUC number B2018-47) at Tufts University and Tufts Medical Center, Boston, MA.

Acute HSV-1 Keratitis

The herpes simplex virus (HSV)-1 McKrae strain (kindly provided by Dr. Homayon Ghiasi, Cedars-Sinai Medical Center, Los Angeles, CA), a stromal disease-causing, neurovirulent HSV-1 strain was used for corneal inoculation. HSV-1 was propagated in Vero cell cultures (American Type Culture Collection, Manassas, VA). Briefly, Vero cells were grown to confluence in T150 cm^3 culture flasks and infected with 2×10^6 plaque forming unit (PFU) of virus stock in 1.5 mL and tilted every 10 min for 1 h. Then, growth media (DMEM plus 5% FBS, both Corning Inc., Corning, NY) was added, and cells cultured for 3 days at 37°C. Afterwards, the maximum viral cytopathic effect was expected, and the infected cells were extracted after 2–3 cycles of cell lysis by using the GentleMACS dissociator (Miltenyi Biotec Inc, San Diego, CA). Then, the lysate was clarified by centrifuging for 10 min at 3,500 rpm at 4°C, followed by a spin down at 17,000 rpm for 30 min at 4°C. The virus pellet was re-suspended, aliquoted and stored at −80°C. Virus titers were determined by standard plaque assay after the infection of Vero cells as previously described (32).

Mice were anesthetized with a mixture of ketamine (120 mg/kg) and xylazine (20 mg/kg) and injected intraperitoneally. A drop of proparacaine hydrochloride (Akorn, Lake forest, IL) was applied for local anesthesia to the eyes before scarifying the cornea. One cornea (previously anesthetized with one drop of 0.5% proparacaine) per mouse was scarified in a 5×5 grid-like pattern along the cornea with a 30-gauge needle. Afterward, 3–5 μL of the virus suspension containing 1×10^5 PFU was applied to the scarified corneas. Following this, the eyelids were closed and opened carefully several times to facilitate the absorption and distribution of the virus. A single dose of sustained release (SR) buprenorphine (1 mg/kg body weight) was injected as an analgesic after infection.

Murine Dry Eye Disease Model

Environmental DS-induced DED was applied as previously described (33). In brief, mice were placed in a controlled environmental chamber at temperature of 21–23°C and humidity of 15% (Percival Scientific, Perry, Iowa). Airflow of 15 L/min using INTELLIS Ultra Control System and desiccant drier 50 cfm was applied. The chamber is sealed avoiding the direct exchange of air between the outside and the inside and is connected to a desiccant, which introduces air with low humidity inside the chamber. Inside the chamber, three sensors are located in order to monitor the humidity, airflow and temperature. Sensors are connected to a router in order to automatically monitor the parameters. In order to maximize exposure, mice were housed in custom-designed perforated cages (Ancare Corp. Bellmore, NY). The cages were built with vents at each side to maximize the airflow through them in order to achieve greater DS at the ocular surface. DED mice were kept under DS for 2 weeks (2 w) or 4 weeks (4 w) and then underwent subsequent experiments. Naïve control animals were housed in a normal laboratory environment with a humidity of 50–60% and a temperature of 21–23°C.

Clinical Scoring and Tear Production

For clinical measurements, mice were anesthetized as above and 1 drop of fluorescein (Akorn Inc., Lake Forest, IL) was added to the ocular surface. Corneal fluorescein staining (CFS) scores were assessed using the National Eye Institute (NEI) scale (0–15), as previously described (34). The CFS was graded in 5 corneal regions, each ranging from 0 to 3 and the sum of the scores of all regions (range 0–15; $n = 4$/group) was measured and used for analysis. Tear secretion was measured on another set of mice using phenol red thread test (Hilco Vision Headquarters, Plainville, MA) (35, 36). The tip of the thread was placed inside the temporal eye canthus for 30 s. The wetted length was then measured to quantify the tear secretion rate.

Histopathological Evaluation of Lacrimal Gland Infiltration

The lacrimal gland was removed and immersed for cryo-protection in sucrose 30% overnight and frozen in OCT until sectioning. Cryo-sections of 20 μm were performed, air dried up to 15 min to remove moisture and stained with 0.1% hematoxylin (Sigma; MHS-16) for 10 min in a 50 ml conical tube. Slides were rinsed in cool running distilled water for 5 min in a coupling jar. Afterwards, slides were stained with 0.5% eosin in ethanol) and dipped in distilled water. Slides were subsequently dipped alternating in 50% ethanol and 70% ethanol 10 times followed by 95% ethanol for 30 sec. Finally, slides were submerged in 100% ethanol for 1 min and washed in 100% xylene several times before imaging by microscopy. At least 10 sections per LG were evaluated morphologically by light microscopy in a masked fashion and the total number

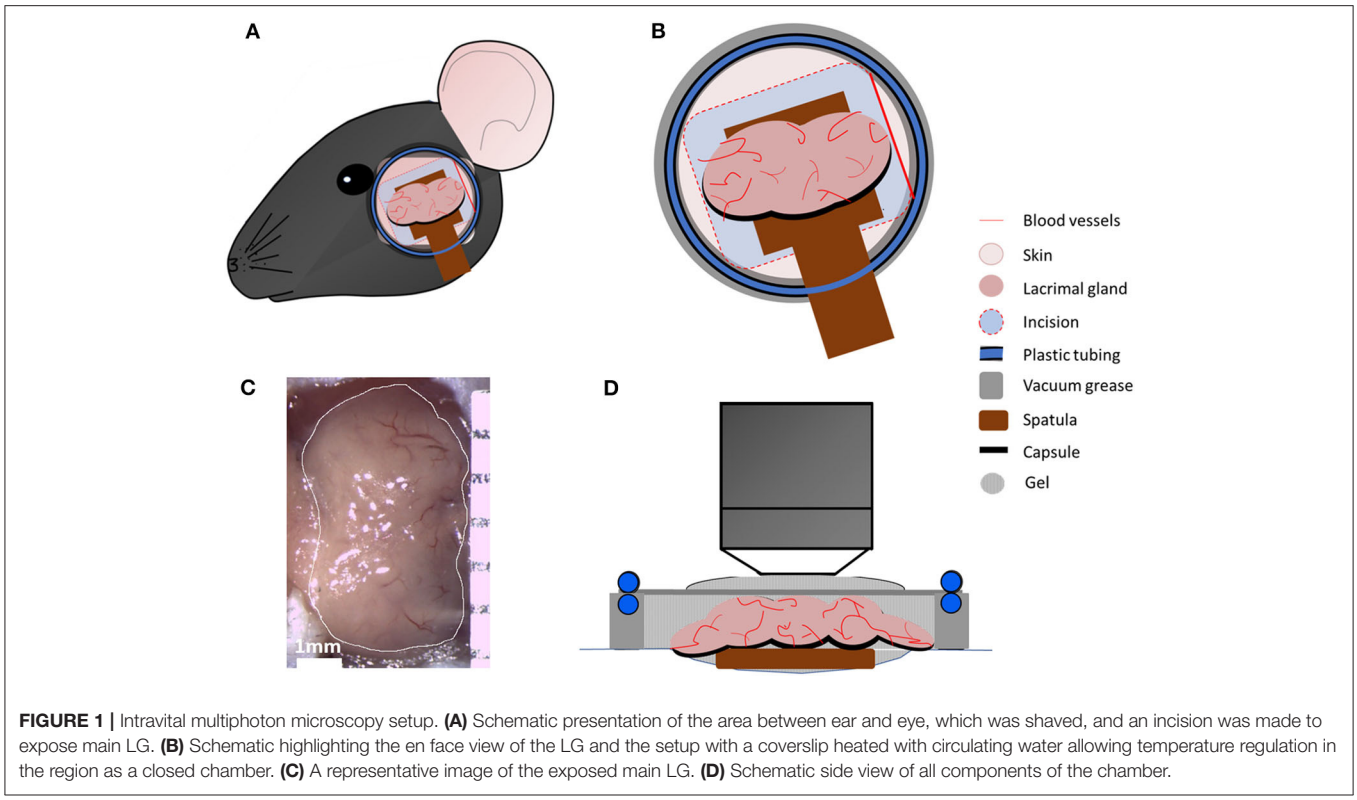

FIGURE 1 | Intravital multiphoton microscopy setup. **(A)** Schematic presentation of the area between ear and eye, which was shaved, and an incision was made to expose main LG. **(B)** Schematic highlighting the en face view of the LG and the setup with a coverslip heated with circulating water allowing temperature regulation in the region as a closed chamber. **(C)** A representative image of the exposed main LG. **(D)** Schematic side view of all components of the chamber.

polymorphonuclear cells (PMNs) and mononuclear cells counted per section using Image J. Cells were quantified and reported as cells per millimeter square (cells/mm^2). Five representative image per animal and 3 animals per each group were used for comparison purposes (**Figure S1**).

Quantification of Lacrimal Gland Edema

To quantify LG edema, the areas between acinar cells were quantified used the software ImageJ (NIH, Bethesda, MD). The images were converted to 8-bit images. The software scanned the 8-bit image and searched for non-stained tissue. Red color was chosen to differentiate non-tissue areas. For each individual image the threshold was adjusted. In the menu, "Analyze" and then "Measure" was selected so that the area in red was quantified for each image. Percentage was determined by dividing the area quantified in red relative to the total area of the image. Three animals per group were used for comparison purposes.

Immunofluorescence Histochemistry

Sections were fixed for 10 min in cold methanol, washed for 5 min with PBS and incubated with blocking solution constituted of 3% BSA (Sigma Aldrich, St. Louis, MO) in PBS with 0.1% of Triton-X (Sigma Aldrich). The following primary antibodies were incubated over night at 4°C to evaluate cell density in the lacrimal gland: CD45 monoclonal antibody rat anti-mouse (1:100; clone 30-F11, eBioscience San Diego, CA) and CD11c monoclonal antibody Armenian hamster anti-mouse (1:100; clone N418, eBioscience). Three washes of 10 min each with PBS were performed, followed by the secondary antibody incubation for 1 h 30 min at room temperature: TRITC- Donkey Anti-Rat (1:500; 712-025-153) and FITC-Goat Anti-Armenian Hamster (1:500; 127-095-160), respectively, both from Jackson ImmunoResearch Labs (West Grove, PA).

Lacrimal Gland Preparation and Intravital Multiphoton Microscopy

Animals were anesthetized by intraperitoneal injection of ketamine (100 mg/kg)/xylazine (20 mg/kg)/acepromazine (3 mg/kg) cocktail, which results in up to 75 min of deep anesthesia (21). Prior to the incision, hair between the eye and ear (∼10 mm wide) was carefully removed using Nair hair removal lotion (Naircare, Princeton, NJ), followed by a single dose injection of 30 µl local analgesic (0.75% Bupivacaine HCl). A ∼5 mm cutaneous incision was made 2 mm away from the eye and 3 mm away from the ear to expose the LG (**Figures 1A–C**). Careful removal of the soft tissues around the LG exposed the gland without damaging blood vessels. In order to stabilize the LG during imaging, a wooden spatula was placed underneath the gland. Afterwards, 5–10 µl of PBS were carefully injected into the LG capsule (the connective tissue that surrounds the lobes of the LG). This created a separation between the capsule and the lobes of the LG to enable removal of the capsule without damaging the underlying lobes.

Mice were then placed onto a custom-designed stage for LG imaging (**Figure 1**). In order to prevent hypothermia during imaging, the body temperature was maintained between 35 and 37°C, using a disposable hand warmer (HotHands, HearMax, Dalton, GA). The depth of anesthesia was also examined

every 50–60 min and an additional dose of anesthesia cocktail was given as necessary. IV-MPM was performed using an Ultima Multiphoton Microscope System (Bruker, Fitchburg, WI) equipped with 2 MaiTai Ti/Sapphire DeepSee lasers (Newport Spectra-Physics, Irvine, CA) as previously described (21) with scanning time between 30 and 75 min and 3 μm optical section slices. Briefly, the simultaneous coaxial illumination was between 800 and 880 nm wavelengths to achieve 2-photon excitation and second harmonic generation. The laser power was set at 95, and the photomultiplier tube gain (PMTs) was set at 650 for all channels. Using a 20x-1.0 NA (Olympus XLUMPLFLN, Tokyo, Japan) water immersion objective, scans of the LG were taken every 30–60 sec during the scanning period with 512 × 512 resolution and 2-fold line averaging. Genteal ophthalmic lubricant gel (Alcon, Fort Worth, TX) was applied onto the LG and the incision to prevent desiccation during IV-MPM. High vacuum grease (Dow Corning, Midland, MI) was applied onto the bare skin surrounding the incision and additional Genteal gel was added to the area. A thin circular coverslip with tubing, for the circulation of heated water, was placed onto the exposed area in order to maintain the heat dissipation and vacuum effect as a sealed chamber during imaging. The temperature regulation during IV-MPM was conducted using a Diba polytetrafluoroethylene fitting unicon connector (Cole Palmer, Vernon Hills, IL) and polyethelene tubing, which was connected to the ring of tubing placed around the coverslip. Heated water was circulated within the tubing using a Masterflex L/S peristaltic pump (Cole Parmer, Vernon Hills, IL) with a flow rate of 30 ml/min (**Figure 1B**). The LG temperature (∼36–37°C) was monitored throughout the IV-MPM imaging by placing a dual input digital thermometer (Omega Engineering, Stamford, CT) on the gland but 1 mm away from the imaging area in the seal chamber (**Figure 1D**).

Image Analysis

In order to examine the cDC kinetics and morphology, a 4D movie was generated by importing the image stacks to the Imaris software (Bitplane, Zurich, Switzerland) as previously described (21). The motility of the transgenic fluorescent-labeled cDCs was then tracked semi-automatically in xyz positions using the 3D rendering and cell tracking function over time. 3D instantaneous velocity (cell velocity between 2 consecutive frames; μm/min), mean track speed (average velocity of a cell over time during imaging, μm/min), track length (total tracking distance of a cell, μm), displacement length (the distance of a cell traveled from start to the end of the imaging; μm) and meandering index (displacement length/track length) were calculated as previously described (21, 37). To assess 3D cell morphology, 3D surface area (μm^2), 3D cell volume (μm^3) and 3D sphericity (score 0–1, where 1 indicates a perfect sphere) were determined by creating a surface object for each YFP cell using the surface tool within the Imaris software.

Flow Cytometry

Lacrimal glands were harvested, chopped and subjected to digestion for up to 30 min at 37°C in 5 mg/ml dispase (Sigma-Aldrich, St. Louis, MO), 2 mg/ml collagenase D (Roche, Indianapolis, IN) and 2 mg/ml DNAse I (MilliporeSigma, Burlington, MA) in HBSS (Thermo Fisher Scientific, Waltham, MA). The digested tissues were strained using a 70 μm nylon mesh to yield single cell suspension and the digestion was inactivated by adding RPMI supplemented with 10% FBS (Corning Inc.). After centrifugation, red blood cells were lysed using ACK (Ammonium-Chloride-Potassium) Lysing Buffer (MilliporeSigma) followed by centrifugation, and washed and resuspended in FACS buffer (Thermo Fisher Scientific).

Single cell suspensions were incubated in FACS buffer with 1% Fc receptor block (CD16/32, BioXCell, West Lebanon, NH) for 15 min to prevent non-specific binding. Samples were then stained with Live/Dead UV Blue (Thermo Fisher Scientific), and combinations of CD45 (FITC-conjugated), CD11c (BV421-conjugated), CD11b (Alexa flour F647-conjugated) or their respective isotype controls (all Biolegend, San Diego, CA) for samples from WT mice or combinations of CD45 (Pacific Blue-conjugated), CD11c (APCCy7-conjugated), CD11b (PercpCy5.5-conjugated), DCIR2 (Alexa flour-647-conjugated), Ly6G (PercpCy5.5-conjugated), NK1.1 (PECy7-conjugated), MHC class II (PerCP/Cy5.5-conjugated, clone M5/114.15.2), CD40 (PE-conjugated clone 1C10), and CD86 (PerCP/Cy5.5-conjugated clone GL-1) and their respective isotype controls (all Biolegend) for samples from $CD11c^{YFP}xThy^{YFP}$ mice for 45 min. Samples were then washed and analyzed via the BD LSR II Analyzer (BD Bioscience, San Jose, CA). Isotype controls and fluorescence minus one control were used for setting the appropriate gates in the analysis. The lists of antibodies are presented in **Table S1**. The sequential gating strategy for all samples, including gating on presumable immune cell population, live cells, single cells, and $CD45^+$ or $CD45^+YFP^+$ cells, are presented in **Figures S2–S4**.

T Cell Proliferation Assays

Splenocytes were collected from naïve WT (C57BL/6N) animals and sorted for naïve $CD4^+$ T cells, identified as live $CD45^+CD3^+CD4^+CD44^{lo}CD62L^{hi}$ cells (**Table S1**). cDCs were sorted from LGs of sham- and HSV-infected animals as live $CD45^+CD11c^+$ cells. After sorting, naïve $CD4^+$ T cells were labeled with Violet Tracer following the manufacturer's protocol (CellTrace Violet Proliferation Kit, Invitrogen, Carlsbad, CA). The cDCs (5,000 cells) were cultured with naïve $CD4^+$ T cells (50,000 cells) at a ratio of 1:10 in RPMI medium supplemented with 10% FBS, and cultured in 96-well round bottom plates (Corning) at 37°C. After 72 h of culture, the $CD4^+$ T cells were analyzed by flow cytometry to monitor for T cell proliferation as indicated by the Violet Tracer. The tracer diffuses into cells and binds to intracellular amines, resulting in stable fluorescent staining. The co-culture with cDCs from sham-infected mice were used as unstimulated controls. On flow cytometry histograms, discrete peaks represent generation of live cells. Presented numbers on the histograms and graphs, indicate the percentage of cells undergoing at least one cycle of proliferation.

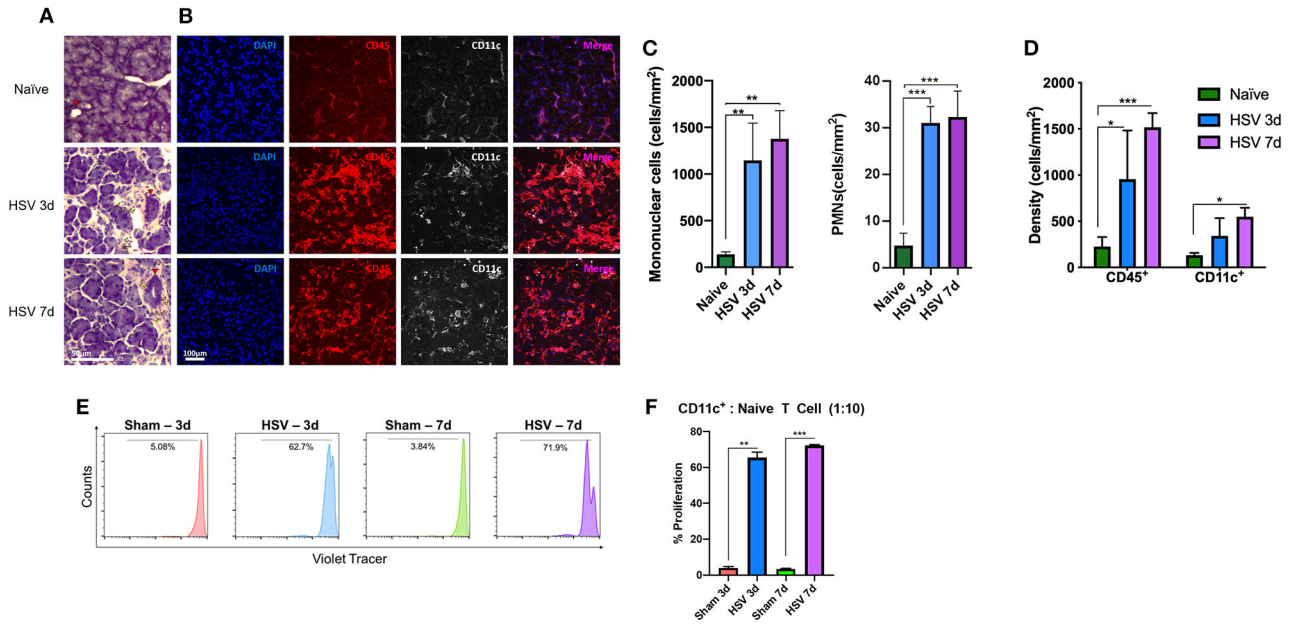

FIGURE 2 | Lacrimal gland immune cell Infiltration after HSV-1 infection. **(A)** After 3- and 7- days post corneal HSV-1 infection mononuclear cells (yellow arrowhead), PMNs and duct hyperplasia (red arrowhead) is observed. **(B)** Corneal HSV-1 infection induces an increase of $CD45^+$ cells and increased density in $CD11c^+$ cells in the LG. **(C)** Quantification of mononuclear and PMNs cells in naïve and after 3- and 7- days post HSV-1 infection. **(D)** Quantification of $CD45^+$ and $CD11c^+$ cells at 3- and 7-days post- HSV-1 infection. **(E)** LG isolated $CD45^+CD11c^+$ cDCs from HSV-infected animals induce naïve T cell proliferation. Histograms are representative of T cell proliferation. **(F)** Quantification of the proliferation assay presented in **(E)**, shows the percentage of proliferating T cells. *T*-test indicates significant differences on day 3 and 7 after HSV-1 infection compared to sham-infections ($^*p < 0.05$, $^{**}p < 0.01$, $^{***}p < 0.001$).

Statistical Analysis

Statistical analyses were performed using GraphPad Prism version 8 (GraphPad Software, La Jolla, CA). Results are presented as mean and SEM. One-way ANOVA was carried out to examine the differences in the studied variables between groups with *post-hoc* comparisons using Bonferroni correction tests. Significance was set at $P < 0.05$. The Spearman rank correlation coefficient was used for correlation purposes.

RESULTS

Corneal Nerve Damage Affects Dendritic Cell Function in The Lacrimal Gland

Considering the key role of the sensory nerves as the afferent pathway of the LFU in regulating tear production, we aimed to investigate if corneal nerve damage may affect the density and function of immune cells in the LG, in particular cDCs, which serve as the professional APCs of the ocular surface (**Figure 2**). In order to induce corneal nerve damage we employed the clinically relevant murine model of HSV-1 keratitis, which causes severe corneal nerve damage (38). Currently, it is well-known that corneal sensory nerves affect tear production in the LG, however, it is not clear if they can affect other aspects of LG homeostasis, including immunologic state of the LG.

Histological analyses (**Figure 2A**) showed a profound increase in mononuclear cells and modest increase in PMNs (**Figure 2C**). While mononuclear cell density in naïve mice exhibited 139.6 ± 25.59 cells/mm^2, they increased after day 3 (1,145.3 ± 400.3 cells/mm^2, $p = 0.008$) and day 7 post-infection (1,377.2 ± 302.1 cells/mm^2, $p = 0.003$). PMN density in naïve mice was 4.4 ± 2.9 cells/mm^2, and significantly increased after 3 days (30.7 ± 3.8 cells/mm^2) and 7 days (32.0 ± 5.9 cells/mm^2; $p < 0.001$ for both; **Figure 2A**) post HSV-1 infection. H&E staining indicated increased LG edema. While naïve mice displayed 5.5 ± 2.4% area between acini, edema significantly increased after day 3 (29.7 ± 3.7%) and day 7 (34.2 ± 4.3%, $p < 0.01$ for both; **Figure S1A**, red area and **Figure S1B**) post HSV infection. Further, signs of duct hyperplasia and fibrosis were observed (**Figures 2A**, **S1A** red arrowhead and delineated by a green dashed area, respectively). Using immunofluorescence histochemistry we observed that compared to naïve mice (179.3 ± 66.6 cells/mm^2), $CD45^+$ cell density significantly increased after 3 and 7 days of HSV-1 infection to 956.5 ± 525.6 cells/mm^2 ($p = 0.003$) and 1,517.5 ± 153.5 cells/mm^2 ($p < 0.001$; **Figures 2B,D**), respectively. In line with the results of the $CD45^+$ cell density, $CD11c^+$ cell density also increased; while naïve mice exhibited 149.6 ± 13.6 cells/mm^2 after 3d and 7d of HSV infection, the density was 343.3 ± 190.3 cells/mm^2 ($p = 0.88$) and 451.7 ± 165.4 cells/mm^2 ($p = 0.04$), respectively (**Figures 2B,D**).

Thus, we next aimed to assess if damage to the ocular surface sensory nerves may affect functionality of cDCs within the LG. After 3- and 7-days post-infection (dpi), we sorted cDCs from the LGs and co-cultured them with naïve $CD4^+$ T cells in order to evaluate if cDCs could induce T cell proliferation. We found

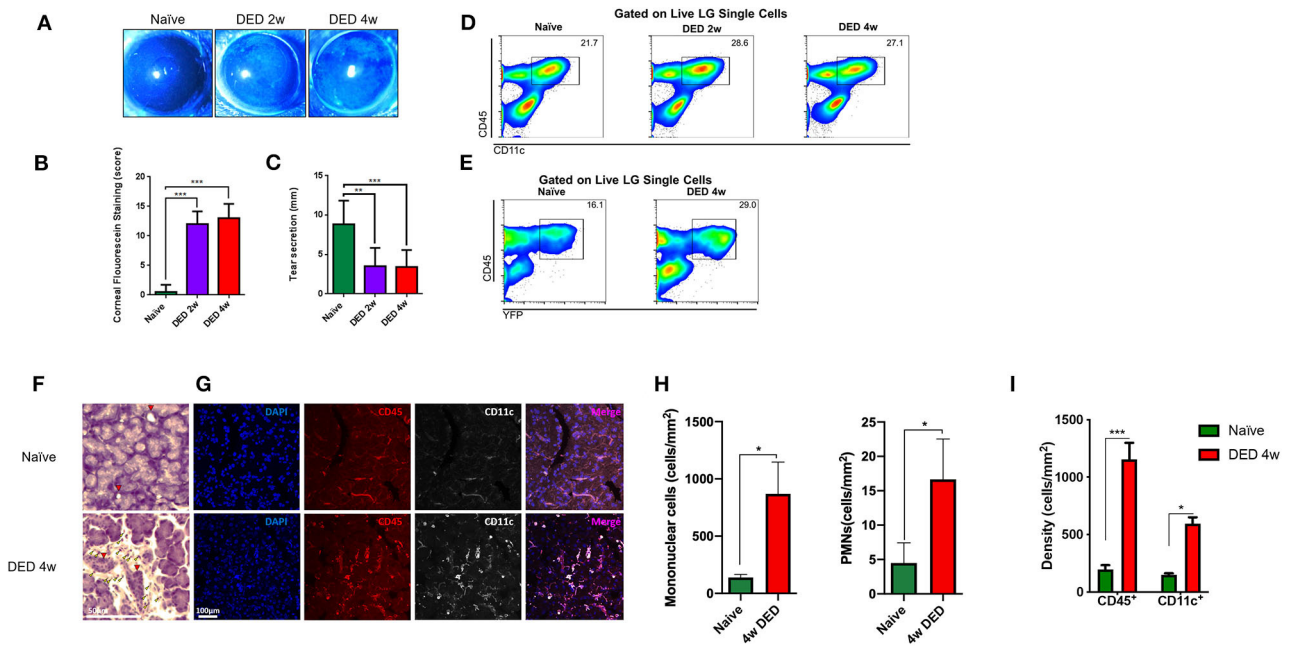

FIGURE 3 | Clinical changes and alterations in conventional dendritic cell density of the lacrimal gland in dry eye disease. **(A)** Representative images of fluorescein staining. **(B)** Quantification of CFS ($n = 4$/group). **(C)** Quantification of the tear secretion using phenol-red thread test ($n = 4$/group). p-values were calculated using one-way ANOVA followed by the Bonferroni multiple comparison test $^{**}p < 0.01$, $^{***}p < 0.001$. **(D)** Percentages of $CD45^{+}CD11c^{+}$ cells in the LG naïve state as well as after 2 and 4 w exposure to DS in C57BL/6N animals. **(E)** Percentage of $CD45^{+}YFP^{+}$ cells in the LG of $CD11c^{YFP}\times Thy1^{YFP}$ transgenic mice in naïve state and after 4 w exposure to DS. **(F)** LG histopathology of naïve and after 4 w of DED (yellow arrowhead indicates infiltrating mononuclear cells, red arrowhead indicated LG ducts). **(G)** Immunofluorescence of $CD11c^{+}$ and $CD45^{+}$ cells within the LG in naïve and 4 w of DED. **(H)** Quantification of mononuclear cells and PMNs in naïve and 4 w of DED. **(I)** Quantification of the cell density presented in **(G)** as cells/mm^2 ($^{*}p < 0.05$, $^{***}p < 0.001$).

that while cDCs sorted from sham-infected mice could induce minimal T cell proliferation (**Figure 2E**), cDCs from HSV-1 infected mice induced considerable T cell proliferation as ∼62.7 and 71.9% of T cells co-cultured with cDCs sorted from HSV-1 infected mice on 3 and 7 dpi underwent at least one cycle of proliferation (**Figures 2E,F**).

Lacrimal Gland Conventional Dendritic Cells Are Increased During Dry Eye Disease

Having established the potential importance of corneal innervation in LG immune homeostasis and functionality of cDCs in this tissue, we next examined if DS, which generally causes milder corneal sensory nerve damage (9) than HSV keratitis, but is more prevalent clinically, has an impact on the density of cDCs in the LG after DS. Greater CFS score (**Figure 3A**) and lower tear secretion were observed in $CD11c^{YFP}\times Thy^{YFP}$ mice exposed to DS compared to naïve controls. The CFS score was 12.0 ± 3.5 at 2 w and 13.0 ± 4.5 at 4 w, compared to naïve mice (1.0 ± 1.5; $p \leq 0.001$; **Figures 3A,B**). Tear secretion in naïve mice was 9.0 ± 4.5 mm, whereas it was reduced to 3.0 ± 2.5 mm at 2 w and remained unchanged (3.0 ± 2.0 mm) at 4 w of exposure to DS ($p \leq 0.004$; **Figure 3C**). Thus, consistent with previous reports, our DS chamber induces decreased tear volume and increased CFS, two hallmarks of DED, as early as 2 weeks.

We next performed flow cytometric analysis on the LGs of naïve and DED C57BL/6N mice. As shown in **Figure S2**, forward and side scatter, as well as viability dye were used to gate on presumed population of immune cells (∼2% of total single cells suspension) by the exclusion of debris (**Figure S2A**), dead cells (**Figure S2B**), and doublets (**Figure S2C**). We next gated on $CD45^{+}$ and $CD11c^{+}$ (**Figure 3D**) to analyze all cDCs in the LG. As depicted in **Figure 3D**, the density of $CD45^{+}CD11c^{+}$ cDCs after 2 and 4 w of DS was higher than the population in naïve mice. Next, we assessed if YFP^{+} cells in our transgenic $CD11c^{YFP}xThy^{YFP}$ mice showed a similar pattern after DS in the LG. Following sequential gating on presumed population of immune cells by excluding debris (**Figure S3A**), dead cells (**Figure S3B**), and doublets (**Figure S3C**), we observed that 16.1% $CD45^{+}YFP^{+}$ cells were found in the naïve LG, while at 4 w of DS this population was increased to 29.0% (**Figure 3E** and **Figure S3**). This population was also positive for CD11c, CD11b, DCIR2, and negative for Ly6G and NK1.1 (**Figure S4**), confirming their cDC phenotype. Importantly, $CD45^{+}CD11c^{+}$ cDCs, after 4 w of DED, exhibited a 1.42-fold increase of the co-stimulatory marker CD40 ($p < 0.05$; **Figure S5**). In contrast, no significant changes were observed for MHC-II and CD86 on LG cDCs after DED.

Furthermore, histological analyses exhibited increased mononuclear cells after 4 w of DED (869.9 ± 277.2 cells/mm^2, $p = 0.063$ **Figures 3F,H** yellow arrowhead) compared to naïve mice and PMNs were also increase after 4 w of DED (16.6 ± 5.9 $p = 0.057$). Edema after 4 w of DED increase to 23.1 ± 0.6% ($p < 0.01$; **Figures S1A,B** red area). Further, CD45$^+$ cells increase after 4 w of DED compared to naïve mice (1,157.8 ± 70.2 vs. 179.3 ± 66.6 vs. cells/mm^2; $p < 0.001$; **Figures 3G,I**). While CD11c after 4 w of DED compared to naïve mice was 594.4 ± 55.8 cells/mm^2 vs. 149.6 ± 13.6 cells/mm^2, respectively ($p < 0.05$, **Figures 3G,I**). H&E staining further indicated increased LG edema. While naïve mice displayed 5.5 ± 2.4% area between acini, edema significantly increased after 4 w of DED to 23.1 ± 0.6% ($p < 0.01$; **Figures S1A,B** red area). In addition, signs of fibrosis were observed (**Figure S1A** first row; green dashed area). Collectively, our findings show that DS-induced DED is accompanied by increased density of cDCs in the LG.

Intravital Multiphoton Microscopy of The Lacrimal Gland

Having shown that DED results in increased cDC density in the LG, we next aimed to study the morphological alterations and kinetic changes of LG cDCs by IV-MPM. Morphologic and

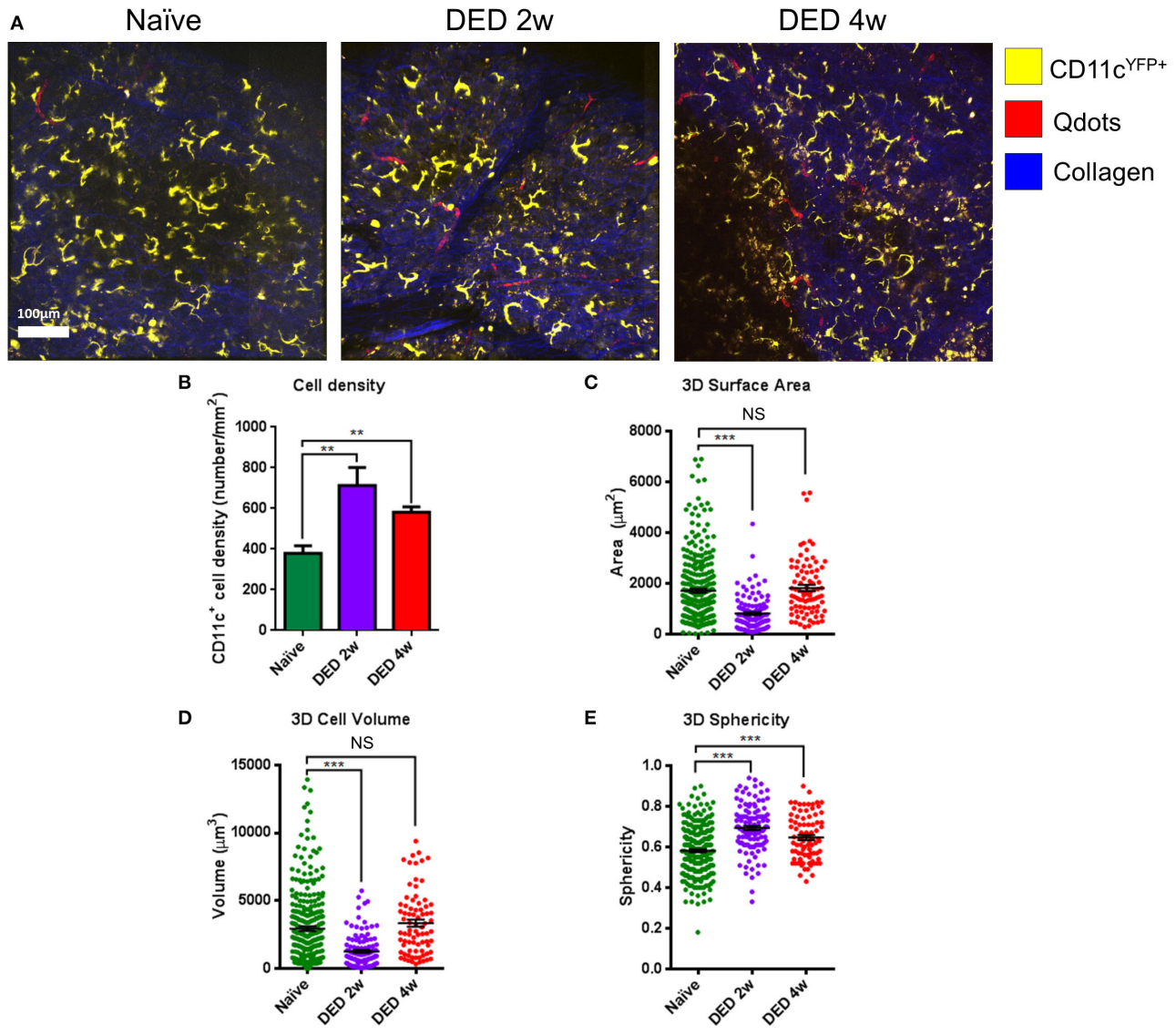

FIGURE 4 | Morphological alterations in lacrimal gland conventional dendritic cells during dry eye disease. **(A)** Representative IV-MPM images of cDCs in the LG of CD11c^{YFP}×Thy1^{YFP} mice in naïve state (left panel), and at 2 w (middle panel) and 4 w (right panel) of exposure to DS. Note increased density and sphericity of cells after exposure to DS. Scale bar: 100 µm. **(B)** Density of cDCs in transgenic CD11c^{YFP}×Thy1^{YFP} mice. **(C–E)** 3D morphologic analyses, including **(C)** 3D surface area, **(D)** 3D cell volume, and **(E)** 3D sphericity. Results are presented as mean ± SEM. One-way ANOVA (upper right) and Bonferroni multiple comparison test. $^{**}p < 0.01$, $^{***}p < 0.001$.

kinetic alterations of naïve cDCs were compared with DED-induced inflammation of the LG.

Analysis of Morphologic Parameters

The analysis of cDC distribution in naïve CD11c^{YFP}×Thy^{YFP} mice demonstrated a range of cell sizes among cDCs. *In vivo* analysis of cDCs revealed uniform distribution of cDCs in the LG lobes in both naïve (**Video S1**) and after 2 w (**Video S2**) and 4 w (**Video S3**) of exposure to DS (**Figure 4A**). However, the cDC density in naïve mice was 379.2 ± 38.2 cells/mm^2, while 2 and 4 w of DS was 712.5 ± 88.4 and 581.2 ± 26.5 cells/mm^2, respectively (**Figure 4B**). The data show that DS induced a robust increase in DC density at 2 w, which became slightly less pronounced at 4 w, once the acute phase had subsided. These new results on CD11c density were correlated with our initial findings by immunofluorescence histochemistry that demonstrated a cDC density 149.6 ± 13.6 cells/mm^2 in naïve mice and 594.4 ± 55.8 cells/mm^2 after 4 w of DED ($p < 0.01$, for naïve $r = 0.94$; for DED $r = 0.95$). This increased number of cDCs after DS compared with naïve animals was previously corroborated by flow cytometry. To have a better understanding of the morphological changes of cDCs after DS we analyzed the cell surface area, volume and sphericity of cDCs at 2 and 4 w after DS. Interestingly, 3D surface area and 3D cell volume were decreased after 2 w of DS compared with steady state. cDCs after 2 w of DS had a 3D cell surface of 809.3 ± 60.4 μm^2 compared with naïve mice showing a cDC surface area of 1,717.4 ± 79.4 μm^2. In addition, the 3D cell volume was 2,929.3 ± 159.4 μm^3 in naïve mice, and 1,274.0 ± 112.3 μm^3 at 2 w post DS

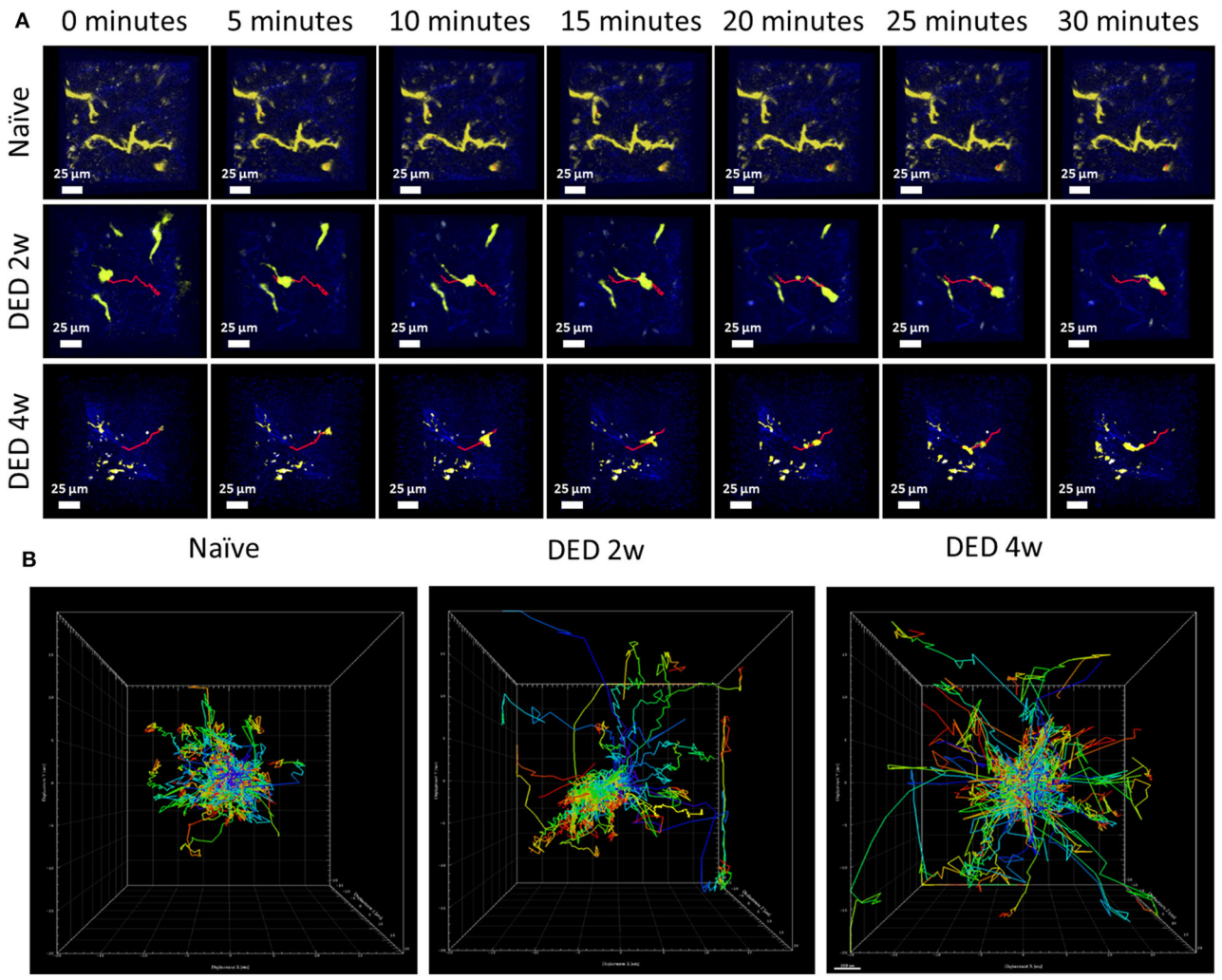

FIGURE 5 | Conventional dendritic cell motility in the lacrimal gland using IV-MPM during dry eye disease. **(A)** Representative en face time course images of cDCs in the LG of CD11c^{YFP}×Thy1^{YFP} mice in naïve mice (21), and mice exposed to DS for 2 w (middle) and 4 w (bottom) over a 30 min time period reveal differences of kinetic and morphological changes of cDCs. Scale bars, 25 μm. **(B)** Representative centered kinetic tracks of cDCs, shows displacement and directionality of the cells in naïve mice and after DS. During naïve state (left panel), the tracks were shorter with sampling movements and no directionality. After exposure to DS (2 w in middle panel, 4 w in right panel), cDCs become more motile with larger tracks with no preferential direction.

(one-way ANOVA with Bonferroni *post-hoc* test $p < 0.001$) (**Figures 4C,D**). In contrast, we found no difference in 3D cell surface area 1,717.4 ± 79.4 vs. 1,819.1 ± 121.8 μm^2 ($p = 0.77$) and 3D cell volume 2,929.3 ± 159.4 vs. 3,340.0 ± 260.6 μm^3 between naïve and 4 w of DED ($p = 0.37$; **Figures 4C,D**). However, the 3D sphericity of cDCs was increased at 2 w (0.694 ± 0.011) and 4 w (0.647 ± 0.012) after DS, compared with naïve mice (0.581 ± 0.007, $p < 0.001$ for both comparisons) (**Figure 4E**). The decreased size and volume, together with the increased sphericity suggest a more migratory phase of cDCs at 2 w during the active phase of inflammation. At 4 w, cell size and volume increase and cDCs show decreased sphericity, demonstrating a more sessile phase during persistent inflammation. Altogether, these results support that there is a shift in the dendritic state (soma and dendrites) characteristic of resting cDCs toward a more dynamic state (round shape with few to no dendrites).

Kinetics and Motility Parameters of Conventional Dendritic Cells in The Lacrimal Gland

Having shown 3D morphological alterations in LG cDCs, we next aimed to analyze if kinetics of cDCs (including 3D instantaneous velocity, mean track speed, track length and displacement length) are altered *in vivo,* following exposure to DS using the transgenic $CD11c^{YFP} \times Thy^{YFP}$ mice. Importantly, previous work has shown that temperature is a critical parameter, since leukocyte function, including kinetics, can be modulated by temperature (23, 39, 40). Thus, in this work, we held the physiological temperature (37°C) during the entire imaging sequence. While we only observed sampling movements of cDCs with minimal displacement in naïve mice (**Video S1**), at 2 w (**Video S2**) and 4 w (**Video S3**) of DS, we observed a considerable alteration in cDC motility, showing more locomotion with longer tracks (**Figure 5A**; a sample track in each panel is represented in red). As depicted in **Figure 5B**, cDCs exposed to DS showed increased motility in all directions (x, y, and z).

Further, after both 2 w (1.135 ± 0.015 μ/min) and 4 w (1.052 ± 0.011 μ/min) following DS, we showed increased 3D instantaneous velocity compared with cDCs from naïve animals (0.771 ± 0.007 μ/min, $p < 0.001$ for both comparisons; **Figure 6A**). The mean track speed of cDCs was also increased at 2 w (2.257 ± 0.069 μ/min) and 4 w (1.645 ± 0.049 μ/min) compared with naïve state (1.265 ± 0.044 μ/min, $p < 0.001$ for both comparisons; **Figure 6B**). Interestingly, mean track speed of cDCs at 2 w of exposure to DS was significantly higher compared with cDCs at 4 w of exposure to DS ($p < 0.001$; **Figure 6B**).

We next examined the changes in track length and displacement length of cDCs in the LG after exposure to DS. Quantifications of these parameters revealed that track length was 44.49 ± 1.22 μm in naïve mice, which was significantly augmented at both 2 w (58.31 ± 2.22 μm, $p < 0.001$) and 4 w (50.78 ± 2.27 μm, $p = 0.041$) after DS (**Figure 6C**). Similar to mean track speed, cDCs at 2 w of exposure to DS, exhibited longer track lengths compared with cDCs after 4 w of exposure ($p = 0.034$; **Figure 6C**). In contrast, we only found significant changes in the displacement length of cDCs in naïve mice (6.27 ± 0.37 μm) compared to cDCs in mice exposed to DS for 4 w (7.88 ± 0.43 μ, $p = 0.009$; **Figure 6D**).

Moreover, while we did not observe a significant difference in the meandering index of cDCs at 2 w following exposure to DS (0.147 ± 0.011, $p = 0.98$) compared with cDCs in naïve mice (0.144 ± 0.006), at 4 w after DS, cDCs demonstrated a significant increase, but still relatively low meandering index (0.201 ± 0.010, $p < 0.001$; **Figure 6E**), suggestive of a random walk pattern. Collectively, we observed considerable alterations in all kinetic parameters of cDCs after exposure to DS compared to naïve mice.

DISCUSSION

In the present work, we establish a novel model of lacrimal gland IV-MPM imaging to study 3D morphology and kinetic properties of cDCs in the LG after DS-induced DED. We demonstrate that the cDC density in the LG is higher during DED, and that cDCs become smaller, more spherical, but more motile in DS-induced DED compared to naïve mice. Histopathological and immunofluorescence histochemistry analyses, showing the increased density of LG mononuclear cells, $CD45^+$ leukocytes, as well as $CD11c^+$ cDCs after both DED and HSV-1 keratitis, confirm our findings as observed by IV-MPM. Altogether, these results suggest that the alterations of cDCs are, at least in part, due to the damage of the sensory nerves on the ocular surface.

DED is a multifactorial disease, and DS is one of the risk factors initiating inflammatory responses at the ocular surface resulting in DED. It has been shown that DS causes reduced tear break-up time and LG dysfunction (17, 41). It is thought that DS contributes to DED pathophysiology by damaging the ocular surface and corneal sensory nerves. Subsequently, the damage to corneal nerves, which comprises the afferent pathway of the LFU, leads to low tear secretion via diminished signaling to the parasympathetic nerve fibers (42). However, the mechanism underlying damage to the corneal sensory nerves on LG immune cell populations is unknown. The LG is mainly responsible for tear secretion through a tightly regulated process incorporating all components of the LFU. Innervation of the ocular surface and the lacrimal gland have been shown to be altered in mice with DED, as compared to naïve mice. Several murine models of DED, including DS-induced DED (43, 44), DS combined with scopolamine to induce suppression of tear production (9), a model in which the LG is removed (45), an experimental autoimmune lacrimal keratoconjunctivitis model (46), as well as $CD25^{-/-}$ and $Aire^{-/-}$ mice that develop Sjögren's syndrome (47, 48) have all demonstrated significantly decreased corneal sub-basal nerve density compared with their respective control mice, irrespective of the model used. Further, in $TSP^{-/-}$ mice that present with aqueous deficient DED, the neuronal innervation of the LG, and in particular the parasympathetic nerves, are substantially decreased when compared to lacrimal glands of age-matched WT mice (49). We show that the density of LG immune cells, in particular cDCs, is increased after nerve damage. Further, the destruction of corneal nerves after corneal HSV-1 infection enhances cDCs capacity in stimulating T cell

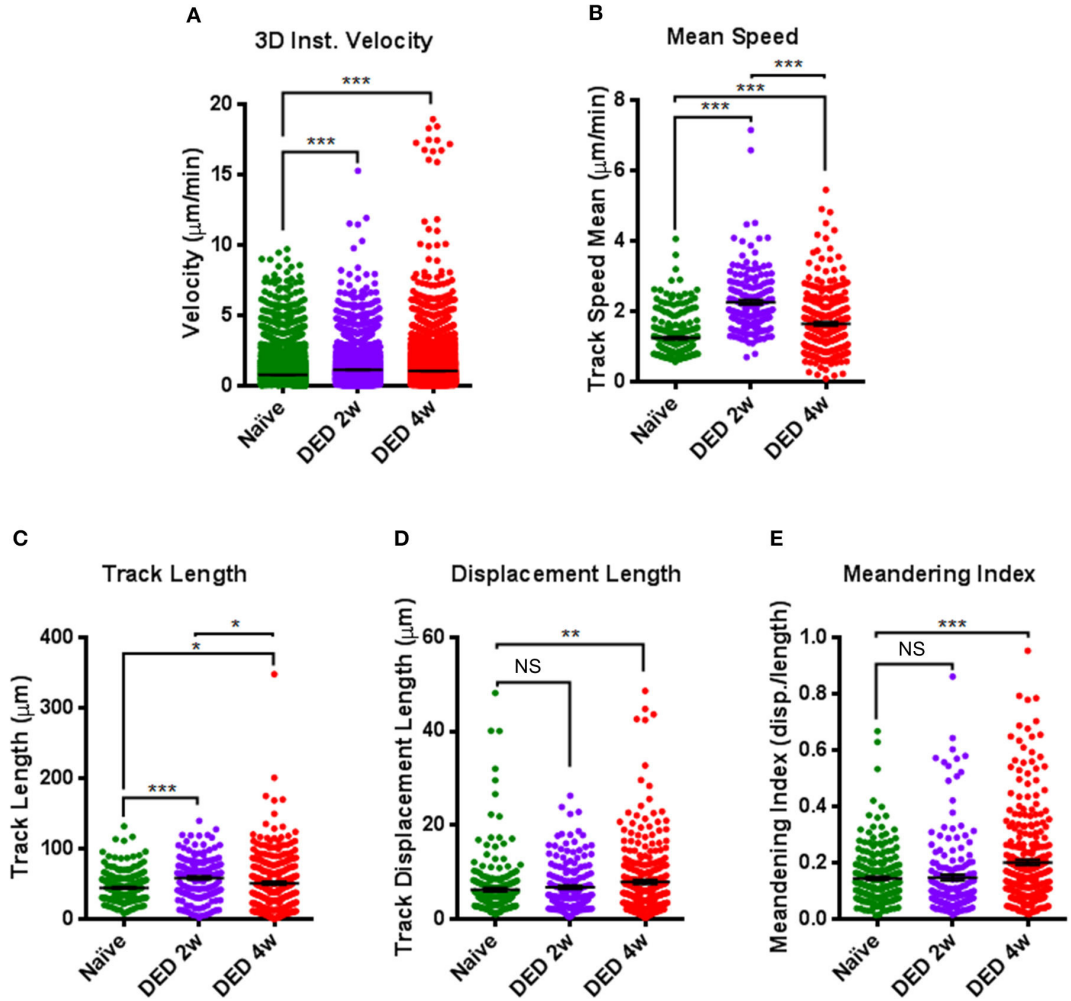

FIGURE 6 | Comparison of kinetic parameters of conventional dendritic cells in the lacrimal gland using IV-MPM during dry eye disease. Analyses of the kinetics of cDCs, including **(A)** 3D instantaneous velocity, **(B)** track speed mean, **(C)** track length, **(D)** displacement length, and **(E)** meandering index. Results are presented as mean ± SEM. One-way ANOVA (upper right) and Bonferroni multiple comparison test. $^{*}p < 0.05$, $^{**}p < 0.01$, $^{***}p < 0.001$.

proliferation. Along with changes in cDC activation, structural changes of the LG after HSV infection are observed with increased edema and increase in fibrosis. Therefore, our results indicate that corneal sensory nerves, as the afferent pathway of the LFU, directly or indirectly modulate the immune cell density and function in the LG. Nonetheless, while DED causes less severe nerve alterations on the ocular surface, HSV-1 infection results in more severe nerve injury (50, 51). However, it is important to note that several factors can contribute to both the nerve and cDC changes observed during HSV-1 keratitis. These include, the severe neurotrophic effect resulting in ocular surface damage, increased inflammation, and the effect of the HSV-1 itself. Thus, while the decrease in nerves during HSV-1 keratitis is more severe than in DED, we cannot rule out an effect from these additional factors that result in morbidity. For example, a recent study has used different strategies to deplete immune cell subpopulations to dissect the contribution of the virus to nerve damage. Reports show higher levels of nerve damage after depletion of cDCs and/or macrophages in PSGL-$1^{-/-}$ mice that prevent *de novo* immune cell recruitment (32), suggesting that the virus itself and not inflammation largely contribute to nerve damage observed during HSV-1 keratitis. Further, increased pro-inflammatory cytokines and chemokines (52–54), changes in neuropeptides (55), as well as leukocyte recruitment, such as T cell activation and recruitment, have been demonstrated in HSV-1 keratitis (56). In addition, viral particles along with $CD4^{+}$ and $CD8^{+}$ T cell infiltration have been found within the LG after HSV-1 infection (57). Thus, alterations in cytokines and chemokines may, in part, explain the more pronounced infiltration of immune cells in the LG after HSV-1 keratitis, as compared to DED.

Based on the literature, inflammation of the ocular surface and corneal sensory nerve damage are observed in mice exposed to DS and individuals with DED (58, 59). The LG cDCs density increases as early as 2 w after DS and remains elevated up to 4 w of exposure to DS. This effect could in part be explained

by increased expression of the pro-inflammatory cytokines IL-1, IL-6, IL-17, IL-23, TNF-α, and IFN-γ that have previously been shown in the LG at 2 and 4 weeks after exposure to DS (9). Thus, cDC density, kinetics and morphological changes presented in our work, could in part be driven by differential expression of these pro-inflammatory cytokines. In line with our findings, a recent study showed that $CD11b^+$ myeloid cells were recruited to the LG at 2 and 4 weeks after exposure to DS (8). The increased density of cDCs and myeloid cells can be explained by the recruitment of circulating cDCs and/or monocytes, which can locally differentiate into cDCs (60, 61). However, this experiment did not examine if the increased density of cDCs is due to potential proliferation of the resident cDCs in the LG or from the infiltrating myeloid-derived cells.

cDCs are highly functional immune cells, inducers of dynamic processes of inflammation and/or tolerance (62), they actively shift their morphology in peripheral tissues such as skin (63) and cornea (21) during inflammation. In recent years, the initiation of immune responses and/or maintenance of central and peripheral tolerance have been studied via cDC kinetics, morphological features, and their interaction with T cells using intravital imaging (27, 64, 65). In this study, we show that LG cDCs are dendritiform with low sphericity during steady state, whereas following DED, they become less dendritiform and more spherical, and demonstrate early signs of activation, as the increased expression of the co-stimulatory marker CD40 shows. This finding is consistent with the previous reports showing that the peripheral cDCs in the naïve setting showed dendritiform morphology with increased surface area to maximize surveillance of the tissue microenvironment. During inflammation, their dendrites are gradually retracted, leaving them with fewer and shorter processes and more spherical cell bodies to facilitate their migration in tissues. While resident populations of cDCs within the skin and gut epithelium are sessile and dendritiform, after different stimuli, such as LPS administration or *Salmonella typhimurium* infection, spherical cells have been demonstrated to become predominant (66, 67). In addition, Linquist et al. have shown that in lymph nodes, LPS-activated cDCs become more motile (27). Furthermore, we have recently shown kinetics and morphological alterations of immune cells following acute sterile inflammation within the cornea, demonstrating that MHC class II^+ cells become more spherical, with increased velocity and larger displacement following inflammation (21). Similarly, in the current work, after inflammation induced by DS, LG cDCs exhibited reduced cell surface, become smaller, acquire a spherical shape, and become motile. The morphological changes during inflammation can also be observed in monocytes, macrophages, T cells, and natural killer cells during inflammation.

Our results show that naïve cDCs in LG are sessile with a low mean speed, while their motility increased after 2 w exposure to DS and remained elevated, although to a lesser extent, at 4 w. Previous studies have demonstrated that activated cDCs within lymph nodes exhibit a mean speed of ∼3 μm/min during inflammation compared to the resident naïve cDCs which had a mean speed of ∼1 μm/min (27). Recently, our group has shown that the mean speed of corneal cDCs was higher following acute thermal injury compared to the naïve setting (21). The differences in mean speed of cDCs reported in the literature and our study could be due to the differences between the tissue microenvironments. This tissue-specific effect is also supported by reports showing that mean speed of cDCs was 6.6 μm/min in paracortical areas of the popliteal lymph nodes (26) and 5.9 ± 1.0 μm/min in explanted lymph nodes (68).

Naïve LG cDCs exhibit sampling movements in concordance with their immature state. This, in part, can be explained by an active role to maintain immune tolerance, also seen within the cornea (21) and epidermis (43). Although cDCs become more motile, as indicated by longer track and displacement lengths after 2 w and 4 w of DS-induced DED compared to controls, we observe no preferential directionality in either time point, suggestive of a random walk pattern. This is consistent with our previous study on corneal cDCs in naïve state and during acute inflammation, in which cDCs exhibit random movements as well (21).

Recently, several studies have shown that the peripheral nervous system (PNS), in addition to mediating communication between the central nervous system and peripheral tissues, also controls innate immune responses via non-specific responses to pathogens (69, 70). However, dysfunction or damage to the PNS may in contrast mediate pro-inflammatory innate responses, called "neurogenic inflammation" (71–74). In addition, sympathetic nerves have been shown to regulate leukocyte homing to tissues (75, 76). Moreover, both sympathetic and sensory innervation of the skin, lung and gut have been shown to influence cDC migration and motility (77, 78). Thus, neurogenic inflammation secondary to DS can result due to dysfunction of ocular surface nerves, resulting in decreased tear production, and alterations of the autonomous nervous system, leading to LG inflammation. A limitation of our study is the lack of detailed mechanistic and signaling data, demonstrating the direct effect of corneal nerve changes on the LG. We hope that the current intravital imaging model of the LG, together with the data provided, will enable and stimulate future research in this important area.

In summary, herein we show a newly developed methodology to study LG immune cell kinetics and 3D morphology in a transgenic murine model by using intravital multi-photon imaging. By using IV-MPM, the spatiotemporal organization of cDCs in the LG of naïve and DS-induced DED can be investigated. We have provided evidence that damage to corneal sensory nerves modulates the immune responses in the LG. This corneal nerve damage resulting from DS could explain the altered cDC kinetics and morphology within the LG. Thus, this study demonstrates that intravital multi-photon imaging offers opportunities for studying *in vivo* immune cell kinetics in diseases affecting the LG.

DATA AVAILABILITY STATEMENT

The raw data supporting the conclusions of this article will be made available by the authors, without undue reservation, to any qualified researcher.

ETHICS STATEMENT

The animal study was reviewed and approved by Tufts Department of Lab Animal Medicine.

AUTHOR CONTRIBUTIONS

GO, CC, YS-R, AJ, BK, DH, DZ, and PH designed the research. GO, AJ, BK, and DH performed the research. CC analyzed the MPM movies. GO, CC, and AJ drafted the manuscript. YS-R, BK, DH, DZ, and PH edited the manuscript. All authors contributed to the article and approved the submitted version.

FUNDING

This work was funded by NIH R01-EY022695 (PH), NIH R01 EY029602 (PH), NIH R01 EY029870 (DZ), Research to Prevent Blindness Challenge Grant to the Department of Ophthalmology, and Tufts Institutional Support (PH).

SUPPLEMENTARY MATERIAL

The Supplementary Material for this article can be found online at: https://www.frontiersin.org/articles/10.3389/fimmu.2020.01713/full#supplementary-material

Figure S1 | LG histopathology in naïve mice, 3 and 7 days post HSV-1 infection, and 4w post DED. **(A)** Converted images of LG histopathology using ImageJ software of all experimental groups. The red extent exhibits the area between acinar cells in all groups. **(B)** Quantification of the area between acinar cells expressed in percentage of area in red of total image area. Results are presented as mean ± SEM. One-way ANOVA and Bonferroni multiple comparison test. $^{**}p < 0.01$, $^{***}p < 0.001$.

Figure S2 | Sequential gating strategy for flow cytometry on the lacrimal gland in naïve and after 2 and 4 w of exposure to DS in WT C57BL/6N mice. **(A)** SSC-A and FSC-A of LG single cell suspension, showing gating out debris and gating on presumable population of immune cells. **(B)** Gating on live cells. **(C)** Gating on single cells. **(D)** Gating on $CD45^+$ immune cells among live single cells.

Figure S3 | Sequential gating strategy for flow cytometry on the lacrimal gland in naïve and after 4 w exposure to DS in $CD11c^{YFP} \times Thy1^{YFP}$ mice**. (A)** SSC-A and FSC-A of LG single cell suspension, showing gating out debris and gating on presumable population of immune cells. **(B)** Gating on live cells. **(C)** Gating on single cells. **(D)** Gating on double positive $CD45^+YFP^+$ cDCs among live single cells.

Figure S4 | Flow cytometric characterization of cells in the lacrimal gland of $CD11c^{YFP} \times Thy1^{YFP}$ mice. Flow cytometry histograms showing expression of CD11c, CD11b, DCIR2, Ly6G, and NK1.1 markers on $CD45^+YFP^+$ cells reveals their identity as cDCs. Light gray histograms show fluorescent minus one isotype controls.

Figure S5 | Flow cytometric characterization of conventional dendritic cells in the lacrimal gland after 4 weeks of exposure to desiccating stress. Histograms showing expression of MHC-II, CD86, and CD40 on $CD45^+CD11c^+$ cells reveal that in cDCs, CD40 is increased after 4w of DED compared to naïve mice. Light gray histograms show fluorescent minus one isotype controls.

Video S1 | Representative IV-MPM movie of lacrimal gland in a naïve transgenic $CD11c^{YFP} \times Thy1^{YFP}$ mouse. The video highlights sampling movement of cDCs with minor displacement in the naïve lacrimal galnd. Blue, second harmonic generation delineating collagen, yellow, yellow fluorescent protein expressed by cDCs.

Video S2 | Representative IV-MPM of lacrimal gland in a transgenic $CD11c^{YFP} \times Thy1^{YFP}$ mouse after 2 weeks of exposure to desiccating stress. The video demonstrates the spherical cDCs with fewer dendrites which move long distances in the lacrimal gland. Blue, second harmonic generation delineating collagen, yellow, yellow fluorescent protein expressed by cDCs.

Video S3 | Representative IV-MPM of lacrimal gland in a transgenic $CD11c^{YFP} \times Thy1^{YFP}$ mouse after 4 weeks of exposure to desiccating stress. The video shows elevated density of cDCs with spherical shape which travel with a high speed in the lacrimal gland. Blue, second harmonic generation delineating collagen, yellow, yellow fluorescent protein expressed by cDCs.

Table S1 | Antibody list.

REFERENCES

1. Farrand KF, Fridman M, Stillman IO, Schaumberg DA. Prevalence of diagnosed dry eye disease in the United States among adults aged 18 years and older. *Am J Ophthalmol.* (2017) 182:90–8. doi: 10.1016/j.ajo.2017.06.033
2. Yu J, Asche CV, Fairchild CJ. The economic burden of dry eye disease in the United States: a decision tree analysis. *Cornea.* (2011) 30:379–87. doi: 10.1097/ICO.0b013e3181f7f363
3. Craig JP, Nichols KK, Akpek EK, Caffery B, Dua HS, Joo CK, et al. TFOS DEWS II definition and classification report. *Ocul Surf.* (2017) 15:276–83. doi: 10.1016/j.jtos.2017.05.008
4. Dartt DA. Signal transduction and control of lacrimal gland protein secretion: a review. *Curr Eye Res.* (1989) 8:619–36. doi: 10.3109/02713688908995762
5. Dartt DA. Regulation of tear secretion. *Adv Exp Med Biol.* (1994) 350:1–9. doi: 10.1007/978-1-4615-2417-5_1
6. Stern ME, Gao J, Siemasko KF, Beuerman RW, Pflugfelder SC. The role of the lacrimal functional unit in the pathophysiology of dry eye. *Exp Eye Res.* (2004) 78:409–16. doi: 10.1016/j.exer.2003.09.003
7. Stern ME, Beuerman RW, Fox RI, Gao J, Mircheff AK, Pflugfelder SC. The pathology of dry eye: the interaction between the ocular surface and lacrimal glands. *Cornea.* (1998) 17:584–9. doi: 10.1097/00003226-199811000-00002
8. Xiao B, Wang Y, Reinach PS, Ren Y, Li J, Hua S, et al. Dynamic ocular surface and lacrimal gland changes induced in experimental murine dry eye. *PLoS ONE.* (2015) 10:e0115333. doi: 10.1371/journal.pone.0115333
9. Stepp MA, Pal-Ghosh S, Tadvalkar G, Williams A, Pflugfelder SC, de Paiva CS. Reduced intraepithelial corneal nerve density and sensitivity accompany desiccating stress and aging in C57BL/6 mice. *Exp Eye Res.* (2018) 169:91–8. doi: 10.1016/j.exer.2018.01.024
10. Schomberg D, Ahmed M, Miranpuri G, Olson J, Resnick DK. Neuropathic pain: role of inflammation, immune response, and ion channel activity in central injury mechanisms. *Ann Neurosci.* (2012) 19:125–32. doi: 10.5214/ans.0972.7531.190309
11. Li J, Wei GH, Huang H, Lan YP, Liu B, Liu H, et al. Nerve injury-related autoimmunity activation leads to chronic inflammation and chronic neuropathic pain. *Anesthesiology.* (2013) 118:416–29. doi: 10.1097/ALN.0b013e31827d4b82
12. Banchereau J, Steinman RM. Dendritic cells and the control of immunity. *Nature.* (1998) 392:245–52. doi: 10.1038/32588
13. Barabino S, Chen Y, Chauhan S, Dana R. Ocular surface immunity: homeostatic mechanisms and their disruption in dry eye disease. *Prog Retin Eye Res.* (2012) 31:271–85. doi: 10.1016/j.preteyeres.2012.02.003

14. Hamrah P, Zhang Q, Liu Y, Dana MR. Novel characterization of MHC class II-negative population of resident corneal Langerhans cell-type dendritic cells. *Invest Ophthalmol Vis Sci.* (2002) 43:639–46.
15. Hamrah P, Liu Y, Zhang Q, Dana MR. The corneal stroma is endowed with a significant number of resident dendritic cells. *Invest Ophthalmol Vis Sci.* (2003) 44:581–9. doi: 10.1167/iovs.02-0838
16. Matthews JB, Mason GI, Lawrence GM. Epithelial expression of major histocompatibility complex (MHC) antigens in normal rat salivary and lacrimal glands. *Arch Oral Biol.* (1992) 37:93–7. doi: 10.1016/0003-9969(92)90003-Q
17. Lee HS, Amouzegar A, Dana R. Kinetics of corneal antigen presenting cells in experimental dry eye disease. *BMJ Open Ophthalmol.* (2017) 1:e000078. doi: 10.1136/bmjophth-2017-000078
18. Shetty R, Sethu S, Deshmukh R, Deshpande K, Ghosh A, Agrawal A, et al. Corneal dendritic cell density is associated with subbasal nerve plexus features, ocular surface disease index, and serum Vitamin D in evaporative dry eye disease. *Biomed Res Int.* 2016:4369750. doi: 10.1155/2016/4369750
19. Gao N, Lee P, Yu FS. Intraepithelial dendritic cells and sensory nerves are structurally associated and functional interdependent in the cornea. *Sci Rep.* (2016) 6:36414. doi: 10.1038/srep36414
20. Cruzat A, Witkin D, Baniasadi N, Zheng L, Ciolino JB, Jurkunas UV, et al. Inflammation and the nervous system: the connection in the cornea in patients with infectious keratitis. *Invest Ophthalmol Vis Sci.* (2011) 52:5136–43. doi: 10.1167/iovs.10-7048
21. Seyed-Razavi Y, Lopez MJ, Mantopoulos D, Zheng L, Massberg S, Sendra VG, et al. Kinetics of corneal leukocytes by intravital multiphoton microscopy. *FASEB J.* (2019) 33:2199–211. doi: 10.1096/fj.201800684RR
22. Cahalan MD, Parker I, Wei SH, Miller MJ. Two-photon tissue imaging: seeing the immune system in a fresh light. *Nat Rev Immunol.* (2002) 2:872–80. doi: 10.1038/nri935
23. Miller MJ, Wei SH, Parker I, Cahalan MD. Two-photon imaging of lymphocyte motility and antigen response in intact lymph node. *Science.* (2002) 296:1869–73. doi: 10.1126/science.1070051
24. Zoumi A, Yeh A, Tromberg BJ. Imaging cells and extracellular matrix *in vivo* by using second-harmonic generation and two-photon excited fluorescence. *Proc Natl Acad Sci USA.* (2002) 99:11014–9. doi: 10.1073/pnas.172368799
25. Miller MJ, Wei SH, Cahalan MD, Parker I. Autonomous T cell trafficking examined *in vivo* with intravital two-photon microscopy. *Proc Natl Acad Sci USA.* (2003) 100:2604–9. doi: 10.1073/pnas.2628040100
26. Mempel TR, Henrickson SE, Von Andrian UH. T-cell priming by dendritic cells in lymph nodes occurs in three distinct phases. *Nature.* (2004) 427:154–9. doi: 10.1038/nature02238
27. Lindquist RL, Shakhar G, Dudziak D, Wardemann H, Eisenreich T, Dustin ML, et al. Visualizing dendritic cell networks *in vivo*. *Nat Immunol.* (2004) 5:1243–50. doi: 10.1038/ni1139
28. Reismann D, Stefanowski J, Gunther R, Rakhymzhan A, Matthys R, Nutzi R, et al. Longitudinal intravital imaging of the femoral bone marrow reveals plasticity within marrow vasculature. *Nat Commun.* (2017) 8:2153. doi: 10.1038/s41467-017-01538-9
29. Roediger B, Ng LG, Smith AL, de St Groth BF, Weninger W. Visualizing dendritic cell migration within the skin. *Histochem Cell Biol.* (2008) 130:1131–46. doi: 10.1007/s00418-008-0531-7
30. Kolesnikov M, Farache J, Shakhar G. Intravital two-photon imaging of the gastrointestinal tract. *J Immunol Methods.* (2015) 421:73–80. doi: 10.1016/j.jim.2015.03.008
31. de Paiva CS. Effects of aging in dry eye. *Int Ophthalmol Clin.* (2017) 57:47–64. doi: 10.1097/IIO.0000000000000170
32. Hu K, Harris DL, Yamaguchi T, von Andrian UH, Hamrah P. A dual role for corneal dendritic cells in herpes simplex keratitis: local suppression of corneal damage and promotion of systemic viral dissemination. *PLoS ONE.* (2015) 10:e0137123. doi: 10.1371/journal.pone.0137123
33. Barabino S, Shen L, Chen L, Rashid S, Rolando M, Dana MR. The controlled-environment chamber: a new mouse model of dry eye. *Invest Ophthalmol Vis Sci.* (2005) 46:2766–71. doi: 10.1167/iovs.04-1326
34. Lemp MA. Report of the national eye institute/industry workshop on clinical trials in dry eyes. *CLAO J.* (1995) 21:221–32.
35. Kilic S, Kulualp K. Tear production rate in a mouse model of dry eye according to the phenol red thread and endodontic absorbent paper point tear tests. *Comp Med.* (2016) 66:367–72.
36. Dursun D, Wang M, Monroy D, Li DQ, Lokeshwar BL, Stern ME, et al. A mouse model of keratoconjunctivitis sicca. *Invest Ophthalmol Vis Sci.* (2002) 43:632–8.
37. Sumen C, Mempel TR, Mazo IB, von Andrian UH. Intravital microscopy: visualizing immunity in context. *Immunity.* (2004) 21:315–29. doi: 10.1016/j.immuni.2004.08.006
38. Chucair-Elliott AJ, Zheng M, Carr DJ. Degeneration and regeneration of corneal nerves in response to HSV-1 infection. *Invest Ophthalmol Vis Sci.* (2015) 56:1097–107. doi: 10.1167/iovs.14-15596
39. Hammarfjord O, Wallin RP. Dendritic cell function at low physiological temperature. *J Leukoc Biol.* (2010) 88:747–56. doi: 10.1189/jlb.0310155
40. Zgair AK. The effect of high temperature on the kinetics of lipopolysaccharide (LPS)-induced human monocytes activity *in vitro*. *Cell Immunol.* (2012) 275:55–60. doi: 10.1016/j.cellimm.2012.03.001
41. Willcox MDP, Argueso P, Georgiev GA, Holopainen JM, Laurie GW, Millar TJ, et al. TFOS DEWS II tear film report. *Ocul Surf.* (2017) 15:366–403. doi: 10.1016/j.jtos.2017.03.006
42. Ding C, Walcott B, Keyser KT. Neuronal nitric oxide synthase and the autonomic innervation of the mouse lacrimal gland. *Invest Ophthalmol Vis Sci.* (2001) 42:2789–94.
43. Simsek C, Kojima T, Dogru M, Tsubota K. Alterations of murine subbasal corneal nerves after environmental dry eye stress. *Invest Ophthalmol Vis Sci.* (2018) 59:1986–95. doi: 10.1167/iovs.17-23743
44. Esquenazi S, He J, Li N, Bazan NG, Esquenazi I, Bazan HE. Comparative *in vivo* high-resolution confocal microscopy of corneal epithelium, sub-basal nerves and stromal cells in mice with and without dry eye after photorefractive keratectomy. *Clin Exp Ophthalmol.* (2007) 35:545–9. doi: 10.1111/j.1442-9071.2007.01543.x
45. Yamazaki R, Yamazoe K, Yoshida S, Hatou S, Inagaki E, Okano H, et al. The Semaphorin 3A inhibitor SM-345431 preserves corneal nerve and epithelial integrity in a murine dry eye model. *Sci Rep.* (2017) 7:15584. doi: 10.1038/s41598-017-15682-1
46. Seo KY, Kitamura K, Han SJ, Kelsall B. TH17 cells mediate inflammation in a novel model of spontaneous experimental autoimmune lacrimal keratoconjunctivitis with neural damage. *J Allergy Clin Immunol.* (2018) 142:96–108.e102. doi: 10.1016/j.jaci.2017.07.052
47. Stepp MA, Pal-Ghosh S, Tadvalkar G, Williams AR, Pflugfelder SC, de Paiva CS. Reduced corneal innervation in the CD25 null model of sjogren syndrome. *Int J Mol Sci.* (2018) 19:3821. doi: 10.3390/ijms19123821
48. Chen FY, Lee A, Ge S, Nathan S, Knox SM, McNamara NA. Aire-deficient mice provide a model of corneal and lacrimal gland neuropathy in Sjogren's syndrome. *PLoS One.* (2017) 12:e0184916. doi: 10.1371/journal.pone.0184916
49. Bhattacharya S, Garcia-Posadas L, Hodges RR, Makarenkova HP, Masli S, Dartt DA. Alteration in nerves and neurotransmitter stimulation of lacrimal gland secretion in the TSP-1(-/-) mouse model of aqueous deficiency dry eye. *Mucosal Immunol.* (2018) 11:1138–48. doi: 10.1038/s41385-018-0002-y
50. Kurbanyan K, Hoesl LM, Schrems WA, Hamrah P. Corneal nerve alterations in acute acanthamoeba and fungal keratitis: an *in vivo* confocal microscopy study. *Eye (Lond).* (2012) 26:126–32. doi: 10.1038/eye.2011.270
51. Rosenberg ME, Tervo TM, Muller LJ, Moilanen JA, Vesaluoma MH. *In vivo* confocal microscopy after herpes keratitis. *Cornea.* (2002) 21:265–9. doi: 10.1097/00003226-200204000-00006
52. Tang Q, Hendricks RL. Interferon gamma regulates platelet endothelial cell adhesion molecule 1 expression and neutrophil infiltration into herpes simplex virus-infected mouse corneas. *J Exp Med.* (1996) 184:1435–47. doi: 10.1084/jem.184.4.1435
53. Tang Q, Chen W, Hendricks RL. Proinflammatory functions of IL-2 in herpes simplex virus corneal infection. *J Immunol.* (1997) 158:1275–83.
54. Biswas PS, Rouse BT. Early events in HSV keratitis–setting the stage for a blinding disease. *Microbes Infect.* (2005) 7:799–810. doi: 10.1016/j.micinf.2005.03.003

55. Muller LJ, Marfurt CF, Kruse F, Tervo TM. Corneal nerves: structure, contents and function. *Exp Eye Res.* (2003) 76:521–42. doi: 10.1016/S0014-4835(03)00050-2
56. Suryawanshi A, Veiga-Parga T, Rajasagi NK, Reddy PB, Sehrawat S, Sharma S, et al. Role of IL-17 and Th17 cells in herpes simplex virus-induced corneal immunopathology. *J Immunol.* (2011) 187:1919–30. doi: 10.4049/jimmunol.1100736
57. Montgomery ML, Carr DJJ. Ocular exocrine glands are infected, harbor T cells, and express select cytokines and chemokines following corneal HSV-1 infection. *J Immunol.* (2018) 200(Suppl. 1):172.17.
58. Tuisku IS, Konttinen YT, Konttinen LM, Tervo TM. Alterations in corneal sensitivity and nerve morphology in patients with primary sjogren's syndrome. *Exp Eye Res.* (2008) 86:879–85. doi: 10.1016/j.exer.2008.03.002
59. Benitez-Del-Castillo JM, Acosta MC, Wassfi MA, Diaz-Valle D, Gegundez JA, Fernandez C, et al. Relation between corneal innervation with confocal microscopy and corneal sensitivity with noncontact esthesiometry in patients with dry eye. *Invest Ophthalmol Vis Sci.* (2007) 48:173–81. doi: 10.1167/iovs.06-0127
60. Robert C, Fuhlbrigge RC, Kieffer JD, Ayehunie S, Hynes RO, Cheng G, et al. Interaction of dendritic cells with skin endothelium: a new perspective on immunosurveillance. *J Exp Med.* (1999) 189:627–36. doi: 10.1084/jem.189.4.627
61. Randolph GJ, Inaba K, Robbiani DF, Steinman RM, Muller WA. Differentiation of phagocytic monocytes into lymph node dendritic cells *in vivo*. *Immunity.* (1999) 11:753–61. doi: 10.1016/S1074-7613(00)80149-1
62. Iberg CA, Jones A, Hawiger D. Dendritic cells as inducers of peripheral tolerance. *Trends Immunol.* (2017) 38:793–804. doi: 10.1016/j.it.2017.07.007
63. Kissenpfennig A, Henri S, Dubois B, Laplace-Builhe C, Perrin P, Romani N, et al. Dynamics and function of Langerhans cells *in vivo*: dermal dendritic cells colonize lymph node areas distinct from slower migrating langerhans cells. *Immunity.* (2005) 22:643–54. doi: 10.1016/j.immuni.2005.04.004
64. Celli S, Albert ML, Bousso P. Visualizing the innate and adaptive immune responses underlying allograft rejection by two-photon microscopy. *Nat Med.* (2011) 17:744–9. doi: 10.1038/nm.2376
65. Gerard A, Khan O, Beemiller P, Oswald E, Hu J, Matloubian M, et al. Secondary T cell-T cell synaptic interactions drive the differentiation of protective CD8+ T cells. *Nat Immunol.* (2013) 14:356–63. doi: 10.1038/ni.2547
66. Chieppa M, Rescigno M, Huang AY, Germain RN. Dynamic imaging of dendritic cell extension into the small bowel lumen in response to epithelial cell TLR engagement. *J Exp Med.* (2006) 203:2841–52. doi: 10.1084/jem.20061884
67. Ng LG, Hsu A, Mandell MA, Roediger B, Hoeller C, Mrass P, et al. Migratory dermal dendritic cells act as rapid sensors of protozoan parasites. *PLoS Pathog.* (2008) 4:e1000222. doi: 10.1371/journal.ppat.1000222
68. Bousso P, Robey E. Dynamics of CD8+ T cell priming by dendritic cells in intact lymph nodes. *Nat Immunol.* (2003) 4:579–85. doi: 10.1038/ni928
69. Tracey KJ. Reflex control of immunity. *Nat Rev Immunol.* (2009) 9:418–28. doi: 10.1038/nri2566
70. Ordovas-Montanes J, Rakoff-Nahoum S, Huang S, Riol-Blanco L, Barreiro O, von Andrian UH. The regulation of immunological processes by peripheral neurons in homeostasis and disease. *Trends Immunol.* (2015) 36:578–604. doi: 10.1016/j.it.2015.08.007
71. Tracey KJ. The inflammatory reflex. *Nature.* (2002) 420:853–9. doi: 10.1038/nature01321
72. Scholz J, Woolf CJ. The neuropathic pain triad: neurons, immune cells and glia. *Nat Neurosci.* (2007) 10:1361–8. doi: 10.1038/nn1992
73. Chiu IM, von Hehn CA, Woolf CJ. Neurogenic inflammation and the peripheral nervous system in host defense and immunopathology. *Nat Neurosci.* (2012) 15:1063–7. doi: 10.1038/nn.3144
74. Riol-Blanco L, Ordovas-Montanes J, Perro M, Naval E, Thiriot A, Alvarez D, et al. Nociceptive sensory neurons drive interleukin-23-mediated psoriasiform skin inflammation. *Nature.* (2014) 510:157–61. doi: 10.1038/nature13199
75. Nakai A, Hayano Y, Furuta F, Noda M, Suzuki K. Control of lymphocyte egress from lymph nodes through beta2-adrenergic receptors. *J Exp Med.* (2014) 211:2583–98. doi: 10.1084/jem.20141132
76. Straub RH, Mayer M, Kreutz M, Leeb S, Scholmerich J, Falk W. Neurotransmitters of the sympathetic nerve terminal are powerful chemoattractants for monocytes. *J Leukoc Biol.* (2000) 67:553–8. doi: 10.1002/jlb.67.4.553
77. Alvarez D, Vollmann EH, von Andrian UH. Mechanisms and consequences of dendritic cell migration. *Immunity.* (2008) 29:325–42. doi: 10.1016/j.immuni.2008.08.006
78. Veres TZ, Rochlitzer S, Shevchenko M, Fuchs B, Prenzler F, Nassenstein C, et al. Spatial interactions between dendritic cells and sensory nerves in allergic airway inflammation. *Am J Respir Cell Mol Biol.* (2007) 37:553–61. doi: 10.1165/rcmb.2007-0087OC

Conflict of Interest: The authors declare that the research was conducted in the absence of any commercial or financial relationships that could be construed as a potential conflict of interest.

Advantages of publishing in Frontiers

OPEN ACCESS
Articles are free to read for greatest visibility and readership

FAST PUBLICATION
Around 90 days from submission to decision

HIGH QUALITY PEER-REVIEW
Rigorous, collaborative, and constructive peer-review

TRANSPARENT PEER-REVIEW
Editors and reviewers acknowledged by name on published articles

Frontiers
Avenue du Tribunal-Fédéral 34
1005 Lausanne | Switzerland

Visit us: www.frontiersin.org
Contact us: info@frontiersin.org | +41 21 510 17 00

REPRODUCIBILITY OF RESEARCH
Support open data and methods to enhance research reproducibility

DIGITAL PUBLISHING
Articles designed for optimal readership across devices

FOLLOW US
@frontiersin

IMPACT METRICS
Advanced article metrics track visibility across digital media

EXTENSIVE PROMOTION
Marketing and promotion of impactful research

LOOP RESEARCH NETWORK
Our network increases your article's readership